Ultracold Dipolar Erbium Atoms: From Scattering Phenomena to Quantum Simulations

DISSERTATION

by

Baier Simon, MSc.

submitted to the Faculty of Mathematics, Computer Science,
and Physics of the University of Innsbruck

in partial fulfillment of the requirements
for the degree of Doctor of Philosophy (PhD)

advisors:
Univ.-Prof. Dr. Francesca Ferlaino,
Institute for Experimental Physics, University of Innsbruck
Institute for Quantum Optics and Quantum Information of the
Austrian Academy of Sciences

Univ.-Prof. Dr. Gerhard Kirchmair,
Institute for Experimental Physics, University of Innsbruck
Institute for Quantum Optics and Quantum Information of the
Austrian Academy of Sciences

Innsbruck, May 2018

Abstract

Remarkable progress in the field of experimental quantum physics has enabled the preparation of quantum systems across various experimental platforms. The ability to precisely control and manipulate quantum states by experimental means, allows to study fundamental laws of quantum mechanics and their impact at the many-body level.

Ultracold atomic gases are a powerful and flexible platform, providing precise control of key parameters, such as temperature, density, internal and external degrees of freedom, dimensionality, or the trapping geometry. With the access of controllable interparticle interaction, a plethora of fascinating quantum phenomena has been observed. While the field was pioneered along studies with short-range contact interaction, nowadays dipolar interactions, featuring a long-range and anisotropic character, are attracting a large attention within the community.

This thesis reports on the investigation of quantum phenomena emerging from dipolar interactions. As a workhorse for our studies, we use ultracold gases of strongly magnetic erbium atoms. Erbium has first been Bose-Einstein condensed in 2012 in our laboratory. Shortly after, we created the first degenerate Fermi gas of erbium. This thesis focuses on the use of both systems as a resource to investigate dipolar quantum phenomena from the few- to the many-body level.

With dipolar fermions, we unveil the universal character of ultracold dipolar scattering, enabling a unique path towards quantum degenerate identical fermions. We further observe a peculiar dependence of the total elastic scattering cross section on the dipole orientation. The few-body collisional physics also impacts the behavior of the system at the many-body level. Reporting on the first observation of a many-body effect in a dipolar Fermi gas, we demonstrate the deformation of the Fermi surface. With bosonic particles, we investigate the origin of a strong level repulsion in Feshbach spectra of magnetic lanthanides and trace it back to the anisotropic van der Waals interaction among the atoms. Utilizing Feshbach resonances, we report on the first production of dipolar Feshbach molecules and reveal a universal behavior of the stabilization of inelastic losses in reduced dimensions by dipolar interactions.

As a major step towards strongly correlated dipolar systems, we investigate the system's behavior in a three-dimensional optical lattice. In particular, we report on the realization of extended Hubbard models with dipolar bosonic and fermionic atoms. In bosonic systems, we directly observe nearest-neighbor interactions activated by the long-range dipolar interaction. We demonstrate the strengthening or weakening of the Mott insulator quantum many-body phase via solely changing the dipole orientation. For the fermionic counterpart, we add the spin-degree of freedom, giving rise to a large spin-$^{19}/_{2}$ system. A lattice protection technique allows to investigate in detail the elastic collisional properties of a two-state mixture. With our method, we realize for the first time a strongly interacting dipolar Fermi gas.

The successful preparation of extended spinor Fermi Hubbard systems brings exciting prospects for future investigations at the interface with solid state physics. Offsite terms emerging from dipolar interactions give rise to clustered states, exotic lattice spin models, resonant demagnetization dynamics, or exotic quantum phases.

Contents

Chapter 1

Introduction

1.1. Motivation

The advent of quantum theory at the beginning of the twentieth century has set the foundation for our current understanding of the microscopic world. Remarkably, already in the early days the theory succeeded in capturing experimental observations such as black-body radiation [Pla06], or the photoelectric effect [Ein05]. However, the description of strongly correlated quantum systems remains fairly difficult, already when they consist only of a relatively small number of particles. Fascinating quantum phenomena emerging in such systems include low-temperature transport, quantum magnetism or most prominently high temperature superconductivity. While these phenomena have been studied extensively within condensed matter physics, a comprehensive description is still lacking.

A promising approach to understand such phenomena can be undertaken via an experimental *bottom-up* method. By forming a model system, where quantum particles are added one-by-one, a *quantum simulator* can be realized, allowing to reveal the properties of a complex quantum system via the well-understood and well controlled model system. This approach, as proposed by Richard Feynman [Fey82], requires the experimental control of single quantum states, a scenario that was formerly thought to be inaccessible.

However, technological developments have made remarkable progress and nowadays coherent control of single quantum states has been realized across many experimental platforms. Indeed, experiments allow for the control and manipulation of single quantum particles such as photons, ions in ion traps, atoms in dipole traps, electrons and nuclei in solid-state systems such as quantum dots or vacancy centers, but also microwave photons in superconducting circuits, see Refs. [Lad10, Tra12] for an overview.

Each experimental platform has different advantages and disadvantages and active research is carried out along distinct lines. A striking advantage of trapped atomic systems, the experimental platform of choice within this thesis, is given by the fact that the used particles are intrinsically identical. This enables the preparation of large uniform quantum systems without suffering from imperfections as often encountered in solid-state systems. An additional advantage arises from the accessibility of both fundamental classes of quantum particles, namely

bosons and fermions. For reaching the quantum regime with this platform ultralow temperatures are required. In particular, the thermal de-Broglie wavelength of the atoms has to exceed the interparticle distance. In 1995 a major breakthrough within the field was achieved with the first production of a Bose-Einstein condensate (BEC) [And95, Bra95, Dav95], a novel quantum state of matter predicted already 70 years before [Bos24, Ein24].

Since then, a leading research has focused on quantum effects that arise from the macroscopic coherence of the interacting many-body system, such as matter-wave interference [And97], the emergence of quantized vortices [Mat99, Mad00], or the creation of a continuous and well-collimated atomic laser [Hag99, Blo99]. With the successful realization of a degenerate Fermi gas (dFg) in 1999 [DeM99], the second fundamental class of quantum particles has become available in experiments. In combination with the observation of Feshbach resonances, which allow to change the strength and sign of the interparticle interaction, see Ref. [Chi10] for a review, the door was opened for experimental studies with tunable *contact interactions*. For a a two-component Fermi gas the tuning from repulsive to attractive interactions across the resonance has enabled studies of the well known BEC-to-BCS crossover, see Ref. [Ing07] for an overview. From peculiar interest has been the *unitary* regime, i. e. the region in the vicinity of the Feshbach resonance, which has been shown to be closely related to the physics of neutron matter in the crusts of neutron stars [Gez08]. Such relations can turn the ultracold atomic system into a model system of complex quantum matter, as discussed above.

The ability of using ultracold atomic systems as quantum simulators, has further a strong foundation in a pioneering theoretical proposal of the late 1990s. Here, the experimental creation of a three-dimensional atomic crystal has been proposed via the use of a three-dimensional optical lattice [Jak98]. Remarkably, the precise control of the optical potentials in combination with tunable atom-atom interaction allows for the preparation and detailed study of condensed matter system Hamiltonians such as the Hubbard model, rendering the ultracold atomic system into an *analog quantum simulator*. The groundbreaking experimental demonstration of the superfluid-to-Mott insulator quantum many-body phase transition [Gre02], set the start to a large number of experimental studies along this lines. Those include the realization of Fermi-Hubbard models [Jör08], the study of orbital physics [Mül07, Wir10], the implementation of superexchange couplings [Tro08], the exploration of sophisticated band structures [Tar12], or the realization of lattice spin models [Kra12]. With the experimental advance of single-site resolution for bosonic and fermionic systems [She10, Bak10, Omr15, Gre16, Che16] via *quantum gas microscopes*, ultracold atom experiments have reached a new era for quantum simulation applications, as nicely accounted for by the spectacular recent experimental preparation of an antiferromagnetic ground state with long-range order [Maz17b].

A natural requirement for the study of correlated states are interactions. Beside the availability of contact interactions, which have been the working horse for almost all the investigations discussed above, a new type of interaction has become available in recent years, namely the *dipole-dipole interaction* (DDI). With its long-range and anisotropic nature it allows to access unique phenomena and quantum phases [Bar08, Lah09, Bar12]. This type of interaction can be found in magnetic atoms, ground-state heteronuclear molecules or Rydberg atoms. An important advantage of magnetic atoms lies in the experimental "simplicity", as the dipolar interaction is intrinsically carried by the atoms, without the need of molecule creation or

Rydberg excitations.

The first magnetic atom brought to quantum degeneracy has been chromium [Gri05, Nay15]. It allowed for the observation of dipolar effects such as demagnetization cooling [Fat06], a characteristic d-wave collapse [Lah08], or spontanous demagnetization at ultralow magnetic fields driven by the DDI [Pas11b]. The realization of even stronger atomic dipoles in the ultracold regime, as dysprosium [Lu11, Lu12] by the group of Benjamin Lev, and erbium [Aik12, Aik14] by our group in Innsbruck, has set the start to the strongly magnetic era. The strong dipolar character of erbium and dysprosium has already led to a fair amount of observations of dipolar effects, among which several will be reported within the present thesis.

Importantly, the long-range nature of the DDI gives also promising prospects in the context of quantum simulations of lattice models. Strikingly, nearest-neighbor interactions emerge purely from offsite interactions and exotic quantum phases with long-range correlations become accessible, see e. g. Ref. [CS10]. Initial studies along this lines have already been performed with lattice confined samples of polar molecules [Yan13], Rydberg atoms [Sch12a, Ber17], and dipolar atoms [dP13b, Bai16], as will also be reported within this thesis. Those promising experimental investigations allow to envision a bright future for the research direction of systems with DDI.

1.2. Thesis overview

This thesis focuses on the study of dipolar quantum effects by utilizing the experimental platform of strongly magnetic ultracold erbium atoms. It reports on complementary studies of the scattering properties of dipolar particles and resonantly interacting lanthanides. A main focus lies on the experimental realization of an analog quantum simulator with dipolar particles. The main scientific achievements of this thesis can be divided into three main sections:

(I) The production of the first degenerate Fermi gas of erbium, which enables clean observations of dipolar effects on the few- and many-body level.

(II) The study of the emergence of chaotic scattering in lanthanides with anisotropic interactions and the creation of the first strongly dipolar Feshbach molecules.

(III) The realization of extended Hubbard models by means of a three-dimensional optical lattice, further allowing for the production of the first strongly interacting dipolar Fermi gas.

On a personal note, I have joined the Erbium team already in 2011 during my master studies. I have contributed to the first realization of a BEC of erbium and my master thesis project, in which I have build an optical dipole trap with dynamically tunable trapping volume, has

served to improve the atom number of our BEC by a factor of three [Bai12a]. As a PhD student, I have valuably contributed to the above mentioned scientific achievements. In the first half of my PhD work, the experiment was in the building and understanding phase. The second part of my PhD work started with the implementation of a three-dimensional optical lattice to the experiment. The ability to pin the atomic dipoles within a crystalline structure has transformed our experiment into an analog quantum simulator of extended Hubbard models. The study of strongly correlated dipolar particles in the optical lattice was the major goal of my PhD work, and thus covers a main part within this thesis.

Additional scientific achievements, to which I have actively participated but that are not the central focus of this thesis, are covered in the Appendix.

Thesis outline

This thesis is based on seven scientific publications, which are grouped in thematic chapters. The main chapters are arranged such that the basic concepts and background information are given prior to the presentation of the publications.

Chapter 2 reviews the state-of-the-art knowledge of the properties of erbium and gives details on our experimental setup. It further summarizes the production of degenerate erbium quantum gases.

Chapter 3 is dedicated to degenerate dipolar Fermi gases. It describes the physics of universal dipolar interactions, discusses the angular dependence of elastic scattering processes of atomic dipoles and investigates on a many-body effects of dipolar Fermi gases. The publication on the production of deeply degenerate Fermi gases via universal dipolar scattering and the observation of the Fermi surface deformation is also part of the PhD thesis of Albert Frisch [Fri14a].

Chapter 4 focuses on the Feshbach spectrum of magnetic lanthanides and reports on the emergence of chaotic scattering. A detailed study of close to treshold molecular bound states allows to identify the underlying molecular quantum numbers and enables the production of strongly magnetic Feshbach molecules.

Chapter 5 contains the study of strongly correlated dipolar quantum systems in three-dimensional optical lattices. The DDI gives rise to extended Hubbard models that are studied in detail. With the access of higher spin states the creation of a strongly interacting dipolar Fermi gas is demonstrated.

Finally, Chapter 6 closes the thesis and briefly discusses a possible route for the Erbium experiment in the future.

Important experimental upgrades, implemented during the course of this thesis, are described in the Appendices B and C, including the optical setup of the three-dimensional optical lattice and the setup for active magnetic field stabilization.

1.3. List of publications

The publications discussed in this thesis are given in chronological order. The thematic chapters for the publications are indicated. Additional publications are covered in Appendix A.

(I) Few- and many-body scattering of dipolar fermions (Chapter 3)

- *Reaching Fermi Degeneracy via Universal Dipolar Scattering.*
  Kiyotaka Aikawa, Albert Frisch, Michael Mark, Simon Baier, Rudolf Grimm, and Francesca Ferlaino,
  Physical Review Letters **112**, 010404 (2014).

- *Observation of Fermi surface deformation in a dipolar quantum gas.*
  Kiyotaka Aikawa, Simon Baier, Albert Frisch, Michael Mark, Cornelis Ravensbergen, and Francesca Ferlaino,
  Science **345**, 6203 (2014).

- *Anisotropic Relaxation Dynamics in a Dipolar Fermi Gas Driven Out of Equilibrium.*
  Kiyotaka Aikawa, Albert Frisch, Michael Mark, Simon Baier, Rudolf Grimm, John L. Bohn, Deborah S. Jin, George M. Bruun and Francesca Ferlaino,
  Physical Review Letters **113**, 263201 (2014).

(II) Resonantly interacting lanthanide quantum gases (Chapter 4)

- *Ultracold Dipolar Molecules Composed of Strongly Magnetic Atoms.*
  Albert Frisch, Michael Mark, Kiyotaka Aikawa, Simon Baier, Rudolf Grimm, Alexander Petrov, Svetlana Kotochigova, Goulven Quéméner, Maxcence Lepers, Olivier Dulieu, and Francesca Ferlaino,
  Physical Review Letters **115**, 203201 (2015).

- *Emergence of Chaotic Scattering in Ultracold Er and Dy.*
  Thomas Maier, Holger Kadau, M. Schmitt, Matthias Wenzel, Igor Ferrier-Barbut, Tilman Pfau, Albert Frisch, Simon Baier, Kiyotaka Aikawa, Lauriane Chomaz, Manfred J. Mark, Francesca Ferlaino, Constantinos Makrides Eite Tiesinga, Alexander Petrov, and Svetlana Kotochigova,
  Physical Review X **5**, 041029 (2015).

(III) Dipolar interactions in optical lattices (Chapter 5)

- *Extended Bose-Hubbard models with ultracold magnetic atoms.*
  Simon Baier, Manfred J. Mark, Daniel Petter, Kiyotaka Aikawa, Lauriane Chomaz, Zi Cai, Mikhail Baranov, Peter Zoller, and Francesca Ferlaino,
  Science **352**, 6282 (2016).

- *Realization of a Strongly Interacting Fermi Gas of Dipolar Atoms.*
  Simon Baier, Daniel Petter, Jan Hendrik Becher, Alexander Patscheider, Gabriele Natale, Lauriane Chomaz, Manfred J. Mark, and Francesca Ferlaino,
  submitted for publication in Physical Review Letters,
  online on arXiv [cond-mat.quant-gas] **1803.11445** (2018).

Additional publications

- *Quantum-Fluctuation-Driven Crossover from a Dilute Bose-Einstein Condensate to a Macrodroplet in a Dipolar Quantum Fluid.*
  Lauriane Chomaz, Simon Baier, Daniel Petter, Manfred J. Mark, Falk Wächtler, Luis Santos, and Francesca Ferlaino,
  Physical Review X **6**, 041039 (2016).

- *Anisotropic polarizability of erbium atoms.*
  Jan Hendrik Becher*, Simon Baier*, Kiyotaka Aikawa, Maxence Lepers, Jean-François Wyart, Olivier Dulieu, and Francesca Ferlaino
  Phys. Rev. A **97**, 012509 (2018).
  * equal contribution

- *Observation of roton mode population in a dipolar quantum gas.*
  Lauriane Chomaz, Rick M. W. van Bijnen, Daniel Petter, Giulia Faraoni, Simon Baier, Jan Hendrik Becher, Manfred J. Mark, Falk Wächtler, Luis Santos, and Francesca Ferlaino,
  Nature Physics **14**, 442 (2018).

Chapter 2

Ultracold erbium atoms

The realization of ultracold quantum gases demands a number of advanced experimental techniques. For instance, ultracold experiments require ultra-high vacuum chambers to minimize scattering with the background gas, dedicated laser sources for laser cooling and trapping of the specific atomic species, high control on magnetic fields, specially designed laser traps for the manipulation of the geometry of the confinement, and high-resolution cameras to visualize the atomic sample. To address a particular atomic species, it is from prime importance to know the atomic properties, such as the energy level spectrum or the detailed physical properties of the atomic ground state.

When in 2009 our group started to plan an ultracold experiment with erbium, very little was known about the properties of this atomic species. While proof-of-principle experiments in NIST showed that erbium atoms can be cooled via laser light [McC06], it still was not clear if the quantum degenerate regime can be reached. The successful realization of the first erbium Bose-Einstein condensate (BEC) in 2012 within our group [Aik12] gave a striking answer to this open question. This thesis connects to this *worlds first* and reports on the following scientific journey undertaken at the Erbium experiment. As to set the stage, within this chapter we will summarize the up-to-date knowledge of the main properties of atomic erbium, see Sec. 2.2, describe our experimental setup, see Sec. 2.3, and follow the route of erbium to the ultracold regime, see Sec. 2.4.

2.1. Erbium - a successful element

Erbium, a rare-earth element, is part of the lanthanide series in the periodic table and has the atomic number 68. In its pure solid form it is a soft, silvery metal and has nowadays several applications. In an alloy it can enhance the workability of metals by lowering their hardness, and as an oxide it allows to give a pink color to glass products [Gup05].

For the major technological application, erbium is used in the form of ions (Er^{3+}). They offer an optical transition around 1.55 μm, a wavelength that is most commonly used for telecommunication as it exhibits minimum loss in optical fibers. When used as a dopant in fused silica fibers, erbium ions enable amplification of this important wavelength regime via

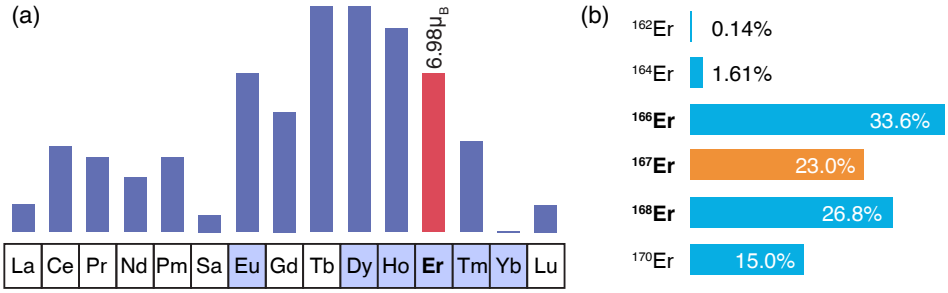

Figure 2.1.: Magnetic moments μ for atoms of the lanthanide series and isotope abundance of erbium. (a) The strength of the magnetic character is indicated by the bar length. The magnitude of erbium's magnetic moment $\mu = 6.98\,\mu_B$ is highlighted in red. Laser cooling and trapping of lanthanide atoms has been demonstrated for ytterbium [Hon99], erbium [McC06], dysprosium [Lu10], thulium [Suk10], holmium [Mia14], and most recently for metastable europium [Ino18]. (b) Erbium offers six stable isotopes - five bosonic (blue) and one fermionic (orange) isotope(s). Their natural abundances are indicated. Isotopes for which quantum degeneracy has been reached are highlighted.

optical pumping and have led to the development of erbium-doped fiber amplifiers (EDFA). The large success of EDFA is nicely accounted for by their wide use within optical communication, where the low required maintenance even allows for in-line amplification in submarine (undersea) telecom cables [Auz99]. Beside the good photoluminescence properties, a very recent experiment shows that also electroluminescence of erbium ions can be accessed via quantum dot arrays [Zha18]. This technological advance would ease optical interconnection application via chip-based near-infrared light generation and amplification.

Further, the key abilities of EDFA have reached research on quantum information and communication applications. Here, single photon protocols at telecom wavelengths are highly recommended due to the low absorption loss, which makes Er^{3+}-based devices a natural choice. Technical limitations have hindered such a fiber-based quantum device, but a recent experiment succeeded in demonstrating single-photon based light-matter interaction in cryogenically cooled erbium-doped fibers [Sag15]. The demonstration of quantum storage and recall of entangled quantum states of light gives exciting prospects for the realization of a fully fiber-based future quantum network. The strength of erbium based devices for telecom quantum applications is further highlighted by the achievement of an over a second coherence time in $^{167}Er^{3+}$ doped Yttrium Orthosilicate crystals [Ran17].

Finally, erbium features remarkable properties in its pure atomic form, as used within this thesis. Atoms of the lanthanide series host among the strongest magnetic moments found in the periodic table. Figure 2.1(a) reports their strength and visualizes that the magnetic moment[1] of erbium ranges at a front position. To reveal this strongly magnetic character it is necessary to enter into the ultracold regime. Here, the dipolar interaction between the atoms becomes strong enough to unveil exotic and unobserved quantum phases. An additional argument that marks erbium as an ideal choice for ultracold experiments is related to its five bosonic and one fermionic isotope(s) with high natural abundance, as shown in Fig. 2.1(b). This feature strongly increases the flexibility of accessible physics in experiments.

[1] The magnetic moment of an element is usually given in units of the Bohr magneton μ_B, which was introduced as a physical constant to express the magnitude of the intrinsic magnetic moment of an electron. The magnetic moment of alkali-metal atoms, which are widely used for ultracold experiments, is $1\mu_B$.

The strong dipole-dipole interaction (DDI) of erbium and the ability to address different quantum statistics by the choice of the isotope are at the heart of the results presented in this thesis.

2.2. Atomic and magnetic properties of erbium

2.2.1. Electron configuration

Erbium atoms host in total 68 electrons that fill the electronic orbitals following the Madelung rule. As the $6s$ shell becomes filled before the $4f$ orbital, this inner shell is left partially unfilled, resulting in a so called *submerged-shell* structure. The electron configuration of the ground state is written as

$$[\mathrm{Xe}]4f^{12}6s^2,$$

where [Xe] denotes the electron configuration of xenon. The two vacant electrons of the $4f$ orbital give rise to large orbital momentum and spin quantum numbers of $L = 5$ and $S = 1$. The ground state of erbium can be written in Russel-Saunders coupling scheme[2]:

$$\text{ground state: } {}^3\mathrm{H}_6,$$

with the standard notation of ${}^{2S+1}L_J$. The unusually large spin-orbit coupling in erbium gives rise to a large magnetic moment, see below. Further, the strongly anisotropic orbitals of the $4f$ shell result in a highly anisotropic van der Waals interaction potential, leading to intriguing scattering properties as discussed in Chapter 4.

2.2.2. Atomic energy spectrum

As a result of the submerged-shell electron configuration, erbium exhibits a complex energy level structure. Reference [Kra18], which is based on the dataset of [Mar78], reports 672 atomic lines with angular momentum quantum numbers $J \in [1, 12]$. The ionization limit of erbium is $49262\,\mathrm{cm}^{-1}$, which corresponds to the energy of a photon with wavelength 203 nm. More recent theoretical work predicts yet unobserved lines for the dipole allowed transitions of the ground state, see Ref. [Lep14] and Appendix A.2, which underlines the developing but still not complete knowledge on erbium spectroscopic data. In Fig. 2.2(a) we plot the atomic energy spectrum up to the strongest transition in erbium, which features an energy of $24943\,\mathrm{cm}^{-1}$ (≈ 401 nm).

For the purpose of laser cooling and trapping it is crucial to precisely know the transition probabilities of the excited levels. Extensive experimental data can be found in Refs. [Law10, Har10]. In general, a large amount of excited states is unfavorable for laser cooling applications, as the probability of pumping atoms to long-lived metastable states

[2] This coupling scheme is also known as LS-coupling and in the case of erbium is only applicable for the ground state. For excited states the electronic spin-orbit interaction becomes more prominent then the individual spin-spin and orbit-orbit interactions. Hence jj-coupling has to be used.

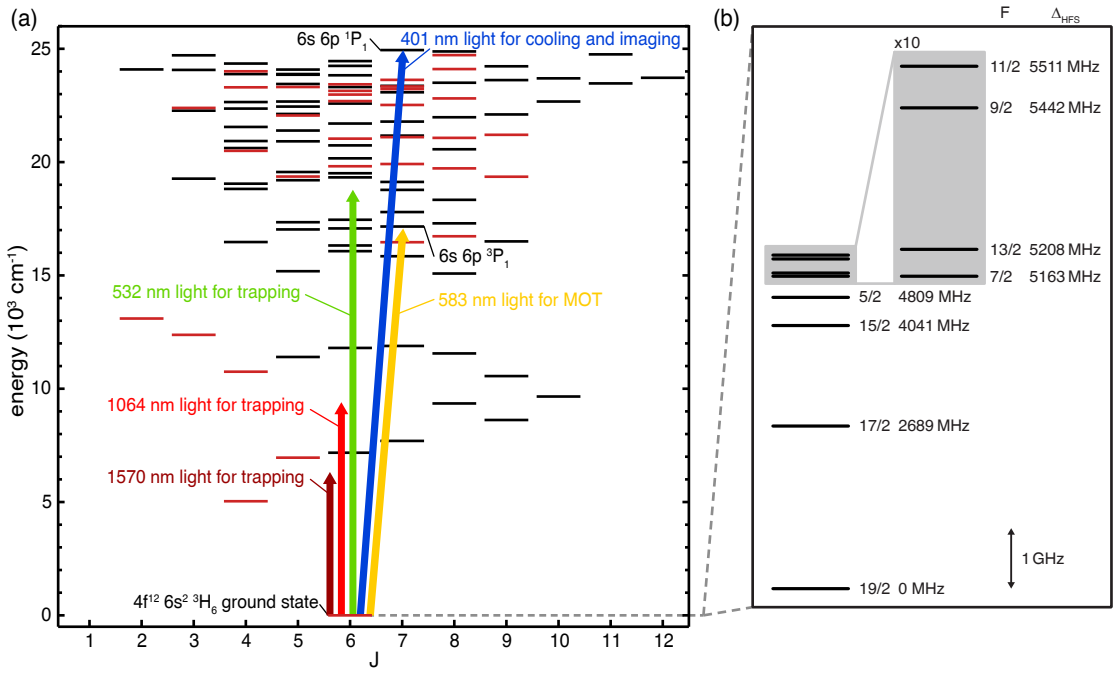

Figure 2.2.: Energy level spectrum of erbium and hyperfine structure of the ground state for the fermionic isotope. (a) Energy levels in the relevant range for laser cooling and trapping. Even and odd parity states are shown in red and black, respectively. All laser colors used in our experiment are indicated. For transversal cooling, Zeeman slowing and imaging 401 nm light (blue) is used. The atoms are captured within a narrow-line magneto-optical trap (MOT) operated at 583 nm (yellow). The optical potentials are formed by 1064 nm, 1570 nm, and 532 nm trapping light (red, dark red, and green, respectively). (b) While bosonic erbium shows no hyperfine structure, fermionic erbium features eight hyperfine manifolds with total angular momentum quantum number $F \in [19/2, 5/2]$. The frequency splitting of the individual levels at zero magnetic field is given with respect to the ground state manifold. Figure adapted from Ref. [Fri14a].

during cycling can be strongly enhanced. However, for the case of erbium, suitable electric-dipole allowed laser transitions have been identified [Ban05], which led to the demonstration of efficient laser cooling and trapping without repumping light via the (in principle) not closed 401 nm line [McC06].

Encouraged by this result, within our experiment we have proposed and realized a simple scheme for the preparation of cold atomic clouds of erbium with temperatures in the order of 10's of μK [Fri12]. Our approach for cooling and trapping is summarized in Fig. 2.2(a) and relies on two electric-dipole transitions with $J \rightarrow J+1$ where one of the $6s$ electrons is excited to a $6p$ state. Initial cooling is performed on the 401 nm singlet ^{1}P$_1$ line. The broad natural linewidth of 29.7 MHz [Bai12a] allows for strong atom-light interaction, ideal for transversal cooling, Zeeman slowing, and imaging applications. For achieving a cold temperature of the atoms when captured in a magneto optical trap, it is from importance to employ an excited state with a narrow linewidth, as the lowest reachable temperature, the Doppler temperature, is directly proportional to this linewidth. Here, we decided for the triplet ^{3}P$_1$ state, an intercombination line that features a linewidth of 190 kHz, which corresponds to a Doppler temperature as low as 4.6 μK.

For the production of ultracold atomic gases with temperatures well below the Doppler temperature an additional approach is needed. The most common method in ultracold experiments relies on optical trapping with off-resonant laser light and subsequent evaporative cooling [Gri00]. The depth of the optical potential for a given trapping wavelength is given by the AC-stark shift on the ground state. This shift depends on the dynamical polarizability, which accounts for the (off-resonant) contributions of all excited states via a sum-over-state formula [Lep14]. In Fig. 2.2(a) all laser wavelengths used for optical trapping at our experiment are indicated. We have experimentally investigated the dynamical polarizability for 1064 nm trapping light in Ref. [Bai12a] and over the years improved our understanding along 532 nm, 1064 nm, and 1570 nm light, as reported in Appendix A.2.

An additional important aspect of the energy spectrum is the energy distribution of the atomic ground state. In the case that the nucleus features a nuclear spin, $I \neq 0$, the ground state will be split by the interaction between the nuclear spin and the electron total angular momentum, resulting in a hyperfine structure. While the bosonic erbium isotopes lack hyperfine splitting, the fermionic isotope ^{167}Er features a nucler spin quantum number of $I = 7/2$, giving rise to a total of eight hyperfine states $F \in [J + I, J - I]$. The states and their corresponding energies are shown in Fig. 2.2(b). A detailed investigation of the hyperfine structure, including also the structures of the $6s6p\,^1\mathrm{P}_1$ and $6s6p\,^3\mathrm{P}_1$ excited states, is given in Ref. [Fri13]. All experiments within this thesis are performed in the $F = 19/2$ hyperfine ground state manifold.

2.2.3. Magnetic properties

One of the landmark properties of several lanthanide elements is their exceptional large magnetic moment, see Fig. 2.1(a). These high values are a direct consequence of the submerged shell structure, as the electron spin-orbit coupling leads to large total angular momentum quantum numbers J. In particular, this results also in large magnetic quantum numbers m_J, which are defined by the projection ot the total angular momentum quantum number $\mathbf{J}$ on the quantization axis, given by an external magnetic field. The m_J values range from $-J$ to $+J$, see Sec. 2.2.4, and are strongly related to the magnetic moment of an atom[3], as it is defined by

$$\mu = m_J g_J \mu_\mathrm{B}. \tag{2.1}$$

To determine the magnetic moment, in addition the Landé g-factor g_J has to be known. In the case of pure spin-orbit coupling it can be calculated via

$$g_J = 1 + (g_S - 1)\frac{J(J+1) - L(L+1) + S(S+1)}{2J(J+1)} \quad \text{with} \quad g_S \approx 2.00232. \tag{2.2}$$

For the case of erbium additional correction have to be included, resulting in a slightly reduced value. The experimentally reported value is $g_J = 1.163801(1)$ [Con63] leading for

[3] We note that the scenario of magnetic dipoles is qualitatively different compared to the scenario of polar molecules. The strength of the electric dipole moment of polar molecules scales with the applied electric field magnitude, while the dipole moment of magnetic atoms is truly permant and persists also at zero magnetic field.

the bosonic isotopes to a magnetic moment of the lowest magnetic state $m_J = -6$ of

$$\mu = -6.982806(6)\mu_\mathrm{B}. \tag{2.3}$$

For the fermionic isotope, the additional hyperfine structure requires to calculate the Landé g-factor g_F via

$$g_F = g_J \frac{F(F+1) - I(I+1) + J(J+1)}{2F(F+1)}, \tag{2.4}$$

resulting in $g_F = 0.735032$. The magnetic moment of the energetically lowest state with $F = 19/2$ and $m_F = -19/2$ is found to be

$$\mu = m_F g_F \mu_\mathrm{B} = -6.982804\mu_\mathrm{B}, \tag{2.5}$$

equaling the bosonic one. When different spin states are prepared the magnetic moment changes accordingly.

2.2.4. Zeeman splitting

When a magnetic field B is applied, the Zeeman manifolds split into $2J+1$ ($2F+1$) Zeeman substates with magnetic quantum numbers m_J (m_F) for bosonic (the fermionic) isotope(s). For the bosonic isotopes the energy of the substates scales linearly with the magnetic field strength, while for the fermionic isotope, as a result of the hyperfine coupling, an additional quadratic field dependence is encountered.

For bosonic erbium the energy of the ground state substates reads as

$$E_\mathrm{Z}^\mathrm{Bo}(B) = m_J g_J \mu_\mathrm{B} B = m_J q(B), \tag{2.6}$$

with $q(B)$ denoting the linear magnetic field dependence. This linear dependence holds for all experimental accessible magnetic field values, as a result of the large spin-orbit coupling constant of erbium [Jud61]. In Fig. 2.3(a) the magnetic field dependence of the 13 m_J states is plotted.

The energy splitting between two adjacent spin states is degenerate across the spin ensemble and reads as

$$\Delta E_\mathrm{Z}^\mathrm{Bo}(B) = \underbrace{(m_J - m_{J+1})}_{1} q(B) = hzB, \quad \text{with} \quad z = 1.628879\,\mathrm{MHz/G} \tag{2.7}$$

being the linear bosonic Zeeman coefficient and h the Plank constant. The knowledge on the energy splitting is from particular relevance as it allows to prepare different spin states via e. g. radiofrequency coupling. In experiments, it is also used to calibrate the magnetic field by driving the $m_J = -6$ to $m_J = -5$ transition and monitoring subsequent atomic loss caused by dipolar relaxation.

For fermionic erbium, due to the Paschen-Back effect, which results in a decoupling of J and I, the energy splitting starts to deviate from a pure linear magnetic field dependence

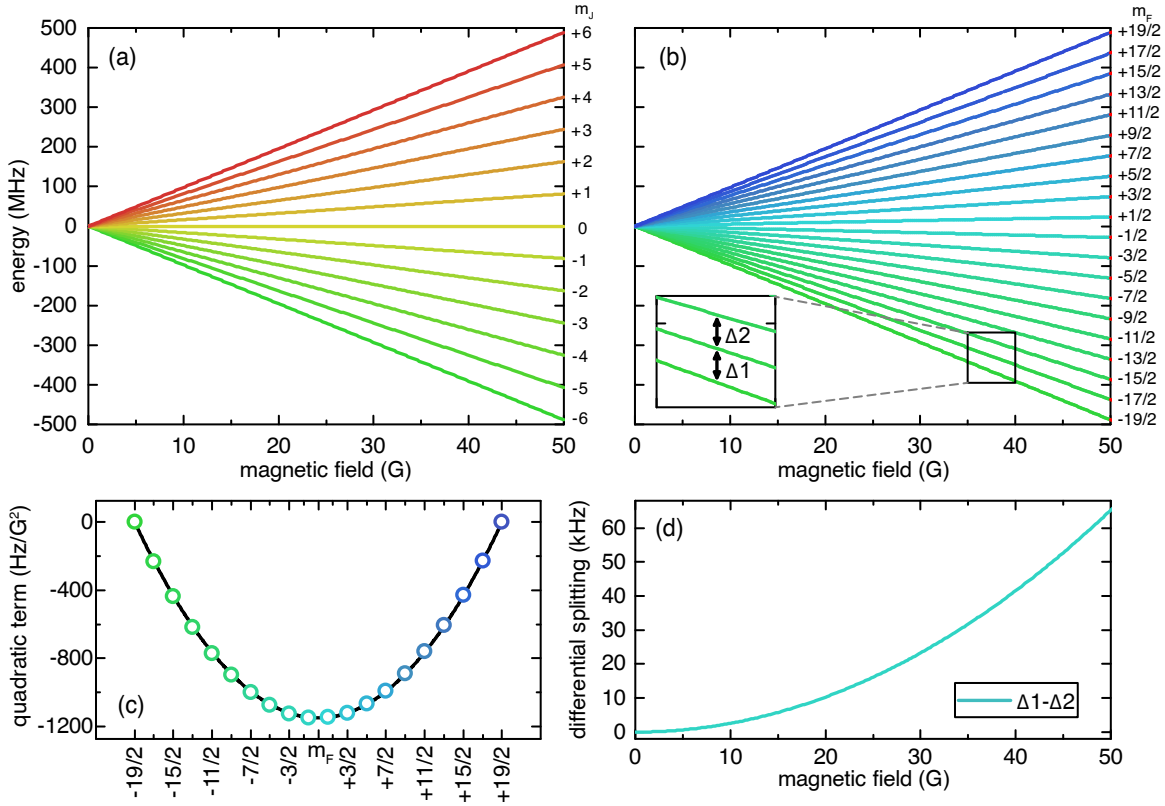

Figure 2.3.: Zeeman energy for bosonic and fermionic erbium in the ground state manifold for magnetic field values up to 50 G. (a) Bosonic erbium shows a linear dependence of the different m_J states on the magnetic field. (b) For the fermionic isotope ($F = 19/2$ manifold) in addition to the linear dependence a quadratic energy shift emerges due to the hyperfine coupling. (c) Extracted quadratic term, see text, from a fit to the data of (b). With a parabolic fit (solid black line) z_{qu} is determined. (d) Difference in the energy splittings between neighboring spin states, see inset of (b).

already at moderate B field values. An additional quadratic field dependence ($E_{\mathrm{Z}}^{\mathrm{Fe}} \propto B^2$) becomes apparent when calculating the hyperfine magnetic levels via exact diagonalization of the atomic Hamiltonian [Smi65]. Figure 2.3(b) shows the 20 Zeeman substates for the ground state manifold of the fermionic isotope. The resulting energy dependence of the m_F substates can be written in good approximation as

$$E_{\mathrm{Z}}^{\mathrm{Fe}}(B) = m_F q_{\mathrm{li}}(B) + (F^2 - m_F^2) q_{\mathrm{qu}}(B^2) = h \underbrace{m_F z_{\mathrm{li}}}_{\text{linear term}} B + h \underbrace{(F^2 - m_F^2) z_{\mathrm{qu}}}_{\text{quadratic term}} B^2. \qquad 2.8$$

Here, $q_{\mathrm{li}}(B)$ and $q_{\mathrm{qu}}(B^2)$ account for the linear and quadratic magnetic field dependence, and z_{li} and z_{qu} are the fermionic linear and quadratic Zeeman coefficients. The m_F dependent linear and quadratic terms can be extracted from a polynomial fit of second order to the calculated Zeeman energies[4]. In Fig. 2.3(c), the quadratic fit term is plotted as a function of the m_F state. It depends on the magnetic sublevels m_F in a quadratic way and results in a down shift in energy for all levels beside the edge states. From a parabolic fit, the quadratic

[4] The fit is restricted up to 50 G and gives residua below 1 kHz. For larger magnetic field ranges a more specialized fitting function should be used.

Zeeman coefficient is determined to be

$$z_{\mathrm{qu}} = -12.76(1)\,\mathrm{Hz/G}^2.$$

A similar treatment gives for the linear Zeeman coefficient $z_{\mathrm{li}} = 1.02874\,\mathrm{MHz/G}$[5].

The major advance of the quadratic term arises for protocols of state selective addressing. Here, it is necessary that the splitting between adjacent spin states in not degenerate, as to allow the coupling of two spin states without a coupling to all other spin states. Following Eq. 2.8, the energy splitting between adjacent spin states reads as

$$\begin{aligned} \Delta E_{\mathrm{Z}}^{\mathrm{Fe}}(B) &= (m_F - m_{F+1})q_{\mathrm{li}}(B) + (-m_F^2 + m_{F+1}^2)q_{\mathrm{qu}}(B^2) \\ &= hz_{\mathrm{li}}B + (2m_F + 1)hz_{\mathrm{qu}}B^2 \end{aligned} \tag{2.9}$$

The lift of the degenerate splitting between adjacent spin states becomes evident when the differential splitting between three neighboring spin states (e. g. $\Delta E_{\mathrm{Z}}^{\mathrm{Fe}}$ between $m_F = -19/2$ and $m_F' = 17/2$ minus $\Delta E_{\mathrm{Z}}^{\mathrm{Fe}}$ between $m_F = 17/2$ and $m_F' = 15/2$, see inset Fig. 2.3(b)) is calculated, as plotted in Fig. 2.3(d). While the linear Zeeman contributions cancel, the quadratic coefficient z_{qu} determines the differential splitting. Within our approximation the differential splitting between three adjacent spin states is found to be

$$\Delta(\Delta E_{\mathrm{Z}}^{\mathrm{Fe}})(B) = -2q_{\mathrm{qu}}(B^2) = -2hz_{\mathrm{qu}}B^2. \tag{2.10}$$

At a magnetic field value of 40 G this gives a differential splitting of 40.83 kHz, which matches the actual value of 41.56 kHz within 2 %. The knowledge on the lift of the degenerate coupling between adjacent spin states allows for a deterministic state preparation of the two lowest spin states in fermionic erbium and enabled us to perform a clean study of the interspin interaction properties, see Sec. 5.6.

2.3. Experimental setup

The building of the erbium apparatus has started in 2010, and led to the successful preparation of the first BEC of erbium already in early 2012. At the heart of the setup are a high-temperature oven, a transversal cooling (TC) section, a Zeeman slower (ZS) setup, and the main chamber for trapping the atoms in a narrow-line magneto-optical trap (MOT), evaporative cooling of the atoms in optical dipole traps, and absorption imaging of the atomic samples.

Within this section, we will summarize the most important experimental parts and report on the performance of the apparatus. For a more detailed description of the experimental setup, including technical details on the vacuum chamber, the blue and yellow laser light setups, and the coil setup of the main chamber, the reader is referred to Ref. [Fri14a]. Updates on the experimental setup, which are from particular importance for this thesis are reported in the Appendices B and C.

[5] This value matches nicely the expectation for a pure linear dependence with $\Delta E_{\mathrm{Z,li}}^{\mathrm{Fe}}(B) = Bg_F\mu_{\mathrm{B}} = B \times h \times 1.0288\,\mathrm{MHz/G}$.

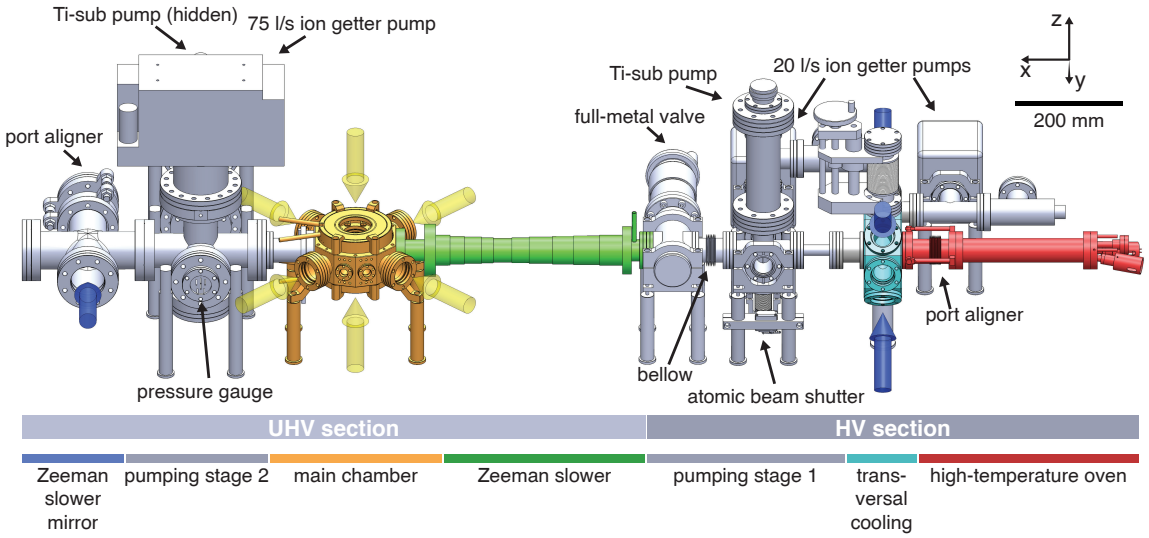

Figure 2.4.: Drawing of the experimental chamber for the erbium experiment. Erbium pieces are heated in the effusion cell section (red) producing an atomic flux traveling from right to left. After a transversal cooling section (light blue), where the transversal velocity spread is reduced by near-resonant 401 nm laser light, the atoms enter the Zeeman slower section (green). The atoms are slowed down by resonant 401 nm light, which enters via the Zeeman slower mirror section (blue). The Zeeman slower also serves as a differential pumping section, which allows pressure differences between the HV and the UHV sections of up to three orders of magnitude. Finally, the atoms are trapped at the main chamber (yellow) with 583 nm yellow laser light within a MOT. Ion getter pumps and Titanium sublimation pumps (gray) maintain the low pressure in the HV and UHV sections. Figure adapted from Ref. [Fri14a].

2.3.1. Vacuum chamber

The erbium apparatus can be divided into two main sections. The high-vacuum (HV) section includes the high-temperature oven and the TC chamber and enables a pressure of about 4×10^{-9} mbar. The ultra-high vacuum (UHV) section is connected via a differential pumping section and includes the ZS and the main experimental chamber. In this section pressures down to 1×10^{-11} mbar are reached, which renders collisions of the trapped atoms with background gas negligible. Figure 2.4 shows a drawing of the whole erbium apparatus, including also to pumping stages for the HV and UHV sections.

The high-temperature oven[6] consists out of two parts, the effusion cell and the hot lip, which are made out of tantalum and are separated by an aperture. Their temperatures are controlled independently to 1100 °C and 1200 °C, respectively. With this temperatures we reach an atomic flux right after the oven of $10^{14} s^{-1} sr^{-1}$, which is sufficient for experimental operations [Sch11]. For a filling of about 10 mG of solid erbium, the oven can be operated for several years without refilling.

[6] model DFC-40-10-WK-2B, from from CreaTec Fischer & Co. GmbH

2.3.2. Laser cooling and trapping of erbium

Right after the effusion cell the atomic beam enters the TC section. While apertures at the oven are implemented to collimate the beam, the remaining transversal velocity spread does not allow all atoms to reach the main chamber through the differential pumping section. As to reduce this spread, a slightly blue-detuned two-dimensional optical molasses in two directions is implemented. This leads to a further collimation of the atomic beam and enhances the amount of atoms captured in the MOT by almost an order of magnitude, see Appendix B.

Subsequentially, the atoms travel through the ZS section. A counter-propagating laser beam reduces the longitudinal velocity via momentum transfer by scattering, which effectively slows down the atoms. The ZS is designed such that the constantly slowing atoms are kept at the atomic resonance, by compensating the varying Doppler shift via the Zeeman shift induced by an external magnetic field. The initial longitudinal velocity of around 450 m/s is reduced to about 5 m/s, which enables to directly capture the atoms in the MOT.

Finally, the atoms enter the main chamber, where they are trapped within a MOT operated at the narrow 583 nm transition. As discussed in Sec. 2.2.2, the narrow linewidth of 190 kHz features a low Doppler temperature and allows for MOT temperatures around 10 μK. To avoid residual light scattering of the ZS beam on the MOT, we use large light detunings of up to 50 linewidths, which leads to an accumulation of the atoms below the ZS beam. With our setup, we can realize MOTs of the five most abundant isotopes of erbium [Fri12]. For an optimized experimental setup, we can achieve MOTs of up to 2×10^8 atoms at a temperature of around 10 μK for the most abundant ^{166}Er isotope. This numbers are fairly sufficient for our experiment and do not limit us. Rather, the maximum atom numbers for further cooling are restricted by the amount of atoms that can be loaded to the optical dipole trap, see Sec. 2.4.1. Hence, we typically work with MOT numbers of 3×10^7 atoms, which are reached for 3 s of MOT loading.

A major advantage of our narrow line MOT is that the atoms are naturally spin-polarized to the lowest Zeeman substate. This is a result of the large detuning of the MOT, which leads to a so called "gravitational sag". As a consequence, atoms preferentially scatter light from the lower σ^--polarized MOT beam, which optically pumps the atoms to the lowest spin state. Indeed, the influence of the top σ^+-polarized MOT beam is negligible, which allowed us to remove it completely without influencing the MOT performance. A more detailed study on such a five-beam MOT configuration has been performed recently [Ilz18]. The increased optical access is particular valuable for our experiment, as it allows for the implementation of additional optical setups.

2.4. Degenerate gases of Erbium

The demonstration of a cold MOT of erbium is the ideal starting point for loading the atoms into an optical dipole trap, and to further cool them by means of forced evaporation. Utilizing this technique, we managed to achieve a BEC of ^{168}Er - a worlds first - in early 2012 [Aik12]. This achievement was the turning point of our experiment and marked the start for many exciting studies within the ultracold regime.

Together with the first BEC of dysprosium atoms in 2011 by the group of Benjamin Lev at Stanford [Lu11], it also led to the beginning of a new era in ultracold experiments - the era of strongly magnetic dipoles. While pioneering work already has been performed with dipolar chromium atoms [Gri05, Lah08, Pas11a], strongly magnetic lanthanides allow to access physical phenomena that are even more governed by the long-range and anisotropic interaction, leading to unexpected quantum phases. The large impact on the community of ultracold gases, is nicely accounted for by the recent building of several more strongly magnetic lanthanide experiments. The groups of Tilman Pfau in Stuttgart as well the group of Giovanni Modugno in Florence with dysprosium [Kad16, Luc18], and the group of Martin Weitz in Bonn with erbium [Uli17] already succeeded in reaching the quantum degenerate regime. Other groups are chasing behind these groups, as the group of Mark Saffman in Wisconsin with holmium [Mia14], the group of Sylvain Nascimbene in Paris with dysprosium [Dre17], our group in Innsbruck with a mixture of erbium and dysprosium [Ilz18], the group of Rudolf Grimm in Innsbruck with a mixture of potassium and dysprosium [Rav18], the group of Mikio Kozuma in Tokyo with europium [Ino18], the group of Patrick Windpassinger in Mainz with dysprosium[7], the group of Markus Greiner at Harvard in Boston with erbium[8], as well as the groups of Zoran Hadzibabic in Cambridge with erbium and Wolfgang Ketterle at MIT in Boston with dysprosium[9].

2.4.1. Optical trapping

Optical dipole traps are based on off-resonant laser light that induces an energy shift on the atomic state. This shift is known as the AC stark shift [Gri00] and is related to the dynamical polarizability. Appendix A.2 summarizes our up-to-date knowledge on the dynamical polarizability of erbium for the three relevant wavelengths used in our experiment.

Directly after the MOT stage, we transfer the atoms to an optical dipole trap, operated at 1064 nm. Good transfer efficiencies of up to 30% are achieved by means of a scanning system that allows to increase the trapping volume of the beam via a technique based on time-averaged potentials [Bai12a]. The maximum transferable atom number is limited by the total power of the dipole trap beam and reaches values of up to 1×10^7 atoms with a temperature of about 20 μK.

[7] Windpassinger dysprosium lab
[8] Greiner erbium lab
[9] private communication

We have further demonstrated optical trapping with 1570 nm and 532 nm light. The use of 1570 nm trapping light turned out to be necessary for the production of degenerate Fermi gases of the ^{167}Er isotope, see Sec. 3.3, as with 1064 nm light significant heating of thermal gases was encountered. Laser light at 532 nm has proven to be particular valuable for the production of optical lattices, as the short wavelength results in a small distance between neighboring atoms in the lattice and enhances the effects from dipolar interactions, see Chapter 5. The optical setups for all optical trapping beams are reported in Ref. [Fri14a] and Appendix B.

2.4.2. Evaporative cooling

To reach the quantum degenerate regime, the technique of forced evaporation is applied. By adiabatically lowering the optical potential depth, the thermal Maxwell-Boltzmann distribution becomes truncated. As only the hottest atoms are removed from the trap, after rethermalization due to elastic collisions, a lower temperature and most importantly a higher phase-space density (PSD) is reached. The PSD of an atomic gas can be expressed as

$$\mathrm{PSD} = N\bar{\omega}^3 \left(\frac{\hbar}{k_\mathrm{B}T}\right)^3, \tag{2.11}$$

with N being the atom number, $\bar{\omega}$ the mean trap frequency, and $k_\mathrm{B}T$ the thermal energy. The transition to a Bose-Einstein condensate, a state where a macroscopically large number of bosons occupies the ground state, is related to a PSD of 2.6.

Efficient evaporative cooling relies on a favorable ratio between elastic and inelastic collisions, as the speed of rethermalization needs to exceed inelastic-loss timescales. For the case of ^{168}Er, ideal conditions are found at a magnetic field value of 0.4 G. At this field we find a s-wave scattering length a_s of $137(1)a_0$, see Sec. 4.1.1 for a definition of a_s, with a_0 being the Bohr radius. At this parameters we achieve an almost pure BEC of up to 2×10^5 atoms within 7 s of forced evaporation [Bai12a]. In Fig. 2.5 the emergence of a BEC is visualized.

In 2015 we also succeeded in Bose-Einstein condensing ^{166}Er, the most abundant erbium isotope. The experimental procedure is very similar to the one for the ^{168}Er isotope. Here, we find best evaporation efficiencies at a magnetic field value of 2.1 G, relating to a s-wave scattering length a_s of $83(2)a_0$, see Appendix A.1. We typically create BECs of 1.1×10^5 atoms with a BEC fraction of $\approx 70\,\%$. This isotope features a conveniently broad Feshbach resonance centered at low magnetic field values of about 50 mG, allowing us to tune the scattering length with a high accuracy *and* precision for arbitrary magnetic field orientations. The high level of control enabled us to investigate in detail the formation of a macro-droplet state, see Appendix A.1, and the birth of Roton quasiparticles, see Appendix A.3.

The formation of a degenerate Fermi gas of ^{167}Er is investigated in detail in Sec. 3.3. Usually, identical fermions do not collide at ultralow temperatures. Hence, spin- or species-mixtures have to be employed to enable an elastic cross section large enough for efficient cooling [DeM99, Tru01, Sch01, Had02, Roa02]. In contrast, our experimental procedure for evaporation is solely based on universal dipolar scattering between single-spin fermions. The

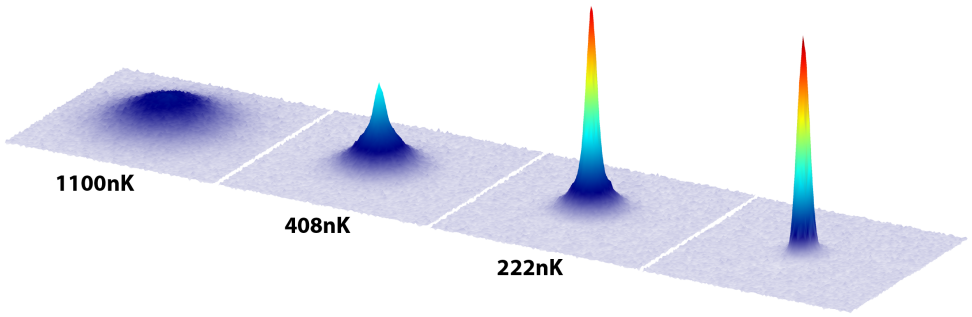

Figure 2.5.: Final evaporation steps to form an almost pure BEC of erbium - a worlds first - realized with ^{168}Er. When the atoms are cooled down below a critical temperature, a sharp peak in the momentum distribution of the atomic cloud (in false color) arises. This resembles the major fingerprint of a quantum degenerate bosonic gas. Temperatures of the thermal distributions are indicated.

large and anisotropic elastic cross section has given new prospects for the study of scattering physics of identical fermions, see Chap. 3.

Chapter 3

Few- and many-body scattering of dipolar atoms

The dipole-dipole interaction (DDI) among particles gives rise to a universal scattering behavior in the ultracold regime [Boh09a]. To access elastic dipolar scattering in a clean manner, it is required to switch off all other types of interactions. With bosonic particles, such a case can be realized when the isotropic contact interaction is lowered to zero by means of Feshbach tuning, see Chap. 4. However, in such a regime the dipolar interactions start to dominate and can lead to a collapse of the atomic sample via the attractive part of the DDI [Lah08]. Nevertheless, for (small) contact interaction, particularly fascinating many-body physics can occur, arising from the competition between the isotropic contact interaction and the anisotropic DDI. Beautiful examples are given by the observation of self-confining quantum droplets, see [Kad16, FB16] and Appendix A.1, or the emergence of roton quasi-particles, see Appendix A.3. Importantly, these works represent scenarios in which, to explain the experimental results by theory, all the different scattering effects, including dipolar interactions, have to be taken into account very carefully. While this is certainly possible, it is not a straightforward method to access dipolar scattering.

A more elegant approach to experimentally treat elastic dipolar scattering does involve spin-polarized fermionic particles. In the fermionic case, contact interactions, due to the Wigner treshold law governed by s-wave scattering, are absent at ultralow temperatures. In contrast, the scattering cross section, resulting from dipolar interactions, does not vanish, but converges to a universal value in the ultracold regime, isolating dipolar effects. In addition, fermionic systems deliver the advantage of being stable against a collapse, even for dominating attractive dipolar interactions. This is a result of quantum statistics where, for low enough temperatures, the fermionic atoms occupy all lowest harmonic oscillator states (up to the Fermi energy) and a further compression (implosion) of the cloud is prohibited by Fermi pressure. These two facts allow for a clean study of dipolar scattering properties with fermionic systems.

Within this chapter we will focus on the description of spin-polarized dipolar fermionic atoms as a platform to investigate the effects of dipolar scattering. Section 3.1 reviews anisotropic dipolar few-body scattering, and Sec. 3.2 focuses on the experimental observation of dipolar many-body effects. The two Secs. 3.3 and 3.4 contain our publication on dipolar few-body effects with fermionic erbium. Finally, Sec. 3.5 presents our publication on the observation of the Fermi surface deformation.

3.1. Dipolar few-body scattering

3.1.1. Dipole-dipole interaction

The DDI has a long-range and anisotropic character. For the case of magnetic atoms, such as erbium, the interaction of two dipoles $\boldsymbol{\mu}_1$ and $\boldsymbol{\mu}_2$ with permanent magnetic moments μ_1 and μ_2, see Sec. 2.2.3, can be written in the general form as

$$U_{\mathrm{dd}}(\mathbf{r}) = \frac{\mu_0}{4\pi r^3}\left[(\boldsymbol{\mu}_1\boldsymbol{\mu}_2) - \frac{3}{r^2}(\boldsymbol{\mu}_1\boldsymbol{r})(\boldsymbol{\mu}_2\boldsymbol{r})\right] \tag{3.1}$$

and depends on the interparticle distance $\boldsymbol{r} = \boldsymbol{r}_1 - \boldsymbol{r}_2$. Here, $r = |\boldsymbol{r}|$ and μ_0 is the magnetic constant. For the case of particles with an electric dipole moment the DDI is calculated by substituting $\boldsymbol{\mu}_i \rightarrow \boldsymbol{d}_i$ and $\mu_0 \rightarrow 1/\epsilon_0$. For electric dipoles the dipolar strength is set by the strength of an external polarizing electric field. In stark contrast, magnetic dipoles intrinsically carry a magnetic moment, where the strength does not depend on the external field $\mathbf{B}$. Nevertheless, the dipole *orientation* is given by the external magnetic field axis $\hat{B}$, even for a weak field amplitude. Hence, for experimental conditions, the magnetic dipoles become polarized and mutually align along the external field that sets the quantization axis. As a result, $\boldsymbol{\mu}_1 \parallel \boldsymbol{\mu}_2$ and Eq. 3.1 simplifies to

$$U_{\mathrm{dd}}(r,\theta) = \frac{\mu_0\mu_1\mu_2}{4\pi}\frac{1-3\cos^2\theta}{r^3} \tag{3.2}$$

with θ denoting the angle between the quantization axis and the interatomic axis of the two dipoles, see Fig. 3.1. Remarkably, the sign of the interaction can be changed when θ is changed from 0° (head-to-tale configuration) to 90° (side-by-side configuration)[1]. The particles repel each other in a side-by-side configuration and experience an attractive force in the head-to-tail configuration, see Fig. 3.1(b). As a consequence of the $1 - 3\cos^2\theta$ term, the absolute strength for negative interaction is twice as large as for positive interaction at the same interparticle separation r. The range of the DDI can be accessed via the so-called *dipolar length*

$$a_{\mathrm{d}} = \frac{m\mu_0\mu_1\mu_2}{4\pi\hbar^2}, \tag{3.3}$$

which in addition to the magnetic moments depends on the mass m of the dipoles. As erbium is a heavy element ($m_{^{166}\mathrm{Er}} = 166\,u$)[2], in the lowest magnetic substate, i. e. $m_J = -6 \rightarrow \mu_1 = \mu_2 \approx -7\mu_{\mathrm{B}}$ (Eq. 2.3), a_{d} takes the value $196.2\,a_0$, which outperforms alkali atoms as rubidium ($a_{\mathrm{d},^{87}\mathrm{Rb}} = 2.1\,a_0$) and even magnetic chromium ($a_{\mathrm{d},^{52}\mathrm{Cr}} = 46.1\,a_0$).

[1] The strength of the interaction does also depend on the magnetic moments μ_1 and μ_2, and the interaction sign can be changed when the signs of the spins are changed from a parallel ($\mathrm{sgn}(\mu_1) = \mathrm{sgn}(\mu_2)$) to an antiparallel ($\mathrm{sgn}(\mu_1) = -\mathrm{sgn}(\mu_2)$) configuration.

[2] The atomic mass unit u equals 1.66×10^{-27} kg, which corresponds to $1/12$ of the mass of carbon-12 atoms.

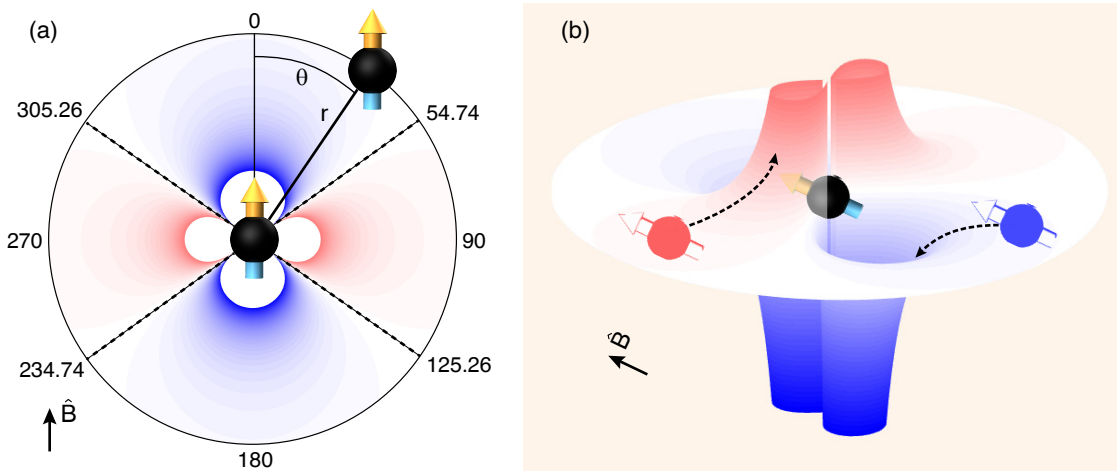

Figure 3.1.: DDI between two magnetic atoms (a) The interaction strength between two dipoles, aligned along $\hat{B}$, relates to their relative distance r and the angle θ between the interatomic axis and the quantization axis. Negative and positive potentials are shown in blue and red, respectively. The dashed lines indicate the angles at which the repulsive and attractive part of the DDI cancel. (b) When a dipole (blue or red dipole) approaches another dipole, it depends crucially on the angle of incidence if it feels a repulsive (red) or attractive (blue) potential. For visualization, the potential is cut off for small distances, at which it starts to diverge.

3.1.2. Ultracold scattering

In quantum mechanics the collision of two particles is described by the scattering theory, see e. g. Ref. [Lan77]. The problem of elastic scattering can be treated as a scattering event of a single particle with reduced mass m_r[3] within the field $U(\mathbf{r})$. The scattered wave function at large distance is given by the sum of the incoming plane wave with wave vector $\mathbf{k}$ and the outgoing spherical wave with wave vector $\mathbf{k}'$. The amplitude $f(\mathbf{k}', \mathbf{k})$ of the outgoing wave depends on the scattering potential $U(\mathbf{r})$ and the included angle with the incoming wave. It is used to evaluate the differential cross section

$$\frac{d\sigma}{d\Omega_{\mathbf{k}'}}(\mathbf{k}', \mathbf{k}) = |f(\mathbf{k}', \mathbf{k})|^2. \tag{3.4}$$

The differential cross section is a measure of the scattering probability of incident direction $\mathbf{k}$ into the outgoing direction $\mathbf{k}'$ with the solid angle $d\Omega_{\mathbf{k}'}$. The total scattering cross section for a given incident direction $\mathbf{k}$ can thus be obtained via integration

$$\sigma(\mathbf{k}) = \int d\Omega_{\mathbf{k}'} \frac{d\sigma}{d\Omega_{\mathbf{k}'}}(\mathbf{k}', \mathbf{k}). \tag{3.5}$$

The collision energy of the scattering event reads as

$$E = \frac{\hbar^2 k}{2m_\mathrm{r}} \tag{3.6}$$

with $k = |\mathbf{k}|$.

[3] The reduced mass of two particles with mass m_1 and m_2 can be calculated via $m_\mathrm{r} = \frac{m_1 m_2}{m_1 + m_2}$, which evaluates to $m_\mathrm{r} = m/2$ for $m_1 = m_2$.

For short-range potentials and in the case of low-energy scattering, i. e. $k \to 0$, the scattering amplitude is governed by scattering in the lowest partial wave $l = 0$, so-called s-wave scattering, and is approximated to

$$f(\mathbf{k}', \mathbf{k}) \approx -a_\mathrm{s}, \tag{3.7}$$

where a_s is the s-wave scattering length. In the case of identical bosons the scattering amplitude has to be symmetrized, i. e. $f_\mathrm{B}(\mathbf{k}', \mathbf{k}) = 1/\sqrt{2}[f(\mathbf{k}', \mathbf{k}) + f(-\mathbf{k}', \mathbf{k})]$, which leads to the total cross section

$$\sigma_\mathrm{B} = 8\pi a_\mathrm{s}^2. \tag{3.8}$$

This cross section is isotropic and thus does not depend on the incident scattering angle. The case of identical fermions is in stark contrast to the bosonic scenario. As the scattering amplitude must be antisymmetrized, i. e. $f_\mathrm{F}(\mathbf{k}', \mathbf{k}) = 1/\sqrt{2}[f(\mathbf{k}', \mathbf{k}) - f(-\mathbf{k}', \mathbf{k})]$, the scattering cross section in the ultracold regime dissapears, i. e.

$$\sigma_\mathrm{F} = 0. \tag{3.9}$$

As a result, identical fermions represent a perfectly non-interacting system. In the context of ultracold experiments, this complicates the approach to cool identical fermions to quantum degeneracy, as evaporative cooling, which is based on elastic scattering, is absent.

3.1.3. Universal dipolar scattering

The scattering behavior changes drastically in the case of DDI [Lan77, Bar08]. As a consequence of the $1/r^3$ long-range character, not only the s-wave but instead *all* partial waves contribute to the scattering event. It has been shown that, in the strong dipolar limit where DDI dominates, the elastic scattering cross section has a universal behavior that only depends on the mass, the dipole moment and the collision energy of the scattered particles [Tic08]. Importantly, in the ultracold regime, the scattering cross section takes a constant value that does not depend on the collision energy anymore [Boh09a]. For dipolar scattering the ultracold regime is reached when the collision energy of Eq. 3.6 is smaller then the natural energy scale of the dipolar interaction

$$E_\mathrm{D} = \frac{\mu_0 \mu_1 \mu_2}{4\pi a_\mathrm{D}^3} \tag{3.10}$$

where the nature length scale a_D for two colliding dipoles is defined as

$$a_\mathrm{D} = \frac{m_\mathrm{r} \mu_0 \mu_1 \mu_2}{4\pi\hbar^2} = a_\mathrm{d}/2. \tag{3.11}$$

For purely dipolar scattering within the first-order Born approximation[4] the scattering amplitude reads as

$$f(\mathbf{k}', \mathbf{k}) = a_\mathrm{D} \left[\frac{2}{3} - \frac{(\hat{k}\hat{B} - \hat{k}'\hat{B})^2}{1 - \hat{k}\hat{k}'} \right]. \tag{3.12}$$

[4] The Born approximation can be applied when the scattering potential can be treated as a perturbation, i. e. when the scattered wave is not significantly changed from the asymptotic incident wave. It has been shown that this approximation can be applied for long-range dipolar interaction potentials, where the scattering happens outside the centrifugal barrier, see e. g. Ref. [Yi01].

In stark contrast to the scattering at an isotropic potential, as it is the case for Eq. 3.7, the scattering amplitude within a dipolar scattering potential, see Eq. 3.2, strongly depends on the angles between the incident, the outgoing, and the quantization axes, i. e. between $\hat{k}$, $\hat{k}'$, and $\hat{B}$.

Following Eq. 3.5 and Eq. 3.12 one can evaluate the total cross section, averaged over all incident directions $\hat{k}$. Depending on the quantum statistics, again the antisymmetrization/symmetrization of the scattering amplitude has to be applied for identical particles, see Sec. 3.1.2.

In the case of fermionic particles, this leads to the total cross section

$$\bar{\sigma}_{\mathrm{F}} = \frac{32\pi}{15} a_{\mathrm{D}}^2. \tag{3.13}$$

For bosonic particles, the s-wave short-range contribution has to be empirically added to the total cross section, which finally results in

$$\bar{\sigma}_{\mathrm{B}} = 8\pi a_{\mathrm{s}}^2 + \frac{32\pi}{45} a_{\mathrm{D}}^2. \tag{3.14}$$

The obtained total cross sections only depend on the dipolar length scale a_{D} (and the scattering length a_{s} for bosons). The found independence on energy reveals the universal behavior of ultracold dipolar elastic collisions.

As a striking consequence of this unversal scattering behavior, dipolar interactions allow for elastic collisions even in the case of spin-polarized fermions. Section 3.3 contains our publication, in which we use universal dipolar scattering for evaporative cooling of fermionic erbium in the streched state. We observe, for the first time, that the deeply quantum degenerate regime can be reached with a single component Fermi gas. Initial work on dysprosium indicated signatures of the very same effect [Lu12]. Our observed evaporation efficiencies are remarkably high, underlining our simple and straightforward method to cool identical fermions. We investigate the total elastic cross section via cross-dimensional thermalization experiments and find a good agreement with the universal value, i. e. Eq. 3.13.

3.1.4. Anisotropic dipolar scattering

While in the case of isotropic interactions, $\sigma(\mathbf{k})$, denoting for the scattering cross section of incident wave vector $\mathbf{k}$ integrated over all outgoing directions $\hat{k}'$, does *not* depend on the incident scattering direction, the behavior is fundamentally different in the dipolar case. On top of the universal behavior, dipolar scattering shows a peculiar angle dependence, as can be seen from Eq. 3.12. The total cross section can be written as a function of the angle η, which is spanned by the incident wave vector $\hat{k}$ and the polarization axis $\hat{B}$ [Boh14], see Fig. 3.2(a).

From Eq. 3.5 and Eq. 3.12 one finds for the scattering cross section of two identical fermionic dipoles

$$\sigma_{\mathrm{F}}(\eta) = \frac{\pi}{3}\left[3 + 18\cos^2\eta - 13\cos^4\eta\right] a_{\mathrm{D}}^2, \tag{3.15}$$

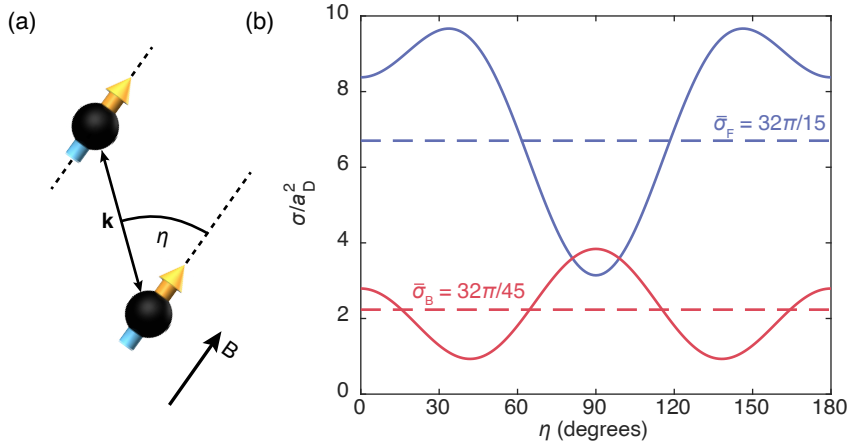

Figure 3.2.: Anisotropic dipolar scattering cross section. (a) Two dipoles collide via an angle η that is defined by the angle between the quantization axis given by $\mathbf{B}$ and the incident wave vector $\mathbf{k}$. (b) Purely dipolar scattering cross section as a function of η for indistinguishable fermions (blue) and bosons (red) summed over all scattering angles $\hat{k}'$. $\sigma(\eta)$ is cylindrically symmetric about the quantization axis. The angular averages $\bar{\sigma}_\mathrm{B}$ and $\bar{\sigma}_\mathrm{F}$ are indicated by the red and blue dashed line, respectively.

while for indistinguishable dipolar bosons the total cross section reads as

$$\sigma_\mathrm{B}(\eta) = \frac{\pi}{9}\left[72\,a_\mathrm{s}^2 - 24\,a_\mathrm{s}\left(1-3\cos^2\eta\right)a_\mathrm{D} + 11\,a_\mathrm{D}^2 - 30\cos^2\eta\,a_\mathrm{D}^2 + 27\cos^4\eta\,a_\mathrm{D}^2\right]. \tag{3.16}$$

Figure 3.2(b) draws their functional form and reveals the strong anisotropy in the scattering behavior. For the bosonic case, the scattering cross section is shown for vanishing contact interactions, i. e. $a_\mathrm{s} = 0$. Interestingly, fermionic and bosonic particles show a markedly different behavior. While bosons scatter strongest when approaching each other in a side-by-side configuration ($\eta = 90°$), fermions preferentially scatter when they meet under an angle of $\eta = 35°$ with respect to the quantization axis. When calculating the angular average of the total cross section

$$\bar{\sigma} = \frac{1}{2}\int_{-1}^{+1} d(\cos\eta)\,\sigma(\eta), \tag{3.17}$$

one finds back the values of $\bar{\sigma}_\mathrm{B}$ and $\bar{\sigma}_\mathrm{F}$, see Eq. 3.13 and Eq. 3.14. For completeness, these mean total cross sections are plotted in Fig. 3.2(b) as dashed lines. We emphasize that dipolar fermions scatter in average three times more often then their bosonic counterparts.

The anisotropy of dipolar scattering can have a strong influence on the rethermalization rate of an out-of-equilibrium atomic sample [Boh14]. Ultracold experiments are typically performed in harmonic traps with an orthogonal coordinate system $\{x, y, z\}$. Collisions in such a trap not only depend on the scattering angle η, but also on the angle β included by the trap symmetry axis and the quantization axis, see Fig. 3.3(a). To access the angle depenendence of the rethermalization rate, cross-dimensional thermalization experiments can be applied. Here, one axis, e. g. the symmetry axis y, is brought out of equilibrium and the time acquired for distributing the induced kinetic energy along the perpendicular axes xz is monitored. This rethermalization time depends on the density and thermal velocity of the atomic sample, but also on the elastic scattering cross section $\bar{\sigma}$. Further, it is directly proportional to the dimensionless constant α, which accounts for the number of collisions

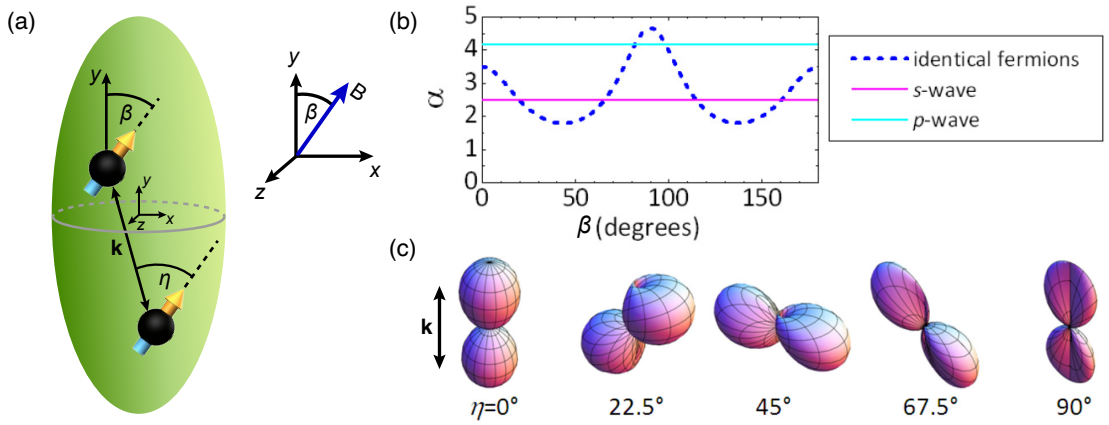

Figure 3.3.: Cross-dimensional thermalization experiments with identical fermionic dipoles. (a) Illustration of a scattering event within a cylindrically symmetric atomic cloud. For experiments, the angle β, included between the symmetry axis y and the quantization axis, is the relevant quantity. The angle η is defined as previously discussed. (b) The number of collisions for rethermalization, α, as a function of the angle β after the atomic cloud is brought out of thermal equilibrium along the y-axis. For comparison, α is also shown for s- and p-wave collisions. (c) Differential cross section $d\sigma/d\Omega_{\mathbf{k}'}$ as a function of the outgoing scattering direction $\mathbf{k}'$ for the incident scattering direction $\mathbf{k}$ aligned along y for various scattering angles η. Figure adapted from Ref. [Boh14].

needed for rethermalization. α can be used as a measure of the efficiency of elastic collisions towards thermal equilibrium.

Figure 3.3(b) shows the dependence of α on the angle β for the case of identical fermions. At an angle $\beta = 45°$ rethermalization happens fast, while for $\beta = 90°$ more than a factor of two more collisions are needed to distribute the energy along the perpendicular directions. To get an intuition for this peculiar angle dependence, one can consider the following scenario: As the trap is excited along the y-axis, it can be assumed that collisions happen mainly along this principle axis, i. e. $\mathbf{k} \parallel y$. For this scenario $\beta \equiv \eta$. As the scattering cross section is found to be lowest for $\eta = 90°$, see Eq. 3.15 and Fig. 3.2, it is not a surprise that at $\beta = 90°$ rethermalization requires the maximum amount of collisions. Further intuition is gained via the angle dependence of the differential scattering amplitude. Thermalization will occur fastest if the differential scattering amplitude is largest for perpendicular outgoing directions, i. e. if $f(\mathbf{k}', \mathbf{k})$ is maximal for $\mathbf{k}' \perp \mathbf{k}$. As can be seen in Fig. 3.3(c) this scenario is found for an angle η of 45°. In contrast, for the cases $\eta = 0°$ and 90° forward and backward scattering is preferred, which hinders energy distribution from y to xz.

Section 3.4 presents our publication on the detailed experimental study of the anisotropic dipolar scattering. Based on the method of cross-dimensional thermalization with an atomic cloud of about 100 000 ^{167}Er atoms, we beautifully reveal that the equilibration rate can vary by as much as a factor of four when we change the dipole orientation with respect to the dynamic axis of the trap. We find remarkable quantitative agreement with the theoretical expectation for our parameters. In addition, we observe that the rethermalization rate in the ultracold regime undergoes a reduction due to Pauli blocking. Our experimental and theoretical investigations reveal that this reduction does not depend on the dipolar angle, i. e. on β.

A complementary approach to directly access the differential scattering cross section of colliding dipoles has more recently been applied with bosonic dysprosium. The method involves the opposed acceleration of two ultracold clouds, which interfere and form a collisional halo. The distribution of this halo depends on the differential cross section and can be observed in time-of-flight (TOF) experiments. While successfully implemented to visualize s- and d-wave collisions of identical bosons in ^{87}Rb [Tho04, Bug04] and p-wave collisions of identical fermions in ^{40}K [Tho16], the work with ^{162}Dy allowed to observe the angle dependence of the differential cross section for dipolar bosons [Bur16].

3.2. Many-body effects in dipolar Fermi gases

Ultracold atoms offer a wealth of possibilities to study the effects of the physics at play. On the one hand, for few-body investigations, where the scattering between two or three particles is of interest, the large number of atoms available in experiments gives a boost to the signal-to-noise ratio, as multiple scattering events are observed simultaneously. On the other hand, ultracold atoms allow to investigate many-body effects, which emerge due to the collective coupling among all particles within the atomic sample. Remarkably, in this scenario one does not need to have information on single scattering events, but rather can describe the atomic system by a single quantum state.

In the case of dipolar particles, which only have been established in the recent years, many-body effects have mainly be explored with bosonic particles. Here, the competition between the isotropic contact interaction and the anisotropic DDI can give rise to many intriguing but also counterintuitive effects. With magnetic chromium atoms it has been observed that, when the dipolar interaction is dominating, the atomic cloud starts to collapse due to the attractive part of the DDI, forming a characteristic d-wave shape [Lah08]. Further, the DDI can affect the collective oscillation frequency of a dipolar Bose-Einstein condensate [Bis10]. More recently, studies along the competing interactions observed the formation of multiple quantum droplets [Kad16], and self-confining quantum liquids, see Ref. [Sch16] and Appendix A.1. It has been shown that the leading role for the stabilization of such quantum droplets is given by beyond mean-field effects, namely quantum fluctuations, see Ref. [FB16] and Appendix A.1, that only can manifest themselves since the other interactions almost cancel[5]. Another intriguing many-body effect, resulting from the competition of contact and dipolar interactions, is given by the emergence of the so-called *Roton spectrum* that features a local minimum in the energy dispersion relation at non-zero momentum, and is closely linked to elementary excitations in superfluid helium [Lan41]. For dipolar systems, the roton mode has been predicted in 2003 [San03], which triggered a large amount of theoretical work along this line [Ron07, Boh09b, Par09, Mar12, Bla12, JL13, Wil10, Nat14]. The first observation of this long-sought mode in dipolar quantum gases is reported in Appendix A.3.

For the case of fermionic dipolar atoms, many-body effects are hardly explored. In contrast to bosonic systems, for spin-polarized fermions contact interactions are absent. For deeply

[5] It should be noted that such self-bound droplets can also be stabilized in purely contact interacting systems, based on the competing attractive and repulsive interactions in e. g. alkali spin mixtures [Pet15, Cab17, Sem17].

degenerate Fermi gases, the relevant energy scale is given by the Fermi energy E_F. In order to manifest themselves, dipolar interactions have to compete with this energy scale. The strength of the expected many-body effect is given by the ratio

$$\frac{n\mu_0\mu^2}{4\pi E_\mathrm{F}}, \tag{3.18}$$

where $n \propto E_\mathrm{F}^{3/2}$ is the peak-number density, and μ is the magnetic moment of the spin-polarized gas. As for magnetic atoms the Fermi energy typically is much larger then the energy of the DDI, dipolar many-body effects are subtle and difficult to observe.

3.2.1. Hartree-Fock theory

To describe many-body effects in a trapped single-component dipolar Fermi gas, Hartree-Fock mean-field theory can be used. Within the semiclassical Thomas-Fermi-Dirac approximiation [Gór01] the total energy of the system can be written as

$$E = E_\mathrm{kin} + E_\mathrm{tr} + E_\mathrm{d} + E_\mathrm{ex} \tag{3.19}$$

with E_kin and E_tr accounting for the kinetic energy and for the external potential energy of the harmonic trap, respectively. The terms

$$E_\mathrm{d} = \frac{1}{2(2\pi)^6}\int d^3r \int d^3r' \int d^3k \int d^3k'\, U_\mathrm{dd}(\mathbf{r}-\mathbf{r}')g(\mathbf{r},\mathbf{k})g(\mathbf{r}',\mathbf{k}') \tag{3.20}$$

and

$$\begin{aligned} E_\mathrm{ex} = -\frac{1}{2(2\pi)^6}\int d^3r \int d^3r' \int d^3k \int d^3k'\, U_\mathrm{dd}(\mathbf{r}-\mathbf{r}') \\ \times e^{i(\mathbf{k}-\mathbf{k}')(\mathbf{r}-\mathbf{r}')} g\left(\frac{\mathbf{r}+\mathbf{r}'}{2},\mathbf{k}\right) g\left(\frac{\mathbf{r}+\mathbf{r}'}{2},\mathbf{k}'\right) \end{aligned} \tag{3.21}$$

are the Hartree direct energy and the Fock exchange energy, respectively, which arise from the DDI, see Eq. 3.1. Here, $\mathbf{r}$ and $\mathbf{k}$ denote for the coordinate and wave vector, respectively. The Wigner distribution function $g(\mathbf{r},\mathbf{k})$ can be written within the variational Ansatz

$$g(\mathbf{r},\mathbf{k}) = \Theta\left(1 - \sum_{i=1}^{3}\frac{r_i^2}{R_i^2} - \sum_{i=1}^{3}\frac{k_i^2}{K_i^2}\right) \tag{3.22}$$

where Θ is the Heaviside step function. Within this Ansatz, which has been confirmed numerically in Ref. [Ron10], the variational paramters R_i and K_i describe the real space and momentum space radii of the atomic cloud in the ith direction, respectively.

The Hartree-Fock theory can be used to calculate the ground state of a dipolar many-body system. For purely contact interacting systems the Hartree and the Fock energy cancel each other, as can be evaluated when $U_\mathrm{dd}(\mathbf{r}-\mathbf{r}')$ is replaced by $\propto \delta(\mathbf{r}-\mathbf{r}')$.

3.2.2. Real and momentum space radii of dipolar atoms

To calculate the ground state of a dipolar gas, the energy of Eq. 3.19 has to minimized. Interestingly, minimal energy is found if the cloud takes a deformed shape in real and momentum space, see Refs. [Gór01, Miy08, Bai12b]. This deformation is a result of E_{d} and E_{ex} and is absent in purely contact interacting systems.

For dipolar bose gases, the deformation of the real space radius has been observed with magnetic Cr [Stu05]. This effect is genuinly known as *magnetostriction* and results from the Hartree direct interaction. Similar to the magnetostriction effect in real space, the surface in momentum space can also be deformed. Here, the relevant term is given by the Fock exchange energy. In the case of dipolar Fermi gases the energy is minimized when the Fermi sphere elongates along the dipole orientation, i. e. along the direction of maximum dipolar attraction [Bai12b].

Section 3.5 presents our publication on the first experimental observation of an anisotropic Fermi surface with a dipolar degenerate Fermi gas. Our investigations, based on TOF experiments with ^{167}Er, reveal that the Fermi sphere indeed elongates along the dipole orientation, and we demonstrate the control of the elongation axis via the external magnetic field. We confirm that the observed deformation in momentum space mainly results from the Fock exchange interaction. To reach an accurate comparison between our experimental observation and the theoretical expectation, we also consider the Hartree direct interaction. During the intial expansion, where the atoms are still interacting, it leads to a non-negligible deformation of the cloud, which we take into account. Remarkably, our observations disclose that the Fermi surface deformation linearly depends on the ratio of the squared magnetic moment to the Fermi energy, see Eq. 3.18, thus confirming the many-body nature of the observed effect.

As we show, the strength of the Fermi surface deformation depends strongly on the competition between the dipolar interaction and the Fermi pressure. If a stronger deformation has to be achieved, one could either increase the dipole moment via the use of polar or dipolar fermionic molecules (e. g. ^{167}Er^{168}Er), or could access the hydrodynamic regime[6], see Ref. [Vac17].

[6] For the measurements in Sec. 3.5 the atomic sample is in the collisionless regime. Here, the mean-free path is larger than the size of the atomic cloud. To enter the hydrodynamic regime the collisional rate has to be increased. The hydrodynamic regime is reached when $\tau\bar{\omega} \ll 1$, where τ is the rethermalization time, see Sec. 3.1.4, and $\bar{\omega}$ the mean trap frequency.

3.3. Publication: Reaching Fermi Degeneracy via Universal Dipolar Scattering[†]

Physical Review Letters **112**, 010404 (2014)
submitted 21 Oct 2013; published 6 Jan 2014
DOI 10.1103/PhysRevLett.112.010404

Kiyotaka Aikawa,[1] Albert Frisch,[1] Michael Mark,[1] Simon Baier,[1] Rudolf Grimm,[1,2] and Francesca Ferlaino[1]

[1] *Institut für Experimentalphysik and Zentrum für Quantenphysik, Universität Innsbruck, Technikerstraße 25, 6020 Innsbruck, Austria*
[2] *Institut für Quantenoptik und Quanteninformation, Österreichische Akademie der Wissenschaften, 6020 Innsbruck, Austria*

[†] The author of the present thesis helped in taking the data, and contributed in writing the manuscript. This publication is also part of the Phd thesis of Albert Frisch.

Reaching Fermi Degeneracy via Universal Dipolar Scattering

K. Aikawa,[1] A. Frisch,[1] M. Mark,[1] S. Baier,[1] R. Grimm,[1,2] and F. Ferlaino[1]
[1]Institut für Experimentalphysik and Zentrum für Quantenphysik, Universität Innsbruck, Technikerstraße 25, 6020 Innsbruck, Austria
[2]Institut für Quantenoptik und Quanteninformation, Österreichische Akademie der Wissenschaften, 6020 Innsbruck, Austria
(Received 21 October 2013; published 6 January 2014)

We report on the creation of a degenerate dipolar Fermi gas of erbium atoms. We force evaporative cooling in a fully spin-polarized sample down to temperatures as low as 0.2 times the Fermi temperature. The strong magnetic dipole-dipole interaction enables elastic collisions between identical fermions even in the zero-energy limit. The measured elastic scattering cross section agrees well with the predictions from the dipolar scattering theory, which follow a universal scaling law depending only on the dipole moment and on the atomic mass. Our approach to quantum degeneracy proceeds with very high cooling efficiency and provides large atomic densities, and it may be extended to various dipolar systems.

DOI: 10.1103/PhysRevLett.112.010404 PACS numbers: 03.75.Ss, 37.10.De, 51.60.+a, 67.85.Lm

Identical fermions with short-range interaction do not collide at very low temperatures [1]. According to the rules of quantum mechanics, the requirement of antisymmetry of the fermionic wave function causes the scattering cross section to vanish in the ultracold regime. This makes ultracold fermions special in many respects. For instance, they realize perfectly noninteracting quantum systems, which can serve for sensitive interferometers [2] and ultraprecise atomic clocks [3]. From another point of view, the absence of collisions means that direct evaporative cooling cannot work.

The inapplicability of direct evaporative cooling to fermions challenged scientists to develop alternative strategies. The common solution is to use mixtures of two distinguishable atomic components [4]. In this scheme, fermions are sympathetically cooled through elastic s-wave collisions with fermions in other spin states [4–8], with atoms belonging to a different isotope [9–13], or with atoms of a different chemical element [14–17].

The scenario is completely different in the presence of the long-range dipole-dipole interaction (DDI). While the effect of the short-range van der Waals interaction still freezes out at low temperatures, as it does for nondipolar fermions, the DDI prevents the elastic cross section between identical fermions from vanishing. The corresponding Wigner threshold law, governing the threshold behavior of two-body scattering, gives a finite and energy-independent elastic cross section [18–20]. As a key consequence, identical dipolar fermions can collide even in the zero-temperature limit.

Ultracold dipolar scattering is currently attracting a renewed interest in connection with recent experiments on polar molecules [21,22] and strongly magnetic atoms [13,23,24]. Early theoretical work on H atoms and atoms in electric fields suggested that dipolar scattering could provide an elastic cross section that is large enough for direct evaporative cooling of identical fermions [25–28]. Recent theoretical work has elucidated the universal character of the dipolar scattering [29–31] and found that the elastic dipolar cross section is determined only by the mass and the dipole moment of the particles [30]. Recent experiments on fermionic ground-state polar KRb molecules have tested this prediction and have obtained evidence for the anisotropic character of the DDI [21]. Experiments on using dipolar scattering for evaporative cooling have been reported for fermionic Dy [13] and KRb molecules [32], both reaching temperatures on the order of the Fermi temperature T_F.

In this Letter, we report on the creation of a quantum degenerate dipolar Fermi gas of ^{167}Er atoms. We demonstrate a powerful approach in which the underlying cooling mechanism relies solely on dipolar scattering between spin-polarized fermions. We observe a remarkably high cooling efficiency, leading to very dense Fermi gases with typically 6.4×10^4 atoms at a temperature of $T/T_F = 0.2$ and a peak density of 4×10^{14} cm^{-3}. Finally, we confirm the prediction of the universal dipolar scattering theory [29,30] by measuring the Er elastic cross section in spin-polarized fermions via cross-dimensional thermalization [33]. Our work opens up a conceptually novel pathway to quantum degeneracy in dipolar systems that can be generalized not only to other strongly magnetic atoms but also to ground-state polar molecules, for which the implementation of sympathetic cooling might be difficult.

The strong dipolar character of Er originates from its large magnetic moment μ of $7\mu_B$, where μ_B is the Bohr magneton, and its large mass [20,34]. Among the six stable isotopes, Er has one fermionic isotope, ^{167}Er, with a large natural abundance of 23%. While the bosonic isotopes have no hyperfine structure, ^{167}Er has a nuclear spin $I = 7/2$, giving rise to a manifold of eight hyperfine levels and 104 magnetic sublevels in the electronic ground state [35]. In spite of the much more complex energy structure of the fermionic isotope, our approach to quantum degeneracy

is very similar to the one we have successfully used to condense the bosonic isotope ^{168}Er [24,36]. It consists of a laser cooling stage followed by direct evaporative cooling in an optical dipole trap (ODT). The fundamental difference with respect to the bosonic case is that the thermalization between spin-polarized fermions proceeds solely through dipolar elastic collisions. In the present work, we focus on spin-polarized fermions in the lowest hyperfine sublevel $|F = 19/2, m_F = -19/2\rangle$, where F is the total spin quantum number and m_F is its projection along the quantization axis.

Our laser cooling scheme relies on a Zeeman slower operating at 401 nm and on a magneto-optical trap (MOT) based on a narrow line at 583 nm [36]. Both light fields act on transitions with quantum numbers $F = 19/2 \rightarrow F' = 21/2$, which are sufficiently closed for laser cooling. In our scheme, fermions in the MOT are naturally spin-polarized into the lowest magnetic sublevel $|19/2, -19/2\rangle$ because of a combined effect of gravity and the MOT light [36]. We typically capture 1×10^7 atoms at $T = 7$ μK in the MOT. All measurements in the present work are performed by absorption imaging on the 401-nm transition.

For evaporative cooling, we first transfer the atoms from the MOT into a single-beam large-volume ODT at 1064 nm and then into a tightly focused ODT at 1570 nm. The first trap is used as an intermediate step to increase the transfer efficiency from the MOT. It consists of a single horizontal beam with a power of 20 W and elliptical focus. The beam waists are approximately 20 and 200 μm in the vertical and horizontal direction, respectively. The corresponding trap depth is roughly 100 μK. From the large-volume trap, the atoms are loaded into a tightly focused ODT at 1570 nm. This second trap is made of a single horizontal beam, which is collinear to the large-volume trapping beam and has a waist of 15 μm. The initial power of the 1570-nm beam is 1.8 W, corresponding to trap frequencies of $(\nu_x, \nu_y, \nu_z) = (2147, 51, 2316)$ Hz and a trap depth of about $k_B \times 190$ μK. Here, z is the direction of gravity. At this stage, we have 1.5×10^6 atoms at $T/T_F = 4.4$ with $T = 28$ μK and a peak density of about 1.2×10^{14} cm^{-3}. The Fermi temperature is defined as $T_F = \hbar\bar{\nu}(6N)^{1/3}/k_B$, where $\bar{\nu}$ is the geometric mean of the trap frequencies and h is the Planck constant. We force evaporation by reducing the power of the horizontal beam in a near-exponential manner. When T_F is reached, we introduce a vertical beam at 1570 nm to confine the fermions into the crossed region created by the two beams and to preserve the atomic density. Its power is gradually increased and reaches 1.2 W at the end of the evaporation. The vertical beam has a beam waist of 33 μm. During evaporation, we apply a homogeneous guiding magnetic field to maintain the spin polarization in the system. At high temperature, the magnetic field value is about 1.7 G, which is large enough to avoid any thermal excitation into higher spin states. For temperature below $3.2T_F$, we decrease the value of the magnetic field to 0.59 G, where we observe a slightly better evaporation efficiency. After 10 s of forced evaporation, we obtain a deeply degenerate Fermi gas.

Figure 1 shows a typical time-of-flight (TOF) absorption image of a degenerate dipolar Fermi gas of $N = 6.4 \times 10^4$ and a peak density of $n_0 = 4 \times 10^{14}$cm^{-3} at $T/T_F = 0.21(1)$ with $T_F = 1.33(2)$ μK. At this point, our trap frequencies are (470,346,345) Hz. Fermi degeneracy reveals itself in a smooth change of the momentum distribution from a Maxwell-Boltzmann to a Fermi-Dirac distribution [37]. Correspondingly, the atomic density profile is expected to change its Gaussian shape into a polylogarithmic one. A fit to TOF images reveals that at temperatures above $\approx 0.5T_F$ the Gaussian and polylogarithmic function are hardly distinguishable from each other and both describe the data well. By further decreasing the temperature, we observe a gradually increasing deviation from the Gaussian shape. This deviation is evident in Fig. 1, which shows a density profile at $T/T_F = 0.21(1)$. A Gaussian fit to the outer wings of the cloud, i.e., outside the disk with radius w, with w being the $1/e$ diameter of the Gaussian fit to the entire cloud, clearly overestimates the population at the center of the cloud. This is a fingerprint of Fermi degeneracy, meaning that the population of low-energy levels is limited by the Pauli exclusion principle.

In all our measurements, we extract T/T_F from fits to the density profiles by using either a polylogarithmic or a Gaussian function. In the former case, the fit gives both the fugacity ζ and the parameter σ characterizing the width of the distribution. The fugacity directly gives $T/T_F = [-6 \times \mathrm{Li}_3(-\zeta)]^{-1/3}$, with Li_n being the nth-order polylogarithmic function [7,9]. The parameter σ is related to the atomic temperature by $T = m\sigma^2/(k_B t_{\mathrm{TOF}}^2)$, where t_{TOF} is the time of flight and m is the mass of ^{167}Er,

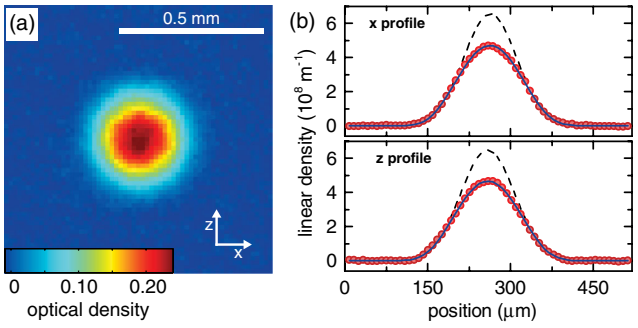

FIG. 1 (color online). Time-of-flight absorption image of a degenerate Fermi gas of Er atoms at $T/T_F = 0.21(1)$ after $t_{\mathrm{TOF}} = 12$ ms of expansion (a) and its density distribution integrated along the z direction (upper panel) and x direction (lower panel) (b). The observed profiles (circles) are well described by fitting a polylogarithmic function to the data (solid lines), while they substantially deviate from a fit using a Gaussian distribution to the outer wings of the cloud, i.e., w (dashed lines). The absorption image is averaged over six individual measurements.

and together with T_F, calculated from N and $\bar{\nu}$, gives a more indirect value for T/T_F. We determine T/T_F by using both methods, which show well consistent results.

To get deeper insights into the evaporation process and the underlying collisional properties, we study the evaporation trajectory. Figure 2 summarizes our results. We observe that the evaporation first proceeds with high efficiency down to temperatures well below T_F and then plateaus at about $T/T_F = 0.2$. The latter behavior suggests that further cooling is limited by Pauli blocking [4,6,7,9] and that more thoroughly optimized evaporation ramps might be needed to reach even lower temperatures. The deepest degeneracy we attained is $T/T_F = 0.19(1)$ with $N = 4.0 \times 10^4$. From the slope of the evaporation trajectory, we obtain the efficiency parameter γ. This parameter quantifies the gain in phase-space density (PSD) at the expense of the atom number and can be written as $\gamma = -d(\ln\ \mathrm{PSD})/d(\ln N) = -3 \times d(\ln T/T_F)/d(\ln N)$. From a linear fit to the data down to $T/T_F = 0.2$, we find $\gamma = 3.5(2)$. This remarkably large number is in the league of the best evaporation efficiencies observed in experiments with ultracold atoms based on s-wave scattering, including our experiments with the bosonic ^{168}Er [24] and experiments on strongly interacting two-component Fermi gases [5,38,39].

Our interpretation of the cooling process in terms of dipolar scattering relies on the full spin polarization of the sample. Another spin state being present would lead to s-wave collisions in the sample. Therefore it is important to make sure that we do not have any other spin state present. For this reason, we carry out a dedicated set of Stern-Gerlach-type measurements at various stages of the evaporation. During the whole evaporation sequence, we never observe any population in spin states different from the $m_F = -19/2$ state. Figure 3 show the relevant portion of the TOF image, where atoms are observed. To identify unambiguously the spatial positions of the different spin components, we intentionally prepare a spin mixture by radio-frequency (rf) transfer; see Fig. 3. It is worth mentioning that we observe fast spin relaxation when a multicomponent mixture is prepared [40].

The effectiveness of our evaporative cooling scheme suggests a very favorable ratio of the elastic scattering rate to the inelastic one. We explore elastic scattering by measuring the elastic dipolar cross section σ_{el} in our spin-polarized fermionic sample via cross-dimensional thermalization experiments [33]. We compress the system in one spatial direction by increasing the power of the vertical beam by about a factor of 3. We then monitor the time evolution of the temperature in the other direction, as shown in the inset in Fig. 4. The time constant τ for cross-dimensional thermalization is directly connected to σ_{el} through the relation $\tau = \alpha/(\bar{n}\sigma_{\mathrm{el}}v)$, where α is the number of collisions required to thermalize, $\bar{n}$ is the mean density, and $v = 4\sqrt{k_B T/(\pi m)}$ is the mean relative velocity. A delicate point of our analysis is the estimation of α, which depends on the underlying scattering mechanism. We employ $\alpha = 4.1$, which has been numerically calculated for nondipolar p-wave collisions and has been applied to KRb polar molecules [21]. Although p-wave collisions are expected to be the leading term in dipolar scattering of identical fermions, more detailed calculations of α might be needed to fully account for the mixing of partial waves resulting from the DDI [41].

In this way, we explore elastic scattering over a wide range of atom numbers from 3×10^4 to 1.1×10^5 and for various final temperatures ranging from 300 to 600 nK. Our findings at 0.59 G [42] are shown in Fig. 4. In the nondegenerate regime ($T \gtrsim T_F$), we obtain a constant elastic cross section with a mean value of $2.0(5) \times 10^{-12}$ cm^2, corresponding to $[2.7(3) \times 10^2 a_0]^2$,

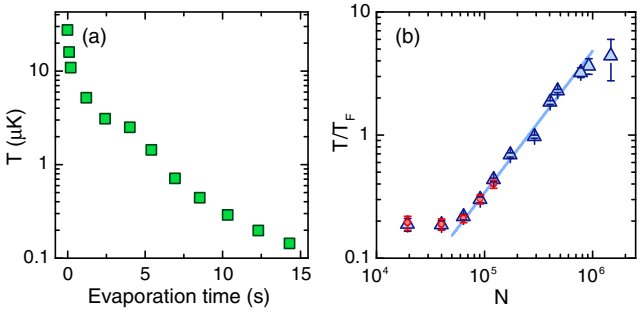

FIG. 2 (color online). Evaporation trajectory to Fermi degeneracy. (a) Temperature evolution during the evaporation ramp and (b) corresponding T/T_F versus N. The ratio T/T_F is obtained from the width σ of the distribution (triangles) and from the fugacity (circles); see the text. The error bars originate from statistical uncertainties in temperature, number of atoms, and trap frequencies for the width measurements and the standard deviations obtained from several independent measurements for the fugacity. The solid line is a linear fit to the data for $0.2 < T/T_F < 4$.

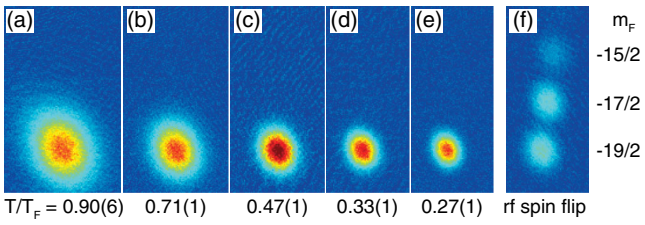

FIG. 3 (color online). Absorption images of the atomic cloud with a Stern-Gerlach separation of the spin components. A magnetic field gradient of about 40 G/cm is applied during the expansion for about 7 ms. (a)–(e) Along the entire evaporative cooling sequence, atoms are always spin-polarized in the lowest hyperfine sublevel $|F = 19/2, m_F = -19/2\rangle$. T/T_F of the atomic samples are indicated in each panel. In (f), the image is obtained right after rf mixing of the spin states for the sample at $T/T_F = 0.33(1)$. The three clouds correspond to the magnetic sublevels $m_F = -19/2, -17/2$, and $-15/2$ from bottom to top.

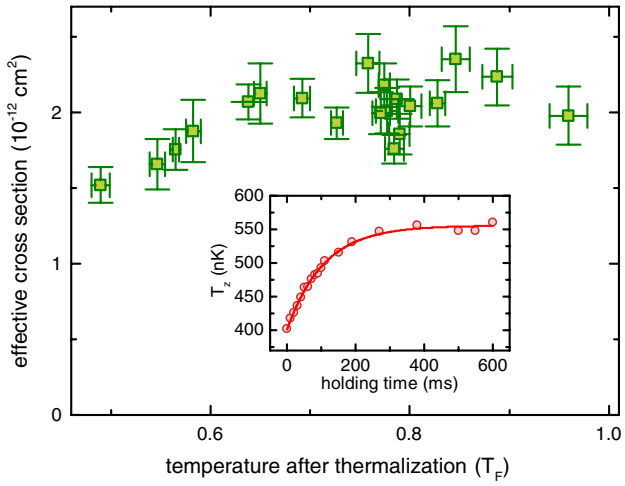

FIG. 4 (color online). Effective elastic cross section as a function of T/T_F after thermalization. In the nondegenerate regime, the effective cross section is constant and gives a mean value of $2.0(5) \times 10^{-12}$ cm^2. The error bars for each point contain the statistical uncertainties of the time constant for cross-dimensional thermalization, of the trap frequencies, and of the temperature. A typical cross-dimensional thermalization measurement with an exponential fit to the data is shown in the inset. T_z is the temperature along the z direction.

where a_0 is the Bohr radius. The error bar is mainly due to systematic uncertainties in trap frequencies, temperature, and number of atoms. Below T_F, the effect of quantum degeneracy becomes visible through a suppression of scattering events caused by Pauli blocking. In this regime, we can interpret our measurements in terms of an effective elastic cross section, which also includes the Pauli suppression factor. As expected, we observe a substantial decrease of the effective σ_{el} for decreasing T/T_F, similarly to the case of s-wave collisions between fermions in different spin states [44].

Dipolar scattering theories predict an energy-independent elastic cross section for identical fermions in the low-energy regime [18–20]. The cross section is predicted to follow a universal scaling law that is fully determined by a single parameter—the dipolar length D [30]—and it reads as

$$\sigma_{\mathrm{el}} = 6.702 \times D^2, \tag{1}$$

where $D = 2\pi^2 d^2 m/h^2$ with $d^2 = \mu_0 \mu^2/(4\pi)$ and μ_0 being the vacuum permeability. This equation shows a clear analogy to the ordinary s-wave scattering, where D plays the role of the scattering length. For the Er parameters, the universal theory predicts $\sigma_{\mathrm{el}} = 1.8 \times 10^{-12}$ cm^2, which is in reasonable agreement with the measured value. The small deviation might be due to the chosen value for α, to systematic errors, or to a residual effect of the short-range physics, which is not included in the theory.

Our observations suggest that inelastic losses are very weak. Since the atoms are fully polarized in the lowest spin state, inelastic losses can be caused only by collisions with the background gas and by three-body decay. To investigate this more quantitatively, we carry out atom-decay measurements by recording the number of atoms as a function of the hold time in an ODT initially loaded with $N \simeq 1 \times 10^5$ atoms at $T/T_F \simeq 0.47$. In spite of the very high peak density of 3×10^{14} cm^{-3}, we find the atom number to decay in a purely exponential manner (time constant 40 s) without showing any signature of three-body processes. From this observation we can derive an upper limit for the three-body recombination rate constant as low as $L_3 \leq 3 \times 10^{-30}$ cm^6/s.

The remarkable efficiency of evaporative cooling in a single-component Fermi gas of Er and the exceptionally high densities together with low inelastic collision rates can be understood in terms of a very favorable combination of the DDI with the p-wave barrier. While DDI is strong enough to provide us with a sufficient cross section for elastic collisions, it is weak enough to preserve a substantial repulsive barrier for any alignment of the colliding dipoles. Even for the case of maximum dipolar attraction (head-to-tail configuration), the effective potential, given by the interplay between the p-wave barrier and the DDI, features a repulsive barrier with a maximum height $V(r_{\mathrm{max}}) = 2\hbar^2/(27mD^2)$ at $r_{\mathrm{max}} = 3D$. For Er, the barrier height still exceeds $k_B \times 7$ μK, which is much larger than all collision energies in the final evaporation stage. This prevents atoms from getting close to each other, and three-body decay, which requires short-range interactions, is strongly suppressed.

In conclusion, we produce a degenerate dipolar Fermi gas of ^{167}Er atoms. We demonstrate direct evaporative cooling of identical fermions via universal dipolar scattering. Our method provides two key advantages: feeble inelastic losses and exceptionally high attainable densities. The former aspect is favorable for reaching low values of T/T_F, which are ultimately limited by the so-called hole-heating mechanism caused by inelastic losses [45,46]. The latter aspect has important consequences for dipolar physics. The relevant energy scale for dipolar phenomena at the many-body level is given by $n_0 d^2$ [20,34]. Given the high densities achieved here, our degenerate Fermi gas of Er currently is the most dipolar quantum gas available in experiments, with $n_0 d^2$ being 0.92% of the Fermi energy. We speculate that even much higher densities than the ones here attained may be achieved, since we do not see any limiting process. This may open a way for observing p-wave pairing in dipolar gases and for the creation of an anisotropic Fermi superfluid [47,48].

We are grateful to J. Bohn, C. Salomon, M. Baranov, and M. Zwierlein for fruitful discussions. We thank M. Springer for technical support and NKT Photonics for lending us the 1570-nm fiber laser. This work is supported by the Austrian

Ministry of Science and Research (BMWF) and the Austrian Science Fund (FWF) through a START grant under Project No. Y479-N20 and by the European Research Council under Project No. 259435. K. A. is supported within the Lise-Meitner program of the FWF.

[1] S. Giorgini, L. P. Pitaevskii, and S. Stringari, Rev. Mod. Phys. **80**, 1215 (2008).
[2] G. Roati, E. de Mirandes, F. Ferlaino, H. Ott, G. Modugno, and M. Inguscio, Phys. Rev. Lett. **92**, 230402 (2004).
[3] T. Nicholson, M. Martin, J. Williams, B. Bloom, M. Bishof, M. Swallows, S. Campbell, and J. Ye, Phys. Rev. Lett. **109**, 230801 (2012).
[4] B. DeMarco and D. S. Jin, Science **285**, 1703 (1999).
[5] S. R. Granade, M. E. Gehm, K. M. O'Hara, and J. E. Thomas, Phys. Rev. Lett. **88**, 120405 (2002).
[6] T. Fukuhara, Y. Takasu, M. Kumakura, and Y. Takahashi, Phys. Rev. Lett. **98**, 030401 (2007).
[7] B. DeSalvo, M. Yan, P. Mickelson, Y. N. Martinez De Escobar, and T. Killian, Phys. Rev. Lett. **105**, 030402 (2010).
[8] S. Taie, Y. Takasu, S. Sugawa, R. Yamazaki, T. Tsujimoto, R. Murakami, and Y. Takahashi, Phys. Rev. Lett. **105**, 190401 (2010).
[9] M. K. Tey, S. Stellmer, R. Grimm, and F. Schreck, Phys. Rev. A **82**, 011608 (2010).
[10] A. G. Truscott, K. E. Strecker, W. I. McAlexander, G. B. Partridge, and R. G. Hulet, Science **291**, 2570 (2001).
[11] F. Schreck, L. Khaykovich, K. L. Corwin, G. Ferrari, T. Bourdel, J. Cubizolles, and C. Salomon, Phys. Rev. Lett. **87**, 080403 (2001).
[12] J. M. McNamara, T. Jeltes, A. S. Tychkov, W. Hogervorst, and W. Vassen, Phys. Rev. Lett. **97**, 080404 (2006).
[13] M. Lu, N. Q. Burdick, and B. L. Lev, Phys. Rev. Lett. **108**, 215301 (2012).
[14] G. Roati, F. Riboli, G. Modugno, and M. Inguscio, Phys. Rev. Lett. **89**, 150403 (2002).
[15] Z. Hadzibabic, C. A. Stan, K. Dieckmann, S. Gupta, M. W. Zwierlein, A. Gorlitz, and W. Ketterle, Phys. Rev. Lett. **88**, 160401 (2002).
[16] C. Silber, S. Gunther, C. Marzok, B. Deh, P. W. Courteille, and C. Zimmermann, Phys. Rev. Lett. **95**, 170408 (2005).
[17] F. M. Spiegelhalder, A. Trenkwalder, D. Naik, G. Hendl, F. Schreck, and R. Grimm, Phys. Rev. Lett. **103**, 223203 (2009).
[18] L. D. Landau and E. M. Lifshitz, *Quantum Mechanics*, Course of Theoretical Physics Vol. 3 (Butterworth-Heinemann, Oxford, 1977).
[19] H. Sadeghpour, J. Bohn, M. Cavagnero, B. Esry, I. Fabrikant, J. Macek, and A. Rau, J. Phys. B **33**, R93 (2000).
[20] M. A. Baranov, Phys. Rep. **464**, 71 (2008).
[21] K. K. Ni, S. Ospelkaus, D. Wang, G. Quemener, B. Neyenhuis, M. H. G. de Miranda, J. L. Bohn, J. Ye, and D. S. Jin, Nature (London) **464**, 1324 (2010).
[22] M. H. G. de Miranda, A. Chotia, B. Neyenhuis, D. Wang, G. Quéméner, S. Ospelkaus, J. L. Bohn, J. Ye, and D. S. Jin, Nat. Phys. **7**, 502 (2011).
[23] M. Lu, N. Q. Burdick, S. H. Youn, and B. L. Lev, Phys. Rev. Lett. **107**, 190401 (2011).
[24] K. Aikawa, A. Frisch, M. Mark, S. Baier, A. Rietzler, R. Grimm, and F. Ferlaino, Phys. Rev. Lett. **108**, 210401 (2012).
[25] J. M. V. A. Koelman, H. T. C. Stoof, B. J. Verhaar, and J. T. M. Walraven, Phys. Rev. Lett. **59**, 676 (1987).
[26] J. M. V. A. Koelman, H. T. C. Stoof, B. J. Verhaar, and J. T. M. Walraven, Phys. Rev. B **38**, 9319 (1988).
[27] M. Marinescu and L. You, Phys. Rev. Lett. **81**, 4596 (1998).
[28] W. Geist, A. Idrizbegovic, M. Marinescu, T. Kennedy, and L. You, Phys. Rev. A **61**, 013406 (1999).
[29] C. Ticknor, Phys. Rev. Lett. **100**, 133202 (2008).
[30] J. L. Bohn, M. Cavagnero, and C. Ticknor, New J. Phys. **11**, 055039 (2009).
[31] Z. Idziaszek and P. S. Julienne, Phys. Rev. Lett. **104**, 113202 (2010).
[32] J. Ye (private communication).
[33] C. R. Monroe, E. A. Cornell, C. A. Sackett, C. J. Myatt, and C. E. Wieman, Phys. Rev. Lett. **70**, 414 (1993).
[34] M. A. Baranov, M. Dalmonte, G. Pupillo, and P. Zoller, Chem. Rev. **112**, 5012 (2012).
[35] A. Frisch, K. Aikawa, M. Mark, F. Ferlaino, E. Berseneva, and S. Kotochigova, Phys. Rev. A **88**, 032508 (2013).
[36] A. Frisch, K. Aikawa, M. Mark, A. Rietzler, J. Schindler, E. Zupanic, R. Grimm, and F. Ferlaino, Phys. Rev. A **85**, 051401 (2012).
[37] Proceedings of the International School of Physics "Enrico Fermi," Course CLXIV, edited by M. Inguscio, W. Ketterle, and C. Salomon (IOS Press, Amsterdam, 2008).
[38] M. Bartenstein, A. Altmeyer, S. Riedl, S. Jochim, C. Chin, J. H. Denschlag, and R. Grimm, Phys. Rev. Lett. **92**, 120401 (2004).
[39] M. W. Zwierlein, C. A. Stan, C. H. Schunck, S. M. F. Raupach, A. J. Kerman, and W. Ketterle, Phys. Rev. Lett. **92**, 120403 (2004).
[40] K. Aikawa, A. Frisch, M. Mark, S. Baier, R. Grimm, and F. Ferlaino (to be published).
[41] J. Bohn and D. Jin (private communication).
[42] The magnetic fields are chosen to avoid Er Feshbach resonances [43].
[43] A. Frisch, M. Mark, K. Aikawa, F. Ferlaino, J. L. Bohn, C. Makrides, A. Petrov, and S. Kotochigova, arXiv:1312.1972.
[44] B. DeMarco, S. B. Papp, and D. S. Jin, Phys. Rev. Lett. **86**, 5409 (2001).
[45] E. Timmermans, Phys. Rev. Lett. **87**, 240403 (2001).
[46] L. D. Carr, T. Bourdel, and Y. Castin, Phys. Rev. A **69**, 033603 (2004).
[47] L. You and M. Marinescu, Phys. Rev. A **60**, 2324 (1999).
[48] M. A. Baranov, M. S. Mar'enko, V. S. Rychkov, and G. V. Shlyapnikov, Phys. Rev. A **66**, 013606 (2002).

3.4. Publication: Anisotropic Relaxation Dynamics in a Dipolar Fermi Gas Driven Out of Equilibrium[†]

Physical Review Letters **113**, 263201 (2014)
submitted 6 May 2014; published 23 Dec 2014
DOI 10.1103/PhysRevLett.113.263201

Kiyotaka Aikawa,[1] Albert Frisch,[1] Michael Mark,[1] Simon Baier,[1] Rudolf Grimm,[1,2] John L. Bohn,[3] Deborah S. Jin,[3] George M. Bruun[4] and Francesca Ferlaino[1,2]

[1] *Institut für Experimentalphysik and Zentrum für Quantenphysik, Universität Innsbruck, Technikerstraße 25, 6020 Innsbruck, Austria*
[2] *Institut für Quantenoptik und Quanteninformation, Österreichische Akademie der Wissenschaften, 6020 Innsbruck, Austria*
[3] *JILA, NIST, and Department of Physics, University of Colorado, Boulder, Colorado 80309, USA*
[4] *Department of Physics and Astronomy, University of Aarhus, Ny Munkegade, DK-8000 Aarhus C, Denmark*

[†] The author of the present thesis helped performing the measurements and analyzing the data together with A. F., M. M. and K. A., and contributed in writing the manuscript. The theoretical calculations of this publication have been contributed by J. B., D. J., and G. B.

Anisotropic Relaxation Dynamics in a Dipolar Fermi Gas Driven Out of Equilibrium

K. Aikawa,[1] A. Frisch,[1] M. Mark,[1] S. Baier,[1] R. Grimm,[1,2] J. L. Bohn,[3] D. S. Jin,[3] G. M. Bruun,[4] and F. Ferlaino[1,2]
[1]*Institut für Experimentalphysik and Zentrum für Quantenphysik, Universität Innsbruck, Technikerstraße 25, 6020 Innsbruck, Austria*
[2]*Institut für Quantenoptik und Quanteninformation, Österreichische Akademie der Wissenschaften, 6020 Innsbruck, Austria*
[3]*JILA, NIST, and Department of Physics, University of Colorado, Boulder, Colorado 80309, USA*
[4]*Department of Physics and Astronomy, University of Aarhus, Ny Munkegade, DK-8000 Aarhus C, Denmark*
(Received 6 May 2014; published 23 December 2014)

We report on the observation of a large anisotropy in the rethermalization dynamics of an ultracold dipolar Fermi gas driven out of equilibrium. Our system consists of an ultracold sample of strongly magnetic ^{167}Er fermions, spin polarized in the lowest Zeeman sublevel. In this system, elastic collisions arise purely from universal dipolar scattering. Based on cross-dimensional rethermalization experiments, we observe a strong anisotropy of the scattering, which manifests itself in a large angular dependence of the thermal relaxation dynamics. Our result is in good agreement with recent theoretical predictions. Furthermore, we measure the rethermalization rate as a function of temperature for different angles and find that the suppression of collisions by Pauli blocking is not influenced by the dipole orientation.

DOI: 10.1103/PhysRevLett.113.263201 PACS numbers: 34.50.Cx, 37.10.De, 47.70.Nd, 67.85.Lm

The behavior of any many-body system follows from the interactions of its constituent particles. In some cases of physical interest, importantly at ultralow temperature, where the de Broglie wavelength is the dominant length scale, these interactions can be simplified by appealing to the Wigner threshold laws [1,2]. These laws, which have been extensively studied for particles interacting via van der Waals forces, both in experiment and theory [3], identify the interactions via simple isotropic parameters such as a scattering length. However, for dipolar particles, the fundamental interaction is anisotropic and the system properties can depend on the orientation of the gas with respect to a particular direction in space [4,5].

One of the major strengths of ultracold matter is its susceptibility to being controlled by various means. Striking examples include traversing the BEC-BES crossover [6,7], welding atoms together into molecules [8,9], and inducing bosons to behave like fermions in one spatial dimension [10,11]. Most often, such control exploits the quantum mechanical nature of a many-body gas at ultralow temperature, and arises from the manipulation of isotropic scattering between constituent particles. However, in the case of dipolar particles the scattering is intrinsically anisotropic, affording novel opportunities to control the behavior of the gas. For example, the anisotropic d-wave collapse of a Bose-Einstein condensate of magnetic atoms [12,13] and the deformation of the Fermi sphere in a dipolar Fermi gas [14] have been observed. These phenomena rely on the collective behavior of all the particles, occurring according to their mean field energy.

Distinct from such many-body effects, dipoles can also influence the properties of the gas via two-body scattering. Since scattering of dipoles is highly anisotropic, properties that require the collisional exchange of energy and momentum between the atoms, such as sound propagation, viscosity, and virial coefficients [15], will be influenced by the presence of dipoles. In particular, differential cross sections of dipolar particles are highly anisotropic, depending on both the initial, as well as scattered, relative directions of the colliding particles, and it has recently been predicted that dipolar anisotropy can exert a profound influence on the nonequilibrium dynamics in such a gas [16].

In this Letter, we demonstrate the control of the thermal relaxation dynamics of a dipolar Fermi gas driven out of equilibrium by adding excess momentum along one axis. The control is achieved by changing the orientation of the dipoles relative to this direction, enabling us to substantially vary the rethermaliztion rate. As a striking consequence of the interaction anisotropy, we find that the rate of equilibration can vary by as much as a factor of 4, depending on the angle between the dipole orientation and the excitation axis. Furthermore, we observe that the rethermalization rate decreases as the temperature is lowered. This effect is due to the lack of available final states into which atoms can scatter and is known as Pauli blocking. Our results provide evidence that the Pauli suppression of collisions does not contribute additional anisotropic effects to the rethermalization.

To realize a dipolar Fermi gas, we use an ultracold spin-polarized sample of strongly magnetic erbium (Er) atoms, which possess a magnetic dipole moment of 7 Bohr magneton. This is an ideal system to study purely dipolar scattering since short-range van der Waals forces give a negligible contribution to the scattering of identical fermions at ultralow temperatures [17]. Our experimental procedure to create a degenerate Fermi gas of ^{167}Er atoms follows the one described in Refs. [18,19]. In brief, it

comprises laser cooling in a narrow-line magneto-optical trap (MOT) [21] and direct evaporative cooling of a spin-polarized sample in an optical dipole trap (ODT) [18]. Evaporative cooling, which was successfully used to reach Bose-Einstein condensation [22,23], relies on efficient thermalization. In our case, this is achieved by elastic dipolar collisions between spin-polarized fermions.

We optimize the evaporative cooling sequence and produce a degenerate Fermi gas of about 3.0×10^4 atoms at a temperature as low as $T/T_F = 0.11(1)$. This gives a peak density of about 3×10^{14} cm^{-3}; see Fig. 1. Here, $T_F = 1.06(5)$ μK. To achieve such a deeply degenerate regime, we confine the atoms more tightly than in our previous work [18] by decreasing the beam waist of the vertical 1570 nm beam from 33 to 21 μm. The trap frequencies in this configuration are $(\nu_x, \nu_y, \nu_z) = (509, 447, 262)$ Hz. Our minimum temperature is comparable to the lowest ones achieved with sympathetic cooling schemes based on s-wave scattering [6,24,25].

While the crucial role of the long-range character of the dipole-dipole interaction (DDI) clearly emerges in the evaporation of spin-polarized fermions, the role of the anisotropy of the interaction is more subtle. We investigate this aspect by studying for various dipole orientations how the system rethermalizes when it is excited out of its equilibrium state. The dipole orientation is controlled by changing the direction of the polarizing magnetic field and is represented by the angle β between the magnetic field and the weak axis of the ODT; see inset in Fig. 2.

The cross-dimensional rethermalization experiments proceed as follows. We first prepare a nearly degenerate Fermi gas of about 8×10^4 atoms at $T/T_F \simeq 0.6$ with $T_F \simeq 600$ nK in a cigar-shaped ODT with frequencies of (393,23,418) Hz. We then change the dipole orientation from $\beta = 90°$, which is used for evaporative cooling, to the desired value and excite the system by increasing the power of the vertical beam by about a factor of 2.8 within 14 ms. After the excitation, the trap frequencies are (393,38,418) Hz. The excitation brings the system out of equilibrium by transferring energy mainly in the direction of the weak axis (y), which we refer to as the *excitation* axis. This process is nearly adiabatic with respect to the trap period for the radial motion and introduces an initial temperature imbalance of about $T_y/T_z = 2$. We follow the reequilibration dynamics by recording the time evolution of the temperature along the z direction T_z and we extract the rethermalization rate for the given dipole orientation.

Figure 2 shows typical temperature evolutions, measured for three different values of β. We observe that the reequilibration dynamics strongly depends on β with T_z approaching the new equilibrium value in a near-exponential way. From an exponential fit to the data, we extract the relaxation time constant τ. The slower rethermalization (i.e., largest τ) is found to occur for dipoles oriented perpendicular to the excitation axis, whereas by changing β by about 45° we observe that the system reequilibrates about 4 times faster. This strong angle dependence clearly shows the anisotropic nature of the relaxation dynamics.

Since rethermalization relies on elastic collisions, its rate $1/\tau$ should be directly proportional to the total elastic cross section $\sigma_{\rm el}$ [16]. The standard way to evaluate the latter is by integrating the differential cross sections $d\sigma_{\rm el}/d\Omega(\mathbf{k}', \mathbf{k})$ over all final directions of the atoms' relative momentum $\mathbf{k}'$, and averaging over incident directions $\mathbf{k}$. For dipolar

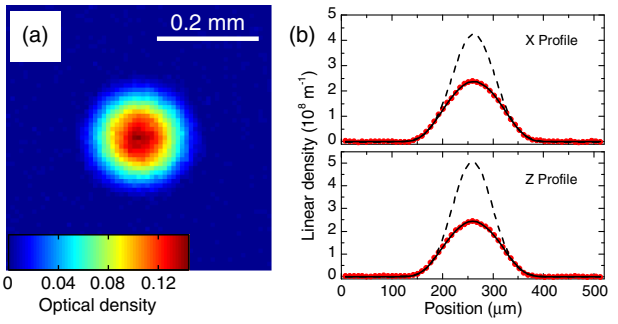

FIG. 1 (color online). Time-of-flight absorption image of a degenerate Fermi gas of 3.0×10^4 Er atoms at $T/T_F = 0.11(1)$ after 12 ms of expansion (a) and its density distribution integrated along the x direction (upper panel) and z direction (lower panel) (b). The observed profiles (circles) are well described by fitting the Fermi-Dirac distribution to the data (solid lines), while they substantially deviate from a fit using a Gaussian distribution to the outer wings of the cloud (dashed lines), i.e., outside the disk with radius w, where w is the $1/e$ radius of the Gaussian fit to the entire cloud. The absorption image is averaged over 20 individual measurements.

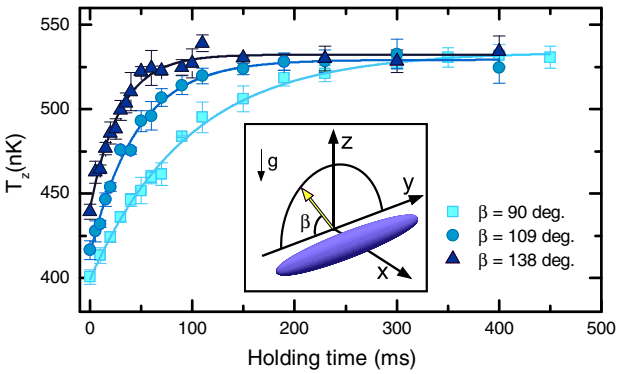

FIG. 2 (color online). Typical cross-dimensional thermalization measurements for three dipole orientations: $\beta = 90°$ (squares), $\beta = 109°$ (circles), and $\beta = 138°$ (triangles). The time evolution of the temperature in the z direction T_z is plotted as a function of holding time after the cloud is excited in the y direction. The geometry of the cigar-shaped trap and the coordinates are indicated in the inset. The yellow arrow represents the dipole orientation. After the equilibration, the Fermi gas is at $T/T_F \simeq 0.75$ with $T_F \simeq 710$ nK.

fermions, the integration yields an energy-independent $\sigma_{\rm el}$, which is universally related to the fermions' dipole moment d by $\sigma_{\rm el} = (32\pi/15)D^2$, where $D = 2\pi^2 d^2 m/h^2$, with m the mass and h the Planck constant, is the characteristic length scale of the dipolar interaction [26]. A collision rate can then be defined as $\bar{n}\sigma_{\rm el} v$, where $\bar{n}$ is the mean number density and $v = \sqrt{16 k_B T'/(\pi m)}$ is the mean relative velocity with T' the effective temperature including a momentum spread by the Fermi energy [27].

The actual reequilibration occurs at a rate different from this collision rate since rethermalization emphasizes those collisions that significantly change the relative direction of the atoms' momenta. The characteristic time for the relaxation is inversely proportional to the collision rate

$$\tau = \frac{\alpha}{\bar{n}\eta\sigma_{\rm el} v}. \quad (1)$$

The dimensionless proportionality constant α is commonly referred to as the number of collisions for thermalization and can be computed from the known differential cross sections. For short-range interactions, Monte Carlo calculations yield $\alpha = 2.7$ and $\alpha = 4.1$ for s- and p-wave collisions, respectively [28,29]. As predicted in Ref. [16], in the case of the DDI, which is long range and anisotropic, α is a function of the angle β. In Eq. (1), we also include a Pauli suppression factor η, which accounts for the reduction of the rethermalization rate in a degenerate Fermi gas caused by Pauli blocking, where $\eta = 1$ for nondegenerate gases; see later discussion.

To explore the angle dependence of α, we perform cross-dimensional rethermalization experiments under the same conditions as in Fig. 2 for various values of β in a range between 30° and 160°. We extract α by using Eq. (1), the experimentally measured τ, and the elastic dipolar cross section $\sigma_{\rm el} = 1.8 \times 10^{-12}\,{\rm cm}^2$ calculated for Er [26]. At $T/T_F \simeq 0.75$, which is our experimental condition after excitation, $\eta = 0.93$; see later discussion. Figure 3 shows our experimental result together with the theoretical value of α, which we calculate using Enskog's equation similarly to Ref. [16]. We observe a remarkably good quantitative agreement between the experiment and the theory, which does not have any free parameter. The theoretical curve is calculated assuming a velocity distribution that is Maxwell-Boltzmann in form that allows the width of the distribution to be characterized by different "temperatures" T_x, T_y, and T_z in the three directions of the trap. We then use the collision integral in Enskog's formulation to calculate the relaxation rate for T_z for the following initial conditions: $T_z = T_x$, and $T_y = 2T_z$. From this we determine the theoretical value of α along the z direction; see Fig. 3. Owing to the anisotropy of the dipolar collision cross section, we find that α is, in general, different in the three directions $i = x, y, z$.

Both the experimental and theoretical results show a strong angular dependence of α, which largely varies in a sinelike manner from about 1 to 4. This behavior is unique to dipolar scattering and occurs because dipolar particles have a spatial orientation dictated by the magnetic field and the collision processes depend on this orientation [16]. Given this angular dependence, dipoles can reequilibrate on a time scale that can be even faster than the one achievable with short-range s-wave collisions ($\alpha = 2.7$). In particular, the rethermalization is the most efficient (smallest α) when $\beta = 45°$. This can be seen qualitatively from the form of the cross sections in Ref. [16]. Consider a simplified scattering event, where the magnetic field $\mathbf{B}$, the relative incident wave vector $\mathbf{k}$, and the relative scattered wave vector $\mathbf{k}'$ all lie in the same plane. Moreover, suppose that $\mathbf{k}$ makes an angle θ with respect to $\mathbf{B}$, while $\mathbf{k}'$ makes an angle θ', defining a scattering angle $\theta_s = \theta' - \theta$. In this reduced case, the differential cross section for scattering of dipolar fermions has the simple angular dependence $d\sigma_{\rm el}/d\Omega \propto \cos^2(2\theta - \theta_s)$; thus, the most likely scattering occurs when $\theta_s = 2\theta$. For the most efficient rethermalization one requires scattering at right angles, $\theta_s = 90°$, and, therefore, collisions in which the atoms approach one another at $\theta = 45°$. At the same time, from the experimental geometry one requires a high collision rate between the radial and axial trap directions. From these considerations, the most efficient rethermalization should occur for a field tilted at an angle $\beta = 45°$ from the trap's axis.

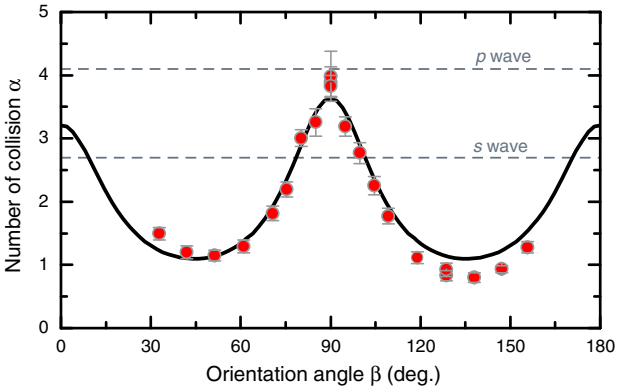

FIG. 3 (color online). Angle dependence of the number of collisions α required to rethermalize ultracold dipolar fermions. The experimental data (circles) are compared with the parameter-free theoretical prediction calculated under our trapping and excitation conditions (solid line).

Another central aspect in the scattering of ultracold fermions in the degenerate regime is related to Pauli blocking of collisions. This effect is caused by the lack of unoccupied final states in a scattering event and leads to a reduction of the elastic collision rate, which has been observed in fermionic systems with short-range interaction [29,30]. In the case of dipolar scattering, it is an interesting question whether or not the Pauli blocking effect exhibits anisotropy.

To address this question experimentally, we explore the temperature dependences of τ for two different angles,

$\beta = 90°$ and 110°, for which α differs by a factor of 2; see Fig. 3. For each temperature, we measure τ, n, v, and we derive η/α using Eq. (1). To extract the Pauli suppression factor η, we normalize η/α to its value in the nondegenerate regime where $\eta = 1$. As shown in Fig. 4, for both angles we observe the same pronounced reduction of η with decreasing temperature. Specifically, η decreases by about 70% from 1 to $0.2T/T_F$. Our results indicate that the reduction of the rethermalization rate is independent from the dipole orientation.

In order to quantitatively confirm that the observed reduction of η is caused by Pauli blocking of collisions, we use a theoretical model following the one developed for nondipolar fermions in Refs. [31,32]. Our model is based on a variational approach for solving the Boltzmann equation to calculate the thermal relaxation rate including the Pauli blocking effect. This gives [33]

$$\frac{1}{\tau} = \frac{\langle \Gamma[\Phi_T]\Phi_T \rangle}{2\langle \Phi_T^2 \rangle}, \tag{2}$$

where the trap and momentum average is defined as $\langle \ldots \rangle = \int d^3r \int d^3\check{k} f(1-f)\ldots$ with $d^3\check{k} = d^3k/(2\pi)^3$, and $f(k,\mathbf{r}) = \{\exp[\beta(k^2/2m + V(\mathbf{r}) - \mu)] + 1\}^{-1}$ is the equilibrium Fermi function with $V(\mathbf{r})$ the trapping potential. We have defined $\Gamma[\Phi_T] = I[\Phi_T]/f(1-f)$ with

$$I[\Phi] = \int d^3\check{k}_2 d\Omega \frac{d\sigma_{\mathrm{el}}}{d\Omega} \frac{|\mathbf{k} - \mathbf{k}_2|}{m} \Delta\Phi f f_2 (1-f_3)(1-f_4) \tag{3}$$

the collision integral describing the rethermalization due to the collision of two particles with incoming momenta $\mathbf{k}$ and $\mathbf{k}_2$ and outgoing momenta $\mathbf{k}_3$ and $\mathbf{k}_4$. Here, $\Delta\Phi = \Phi_1 + \Phi_2 - \Phi_3 - \Phi_4$ and Ω is the solid angle of the outgoing relative momentum $(\mathbf{k}_4 - \mathbf{k}_3)/2$. We use $\Phi_T = k_y^2 - k^2/3$ as a variational expression for the deviation function corresponding to a thermal anisotropy in the y direction. This is also the approach used to calculate α as a function of β for a Maxwell-Boltzmann distribution in Ref. [16] and used to calculated the shear viscosity in a gas interacting with s-wave interactions [31,32].

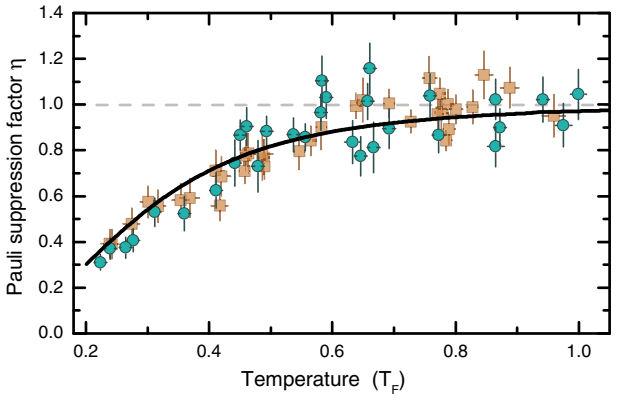

FIG. 4 (color online). The Pauli suppression factor η as a function of the temperature. The experimental data are taken for two different orientations of the dipoles, i.e., for $\beta = 90°$ (squares) and for $\beta = 110°$ (circles). The experimental values are compared with the theoretical predictions on Pauli blocking (solid line); see text.

By calculating the thermal relaxation rate using Eq. (2) with either a pure s-wave or a pure p-wave interaction, we find that the relative suppression of the rate compared to the classical value is essentially the same in the two partial wave channels for a given temperature. This indicates that the Pauli blocking effect is largely insensitive to the angular dependence of the cross section of the atoms. Hence, we can safely use the p-wave cross section as a stand-in for the true dipolar scattering in this calculation. In the high-temperature limit $T \gg T_F$, the integrals in Eqs. (2)–(3) can be solved analytically and we get Eq. (1) with $\alpha = 25/6$ for p-wave scattering and $\alpha = 5/2$ for s-wave scattering. These variational values agree well with the Monte Carlo results stated above.

In Fig. 4, we plot the theoretically predicted temperature dependence of η using Eqs. (2) and (3) and assuming a p-wave cross section, together with the experimental values. As explained above, the calculation yields essentially the same result when we assume s-wave scattering. By fitting the theoretical curve to the observed rethermalization rates with a single free scaling parameter for each angle, we determine the values of $\sigma_{\mathrm{el}}/\alpha$ to be $0.51(1)(12) \times 10^{-12}$ cm^2 at $\beta = 90°$ and $1.00(2)(24) \times 10^{-12}$ cm^2 at $\beta = 110°$, where the errors are statistical errors of fitting and systematic uncertainties on temperature, trap frequencies, and atom number, respectively. The theory and experimental results are in good agreement. Our findings show that the reduction of the rethermalization rate is indeed due to Pauli blocking and that it is not significantly influenced by the polarization angle.

In conclusion, we have studied the rethermalization dynamics of indistinguishable dipolar fermions after the system is excited out of thermal equilibrium. We have observed that the rate of equilibration can strongly vary depending on the polarization direction of the atoms' magnetic dipole moments, which demonstrates a remarkable influence of anisotropic scattering. Further, we note that the anisotropy has no significant influence on the Pauli blocking effect. Our results are fundamentally important for understanding the collisional behavior of dipolar particles, such as strongly magnetic atoms and polar molecules.

We are grateful to M. Baranov for fruitful discussions. This work is supported by the Austrian Ministry of Science and Research (BMWF) and the Austrian Science Fund (FWF) through a START Grant under Project No. Y479-N20 and by the European Research Council under Project

No. 259435. K. A. is supported within the Lise-Meitner program of the FWF. J. L. B. and D. S. J. acknowledge support from U.S. National Science Foundation Grant No. 1125844.

[1] E. P. Wigner, Phys. Rev. **73**, 1002 (1948).
[2] H. Sadeghpour, J. Bohn, M. Cavagnero, B. Esry, I. Fabrikant, J. Macek, and A. Rau, J. Phys. B **33**, R93 (2000).
[3] J. Weiner, V. S. Bagnato, S. Zilio, and P. S. Julienne, Rev. Mod. Phys. **71**, 1 (1999).
[4] T. Lahaye, C. Menotti, L. Santos, M. Lewenstein, and T. Pfau, Rep. Prog. Phys. **72**, 126401 (2009).
[5] M. A. Baranov, M. Dalmonte, G. Pupillo, and P. Zoller, Chem. Rev. **112**, 5012 (2012).
[6] *Ultra-Cold Fermi Gases, Proceedings of the International School of Physics "Enrico Fermi," Course CLXIV, Varenna, 2006*, edited by M. Inguscio, W. Ketterle, and C. Salomon (IOS Press, Amsterdam, 2008).
[7] S. Giorgini, L. P. Pitaevskii, and S. Stringari, Rev. Mod. Phys. **80**, 1215 (2008).
[8] L. D. Carr, D. DeMille, R. V. Krems, and J. Ye, New J. Phys. **11**, 055049 (2009).
[9] D. S. Jin and J. Ye, Chem. Rev. **112**, 4801 (2012).
[10] M. A. Cazalilla, R. Citro, T. Giamarchi, E. Orignac, and M. Rigol, Rev. Mod. Phys. **83**, 1405 (2011).
[11] A. Imambekov, T. L. Schmidt, and L. I. Glazman, Rev. Mod. Phys. **84**, 1253 (2012).
[12] T. Lahaye, J. Metz, B. Fröhlich, T. Koch, M. Meister, A. Griesmaier, T. Pfau, H. Saito, Y. Kawaguchi, and M. Ueda, Phys. Rev. Lett. **101**, 080401 (2008).
[13] K. Aikawa, A. Frisch, M. Mark, S. Baier, A. Rietzler, R. Grimm, and F. Ferlaino, Phys. Rev. Lett. **108**, 210401 (2012).
[14] K. Aikawa, S. Baier, A. Frisch, M. Mark, C. Ravensbergen, and F. Ferlaino, Science **345**, 1484 (2014).
[15] K. M. Daily and D. Blume, Phys. Rev. A **89**, 013606 (2014).
[16] J. L. Bohn and D. S. Jin, Phys. Rev. A **89**, 022702 (2014).
[17] According to the Wigner threshold law for the short-range van der Waals interaction, the cross section for identical fermions rapidly vanishes with temperature. As a consequence, both the isotropic and anisotropic part of the van der Waals interaction plays a negligible role in the scattering.
[18] K. Aikawa, A. Frisch, M. Mark, S. Baier, R. Grimm, and F. Ferlaino, Phys. Rev. Lett. **112**, 010404 (2014).
[19] See Supplemental Material at http://link.aps.org/supplemental/10.1103/PhysRevLett.113.263201, which includes Ref. [20], for experimental details.
[20] A. Frisch, M. Mark, K. Aikawa, F. Ferlaino, J. L. Bohn, C. Makrides, A. Petrov, and S. Kotochigova, Nature (London) **507**, 475 (2014).
[21] A. Frisch, K. Aikawa, M. Mark, A. Rietzler, J. Schindler, E. Zupanic, R. Grimm, and F. Ferlaino, Phys. Rev. A **85**, 051401 (2012).
[22] M. H. Anderson, J. R. Ensher, M. R. Matthews, C. E. Wieman, and E. A. Cornell, Science **269**, 198 (1995).
[23] K. B. Davis, M.-O. Mewes, M. R. Andrews, N. J. Van Druten, D. S. Durfee, D. M. Kurn, and W. Ketterle, Phys. Rev. Lett. **75**, 3969 (1995).
[24] S. Taie, Y. Takasu, S. Sugawa, R. Yamazaki, T. Tsujimoto, R. Murakami, and Y. Takahashi, Phys. Rev. Lett. **105**, 190401 (2010).
[25] S. Stellmer, R. Grimm, and F. Schreck, Phys. Rev. A **87**, 013611 (2013).
[26] J. L. Bohn, M. Cavagnero, and C. Ticknor, New J. Phys. **11**, 055039 (2009).
[27] For estimating v, T' is determined by fitting a Gaussian distribution to the observed TOF absorption images over the entire temperature range such that v includes the effect of a momentum spread by the Fermi energy, as performed in Ref. [29].
[28] C. R. Monroe, E. A. Cornell, C. A. Sackett, C. J. Myatt, and C. E. Wieman, Phys. Rev. Lett. **70**, 414 (1993).
[29] B. DeMarco, J. L. Bohn, J. P. Burke, M. Holland, and D. S. Jin, Phys. Rev. Lett. **82**, 4208 (1999).
[30] S. Riedl, E. R. Sánchez Guajardo, C. Kohstall, A. Altmeyer, M. J. Wright, J. Hecker Denschlag, R. Grimm, G. M. Bruun, and H. Smith, Phys. Rev. A **78**, 053609 (2008).
[31] P. Massignan, G. M. Bruun, and H. Smith, Phys. Rev. A **71**, 033607 (2005).
[32] G. M. Bruun and H. Smith, Phys. Rev. A **72**, 043605 (2005).
[33] C. J. Pethick and H. Smith, *Bose-Einstein Condensation in Dilute Gases* (Cambridge University Press, Cambridge, England, 2002).

SUPPLEMENTARY MATERIAL: ANISOTROPIC RELAXATION DYNAMICS IN A DIPOLAR FERMI GAS DRIVEN OUT OF EQUILIBRIUM

Creation of a spin-polarized sample of ^{167}Er

After the MOT stage, in which the sample is simultaneously cooled and spin-polarized into the lowest hyperfine sublevel, we typically transfer 1.5×10^6 atoms at a temperature of $T = 28\,\mu$K into a crossed ODT. The latter consists of a horizontal beam, which propagates along the y direction, and a vertical beam, propagating along the z direction (direction of gravity). The horizontal beam has a beam waist of $15\,\mu$m and a wavelength of 1570 nm. For the vertical beam, we use light that operates either at 1570 nm or at 1064 nm and various values of the beam waist, depending on the final temperatures and densities required for the specific experiments.

Magnetic field control

We apply a magnetic bias field of 0.58 G, oriented along the z direction. We select this value of the magnetic field to avoid loss features associated to the recently observed Fano-Feshbach resonances [1]. At 0.58 G, the Zeeman energy splitting between magnetic sublevels is $0.6\,\text{MHz} \times h$. This value is much larger than the typical Fermi energy (about $20\,\text{kHz} \times h$) and the typical energy of the DDI (about $100\,\text{Hz} \times h$).

The angle β and the amplitude of the magnetic field are controlled by three independent sets of coils along the x, y, and z directions. Each coil set is independently calibrated by using radio-frequency spectroscopy to within 5 mG, from which we estimate the error on angle to be within 1 degree.

[1] A. Frisch, M. Mark, K. Aikawa, F. Ferlaino, J. L. Bohn, C. Makrides, A. Petrov, and S. Kotochigova, Nature **507**, 475 (2014).

3.5. Publication: Observation of Fermi surface deformation in a dipolar quantum gas[†‡]

Science **345**, 6203 (2014)
submitted 25 Apr 2014; published 15 Aug 2014
DOI 10.1126/science.1255259

Kiyotaka Aikawa,[1] Simon Baier,[1] Albert Frisch,[1] Michael Mark,[1] Cornelis Ravensbergen,[1,2] Francesca Ferlaino[1,2]

[1] *Institut für Experimentalphysik and Zentrum für Quantenphysik, Universität Innsbruck, Technikerstraße 25, 6020 Innsbruck, Austria*
[2] *Institut für Quantenoptik und Quanteninformation, Österreichische Akademie der Wissenschaften, 6020 Innsbruck, Austria*

[†] The author of the present thesis performed the measurements together with K. A. and the help of C. R., M. M., and A. F., and contributed in writing the manuscript. This publication is also part of the Phd thesis of Albert Frisch.

[‡] The post-print version of the publication is attached for online access of this thesis.

Observation of Fermi surface deformation in a dipolar quantum gas

K. Aikawa,[1] S. Baier,[1] A. Frisch,[1] M. Mark,[1] C. Ravensbergen,[1,2] and F. Ferlaino[1,2]

[1] *Institut für Experimentalphysik and Zentrum für Quantenphysik, Universität Innsbruck, Technikerstraße 25, 6020 Innsbruck, Austria*

[2] *Institut für Quantenoptik und Quanteninformation,Österreichische Akademie der Wissenschaften, 6020 Innsbruck, Austria*

(Dated: July 18, 2014)

The deformation of a Fermi surface is a fundamental phenomenon leading to a plethora of exotic quantum phases. Understanding these phases, which play crucial roles in a wealth of systems, is a major challenge in atomic and condensed-matter physics. Here, we report on the observation of a Fermi surface deformation in a degenerate dipolar Fermi gas of erbium atoms. The deformation is caused by the interplay between strong magnetic dipole-dipole interaction and the Pauli exclusion principle. We demonstrate the many-body nature of the effect and its tunability with the Fermi energy. Our observation provides basis for future studies on anisotropic many-body phenomena in normal and superfluid phases.

PACS numbers: 03.75.Ss, 37.10.De, 51.60.+a, 67.85.Lm

The Fermi-liquid theory, formulated by Landau in the late 50's, is one of the most powerful tools in modern condensed-matter physics [1]. It captures the behavior of interacting Fermi systems in the normal phase, such as electrons in metals and liquid ^{3}He [2]. Within this theory the interaction is accounted by dressing the fermions as *quasi-particles* with an effective mass and an effective interaction. The ground state is the so-called *Fermi sea*, in which the quasi-particles fill one-by-one all the states up to the Fermi momentum, k_{F}. The Fermi surface (FS), which separates occupied from empty states in k-space, is a sphere of radius k_{F} for isotropically interacting fermions in uniform space. The FS is crucial for understanding system excitations and Cooper pairing in superconductors. When complex interactions act, the FS can get modified. For instance, strongly-correlated electron systems violates the Fermi-liquid picture, giving rise to a deformed FS, which spontaneously breaks the rotational invariance of the system [3]. Symmetry-breaking FSs have been studied in connection with electronic liquid crystal phases [4] and Pomeranchuk instability [5] in solid state systems. Particularly relevant is the nematic phase, in which anisotropic behaviors spontaneously emerge and the system acquires an orientational order, while preserving its translational invariance. This exotic phase has recently been observed by transport and thermodynamics studies in ruthenates [6], in high-transition-temperature superconductors such as cuprates [7], and in other systems [3].

A completely distinct approach to study FSs is provided by ultracold quantum gases. These systems are naturally free from impurities and crystal structures, realizing a situation close to the ideal uniform case. Here, the shape of the FS can directly reveal the fundamental interactions among particles. Studies of FSs in strongly interacting Fermi gases have been crucial in understanding the BEC-to-BCS crossover, where the isotropic s-wave (contact) interaction causes a broadening of the always-spherical FS [8]. Recently, Fermi gases with anisotropic interactions have attracted remarkable attention in the context of p-wave superfluidity [9, 10] and dipolar physics [11]. Many theoretical studies have focused on dipolar Fermi gases, predicting the existence of a deformed FS [12–17]. These studies also include an extension of the Landau Fermi-liquid theory to the case of anisotropic interactions [18]. Despite recent experimental advances in polar molecules and magnetic atoms [19–22], the observation of anisotropic FSs has so far been elusive.

In this letter, we present the direct observation of the deformed FS in dipolar Fermi gases of strongly magnetic erbium (Er) atoms. By virtue of the anisotropic dipole-dipole interaction (DDI) among the particles, the FS is predicted to be deformed into an ellipsoid, reflecting the underlying symmetry of the interaction for polarized gases. To minimize the system's energy, the FS elongates along the direction of the maximum attraction of the DDI, where the atomic dipoles have a 'head-to-tail' orientation. To understand the origin of the Fermi surface deformation (FSD), one has to account for both the mechanical action of the DDI in k-space and the Pauli exclusion principle, which imposes the many-body wave-function to be anti-symmetric. In the Hartree-Fock formalism, the FSD comes from the exchange interaction among fermions, known as the Fock term ([12, 16] and Supplementary Materials). Our observations agree very well with parameter-free calculations based on the Hartree-Fock theory [12, 15, 17]. We demonstrate that the degree of deformation, related to the *nematic susceptibility* in the liquid-crystal vocabulary, can be controlled by varying the Fermi energy of the system and vanishes at high temperatures.

Our system is a single-component quantum degenerate dipolar Fermi gas of Er atoms. Like other lanthanoids, a distinct feature of Er is its large permanent magnetic dipole moment μ (7 Bohr magneton), entailing the strong DDI among the fermions. Similarly to our previous work [22], we take advantage of elastic dipole-dipole collisions to drive efficient evaporative cooling in spin-polarized fermions. The sample is confined into a three-dimensional optical harmonic trap and typically contains 7×10^4 atoms at a temperature of $0.18(1)\,T_F$ with $T_F = 1.12(4)\,\mu$K (Supplementary Materials). We control the alignment of the magnetic dipole moments by setting the orientation of an external polarizing magnetic field. The quan-

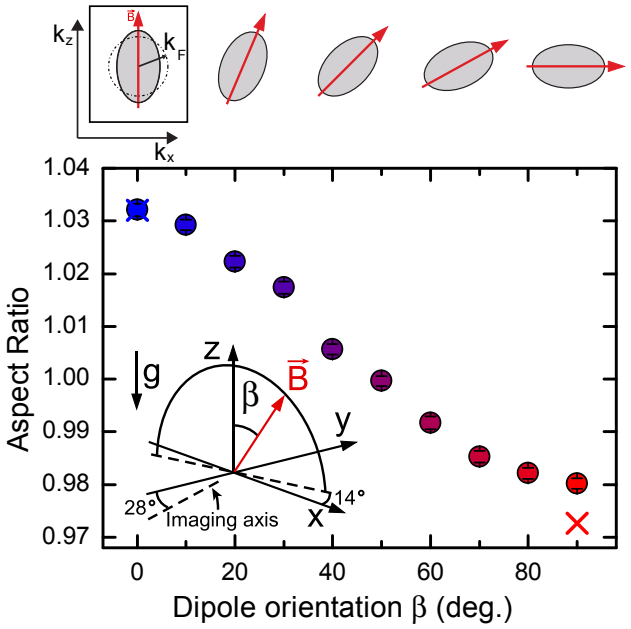

FIG. 1: (color online) AR of an expanding dipolar Fermi gas as a function of the angle β. In this measurement, the trap frequencies are $(f_x, f_y, f_z) = (579, 91, 611)$ Hz. The data are taken at $t_{\mathrm{TOF}} = 12$ ms. Each individual point is obtained from about 39 independent measurements. The error bars indicate the standard errors of the mean. For comparison, the calculated values are also shown for 0° and 90° (crosses). The inset schematically illustrates the geometry of the system. Gravity is along the z direction. The atomic cloud is imaged with an angle of 28° with respect to the y axis (Supplementary Materials). The magnetic field orientation is rotated on the plane with an angle of 14° with respect to the xz plane. Schematic illustrations of the deformed FS are also shown above the panel. Here, the Fermi momentum for an ideal Fermi gas is shown as k_F.

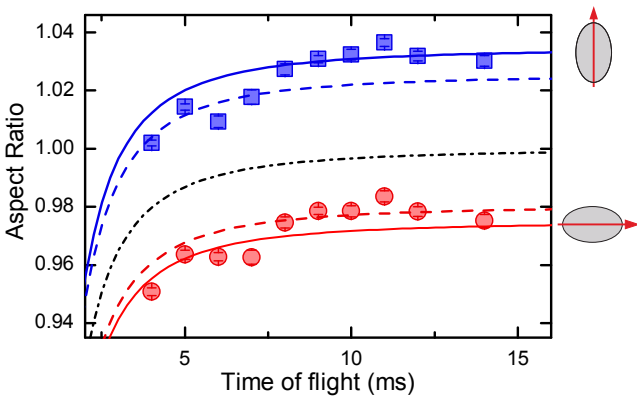

FIG. 2: (color online) Time evolution of the AR of the atomic cloud during the expansion. Measurements are performed for two dipole angles, $\beta = 0^\circ$ (squares) and $\beta = 90^\circ$ (circles) under the same conditions as in Fig. 1. The error bars are standard errors of the mean of about 17 independent measurements. The possible origin of the fluctuations in the AR is carefully discussed in the Supplementary Materials. The theoretical curves show the full numerical calculations (solid lines), which include both the FSD and the NBE effects, and the calculation in the case of ballistic expansions (dashed lines), i. e. in the absence of the NBE effect. For comparison, the calculation for a non-interacting Fermi gas is also shown (dot-dashed line).

tity β symbolizes the angle between the magnetic field and the z axis (inset Fig. 1).

To explore the impact of the DDI on the momentum distribution, we perform time-of-flight (TOF) experiments. Since its first use as "smoking-gun" evidence for Bose-Einstein condensation [23, 24], this technique has proved its power in revealing many-body quantum phenomena in momentum space [8, 25]. TOF experiments are based on the study of the expansion dynamics of the gas when released from a trap. For sufficiently long expansion time, the size of the atomic cloud is dominated by the velocity dispersion and, in the case of ballistic (free) expansions, the TOF images purely reflect the momentum distribution in the trap.

In our experiment, we first prepare the ultracold Fermi gas with a given dipole orientation and then we let the sample expand by suddenly switching off the optical dipole trap (ODT). From the TOF images, we derive the cloud aspect ratio (AR), which is defined as the ratio of the vertical to horizontal radius of the cloud in the imaging plane (Supplementary Materials). Figure 1 shows the AR for various values of β. For vertical orientation ($\beta = 0^\circ$), we observe a clear deviation of the AR from unity with a cloud anisotropy of about 3 %. TOF images show that the cloud has an ellipsoidal shape with elongation in the direction of the dipole orientation. When changing β, we observe that the cloud follows the rotation of the dipole orientation, keeping the major axis always parallel to the direction of the maximum attraction of the DDI. In a second set of experiments, we record the time evolution of the AR during the expansion for $\beta = 0^\circ$ and $\beta = 90^\circ$ (Fig. 2). For both orientations, the AR differs from unity at long expansion times. Our results are strikingly different from the ones of conventional Fermi gases with isotropic contact interactions, in which the FS is spherical (AR $= 1$) and the magnetic field orientation has no influence on the cloud shape.

The one-to-one mapping of the original momentum distribution in the trap and the density distribution of the cloud after long expansion time strictly holds only in the case of pure ballistic expansions. In our experiments, the DDI is acting even during the expansion and could potentially mask the observation of the FSD. We evaluate the effect of the non-ballistic expansion (NBE) by performing numerical calculations based on the Hartree-Fock mean-field theory at zero temperature and the Boltzmann-Vlasov equation for expansion dynamics [15, 17] (Supplementary Materials). In Fig. 2, the theoretical curves do not have any free parameter and are calculated both in presence (solid lines) and absence (dotted lines) of the NBE effect. We observe an excellent agreement between experiment and theory, showing that our model accurately describes the behavior of the system. In addition, the comparison between ballistic and non-ballistic expansion

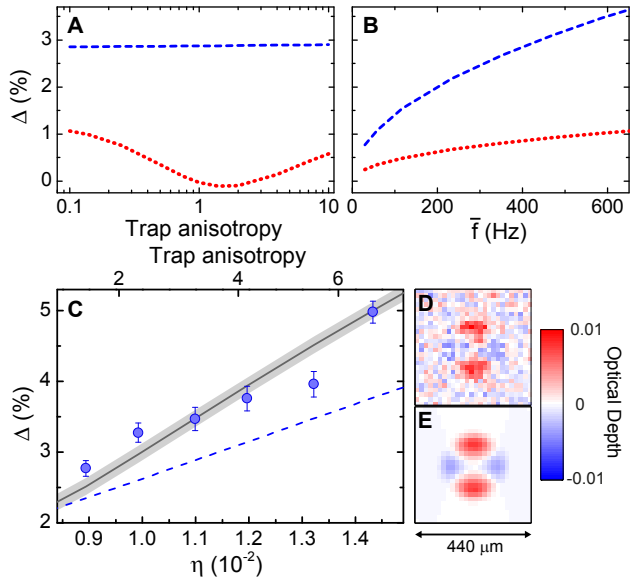

FIG. 3: (color online) Δ for various trap geometries. We consider a cigar-shaped trap with $f_x = f_z$ in the calculations and show the behaviors of the FSD (dashed lines) and the NBE (dotted lines) separately as a function of the trap anisotropy $\sqrt{f_x f_y}/f_z$ at $\bar{f} = 400\,\mathrm{Hz}$ (A) and as a function of $\bar{f}$ at $\sqrt{f_x f_y}/f_z = 5$ (B). (C) Experimentally observed Δ at $t_{\mathrm{TOF}} = 12\,\mathrm{ms}$ are plotted as a function of η, together with the full calculation (solid line) and the calculation considering only FSD (dashed line). The shaded area shows the uncertainty originating from the uncertainty in determining η in our experiments. The sample contains 6×10^4 atoms at a typical temperature of $T/T_F = 0.15(1)$. The error bars represent standard errors of the mean of about 15 independent measurements. The variation of the trap anisotropy in the experiment is indicated in the top axis. Visualization of the FSD at $\eta = 0.009$ from the experimental TOF image (D) and from the fitted image (E).

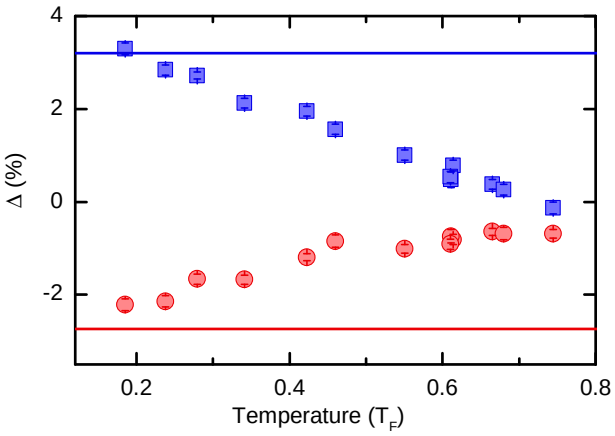

FIG. 4: (color online) Δ as a function of the temperature of the cloud. Measurements are performed for two dipole angles, $\beta = 0^\circ$ (squares) and $\beta = 90^\circ$ (circles) under the same conditions as in Fig. 1. The error bars are standard errors of the mean of about 26 independent measurements. The solid lines show the numerically calculated values at zero temperature for $\beta = 0^\circ$ and $\beta = 90^\circ$.

reveals that the latter plays a minor role in the final AR, showing that the observed anisotropy dominantly originates from the FSD.

Theoretical works have predicted that the degree of deformation depends on the Fermi energy and the dipole moment [12, 14–18]. In the limit of weak DDI, the magnitude of the FSD in a trapped sample is expected to be linearly proportional to the ratio of the DDI to the Fermi energy, $\eta = nd^2/E_F$ [16]. Here, $n = 4\pi(2mE_F/h^2)^{3/2}/3$ is the peak number density at zero temperature with h the Planck constant, m the mass, $d^2 = \mu_0\mu^2/(4\pi)$ the coupling constant for the DDI, and μ_0 the magnetic constant. For a harmonically trapped ideal Fermi gas, the Fermi energy E_F depends on the atom number N and the mean trap frequency $\bar{f} = (f_x f_y f_z)^{1/3}$, $E_F = h\bar{f}(6N)^{1/3}$. Given that $\eta \propto \sqrt{E_F}$, the FSD can be tuned by varying E_F.

To test the theoretical predictions, we first numerically study the degree of cloud deformation Δ, defined as $\Delta = \mathrm{AR} - 1$, as a function of the trap anisotropy, $\sqrt{f_x f_z}/f_y$, and/or $\bar{f}$. To distinguish the effect of the FSD and of the NBE, we keep the two contributions separated in the calculations (Fig. 3A and 3B). Our results clearly convey the following information: (i) the FSD gives the major contribution to Δ, (ii) the FSD is independent from the trap anisotropy, while it increases with $\bar{f}$, (iii) the NBE effect is reminiscent of the trap anisotropy and vanishes for a spherical trap [15].

In the experiment, we explore the dependence of Δ on the trap geometry for $\beta = 0^\circ$ by keeping the axial frequency (f_y) constant and varying the radial frequencies ($f_x = f_z$ within 5 %) (Fig. 3C). This leads to a simultaneous variation of both the trap anisotropy and $\bar{f}$. We observe an increase of Δ with η, which is consistent with the theoretically predicted linear dependence [16].

In analogy with studies in superconducting materials [26], we graphically emphasize the FSD in the measurements at $\eta = 0.009$ by subtracting the TOF absorption image taken at $\beta = 90^\circ$ from the one at $\beta = 0^\circ$ (Fig. 3D). The resulting image exhibits a clover-leaf-like pattern, showing that the momentum spread along the orientation of the dipoles is larger than in the other direction. For comparison, the same procedure is applied for images obtained by a fit to the observed cloud (Fig. 3E). At $\eta = 0.009$, the trap anisotropy is so small that the NBE effect is negligibly small and the deformation is caused almost only by the FSD.

Finally, we investigate the temperature dependence of Δ (Fig. 4). We prepare samples at various temperatures by stopping the evaporative cooling procedure at various points. The final trap geometry is kept constant. When reducing the temperature, we observe the emergence of the FSD, which becomes more and more pronounced at low temperatures and eventually approaches the zero-temperature limit. The qualitative behavior of the observed temperature dependence is consistent with a theoretical result at finite temperatures [16], although further theoretical developments are needed for a

more quantitative comparison.

Our observation clearly shows the quantum many-body nature of the FSD and sets the basis for future investigations on more complex dipolar phenomena, including collective excitations [15, 17, 27, 28] and anisotropic superfluid pairing [29, 30]. Taking advantage of the wide tunability of cold atom experiments, dipolar Fermi gases are ideally clean systems for exploring exotic and topological phases in a highly controlled manner [11].

We are grateful to A. Pelster, M. Ueda, M. Baranov, R. Grimm, T. Pfau, B. L. Lev, and E. Fradkin for fruitful discussions. This work is supported by the Austrian Ministry of Science and Research (BMWF) and the Austrian Science Fund (FWF) through a START grant under Project No. Y479-N20 and by the European Research Council under Project No. 259435. K. A. is supported within the Lise-Meitner program of the FWF.

Supplementary Materials

Experimental setup

We obtain a quantum gas of fermionic ^{167}Er atoms via laser cooling in a narrow-line magneto-optical trap [31] followed by evaporative cooling in an ODT [22]. The sample is trapped in a crossed ODT consisting of a horizontally (y axis) and a vertically (z axis) propagating beam at 1570 nm. The beam waist of the horizontal beam is 15 μm, while the one of the vertical beam is tuned in a range from 20 μm to 90 μm to vary the trap geometry from a nearly spherical shape to a nearly cigar shape. During the entire experimental procedure, the fermions are fully polarized into the lowest hyperfine sublevel $|F = 19/2, m_F = -19/2\rangle$, where F is the total angular momentum quantum number and m_F is its projection along the quantization axis. For maintaining the spin polarization of the trapped sample, we apply an external magnetic field of 0.58 G. At this field value, we do not observe any influence of Feshbach resonances [32]. The magnetic field orientation is controlled with two sets of coils. During evaporative cooling, the magnetic field is vertically oriented ($\beta = 0^\circ$). For imaging, we rotate the magnetic field orientation to the direction of the imaging axis to attain a maximum optical depth.

Measurement of the AR

We measure the deformation of the cloud shape in TOF absorption images by using a standard poly-logarithmic fit for the integrated density distribution of an ideal Fermi gas [33–35]

$$n(X,Z) = B\mathrm{Li}_2\left(-\zeta\exp\left(-\frac{(h-h_0)^2}{2\sigma_h^2} - \frac{(z-z_0)^2}{2\sigma_z^2}\right)\right) \quad (1)$$

where Li_n is the n-th order poly-logarithmic function, ζ is the fugacity, h and z indicate horizontal and vertical coordinates on the imaging plane, respectively, h_0 and z_0 are the positions, and σ_h and σ_z are the radii. We define the AR of the observed cloud as σ_z/σ_h. The imaging axis has an angle of 28° with respect to the y axis (inset Fig. 1) and thus the horizontal radius in the imaging plane σ_h is related to the radii in the x and y directions, σ_x, σ_y, by

$$\sigma_h = \sqrt{\sigma_x^2\cos^2(28^\circ) + \sigma_y^2\sin^2(28^\circ)} \quad (2)$$

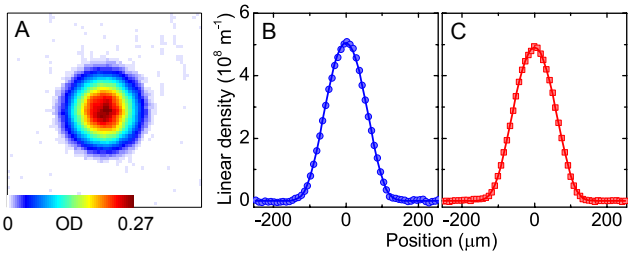

FIG. 5: (color online) Time-of-flight absorption image (A) and its integrated profiles in the horizontal (B) and vertical (C) directions. The image corresponds to the measurement at $\beta = 0^\circ$ in Fig. 1 and is averaged over 39 independent measurements. The integrated profiles of the fit with a poly-logarithmic function are shown by solid lines. The AR of the cloud is about 1.03.

The fugacity ζ is directly connected to T/T_F through the relation $T/T_F = [-6\times\mathrm{Li}_3(-\zeta)]^{-1/3}$. The optical depth is proportional to N. Although the optical depth is also related to ζ through N and T_F by $T_F = \hbar\bar{f}(6N)^{1/3}/k_B$, we leave both free in the fitting procedure and confirm that they are consistent with each other. Here, we assume that the cloud has a constant fugacity over the entire cloud because the momentum deformation is small. Rigorously speaking, T_F is anisotropic and T is constant over the cloud, and thus ζ should be anisotropic. Dealing with such a distribution is beyond the scope of the present work. Figure 5 shows a typical TOF absorption image and its integrated profiles as well as the integrated profiles of the poly-logarithmic fit. The fit is in excellent agreement with the observed distribution.

By taking the average of about 20 independent measurements, we are able to determine the AR with a typical precision of 0.1 %, corresponding to the standard error of the mean for multiple measurements. In addition, we find six possible sources of systematic errors in the measured AR. (a) Variation in pixel sizes. The variation in pixel sizes over the area of the cloud can introduce a systematic error in the AR. There is no measured data available for our CCD camera (Andor, iXon3). (b) Residual interference fringes. Interference fringes, arising from dusts on the imaging optics, can produce a fixed background pattern on the image. (c) Finite pixel number. The finite number of pixels can limit the resolution of the measurement of the AR, in particular at short TOF. From the TOF measurements shown in Fig. 2, where the position of the atomic cloud varies with TOF by a free fall, we estimate the combined effect of (a), (b), and (c) to be within ± 0.5 %. (d) Error in the fitting procedure. Although our fitting procedure

assuming a constant fugacity may give rise to a systematic error in deriving the AR, it is difficult to quantitatively estimate it owing to the lack of an appropriate model. Investigating this effect will be an important future work. (e) Fluctuations in the magnetic field. The influence of the fluctuation in magnetic field, which results in a fluctuation in the dipole orientation, is negligibly small at $\beta = 0^\circ$ and $\beta = 90^\circ$ ($< 0.05\,\%$ in deformation). (f) Tilt of the camera. Assuming that the camera is aligned perpendicular to the imaging beam path within 1°, we infer that the influence of the tilt of the camera on the AR is negligible ($< 0.02\,\%$).

Physical origin of the deformation of the FS

Within the Hartree-Fock theory for a many-body system, the DDI contributes to the total energy of the system in two distinct ways: the Hartree direct interaction and the Fock exchange interaction [12, 16]. As compared to the case with a non-interacting gas, the Hartree term gives rise to a distortion in position space, whereas the exchange term gives rise to a distortion in momentum space. Previously, magnetostriction in position space was observed in a dipolar BEC of chromium atoms [36]. In a BEC, the Fock term is zero because of the symmetric character of the many-body wave function. In an isotropically interacting Fermi gas, the Hartree and the Fock terms cancel out [12]. The existence of the exchange term in dipolar Fermi gases arises from the combined effect of the DDI and the Pauli exclusion principle. In our expansion measurements, both the Hartree and the Fock terms need to be considered. The first is responsible for the NBE, while the second gives the FSD.

Calculation of the deformation

In the present work, the collision rate associated with universal dipolar scattering [22, 37] is lower than the lowest trap frequency. Therefore, our sample is in the collisionless regime, where the mean free path is longer than the size of the cloud [38]. We describe the trapped dipolar Fermi gas in the collisionless regime in the zero temperature limit with an ansatz that the Wigner distribution function is given as an ellipsoid

$$g(\mathbf{r},\mathbf{k},t) = \Theta\left(1 - \sum_{j=1}^{3} \frac{r_j^2}{R_j^2} - \sum_{j=1}^{3} \frac{k_j^2}{K_j^2}\right) \tag{3}$$

where Θ denotes the Heaviside's step function, and $\mathbf{r}$, $\mathbf{k}$, and t denote coordinate, wave vector, and time, respectively. The parameters R_j and K_j represent the Thomas-Fermi radius and the Fermi momentum in the jth direction, respectively. These parameters are numerically determined by minimizing the total energy in the presence of the DDI. The validity of this approach was numerically confirmed [39]. At equilibrium, the parameters K_j contain the information of the anisotropic FS.

The expansion dynamics is calculated using the Botzmann-Vlasov equation for the Wigner distribution function under the scaling ansatz [40–42]. The scaling parameters, representing variations from the equilibrium condition, are described by a set of coupled time-dependent differential equations. The NBE effect is naturally included in this framework and occurs predominantly within 1 ms after the release from the trap. We numerically solve the equations for the general triaxial geometry, where the trap frequencies in three directions are different and the dipoles are oriented in the direction of one of the trap axes. This reflects our experimental situation at $\beta = 0^\circ$. Although at $\beta = 90^\circ$ the dipole orientation has an angle of 14° with respect to the x axis, we assume that the dipole orientation is parallel to the x axis in our calculation.

We calculate the radii of the cloud on the image plane, taking into account the angle of 28° between the imaging axis and the y axis by using eq. (2). In all our measurements, we observe an asymmetry between $\beta = 0^\circ$ and $\beta = 90^\circ$, i. e. $|\Delta|$ is larger at $\beta = 0^\circ$ than at $\beta = 90^\circ$. We observe this asymmetry also in the subtracted images in Fig. 3D and Fig. 3E as a higher contrast in the vertical direction than in the horizontal direction. This asymmetry is well reproduced by our calculation and is understood as follows. At $\beta = 0^\circ$, the major axis of the ellipsoid is oriented to the z direction and is fully imaged. By contrast, at $\beta = 90^\circ$, the major axis is not perpendicular to the imaging plane and we observe a combined radius between the major and the minor axis of the ellipsoid. Therefore, the observed deformation at $\beta = 90^\circ$ is always smaller than the one at $\beta = 0^\circ$.

Image subtraction for Fig. 3D,E

The image shown in Fig. 3D is obtained as follows. The TOF absorption images from 18 independent measurements are averaged and binned by 2×2 pixels to reduce background noise. This procedure is applied for the measurements at $\beta = 0^\circ$ and $\beta = 90^\circ$. We subtract the image at $\beta = 90^\circ$ from the one at $\beta = 0^\circ$. This image subtraction is very sensitive to the relative position of the clouds on the two images down to a sub-pixel level. We obtain accurate positions of the center of the cloud from the fit and shift the coordinate of the image at $\beta = 90^\circ$ such that the center positions of two images exactly agree. We then apply spline interpolation for the image at $\beta = 90^\circ$ to estimate the optical depth of the cloud at each pixel position in the image at $\beta = 0^\circ$. Unlike the procedure used in Ref. [26], where the anisotropy is extracted by rotating a single image by 90° and subtracting it from the original image, our procedure with two images at two dipole orientations allows us to extract only the anisotropy originating from the DDI.

[1] L. D. Landau and E. M. Lifshitz, *Statistical Physics, Part 2* (Pergamon, Oxford, 1980).
[2] A. J. Leggett, Rev. Mod. Phys. **47**, 331 (1975).
[3] E. Fradkin, S. A. Kivelson, M. J. Lawler, J. P. Eisenstein, and A. P. Mackenzie, Annu. Rev. Condens. Matter Phys. **1**, 153 (2010).
[4] S. A. Kivelson, E. Fradkin, and V. J. Emery, Nature **393**, 550 (1998).
[5] I. I. Pomeranchuk, Sov. Phys. JETP-USSR **8**, 361 (1959).
[6] R. Borzi, S. Grigera, J. Farrell, R. Perry, S. Lister, S. Lee, D. Tennant, Y. Maeno, and A. Mackenzie, Science **315**, 214 (2007).
[7] Y. Ando, K. Segawa, S. Komiya, and A. Lavrov, Phys. Rev. Lett. **88**, 137005 (2002).
[8] S. Giorgini, L. P. Pitaevskii, and S. Stringari, Rev. Mod. Phys. **80**, 1215 (2008).
[9] C.-H. Cheng and S.-K. Yip, Phys. Rev. Lett. **95**, 070404 (2005).
[10] V. Gurarie, L. Radzihovsky, and A. Andreev, Phys. Rev. Lett. **94**, 230403 (2005).
[11] M. A. Baranov, M. Dalmonte, G. Pupillo, and P. Zoller, Chem. Rev. **112**, 5012 (2012).
[12] T. Miyakawa, T. Sogo, and H. Pu, Phys. Rev. A **77**, 061603 (2008).
[13] B. M. Fregoso and E. Fradkin, Phys. Rev. Lett. **103**, 205301 (2009).
[14] B. M. Fregoso, K. Sun, E. Fradkin, and B. L. Lev, New J. Phys. **11**, 103003 (2009).
[15] T. Sogo, L. He, T. Miyakawa, S. Yi, H. Lu, and H. Pu, New J. Phys. **11**, 055017 (2009).
[16] D. Baillie and P. Blakie, Phys. Rev. A **86**, 023605 (2012).
[17] F. Wächtler, A. R. Lima, and A. Pelster, arXiv preprint arXiv:1311.5100 (2013).
[18] C.-K. Chan, C. Wu, W.-C. Lee, and S. Das Sarma, Phys. Rev. A **81**, 023602 (2010).
[19] A. Griesmaier, J. Werner, S. Hensler, J. Stuhler, and T. Pfau, Phys. Rev. Lett. **94**, 160401 (2005).
[20] K. K. Ni, S. Ospelkaus, M. H. G. de Miranda, A. Pe'er, B. Neyenhuis, J. J. Zirbel, S. Kotochigova, P. S. Julienne, D. S. Jin, and J. Ye, Science **322**, 231 (2008).
[21] M. Lu, N. Q. Burdick, and B. L. Lev, Phys. Rev. Lett. **108**, 215301 (2012).
[22] K. Aikawa, A. Frisch, M. Mark, S. Baier, R. Grimm, and F. Ferlaino, Phys. Rev. Lett. **112**, 010404 (2014).
[23] M. H. Anderson, J. R. Ensher, M. R. Matthews, C. E. Wieman, and E. A. Cornell, Science **269**, 198 (1995).
[24] K. Davis, M. Mewes, M. Andrews, N. Van Druten, D. Durfee, D. Kurn, and W. Ketterle, Phys. Rev. Lett. **75**, 3969 (1995).
[25] I. Bloch, J. Dalibard, and W. Zwerger, Rev. Mod. Phys. **80**, 885 (2008).
[26] E. Rosenthal, E. Andrade, C. Arguello, R. Fernandes, L. Xing, X. Wang, C. Jin, A. Millis, and A. Pasupathy, Nat. Phys. **10**, 225 (2014).
[27] M. Babadi and E. Demler, Phys. Rev. A **86**, 063638 (2012).
[28] Z.-K. Lu, S. Matveenko, and G. Shlyapnikov, Phys. Rev. A **88**, 033625 (2013).
[29] L. You and M. Marinescu, Phys. Rev. A **60**, 2324 (1999).
[30] M. A. Baranov, M. S. Mar'enko, V. S. Rychkov, and G. V. Shlyapnikov, Phys. Rev. A **66**, 013606 (2002).
[31] A. Frisch, K. Aikawa, M. Mark, A. Rietzler, J. Schindler, E. Zupanic, R. Grimm, and F. Ferlaino, Phys. Rev. A **85**, 051401 (2012).
[32] A. Frisch, M. Mark, K. Aikawa, F. Ferlaino, J. L. Bohn, C. Makrides, A. Petrov, and S. Kotochigova, Nature **507**, 475 (2014).
[33] M. Inguscio, W. Ketterle, and C. Salomon, eds., *Ultra-cold Fermi Gases* (IOS Press, Amsterdam, 2008), Proceedings of the International School of Physics "Enrico Fermi", Course CLXIV, Varenna, 20-30 June 2006.
[34] B. DeSalvo, M. Yan, P. Mickelson, Y. M. De Escobar, and T. Killian, Phys. Rev. Lett. **105**, 030402 (2010).
[35] M. K. Tey, S. Stellmer, R. Grimm, and F. Schreck, Phys. Rev. A **82**, 011608 (2010).
[36] J. Stuhler, A. Griesmaier, T. Koch, M. Fattori, T. Pfau, S. Giovanazzi, P. Pedri, and L. Santos, Phys. Rev. Lett. **95**, 150406 (2005).
[37] J. L. Bohn, M. Cavagnero, and C. Ticknor, New J. Phys. **11**, 055039 (2009).
[38] C. J. Pethick and H. Smith, *Bose-Einstein condensation in dilute gases* (Cambridge University Press, 2002).
[39] S. Ronen and J. L. Bohn, Phys. Rev. A **81**, 033601 (2010).
[40] D. Guéry-Odelin, Phys. Rev. A **66**, 033613 (2002).
[41] C. Menotti, P. Pedri, and S. Stringari, Phys. Rev. Lett. **89**, 250402 (2002).
[42] H. Hu, X.-J. Liu, and M. Modugno, Phys. Rev. A **67**, 063614 (2003).

Chapter 4

Resonantly interacting lanthanide quantum gases

Ultracold gases owe their success to the high degree of parameter control available in experiments. In particular, a major step forward has been the access of controllable *contact interactions*. Interaction tuning is nowadays a well established tool, which allows to enter various physical regimes. Importantly, contact interaction can be changed from positive to negative values. Repulsive interactions can be crucial to attain stable Bose-Einstein condensates (BEC), and the access of tunable interactions has been necessary to condense e. g. ^{85}Rb [Cor00], ^{133}Cs [Web03], or ^{39}K [Roa07]. Attractive interactions can result in an implosion of the BEC, a so-called *Bosenova*, as beautifully demonstrated with ^{85}Rb [Don01], or allow for the spectacular observation of bright solitons in one-dimensional geometries [Str02, Kha02, Mar13]. The tuning can further be used for periodic modulation of the interaction strength, which enables to access highly correlated states such as matter-wave jets [Cla17], or to mimic occupation-dependent tunneling processes via Floquet engineering in an atomic Bose-Hubbard model [Mei16]. In the case of degenerate Fermi gases, interaction tuning opens the way for studies along the BEC-to-BCS crossover [Ing07].

When dipolar interactions are added to the scenario, tuning of the contact interaction can give rise to even more intriguing scenarios. It is the competition of the isotropic contact interaction with the anisotropic dipolar interaction that can disclose new quantum phases. For dominating attractive dipolar interactions, a d-wave collapse of a BEC of chromium has been observed [Lah08], and with the advent of strongly magnetic lanthanides the formation of quantum droplets, see [Kad16, FB16] and Appendix A.1, or the observation of roton excitations, see Appendix A.3, has been made possible.

The list of observations, which is far from being complete, relies on the experimental control of the s-wave scattering length a_s, which is directly proportional to the isotropic contact interaction. Its tunability is based on the existence of *Feshbach resonances* (FRs), which arise when a molecular state is brought into resonance with the two-body scattering state. The resonantly enhanced coupling can strongly change the scattering behavior [Chi10]. The availability of FRs crucially depends on the employed atomic species and isotope. To access physical phenomena as discussed above, it is thus from prime importance to acquire knowledge on the Feshbach spectrum of the specific atomic species. In the case of alkali atoms, Feshbach spectra are rather dilute, i. e. the density of FRs is low. Further, theoretical

calculation, based on coupled-channel models and predicted interaction potentials, provide good expectations of resonance positions and enable to assign specific resonances to single molecular states. The story changes drastically for the case of lanthanide atoms with anisotropic interactions where a very high density of resonances is encountered [Fri14b, Bau14]. This high density is explained by a large number of molecular states that contribute to the atomic scattering process. A strong coupling between many different molecular states greatly challenges theoretical models and so far a direct assignment of the entire observed Feshbach spectra is absent.

Beside the application of interaction tuning, FRs allow to access molecular bound states and to form molecules out of two free atoms. With the platform of cold and ultracold molecules exciting physics becomes available, ranging from chemical reactions and collisional studies, over precision measurements of fundamental constants, up to the creation of new quantum phases or quantum information and simulation applications; for a review see e. g. Ref. [Car09]. A routinely used method for molecule creation uses an adiabatic sweep of the molecular channel across the two-atom scattering channel. The resonant channel-channel interaction results in an avoided crossing, enabling association of so-called *Feshbach molecules*. Initially, molecules have been formed out of single atomic species [Reg03, Cub03, Joc03a, Str03, Her03]. Molecule-creation methods have been further utilized for the successful creation of heteronuclear molecules [Osp06], and can also be applied to magnetic atoms.

This chapter is dedicated to resonantly interacting dipolar quantum gases. In Sec. 4.1 we will give the framework for Feshbach resonances and discuss the emergence of FRs in magnetic lanthanides. Our publication on the emergence of quantum chaos in lanthanides is covered in Sec. 4.3. Section 4.2 reviews the creation of ultracold molecules, and finally, Sec. 4.4 contains our publication on the creation of Feshbach molecules of bosonic erbium atoms at low magnetic field values. Our measurements of the molecules' magnetic moment prove to be key for the assignment of specific FRs in lanthanides with anisotropic interactions.

4.1. Quantum chaos in lanthanides

4.1.1. Feshbach resonances

In Sec. 3.1 we have seen that in ultracold experiments the two-body scattering behavior can be captured within a simple description. For isotropically interacting bosons, the interaction is described by s-wave scattering and quantified via the s-wave scattering length a_s. This simple description does not come without surprises, as in principal the interaction of two particles is determined by their interaction potential, i. e. the Born-Oppenheimer potential, which can have a complicated form [Chi10]. However, at ultralow temperatures T the thermal de Broglie wavelength $\lambda_\mathrm{dB} \propto T^{-1/2}$ has a large extension, and hence the real shape of the short-range interaction potential becomes irrelevant. Indeed, it is only necessary to know the impact of the underlying potential on the scattering wave at large interatomic separation $\mathbf{R}$. The real interatomic potential can then be replaced by a spherically symmetric

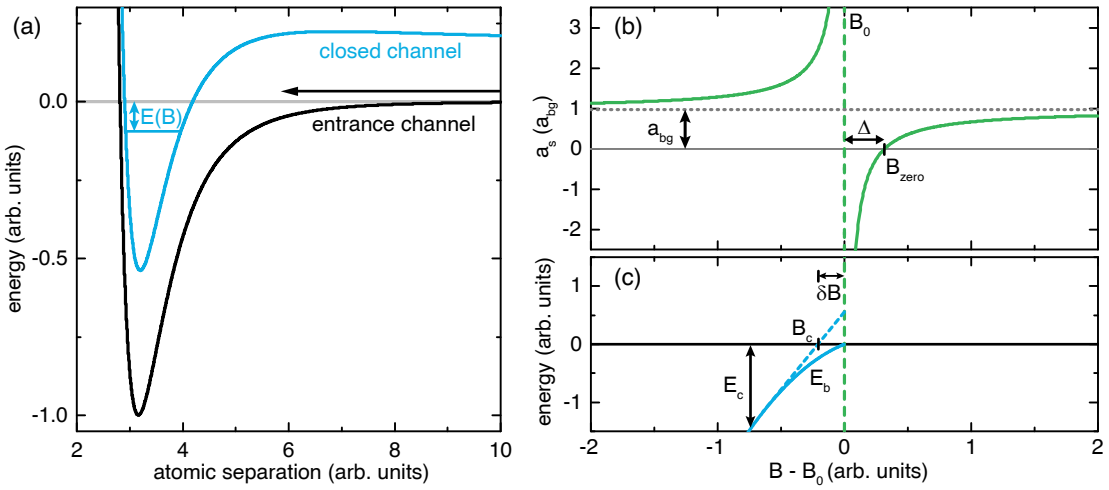

Figure 4.1.: FR in a two-channel model (a) The energy $E(B)$ of a molecular bound state can be tuned by a magnetic field B such that a resonant coupling to the entrance channel of two scattered atoms arises. At the atomic threshold a FR appears. (b) In the vicinity of such a FR the interparticle scattering length a_s diverges. The width Δ of the resonance is defined by the magnetic field separation between the pole at B_0 and the zero crossing of a_s at B_zero. Away from resonance the scattering length approaches the background value a_bg. (c) At the pole position the molecular state (blue) resonantly couples to the two-body entrance channel (black). In the universal regime, see text, due to the coupling between the states, the bound states' energy evolves quadratically, while it evolves linearly further away from the resonance.

pseudopotential with the same effective interaction

$$U_\mathrm{c}(\mathbf{R}) = \frac{4\pi\hbar^2}{m} a_\mathrm{s} \delta(\mathbf{R}) \tag{4.1}$$

where m is the particle mass, $\delta(\mathbf{R})$ the Dirac delta function, and a_s the remaining relevant parameter. A positive a_s results in a repulsive interaction while a negative a_s leads to an attractive interaction.

To understand the concept of FRs, we have to add the internal structure of the collision partners to the description. Due to the e. g. atomic Zeeman structure, different internal Zeeman states become available, resulting in additional molecular potentials as exemplified in Fig. 4.1(a). For large separation $\mathbf{R}$, these potential connect to two free atoms of the corresponding spin states. The scattering behavior of two atoms that approach each other in the lowest energy channel, the so-called *entrance channel*, dramatically depends on the coupling to a molecular level within the other scattering potential, the so-called *closed channel*. In particular, when the molecular bound state of the closed channel energetically approaches the two-body atomic threshold, the coupling becomes resonantly enhanced and the two channels strongly mix. As a result of this strong mixing, a FR emerges and the interparticle interaction diverges. In order to tune the energy of the bound state, $E(B)$, with respect to the atomic threshold, the states need to feature a differential magnetic moment $\delta\mu$[1], as to allow tuning via the bias magnetic field B.

[1] The differential magnetic moment is defined via $\delta\mu = 2\mu_\mathrm{a} - \mu_\mathrm{m}$. Here, μ_a and μ_m denote the magnetic moment of the free atom and the bound molecule, respectively.

Surprisingly, despite the complex underlying process for the emergence of FRs, the dependence of the scattering length a_s on the magnetic field takes the simple expression [Chi10]

$$a_s(B) = a_{bg}\left(1 - \frac{\Delta}{B - B_0}\right), \tag{4.2}$$

see Fig. 4.1(b), with a_{bg} denoting the background scattering length away from resonance, B_0 determining the resonance position, and Δ defining the resonance width. The coupling strength between the entrance and the closed channel affects the resonance width as well as the resonance position $B_0 = B_c + \delta B$, see Fig. 4.1(c). Close to the atomic threshold the coupling results in an avoided crossing, leading to a bending of the energy of the molecular state. In this *universal* regime the s-wave scattering length particularly proves its importance as it solely determines the binding energy of the crossing molecular state

$$E_b = \frac{\hbar^2}{2m_r a_s^2}, \tag{4.3}$$

with m_r being the reduced mass, see Sec. 3.1.2. The binding energy is defined to be a positive value [Chi10]. Away from resonance, the binding energy shows a linear dependence on B and is given by

$$E_c = \delta\mu(B_0 - B). \tag{4.4}$$

As we have seen, FRs arise if a coupling between the entrance and the closed channel is present. This coupling is a result of the underlying interactions [Chi10]. For broad FRs, typically electronic interactions, consisting of exchange interaction at short range and the van der Waals interaction potential $V_{vdW} = -C_6/R^6$ at long range, are responsible for the coupling. Here, C_6 is the isotropic van der Waals coefficient. Due to the isotropy of this interaction, the angular momentum quantum number l is preserved and for an s-wave entrance channel only s-wave closed channels can be coupled, i. e. molecular states without rotation. To access molecular levels with $\Delta l \neq 0$, additional interactions such as spin-spin dipole or second-order spin-orbit interactions are required. Those interactions can couple partial waves with $\Delta l = 2$ and give rise to e. g. d-wave and g-wave resonances, which are typically narrow. In lanthanides that feature an anisotropic van der Waals potential more exotic couplings arise as will be discussed below.

To distinguish between broad and narrow resonances, it is convenient to define the dimensionless resonance strength parameter[2] [Chi10]

$$s_{res} = \frac{a_{bg}\delta\mu\Delta}{\bar{a}\bar{E}}. \tag{4.5}$$

Here,

$$\bar{a} = 0.955978R_{vdW} \text{ with } R_{vdW} = \frac{1}{2}\left(\frac{2m_r C_6}{\hbar^2}\right)^{1/4} \tag{4.6}$$

and

$$\bar{E} = 1.09422E_{vdW} \text{ with } E_{vdW} = \frac{\hbar^2}{2m_r}\frac{1}{R_{vdW}^2} \tag{4.7}$$

[2] We note that an alternative method to determine the strength of a FR is given by the length parameter $R^* = \hbar^2/(2m_r a_{bg}\delta\mu\Delta)$, see Ref. [Pet04a].

define the relevant length and energy scales of the underlying van der Waals potential. For $s_{\mathrm{res}} \gg 1$ the resonance is called entrance-channel dominated while for $s_{\mathrm{res}} \ll 1$ it is called a closed-channel dominated resonance. Typically, this is related to broad and narrow widths Δ, respectively. For closed-channel dominated resonances a universal bound state only extends over a small fraction of Δ, imposing challenges on the experimental access of the universal regime.

4.1.2. Feshbach spectrum of lanthanides

In stark contrast to alkali atoms, in lanthanide atoms orbital anisotropy can be found. This is a consequence of a submerged shell structure, see Sec. 2.2.1, and results in an anisotropic van der Waals potential, see Refs. [Kot11, Kot14]. This additional anisotropy gives qualitatively new possibilities for the coupling to molecular bound states, and hence strongly influences the Feshbach spectrum. Before we turn to the theoretical description of Feshbach spectra in lanthanides with anisotropic interactions, we will briefly review the experimental study of FRs with magnetic atoms.

The first element used for investigations of the magnetic dipole-dipole interaction (DDI) in the ultracold regime has been chromium, which features a magnetic moment of $6\,\mu_{\mathrm{B}}$. Measurements of the Feshbach spectrum of ^{52}Cr in the stretched state $m_j = -3$ [Wer05] have revealed a density of ≈ 0.02 resonances per gauss, see Fig. 4.2(a). Chromium has a zero nuclear spin and hence hyperfine interaction is absent. As a result, isotropic electronic interactions can only couple molecular states that have the same magnetic moment as the free atom entrance channel. In such a scenario, a tuning of the bias magnetic field B does not change the relative energy $E(B)$, see Fig. 4.1, and no FRs would appear. The observed resonances in ^{52}Cr are thus a result of first- and second-order spin-spin dipole interactions, which are 36 times stronger than in alkali-metal atoms.

An additional class of magnetic atoms has become available in experiments with the creation of ultracold atomic clouds of dysprosium and erbium. The first investigation of their Feshbach spectra has been performed by our group with bosonic ^{168}Er in a magnetic field range of 0–3 G [Aik12]. Feshbach resonances have been observed via increased three-body loss in the vicinity of the resonance. Remarkably, already in this small field region six FRs have been identified, which pointed towards a high density of resonances in magnetic lanthanides. A more detailed study for two bosonic and one fermionic isotopes of erbium in a large magnetic field range [Fri14b], see also Fig. 4.2(b), and three bosonic and one fermionic isotopes of dysprosium in a smaller magnetic field range [Bau14] followed shortly after by our group and the group of Benjamin Lev, respectively. Both experiments confirmed the initial work and revealed for the bosonic isotopes a density of resonances in the order of 3 per gauss, a value previously unseen for elements in the ultracold regime. The fermionic isotopes exhibit an even higher density with ≈ 27 and ≈ 11 resonances per gauss for ^{167}Er and ^{161}Dy, respectively.

Remarkably, for erbium a two orders of magnitude higher density of FRs is observed when compared to the spectrum of chromium, see Fig. 4.2. Both elements feature DDI that couples partial waves with $\Delta l = 2$. In addition, for erbium the anisotropic dispersion relation allows

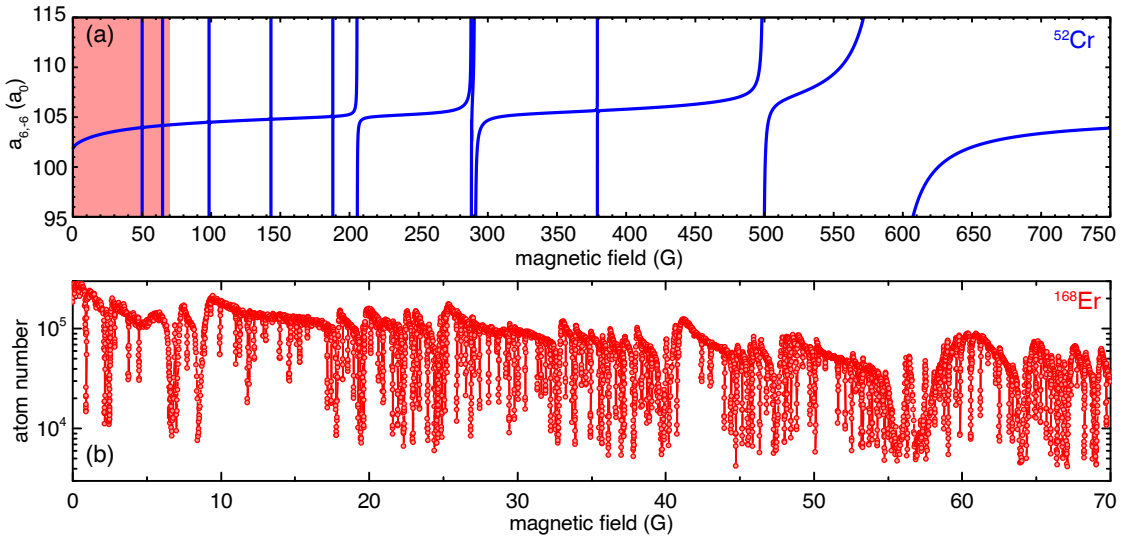

Figure 4.2.: Feshbach spectrum of chromium (a) and erbium (b). (a) Calculated scattering length based on experimental Feshbach spectroscopy for ^{52}Cr in the lowest Zeeman state $m_j = -3$ as a function of the magnetic field. Figure adapted from Ref. [Wer05] (b) Feshbach spectrum for ^{168}Er in the lowest Zeeman state $m_j = -6$ within a magnetic field region as indicated by the red shading in (a). Every loss feature corresponds to a FR. Figure adapted from Ref. [Fri14b].

to couple rotational states with $\Delta l = 4$. Moreover, as a consequence of the large angular momentum quantum number j of bosonic erbium atoms, a large number of $(j+1)^2 = 49$ gerade molecular Born-Oppenheimer potential exist in the lowest Zeeman state. Those potentials provide a significant amount of molecular bound states that can be coupled, giving an intuition for the observed high density of FRs.

To understand the experimental observations in more detail, theoretical models based on coupled-channel calculation can be applied. Reference [Pet12] has studied the Feshbach spectrum of dysprosium by taking into account the Zeeman, the magnetic dipole-dipole $V_{\mu\mu} \propto 1/R^3$, the electrostatic isotropic and anisotropic dispersion $V_{\text{disp}} \propto 1/R^6$, and the weak quadrupole-quadrupole $V_{\text{qq}} \propto 1/R^5$ interaction. The different anisotropies contribute differently to the coupling of rotational states, as can be seen in Fig. 4.3(a). When all interactions are included, the highest amount of resonances appears (upper panel), where a lower number of resonances is present when either the anisotropic V_{disp} (middle panel) or $V_{\mu\mu}$ (lower panel) are excluded. A similar behavior is found for erbium, see Ref. [Fri14a]. Still, the experimentally observed density of FRs has not been captured by the theoretical study of Ref. [Pet12].

Interestingly, the amount of resonances depends strongly on how many molecular states, i. e. states with rotational quantum numbers l, are included into the theory, a scenario that cannot be observed for collisions of alkali-metal atoms or chromium. The more higher partial wave states are added, the more resonances appear, which suggests that the different partial waves are strongly mixed. Indeed, it has been shown that the experimentally observed density of resonances can only be reproduced if partial waves up to $l = 40$ are included, see Fig. 4.3(b). The even higher density observed for fermionic erbium and dysprosium is a result of the additional hyperfine structure that leads to an increased number of possible

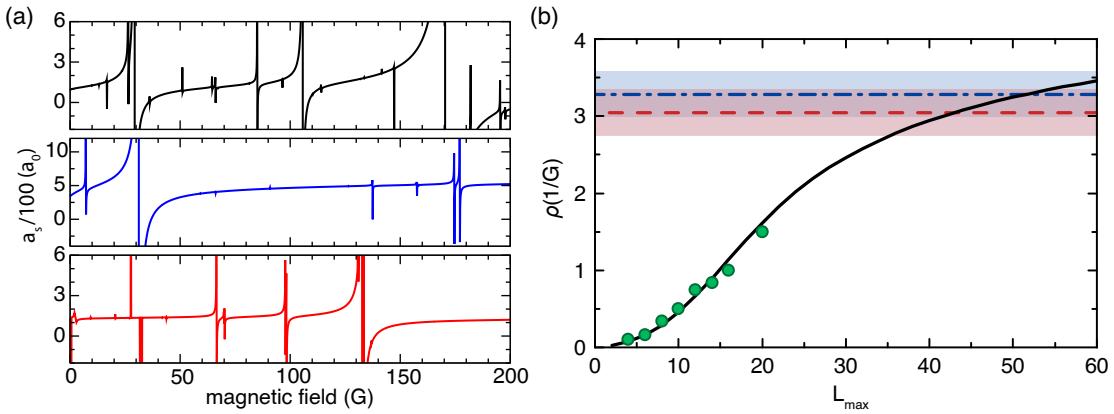

Figure 4.3.: Interaction and partial wave contributions to the Feshbach spectrum of lanthanides (a) Calculated scattering length for ^{164}Dy in the lowest Zeeman state $m_j = -8$ as a function of magnetic field with all interactions included (top panel), when the anisotropic dispersion interaction is set to zero (middle panel), and when the dipole-dipole contribution is excluded (lower panel). For the simulation even partial waves up to $L_{\max} = 10$ are taken into account. Figure adapted from Ref. [Pet12] (b) Calculation of the mean resonance density ρ for bosonic erbium when the number of included partial waves $L_{\max}$ is varied. Coupled-channel calculation (green circles) and analytical estimate (black line) are compared to the experimentally measured ρ for ^{168}Er (dashed line) and ^{166}Er (dashed-dotted line). Figure adapted from Ref. [Fri14b].

collisional channels.

Beside that many partial waves contribute to the Feshbach spectrum, the resonance positions also show a significant dependence on the number of included partial waves [Pet12]. As a consequence, the assignment of specific resonances by a single quantum number, as it is typically done for alkalis, is difficult. Hence, a different approach has to be applied to analyze the Feshbach spectrum of lanthanides with anisotropic interactions.

4.1.3. Chaotic scattering

For the analysis of the Feshbach spectra of magnetic lanthanides a statistical method can be utilized. This approach is based on the Random Matrix Theory (RMT), which has been developed by Wigner and Dyson [Wig51, Meh63] and finds applications across various problems, ranging from nuclear physics [Lio72a, Lio72b], to atomic physics [Guh98], towards neural networks [Raj06] or to the context of financial markets [Bou11]. In the case of the scattering of lanthanide atoms with anisotropic interactions, the theory captures the correlation of the individual molecular levels among each other. In brief, the combination of magnetic field and level coupling results in a certain distribution of FRs at the atomic threshold. Hence, the statistical analysis of the nearest-neighbor-spacing (NNS) distribution of the Feshbach spectrum can give insights into the correlations of different channels.

An analysis of bosonic erbium [Fri14b] based on RMT has revealed that a strong level repulsion has to be present[3]. This is e. g. captured by the observed NNS distribution, which shows that the magnetic field distance between neighboring resonances tends to maximize. The distribution is well described by the Brody distribution

$$P_{\mathrm{B}}(s) = b(1+\eta)s^{\eta}\exp\left(-bs^{\eta+1}\right), \tag{4.8}$$

which interpolates between the standard Poisson distribution $P_{\mathrm{P}}(s) = \exp(-s)$ and the Wigner-Dyson distribution $P_{\mathrm{WD}}(s) = \frac{\pi}{2}s\exp(-\pi s^2/4)$. The dimensionless quantity s denotes the level spacing in units of the mean level spacing, η is the single fitting parameter, and $b = [\Gamma(\eta+2)/(\eta+1)]^{\eta+1}$ is a normalization constant where Γ depicts the Gamma function. The observed distribution, matching better to a Wigner-Dyson distribution, is a strong signature of chaotic scattering [Fri14b][4]. The approach utilizing RMT has proven its strength, as it allows to genuinely compare the experimental observation with theoretical calculations without the need of an individual assignment of the resonances. While the work of Ref. [Fri14b] has given beautiful insights into the physical origin of resonant scattering behavior of erbium atoms, it did not tackle the questions if lanthanides with anisotropic interactions show a universal behavior and what is the dominating interaction for the level correlation.

To address such questions we have formed a collaboration between the group of Tilman Pfau in Stuttgart, the group of Svetlana Kotochigova in Philadelphia, and our group in Innsbruck. In our joined effort we have investigated experimentally and theoretically in detail the Feshbach spectrum of erbium and dysprosium atoms in a magnetic field range up to 70 G. Our publication, reported in Sec. 4.3, shows that both, erbium and dysprosium, exhibit a large amount of FRs. The observed densities can be nicely reproduced in theory when including higher partial waves l up to a total $J_{\mathrm{max}} = 39$ and $J_{\mathrm{max}} = 36$, respectively. Further, we theoretically show that a convergence of the resonance position requires $J_{\mathrm{max}} > 22$, disclosing the strong mixing of such partial waves. We reveal that the emergence of chaotic scattering is mainly determined by the anisotropic dispersion interaction and does not depend on the contribution of the anisotropic DDI. Finally, we report on a strong temperature dependence of a significant number of resonances in ^{168}Er, in analogy to previous studies with Dy [Bau14]. We find that this dependency, which cannot be explained by higher-partial wave two-body scattering, can be traced back to the temperature dependence of the recombination rate of three free particles into a resonant trimer state via a d-wave three-atom entrance channel.

4.1.4. Interaction tuning

Beside the high complexity of the Feshbach spectra of lanthanides with anisotropic dispersion interactions, interaction tuning via the s-wave scattering length does become possible if isolated FRs are observed, see Eq. 4.2. In the context of atoms with DDI this gives the possibility to change the relative strength between isotropic and anisotropic interactions.

[3] Reference [Fri14a] gives further details on RMT and its application to the resonant scattering of erbium atoms.

[4] For an introduction to quantum chaos the reader is referred to e. g. Ref. [Jen92].

In recent years, several works have investigated the s-wave scattering length of dipolar lanthanides, both, away and in the vicinity of different FRs. The values of a_s for erbium and dysprosium have been studied via cross-dimensional thermalization experiments in thermal gases [Fri14a, Tan15], via the measurement of the anisotropic thermal expansion of a dipolar Bose gas [Tan16, Luc18], by comparing experimental measurements of the molecular binding energy of dysprosium to a universal model [Mai15], or by comparing theoretical simulations with experimental measurements of the critical atom number of the liquid-to-gas phase transition [Sch16] or the frequency of collective excitations in a dipolar quantum droplet [FB18].

A very precise method to derive s-wave interactions within a broad magnetic field range is based on modulation-spectroscopy in a three-dimensional optical lattice, see Sec. 5.4.1. This method is very successful as demonstrated within this thesis for ^{168}Er, ^{167}Er, and ^{166}Er, see Sec. 5.5, Sec. 5.6, and Appendix A.1, respectively. Our obtained knowledge allows us to precisely tune the atomic interactions in the vicinity of isolated FRs, as needed for the study of dipolar phenomena that emerge from the competition between s-wave and contact interactions, see Appendix A.1 and Appendix A.3, or for reaching the strongly interacting regime of a two-component Fermi gas, see Sec. 5.6.

A further prospect emerging from the observation of isolated FRs is given by the possibility to access ultracold molecules. Details along this line will be discussed in the following section.

4.2. Dipolar Feshbach molecules

4.2.1. Molecule formation

In the vicinity of a FR the coupling between the two-body atomic threshold and the molecular state is strongly enhanced, see Fig. 4.1. As a result, it becomes possible to associate Feshbach molecules out of two free atoms [Köh06]. Further, the strength of the bond, see Eq. 4.4, can be tuned by the magnetic field. For the creation of such molecules, different techniques can be applied. Figure 4.4 gives two examples. The method of magnetic-field modulation allows to directly couple to the bound state, even when the atomic sample is prepared away from the resonance [Tho05], see Fig. 4.4(a). Here, molecule formation is typically observed via a resonant atomic loss feature. By preparing the atoms at various magnetic field values, this method allows to directly map the molecular binding energy as a function of the magnetic field. Hence, it is a convenient method to access the magnetic moment μ_m of a molecular state, see Eq. 4.4.

Another method used for Feshbach molecule creation is based on adiabatic magnetic field sweeps, see Fig. 4.4(b). Two free atoms are prepared above the resonance and when adiabatically ramped across the resonance can follow into the molecular bound state along an avoided crossing. Atom-to-molecule conversion efficiencies are strongly related to the phase-space density n of the atomic sample, the resonance strength, and the magnetic field sweep rate $\dot{B}$ via $na_{bg}\Delta/\dot{B}$ [Hod05]. Initially, such molecule creation has been achieved for

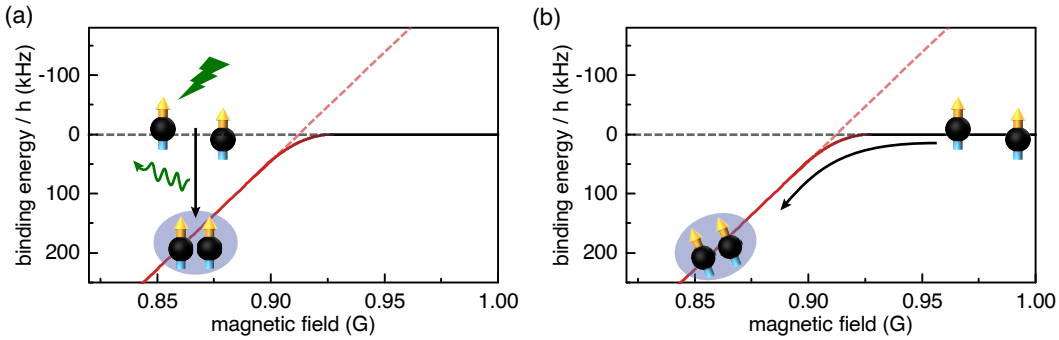

Figure 4.4.: Creation of Feshbach molecules exemplified for ^{168}Er atoms via magnetic-field modulation (a) and magnetoassosciation (b) techniques. (a) The atoms are prepared below the FR. If the energy of an oscillatory magnetic field matches the binding energy, Feshbach molecules are associated. The excess energy is taken away by the modulated field (green arrow). The resonant condition typically is observed via increased loss, triggered by atom-dimer collisions, once the molecules are formed. (b) Adiabatic creation of Feshbach molecules via a magnetic field sweep across the avoided crossing of the free-atom (black line) to the bound state (red line).

^{40}K [Reg03], ^{6}Li [Cub03, Joc03a, Str03], ^{133}Cs [Her03] ^{23}Na [Xu03], and also ^{87}Rb [Dür04], all within one year. Collisional studies revealed a large loss rate of bosonic molecules caused by atom-dimer or dimer-dimer collisions, see e. g. Refs. [Muk04, Chi05, Sya06, Fer10], while molecules formed from two fermionic spin states can remain remarkably stable. This is a result of the Pauli exclusion principle, which suppresses few-body processes of three and more particles [Pet04b]. This collisional stability has paved the way for the creation of molecular BECs out of weakly-bound Feshbach molecules [Joc03b, Gre03].

4.2.2. Polar and dipolar molecules

Molecule creation can also be used to access strongly dipolar systems. Such systems are ideal candidates for e. g. quantum simulation of condensed matter [Bar12]. To realize this systems, different experimental approaches are followed. One approach is based on the production of ground state heteronuclear molecules that exhibit a strong electric dipole moment. After Feshbach association the molecules can be transferred to the rovibrational ground state via an optical *stimulated Raman adiabatic passage* (STIRAP) technique with high conversion efficiencies [Ber98, Vit17]. The access of lower-lying vibrational levels has first been demonstrated with Rb_2 [Win07]. Today, STIRAP is a well established method and has led to the production of rovibrational ground state polar molecules such as KRb [Ni08], RbCs [Tak14, Mol14], NaK [Par15], and NaRb [Guo16], which all posses a tunable electric dipole moment.

A distinct approach towards the goal of ultracold polar molecules, involves the direct cooling of hot molecular samples. For certain molecular species remarkable progress has been made in recent years and laser cooling and magneto-optical trapping have now been demonstrated for polar SrF and CaF molecules [Bar14, Nor16, Tru17, And17, And18]. While temperatures down to milikelvin and submilikelvin already have been reached, further cooling to the ultracold regime remains an outstanding challenge.

A different method to access strongly dipolar interactions is given by elements that intrinsically carry a magnetic dipole moment such as chromium, dysprosium and erbium. When atoms of such elements are bond together to Feshbach molecules, a strong dipolar interactions can be accessed. Remarkably, the dipolar interaction comes for free without the need of bringing the weakly-bound molecules to the rovibrational ground state.

Our publication in Sec. 4.4, a joint effort between the group of Svetlana Kotochigova in Philadelphia, the group of Olivier Dulieu in Orsay, and our group in Innsbruck, reports on the first realization of magnetic dipolar molecules. We create them with strongly magnetic ^{168}Er atoms via the magnetoassociation technique, see Fig. 4.4(b), and explore the magnetic moment of four molecular states by magnetic-field modulation spectroscopy[5], see Fig. 4.4(a). For the strongest dipolar molecule we find $a_{\mathrm{d}} = 1140a_0$, see Eq. 3.3 for the definition of the dipolar length, which exceeds our typical s-wave scattering length by one order of magnitude. Applying a new theoretical approach based on approximate adiabatic potentials allows us, together with the experimental input, to assign the dominant quantum numbers of the investigated molecular states. We prove the dipolarity of the produced molecules via the observation of a reduction of inelastic losses for a perpendicular dipole orientation with respect to the weak confinement axes. Finally, we unveil that the observed ratios of the loss-rate between dominant repulsive and dominant attractive dipolar interactions follow a universal behavior.

Our work sets the start for future investigations with magnetic dipolar molecules. A particularly interesting scenario is given by the creation of fermionic dipolar molecules. In such a system inelastic losses are suppressed by Pauli pressure and the attainment of molecular BECs is accessible, as demonstrated with alkalis [Joc03b, Gre03]. For the fermionic erbium isotope ^{167}Er we already have achieved precise knowledge of the interaction between two spin states along a comparatively broad FR, see Sec. 5.6, which brings the scenario of studies along the BEC-to-BCS crossover with dipolar interactions and the creation of a dipolar molecular BEC at reach.

[5] Magnetic-field modulation spectroscopy more recently has also been applied to detect the molecular binding energy for broad resonances in ^{164}Dy [Mai15] and ^{162}Dy [Luc18].

4.3. Publication: Emergence of Chaotic Scattering in Ultracold Er and Dy[†]

Physical Review X **5**, 041029 (2015)
submitted 7 Jun 2015; published 21 Sep 2015
DOI 10.1103/PhysRevX.5.041029

Thomas Maier,[1] Holger Kadau,[1] M. Schmitt,[1] Matthias Wenzel,[1] Igor Ferrier-Barbut,[1] Tilman Pfau,[1]

[1] *5. Physikalisches Institut and Center for Integrated Quantum Science and Technology, Universität Stuttgart, Pfaffenwaldring 57, 70569 Stuttgart, Germany*

Albert Frisch,[2,3] Simon Baier,[2] Kiyotaka Aikawa,[2] Lauriane Chomaz,[2,3] Manfred J. Mark,[2,3] Francesca Ferlaino,[2,3]

[2] *Institut für Experimentalphysik, Universität Innsbruck, Technikerstraße 25, 6020 Innsbruck, Austria*
[3] *Institut für Quantenoptik und Quanteninformation, Österreichische Akademie der Wissenschaften, 6020 Innsbruck, Austria*

Constantinos Makrides,[4] Eite Tiesinga,[5] Alexander Petrov,[4] and Svetlana Kotochigova[4]

[4] *Department of Physics, Temple University, Philadelphia, Pennsylvania 19122, USA*
[5] *Joint Quantum Institute and Center for Quantum Information and Computer Science, National Institute of Standards and Technology and the University of Maryland, 100 Bureau Drive, Stop 8423, Gaithersburg, Maryland 20899, USA*

[†] The author of the present thesis performed the measurements for erbium together with A. F., and K. A., and contributed in writing the manuscript. The theoretical calculations of this publication have been contributed by C. M., E. T., A. P., and S. K.

Emergence of Chaotic Scattering in Ultracold Er and Dy

T. Maier,[1,*] H. Kadau,[1] M. Schmitt,[1] M. Wenzel,[1] I. Ferrier-Barbut,[1] T. Pfau,[1] A. Frisch,[2,3] S. Baier,[2] K. Aikawa,[2,†] L. Chomaz,[2,3] M. J. Mark,[2,3] F. Ferlaino,[2,3] C. Makrides,[4] E. Tiesinga,[5] A. Petrov,[4,‡] and S. Kotochigova[4]

[1]*5. Physikalisches Institut and Center for Integrated Quantum Science and Technology, Universität Stuttgart, Pfaffenwaldring 57, 70569 Stuttgart, Germany*

[2]*Institut für Experimentalphysik, Universität Innsbruck, Technikerstraße 25, 6020 Innsbruck, Austria*

[3]*Institut für Quantenoptik und Quanteninformation, Österreichische Akademie der Wissenschaften, 6020 Innsbruck, Austria*

[4]*Department of Physics, Temple University, Philadelphia, Pennsylvania 19122, USA*

[5]*Joint Quantum Institute and Center for Quantum Information and Computer Science, National Institute of Standards and Technology and the University of Maryland, 100 Bureau Drive, Stop 8423, Gaithersburg, Maryland 20899, USA*

(Received 7 June 2015; revised manuscript received 21 September 2015; published 19 November 2015)

We show that for ultracold magnetic lanthanide atoms chaotic scattering emerges due to a combination of anisotropic interaction potentials and Zeeman coupling under an external magnetic field. This scattering is studied in a collaborative experimental and theoretical effort for both dysprosium and erbium. We present extensive atom-loss measurements of their dense magnetic Feshbach-resonance spectra, analyze their statistical properties, and compare to predictions from a random-matrix-theory-inspired model. Furthermore, theoretical coupled-channels simulations of the anisotropic molecular Hamiltonian at zero magnetic field show that weakly bound, near threshold diatomic levels form overlapping, uncoupled chaotic series that when combined are randomly distributed. The Zeeman interaction shifts and couples these levels, leading to a Feshbach spectrum of zero-energy bound states with nearest-neighbor spacings that changes from randomly to chaotically distributed for increasing magnetic field. Finally, we show that the extreme temperature sensitivity of a small, but sizable fraction of the resonances in the Dy and Er atom-loss spectra is due to resonant nonzero partial-wave collisions. Our threshold analysis for these resonances indicates a large collision-energy dependence of the three-body recombination rate.

DOI: 10.1103/PhysRevX.5.041029

Subject Areas: Atomic and Molecular Physics, Quantum Physics

I. INTRODUCTION

Anisotropic interactions are a central and modern tool for engineering quantum few- and many-body processes [1]. A prominent example of such an interaction is the long-range dipole-dipole interaction (DDI) acting, for instance, between polar molecules [2], Rydberg atoms [3], or magnetic atoms [4]. Over the years, fascinating quantum effects of the anisotropy have been observed, such as the d-wave collapse of a dipolar Bose-Einstein condensate [5], the deformation of the Fermi surface [6], and the control of stereodynamics in dipolar collisions [7]. Moreover, the DDI is expected to give rise to a plethora of few- and many-body phenomena, which still await observation, such as universal few-body physics [8,9], rotonic features [10,11], two-dimensional stable solitons [12], and the supersolid phase [13].

Recently, atomic species in the lanthanide family became available to the field of ultracold quantum gases. The interaction between magnetic lanthanide atoms, such as Er [14,15] and Dy [16,17], is highly anisotropic. This is not only due to the long-range DDI, originating from their large magnetic moment, but also to the shorter-ranged van der Waals interaction [18], which exhibits anisotropic contributions arising from the large orbital angular momentum of their valence electrons.

For magnetic lanthanides, which also include the successfully laser-cooled elements Ho [19] and Tm [20], the orbital anisotropy is a consequence of a partially filled submerged $4f$ electron shell that underlies a closed outer $6s$ shell. This leads to an electronic ground state with a total atomic angular momentum $\vec{j}$ with $j \gg 1$. Consequently, in

*Corresponding author.
t.maier@physik.uni-stuttgart.de

†Present address: Department of Physics, Graduate School of Science and Engineering, Tokyo Institute of Technology, Meguro-ku, Tokyo 152-8550, Japan.

‡Also at: NRC "Kurchatov Institute" PNPI 188300, Division of Quantum Mechanics, St. Petersburg State University, 198904, Russia.

collisions between such atoms there exist $(j+1)^2$ nondegenerate (gerade) molecular Born-Oppenheimer (BO) potentials and a correspondingly large manifold of collision channels with associated molecular bound states. This is in sharp contrast to the one or two BO potentials encountered in alkaline-earth and alkali-metal atom collisions. In addition, the anisotropy or orientation dependence of the BO potentials strongly mixes collision channels with large relative orbital angular momentum $\vec{\ell}$ between the atoms even for our ultracold collisions with a $\ell = 0$, s-wave initial channel. The complexity of the molecular forces are reflected in a dense spectrum of Fano-Feshbach resonances as a function of magnetic field B, as recently observed in Er [14,21] and Dy [22]. In Er a statistical analysis of the spacings between resonances has shown correlations that revealed chaotic scattering. The data set of the initial Dy experiments was too small to extract statistically significant correlations.

Chaotic behavior is manifest in a variety of complex systems ranging from atomic to nuclear and solid-state physics. In atomic physics, chaos was originally studied with Rydberg states of H and He in a magnetic field [23]. Later on, a variety of more complex atoms and ions in highly excited states showed signatures of chaotic spectral distributions [24]. The origin of chaos in these systems was traced back to a strong mixing of many-electron excited states by the Coulomb interaction [25]. A chaotic level distribution is also common in a variety of solid-state systems ranging from those with strong many-body interactions to the motion of particles in irregular potentials [26,27]. Experiments in nuclear physics [28,29] have also produced substantial evidence for chaotic neutron resonance spectrum fluctuations, which agree with predictions of random matrix theory (RMT). Similar agreement was found from numerical simulations based on nuclear shell models [30,31]. Moreover, Refs. [32,33] suggested that chaos is a generic property of nuclei with multiple degrees of freedom (i.e., multiple active shells), which become completely mixed.

This article describes a joint effort to understand ultracold scattering and Fano-Feshbach spectra of strongly magnetic Er and Dy atoms. In particular, we report on the measurement and statistical analysis of Fano-Feshbach spectra for Dy and Er between $B = 0$ and 70 G at gas temperatures T below and around 1 μK. Here, 1 G = 0.1 mT. We observe that both elements have similar chaotic scattering. We present a RMT-inspired model to gain insight into their statistical properties as well as theoretical evidence based on coupled-channels calculations with a microscopic Hamiltonian that chaotic scattering requires both strong molecular anisotropy and Zeeman mixing to fully develop. Limitations of the RMT are also discussed. Finally, we present experimental data and a comparison to a resonant trimer model to show that our increase in resonance density with temperature is a consequence of the strong collision-energy dependence of transitions from entrance d-wave channels of three free atoms to resonant trimer states.

II. EXPERIMENT

A. Measurement

The experimental study of Fano-Feshbach resonances in Er and Dy is based on high-resolution trap-loss spectroscopy on spin-polarized thermal samples. Ultracold bosonic ^{164}Dy samples are created by direct loading from a narrow-line magneto-optical trap, operating on the 626 nm cycling transition, into a single-beam optical dipole trap (ODT) [34]. By moving the last focusing lens of the ODT, the atoms are transported from the magneto-optical trap chamber to the science cell. The ODT is created with a 100 W fiber laser at a wavelength of 1070 nm. We achieve a transport efficiency close to unity. This fiber laser, however, causes atom loss due to its longitudinal multimode structure [35]. Therefore, we transfer the atoms into a second single-beam ODT, created by a 55 W solid-state laser at a wavelength of 1064 nm. Finally, forced evaporative cooling in a crossed ODT leads to a sample of 10^5 atoms in the energetically lowest Zeeman sublevel, $m_j = -8$ at $T = 600$ nK.

High-resolution trap-loss spectroscopy is performed on a spin-polarized bosonic ^{168}Er sample at $T = 1400$ nK and compares this spectrum with that obtained at a 4 times lower temperature measured in previous work for ^{168}Er as well as for fermionic ^{167}Er [21]. The experimental procedures for creating bosonic and fermionic samples are described in Refs. [14,15], respectively. Bosons (fermions) are prepared in the lowest Zeeman sublevel, $m_j = -6$ ($m_f = -19/2$). Erbium samples are trapped in a crossed ODT and contain about 10^5 atoms.

B. Feshbach spectroscopy

Feshbach spectroscopy is performed in a similar manner for the two species. The magnetic field is ramped up over a few milliseconds to a magnetic-field value B, where the atoms are held in the ODT for 500 ms for Dy, 400 ms for ^{168}Er, and 100 ms for ^{167}Er. During this time, inelastic three-body recombination causes atom loss from the ODT. At resonance, the recombination process is enhanced because of the coupling between the atomic-threshold state and a molecular state leading to a resonant increase of the atom loss. We identify the field locations of maximum loss as the positions of Fano-Feshbach resonances [36]. The atom number is probed by standard time-of-flight absorption imaging at low magnetic field. We record atom-loss features for magnetic-field values between 0 and 70 G in steps of a few mG. Figure 1(a) shows the normalized loss spectrum for the ^{164}Dy isotope, where we identify 309 resonances. For ^{168}Er at $T = 1.4$ μK, there are

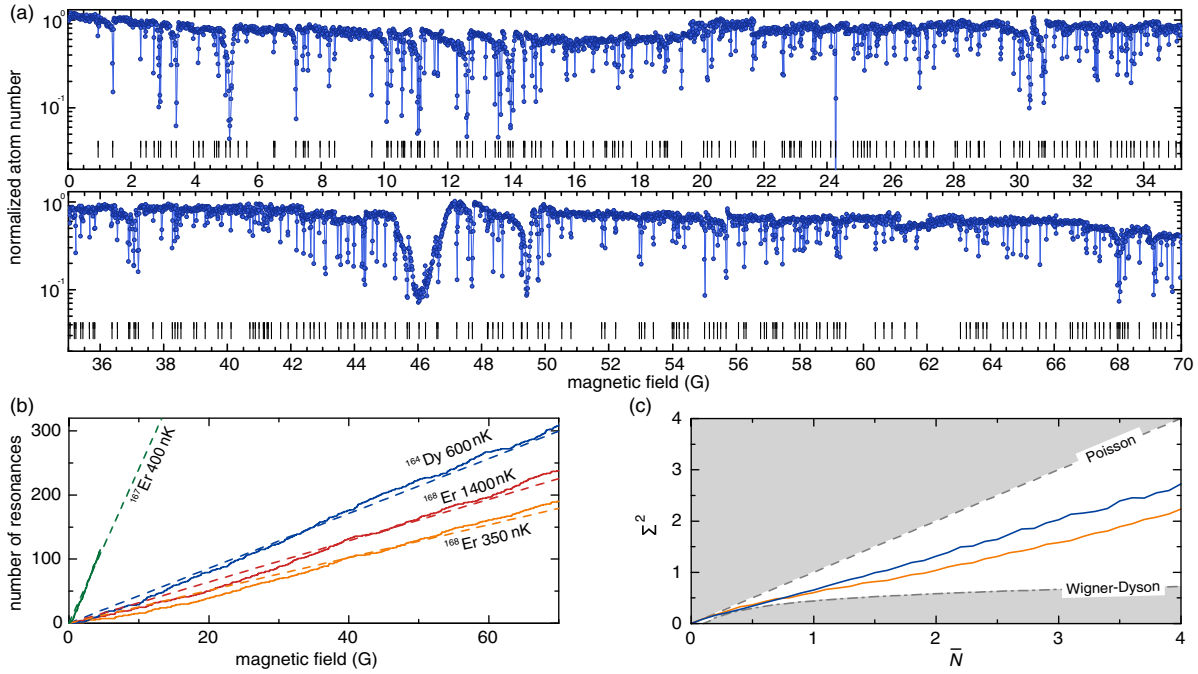

FIG. 1. (a) Trap-loss spectroscopy mapping of the Fano-Feshbach spectrum of ^{164}Dy as a function of magnetic field between $B = 0$ and 70 G with a data point every 14.5 mG and temperature $T = 600$ nK. Each data point is an average of three measurements. (b) Staircase function for the number of resonances as a function of B for ^{164}Dy, ^{168}Er at two temperatures, and fermionic ^{167}Er. Dashed lines are linear fits forced to pass through the origin. Their slopes give a mean density of resonances of $\bar{\rho} = 4.3$ G^{-1} for ^{164}Dy, 2.7 G^{-1} for ^{168}Er at $T = 350$ nK, 3.4 G^{-1} for Er at $T = 1.4$ μK, and 25.6 G^{-1} for ^{167}Er. (c) Number variance of the experimental data as a function of scaled B-field interval $\bar{N} = \Delta B\bar{\rho}$. The experimental data for ^{164}Dy (blue line) and ^{168}Er at $T = 350$ nK (orange line) lie between the variances for an uncorrelated Poisson distribution (dashed line) and the correlated Wigner-Dyson distribution (dot-dashed line).

238 resonances. The Fano-Feshbach scan of fermionic ^{167}Er is carried out from 0 to 4.4 G and yields 115 resonances.

The understanding of the richness of the scattering in Er and Dy requires the development of sophisticated microscopic coupled-channels scattering models. We defer such analysis until later in this paper and first analyze our data following the statistical approach based on the RMT advocated by Ref. [21]. In particular, we study the correlations between resonance locations via the nearest-neighbor spacing (NNS) distribution and set up a RMT-like model, which accounts for the structure of our B-dependent microscopic Hamiltonian, to get intuition about these NNSs. In our description of the coupled-channels calculations, limitations of such a RMT-like model are discussed.

C. Statistical analyses

Our statistical analysis starts with the construction of the staircase function, which is a steplike function that counts the number of resonances below magnetic-field value B [37]. Figure 1(b) shows the staircase function for Dy and Er. For both species the function is well fit by a linear curve forced to pass through the origin. Its slope $\bar{\rho}$ corresponds to the density of resonances. Deviations below and above the fit occur for small and large B, respectively. The fitted resonance densities are given in the caption. Remarkably, the density of resonances of ^{168}Er at $T = 1.4$ μK is 25% higher than the one observed at 350 nK. The discussion of the origin of this sensitivity is postponed until Sec. V. The density $\bar{\rho}$ for bosonic Dy is 50% larger than for bosonic Er. This is caused by the larger $\vec{j}$ of Dy and, thus, its larger number of allowed collision channels. The much larger density $\bar{\rho}$ of 25.6 G^{-1} for the fermionic ^{167}Er is due to its additional hyperfine structure.

Fluctuations in the number of resonances within a magnetic-field interval ΔB is a second measure of the statistical properties of the spacings between resonances. Formally, it is defined as the dimensionless number variance $\Sigma^2 = \overline{N^2} - \bar{N}^2$, where $\bar{N} = \sum_{i=0}^{M-1} N_i/M$, $\overline{N^2} = \sum_{i=0}^{M-1} N_i^2/M$, and N_i is the number of resonances in the field interval $[i\Delta B,\ (i+1)\Delta B]$, with $i = 0, \ldots, M-1$, such that $M\Delta B = B_{\max}$ and $B_{\max} = 70$ G for both species. Consequently, $\bar{N} \equiv \Delta B\bar{\rho}$. For shot noise or a Poissonian distribution, we expect $\Sigma^2 = \bar{N}$. Figure 1(c) compares Σ^2 for our Dy and Er data as a function of $\bar{N}$. The fluctuations for both species monotonically increase with ΔB but are

substantially less than the shot-noise limit. While this behavior was previously demonstrated for Er [21], the present results provide the first evidence of correlation in Dy and indicate similarity between the species.

These correlations between resonance locations are further studied using the nearest-neighbor spacings distribution $P(s)$, where $s = \delta B\bar{\rho}$ and δB is the field spacing between two adjacent resonances in the spectrum. Figures 2(a) and 2(b) show the computed NNS distribution of our experimental data, derived from the number of NNS, S_i, with spacings s between $i\delta s$ and $(i+1)\delta s$, where $i = 0, 1, \ldots$ and $\delta s \approx 0.3$. The NNS distributions have clear deviations from both the Poisson $P_P(s) = \exp(-s)$ and Wigner-Dyson $P_{\mathrm{WD}}(s) = (\pi/2)s\exp[-(\pi/4)s^2]$ distribution, two well-known distributions within RMT [21]. A Poisson distribution corresponds to a random distribution of resonance locations, while a Wigner-Dyson distribution corresponds to a situation where neighboring resonances "avoid" each other and $P_{\mathrm{WD}}(s) \propto s$ for $s \to 0$. Deviations are also seen in Fig. 1(c), where for both atomic species the variance Σ^2 does not agree with the corresponding predictions for these distributions. The experimental NNS distributions in Figs. 2(a) and 2(b) have also been fit to the Brody distribution $P_B(s,\eta) = b(1+\eta)s^\eta \exp[-bs^{\eta+1}]$, an empirical function that interpolates between $P_P(s)$ and $P_{\mathrm{WD}}(s)$ for $\eta = 0$ and 1, respectively, and b is a normalization constant [38]. The values for η reported in the caption indicate intermediate or mixed behavior of the data.

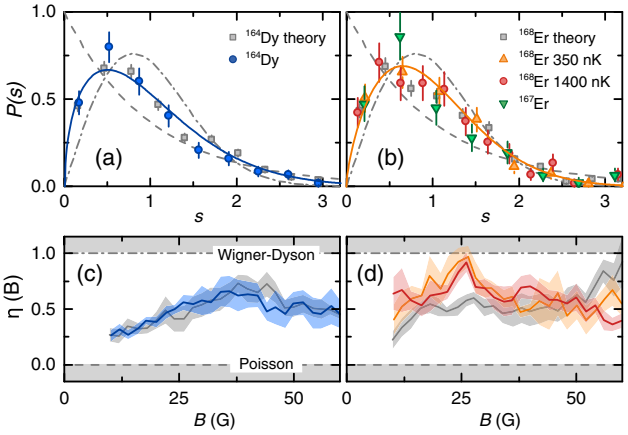

FIG. 2. (a) Nearest-neighbor spacing distribution $P(s)$ determined from all observed Fano-Feshbach resonances for ^{164}Dy (blue markers). Dashed and dot-dashed curves are the Poisson and Wigner-Dyson distribution, respectively. The solid line is a Brody distribution with $\eta = 0.45(7)$ fit to the experimental data. (b) Distributions $P(s)$ for ^{168}Er at $T = 350$ nK and $T = 1.4$ μK (orange and red markers, respectively), and ^{167}Er at $T = 0.4T_F$ (green markers), where T_F is the Fermi temperature of the gas. The solid line is a Brody distribution with $\eta = 0.68(9)$ fit to the ^{168}Er data at $T = 350$ nK. Panels (c) and (d) show the magnetic-field-resolved Brody parameter $\eta(B)$ as a function of magnetic field for ^{164}Dy and ^{168}Er, respectively. The Brody parameters for the Poisson and Wigner-Dyson distribution are 0 and 1, respectively. Gray markers and lines in all four panels are results from our coupled-channels calculations. The 1σ error bars in (a) and (b) correspond to Poisson counting errors, while shaded bands in (c) and (d) are 1σ statistical uncertainties of the fits to the data.

We present the magnetic-field resolved Brody parameter $\eta(B)$ in Figs. 2(c) and 2(d) obtained from a fit to the NNS distribution of resonances located in moving intervals $[B - \Delta B/2, B + \Delta B/2]$, with $\Delta B = 20$ G. It has a non-negligible 1σ uncertainty equally limited by the quality of the fit and the number of Feshbach resonances in an interval or bin. The latter uncertainty is reflected in the bin-to-bin variation of $\eta(B)$. For Dy we observe that η increase linearly with field for small B, which saturates at a value of $\approx$0.5 for $B > 30$ G. For Er the Brody parameter fluctuates around 0.5. Interestingly, the Er data at our two temperatures have a similar behavior, indicating that the larger density of resonances at higher T does not impact the degree of correlation between their spacings.

III. RMT ENSEMBLE MODEL

Random matrix theory is based on the powerful notion that the statistics of eigenvalues and eigenfunctions of a complex system can be studied by replacing the microscopic Hamiltonian by an ensemble of random Hamiltonians. In this spirit, we construct a RMT-inspired model for weakly bound molecular dimer states to test the distribution of Fano-Feshbach resonances.

Our RMT model is based on the statistics of eigenvalues of the $N \times N$ real, symmetric matrix $H_{\mathrm{RMT}} = H_0 + H_Z$, where matrices H_0 and H_Z represent the $B = 0$ Hamiltonian and the Zeeman interaction of the two atoms, respectively. Without loss of generality we can assume that H_Z is a diagonal matrix with matrix elements given by $mg\mu_B B$, where m is an integer between $-2j$ and $2j$, corresponding to the sum of the projection quantum numbers of the atomic angular momenta, g is the atomic Landé factor, and μ_B is the Bohr magneton. The Zeeman interaction does not depend on the rotational state of the molecule and, thus, entries in H_Z correspond to states with a definite value for ℓ and its projection. H_0 is then the $B = 0$ Hamiltonian expressed in this basis. It is also convenient to define $H_0 = H_d + H_{\mathrm{cpl}}$, where diagonal matrix H_d contains the diagonal matrix elements of H_0 and H_{cpl} is the matrix of all its off-diagonal elements. The eigenvalues of H_d can then be interpreted as the energies of rovibrational levels of the isotropic contribution of the molecular BO potentials, while H_{cpl} describes mixing due to the anisotropic contributions of these potentials.

We generate members of our ensemble of H_{RMT} by choosing random matrix elements for H_Z, H_d, and H_{cpl} based on specific distributions. The values of m in H_Z are uniformly distributed integers between $-2j$ and $2j$. The matrix elements of H_d are chosen according to a Brody distribution with variable Brody parameter $\eta_d \in [0, 1]$ and

with a mean energy spacing between bound states ϵ_d. Finally, matrix elements of $H_{\rm cpl}$ are chosen as Gaussian-distributed real numbers with zero mean and standard deviation $\nu_{\rm cpl}$, thereby on average coupling all diagonal elements equally. Notice that this construction deviates from that for a true Gaussian orthogonal ensemble, where all matrix elements of a symmetric Hamiltonian are Gaussian distributed [39].

We apply the RMT model to the case of ^{168}Er. The relevant species-specific quantities are $j = 6$, $g = 1.16$, and ϵ_d is chosen to roughly reproduce the observed density of Fano-Feshbach resonances of ^{168}Er and is set to $\epsilon_d/h = 6.4$ MHz, where h is Planck's constant. Figure 3(a) shows an example of a molecular spectrum, the eigenvalues of $H_{\rm RMT}$ obtained with our RMT model as a function of B with $\eta_d = 0$ and $\nu_{\rm cpl}/h = 2$ MHz. We observe that as B increases, weakly bound molecular states avoid each other multiple times before reaching the two-atom threshold creating a Feshbach resonance. When we turn off $H_{\rm cpl}$, the levels cross. Similar B-field dependencies of the eigenvalues occur for $\eta_d > 0$.

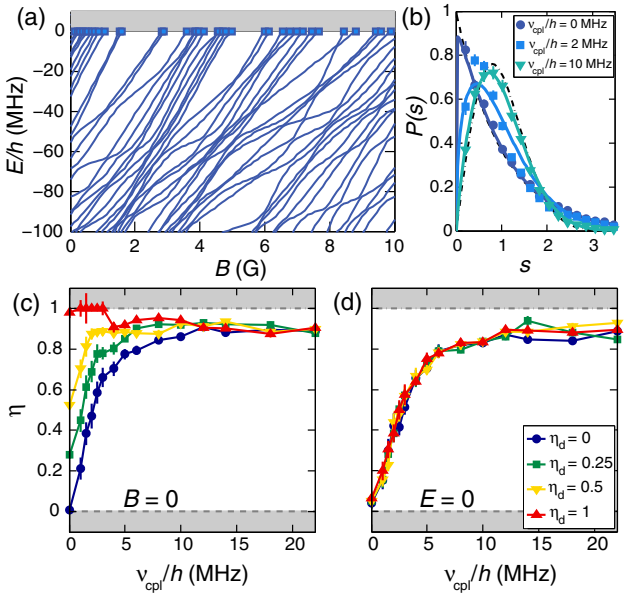

FIG. 3. Molecular spectrum and NNS distributions of Fano-Feshbach resonances of ^{168}Er calculated from our RMT model. (a) Example of a spectrum of molecular binding energies as a function of B for $\nu_{\rm cpl}/h = 2$ MHz, $\eta_d = 0$. Here, h is Planck's constant. Squares at $E/h = 0$ MHz indicate crossings of molecular levels with the threshold of two $m_j = -6$ atoms and correspond to the position of Feshbach resonances. For the sake of visibility, we show only the spectrum between $B = 0$ and 10 G. (b) NNS distributions of simulated Feshbach resonances for $\eta_d = 0$ and $\nu_{\rm cpl}/h = 0$ MHz (circles), 2 MHz (squares), and 10 MHz (triangles). The dashed and dash-dotted lines are Poisson and Wigner-Dyson distributions, respectively. Solid lines are best-fit Brody distributions with $\eta = 0.03(1)$, $\eta = 0.41(5)$, and $\eta = 0.82(1)$ for $\nu_{\rm cpl}/h = 0$, 2, and 10 MHz, respectively. (c) Fitted Brody parameters of the nearest-neighbor energy-spacing distribution of the eigenvalues of $H_{\rm RMT}$ at $B = 0$ G as a function of $\nu_{\rm cpl}$. Circles, squares, down triangles, and up triangles correspond to $\eta_d = 0$, 0.25, 0.5, and 1, respectively. (d) Fitted Brody parameters of the NNS distribution of the Feshbach resonances as a function of $\nu_{\rm cpl}$ and for four η_d using the same marker code as in (c). In panels (b)–(d) distributions are obtained by averaging over 15 realizations of $H_{\rm RMT}$, each of dimension 500×500 and using Feshbach resonances computed up to $B = 85$ G.

We investigate the effect of the parameters $\nu_{\rm cpl}$ and η_d on the NNS distribution of the Fano-Feshbach resonances as well as that of the $B = 0$ molecular levels. Figure 3(b) shows the NNS distribution of Feshbach resonances, obtained by averaging over 15 realizations of $H_{\rm RMT}$, for four values of $\nu_{\rm cpl}$ and $\eta_d = 0$. For negligible $\nu_{\rm cpl}$, the distribution follows $P_P(s)$ and approaches $P_{\rm WD}(s)$ when the anisotropic coupling strength $\nu_{\rm cpl}$ is large compared to ϵ_d. In fact, we find that a larger ϵ_d requires a larger $\nu_{\rm cpl}$ to develop correlations.

Figures 3(c) and 3(d) show Brody parameters fit to NNS distributions as functions of $\nu_{\rm cpl}$ and η_d. Figure 3(c) shows η for the $B = 0$ molecular binding energies. For $\nu_{\rm cpl} = 0$, the Brody parameter is simply η_d, as expected from the distribution of the diagonal H_d, while for larger interaction anisotropy $\nu_{\rm cpl}$, the parameter $\eta \approx 0.9$, close to a Wigner-Dyson distribution, independent of η_d. Figure 3(d) shows η extracted from the RMT Feshbach resonance locations as a function of $\nu_{\rm cpl}$. It suggests that the correlation in the NNS of the resonances is caused by $\nu_{\rm cpl}$, whereas it appears fairly independent of η_d. More precisely, the Brody parameter fitted to these distributions rapidly increases from $\eta \approx 0$ to $\eta \approx 0.8$ for $\nu_{\rm cpl} \lesssim \epsilon_d$ and tends to one for larger $\nu_{\rm cpl}$. We conclude from the RMT model that the correlations between the locations of the Fano-Feshbach resonance are essentially due to the avoided crossings between weakly bound molecular states at finite B and are only weakly dependent on the energy distribution at $B = 0$. In fact, these correlations increase for increasing $\nu_{\rm cpl}$.

IV. MICROSCOPIC COUPLED-CHANNELS MODEL

A. Realistic setup

A quantitative understanding of the origin of the chaotic resonance distribution requires coupled-channels and bound-state calculations with physically realistic angular-momentum couplings and interaction potentials. We do so here based on the time-reversal symmetric Hamiltonian for the relative motion of Dy and Er described in Refs. [21,40]. It contains the Zeeman Hamiltonian, the molecular vibration and rotation, and the molecular interactions with isotropic (orientation-independent) and anisotropic (orientation-dependent) contributions, $\hat{V}_i(R)$ and $\hat{V}_a(\vec{R})$, respectively, where $\vec{R}$ describes the separation R and orientation of the atom pair $\hat{R}$. The potential has eight

tensor operators coupling the two atomic and relative orbital angular momenta, $\vec{j}_1$, $\vec{j}_2$, and $\vec{\ell}$. For $B = 0$, the total angular momentum $\vec{J} = \vec{j}_1 + \vec{j}_2 + \vec{\ell}$ is conserved. For $B > 0$ G, only the projection M of $\vec{J}$ along $\vec{B}$ is conserved. The zero of energy of the Hamiltonian is the energy of an atom pair in the absolute lowest Zeeman sublevel, $m_{j\alpha} = -j_\alpha$.

The potentials $\hat{V}_i(R)$ and $\hat{V}_a(\vec{R})$ contain short-ranged exchange, medium-ranged van der Waals, as well as long-range magnetic dipole-dipole interactions. We use the isotropic van der Waals coefficient $C_6 = 1723 E_h a_0^6$ and anisotropic coefficients spread over $\Delta C_6 = 174 E_h a_0^6$ for Er [21]. For Dy we have improved the value of van der Waals coefficients of Ref. [40] by including additional experimental and theoretical transition frequencies and oscillator strengths [41–44] and now use $C_6 = 2003 E_h a_0^6$ and spread $\Delta C_6 = 188 E_h a_0^6$. In particular, the anisotropic spread for Dy has significantly increased. Here, $E_h = 4.360 \times 10^{-18}$ J is the Hartree energy and $a_0 = 0.052\,97$ nm is the Bohr radius.

B. Bound-state calculations

In Ref. [21] we performed initial coupled-channels calculations of the scattering between ultracold Er atoms and predicted that tens of partial waves ℓ should have been included as the strength of the anisotropic contribution is large. We, however, were unable to reach numerical convergence with respect to the number of coupled equations.

Here, we circumvent this limitation by performing multichannel bound-state calculations, in which we use $B = 0$ eigenstates as a basis for those at $B > 0$ G. For $B = 0$, where J is a good quantum number, at most 49 and 81 Bose-symmetrized and parity-conserving channels are coupled for Er and Dy, respectively. The $B = 0$ coupled Schrödinger equations are discretized on the interval $R \in [0, R_{\max}]$ assuming zero boundary conditions and solved as a matrix eigenvalue problem [45–48]. For each J, only eigenstates with energies between $[E_0, E_1]$ surrounding the zero of energy are computed and stored. The bound states for $B > 0$ G are solutions of the matrix eigenvalue problem that includes all computed $B = 0$ solutions with $|M| \le J \le J_{\max}$ and their coupling due to the Zeeman interaction. Selection rules of the Zeeman interaction ensure that there only exists direct coupling between J and J' zero-field eigenstates with $J - J' = 0, \pm 1$. For both species, $R_{\max} = 1000 a_0$, $E_0/h = -3$ GHz, and $E_1/h = 0.9$ GHz, ensuring that Feshbach resonance locations below 70 G are converged.

In this section on the microscopic calculations we focus on analyzing the spectra at our coldest temperatures, where the initial collision channel has s-wave ($\ell = 0$) character. Hence, we need to consider only even-ℓ channels with total projection quantum number $M = -12$ and -16 for ^{168}Er and ^{164}Dy, respectively, and inclusion of zero-field solutions up to $J_{\max} = 36$ for Dy and 39 for Er is sufficient to reproduce the experimental resonance densities. In Sec. V, we discuss higher-temperature collisions between Er atoms, where d-wave ($\ell = 2$) entrance channels must be considered and, hence, spectra at other M values (i.e., M between -14 and -10 for ^{168}Er) contribute.

C. Interaction anisotropies

We first look into the role of interaction anisotropies on the level distribution of the most weakly bound molecular energy levels at zero magnetic field. There are two dominant components to the anisotropy, the dispersion $V_{\Delta C_6}(\vec{R})$ and magnetic dipole-dipole $V_{\mathrm{MDD}}(\vec{R})$ contribution. To distinguish the contributions of these two terms, we define

$$\hat{V}_a(\vec{R}) = \lambda_{\Delta C_6} V_{\Delta C_6}(\vec{R}) + \lambda_{\mathrm{MDD}} V_{\mathrm{MDD}}(\vec{R}), \qquad (1)$$

with variable strength $\lambda_{\Delta C_6}$ and λ_{MDD}. We systematically increase the strengths $\lambda_{\Delta C_6}$ and λ_{MDD} from zero, where we recover the full physical strength for $\lambda_{\mathrm{MDD}} = \lambda_{\Delta C_6} = 1$.

For completeness, we note that the dominant tensor operator for the anisotropic dispersion contribution is

$$V_{\Delta C_6}(\vec{R}) = \frac{c_a}{R^6} \sum_{i=1,2} \frac{1}{\sqrt{6}} \{3(\hat{R}\cdot\vec{j}_i)(\hat{R}\cdot\vec{j}_i) - \vec{j}_i\cdot\vec{j}_i\} + \cdots,$$

with strength $c_a < 0$ found with the methodology discussed in Sec. IV A. Weaker contributions indicated by dots are included in our calculations. Moreover,

$$V_{\mathrm{MDD}}(\vec{R}) = -\frac{\mu_0}{4\pi}\frac{(g\mu_B)^2}{R^3}\{3(\hat{R}\cdot\vec{j}_1)(\hat{R}\cdot\vec{j}_2) - \vec{j}_1\cdot\vec{j}_2\},$$

where μ_0 is the magnetic constant.

Figures 4(b) and 4(d) show the most weakly bound $B = 0$, $J = 16$ levels of $^{164}Dy_2$ as a function of anisotropy strength for purely dipolar ($\lambda_{\Delta C_6} = 0$, varying λ_{MDD}) and dispersive ($\lambda_{\mathrm{MDD}} = 0$, varying $\lambda_{\Delta C_6}$) anisotropic interaction, respectively. For $\lambda_{\mathrm{MDD}} = \lambda_{\Delta C_6} = 0$, the binding energies are regularly structured with many near degeneracies. In fact, the corresponding states are rovibrational levels of the isotropic centrifugal potentials $\hat{V}_i(R)$ and labeled by ℓ. In our 3-GHz energy window an s-wave channel has at most three bound states, while even $\ell > 0$ channels with their centrifugal barriers have fewer [21,49]. For small $\lambda_{\Delta C_6}$ and λ_{MDD}, the degeneracy is lifted and levels shift linearly. The linear dependence for increasing strength of the dipole-dipole is approximately valid up to the physical value of $\lambda_{\mathrm{MDD}} = 1$. Hence, the dipole-dipole interaction does not lead to our chaotic level distributions. In fact, Fig. 4(a) shows that at $\lambda_{\mathrm{MDD}} = 1$ and $\lambda_{\Delta C_6} = 0$ the NND distribution is Poissonian.

On the other hand, for a relatively small anisotropic dispersion strength $\lambda_{\Delta C_6} \approx 0.1$, levels start to avoid each

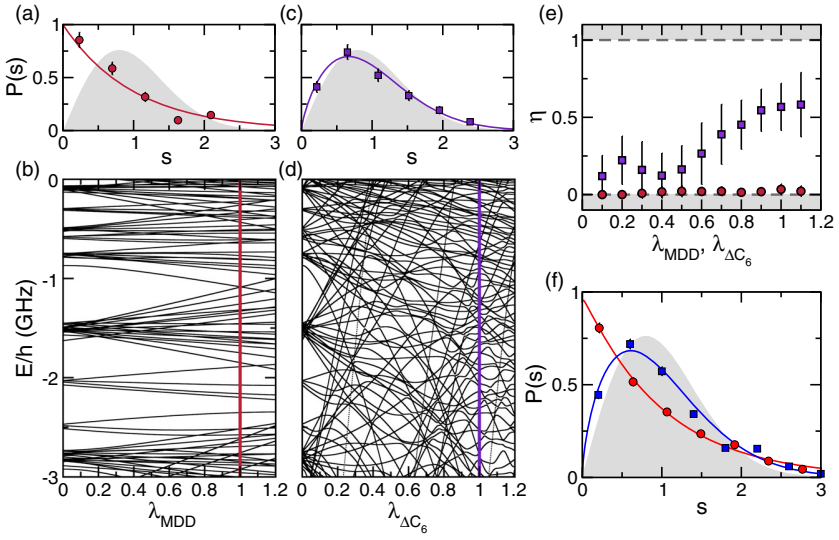

FIG. 4. Interaction-anisotropy-induced chaos of $B = 0$ near-threshold bound states. (b) Weakly bound $J = 16$ bound-state energies of $^{164}Dy_2$ as a function of the anisotropy scale λ_{MDD} with $\lambda_{\Delta C_6} = 0$. (a) NNS distribution (red circles) for the $J = 16$ bound-state data in (b) at $\lambda_{\mathrm{MDD}} = 1$ and $\lambda_{\Delta C_6} = 0$. The solid red line is a Brody distribution fit to the data and agrees well with a Poisson distribution. (d) Weakly bound $J = 16$ bound-state energies of $^{164}Dy_2$ as a function of the anisotropy scale $\lambda_{\Delta C_6}$ with $\lambda_{\mathrm{MDD}} = 0$. (c) NNS distribution (purple squares) for the $J = 16$ bound-state data in (d) at $\lambda_{\mathrm{MDD}} = 0$ and $\lambda_{\Delta C_6} = 1$. The solid purple line is a Brody distribution fit to the data and is close to a Wigner-Dyson distribution. (e) Moving average of the Brody parameter η as a function of $\lambda_{\Delta C_6}$ (purple squares) or λ_{MDD} (red circles) with bins $\Delta\lambda = 0.2$ obtained by fitting the NNS distribution for the $J = 16$ bound-state data in (b) and (d) to Brody distributions, respectively. The horizontal lines at $\eta = 0$ and 1 correspond to the Brody parameter for a Poisson and Wigner-Dyson distribution, respectively. The 1σ error bars combine statistical and fitting uncertainties. (f) The individual-J (blue squares) and combined-J (red circles) NNS distributions $P(s)$ at $\lambda_{\mathrm{MDD}} = \lambda_{\Delta C_6} = 1$ as a function of the normalized energy spacing s. The distributions are derived from $B = 0$ bound-state data for $J = 16, \ldots, 25$. The gray shaded areas in (a), (b), and (f) indicate the Wigner-Dyson distribution.

other. Starting from $\lambda_{\Delta C_6} \approx 0.5$, most avoided crossings are noticeable on the 3-GHz scale of the figure. At the nominal $\lambda_{\Delta C_6} = 1$, where there are 56 levels with $-3 < E/h < 0$ GHz, a significant fraction of the levels have undergone multiple avoided crossings and cannot be described by a single dominant partial wave. The level spacing is chaotic as confirmed by the NND distribution for $\lambda_{\Delta C_6} = 1$ and $\lambda_{\mathrm{MDD}} = 0$ in Fig. 4(c). We compute the weakly bound $J = 16$ levels for $\lambda_{\mathrm{MDD}} = \lambda_{\Delta C_6} = 1$. Visually the level distribution is much the same as the one shown in Fig. 4(d). Similar results have been obtained for $^{168}Er_2$.

Figure 4(e) quantifies the intuition gained from Figs. 4(a)–4(d) by showing the Brody parameter η of the $B = 0$ $J = 16$ $^{164}Dy_2$ levels as a function of $\lambda_{\Delta C_6}$ or λ_{MDD}. The Brody parameter is obtained by fitting a Brody distribution to the NNS distribution of the bound state data in Figs. 4(b) and 4(d). For increasing dipole-dipole strength λ_{MDD} and no anisotropic dispersion ($\lambda_{\Delta C_6} = 0$), the parameter is always zero, indicating the prevalence of small level spacings. On the other hand, in the absence of the DDI, increasing $\lambda_{\Delta C_6}$ leads to an increasing η. It evolves from $\eta = 0.2$ for $\lambda_{\Delta C_6} \lesssim 0.5$ to $\eta = 0.7$ for $\lambda_{\Delta C_6} = 1$, indicating a depopulation of small energy spacings. Note that our systems does not reach a Wigner-Dyson distribution, which corresponds to $\eta = 1$.

In Fig. 4(f), we compare two NNS distributions of $B = 0$ weakly bound states of $^{164}Dy_2$ obtained for the full anisotropic interaction ($\lambda_{\mathrm{MDD}} = \lambda_{\Delta C_6} = 1$). Both distributions are based on $|E/h| < 3$ GHz bound states computed for $J = 16$ up to 25. The first so-called individual-J distribution is constructed by averaging the NNS distribution of levels for individual J's assuming that individual distributions are the same. The second, combined-J NNS distribution, is calculated from a sorted list of all $J = 16, \ldots, 25$ levels. Data for $J > 25$ are not included as the number of bound states is too small for a reliable determination of the NNS distribution.

The individual-J NNS distribution is non-Poissonian as levels with the same J repel each other. The combined-J distribution, however, follows a Poisson distribution indicating that energies of bound states with different J are uncorrelated. In other words, even though the Hamiltonian, i.e., the set of coupling operators between $\vec{j}_1$, $\vec{j}_2$ and $\vec{\ell}$, is the same, differences in the matrix elements and thus coupling strengths between channels lead to uncorrelated eigenenergies.

D. Atom scattering in a magnetic field

The study of the $B = 0$ G multichannel bound states has shown that interaction anisotropies mix channels with the same J, while states with different J are uncorrelated. The Zeeman interaction mixes these molecular levels and leads to the Fano-Feshbach spectrum. Figures 5(a) and 5(b) show example $^{164}Dy_2$ $M = -16$ bound-state spectra as a function of B on two binding-energy and field regions. Similarly, Figs. 5(c) and 5(d) show $M = -12$ $^{168}Er_2$ bound states. In all cases, the full nominal anisotropy ($\lambda_{\Delta C_6} = 1$ and $\lambda_{\mathrm{MDD}} = 1$) is used. For Dy and Er, channels with J up to 36 and 39 are included, respectively. The figure shows that the Dy level density is higher than that for Er. This simply follows from the larger atomic angular momentum of Dy, leading to a larger number of channels with the same $J - |M|$. We also observe that for both species the level structure in the 0–10 G, small field region is qualitatively different from that in the larger field region. For small B, the avoided crossings are substantially narrower than for larger B. Moreover, at small field the levels cluster, while at larger field they are more uniformly distributed. These changes are a consequence of the linearly increasing Zeeman coupling between vibrational levels with different J's as a function of B.

Figure 6(a) shows effective length $a_s(B)$ as a function of B. It diverges at every resonance location and is closely related to the scattering length of a zero-energy collision. Our calculations cannot be directly used to define the scattering length as we use a hard-wall potential for $R \geq R_{\mathrm{max}}$. This wall leads to a discrete set of states with positive energy, and using the lowest of these $E_s(B)$, we can define the effective length $a_s(B)$ shown in the figure by solving for $E_s(B) = \hbar^2\pi^2/\{2\mu_r[R_{\mathrm{max}} - a_s(B)]^2\}$, with $\mu_r = m/2$ and atomic mass m [50].

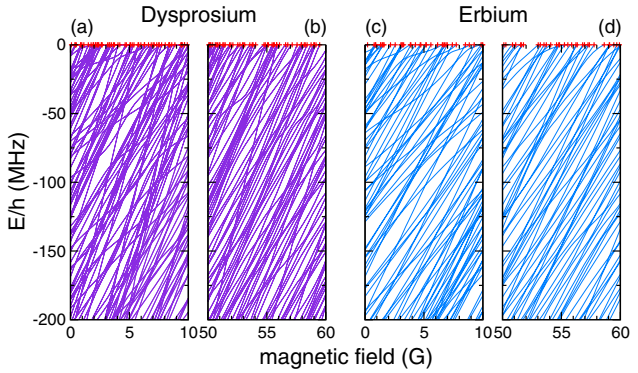

FIG. 5. Theoretical $^{164}Dy_2$ [(a),(b)] and $^{168}Er_2$ [(c),(d)] near-threshold bound states as a function of magnetic field. Calculations have been performed with the full nominal anisotropy. Panels (a) and (c) show the near-threshold region between $B = 0$ and 10 G, while panels (b) and (d) show the region between $B = 50$ and 60 G. Red crosses indicate the location of Feshbach resonances.

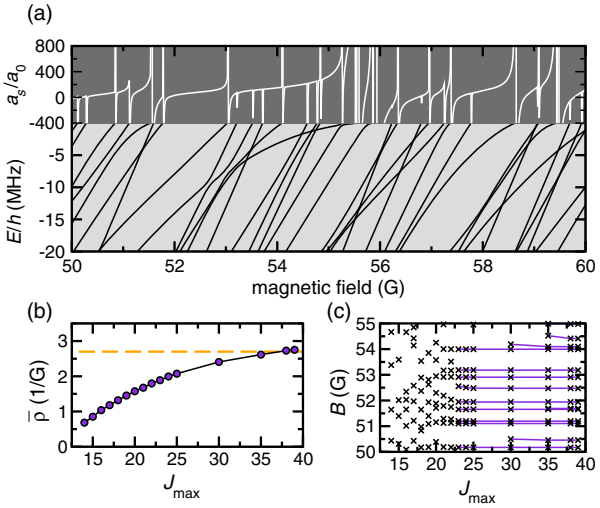

FIG. 6. Theoretical near-threshold bound states and Feshbach resonances in a magnetic field. (a) Near-threshold bound states for $M = -12$ $^{168}Er_2$ for fields between $B = 50$ and 60 G (bottom half of image). The top half of the image shows the effective scattering length, defined in the text, as a function of B. It is infinite at a resonance location where a bound state has zero energy. Calculations use the physical interaction anisotropies and channel states with $J \leq J_{\mathrm{max}} = 39$. (b) Theoretical Feshbach-resonance density $\bar{\rho}$ as a function of J_{max} (purple circles) computed from resonance locations between 0 and 70 G. The dashed horizontal line indicates the experimental density for $^{168}Er_2$. (c) Convergence study of resonance locations (crosses) between 50 and 55 G as a function of J_{max}. Purple lines connect resonances when their location has converged.

It is of interest to briefly discuss the convergence properties of our calculations. The data in Figs. 6(a), 5(c), and 5(d) are based on computations with channels with J up to $J_{\mathrm{max}} = 39$. Figure 6(b) shows the $^{168}Er_2$ Feshbach-resonance density $\bar{\rho}$ as a function of J_{max}. The resonance density increases linearly from ≈ 0.5 1/G at $J_{\mathrm{max}} = 12$ but then is seen to "saturate" for larger J_{max}. At $J_{\mathrm{max}} = 39$ the experimental density is reproduced. In addition, Fig. 6(c) shows the field location of resonances between 50 and 55 G as a function of J_{max}. The resonance locations change significantly for $J_{\mathrm{max}} < 22$, but then rapidly converge. This implies strong mixing among bound states with those J. On the other hand, the location of resonances that appear for $J \geq 22$ is almost immediately converged indicating weak mixing to smaller J states.

E. Comparison of experiment and coupled-channels model

In Figs. 2(a) and 2(b), we show the NNS distribution of converged Feshbach-resonance locations based on our multichannel data between $B = 0$ and 70 G for $^{164}Dy_2$ with $J_{\mathrm{max}} = 36$ and $^{168}Er_2$ with $J_{\mathrm{max}} = 39$, respectively. For both species the distribution clearly deviates from a

Poisson distribution, consistent with the experimental distributions that are also shown. The fitted experimental and coupled-channel Brody parameters agree within their error bars.

The anisotropy parameters $\lambda_{\Delta C_6}$ and λ_{MDD} in the coupled-channels calculations and the parameter ν_{cpl} in the RMT play analogous roles in the Hamiltonian and in the emergence of chaotic level distributions, even though no explicit quantitative connection exists. This role is most manifest in the Brody parameters of the $B = 0$ G bound states and that of the Feshbach-resonance spectra for the two models. For ^{168}Er the corresponding Brody parameters from the coupled-channels calculations are $\approx$0.01 and 0.68 at the physical $\lambda_{\mathrm{MDD}} = \lambda_{\Delta C_6} = 1$, respectively. Within the RMT model, the small η value for the $B = 0$ G level distribution requires weak coupling $\nu_{\mathrm{cpl}} \ll \epsilon_d$ and $\eta_d \approx 0$. In contrast, the Brody parameter for the Feshbach-resonance spectrum requires $\nu_{\mathrm{cpl}} \approx \epsilon_d$ and points at limitations of the current RMT model. Similar conclusions hold for bosonic Dy. Future advanced RMT models might circumvent these limitations by incorporating overlapping, uncoupled chaotic series as is found from our $B = 0$ G coupled-channels calculations.

We plot the B-field-resolved Brody parameter $\eta(B)$ of the theoretical coupled-channels data in Figs. 2(c) and 2(d). A comparison with the experimental $\eta(B)$ shows excellent agreement for ^{164}Dy, while the agreement for ^{168}Er is less satisfactory. A possible explanation for the discrepancies in ^{168}Er is the larger bin-to-bin fluctuations as bins contain fewer resonances than for ^{164}Dy.

For ^{164}Dy the theoretical field-resolved Brody parameter in Fig. 2(c) linearly increases from zero for small B fields and saturates at $\eta(B) \approx 0.5$ for fields larger than 35 G, where the size or width of the avoided crossings between weakly bound states is larger. For ^{168}Er in Fig. 2(d) we find a much more rapid increase of $\eta(B)$ at small fields. This is followed by a plateau at $\eta(B) \approx 0.5$ between $B = 20$ and 50 G, after which $\eta(B) \to 0.9$ with an uncertainty of 0.2 close to a Wigner distribution. The initial rise of $\eta(B)$ for both atomic species is a consequence of weakly bound vibrational levels, uncoupled and randomly distributed when $B = 0$ G, that start to repel each other as the Zeeman interaction increases in strength for increasing B. The plateau at $\eta(B) \approx 0.5$ and the sudden increase of $\eta(B)$ to one for ^{168}Er have no simple explanation and are determined by the not-fully-explored complex interplay between the Zeeman and anisotropic interatomic interactions. It does, however, indicate that Wigner's assumptions on ensembles of Hamiltonians do not hold for fields below 50 G.

V. TEMPERATURE DEPENDENCE OF THE RESONANCE DENSITY

We now describe the origin of the strong temperature dependence of some of the resonances in our atom-loss spectra and thus explain the accompanying increase of the resonance density. Here, atom loss is solely due to three-body recombination, where three ultracold atoms collide to form a diatomic molecule and an atom that are both lost from the atom trap. Figure 7(a) shows atom-loss spectra for one such resonance for ^{168}Er at four temperatures below 2 μK. Atom loss, indeed, is larger for larger temperatures, but we also observe a broadening of the B-field width and a shift of the maximum loss position to larger B fields.

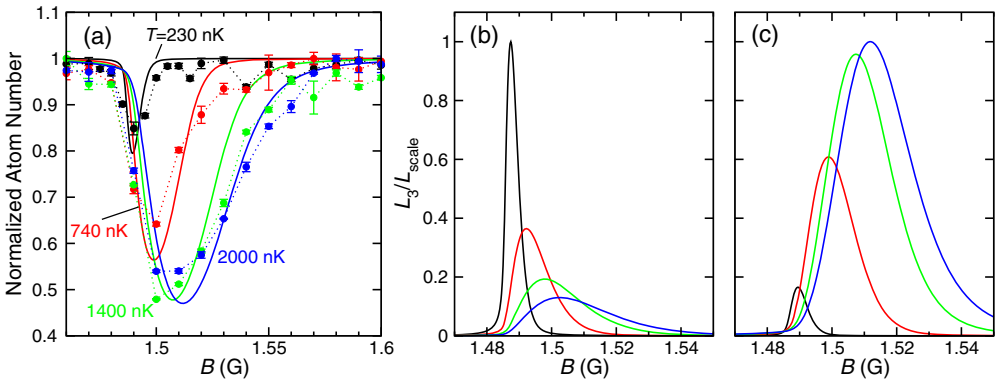

FIG. 7. Line shapes for a strongly temperature-dependent ^{168}Er Feshbach resonance near $B = 1.48$ G. Panel (a) shows experimental data (markers with error bars) as a function of B of the remaining atom number divided by the atom number away from resonance measured 400 ms after initial preparation. Black, red, green, and blue markers correspond to data for temperatures $T = 230$, 740, 1400, and 2000 nK, respectively. Dashed lines connecting the markers guide the eye. Solid lines are theoretical line shapes of the remaining atom number based on the d-wave ($\mathcal{N} = 2$) recombination rates shown in (c). Panels (b) and (c) show simulated three-body recombination rates for the same four temperatures assuming three-body entrance s- ($\mathcal{N} = 0$) and d-wave ($\mathcal{N} = 2$) scattering, respectively. Curves are based on a thermally averaged line shape discussed in the text. Recombination rates are scaled such that the largest value in each panel is one. For both panels, $\mu = 3.1\mu_B$ and $\Gamma_{\mathrm{br}}/k_B = 250$ nK, while $\Gamma(E)/k_B = 0.2(E/E_{\mathrm{ref}})^2$ nK in (b) and $\Gamma(E)/k_B = 0.1(E/E_{\mathrm{ref}})^4$ nK in (c), where $E_{\mathrm{ref}}/k_B = 1000$ nK.

Resonances with a weak temperature dependence show none of these behaviors.

We show with an intuitive resonant "trimer" model that a strongly temperature-dependent resonance is due to scattering processes with entrance d-wave channels even though the two-body d-wave centrifugal barrier, $V_b/k_B = 250\ \mu$K, is 100 times larger than our highest temperature, where k_B is the Boltzmann constant. The difference in the power-law Wigner-threshold behavior of the recombination rate with collision energy for s- and d-wave entrance-channel collisions can explain our observations.

Three-body recombination has been extensively studied in the context of Efimov physics [51–54]. We follow Refs. [55–57] and start from a coupled-channels description in the (mass-scaled) hyperradius ρ, which describes the size of the three-atomic system, and basis functions in the five other hyperspherical coordinates that are ρ-dependent eigenstates of the squared "grand-angular-momentum operator." Similar to the coupled-channels description for two atoms, there are entrance, open, and closed channels. The collision starts in one of the entrance channels with atoms in the energetically lowest Zeeman state and relative three-body kinetic energy E_3, the dimer plus atom are the open channels, and bound states in closed channels can lead to resonances. These closed channels dissociate to three free-atom states with at least one atom in a Zeeman level with higher internal energy. The bound states are resonant trimer states giving us our name for the model. It should, however, be realized that their origin lies in bound states of pairs of atoms and that the resonant state is better thought of as a pair bound state that hops from pair to pair. We define $E_3 \equiv \hbar^3 k_3^2/(2\mu_3) \equiv \mu_3 v_3^2/2$ with the three-body reduced mass $\mu_3 = m/\sqrt{3}$, where k_3 and v_3 are the relative wave vector and velocity, respectively.

The potentials in the entrance channels have long-range repulsive centrifugal potentials, governed by the asymptotic behavior of the grand-angular-momentum operator, and depend on the relative orbital angular momentum $\vec{\mathcal{N}}$ of the three atoms. In fact, the centrifugal potentials are $\hbar^2(\lambda+3/2)(\lambda+5/2)/(2\mu_3\rho^2)$ with non-negative integer quantum number λ [55]. For $\mathcal{N}=0$, the least repulsive potential has $\lambda = 0$, while that for $\mathcal{N}=2$ has $\lambda = 2$.

For an isolated trimer resonance in a closed channel coupled to both entrance and other open channels, we can apply the resonance theories by Fano and Feshbach and derive that the recombination rate coefficient at collision energy E_3 and entrance channel with quantum number λ is given by $L_3(E_3, B) = v_3\sigma(E_3, B)$, where the cross section $\sigma(E_3,B)=(2\mathcal{N}+1)192\pi^2|S(E_3,B)|^2/k_3^5$ and

$$|S(E_3, B)|^2 = \frac{\Gamma(E_3)\Gamma_{\rm br}}{[E_3 - \mu(B - B_0)]^2 + [\Gamma_{\rm tot}(E_3)/2]^2}$$

is a resonant expression for the square of a dimensionless S-matrix element, where B_0 is the trimer resonance location and μ is the magnetic moment of the resonant trimer relative to that of the entrance channel. The definition for $|S(E_3, B)|^2$ also contains the entrance-channel energy width $\Gamma(E_3) = A_\lambda E_3^{\lambda+2}$ to the trimer resonance with a characteristic power-law energy dependence that reflects the threshold behavior of the scattering solutions in the centrifugal potentials. The energy width $\Gamma_{\rm br}$ determines the decay or breakup rate of the resonance into the fast atom and dimer pair and is independent of E_3. Finally, $\Gamma_{\rm tot}(E_3) = \Gamma(E_3) + \Gamma_{\rm br}$. For simplicity, we assume that nonresonant, direct recombination from the entrance to open channels is weak. We also note that for $\mathcal{N}=0$ and $\lambda = 0$, $L_3(E_3, B)$ approaches a finite constant for $E_3 \to 0$ as expected.

In our experiments we have thermal samples of Er and we require the thermally averaged rate coefficient

$$L_3(T, B) = \frac{1}{Z}\int_0^\infty E^2 dE L_3(E, B) e^{-E/kT}$$

and normalization $Z = \int_0^\infty E^2 dE e^{-E/kT} = 2(kT)^3$. In order to increase the signal-to-noise ratio, we allow a significant fraction of atoms to be lost [see Fig. 7(c)], which, assuming a homogeneous sample, can be modeled by the rate equation $dn(t)/dt = -3L_3(T, B)n^3(t)$ for atom density $n(t)$ [53] with solution

$$N(t_h, B) = \frac{N_0}{\sqrt{1 + 6L_3(T, B)n_0^2 t_h}},$$

where $N(t_h, B)$ is the remaining atom number after hold time t_h, N_0 is the initial atom number, and n_0 is the initial density. This nonlinear time evolution adds additional broadening to the lines.

Figures 7(b) and 7(c) show our model event rates $L_3(T, B)$ as a function of B for $\mathcal{N}=0$, $\lambda=0$ and $\mathcal{N}=2$, $\lambda=2$, respectively. Curves are for the same four temperatures as in Fig. 7(a). A comparison of Figs. 7(b) and 7(c) shows a striking difference. The strongest features in Fig. 7(b) are for the smallest temperatures, while those in Fig. 7(c) are for the largest temperatures. This behavior naturally follows from an approximation of the integrant in $L_3(T, B)$ under the conditions $kT \gg \Gamma_{\rm br} \gg \Gamma(E)$ [58]. In this limit the Lorentzian is sharply peaked around $E_3 = \mu(B - B_0)$ for $B > B_0$, and after some algebra it follows that $L_3(T, B)$ as a function of B has a maximum value proportional to $(kT)^{\lambda-1}$ located at $B = B_0 + (\lambda+2)kT/\mu$. Consequently, for $\lambda = 0$ and 2 the maximum loss rate decreases and increases with T, respectively. Even for less restrictive parameter values as used in Fig. 7 this trend remains.

Our experimental data have a temperature trend as in Fig. 7(c). In fact, Fig. 7(a) compares our experimental loss data with model $N(t_h, B)$ for $\mathcal{N}=2$, $\lambda=2$ using the same parameters as in Fig. 7(c) and requiring a $\approx 50\%$

maximum atom loss as in the experiment. It is worth noting that, from our theoretical calculations, the magnetic-field width of $L_3(T,B)$ is noticeably smaller than that for $N(t_h,B)$, indicating that the finite hold time does indeed lead to broadening. The agreement of the experimental data and the prediction of our model for the losses is satisfactory for all four temperatures given the limitations and approximations within our modeling. We conclude that our strongly T-dependent resonances correspond to d-wave or more precisely $\mathcal{N}=2$ entrance-channel collisions. Note that we have not observed any resonances with temperature dependence similar to Fig. 7(b) in our spectra. In the case of resonances with a three-body s-wave entrance channel, which would correspond to such a dependence, we infer that the loss spectra are saturated. This will be subject for future investigations.

As a corollary, this implies that for two colliding atoms, as described in Sec. IV, temperature-dependent resonances are due to collisions with entrance d waves for which there are multiple allowed values of the total angular projection quantum number M. Here, $M=-14$ to -10 for bosonic Er and $M=-18$ to -14 for bosonic Dy. Numerical computations, not presented here, show that their zero-field bound states and thus resonance locations are again uncorrelated and random.

VI. CONCLUSION

In summary, we experimentally and theoretically study the resonant scattering of ultracold Er and Dy atoms in a magnetic field. We show that chaotic scattering as witnessed by chaotic nearest-neighbor spacings between Feshbach-resonance locations emerges due to the anisotropy in the molecular dispersion.

Our study also reveals several unique features of colliding magnetic lanthanides that have not been observed in any other ultracold atomic system. These lanthanides are characterized by their exceptionally large electron orbital angular momentum, which leads to large anisotropic dispersion interactions between these atoms. Our theoretical estimate shows that in both Er and Dy collisions the ratio of anisotropic to isotropic dispersion interaction $\Delta C_6/C_6$ is about 10%. This anisotropy leads to significant splittings among the 48 and 81 gerade short-range potentials that dissociate to the ground-state atomic limits of Er and Dy, respectively. We show that each potential has its own rovibrational structure, which by Coriolis forces and the Zeeman interaction interacts with that of other potentials, creating a dense distribution of levels near the threshold and initiating chaos. In fact, we find a very large number of partial waves contributing to the creation of Fano-Feshbach resonances.

On the other hand, if we just consider the anisotropy from the magnetic dipole-dipole interaction alone, our coupled-channel calculations indicate that chaos in the level distribution does not appear. The strength of the dipole-dipole interaction is too small. In addition, we show that the NNS distributions for Dy and Er are very similar, as can be expected from their similar $\Delta C_6/C_6$ ratio. The difference in their magnetic moment plays only a small role. This further confirms that chaos is due to the anisotropic dispersion interaction.

The distribution of Feshbach resonances of ultracold ground-state alkali-metal, alkaline-earth, Yb, and Cr atoms, as experimental studies have shown, is not chaotic. This is because these atoms have a zero electron orbital angular momentum and, hence, only an isotropic dispersion interaction. Even though alkali-metal and Cr atoms have a nonzero magnetic moment of $1\mu_B$ and $6\mu_B$, respectively, these moments do not lead to chaos. We would expect that other magnetic lanthanides and actinides with nonzero orbital angular momentum will exhibit chaotic properties in their collisions. In addition, collisions between mixed species, such as magnetic lanthanides and alkali metals, like K + Dy or Na + Er, might be susceptible to chaos. A first theoretical analysis for Li + Er [59], however, estimates a small 2% dispersion anisotropy and no chaos is predicted.

Another interesting property of magnetic lanthanide gases is the extreme sensitivity of the atom-loss spectra and, in essence, three-body recombination to the temperature. This phenomenon was first observed in Ref. [22] for loss spectra of Dy. The number of Dy resonances increases by 50% when the temperature is increased from 420 to 800 nK. Here, we observe a 25% increase in the Er resonance density when the temperature rises from 250 to 1400 nK. We show by a comparison of resonance profiles taken at several temperatures and predictions of a theoretical model of three-body recombination via the formation of a trimer, or, more precisely, of a shared pair bound state, that the origin of the temperature-dependent resonances lies in the "partial wave" of the three-atom entrance channel. Entrance channels with zero and nonzero total orbital angular momentum $\mathcal{N}$ lead to line shapes with a different temperature behavior. Those with $\mathcal{N}=0$ or "s-wave" entrance channels have sharply decreasing recombination rates with temperature, whereas those with $\mathcal{N}=2$ or "d-wave" entrance channels have an increasing recombination rate. Temperature-sensitive resonances can be explained only by "d-wave" collisions. It is worth noting that for alkali-metal-atom collisions a number of entrance-channel p-wave resonances have been observed (see, for example, Ref. [60] for cesium). Analysis of the temperature-dependent rate coefficient, however, was not performed.

ACKNOWLEDGMENTS

The Stuttgart group thanks Axel Griesmaier for the support at the early stage of the experiment. The Dy work is supported by the German Research Foundation (DFG) within SFB/TRR21. H. K. acknowledges support by the

"Studienstiftung des deutschen Volkes." The Er work is supported by the Austrian Ministry of Science and Research (BMWF) and the Austrian Science Fund (FWF) through a START grant under Project No. Y479-N20 and by the European Research Council under Project No. 259435. K. A. was supported within the Lise-Meitner program of the FWF. L. C. acknowledges support by the FWF through SFB FoQuS. Work at Temple University is supported by the AFOSR Grant No. FA9550-14-1-0321 and the NSF Grant No. PHY-1308573. The work at JQI is supported by the NSF Grant No. PHY-1506343.

[1] M. A. Baranov, M. Dalmonte, G. Pupillo, and P. Zoller, *Condensed Matter Theory of Dipolar Quantum Gases*, Chem. Rev. **112**, 5012 (2012).
[2] G. Quemener and P. S. Julienne, *Ultracold Molecules under Control!*, Chem. Rev. **112**, 4949 (2012).
[3] M. Saffman, T. G. Walker, and K. Mølmer, *Quantum Information with Rydberg Atoms*, Rev. Mod. Phys. **82**, 2313 (2010).
[4] T. Lahaye, C. Menotti, L. Santos, M. Lewenstein, and T. Pfau, *The Physics of Dipolar Bosonic Quantum Gases*, Rep. Prog. Phys. **72**, 126401 (2009).
[5] T. Lahaye, J. Metz, B. Fröhlich, T. Koch, M. Meister, A. Griesmaier, T. Pfau, H. Saito, Y. Kawaguchi, and M. Ueda, *d-Wave Collapse and Explosion of a Dipolar Bose-Einstein Condensate*, Phys. Rev. Lett. **101**, 080401 (2008).
[6] K. Aikawa, S. Baier, A. Frisch, M. Mark, C. Ravensbergen, and F. Ferlaino, *Observation of Fermi Surface Deformation in a Dipolar Quantum Gas*, Science **345**, 1484 (2014).
[7] M. H. G. de Miranda, A. Chotia, B. Neyenhuis, D. Wang, G. Quéméner, S. Ospelkaus, J. L. Bohn, J. Ye, and D. S. Jin, *Controlling the Quantum Stereodynamics of Ultracold Bimolecular Reactions*, Nat. Phys. **7**, 502 (2011).
[8] J. L. Bohn, M. Cavagnero, and C. Ticknor, *Quasi-Universal Dipolar Scattering in Cold and Ultracold Gases*, New J. Phys. **11**, 055039 (2009).
[9] Y. Wang, J. P. D'Incao, and C. H. Greene, *Universal Three-Body Physics for Fermionic Dipoles*, Phys. Rev. Lett. **107**, 233201 (2011).
[10] L. Santos, G. V. Shlyapnikov, and M. Lewenstein, *Roton-Maxon Spectrum and Stability of Trapped Dipolar Bose-Einstein Condensates*, Phys. Rev. Lett. **90**, 250403 (2003).
[11] S. Ronen, D. C. E. Bortolotti, and J. L. Bohn, *Radial and Angular Rotons in Trapped Dipolar Gases*, Phys. Rev. Lett. **98**, 030406 (2007).
[12] I. Tikhonenkov, B. A. Malomed, and A. Vardi, *Anisotropic Solitons in Dipolar Bose-Einstein Condensates*, Phys. Rev. Lett. **100**, 090406 (2008).
[13] I. Danshita and C. A. R. Sá de Melo, *Stability of Superfluid and Supersolid Phases of Dipolar Bosons in Optical Lattices*, Phys. Rev. Lett. **103**, 225301 (2009).
[14] K. Aikawa, A. Frisch, M. Mark, S. Baier, A. Rietzler, R. Grimm, and F. Ferlaino, *Bose-Einstein Condensation of Erbium*, Phys. Rev. Lett. **108**, 210401 (2012).
[15] K. Aikawa, A. Frisch, M. Mark, S. Baier, R. Grimm, and F. Ferlaino, *Reaching Fermi Degeneracy via Universal Dipolar Scattering*, Phys. Rev. Lett. **112**, 010404 (2014).
[16] M. Lu, N. Q. Burdick, S. H. Youn, and B. L. Lev, *Strongly Dipolar Bose-Einstein Condensate of Dysprosium*, Phys. Rev. Lett. **107**, 190401 (2011).
[17] M. Lu, N. Q. Burdick, and B. L. Lev, *Quantum Degenerate Dipolar Fermi Gas*, Phys. Rev. Lett. **108**, 215301 (2012).
[18] A. Petrov, E. Tiesinga, and S. Kotochigova, *Anisotropy-Induced Feshbach Resonances in a Quantum Dipolar Gas of Highly Magnetic Atoms*, Phys. Rev. Lett. **109**, 103002 (2012).
[19] J. Miao, J. Hostetter, G. Stratis, and M. Saffman, *Magneto-optical Trapping of Holmium Atoms*, Phys. Rev. A **89**, 041401 (2014).
[20] D. Sukachev, A. Sokolov, K. Chebakov, A. Akimov, S. Kanorsky, N. Kolachevsky, and V. Sorokin, *Magneto-optical Trap for Thulium Atoms*, Phys. Rev. A **82**, 011405 (2010).
[21] A. Frisch, M. Mark, K. Aikawa, F. Ferlaino, J. L. Bohn, C. Makrides, A. Petrov, and S. Kotochigova, *Quantum Chaos in Ultracold Collisions of Gas-Phase Erbium Atoms*, Nature (London) **507**, 475 (2014).
[22] K. Baumann, N. Q. Burdick, M. Lu, and B. L. Lev, *Observation of Low-Field Fano-Feshbach Resonances in Ultracold Gases of Dysprosium*, Phys. Rev. A **89**, 020701 (2014).
[23] R. Blümel and W. P. Reinhardt, *Chaos in Atomic Physics* (Cambridge University Press, Cambridge, England, 1997).
[24] V. V. Flambaum, A. A. Gribakina, and G. F. Gribakin, *Statistics of Electromagnetic Transitions as a Signature of Chaos in Many-Electron Atoms*, Phys. Rev. A **58**, 230 (1998).
[25] V. V. Flambaum, M. G. Kozlov, and G. F. Gribakin, *Coherent and Stochastic Contributions of Compound Resonances in Atomic Processes: Electron Recombination, Photoionization, and Scattering*, Phys. Rev. A **91**, 052704 (2015).
[26] O. Agam, B. L. Altshuler, and A. V. Andreev, *Spectral Statistics: From Disordered to Chaotic Systems*, Phys. Rev. Lett. **75**, 4389 (1995).
[27] T. Zelevinsky, S. Kotochigova, and J. Ye, *Precision Test of Mass-Ratio Variations with Lattice-Confined Ultracold Molecules*, Phys. Rev. Lett. **100**, 043201 (2008).
[28] H. I. Liou, H. S. Camarda, and F. Rahn, *Application of Statistical Tests for Single-Level Populations to Neutron-Resonance-Spectroscopy Data*, Phys. Rev. C **5**, 1002 (1972).
[29] H. I. Liou, H. S. Camarda, S. Wynchank, M. Slagowitz, G. Hacken, F. Rahn, and J. Rainwater, *Neutron-Resonance Spectroscopy. VIII. The Separated Isotopes of Erbium: Evidence for Dyson's Theory Concerning Level Spacings*, Phys. Rev. C **5**, 974 (1972).
[30] V. Zelevinsky, B. A. Brown, N. Frazier, and M. Horoi, *The Nuclear Shell Model as a Testing Ground for Many-Body Quantum Chaos*, Phys. Rep. **276**, 85 (1996).
[31] N. Frazier, B. A. Brown, and V. Zelevinsky, *Strength Functions and Spreading Widths of Simple Shell Model Configurations*, Phys. Rev. C **54**, 1665 (1996).
[32] A. Molinari and H. A. Weidenmüller, *Nuclear Masses, Chaos, and the Residual Interaction*, Phys. Lett. B **637**, 48 (2006).

[33] H. A. Weidenmüller and G. E. Mitchell, *Random Matrices and Chaos in Nuclear Physics: Nuclear Structure*, Rev. Mod. Phys. **81**, 539 (2009).
[34] T. Maier, H. Kadau, M. Schmitt, A. Griesmaier, and T. Pfau, *Narrow-Line Magneto-optical Trap for Dysprosium Atoms*, Opt. Lett. **39**, 3138 (2014).
[35] T. Lauber, J. Küber, O. Wille, and G. Birkl, *Optimized Bose-Einstein-Condensate Production in a Dipole Trap based on a 1070-nm Multifrequency Laser: Influence of Enhanced Two-Body Loss on the Evaporation Process*, Phys. Rev. A **84**, 043641 (2011).
[36] C. Chin, R. Grimm, P. Julienne, and E. Tiesinga, *Feshbach Resonances in Ultracold Gases*, Rev. Mod. Phys. **82**, 1225 (2010).
[37] H. A. Weidenmüller and G. E. Mitchell, *Random Matrices and Chaos in Nuclear Physics: Nuclear Structure*, Rev. Mod. Phys. **81**, 539 (2009).
[38] T. A. Brody, J. Flores, J. B. French, P. A. Mello, A. Pandey, and S. S. M. Wong, *Random-Matrix Physics: Spectrum and Strength Fluctuations*, Rev. Mod. Phys. **53**, 385 (1981).
[39] F. J. Dyson, *Statistical Theory of the Energy Levels of Complex Systems. I*, J. Math. Phys. (N.Y.) **3**, 140 (1962).
[40] A. Petrov, E. Tiesinga, and S. Kotochigova, *Anisotropy-Induced Feshbach Resonances in a Quantum Dipolar Gas of Highly Magnetic Atoms*, Phys. Rev. Lett. **109**, 103002 (2012).
[41] M. E. Wickliffe, J. E. Lawler, and G. Nave, *Atomic Transition Probabilities for Dy I and Dy II*, J. Quant. Spectrosc. Radiat. Transfer **66**, 363 (2000).
[42] J. J. Curry, E. A. Den Hartog, and J. E. Lawler, *Radiative Lifetimes of Dy I and Dy II*, J. Opt. Soc. Am. B **14**, 2788 (1997).
[43] V. N. Gorshkov, V. A. Komarovskii, A. L. Oserovich, N. P. Penkin, and R. Khefferlin, *Lifetimes of Dy I and Dy II Excited Levels. Oscillator Strengths of Dy I Spectral Lines*, Opt. Spectrosc. **48**, 362 (1980).
[44] V. A. Dzuba, V. V. Flambaum, and B. L. Lev, *Dynamic Polarizabilities and Magic Wavelengths for Dysprosium*, Phys. Rev. A **83**, 032502 (2011).
[45] C. J. Williams, E. Tiesinga, and P. S. Julienne, *Hyperfine Structure of the* Na_2 0_g^- *Long-Range Molecular State*, Phys. Rev. A **53**, R1939 (1996).
[46] E. Tiesinga, C. J. Williams, and P. S. Julienne, *Photoassociative Spectroscopy of Highly Excited Vibrational Levels of Alkali-Metal Dimers: Green-Function Approach for Eigenvalue Solvers*, Phys. Rev. A **57**, 4257 (1998).
[47] V. Kokoouline, O. Dulieu, and F. Masnou-Seeuws, *Theoretical Treatment of Channel Mixing in Excited* Rb_2 *and* Cs_2 *Ultracold Molecules: Perturbations in* 0_u^+ *Photoassociation and Fluorescence Spectra*, Phys. Rev. A **62**, 022504 (2000).
[48] D. T. Colbert and W. H. Miller, *A Novel Discrete Variable Representation for Quantum-Mechanical Reactive Scattering via the S-Matrix Kohn Method*, J. Chem. Phys. **96**, 1982 (1992).
[49] B. Gao, E. Tiesinga, C. J. Williams, and P. S. Julienne, *Multichannel Quantum-Defect Theory for Slow Atomic Collisions*, Phys. Rev. A **72**, 042719 (2005).
[50] K. Burnett, P. S. Julienne, P. D. Lett, E. Tiesinga, and C. J. Williams, *Quantum Encounters of the Cold Kind*, Nature (London) **416**, 225 (2002).
[51] D. S. Petrov, *Three-Boson Problem near a Narrow Feshbach Resonance*, Phys. Rev. Lett. **93**, 143201 (2004).
[52] T. Kraemer, M. Mark, P. Waldburger, J. G. Danzl, C. Chin, B. Engeser, A. D. Lange, K. Pilch, A. Jaakkola, H. C. Nägerl, and R. Grimm, *Evidence for Efimov Quantum States in an Ultracold Gas of Caesium Atoms*, Nature (London) **440**, 315 (2006).
[53] E. Braaten and H.-W. Hammer, *Universality in Few-Body Systems with Large Scattering Length*, Phys. Rep. **428**, 259 (2006).
[54] P. Massignan and H. T. C. Stoof, *Efimov States near a Feshbach Resonance*, Phys. Rev. A **78**, 030701 (2008).
[55] H. Suno, B. D. Esry, C. H. Greene, and J. P. Burke, *Three-Body Recombination of Cold Helium Atoms*, Phys. Rev. A **65**, 042725 (2002).
[56] J. Wang, J. P. D'Incao, and C. H. Greene, *Numerical Study of Three-Body Recombination for Systems with Many Bound States*, Phys. Rev. A **84**, 052721 (2011).
[57] J. Wang, J. P. D'Incao, Y. Wang, and C. H. Greene, *Universal Three-Body Recombination via Resonant d-Wave Interactions*, Phys. Rev. A **86**, 062511 (2012).
[58] K. M. Jones, P. D. Lett, E. Tiesinga, and P. S. Julienne, *Fitting Line Shapes in Photoassociation Spectroscopy of Ultracold Atoms: A Useful Approximation*, Phys. Rev. A **61**, 012501 (1999).
[59] M. L. González-Martínez and P. S. Zuchowski, *Magnetically Tunable Feshbach Resonances in* Li + Er, Phys. Rev. A **92**, 022708 (2015).
[60] C. Chin, V. Vuletić, A. J. Kerman, S. Chu, E. Tiesinga, P. J. Leo, and C. J. Williams, *Precision Feshbach Spectroscopy of Ultracold* Cs_2, Phys. Rev. A **70**, 032701 (2004).

4.4. Publication: Ultracold Dipolar Molecules Composed of Strongly Magnetic Atoms[†]

Physical Review Letters **115**, 203201 (2015)
submitted 17 April 2015; published 9 Nov 2015
DOI 10.1103/PhysRevLett.115.203201

Albert Frisch,[1,2] Michael Mark,[1] Kiyotaka Aikawa,[1] Simon Baier,[1] Rudolf Grimm,[1,2] Alexander Petrov,[3] Svetlana Kotochigova,[3] Goulven Quéméner,[4] Maxcence Lepers,[4] Olivier Dulieu,[4] and Francesca Ferlaino[1,2]

[1] *Institut für Experimentalphysik and Zentrum für Quantenphysik, Universität Innsbruck, Technikerstraße 25, 6020 Innsbruck, Austria*
[2] *Institut für Quantenoptik und Quanteninformation, Österreichische Akademie der Wissenschaften, 6020 Innsbruck, Austria*
[3] *Department of Physics, Temple University, Philadelphia, Pennsylvania 19122, USA*
[4] *Laboratoire Aimé Cotton, CNRS, Université Paris-Sud, ENS Cachan, 91405 Orsay, France*

[†] The author of the present thesis helped in performing the measurements, and contributed in writing the manuscript. The theoretical calculations of this publication have been contributed by A. P., S. K., G. Q., M. L., and O. D.

Ultracold Dipolar Molecules Composed of Strongly Magnetic Atoms

A. Frisch,[1,2] M. Mark,[1] K. Aikawa,[1,*] S. Baier,[1] R. Grimm,[1,2] A. Petrov,[3,†] S. Kotochigova,[3] G. Quéméner,[4] M. Lepers,[4] O. Dulieu,[4] and F. Ferlaino[1,2]

[1]*Institut für Experimentalphysik, Universität Innsbruck, Technikerstrasse 25, 6020 Innsbruck, Austria*

[2]*Institut für Quantenoptik und Quanteninformation, Österreichische Akademie der Wissenschaften, 6020 Innsbruck, Austria*

[3]*Department of Physics, Temple University, Philadelphia, Pennsylvania 19122, USA*

[4]*Laboratoire Aimé Cotton, CNRS, Université Paris-Sud, ENS Cachan, 91405 Orsay, France*

(Received 17 April 2015; published 9 November 2015)

In a combined experimental and theoretical effort, we demonstrate a novel type of dipolar system made of ultracold bosonic dipolar molecules with large magnetic dipole moments. Our dipolar molecules are formed in weakly bound Feshbach molecular states from a sample of strongly magnetic bosonic erbium atoms. We show that the ultracold magnetic molecules can carry very large dipole moments and we demonstrate how to create and characterize them, and how to change their orientation. Finally, we confirm that the relaxation rates of molecules in a quasi-two-dimensional geometry can be reduced by using the anisotropy of the dipole-dipole interaction and that this reduction follows a universal dipolar behavior.

DOI: 10.1103/PhysRevLett.115.203201 PACS numbers: 34.50.Cx, 31.10.+z

Ultracold dipolar particles are at the heart of very intense research activities that aim to study the effect of interactions that are anisotropic and long range [1,2]. Dipolar quantum phenomena require ultracold gases and a strong dipole-dipole interaction (DDI). So far, strongly dipolar gases have been obtained using either atoms with a large magnetic dipole moment or ground-state polar molecules with an electric dipole moment [2]. With both systems, many fascinating many-body quantum effects have been observed and studied, such as the d-wave collapse of a dipolar Bose-Einstein condensate [3,4], the deformation of the Fermi sphere [5], and the spin-exchange phenomena [6,7].

Here, we introduce a novel kind of strongly dipolar particles. These are weakly bound dipolar molecules produced from a pair of atoms with large magnetic dipole moments, such as erbium (Er). The central idea is that these molecules can possess a very large magnetic moment μ up to twice that of atoms (e.g., 14 Bohr magneton, μ_B, for Er_2) and have twice the mass of the atoms. As a consequence, the degree of "dipolarity" of the magnetic molecules is much larger than the one of atoms. This can be quantified in terms of the dipolar length $a_d = m\mu_0\mu^2/(4\pi\hbar^2)$ [1], which solely depends on the molecular mass m and on μ; $\hbar$ is the Planck constant divided by 2π. To give an example, Er_2 with $\mu = 14\mu_B$ has an a_d of about 1600 a_0, which largely exceeds the typical values of the s-wave scattering length. Here, a_0 is the Bohr radius. Moreover, in contrast to ground-state heteronuclear molecules, the dipole moment of the magnetic molecules does not vanish at zero external (magnetic) field, opening the intriguing possibility of investigating the physics of unpolarized dipoles.

In a joined experimental and theoretical effort, we study the key aspects of ultracold dipolar Er_2 molecules, including the association process, the molecular energy spectrum, the magnetic dipole moments, and the scattering properties in both three- (3D) and quasi-two-dimensional (Q2D) geometries.

Erbium belongs to the class of strongly magnetic lanthanides, which are currently attracting great attention in the field of ultracold quantum gases [4,8–10]. Indeed, these species exhibit unique interactions. Beside the long-range magnetic DDI, these species have both an isotropic and an anisotropic contribution in the short range van der Waals (vdW) potential. The latter results from the large nonzero orbital momentum quantum number of the atoms [11,12]. This manifold leads to an extraordinary rich molecular spectrum, reflecting itself in a likewise dense spectra of Feshbach resonances as demonstrated in recent scattering experiments [4,13,14]. Each resonance position marks an avoided crossing between the atomic scattering threshold and a molecular bound state, which can be used to associate molecules from atom pairs [15].

We create and probe Er_2 dipolar molecules by using standard magnetoassociation and imaging techniques [15]. Details of the production schemes are described in the Supplemental Material [16]. In brief, we begin with an ultracold sample of ^{168}Er atoms in an optical dipole trap (ODT) in a crossed-beam configuration. The atoms are spin polarized into the lowest Zeeman sublevel ($j = 6$, $m_j = -6$). Here, j is the atomic electronic angular momentum quantum number and m_j is its projection on the quantization axis along the magnetic field. To associate Er_2 molecules, we ramp the magnetic field across one of the low-field Feshbach resonances observed in Er [4,13]. We experimentally optimize the ramping parameters, such as the ramp speed and the magnetic-field sweep interval, by maximizing the conversion efficiency. In our experiment we typically achieve a conversion efficiency of 15%, which

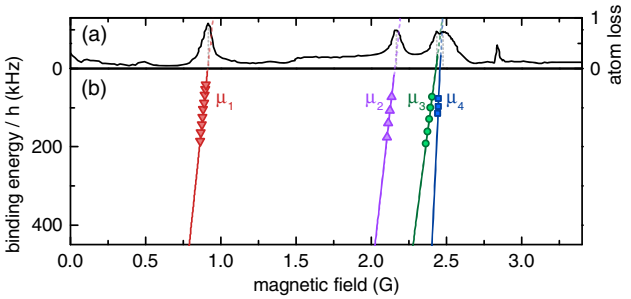

FIG. 1 (color online). Er_2 weakly bound molecules. (a) Atom-loss spectrum [4] from 0 to 3 G and (b) near-threshold binding energy of the corresponding molecular states. The solid lines are fits to the experimental data and extrapolated to larger E_b up to $h \times 500$ kHz. The error bars are smaller than the symbols.

is a common value for boson-composed Feshbach molecules [15]. To obtain a pure molecular sample, we remove all the remaining atoms from the ODT by applying a resonant laser pulse. Our final molecular sample contains about 2×10^4 Er_2 Feshbach molecules at a temperature of 300 nK and at a density of about 8×10^{11} cm^{-3} [16].

A central question regards the magnitude of the dipole moment owned by the magnetic molecules. We experimentally determine μ by using magnetic-field modulation spectroscopy, a technique which was successfully applied to alkali atoms [20–22]. With this method, we measure the molecular binding energy E_b near the atomic threshold as a function of the magnetic field B. The binding energy is related to the differential magnetic moment of the molecules with respect to the atom-pair magnetic moment $2\mu_a$. Here, $\mu_a = -gm_j\mu_B = 6.98\mu_B$ in the case of Er, where $g = 1.16$ is the Er atomic Landé factor. We thus extract μ by using the relation $\mu = 2\mu_a - |dE_b(B)/dB|$. Our spectroscopic measurement begins with an ultracold atomic sample near a Feshbach resonance. We then add a small sinusoidal modulation to the bias magnetic field for 400 ms. The modulation frequency is varied at each experimental run. When it matches E_b/h, prominent atom losses appear because of molecule formation. We trace the near-threshold molecular spectrum by repeating the measurement for various magnetic-field values. Figure 1 shows the Er_2 molecular spectrum in a magnetic-field range up to 3 G. In our range of investigation, we identify four molecular energy levels, which, near threshold, exhibit a linear dependence on B. For each state, we obtain a different μ value, ranging from 8 to $12\mu_B$ [23], as listed in Table I.

For alkali-metal atoms, which possess much simpler interaction properties than lanthanides, theoretical approaches based on coupled-channel calculations have been extremely successful in assigning the quantum numbers of the molecular energy levels and reproducing molecular spectra [15]. However, a straightforward extension of these methods to the lanthanide case is out of reach because of their complex scattering physics involving highly anisotropic interactions and many partial waves [13]. Inspired by work on alkali-metal collisions [24–27], we develop a new theoretical approach to identify the molecular quantum numbers, based on approximate adiabatic potentials and on the experimentally measured μ as input parameters. Our scattering model is detailed in the Supplemental Material [16], whereas we here summarize the central ideas of our approach.

TABLE I. Experimental (Expt.) and theoretical (Theo.) magnetic moments of four molecular states near the atomic threshold, Feshbach-resonance positions B_{FR}, dipolar lengths, outer turning points R^*, and dominant quantum numbers ℓ, J, and M. For convenience, the molecular states are labeled as μ_i with $i = 1, \ldots, 4$. The specified uncertainties correspond to the 1σ statistical errors.

	B_{FR} (G)	μ/μ_B Expt.	Theo.	a_d (a_0)	R^* (a_0)	$\lvert\ell, J, M\rangle$
μ_1	0.91	11.30(7)	11.20	1041(13)	72.0	$\lvert 4, 12, -12/-10/-9\rangle$
μ_2	2.16	11.51(4)	11.46	1080(8)	71.0	$\lvert 4, 10, -10\rangle$
μ_3	2.44	11.84(2)	11.75	1143(4)	86.0	$\lvert 2, 12, -10\rangle$
μ_4	2.47	7.96(3)	7.92	517(4)	57.0	$\lvert 6, 10, -7/-6\rangle$

We first solve the eigenvalue problem of the full atom-atom interaction potential operator [16], whose eigenvalues are the adiabatic potentials $U_n(R;B)$. The corresponding eigenfunctions read as $|n;R\rangle = \sum_i c_{n,i}(R)|i\rangle$, where $n = 1, 2, \ldots$, and $c_{n,i}(R)$ are R-dependent coefficients. The molecular state $|i\rangle$ is uniquely determined by the set of angular momentum quantum numbers (ℓ, J, M), where ℓ is the molecular orbital quantum number, $\vec{J} = \vec{j}_1 + \vec{j}_2$ the total atomic angular momentum, and M its projection on the internuclear axis.

To derive the corresponding "adiabatic" molecular magnetic moments, we calculate $\mu^{\text{calc}} \approx -dU_n(R;B)/dB$ at the position of the outer classical turning point $R = R^*$. This choice is justified by the fact that most of the vibrational wave function is localized around R^*.

From the Hellmann-Feynman theorem it then follows that $\mu^{\text{calc}} = -g\mu_B \sum_i M_i |c_i(R^*)|^2$. Finally, we assume that for each Feshbach resonance a vibrational state is on resonance and we find the adiabatic potential that has a magnetic moment closest to the measured one within 1%. Once the best match is identified, the corresponding $|n;R\rangle$ sets the molecular state $|i\rangle$, characterized by ℓ, J, and M, with the largest, dominant contribution. In our range of investigation we observe d-, g-, and i-wave molecular states; see Table I. These states show several dominant M contributions. This fact is unusual and reflects the dominant role of the DDI, which couples several adiabatic potentials and M components. As shown in Fig. 2, this mixing effect is particularly dominant below 10 G, where the DDI at R^* is larger than the Zeeman interaction. Above 10 G, we predict μ to be equal to integer multiples of $g\mu_B$ [16].

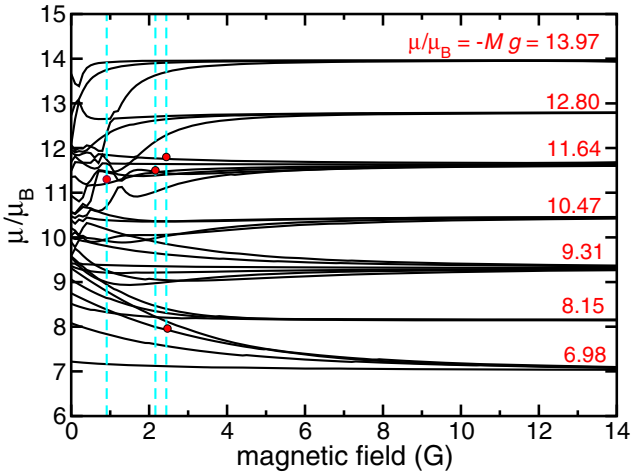

FIG. 2 (color online). Adiabatic magnetic moment as a function of magnetic-field strength evaluated at the entrance channel energy. Each curve corresponds to the adiabatic magnetic moment of one adiabatic potential $U_n(R;B)$. The magnetic moments in the asymptotic limit of large B are given. The dashed vertical lines correspond to the field strength where we have observed Feshbach resonances. The red-filled circles represent the experimentally measured magnetic moments at these resonance locations.

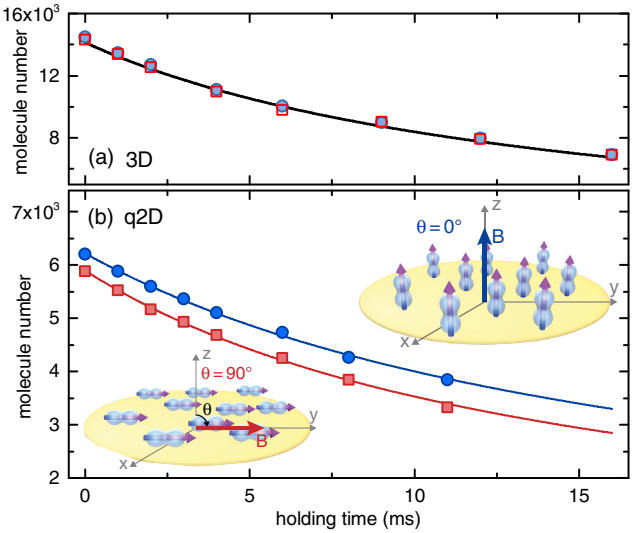

FIG. 3 (color online). Typical time evolution of the number of molecules for $\theta = 90°$ (squares) and $\theta = 0°$ (circles) in a 3D (a) and in a Q2D trap (b). The data refer to molecules in the state μ_1 for the 3D case (a) and molecules in the state μ_2 in Q2D (b). The insets in (b) show an illustration of molecules in pancake-shaped traps with out-of-plane (right) and in-plane (left) orientations. The solid lines are two-body decay fits to the data. The error bars for (a) and (b) are smaller than the data points and are not shown. The data points in (a) are obtained by averaging five independent measurements and in (b) about 50 measurements have been averaged.

As summarized in Table I, we find very good overall agreement between the measured and the calculated molecular magnetic moments. For the largest observed μ, we calculate a corresponding dipolar length, $a_d \approx 1150a_0$. This value exceeds the typical range of the vdW potentials, setting the DDI as the dominant interaction in the system. Remarkably, a_d for Er_2 is comparable to the one realized with ground-state KRb molecules [28], which are an extensively investigated case serving as a benchmark dipolar system.

Following the methods introduced for KRb [29–31], we test the dipolar character of Er_2 by performing scattering experiments in a 3D and in a Q2D optical dipole trap. We control the DDI between molecules by tuning the dipole orientation, which is controlled by changing the direction of the magnetic field and is represented by the angle θ between the magnetic-field axis and the gravity axis. Our experiment begins with the atomic sample trapped either in a 3D or in a Q2D ODT. The Q2D trap is created by superimposing a vertically oriented, one-dimensional optical lattice [16]. After the magnetoassociation and the removal of the remaining atoms, we probe the number of molecules as a function of the holding time in the ODT. We perform measurements for the molecular states μ_1, μ_2, and μ_4 [32]. For each of these states, we measure the collisional stability of the sample for both in-plane ($\theta = 90°$) and out-of-plane ($\theta = 0°$) dipole orientation, and extract the corresponding relaxation rate coefficients, $\beta_\perp$ and $\beta_\parallel$, using a standard two-body rate equation [33].

Figure 3 shows typical molecular decay curves in (a) 3D and in (b) Q2D. In 3D, we confirm that the inelastic decay does not depend on θ. We obtain $\beta_{3D} = 1.3(2) \times 10^{-10}$ cm^3/s. This is a typical value for boson-composed Feshbach molecules, which undergo a rapid vibrational quenching into lower-lying molecular states, as demonstrated with alkali atoms [33]. Contrary, in Q2D the decay rates clearly depend on the dipole orientation. For each investigated molecular state, $\beta_\perp$ is larger than $\beta_\parallel$. We find a reduction of losses of up to 30% for out-of-plane orientation, for which the DDI is predominantly repulsive. The ratio $(\beta_\perp(T)/\beta_\parallel(T))$ increases with increasing μ; see Table II. We note that stronger suppression of losses can be obtained using a tighter two-dimensional confinement [29], which is presently not reachable with our experimental parameters.

TABLE II. Experimental and theoretical loss rate coefficients β for $T = 400$ nK and for various μ and θ at $B = 200$ mG. Uncertainties of β are statistical from fitting and systematic due to number density uncertainty. For the slightly different values of μ compared to Table I and the error discussion see the Supplemental Material [16].

		$\beta_\perp$ (10^{-6} cm^2/s)		$\beta_\parallel$ (10^{-6} cm^2/s)	
	μ/μ_B	Expt.	Theo.	Expt.	Theo.
μ_4	8.7(6)	$12.5 \pm 0.3 \pm 3.3$	6.00	$10.6 \pm 0.3 \pm 2.8$	4.79
μ_1	10.9(5)	$9.5 \pm 0.2 \pm 2.5$	6.81	$7.3 \pm 0.1 \pm 2.1$	5.07
μ_2	11.7(3)	$11.3 \pm 0.2 \pm 2.9$	7.12	$8.6 \pm 0.2 \pm 2.3$	5.13

The reduction of losses in Q2D draws a natural analogy with the observations obtained with KRb molecules [31]. From a comparative analysis between Er_2 and KRb, one can unveil universal behavior attributed to the DDI, for systems being different in nature, but sharing a similar degree of dipolarity. We thus theoretically study the scattering behavior of Er_2 using a theoretical approach similar to the one successfully applied to KRb. Our formalism, which accounts for the DDI and the isotropic vdW interaction, is described in Refs. [16,34].

We compute the $Er_2 + Er_2$ loss rate coefficients $\beta(T)$ in 3D and in Q2D for given values of μ, θ, and T. By averaging over a 3D and a 2D Maxwell-Boltzmann distribution, we obtain the thermalized loss rate coefficients $\beta(T)$ in 3D and in Q2D, respectively. In 3D, we find a rate coefficient of 1.0×10^{-10} cm^3/s at $T = 300$ nK, which is close to the experimental value [35]. In Q2D, our calculations show that the collision dynamics at long range, and thus the value of β, depends on the dipole orientation and monotonically increases with μ. As in the experiments, our calculations show that collisions for in-plane orientation ($\beta_\perp$) lead to larger molecular losses than for out-of-plane orientation ($\beta_\parallel$). In Table II, we compare theory and experiment. The absolute values of β agree within a factor of 2. This difference is well explained by the fact that our model does not include details of the short-range physics, with the Er_4 potential energy surfaces currently unknown [16].

Remarkably, the experimental and calculated ratios $\beta_\perp(T)/\beta_\parallel(T)$ agree very well with each other; see Fig. 4. This suggests that $\beta_\perp(T)/\beta_\parallel(T)$ for Er_2 Feshbach molecules is determined by the DDI and not by the short-range physics, and that it can be correctly described using a point-like-dipole formalism [16]. Figure 4 shows the comparative analysis between bosonic $^{41}K^{87}Rb$ and $^{168}Er_2$, and fermionic $^{40}K^{87}Rb$ and $^{167}Er^{168}Er$ based on our numerical calculations. Independent of the nature of the magnetic or electric dipolar system, we find universal curves as a function of $a_d/\tilde{a}$: one for bosons with $\tilde{a} = a_{\rm ho}$ and one for fermions when $\tilde{a} = a_{\rm vdW}$. Here, $a_{\rm ho}$ is the harmonic oscillator length and $a_{\rm vdW} = (2mC_6/\hbar^2)^{1/4}$ is the vdW length with C_6 the vdW coefficient. The faster increase of $\beta_\perp/\beta_\parallel$ for fermions with respect to bosons is due to the statistical fermionic suppression of $\beta_\parallel$ in Q2D that does not occur for bosons as explained in Ref. [36].

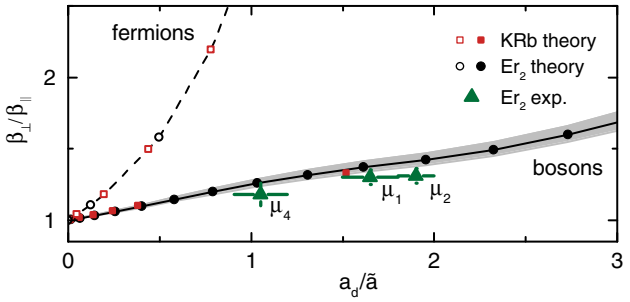

FIG. 4 (color online). Universal loss rate ratio $\beta_\perp/\beta_\parallel$ as a function of $a_d/\tilde{a}$ for Er_2 (circles) and KRb (squares) for a fixed value $a_{\rm dB}/a_{\rm ho} = 4.85$ corresponding to $T = 400(40)$ nK and $\nu_z = 31.2(1)$ kHz [16]. The gray shaded area is due to the uncertainty of T. Here, $\tilde{a} = a_{\rm ho}$ for bosonic molecules (filled symbols) and $\tilde{a} = a_{\rm vdW}$ for fermionic molecules (open symbols). The calculated loss rate ratios of Er_2 are compared with the experimental data for states μ_1, μ_2, and μ_4 (triangles).

The universal behavior of ultracold dipolar scattering has been previously pointed out in Ref. [37]. In the Wigner regime, we derive simple universal scaling laws for dipolar bosonic and fermionic molecules [16,37]. For bosons with a_d, $a_{\rm ho} > a_{\rm vdW}$, which is the case of our Er_2 molecules, we find $[\beta_\perp(T)/\beta_\parallel(T)] \sim (a_{\rm dB}/a_{\rm ho})^4 (a_d/a_{\rm ho}) \exp[2(a_d/a_{\rm ho})^{2/5}]$. For fermions with $a_d, a_{\rm vdW} < a_{\rm ho}$, $(\beta_\perp/\beta_\parallel) \sim (a_d/a_{\rm vdW})^3$. Here, $a_{\rm dB} = h/\sqrt{2\pi m k_B T}$ is the thermal de Broglie wavelength.

To conclude, our work reports on the study of strongly dipolar molecules created by pairing ultracold atoms with large magnetic dipole moments. We anticipate that our scheme can be generalized to other magnetic lanthanide species and has the potential to open regimes of investigations, which have been unaccessible so far. First, the extraordinarily dense and rich molecular energy spectrum of Er opens the exciting prospect of cruising through molecular states of different magnetic moments or even creating molecular-state mixtures with dipole imbalance [22,38,39]. Second, in contrast to electric polar molecules where the electric dipole moment is zero in the absence of a polarizing electric field, magnetic dipolar molecules have a permanent dipole moment allowing us to study the physics of unpolarized dipoles. In addition, strongly magnetic Feshbach molecules offer a novel case of study for scattering physics. These molecules are in fact diffuse in space with a typical size on the order of the vdW length. This novel situation can also have interesting consequences and trigger the development of extended scattering models, which account for multipolar effects and truly four-body contributions when the molecule size becomes comparable to a_d [40]. Finally, a very promising development will be to create fermionic Er_2 dipolar molecules where vibrational quenching processes are intrinsically suppressed because of the Pauli exclusion principle [41,42].

The Innsbruck team acknowledges support by the Austrian Ministry of Science and Research (BMWF) and the Austrian Science Fund (FWF) through a START Grant under Project No. Y479-N20 and by the European Research Council under Project No. 259435. Research at Temple University is supported by an AFOSR Grant No. FA9550-14-1-0321 and NSF Grant No. PHY-1308573. G. Q., M. L., and O. D. acknowledge the financial support of "Projet Attractivité" from Université Paris-Sud and the COPOMOL project (No. ANR-13-IS04-0004) from Agence Nationale de la Recherche.

*Present address: Department of Physics, Graduate School of Science and Engineering, Tokyo Institute of Technology, 2-12-1-S5-9, Ookayama, Meguro-ku, Tokyo 152-8551, Japan.

†Also at: NRC Kurchatov Institute PNPI 188300, Division of Quantum Mechanics, St. Petersburg State University, St. Petersburg 198904, Russia.

[1] M. A. Baranov, M. Dalmonte, G. Pupillo, and P. Zoller, Chem. Rev. **112**, 5012 (2012).

[2] T. Lahaye, C. Menotti, L. Santos, M. Lewenstein, and T. Pfau, Rep. Prog. Phys. **72**, 126401 (2009).

[3] T. Lahaye, T. Koch, B. Fröhlich, M. Fattori, J. Metz, A. Griesmaier, S. Giovanazzi, and T. Pfau, Nature (London) **448**, 672 (2007).

[4] K. Aikawa, A. Frisch, M. Mark, S. Baier, A. Rietzler, R. Grimm, and F. Ferlaino, Phys. Rev. Lett. **108**, 210401 (2012).

[5] K. Aikawa, S. Baier, A. Frisch, M. Mark, C. Ravensbergen, and F. Ferlaino, Science **345**, 1484 (2014).

[6] B. Yan, S. A. Moses, B. Gadway, J. P. Covey, K. R. A. Hazzard, A. M. Rey, D. S. Jin, and J. Ye, Nature (London) **501**, 521 (2013).

[7] A. de Paz, A. Sharma, A. Chotia, E. Maréchal, J. H. Huckans, P. Pedri, L. Santos, O. Gorceix, L. Vernac, and B. Laburthe-Tolra, Phys. Rev. Lett. **111**, 185305 (2013).

[8] M. Lu, N. Q. Burdick, S. H. Youn, and B. L. Lev, Phys. Rev. Lett. **107**, 190401 (2011).

[9] D. Sukachev, A. Sokolov, K. Chebakov, A. Akimov, S. Kanorsky, N. Kolachevsky, and V. Sorokin, Phys. Rev. A **82**, 011405 (2010).

[10] J. Miao, J. Hostetter, G. Stratis, and M. Saffman, Phys. Rev. A **89**, 041401 (2014).

[11] A. Petrov, E. Tiesinga, and S. Kotochigova, Phys. Rev. Lett. **109**, 103002 (2012).

[12] M. Lepers, J.-F. Wyart, and O. Dulieu, Phys. Rev. A **89**, 022505 (2014).

[13] A. Frisch, M. Mark, K. Aikawa, F. Ferlaino, J. L. Bohn, C. Makrides, A. Petrov, and S. Kotochigova, Nature (London) **507**, 475 (2014).

[14] K. Baumann, N. Q. Burdick, M. Lu, and B. L. Lev, Phys. Rev. A **89**, 020701 (2014).

[15] C. Chin, R. Grimm, P. Julienne, and E. Tiesinga, Rev. Mod. Phys. **82**, 1225 (2010).

[16] See Supplemental Material at http://link.aps.org/supplemental/10.1103/PhysRevLett.115.203201, which includes Refs. [17–19], for details regarding the creation of Er_2 molecules, the theoretical description of the collision formalism, and the adiabatic model.

[17] Z. Idziaszek and P. S. Julienne, Phys. Rev. Lett. **104**, 113202 (2010).

[18] S. Kotochigova and A. Petrov, Phys. Chem. Chem. Phys. **13**, 19165 (2011).

[19] A. Frisch, K. Aikawa, M. Mark, A. Rietzler, J. Schindler, E. Zupanic, R. Grimm, and F. Ferlaino, Phys. Rev. A **85**, 051401(R) (2012).

[20] N. R. Claussen, S. J. J. M. F. Kokkelmans, S. T. Thompson, E. A. Donley, E. Hodby, and C. E. Wieman, Phys. Rev. A **67**, 060701 (2003).

[21] S. T. Thompson, E. Hodby, and C. E. Wieman, Phys. Rev. Lett. **95**, 190404 (2005).

[22] M. Mark, F. Ferlaino, S. Knoop, J. G. Danzl, T. Kraemer, C. Chin, H.-C. Nägerl, and R. Grimm, Phys. Rev. A **76**, 042514 (2007).

[23] For future experiments, it will be very interesting to access molecular levels parallel to the atomic threshold for which $\mu = 2\mu_a$ [22].

[24] A. J. Moerdijk, B. J. Verhaar, and A. Axelsson, Phys. Rev. A **51**, 4852 (1995).

[25] C. A. Stan, M. W. Zwierlein, C. H. Schunck, S. M. F. Raupach, and W. Ketterle, Phys. Rev. Lett. **93**, 143001 (2004).

[26] E. Wille, F. M. Spiegelhalder, G. Kerner, D. Naik, A. Trenkwalder, G. Hendl, F. Schreck, R. Grimm, T. G. Tiecke, J. T. M. Walraven, S. J. J. M. F. Kokkelmans, E. Tiesinga, and P. S. Julienne, Phys. Rev. Lett. **100**, 053201 (2008).

[27] T. G. Tiecke, M. R. Goosen, J. T. M. Walraven, and S. J. J. M. F. Kokkelmans, Phys. Rev. A **82**, 042712 (2010).

[28] K. K. Ni, S. Ospelkaus, D. Wang, G. Quéméner, B. Neyenhuis, M. H. G. de Miranda, J. L. Bohn, J. Ye, and D. S. Jin, Nature (London) **464**, 1324 (2010).

[29] G. Quéméner and J. L. Bohn, Phys. Rev. A **81**, 060701 (2010).

[30] A. Micheli, Z. Idziaszek, G. Pupillo, M. A. Baranov, P. Zoller, and P. S. Julienne, Phys. Rev. Lett. **105**, 073202 (2010).

[31] M. H. G. de Miranda, A. Chotia, B. Neyenhuis, D. Wang, G. Quéméner, S. Ospelkaus, J. L. Bohn, J. Ye, and D. S. Jin, Nat. Phys. **7**, 502 (2011).

[32] The state μ_3 is difficult to access because of its proximity with μ_4.

[33] F. Ferlaino, S. Knoop, M. Berninger, M. Mark, H.-C. Nägerl, and R. Grimm, Laser Phys. **20**, 23 (2010).

[34] G. Quéméner, M. Lepers, and O. Dulieu, Phys. Rev. A **92**, 042706 (2015).

[35] Note that this value is 2 orders of magnitude larger than that of p-wave dominated fermionic KRb molecules [28].

[36] G. Quéméner and J. L. Bohn, Phys. Rev. A **83**, 012705 (2011).

[37] G. Quéméner, J. L. Bohn, A. Petrov, and S. Kotochigova, Phys. Rev. A **84**, 062703 (2011).

[38] M. Mark, T. Kraemer, P. Waldburger, J. Herbig, C. Chin, H.-C. Nägerl, and R. Grimm, Phys. Rev. Lett. **99**, 113201 (2007).

[39] F. Lang, P. van der Straten, B. Brandstätter, G. Thalhammer, K. Winkler, P. S. Julienne, R. Grimm, and J. Hecker Denschlag, Nat. Phys. **4**, 223 (2008).

[40] M. Lepers, G. Quéméner, E. Luc-Koenig, and O. Dulieu, arXiv:1508.06066 [J. Phys. B (to be published)].

[41] M. Greiner, C. A. Regal, and D. S. Jin, Nature (London) **426**, 537 (2003).

[42] S. Jochim, M. Bartenstein, A. Altmeyer, G. Hendl, S. Riedl, C. Chin, J. Hecker Denschlag, and R. Grimm, Science **302**, 2101 (2003).

Ultracold Dipolar Molecules Composed of Strongly Magnetic Atoms: Supplemental Material

A. Frisch,[1,2] M. Mark,[1] K. Aikawa,[1,*] S. Baier,[1] R. Grimm,[1,2] A. Petrov,[3,†]
S. Kotochigova,[3] G. Quéméner,[4] M. Lepers,[4] O. Dulieu,[4] and F. Ferlaino[1,2]

[1] *Institut für Experimentalphysik, Universität Innsbruck, Technikerstrasse* 25, 6020 *Innsbruck, Austria*
[2] *Institut für Quantenoptik und Quanteninformation, Österreichische Akademie der Wissenschaften,* 6020 *Innsbruck, Austria*
[3] *Department of Physics, Temple University, Philadelphia, Pennsylvania* 19122, *USA*
[4] *Laboratoire Aimé Cotton, CNRS, Université Paris-Sud, ENS Cachan,* 91405 *Orsay, France*

Creation of Er_2 in 3D and Q2D

We create Feshbach molecules using standard techniques of magneto-association across a Feshbach resonance. As demonstrated in Refs. [1, 2], Er features an enormous number of Feshbach resonances. Here, we focus on the resonances observed below 3 G. In particular, we first create an ultracold atomic sample of about 3×10^5 ^{168}Er atoms at a temperature of $T \approx 150$ nK, which is just above the onset of Bose condensation, see Ref. [1]. The atoms are confined into a three-dimensional (3D) crossed optical dipole trap with frequencies $\nu_x = 51.5(2)$ Hz, $\nu_y = 13.2(3)$ Hz, and $\nu_z = 207(1)$ Hz. We choose magnetic fields of 1.4 G, 2.3 G, and 2.8 G for the molecular states μ_1, μ_2, and μ_4, respectively. We then magneto-associate molecules by ramping the magnetic field 150 mG below the Feshbach resonance. The typical ramp speed is 90 mG/ms. After the molecule association, we remove all the residual atoms from the optical dipole trap by applying a short laser pulse. The pulse is on resonance with the strong atomic transition at 401 nm [3] and has a duration of 1 μs with an intensity of $\sim 40\,\mathrm{mW/cm^2}$.

To realize a Q2D geometry, we superimpose a one dimensional optical lattice beam to the system after finishing evaporation in the 3D trap. The lattice is realized from a retro-reflected laser beam at 1064 nm, propagating along the vertical direction. The beam has a waist of 250 μm and a typical power of 8 W. As a result, the particles are confined into an array of Q2D pancakes with frequencies $\nu_r = 33.0(3)$ Hz in the radial direction and $\nu_z = 31.2(1)$ kHz in the tightly confining axial direction. We first load the lattice from the atomic sample and we then magneto-associate Er_2 in the lattice. The molecule conversion efficiency in the Q2D geometry is $\lesssim 5\,\%$, which is below the one observed in the 3D trap. With this scheme, we produce about 1.1×10^4 molecules at a temperature of 400 nK, corresponding to a density of $3.8 \times 10^7\,\mathrm{cm^{-2}}$. The molecules fill about 35 lattice layers.

We control the molecular dipole orientation by changing the orientation of the magnetic field. The orientation is quantified in term of the angle θ, which defines the angle between the quantization axis, set by the magnetic field orientation, and the z-axis of the lattice trap. We prepare the molecular samples at either $\theta = 0°$ or $90°$, correspondingly side-by-side (repulsive) or head-to-tail (attractive) dipolar collisions. The magnetic field is rotated by using three pairs of independently-controlled magnetic-field coils. We pay particular attention that when changing the orientation of the magnetic field we keep its magnitude constant. We check this by performing radio-frequency spectroscopy between Zeeman sublevels for different angles of rotation. We typically rotate the field within ~ 6 ms.

For all our loss-rate measurements, we jump to a magnetic field of about 200 mG after molecule association. At this field, E_b is of the order of few $h \times 1$ MHz. We choose to perform our measurement at this magnetic-field value because around 200 mG there are no Feshbach resonances and the molecular spectrum might be less dense. Using a Stern-Gerlach technique [4], we measure μ at 200 mG for all the three target molecular states. We find a slight shift of μ in comparison with the values from Table II of a few percent to $10.9(5)\,\mu_B$ for μ_1, $11.7(3)\,\mu_B$ for μ_2, and $8.7(6)\,\mu_B$ for μ_4.

The given uncertainties for the measured loss rates in Table II are composed of a statistical error with one standard deviation derived from fitting a two-body rate equation to the measured data, and a systematic uncertainty coming from number density calibration. Due to the distribution of molecules across many lattice layers this is by far the greatest uncertainty in the Q2D geometry. The average 2D density and its uncertainty was calculated using a number-weighted average over occupied lattice layers similar to Ref. [5]. When calculating the loss rate ratio $\beta_\perp/\beta_\parallel$, the systematic uncertainty in the density can be neglected as it is highly correlated for the measurement of $\beta_\perp$ and $\beta_\parallel$.

Collision Formalism

We briefly describe the theoretical formalism used in this article to determine the collisional properties of Er_2 molecules in free space (3D collisions) and in an one-dimensional optical lattice (Q2D collisions), in an arbitrary magnetic field $\vec{B}$. More details can be found in Ref. [6, 7].

We use a time-independent quantum formalism based

on spherical coordinates $\vec{r} = (r, \theta_r, \phi_r)$ describing the relative motion of two Er_2 molecules. The quantization axis $\hat{z}$ is chosen to be the confinement axis of the optical lattice. A spherical harmonic basis set, summed over different partial waves ℓ with projections m_ℓ on the quantization axis, is used to expand the total colliding wave function. The one dimensional optical lattice is supposed to be deep enough to consider the collision taking place in an individual pancake. One pancake is represented as an harmonic trap for the relative motion of reduced mass $m_{\rm red}$

$$V_{\rm ho} = \frac{1}{2} m_{\rm red}\, \omega^2 z^2 \tag{1}$$

with $\omega = 2\pi\nu$ and $\nu = 31.2\,$kHz. The 3D collisions are recovered by setting $\nu = 0$. We consider molecules in the ground state of the harmonic oscillator. A given state of an Er_2 Feshbach molecule is described by a rather complicated linear combination of atomic states which cannot be precisely calculated as mentioned in the next section of this Supplemental Material. Therefore we consider that the molecule has a magnetic moment of magnitude μ aligned along the magnetic field which makes an angle θ with the confinement axis. The interaction between two molecules is provided by the magnetic dipole-dipole interaction

$$V_{\rm dd} = \frac{\mu^2\,(1 - 3\cos^2(\theta_r - \theta))}{(4\pi/\mu_0)\, r^3}. \tag{2}$$

We also used an isotropic Er_2 + Er_2 van der Waals interaction given by

$$V_{\rm vdW} = -\frac{C_6}{r^6} \tag{3}$$

with $C_6 = 4 \times 1760 = 7040\,$a.u. which amounts to four times the value of an isotropic atom-atom coefficient of 1760 a.u. from the theoretical work of Ref. [8]. Note that an alternative value of 1723 a.u. based on observed transitions was obtained in Ref. [2]. The Schrödinger equation is solved for each radial intermolecular separations r using a log-derivative propagation method. Matching the colliding wavefunction and its derivative with appropriate two-dimensional asymptotic boundary conditions at long-range [6] provides the cross section and the rate coefficient as a function of the collision energy for any arbitrary configurations of magnetic fields and confinements. Averaging the cross sections over a 3D and 2D dimensional Maxwell-Boltzmann distribution provides the corresponding thermalized rate coefficients $\beta(T)$ for a given temperature.

At short range, we assume that the molecules undergo a full loss mechanism process with a unit probability (it can be either an inelastic or a possible reactive process). This assumption, which corresponds to the so-called universal regime in ultracold collisions, considers that the physics is independent of the initial short-range scattering phase-shift [9] of the full potential energy surfaces of Er_4. This is what it is usually assumed for theory as nothing is known about this potential energy surface at short range. Then, if the magnitude of the rates differs between experiment and theory, one can learn that an experimental system deviates from this universal regime and short-range effects play a role.

To circumvent this, it is more convenient to compute the ratio of the theoretical rates of two different magnetic field orientations since we will start with the same short-range physics condition for both orientations, and compare it with the corresponding experimental ratio. An analysis based on the universal behavior of dipolar collisions in confinement of Ref. [10] using a Quantum Threshold model leads to the following formula for the ratio $\beta_\perp(T)/\beta_\parallel(T)$. For bosons, using Eq. 30 of Ref. [10] to describe $\beta_\perp$ (dipole dominated) and Eq. 32 of the same reference for $\beta_\parallel$ (confinement dominated) we find

$$\left.\frac{\beta_\perp(T)}{\beta_\parallel(T)}\right|_{\rm bos} \sim \left(\frac{a_{\rm dB}}{a_{\rm ho}}\right)^4 \frac{a_d}{a_{\rm ho}}\, e^{2(a_d/a_{\rm ho})^{2/5}} \tag{4}$$

when $a_d, a_{\rm ho} > a_{\rm vdW}$ for a fixed value of $a_{\rm dB}/a_{\rm ho}$ where $a_{\rm dB}$ is the thermal de Broglie wavelength. For fermions, using Eq. 16 of Ref. [10] to describe $\beta_\perp$ (dipole dominated) and Eq. 14 of the same reference for $\beta_\parallel$ (van der Waals dominated), along with Eq. 27, we find

$$\left.\frac{\beta_\perp}{\beta_\parallel}\right|_{\rm fer} \sim \left(\frac{a_d}{a_{\rm vdW}}\right)^3 \tag{5}$$

when $a_d, a_{\rm vdW} < a_{\rm ho}$. These formulas suggest to plot the ratio as a function of $a_d/a_{\rm ho}$ for bosons for a fixed ratio $a_{\rm dB}/a_{\rm ho} = 2\pi\sqrt{\nu/k_B T}$ and as a function of $a_d/a_{\rm vdW}$ for fermions, as it has been done in Fig. 4 for the magnetic dipolar molecules of Er_2 and the electric polar molecules of KRb.

Adiabatic Model

In Ref. [2] we presented the theoretical bosonic-erbium Feshbach spectra derived from coupled-channels calculations. We concluded there that such first-principle evaluations can not quantitatively capture the complex scattering behavior of Er. In fact with the current computing capabilities, the calculations can not be converged with respect to the number of basis states required to explain the experimental Feshbach-resonance density. For this reason, we developed a novel approach based on adiabatic potentials (adiabats) $U_n(R; B)$.

Our adiabatic model starts from the Hamiltonian $H = -(\hbar^2/2m_r)d^2/dR^2 + V(\vec{R})$. The first term is the radial kinetic-energy operator with $\vec{R}$ describing the orientation and the separation between the two atomic dipoles, and m_r is the reduced mass. The second term of the Hamiltonian is the potential operator $V(\vec{R})$, which describes the Zeeman and interatomic interactions. It reads

$V(\vec{R}) = \hbar^2\vec{\ell}^2/(2m_rR^2)+H_Z+W^{\rm elec}(\vec{R})$ and incorporates the rotational energy operator with molecular orbital angular momentum $\vec{\ell}$, the Zeeman interaction of two atoms H_Z, and the electronic potential operator $W^{\rm elec}(\vec{R})$ between the particles. Our model assumes that the relative vibrational motion of two Er atoms is slow compared to the timescales of the rotational, Zeeman, and "electronic" atom-atom interactions.

The Zeeman interaction is $H_Z = g\mu_B(j_{1z} + j_{2z})B$. Here, $g = 1.16$ is the Er g-factor, a magnetic field B is aligned along the $\hat{z}$ direction, and j_{iz} is the z component of the angular momentum operator $\vec{j}_i$ of atom $i = 1, 2$. The electronic potential operator $W^{\rm elec}(\vec{R})$, described in Refs. [2, 11, 12], is anisotropic, as it depends on the orientation of $\vec{R}$. At large separation R, $W^{\rm elec}(\vec{R})$ is given by the magnetic dipole-dipole interaction plus both the isotropic and anisotropic contribution of the van der Waals interaction. For $R \to \infty$ the interaction $W^{\rm elec}(\vec{R}) \to 0$.

The Hamiltonian is evaluated in the basis $|i\rangle = |(j_1j_2)JM\rangle Y_{\ell m_\ell}(\hat{R})$, where $\vec{J} = \vec{j}_1 + \vec{j}_2$ and $Y_{\ell m_\ell}(\hat{R})$ is a spherical harmonic. It conserves $m_\ell + M$ and parity $p = (-1)^\ell$. In addition, for bosonic isotopes $(-1)^{\ell+J} = 1$. We focus on ultracold collisions between atomic states $|j_1m_1\rangle = |j_2m_2\rangle = |6, -6\rangle$ and, therefore, only include basis functions satisfying $m_\ell + M = -12$. We limit the included partial waves to even $\ell \leq 6$ and thus to states with even J, as the "adiabatic" magnetic moments of the resonances quickly converge with the included number of partial waves (In our calculation there is one s-wave channel, four d-wave channels, nine g-wave channels, and 16 i-wave channels.).

The adiabats $U_n(R; B)$ with $n = 1, 2, \ldots$ are eigenvalues of the operator $V(\vec{R})$ at a given field strength B. Their eigenfunctions are $|n; R\rangle = \sum_i c_{n,i}(R)|i\rangle$ with R-dependent coefficients $c_{n,i}(R)$. Note that we neglect the coupling between $U_n(R; B)$ due to the radial part of kinetic-energy operator.

Figure S1 shows the adiabats at $B = 2.44$ G. The scattering starts from the s-wave entrance channel correlating to the energetically lowest adiabat. All other potentials either have a centrifugal barrier and dissociate to two atoms with $M = -12$, or dissociate to closed-channel Zeeman sublevels with $M > -12$. We distinguish four groups of potentials, each associated with a dominant partial wave ℓ. Within a group, the potentials are split by the Zeeman energy and the magnetic DDI and dissociate at different atomic thresholds. For each potential $U_n(R; B)$ we can further assign the dominant J and M, where $\vec{J} = \vec{j}_1 + \vec{j}_2$ is the sum of electronic angular momenta of two atoms and M is the projection of J on the internuclear axis. The figure also shows an example of predominantly d-wave Feshbach molecules with an outer classical turning point R^*. Its "adiabatic" molecular magnetic moment is to good approximation given

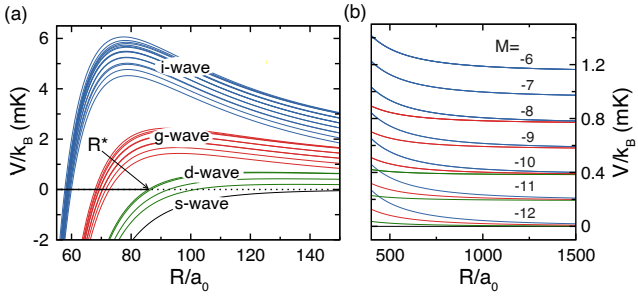

Figure S1. Adiabatic interaction potentials of two Er atoms at medium- (a) and long- (b) interatomic separation R. The calculation is performed at $B = 2.44$ G with $m_\ell + M = -12$ and includes only states with even $\ell \leq 6$. The zero of energy is at the dissociation limit of two $|j, m\rangle = |6, -6\rangle$ atoms. Black, green, red, and blue curves indicate the dominant ℓ-wave character. The horizontal black line indicates a d-wave Feshbach molecule with an outer turning point $R = R^*$ resonant with the s-wave entrance channel. Panel (b) also shows the M projection for each of the Zeeman dissociation limit.

by $\mu^{\rm calc} \approx -dU_n(R^*; B)/dB$, where we further use that most of the vibrational wavefunction is localized around R^*. Interestingly, we observe that the $\mu^{\rm calc}$ value quickly converges with the number of included ℓ (even $\ell \leq 6$ is sufficient) and that it strongly depends on the DDI but only weakly on the vdW dispersion potential. In fact, at R^* the DDI dominates over the anisotropic part of the dispersion potential.

The adiabatic magnetic moment of a resonance is given by $\mu_{nv}^{\rm adiab} \equiv -dE_{nv}(B)/dB \approx -dU_n(R^*; B)/dB$, where we realize that to good approximation most of the adiabatic vibrational wavefunction is localized around the outer classical turning point. We further note that $dU_n(R^*; B)/dB = \langle n; R^*|dH_Z/dB|n; R^*\rangle$ from the Hellmann-Feyman theorem and, hence, $\mu_{nv}^{\rm adiab} = -g\mu_B \sum_i M_i|c_i(R^*)|^2$, where M_i is the total atomic projection quantum number of state $|i\rangle$. We assign a resonance by the quantum numbers of the basis state $|i\rangle$ for which $|c_i(R^*)|^2$ is largest and note that the absolute value of the magnetic moment of a resonance is always smaller that $12g\mu_B \approx 14\mu_B$.

We further assume that the non-adiabatic coupling between the adiabatic potentials is significantly smaller than their spacings for $R < 100a_0$. Then a weakly bound level of adiabatic potential n can lead to a Feshbach resonance when its energy $E_{nv}(B)$ coincides with the entrance channel energy. The outer turning point R^* of this level satisfies $U_n(R; B) = 0$. The resonance acquires a width due to non-adiabatic coupling to the entrance channel.

Finally, we determine the approximate quantum numbers of experimentally-observed resonances with $B_{\rm res} < 3$ G, listed in Table I, based on a comparison of the experimental magnetic moment with those predicted by the adiabatic model at the same resonant field. We find that

for these resonances there exist adiabats with a magnetic moment that agrees within 1% uncertainty with the experimental values. A study of the largest coefficients $c_{n,i}(R)$ at $R = R^*$ then enables us to assign the dominant quantum states shown in Table I.

Figure 2 (main text) shows the magnetic-field dependence of the adiabatic magnetic moment at the entrance channel energy for each of the adiabatic potentials $U_n(R;B)$. We see that for $B > 10$ G the magnetic moment values equal integer multiples of $g\mu_B$ corresponding to those of the atomic limits. For smaller field strengths the adiabatic magnetic moments show mixing of the Zeeman sublevels. Here, the magnetic moment value depends on the magnetic dipole-dipole interaction but only weakly on the strength and anisotropy of the dispersion potential. The figure also shows our experimentally studied Feshbach resonance locations as well as their magnetic moments $\mu^{\rm exp}$; see Table I.

* Current address: Department of Physics, Graduate School of Science and Engineering, Tokyo Institute of Technology, 2-12-1-S5-9, Ookayama, Meguro-ku, Tokyo 152-8551, Japan.
† Alternative address: NRC "Kurchatov Institute" PNPI 188300, Division of Quantum Mechanics, St. Petersburg State University, 198904, Russia.

[1] K. Aikawa, A. Frisch, M. Mark, S. Baier, A. Rietzler, R. Grimm, and F. Ferlaino, Phys. Rev. Lett. **108**, 210401 (2012).
[2] A. Frisch, M. Mark, K. Aikawa, F. Ferlaino, J. L. Bohn, C. Makrides, A. Petrov, and S. Kotochigova, Nature **507**, 475 (2014).
[3] A. Frisch, K. Aikawa, M. Mark, A. Rietzler, J. Schindler, E. Zupanic, R. Grimm, and F. Ferlaino, Phys. Rev. A **85**, 051401(R) (2012).
[4] M. Mark, F. Ferlaino, S. Knoop, J. G. Danzl, T. Kraemer, C. Chin, H.-C. Nägerl, and R. Grimm, Phys. Rev. A **76**, 042514 (2007).
[5] M. H. G. de Miranda, A. Chotia, B. Neyenhuis, D. Wang, G. Quéméner, S. Ospelkaus, J. L. Bohn, J. Ye, and D. S. Jin, Nature Phys. **7**, 502 (2011).
[6] G. Quéméner and J. L. Bohn, Phys. Rev. A **83**, 012705 (2011).
[7] G. Quéméner, M. Lepers, and O. Dulieu, Phys. Rev. A **92**, 042706 (2015).
[8] M. Lepers, J.-F. Wyart, and O. Dulieu, Phys. Rev. A **89**, 022505 (2014).
[9] Z. Idziaszek and P. S. Julienne, Phys. Rev. Lett. **104**, 113202 (2010).
[10] G. Quéméner, J. L. Bohn, A. Petrov, and S. Kotochigova, Phys. Rev. A **84**, 062703 (2011).
[11] S. Kotochigova and A. Petrov, Phys. Chem. Chem. Phys. **13**, 19165 (2011).
[12] A. Petrov, E. Tiesinga, and S. Kotochigova, Phys. Rev. Lett. **109**, 103002 (2012).

Chapter 5

A quantum simulator of extended Hubbard models

A major advantage with ultracold atomic systems is the outstanding experimental flexibility to tailor the confinement for the atoms via optical potentials. This unique control allows to conveniently realize different trapping geometries, where the potentials are formed by off-resonant laser light, exploiting the AC-stark effect [Gri00]. The first realization of optical traps for cold atom experiments featured harmonic potentials [Chu86], which are still widely used in experiments today. In recent years also different potentials have become available as e. g. box-like potentials [Gau13]. However, one of the cornerstones in experiments with ultracold atoms is the ability to restrict the motion of the atoms along different directions via strong confinements, allowing to access quantum effects in reduced dimensions.

A famous realization of reduced dimensions is given by the implementation of a three-dimensional (3D) optical lattice. For very deep lattice potentials, this leads to a pinning of the atoms to individual lattice sites, effectively reducing the dimension to zero. Additionally, the precise and individual control of the depth of the periodic potentials along the different geometrical axis also allows to relax the confinement along specific axis. This enables the study of physical phenomena in tube- or pancake-traps, mimicking a one- or two-dimensional world, respectively.

Three-dimensional optical lattices are nowadays one of the most important tools in ultracold quantum-gas experiments, as they can access physical phenomena found in solid state systems via quantum simulations of the underlying Hamiltonians, see Ref. [Fey82] for the basic idea. Several experimental milestones have been achieved in the past years, including the observation of quantum many-body phase transitions [Gre02, Köh05, Jör08], the access of orbital physics [Mül07, Wir10], the observation of superexchange coupling [Tro08], the implementation of sophisticated band structures via specialized lattice geometries [Tar12], the realization of lattice spin models with short-range [Kra12] and long-range interactions [dP13b, Yan13], and the creation of peculiar ground states, such as the antiferromagnet [Maz17b]. This list is far from being complete but strikingly shows how the remarkable experimental progress in the engineering of ultracold atomic systems enables the access of fascinating quantum phenomena in a controlled manner and allows to prepare peculiar quantum phases.

Within this thesis, we have upgraded our experimental apparatus by implementing a 3D optical lattice, see Appendix B, transforming our system into an *analog quantum simulator* of Hamiltonians with long-range correlations. The strongly magnetic character of erbium atoms can allow to prepare exotic quantum phases resulting from the long-range and anisotropic dipole-dipole interaction (DDI) between the particles. In order to set the stage for the results presented in this chapter, in Sec. 5.1 we will discuss the framework of an optical lattice in the single particle picture. Section 5.2 introduces the underlying extended Hubbard Hamiltonians of the engineered systems for bosonic and fermionic dipolar particles. We will stress the influence of the DDI on the physical observables and its effect on the quantum many-body phase transitions, see Sec. 5.3. Finally, Sec. 5.4 sets the foundation for the scientific results that are presented in Sec. 5.5 and Sec. 5.6. These sections contain our publications on the implementation of extended Bose-Hubbard models and the realization of strongly interacting dipolar Fermi gases, respectively.

5.1. Periodic potentials

5.1.1. Bloch waves

For a freely propagating particle in one dimension, the Schrödinger equation takes the form, see e. g. Ref. [Hum85],

$$H\Phi(x) = \frac{\hat{p}^2}{2m}\Phi(x) = E\Phi(x) \tag{5.1}$$

where the solution is found to consist of plane waves $\Phi(x) = e^{ikx}$, and the particle is well described by the energy-momentum relation $E = \hbar^2 k^2/2m$, where k is the wavevector of the particle and m its mass. Here, the energy consists of a continuum of states. The situation changes drastically when the particle is confined in a periodic potential, which leads to a discretization of energy states, as will be shown below.

In nature, periodic potentials are typically found in solid state systems where nuclei are arranged in a crystalline structure. The coulomb attraction of the nuclei forms a periodical potential $V(x)$ that restricts the motion of the *electrons* along x, see e. g. Ref. [Ash76]. In this paradigmatic case, the solutions of the Schrödinger equation with $H = \frac{\hat{p}^2}{2m} + V(x)$ are given by the *Bloch wave functions*

$$\Phi_q^{(n)}(x) = e^{iqx} u_q^{(n)}(x) \quad \text{where} \quad u_q^{(n)}(x) = u_q^{(n)}(x+d) \tag{5.2}$$

is a completely delocalized periodic function reflecting the periodicity d of the lattice, with q denoting the *quasimomentum* and n being the Bloch-band index.

In ultracold-atom experiments the role of the nuclei in solid state systems is taken by an optical lattice, which in this case forms a periodic potential for the individual *atoms*. The optical lattice can be formed by a retro-reflected gaussian laser beam, propagating along the x axis and being radially symmetric in r. The potential is described as

$$V(r,x) = -V_0\, e^{-2r^2/w_0^2} \cos^2(kx) \approx -V_0 \left(1 - 2\frac{r^2}{w_0^2}\right) \cos^2(kx), \tag{5.3}$$

with V_0 representing the lattice depth and $k = 2\pi/\lambda$ denoting the lattice wave vector. The finite focal waist of the lattice beam w_0 results in an radial harmonic confinement of the atoms, which for the purpose of this introduction will be neglected, i. e. r is set to be zero. In order to avoid inelastic atom-light scattering, the wavelength λ should be chosen such that it is far detuned from atomic transitions. The depth of the optical lattice is conveniently given in recoil energy E_R as $V_0 = sE_\mathrm{R}$ with $E_\mathrm{R} = \hbar^2k^2/2m$ linked to the absorption or emission of a lattice photon for an atom with mass m.

Following from equation 5.2, the periodicity of the lattice allows to expand $u_q^{(n)}(x)$ and $V(x)$ as discrete Fourier sums, leading to the expressions

$$u_q^{(n)}(x) = \sum_l c_l^{(n,q)} e^{i2lkx} \quad \text{and} \quad V(x) = -V_0\cos^2(kx) = -(V_0/4)\left(e^{2ikx} + e^{-2ikx} + 2\right). \tag{5.4}$$

The kinetic energy term reads as

$$\frac{\hat{p}^2}{2m} = \sum_l \frac{(l \times 2\hbar k + q)^2}{2m} = \sum_l \left(2l + \frac{q}{\hbar k}\right)^2 E_\mathrm{R}. \tag{5.5}$$

By inserting 5.4 and 5.5 into the stationary Schrödinger equation one can obtain its matrix form expression:

$$\sum_l H_{l,l'} c_l^{(n,q)} = E_q^{(n)} c_l^{(n,q)} \quad \text{with} \quad H_{l,l'} = \begin{cases} (2l + q/\hbar k)^2 E_\mathrm{R} - V_0/2 & \text{if } \ l = l' \\ -V_0/4 & \text{if } \ |l - l'| = 1 \\ 0 & \text{else.} \end{cases} \tag{5.6}$$

Periodicity allows to confine q to the first Brillouin zone $[-\hbar k, \hbar k]$ without the loss of generality. We can now solve the eigenvalue problem by numerically diagonalizing the Hamiltonian. The extracted eigenvalues $E_q^{(n)}$ give the energy at the quasimoment q for the n-th Bloch band. The energy spread within q for a given lattice band is associated to the width of the band.

5.1.2. Band structure

In Fig. 5.1(a) we plot the energies of the five lowest bands as a function of the lattice depth. The evolution of the different bands captures three different regimes. For zero lattice depth the particle is well described by the free-particle dispersion relation, where no gaps between the different bands are found, correspoding to a continuum of states. With increasing lattice depth, band gaps open up, leading to a quantization of energy states. Finally, for an infinitely deep lattice the width of the bands would reduce to zero and their energies would correspond to the energies of an harmonic oscillator $E^{(n)} = \hbar\omega_\mathrm{lat}(1/2 + n)$ with $\omega_\mathrm{lat} = 2\sqrt{s}E_\mathrm{R}$.

In contrast to solid state systems, ultracold atoms allow to conveniently explore the different regimes, as the depth of the lattice potential can be tuned via $V_0 \propto I\,\alpha$. This *magic knob* is provided by the direct access to the intensity $I = 2P/(\pi w_0^2)$ of the lattice beam, where P denotes the power of the laser light. In order to precisely know the resulting lattice depth, it is crucial to determine the dynamical polarizability α of the specific element at

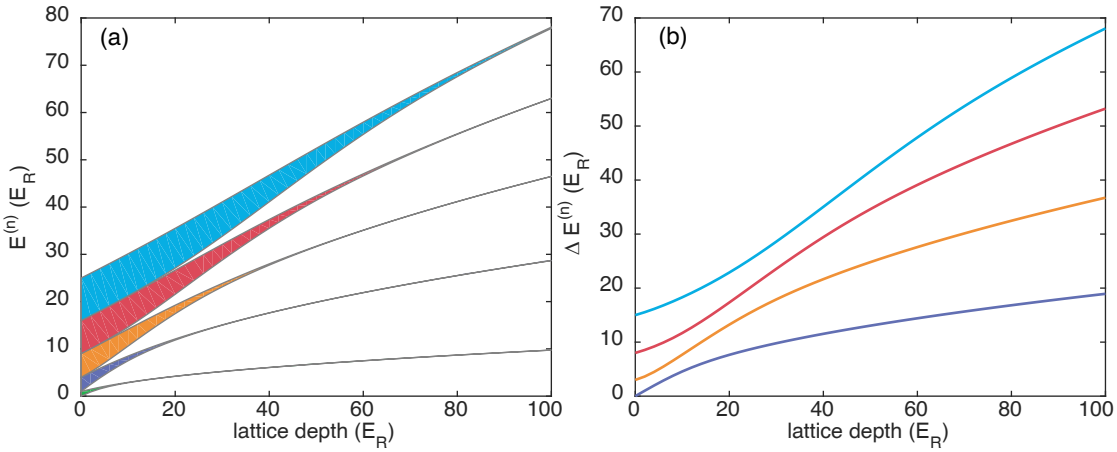

Figure 5.1.: Energy of bands in a 1D optical lattice. (a) The energy of the five lowest Bloch bands (depicted by green, dark blue, orange, red, light blue from lowest to higher bands) evolve and the energy spreads become narrower as the lattice depth is increased. In addition bandgaps emerge. The energy of the gaps between the ground band and the higher bands is shown in (b), respectively. Same color notation as in (a). The energies and the lattice depths are given in recoil energy E_{R}.

the required laser wavelength. In the case of erbium, the dynamical polarizability prior to our work was unknown. With our experiment, we have measured α for experimentally relevant wavelengths as reported in Appendix A.2. For a calculation of the polarizability, the contributions of all dipole-allowed transitions in erbium have to be taken into account via a sum-over-state formula [Lep14].

A majority of ultracold atom experiments focus on physics of the ground band in deep optical lattices, where effects arising from coupling to higher lattice bands are negligible [Lew12]. Still, the knowledge on the energy gap to higher bands is important as it can be used e. g. to calibrate the lattice depth by measuring the excitation energy from the ground to higher bands. Figure 5.1(b) depicts the band gap $\Delta E^{(n)}$ between the ground and the excited bands for a one-dimensional (1D) optical lattice.

Beside the physics in the ground band, an interesting direction is the investigation of orbital physics, accessed by transferring atoms to higher bands. Pioneering work have shown that coherent states in higher lattice orbits indeed can be prepared, in the orbit of one axis in an anisotropic 3D lattice [Mül07] and in the coupled two-dimensional orbit of a 2D lattice [Wir10]. The access of higher orbits enables the studies of complex quantum many-body phases as e. g. p-wave superfluidity [Li16]. It should be noted that in the case of a more-dimensional lattice the wavevector $\mathbf{q}$ consists of components along all the orthogonal lattice axes, leading both, to degeneracies of higher bands for certain quasimomenta $\mathbf{q}$, and to different band gaps as compared to the 1D situation. As the investigation of higher orbits is not the scope of the present thesis, the reader is referred to e. g. Ref. [Mül06] for more details.

5.1.3. Wannier functions

For experiments in deep optical lattices, it is convenient to switch from the description with delocalized Bloch functions to a set of states that are localized at single lattice sites x_i. This set of wavefunctions is given by the so-called *Wannier functions* that form a single-particle basis for each band n and that are orthogonal to each other with respect to different lattice sites and different bands. They are formed by a linear combination of all Bloch waves[1] of a given band as

$$w_n(x - x_i) = \frac{1}{\sqrt{M}} \sum_q e^{-iqx_i} \Phi_q^{(n)}(x) \tag{5.7}$$

where q is again confined to the first Brillouin zone and M is a normalization factor [Wan37]. Within this thesis, we work with Wannier states in the lowest lattice band and hence the band index n is omitted from now on. Working with well localized Wannier functions gives the advantage of easily placing an atomic wavefunction on an arbitrary lattice site. Indeed, the Wannier function at lattice site j is constructed by a simple translation of the Wannier function at lattice site i, as $w_j(x) = w(x - x_j) = w(x - (x_i + (j - i)d)$. For deep enough optical lattices, i. e. in the tight binding regime, the ground state of a lattice site can also be described by the harmonic oscillator ground state

$$w_{\mathrm{ho}}(x) = \frac{1}{\pi^{1/4} l_{\mathrm{ho}}^{1/2}} e^{-\frac{x^2}{2l_{\mathrm{ho}}^2}} \quad \text{with} \quad l_{\mathrm{ho}} = \frac{d}{\pi s^{1/4}} \tag{5.8}$$

being the single-site harmonic oscillator length. To visualize the validities of these two possible descriptions, we compare their functional form in Fig. 5.2 for various lattice depths (Fig. 5.2(a)). For an atom occupying the lattice site $i = 0$, the Wannier function $w_i(x)$ (Fig. 5.2(b)) and the harmonic oscillator ground state $w_{\mathrm{ho}}(x)$ (Fig. 5.2(c)) as well as their difference $w_0(x) - w_{\mathrm{ho}}(x)$ (Fig. 5.2(d)) are depicted. For small lattice depths the Wannier function extends over more lattice sites featuring side lobes, whereas it becomes more and more localized for deeper lattices. While the harmonic oscillator state gives very similar results for deep lattices, it particularly underestimates the occupation at neighboring lattice sites for shallow lattices, as nicely captured by the residual of the two descriptions (Fig. 5.2(d)). This can have a strong influence on the kinetic and potential energy terms of the system's underlying Hamiltonian, i. e. the tunneling of a particle to a neighboring lattice site and the interaction energy of neighboring particles, as this terms are directly related to the wavefunction overlap between neighboring sites as will be discussed below. The description with harmonic oscillator states has therefore to be used with care.

[1] The complex phases of $\Phi_q^{(n)}(x)$ have to be chosen such that the Wannier function of each band are real, symmetric or antisymmetric around $x = 0$ or $x = d/2$ and fall of exponentially in x [Koh59].

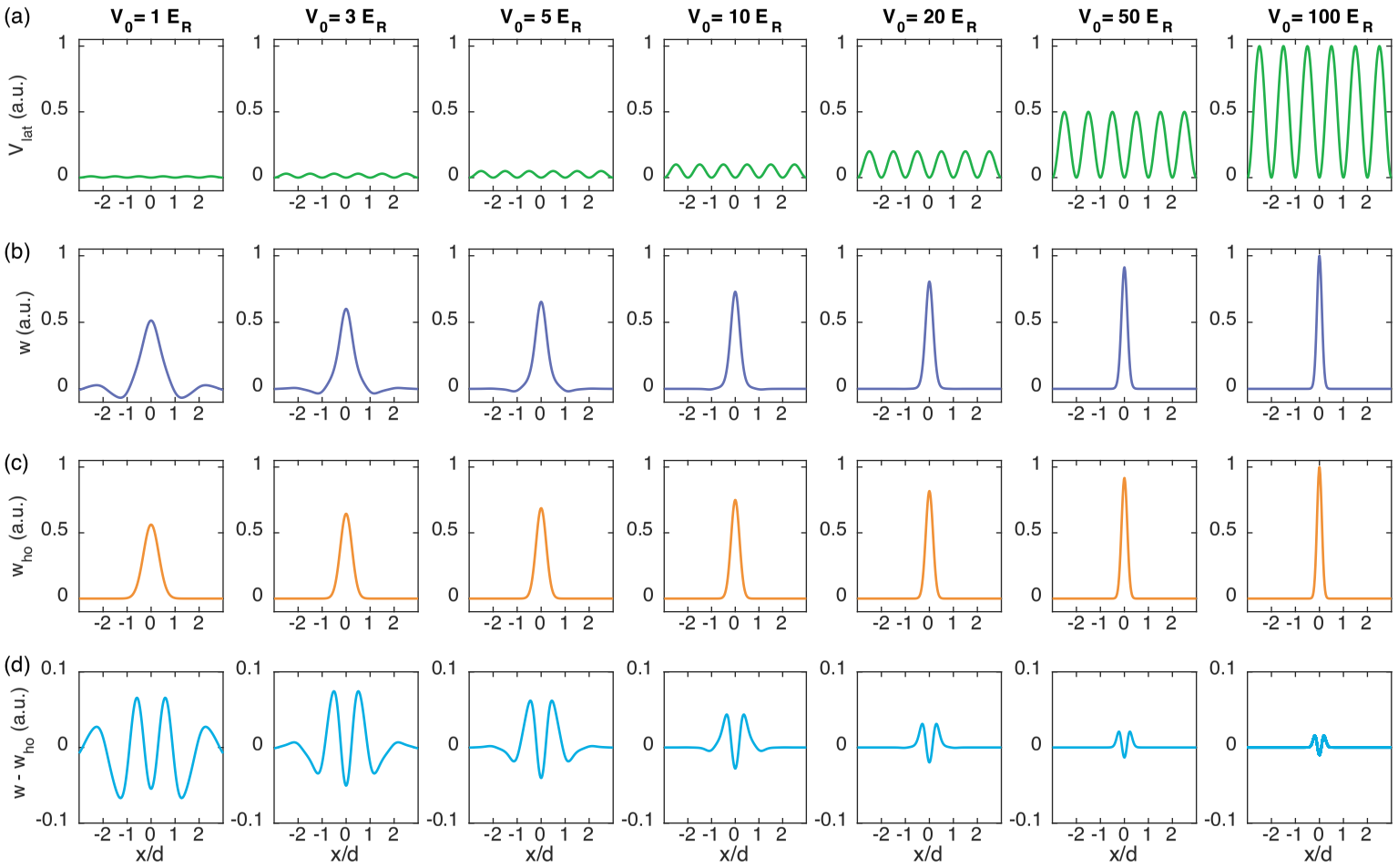

Figure 5.2.: Wannier functions (b) and the harmonic oscillator ground state (c) for an atom at site $i = 0$ for different lattice dephts V_0 (a) as a function of the position x in the lattice in units of the distance d between neighboring lattice sites. The individual data of (a-c) is renormalized by their respective maximum values for the case $V_0 = 100\,\mathrm{E_R}$. The residuum $w - w_{\mathrm{ho}}$ (d) reveals the difference between the two functions used to describe the population of a single lattice site.

5.2. Extended Hubbard models

5.2.1. The Hubbard model

The single-particle description in a periodic potential by itself leads to interesting phenomena such as coherent Bloch oscillation in momentum space within the first Brillouin zone when the particle is accelerated by an external force [Blo29, Dah96, Gus08, Fat08], or the tunneling to higher bands at the edge of the Brillouin zone for small enough band gaps, known as Landau-Zener tunneling [Lan32, Zen34, Tay10].

To capture real physical systems, in addition to the single particle description it is crucial to take into account the correlations between the particles on the microscopic level, e. g. the electron-electron interaction in solid state systems. In particular, the many-body dynamics at low temperature depend critically on the interparticle interactions on single lattice sites and are well described by the famous Hubbard model. The Hubbard Hamiltonian captures the physical observables of a correlated many-body system in a lattice, i. e. the tunneling of particles between neighboring sites, known as the term J, as well the onsite energy for multiple particles occupying the same lattice site, denoted by the term U. Indeed this model, being simple in its representation but still comprehensive with its description, is one of the prime examples of a many-body model in physics, and has since its developement [Hub63] received significant attention. Originally, it was intended to explain the correlated behavior of fermionic particles, i. e. electrons, in a solid state system interacting via Coulomb repulsion, resulting in more stringent conditions for the emergence of ferromagnetism. The proposal to experimentally access the Hubbard model via ultracold atomic systems [Jak98] led to a major popularization, resulting in the observation of the quantum phase transition from a superfluid state to a Mott insulator (SF-MI) within a bosonic system [Gre02], as well as to the realization of the Hubbard model in the original context with fermionic particles [Jör08]. These milestones have been followed by a vast amount of theoretical and experimental studies, see Ref. [Lew12] for an overview.

More recently the Hubbard model has become accessible across different experimental platforms. Here, Fermi-Hubbard physics has been demonstrated with a 2D electron gas in an artificial honeycomb lattice formed by a gallium arsenide heterostructure [Sin11], is modeled by digital quantum simulation via the use of a X-mon transmon qubit array in superconducting circuits [Bar15], and is realized for two sites by single-site resolution of subsurface boron dopants in silicon [Sal16]. Increasing experimental control nowadays allows to emulate Fermi-Hubbard models in solid state systems without suffering from electrostatic disorder, as beautifully demonstrated by single-electron control with gate-defined quantum dots [Hen17]. Despite that for superconducting circuits photonic excitations are used as "quantum particles" [Hou12], theoretical works show that simulation of Bose-Hubbard physics including the SF-MI phase transition is at reach, e. g. by coupling a charge qubit to a superconducting transmission line resonator to form a lattice site [Den15]. An attractive 1D Bose-Hubbard model already has been realized with a three-qubit transmon array [HG15]. This ongoing experimental and theoretical explorations of the Hubbard model throughout different quantum system platforms underline its unbroken currentness.

Quantum statistics

As discussed, the Hubbard model can be accessed with both classes of quantum particles, namely bosons and fermions. The differences for this two classes arises from quantum statistics. While for identical bosons multiple particles can occupy the same lattice site, in the case of identical fermions a multi-occupancy is forbidden by the Pauli exclusion principle. As a result, the Fermi-Hubbard model of identical fermions includes only the tunneling term J, while for a Bose-Hubbard system additionally the onsite interaction term U has to be considered. To realize the onsite term U also with a fermionic system, an additional spin state has to be considered.

In the following, we will discuss Bose-Hubbard and Fermi-Hubbard models for the case of dipolar particles, which open the opportunity to access new Hamiltonian terms that arise from the long-range character of the DDI.

5.2.2. Extended Bose-Hubbard model

While the Bose-Hubbard model already gives a solid framework for the exploration of lattice models, an enriched system can be achieved when correlations are extended beyond single lattice sites as accessible with long-range interactions. Here, a possible route involves dipolar particles, where the DDI gives significant nearest-neighbor interaction leading to exotic quantum phases [Gór02, Dut15]. The many-body dynamics of this system can be captured by the so-called *extended Hubbard model*, which is at the heart of the presented results within this chapter. Here, we will review the theoretical description of this model for the case of bosonic dipolar atoms resulting in the extended Bose-Hubbard (eBH) model. A similar treatement leads to the extended Fermi-Hubbard model, see Sec. 5.2.3.

Let us consider a dipolar Bose-Einstein condensate within a 3D periodic potential $V(\mathbf{r})$. The many-body Hamiltonian in second quantization reads as

$$\hat{H} = \int d\mathbf{r}\Psi^\dagger(\mathbf{r})\left[-\frac{\hbar^2\nabla^2}{2m} + V(\mathbf{r})\right]\hat{\Psi}(\mathbf{r}) + \frac{1}{2}\int d\mathbf{r}\int d\mathbf{r}'\hat{\Psi}^\dagger(\mathbf{r})\hat{\Psi}^\dagger(\mathbf{r}')U(\mathbf{r}-\mathbf{r}')\hat{\Psi}(\mathbf{r}')\hat{\Psi}(\mathbf{r}), \quad 5.9$$

where $\hat{\Psi}^\dagger(\mathbf{r})$ and $\hat{\Psi}(\mathbf{r})$ are the bosonic creation and annihilation field operators, respectively. The first integral of Eq. 5.9 describes the energy of a single particle in the periodic potential $V(\mathbf{r})$ and the second part considers the interaction $U(\mathbf{r}-\mathbf{r}')$ between two particles. They interact with each other via the short-range contact interaction ($\propto a_\mathrm{s}$), see Eq. 4.1, and the long-range DDI ($\propto \mu^2$), see Eq. 3.2,

$$U(\mathbf{r}-\mathbf{r}') = \frac{4\pi\hbar^2 a_\mathrm{s}}{m}\delta(\mathbf{r}-\mathbf{r}') + \frac{\mu_0\mu^2}{4\pi}\frac{1-3\cos^2\theta_{\mathbf{r}-\mathbf{r}'}}{|\mathbf{r}-\mathbf{r}'|^3}. \quad 5.10$$

The field operators can be expanded in the basis of Wannier functions as $\hat{\Psi}(\mathbf{r}) = \sum_i \hat{b}_i w_i(\mathbf{r})$ where b_i is the bosonic annihilation operator for a particle on lattice site i. Here, the Wannier function is a three dimensional object and is given by the product of the individual orthogonal

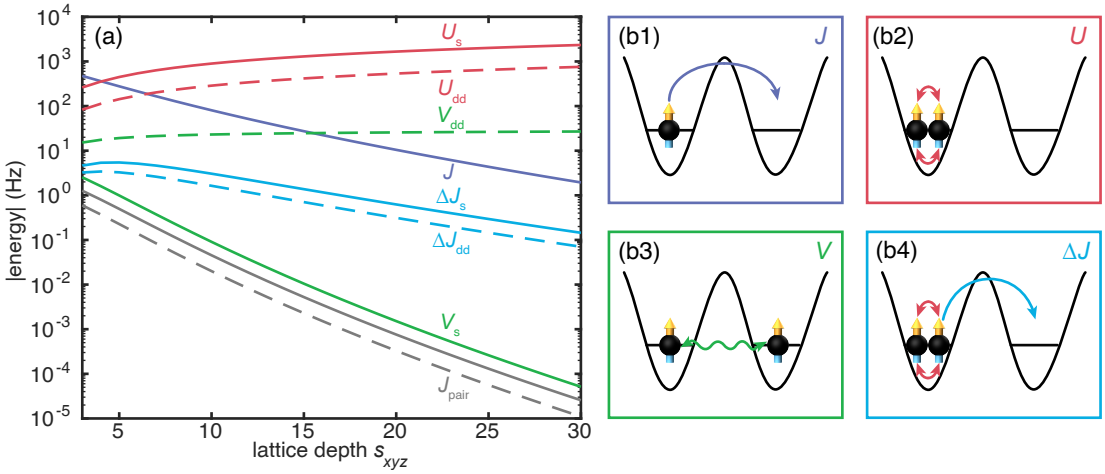

Figure 5.3.: Non-standard extended Bose-Hubbard terms. (a) Absolut energies of the individual matrix elements for the case of erbium in a 3D lattice for our experimental lattice setup, see Appendix B, as a function of the 3D lattice depth $s_{xyz} = s_x = s_y = s_z$. The terms are calculated along the horizontal plane (xy) with a lattice spacing of $d = 266\,\mathrm{nm}$ and a dipole orientation along the vertical z axis. The s-wave scattering length is set to $a_s = 100\,a_0$. Beside the tunneling amplitude J, all terms have contribution from the contact interaction (solid lines) and the dipolar interactions (dashed lines), see text. (b1-b4) Illustrations of the relevant terms of the non-standard eBH model.

Wannier states $w(\mathbf{r}) = w(x)w(y)w(z)$. The two-body interaction of Eq. 5.9 then takes the form

$$\hat{H}_{\mathrm{int}} = \frac{1}{2}\sum_{ijkl} U_{ijkl} b_i^\dagger b_j^\dagger b_k b_l \tag{5.11}$$

where the interaction strength

$$U_{ijkl} = \int d\mathbf{r} \int d\mathbf{r}' w_i^*(\mathbf{r}) w_j^*(\mathbf{r}') U(\mathbf{r}-\mathbf{r}') w_k(\mathbf{r}) w_l(\mathbf{r}') \tag{5.12}$$

results from the wavefunction overlap of lattice sites i, j, k and l. Equation 5.12 contains the matrix elements of all possible processes involving two particles in a lattice. Taking only onsite and nearest-neighbor scattering events into account, finally leads to the non-standard extended Bose-Hubbard Hamiltonian in single-band approximation [Dut15]

$$\begin{aligned} H &= H_{\mathrm{single}} + H_{\mathrm{onsite}} + H_{\mathrm{offsite}}, \quad \text{with} \\ H_{\mathrm{single}} &= -J\sum_{\langle ij\rangle}(b_i^\dagger b_j + h.c.) + \sum_i V_{\mathrm{h},i}\, n_i, \\ H_{\mathrm{onsite}} &= \frac{U}{2}\sum_i n_i(n_i-1), \quad \text{and} \\ H_{\mathrm{offsite}} &= V\sum_{\langle ij\rangle} n_i n_j - \Delta J \sum_{\langle ij\rangle}\left[b_i^\dagger b_j (n_i + n_j - 1) + h.c.\right] + J_{\mathrm{pair}}\sum_{\langle ij\rangle} b_i^{\dagger 2} b_j^2. \end{aligned} \tag{5.13}$$

Here, $\langle ij\rangle$ denotes a pair of nearest-neighboring sites and $n_i = b_i^\dagger b_i$ is the onsite occupation number. The Hamiltonian consists of three contributions: the single particle part H_{single}, the onsite part H_{onsite}, and the offsite part H_{offsite} that results from correlations between particles

in neighboring lattice sites. The last part of the Hamiltonian represents new terms compared to the standard Bose-Hubbard model. The two Hamiltonian parts H_{onsite} and H_{offsite} arise from the interaction $U(\mathbf{r}-\mathbf{r}')$, where contact and dipolar interactions are at play. To access the terms of the Hamiltonian in experiments it is crucial to know their respective strength for experimental relevant parameters. In Fig. 5.3 we plot the individual contribution of the eBH terms as a function of equal lattice depths s_{xyz} in the three orthogonal directions for our experimental conditions, see Appendix B. It should be stressed that, in contrast to solid state systems, the individual terms and especially the relative strengths of the eBH terms can be tuned conveniently via the control of the lattice depth, which allows to access different regimes and quantum phases. The individual terms of the Hamiltonian will be discussed below.

Single particle terms

Single particles can hop between neighboring lattice sites with a tunneling rate J/h (Fig. 5.3(b1)), which reads as

$$J = -\int d\mathbf{r} w_i^*(\mathbf{r})[-\frac{\hbar^2\nabla^2}{2m} + V(\mathbf{r})]w_j(\mathbf{r}). \tag{5.14}$$

Its strength depends on the overlap between the involved wavefunctions of neighboring lattice sites i and j. As has been shown in Fig. 5.2, for deeper lattices the Wannier functions become more and more localized, resulting in a diminishing overlap. Hence, while for shallow lattices the tunneling J dominates the system dynamics it decreases for increasing lattice depths (dark blue line, Fig. 5.3(a)) and eventually vanishes for infinitely deep lattices.

Additional single particle contributions can arise from potential gradients that lead to an energy offsets between different lattice sites [Sac02]. In particular, an important role can be played by the radial harmonic confinement of the lattice beam, see Eq. 5.3, which leads to a position dependent potential energy $V_{\text{h},i}$. Particles away from the center of the red-detuned lattice beams experience a higher potential energy as compared to the central particles. This can influence the hopping dynamics and can lead to different spatial regions of quantum phases across the lattice for sufficient lattice dephts [Cam06, Föl06].

Onsite contributions

When a number of interacting atoms occupy the same lattice site, the particle correlations lead to an energy change of the occupied state, i. e. the energy is increased (decreased) for repulsive (attractive) interactions. In standard Bose-Hubbard models this onsite energy U is solely given by the contact interaction between the particles, which is related to the scattering length a_{s}. In the case of dipolar particles the onsite energy reads as $U = U_{\text{s}}+U_{\text{dd}} = U_{iiii}$ and captures both the contact and the dipolar interactions (Fig. 5.3(b2)). As depicted in Fig. 5.3(a), the contact interaction (solid red line) dominates the onsite energy for the experimental relevant scenario and in particular for deep lattices exceeds the energy of all

other eBH terms. This is a direct consequence of the localization of the 3D Wannier functions, effectively resulting in a compression of the particles. The dipolar contribution (dashed red line) scales similarly as the contact contribution but additionally depends on the shape of the 3D Wannier function and the orientation of the atomic dipoles with respect to the symmetry axis of the confinement potential [Wal13], i. e. $U_{\mathrm{dd}}(w, \theta)$.

As a result of the onsite energy, a gap opens up between e. g. the energies of a singly-occupied and a doubly-occupied lattice site [Gre02]. The energy of this gap is also known as the particle-hole excitation energy and in experiments can be conveniently accessed via modulation spectroscopy, see Sec. 5.4.1.

Offsite contributions

The particle correlations can also give rise to offsite terms in the Hamiltonian. The probably most exotic term is the nearest-neighbor interaction (NNI) term $V = V_{\mathrm{s}} + V_{\mathrm{dd}} = U_{ijij}$ (Fig. 5.3(b3)). We emphasize that the contribution of the DDI (V_{dd}) to the NNI in a deep lattice exceeds the contribution of the contact interaction (V_{s}) by several orders of magnitude (dashed and solid green line in Fig. 5.3(a)), underlining the prominent role of the long-range nature of the DDI. Especially for deep lattices V_{s}, can safely be neglected. Offsite interactions are from particular interest as they can lead to special ordering of the particles within the optical lattice, associated to exotic quantum phases. A promising theoretical study of such quantum phases is performed in Ref. [CS10]. A system of hardcore dipolar bosons in a 2D lattice studied via the path integral Monte Carlo method reveals the existence of various Mott lobes depending on the filling fraction. In particular for half filling, the out-of-plane oriented dipoles arrange in a checkerboard order. Remarkably, the investigations, where no cut-off on the dipolar interaction potential is used, identify parameter regions where the ordered crystalline phase remains superfluid, resembling a supersolid phase. This phase is shown to remain stabilized even at finite temperature [CS10]. The experimental realization of a supersolid phase, proposed for Helium already in the 1960s, is still of prime interest within the quantum physics' community[2].

It has been observed that offsite interactions can also arise from the so-called *superexchange interaction*, assosciated to two virtual tunneling processes of neighboring particles [Aue94]. The coupling strength J^2/U of this second-order process can be large enough to study lattice spin models with two-component mixtures. While first observed locally for a pair of bosonic atoms in a double well [Tro08], super-exchange coupling allowed to realize short-range magnetic correlations in the fermionic Hubbard model in lower and later also in three dimensions [Gre13, Har15], and led to the observation of the propagations of single spin-excitations [Fuk13a] and magnon bound states [Fuk13b] in a 1D-Bose-Hubbard spin chain. Remarkably, when temperatures well below the superexchange scale are prepared, the correlations even can give rise to a long-range antiferromagnetic ordering, as recently observed in a 2D Fermi-Hubbard system [Maz17b]. However, superexchange interactions vanish for

[2] It should be noted that very recently experimentalists from ETH and MIT have managed to realize a supersolid phase by coupling a BEC to the modes of two optical cavities [Léo17] and by introducing a spin-orbit coupling of BECs in an array of double-well potentials [Li17], respectively.

very deep lattices. In stark contrast, nearest-neighbor correlations arising from the DDI are only weakly affected by the lattice depth, see Fig. 5.3(a), and also enable direct coupling of particles beyond nearest-neighbors.

An additional term in the Hamiltonian of Eq. 5.13 resulting from offsite correlations is given by the occupation dependent hopping ΔJ, known as density-induced tunneling (DIT) [Lüh12, Bis12] (Fig. 5.3(b4)). For the case of dipolar atoms, it has contributions both from the contact and the DDI and reads as $\Delta J = \Delta J_\mathrm{s} + \Delta J_\mathrm{dd} = -U_{iiij}$. As can be seen in Fig. 5.3(a) (light blue lines) the values of the DITs reach values of up to 10% of J and hence can significantly influence the SF-to-MI quantum phase transition, see Ref. [Lüh12] and Sec. 5.3.1. While direct observations of DIT in a contact interacting tilted 1D Mott insulator nicely showed how strong (isotropic) interaction can alter the tunneling dynamics [Jür14], the investigation of DIT caused by DDI has been first performed with our system, see Sec. 5.5.

A final term involves the correlated pair tunneling $J_\mathrm{pair} = J_\mathrm{pair,s} + J_\mathrm{pair,dd} = U_{iijj}/2$ of two atoms originally occupying the same lattice site. As this term features very small energies (grey lines in Fig. 5.3(a)) it will not be further discussed.

5.2.3. Extended spinor Fermi-Hubbard model

Fermi-Hubbard models

Fermi-Hubbard models are very relevant as they can be directly related to the description of electrons in solid state systems. Fermionic particles show completely distinct quantum statistics with respect to their bosonic opponents as Pauli exclusion principle prohibits two identical fermions to occupy the same quantum state. This has striking consequences for the case of spin-polarized particles, as double occupancies (in the single-band picture) are suppressed and the lattice Hamiltonian includes solely the tunneling term J.

The description changes once a fermionic spin-$1/2$ system is considered. Due to the distinguishability of the particles double occupancies become allowed, adding onsite interaction U to the Hamiltonian. Additionally, nearest-neighbor exchange interactions can arise due to superexchange correlations. For the case of $U \gg J$ the Hamiltonian resembles the celebrated $t-J$ model[3] [Aue94]. Here, for the case of half-filling, i. e. one atom per lattice site and an in total equal spin number, the system is in a Mott insulator state and an antiferromagnetic ground state is expected [Man91]. A particular relevant scenario emerges when the system undergoes doping, i. e. when the filling fraction is lowered. Here, strong relations to high-temperature (high-T_c) superconductors such as cuprates [And87] can be drawn. The microscopic description of high-T_c superconductors still puzzles the community and it is believed that with the use of ultracold spin-$1/2$ fermions as a model system for electronic spins in solids important insights can be be gained, see Ref. [Lee06] for a review. Indeed, the high control on parameters such as temperature, interaction, and doping, nowadays reached

[3] This model is well discussed in literature. Here, the notation typically differs from ours. t denotes for the tunneling rate and $J = 4t^2/U$ for a spin conserving nearest-neighbor correlation due to superexchange coupling.

the single-atom level via quantum gas microscopes techniques, see e. g. Ref. [Maz17b]. This gives exciting prospects for future explorations with this already comprehensive quantum simulators of regimes where theoretical simulations fail.

While the rather simple Hamiltonian of the $t-J$ model already provides surprisingly rich physics along the phase diagram, ultracold atoms give possibilities to further enrich the systems description. Adding long-range interactions yields Hubbard systems where the interparticle interaction ranges beyond nearest neighbors. Further, by upgrading the spin degree of freedom, high spin Hubbard models can be accessed. Both upgrades can be implemented via the use of fermionic erbium. First, erbium provides long-range dipolar interactions and second, the fermionic isotope features a large number of 20 spin states in the atomic ground state, see Sec. 2.2.4. This gives promising prospects for the implementation of exotic lattice models.

Fermi-Hubbard model with dipolar interaction

For single-spin dipolar particles, the extended Fermi Hubbard model includes in addition to the tunneling term J the long-range NNI term V while the onsite term U remains absent. To enrich the scenario, additional spin states can be added, resulting in the *extended spinor Fermi Hubbard* (eFH) Hamiltonian. This Hamiltonian is derived via a very similar treatment as for the bosonic case, see Sec. 5.2.2, and reads as [Aue94, Dut15]

$$\begin{aligned} H = & -J \sum_{\langle ij\rangle,\sigma} \left(b^\dagger_{\sigma_i} b_{\sigma_j} + h.c. \right) + \sum_{i,\sigma} V_{\mathrm{h},i}\, n_{\sigma_i} + U \sum_{i,\sigma\neq\sigma'} n_{\sigma_i} n_{\sigma'_i} \\ & + \sum_{i<j,\sigma} V_{\sigma_i,\sigma_j} \left[F^z_{\sigma_i} F^z_{\sigma_j} - \frac{1}{4}(F^+_{\sigma_i} F^-_{\sigma_j} + F^-_{\sigma_i} F^+_{\sigma_j}) \right]. \end{aligned} \tag{5.15}$$

Similarly to the bosonic case, $\langle ij\rangle$ denote pairs of adjacent sites, $b^\dagger_{\sigma_i}$ (b_{σ_i}) are the fermionic creation (annihilation) operators of an atom at site i, and $n_{\sigma_i} = b^\dagger_{\sigma_i} b_{\sigma_i}$ is the associated number operator. The spin degree of freedom is encoded in σ, which for the case of fermionic erbium can be replaced by the state $|F, m_F\rangle$. For the sake of simplicity the terms accounting for density induced tunneling and pair hopping, see Sec. 5.2.2, are not included, while the potential energy gradient term $V_{\mathrm{h},i}$ is given for completeness. Figure 5.4 gives all relevant terms of the eFH model.

The single-particle tunneling J (Fig. 5.4(b1)) and the onsite energy U_s that arises from interspin contact interactions between two distinguishable fermions, show the same strengths as for the bosonic case (compare blue and red solid lines in Fig. 5.4(a) and Fig. 5.3(a))[4]. The dipolar contribution to the onsite energy (red dashed line in Fig. 5.4(a)) gives similar results as for the bosonic case. However, it should be noted that this energy crucially depends on the composition of spin states.

In the case of a spinor dipolar Fermi gases in a 3D lattice the most prominent offsite terms are given by the NNI $F^z_{\sigma_i} F^z_{\sigma_j}$ (Fig. 5.4(b3)) and the flip-flop term $F^+_{\sigma_i} F^-_{\sigma_j}$ (Fig. 5.4(b4)). The

[4] We note that the tunneling term J is equal for all spin states.

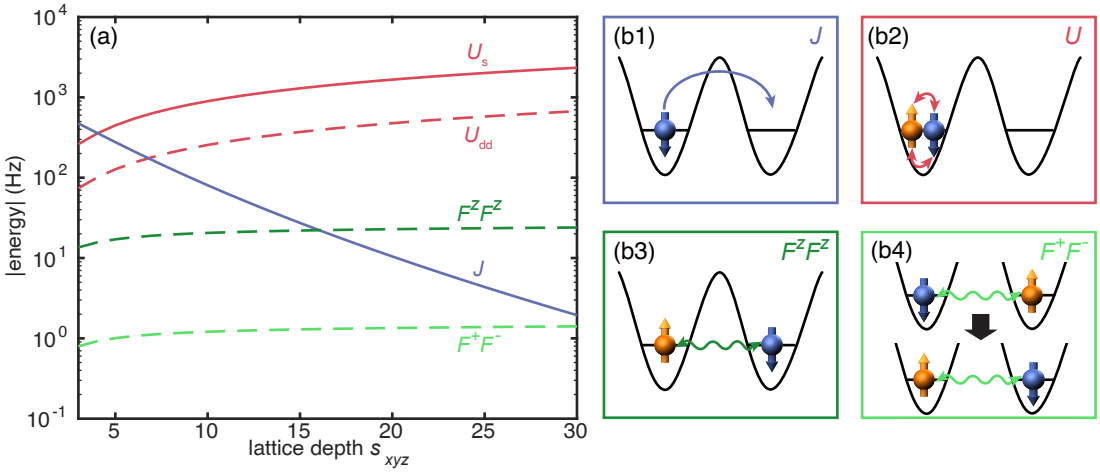

Figure 5.4.: Extended Fermi-Hubbard terms. (a) Absolut energies of the individual matrix elements for the case of the two lowest spin states of fermionic erbium in a 3D lattice for our experimental lattice setup, see Appendix B, as a function of the 3D lattice depth $s_{xyz} = s_x = s_y = s_z$. The terms are calculated along the horizontal plane (xy) with a lattice spacing of $d = 266\,\mathrm{nm}$ and a dipole orientation along the vertical z axis. The interspin s-wave scattering length is set to $a_\mathrm{s} = 100\,a_0$. Beside the tunneling amplitude J all terms have contributions from the interspin contact interaction (solid lines) and the dipolar interactions (dashed lines), see text. (b1-b4) Illustrations of the relevant terms of the eFH model for the case of two spin states $|\downarrow\rangle$ and $|\uparrow\rangle$ (blue and orange dipole, respectively). Nearst-neighbor terms arising from the F^zF^z and the F^+F^- coupling are included.

spin operators obey the rules

$$F^z|F, m_F\rangle = m_F|F, m_F\rangle \tag{5.16}$$

and

$$F^\pm|F, m_F\rangle = \sqrt{F(F+1) - m_F(m_F \pm 1)}|F, m_F \pm 1\rangle. \tag{5.17}$$

V_{σ_i,σ_j}, see Eq. 5.15, denotes the dipolar coupling strength and can be derived via

$$V_{\sigma_i,\sigma_j} = \int d\mathbf{r} \int d\mathbf{r}' w_i^*(\mathbf{r}) w_j^*(\mathbf{r}') \left(\frac{\mu_0 (g_F \mu_\mathrm{B})^2}{4\pi} \frac{1 - 3\cos^2\theta_{\mathbf{r}-\mathbf{r}'}}{|\mathbf{r} - \mathbf{r}'|^3} \right) w_i(\mathbf{r}) w_j(\mathbf{r}'). \tag{5.18}$$

While the NNI term features larger energies as the flip-flop term (dark and light green dashed lines in Fig. 5.4(a)), the flip-flop term can lead to resonant spin dynamics, see Sec. 6.2.

Additional (single particle) terms that have to be considered in experiments result from spin-dependent potential energies. This energies arise from the Zeeman energy

$$H_\mathrm{Zeeman} = \sum_{i,\sigma} \left[q_\mathrm{li}(B)\sigma + q_\mathrm{qu}(B^2)(\sigma^2 - F^2) \right] n_{\sigma_i}, \tag{5.19}$$

see Sec. 2.2.4, and from spin-dependent light shifts

$$H_\mathrm{light} = \sum_{i,\sigma} q_\mathrm{L}(I)\sigma_i^2 n_{\sigma_i}. \tag{5.20}$$

The light shift, being a consequence of the tensorial dynamical polarizability, see Appendix A.2, is proportional to the intensity I of the confining laser traps. It should be noted that the presented Hamiltonian can also feature terms that do not conserve the total magnetization $F^z_\mathrm{tot} = \sum_i S_i^z$ as discussed in Sec. 6.2.

5.3. Quantum phase transitions

The extended Hubbard models discussed in Sec. 5.2.2 and Sec. 5.2.3 do not only determine the relevant energy scales of the underlying system, but also give access to the dynamics of the strongly correlated many-body wavefunction. In particular, quantum phase transitions can be driven by changing the strength and the ratio of the different Hamiltonian parameters. Within this section, we will briefly review the different phases expected for bosonic and fermionic systems in 3D lattices, and will set them in context with our experiment. In the case of bosons, a superfluid-to-Mott insulator quantum phase transition can be driven, where for a two-component Fermi gas the initial metal phase can undergo phase transitions to either a band or a Mott insulating state.

5.3.1. Superfluid-to-Mott insulator transition

A seminal example where the many-body dynamics of a system are changed in a dramatic way is the superfluid-to-Mott insulator (SF-MI) quantum phase transition. The superfluid phase is characterized by a large (integer) number fluctuation on a single lattice site, resulting from a delocalized phase-coherent matter wave across the lattice. In contrast, in the insulating regime, the ground state consists of exponentially localized bosonic wavefunctions leading to a loss of global phase coherence. In the MI phase the excitations spectrum, associated to the onsite energy U, is gapped and an incompressible state is formed. The quantum phase transition can be driven by tuning the strength of the interaction term U with respect to the tunneling term J. From a mean-field treatment for an average site occupation of $\langle n \rangle = 1$, the phase transition is predicted to occur at the critical value $(U/J)_\mathrm{c} = z \times 5.8$ with z associated to the system's dimensionality via the number of nearest neighbors. While this value is found to be in reasonable agreement with Quantum Monte carlo simulations for the 3D case, $(U/J)_\mathrm{c} \approx 29.3$ [CS07], it differs significantly from Quantum Monte carlo simulations for the 2D case, $(U/J)_\mathrm{c} \approx 16.7$ [CS08], and from DMRG simulations in the 1D case, $(U/J)_\mathrm{c} \approx 3.4$ [Küh00].

In ultracold experiments, the respective Hamiltonian parameters can be conveniently tuned via the lattice depth s. This technique led to the first experimental demonstration of the SF-MI quantum phase transition in 2002 [Gre02]. Nowadays, the phase transition can even be studied on the single-atom level via quantum gas microscope techniques [She10, Bak10]. This methods allow to directly visualize the typical Mott structure, consisting of concentric shells with commensurate fillings of density $\langle n \rangle = 1, 2, 3 \ldots$ (from outside to the lattice center), resulting from a weak transversal confinement of the optical lattice beams.

As the SF-MI transition is driven by the competition of U and J, for the case of dipolar particles the contributions of the DDI to these terms has to be taken into account. Precisely, one has to consider the ratio between the *total* onsite energy $U_\mathrm{total} = U_\mathrm{s} + U_\mathrm{dd}$ and the *total* tunneling rate $J_\mathrm{total} = J + \Delta J_\mathrm{s} + \Delta J_\mathrm{dd}$ along the three directions. In Sec. 5.5 we study the phase transition in such a dipolar system, proving a unique tunability of the critical value via the dipole orientation. Further, for dipolar interactions, the phase diagram becomes enriched by new and exotic quantum phases such as the checkerboard or the stripe phase [CS10]. The preparation of such phases is at reach with our system.

5.3.2. Metal to band and Mott insulator transition

A two-state fermionic mixture in an optical lattice shows a rich phase diagram. The relevant energy scales that have to be compared are the onsite energy U, the width of the lowest Bloch band W that is related to the tunneling rate[5], and the chemical potential μ[6]. For the case of weak interactions and a shallow trap ($U \ll \mu \ll W$), the system is in a metallic state and the atomic wave functions are delocalized. The system is compressible and the central filling per spin state $\langle n_\sigma \rangle$ remains below 1, resulting in the occurrence of holes but also doubly occupied sites (doublons). When the interaction energy U is dominating ($U \gg \mu \gg W$) doublons become suppressed and the system enters into the Mott insulating phase with $\langle n_\sigma \rangle = 1/2$. This phase shows a gapped excitation spectrum and can be described by two Hubbard bands, where the upper band relates to the case of double occupancies. When the chemical potential exceeds the onsite energy ($\mu \gg U, W$) filling of this upper band becomes favorable and a band insulator forms with $\langle n_\sigma \rangle = 1$ at zero temperature. Here, every site is occupied by each spin state and a further compression of the sample is not possible due to the Pauli exclusion principle. It should be noted that in the case of a single spin system a Mott insulating phase is absent, and the system enters into a band insulator, i. e. $\langle n_\sigma \rangle = 1$, when μ exceeds W.

Pioneering experiments succeeded in observing band- [Köh05] and Mott-insulating phases [Jör08, Sch08] by studying global observables. With the advent of fermionic quantum gas microscopes, the investigation of the phase transitions with single-site resolution has become available. As a result of the variation of the (local) density across the lattice due to the harmonic confinement, the coexistance of all quantum phases within a single sample is possible, which was nicely visualized with quantum gas microscope techniques [Omr15, Gre16, Che16].

All this experiments set the stage to further explore the fermionic phase diagram. Indeed, for low enough temperature, the Mott insulator state can undergo a phase transition to an antiferromagnetically ordered state owing to spin-spin interactions via superexchange coupling. While already in 2013 a promising experiment demonstrated short-range magnetic ordering [Gre13], it remained an outstanding challenge to reach temperatures well below the superexchange energy scale. It was not before 2017 that the group of Markus Greiner in Harvard managed to engineer the entropy in such a way that a long-range ordered antiferromagnet was formed [Maz17b].

For the case of dipolar particles, additional quantum phases are expected due to the anisotropic and long-range nature of the DDI. While superexchange coupling remains isotropic, dipolar interaction can show different strengths and even a different sign along perpendicular lattice directions. A recent theoretical work explores the possibility to adiabatically prepare a striped ground state with dipolar atoms aligned within the plane of a 2D optical lattice. The formation of the stripe state is driven by the competition of the long-range dipolar correlations of neighboring spins that reside in adjacent Zeeman states [Maz17a].

[5] For the case of an isotropic 3D lattice $W = 12J$.

[6] The chemical potential scales with the strength of the radial harmonic confinement, see $V_{\mathrm{h},i}$ in Eq. 5.15, and with the total atom number.

While the study of quantum phase transitions is one of the prime research directions with ultracold experiments, the ability to prepare insulating phases is also a powerful tool to protect the atomic sample from inelastic collisions. Pinning particles within a deep 3D optical lattice strongly restricts their movement and their ability to interact with each other. As a consequence, a large collisional protection can be realized [Tha06]. This can also nicely facilitate the study of *dipolar* spin mixtures, as dipolar relaxations [Bur15] can be strongly suppressed. In Sec. 5.6 we apply the method of lattice protection to prepare spin mixtures of the two lowest magnetic substates of fermionic erbium in a Mott-type state.

5.4. Extended Hubbard models in experiments with dipolar particles

In order to experimentally access the extended Hubbard models that we have discussed in Sec. 5.2.2 and Sec. 5.2.3 we have upgraded our experiment by implementing a 3D optical lattice. The lattice is formed by three retro-reflected orthogonal red-detuned laser beams[7] operated at 532 nm along two horizontal axes and at 1064 nm along the vertical axis. The resulting standing waves along the three orthogonal axes impose a 3D lattice structure on the atomic cloud. The experimental setup of our optical lattice is described in detail in Appendix B.

Importantly, the high natural abundance of bosonic and fermionic isotopes in erbium, see Sec. 2.1, allows us to prepare both eBH *and* eFH systems and gives us a large flexibility for the study of different quantum models and quantum phases. Prior to the study of new and exotic quantum phases, it is necessary to properly understand and characterize our system. This has been one of the major goals of this thesis. In particular, we have quantitatively analyzed the eBH terms prepared with our dipolar bosonic system. Similar investigations for our dipolar fermionic system are currently carried out, see Sec. 6.2. To characterize the individual terms of the Hamiltonian, lattice spectroscopy can be applied. As a result of the interaction terms, an energy gap can open up between neighboring lattice sites. This gap can be measured via lattice modulation spectroscopy and carries information on the onsite term U and the offsite term V of the Hamiltonian. As this method is one of the major tools of our experiment, we will discuss it in the following section.

5.4.1. Lattice modulation spectroscopy

Depending on the number of particles occupying a given lattice site and on their interactions the ground state energy of this lattice site can be modified. This is a direct consequence of the onsite energy U and results in an up- or downshift of the state for repulsive and attractive interactions, respectively. This energy shift can be accessed by resonantly driving particle-hole excitations, e. g. by forming a double occupancy (doublon) out of two single occupancies on neighboring lattice sites. To allow for such a process, energy has to be deposited into the

[7] See Appendix A.2 for a definition of the red- and blue-detuned regions of the dynamical polarizability of erbium.

system. This can be conveniently utilized via amplitude modulation of the lattice potential with a certain modulation frequency ν_{mod}, see Refs. [Stö04, Kol06, Cla06]. If the energy of the lattice modulation $E_{\mathrm{mod}} = h\nu_{\mathrm{mod}}$ matches the onsite energy U a particle-hole excitation is resonantly driven.

As a probe of this resonant feature different methods are available. For the case of bosonic particles, one can monitor the remaining fraction of atoms in the Bose-Einstein condensate (BEC) after adiabatically melting the lattice, see also Ref. [Mar11]. If particle-hole excitations have been driven, the system has gained energy and hence the final BEC fraction will be reduced. In the case of fermionic particles, particle-hole excitations are only allowed if additional spin states are available, as for spin-polarized fermions the Pauli exclusion principle prohibits doublons in a single lattice band. The resonant condition of the modulation spectroscopy can be extracted via the increase in temperature after going back to a degenerate Fermi gas. For dipolar particles, the formation of two-spin state doublons can also be monitored via particle loss if dipolar relaxations take place.

In the case of dipolar systems, the onsite energy U consists of contributions from the isotropic contact interaction and the anisotropic DDI, as discussed in Sec. 5.2.2. Comparing the measured energy to numerical simulations of the system at hand enables to extract the individual contributions. In particular, one can determine the s-wave scattering length a_{s}, which is directly proportional to U_{s}. This is a powerful method to precisely measure the scattering properties of the system. This information can in turn be used to investigate fascinating physical phenomena, see also Sec. 4.1.4.

Further details on the modulation spectroscopy method and on how to extract a_{s} are given in the publications presented in Sec. 5.5 and Sec. 5.6. Remarkably, the lattice modulation spectroscopy also allows to extract the offsite interaction V, a method invented by our group and reported in Sec. 5.5.

5.4.2. A dipolar bosonic quantum simulator

To prepare an analog quantum simulator of the eBH model, we adiabatically load a BEC of erbium atoms into a deep 3D optical lattice. In our publication contained in Sec. 5.5 we investigate the effects of the individual terms of the eBH model and quantify their strength. We show the first observation of the offsite dipolar interaction V_{dd} in eBH dynamics and set the stage for future investigations with lattice models influenced or even governed by dipolar long-range interactions [CS10]. In addition, we study the SF-to-MI phase transition, see Sec. 5.3.1, and reveal that the dipole orientation can significantly alter the phase transition point. Here, the main influence can be traced back to the angle dependence of the onsite dipolar interaction U_{dd}, but in order to find a better agreement between our experimental observations and theory, the dipolar DIT ΔJ_{dd} has to be taken into account.

5.4.3. A dipolar fermionic quantum simulator

To realize the Hamiltonian of Eq. 5.15 within our experiment, we first load a degenerate Fermi gas of spin-polarized ^{167}Er atoms into the 3D optical lattice and subsequentially deterministically prepare a spin mixture[8]. For our first investigation, we switch off the dipolar spin exchange term $F^+_{\sigma_i}F^-_{\sigma_j}$ by utilizing spin-dependent quadratic shifts via $H_{\text{Zeeman}} + H_{\text{light}}$. This allows us to investigate in detail the interaction properties of an effective spin-$^1/_2$ system consisting of the two lowest spin state $m_F = |{-}19/2\rangle$ and $m_F = |{-}17/2\rangle$. The interspin scattering length is extracted by modulation spectroscopy, see Sec. 5.4.1, in combination with our theoretical knowledge of the Hamiltonian terms in Eq. 5.15. Our publication that is contained in Sec. 5.6 reports on the finding of a relatively broad interspin Feshbach resonance, on which we demonstrate interaction tuning. Our investigation realizes for the first time a strongly interacting dipolar Fermi gas. Importantly, our preparation method via the lattice-protection technique, see Sec. 5.3.2, allows to access deeply degenerate fermionic mixtures at any magnetic field, since the pinning of atoms to individual lattices sites in deep lattices strongly suppresses dipolar relaxation losses.

Importantly, the performed study only sets the starting point for our experiment, as with our dipolar fermionic quantum simulator at hand, a large amount of investigations become accessible. A promising direction emerges from studies of spin dynamics along the Heisenberg model, see Sec. 6.2. Further, the realization of a magnetically ordered ground state is at reach [Maz17a].

[8] For the deterministic preparation of the spin states, we utilize the spin-dependent quadratic Zeeman shift, which leads to a lifting of the degenerate coupling between three adjacent spin states, see Eq. 2.10. The differential splitting allows for selective spin-addressing already at moderate magnetic field values via radio-frequency techniques.

5.5. Publication: Extended Bose-Hubbard models with ultracold magnetic atoms[†‡]

Science **352**, 6282 (2016)
submitted 10 Jul 2015; published 8 Apr 2016
DOI 10.1126/science.aac9812

Simon Baier,[1] Manfred J. Mark,[1,2] Daniel Petter,[1] Kiyotaka Aikawa,[1] Lauriane Chomaz,[1,2] Zi Cai,[2] Mikhail Baranov,[2] Peter Zoller,[2,3] F. Ferlaino[1,2]

[1] *Institut für Experimentalphysik, Universität Innsbruck, Technikerstraße 25, 6020 Innsbruck, Austria*
[2] *Institut für Quantenoptik und Quanteninformation, Österreichische Akademie der Wissenschaften, 6020 Innsbruck, Austria*
[3] *Institut für Theoretische Physik, Universität Innsbruck, Technikerstraße 21A, 6020 Innsbruck, Austria*

[†] The author of the present thesis developed the experimental procedures together with K. A., and M. J. M., performed the measurements with the help of D. P., K. A., and L. C., analyzed the data, and contributed strongly in writing the manuscript. The theoretical calculations of this publication have been contributed by Z. C., and M. B.

[‡] The post-print version of the publication is attached for online access of this thesis.

Extended Bose-Hubbard Models with Ultracold Magnetic Atoms

S. Baier,[1] M. J. Mark,[1,2] D. Petter,[1] K. Aikawa,[1,*] L. Chomaz,[1,2] Z. Cai,[2] M. Baranov,[2] P. Zoller,[2,3] and F. Ferlaino[1,2]

[1]*Institut für Experimentalphysik, Universität Innsbruck, Technikerstraße 25, 6020 Innsbruck, Austria*
[2]*Institut für Quantenoptik und Quanteninformation, Österreichische Akademie der Wissenschaften, 6020 Innsbruck, Austria*
[3]*Institut für Theoretische Physik, Universität Innsbruck, Technikerstraße 21A, 6020 Innsbruck, Austria*

(Dated: May 4, 2018)

The Hubbard model underlies our understanding of strongly correlated materials. Whereas its standard form only comprises interactions between particles at the same lattice site, extending it to encompass long-range interactions is predicted to profoundly alter the quantum behavior of the system. We realize the extended Bose-Hubbard model for an ultracold gas of strongly magnetic erbium atoms in a three-dimensional optical lattice. Controlling the orientation of the atomic dipoles, we reveal the anisotropic character of the onsite interaction and hopping dynamics, and their influence on the superfluid-to-Mott insulator quantum phase transition. Moreover, we observe nearest-neighbor interactions, a genuine consequence of the long-range nature of dipolar interactions. Our results lay the groundwork for future studies of exotic many-body quantum phases.

PACS numbers: 67.85.Hj, 37.10.De, 51.60.+a, 05.30.Rt

Dipolar interactions, reflecting the forces between a pair of magnetic or electric dipoles, account for many physically and biologically important phenomena. These range from quantum many-body phases [1, 2], to liquid crystals and ferrofluids [3, 4], to the mechanisms underlying protein folding [5]. The distinguishing feature of the dipole-dipole interaction (DDI) is its long-range and anisotropic character [6]: two dipoles oriented in parallel repel each other, whereas the interaction between two head-to-tail dipoles is attractive. Notable progress towards the ability to study DDI has been made recently in systems containing electric dipoles, such as gases of polar molecules [7] and Rydberg ensembles [8]; similarly, the recent experimental advances in creating quantum degenerate gases of bosonic and fermionic magnetic atoms, including Cr [9–11] and the Lanthanides Er [12, 13] and Dy [14, 15], have now opened the door to a study of magnetic dipolar interactions.

Ultracold Lanthanide atoms have an open electronic f-shell, and anisotropic interactions; they are characterized by unconventional low-energy scattering properties, including the proliferation of Feshbach resonances [16]. This complexity manifests itself in quantum many-body dynamics: by preparing quantum degenerate Lanthanide gases in optical lattices we can realize extended Hubbard models for bosonic and fermionic atoms [2, 17]. In addition to the familiar single-particle tunneling and isotropic onsite interactions (as for contact interactions in Alkali), dipolar interactions give rise to anisotropic onsite interactions and density-induced tunneling (DIT), and activate nearest-neighbor (offsite) interactions (NNI). Such extended Hubbard models have been extensively studied in theoretical condensed matter physics and quantum material science [18, 19], and it is the competition between these unconventional Hubbard interactions that underlies the prediction of exotic quantum phases such as supersolids, stripe and checkerboard phases [17, 20–26].

Here we report a first observation of the unique manifestations of magnetic dipolar interactions in extended Hubbard dynamics. These observations are enabled by preparing an ultracold sample of bosonic Er atoms in an three-dimensional (3D) optical lattice. It is the control of the optical lattice via laser parameters in combination with a flexible alignment of the magnetic dipoles in an external magnetic field, which allows us to reveal and explore the anisotropic onsite and offsite interactions. Measurements of the excitation spectrum in the Mott insulator state, and of the superfluid-to-Mott-insulator (SF-to-MI) quantum phase transition are employed as a tool to detect these interactions and their competitions.

In our experiment an ultracold dipolar gas of ^{168}Er atoms is prepared in a 3D optical lattice. The atoms are fully spin-polarized in their lowest Zeeman sublevel [12] and feature a magnetic moment μ of 7 Bohr magneton. The experiment starts by adiabatically loading a Bose-Einstein condensate (BEC) of about 1.5×10^5 atoms from an optical dipole trap (ODT) into a 3D optical lattice. The lattice is created by two retroreflected 532-nm laser beams, defining the horizontal xy-plane, and one 1064-nm beam, nearly collinear with the vertical (z) direction, defined by gravity (Fig. 1A) [27]. The lattice has a cuboid unit cell with lattice constants $d_{x,y} = 266\,\mathrm{nm}$ and $d_z = 532\,\mathrm{nm}$, which for ^{168}Er correspond to the recoil energies $\mathrm{E_{R},}_x = \mathrm{E_{R},}_y = h \times 4.2\,\mathrm{kHz}$ and $\mathrm{E_{R},}_z = h \times 1.05\,\mathrm{kHz}$, h being Planck's constant. The lattice can be controlled by independently changing the depths associated with the lattice beams in each direction, (s_x, s_y, s_z), measured here in units of the corresponding recoil energies. The dipole orientation, quantified by the polar angles θ and ϕ (Fig. 1A, inset), is varied by changing the direction of the polarizing magnetic field [27]. When increasing the lattice depths we can prepare the Er atoms in the Mott Insulator (MI) state, by driving the superfluid (SF)-to-MI phase transition, as described below.

The dynamics of Er atoms in the optical lattice are described by an extended Bose-Hubbard (eBH) model with

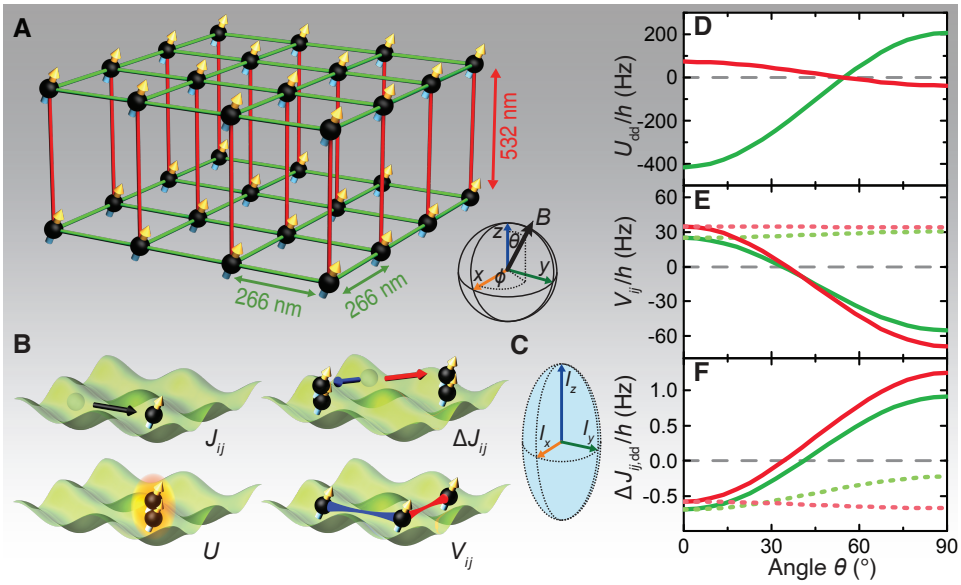

FIG. 1. **Magnetic dipoles in a 3D optical lattice.** (A) Schematic of our lattice geometry, where the lattice spacings are indicated. The dipole orientation, given by the polarizing magnetic field B, is quantified by the polar angles θ and ϕ with respect to our coordinate system. (B) Illustration of the contributing terms in the eBH model: Tunneling matrix element J_{ij}, DIT matrix elements ΔJ_{ij}, onsite interaction U, and NNI V_{ij}. (C) Illustration of the single-site density distribution, where the harmonic oscillator lengths are indicated. (D to F) Calculated values of the DDI-dependent terms as a function of θ for $\phi = 0^\circ$ in the MI phase, $(s_x, s_y, s_z) = (15, 15, s_z)$ with s_z set by the AR for the cases AR $= 1$ (red) and AR $= 2$ (green). (D) shows $U_{\rm dd}$. (E) and (F) show V_{ij} and $\Delta J_{ij,\rm dd}$ respectively, for bond and hopping directions ij both along x (solid lines) and y (dotted lines). The dashed lines indicate the case without DDI. $U_{\rm s}$ and J_{ij} are independent of θ and their values for the two configurations considered are $U_{\rm s} = 3749\,$Hz (1775 Hz) for AR $= 1$ (2) and $J_{ij} = 27\,$Hz for $ij = x$ or y.

Hamiltonian [17, 28]

$$H = -\sum_{\langle ij\rangle}\left[\left(J_{ij} + \Delta J_{ij}(n_i + n_j - 1)\right) b_i^\dagger b_j + \text{h.c.}\right] + \frac{U}{2}\sum_i n_i(n_i - 1) + \sum_{\langle ij\rangle} V_{ij} n_i n_j. \quad (1)$$

Here $b_i^\dagger$ (b_i) are the bosonic creation (annihilation) operators of an atom at site i, $n_i = b_i^\dagger b_i$ is the associated number operator, and $\langle ij\rangle$ denotes pairs of adjacent sites. All terms of the eBH are illustrated in Fig. 1B. The interactions manifest themselves in both the tunneling dynamics, the onsite (U) and the offsite (V_{ij}, approximated to NNI) interaction. In addition to the single-particle hopping, which here has amplitudes J_{ij} reflecting the anisotropy of the optical lattice, Eq. 1 includes DIT terms (ΔJ_{ij}). The onsite interaction (U) and DIT terms (ΔJ_{ij}) have contributions ($U_{\rm s}$ and $\Delta J_{ij,\rm s}$) from the short-range contact interaction, which is proportional to the s-wave scattering length $a_{\rm s}$; they also have contributions ($U_{\rm dd}$ and $\Delta J_{ij,\rm dd}$) from the long-range DDI, which is proportional to μ^2 [17, 27]. The DIT have recently been observed in purely contact interacting systems [29, 30]. The NNI (V_{ij}) is a term that genuinely originates from the long-range DDI. The NNI in spin-polarized dipolar systems is qualitatively different from Heisenberg spin-spin interaction between atoms at neighboring sites $\langle ij\rangle$ [31, 32], which arises from superexchange processes in Hubbard dynamics in second-order virtual hopping processes ($\sim J_{ij}^2/U$) in the limit of large onsite interaction, and different from dipolar spin-exchange interactions [7] and full Heisenberg type interactions [10], driving flip-flop dynamics.

The angle dependence of the DDI reveals itself more prominently in combination with anisotropic geometries [33]. By changing the lattice depths (s_x, s_y, s_z) in the three directions independently, we can control the aspect ratio (AR) of the three-dimensional density distribution at a given lattice site (Fig. 1C), i.e. we can shape the anisotropy of the three-dimensional Wannier function. For simplicity, we define the AR using the harmonic approximation, AR $= l_z/l_{x,y}$, where l_z ($l_x = l_y$) is the harmonic oscillator length along the z (xy) direction of the local atomic well. In our experiment $s_x = s_y$, such that z is the anisotropy axis. The symmetric condition, defined as $U_{\rm dd} = 0$, is slightly shifted with respect to AR $= 1$, when using Wannier functions (e.g. AR $= 1.05$ for $s_x = s_y = 15$ and AR $= 1.07$ for $s_x = s_y = 10$) [34]. For $U_{\rm dd}$, the relative weight between the attractive and repulsive contributions can be tuned by changing the dipole orientation relative to the anisotropy axis of the onsite density distribution, and the AR (Fig. 1D). In contrast, the NNI V_{ij} is controlled mainly through the orientation of the dipoles with respect to the bond direction ij (Fig. 1E). Finally, $\Delta J_{ij,\rm dd}$ depends both on the orientation of the dipoles relative to the bond direction and the anisotropy axis, and on the AR (Fig. 1F).

We first investigate the impact of the DDI on the onsite in-

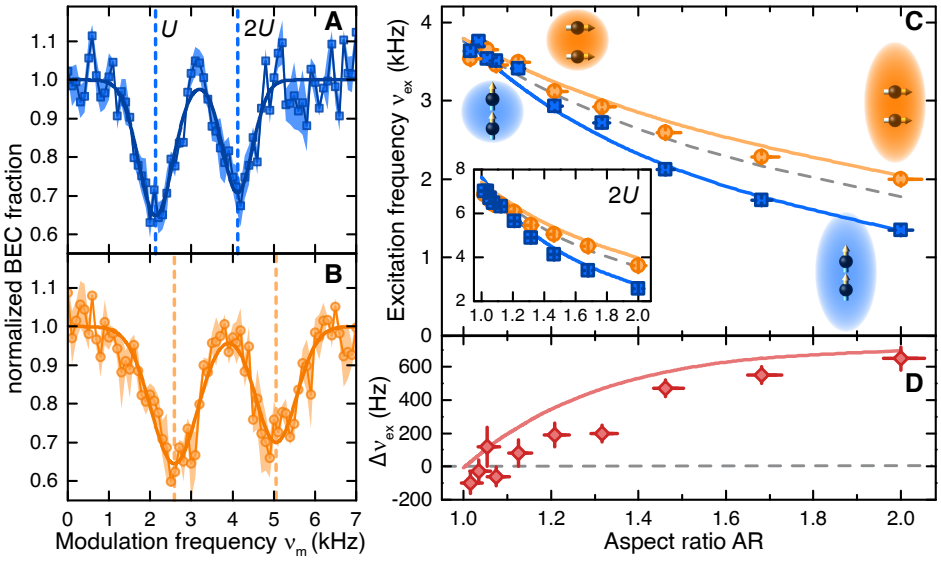

FIG. 2. **Measurement of the onsite interactions.** (A and B) Excitation spectrum of the MI state for dipole orientations $\theta = 0°$ (A) and $\theta = 90°$ (B) with $\phi = 0°$. The modulation spectroscopy is performed along the x-axis at $(s_x, s_y, s_z) = (15, 15, 52.5)$, corresponding to AR ≈ 1.46 and the remaining BEC fraction is measured after adiabatically ramping down the lattice depths to zero. From a double Gaussian fit to the data (solid line) we extract the resonant excitation frequency ν_{ex} for the U and $2U$ feature. (C) ν_{ex} for the loss feature at U and $2U$ (inset) as a function of AR for $\theta = 0°$ (squares) and $\theta = 90°$ (circles). (D) Difference in excitation frequencies ν_{ex} relative to the two dipole orientations, $\Delta\nu_{\mathrm{ex}}$, as a function of AR. The error bars for all figures are the sum of the SEM and systematic errors [27]. The theoretical model (solid lines in C and D) also includes the effect of the NNI, which shifts the excitation frequency by up to 3 % (see Fig. 3). Dashed lines: calculations accounting only for the isotropic (contact) interaction.

teraction (U_{dd}) by performing spectroscopic measurements. We prepare our system deep in the MI phase and probe the energy gap in the excitation spectrum for different dipole orientations. This energy gap, associated with particle-hole excitations, is U for atoms in singly- or doubly-occupied Mott shells and $2U$ at the border between the two shells and at doublon defects within the first Mott-shell [35–38]. We excite the MI state by applying a sinusoidal modulation of frequency ν_{ex} on the intensity of the x-lattice beam. When $h\nu_{\mathrm{ex}}$ matches U or $2U$, we observe a resonant depletion of the remaining condensate fraction after ramping down the lattice [27]. We perform the measurement for $\theta = 0°$ and $\theta = 90°$ (Fig. 2, A and B) with $\phi = 0°$ and observe that the resonance positions clearly depend on the dipole orientation, consistent with our expectation.

To further explore this effect, we repeat the measurement for different values of the AR (Fig. 2C). At the symmetric condition (AR $= 1.05$), we observe that the excitation gap looses its angle dependence showing that U_{dd} averages to zero [39]. As the spatial distribution is deformed towards larger AR, we find a clear deviation from the purely contact-interaction case (dashed lines), with a smaller energy gap for dipoles at $\theta = 0°$, and a larger one for dipoles at $\theta = 90°$. For large ARs, the dipole orientation substantially affects the incompressibility of the corresponding Mott state with the energy difference between the two dipole configurations of up to $h \times \Delta\nu_{\mathrm{ex}} = h \times 600\,\mathrm{Hz}$ (Fig. 2D). The observed angle dependence is well described within our eBH model (Fig. 2, C and D, solid lines). The theory for Fig. 2D is parameter free, whereas for Fig. 2C a_{s} is the only fit parameter. From the fit we find $a_{\mathrm{s}} = 137(1)\,\mathrm{a}_0$, with a_0 being the Bohr radius, which is consistent with previous measurements based on thermalization experiments [12]. Our measurement shows that U_{dd} plays a fundamental role in the stability of the MI phase: it can either protect the MI phase for the dominantly repulsive DDI ($\theta = 90°$) or make it more susceptible to excitations for the dominantly attractive case ($\theta = 0°$).

The energy gap in the MI phase also depends on the NNI between atoms occupying adjacent lattice sites. To isolate the contribution of the NNI in the eBH, we design a dedicated measurement scheme based on modulation spectroscopy in the 2D short-spacing lattice plane (xy-plane), where the NNI is stronger (Fig. 3A). For a system with only onsite interactions the energy gap associated with the particle-hole excitation does not depend on the direction of excitation, i.e. on the direction of the modulated beam. In contrast, a system including anisotropic NNI will exhibit a modification of the energy gap according to the excitation direction as the energy gap equals $U - V_{ij}$ for excitations along the bond direction ij. Hence the difference between the two resonance frequencies measured by modulating s_x and s_y, denoted as $\Delta V_{\mathrm{NNI}}/h$, directly reveals the existence of the NNI as the onsite contribution cancels. Our scheme is illustrated in Fig. 3, A to C, for the case $\theta = 90°, \phi = 90°$. Here, one bond of attractive (repulsive) NNI with energy V^{att} (V^{rep}) is destroyed during the excitation along (perpendicular to) the dipole orien-

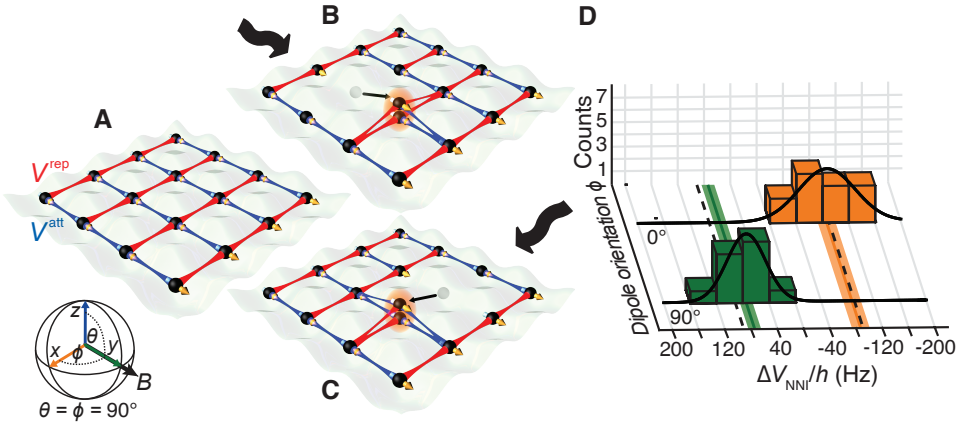

FIG. 3. **Nearest neighbor interactions.** (A) Initial system in the MI regime with dipole orientation $\theta = 90°$, $\phi = 90°$. Driving excitations along y (B) or x (C) leads to two different particle-hole energy gaps $U - V^{\rm att}$ and $U - V^{\rm rep}$, respectively. Here, $V^{\rm att} = V_{ij}$ with in-plane head-to-tail dipole orientations and $V^{\rm rep} = V_{ij}$ for the in-plane side-by-side orientation. The difference between the two resonant energies $\Delta V_{\rm NNI}$, equal to $-V^{\rm att} + V^{\rm rep}$, reveals the NNI. (D) Histogram of our measurements of $\Delta V_{\rm NNI}$ for two dipole orientations $\phi = 0°$ and $\phi = 90°$. The black solid curves are the normal distributions of the corresponding data. The two dashed lines show the theoretical expectation values, whereas the orange and green lines show the corresponding measured values with the shaded areas indicating the SEM.

tation such that $\Delta V_{\rm NNI} = -V^{\rm att} + V^{\rm rep}$. Our measurement for two dipole orientations in the plane with $\phi = 90°$ ($0°$) give $\Delta V_{\rm NNI}/h = +74(10)\,$Hz ($-87(14)\,$Hz). Remarkably, $|\Delta V_{\rm NNI}|$ is similar for both values of ϕ as expected from the symmetry between these two configurations and is close to the theoretical expectation $h \times 91\,$Hz [27], as shown in Fig. 3D.

Finally, we use our understanding of the angle dependence of the Hamiltonian, to modify the many-body phase transition from a SF to a MI state by changing θ and AR. Figure 4A shows the textbook signature of the phase transition in the momentum distribution of a lattice-confined gas [40]: the interference pattern of the SF phase progressively disappears as the system is driven into the MI phase by increasing the lattice depths. However, in stark contrast with the purely contact-interaction case as in previous alkali experiments, we observe that the dynamics of the phase transition has a clear angle dependence. The full width at half maximum (FWHM) of the central interference peak reveals a different evolution with lattice depths for $\theta = 90°$ as compared to $\theta = 0°$, particularly for the largest AR (Fig. 4, B to D). This behavior is qualitatively consistent with our previous observations on $U_{\rm dd}$ because the phase transition is governed by the competition between the total onsite interaction, i. e. the sum of the dipolar and contact part, and the tunneling, U/J. For large ARs and $\theta = 90°$, the DDI is mainly repulsive and thus strengthens the pinning of particles in the MI phase with respect to the SF phase, whereas the contrary happens for $\theta = 0°$ where the SF phase is favored (Fig. 4B).

We systematically study the critical value of the lattice depth, $s_c(\theta)$, corresponding to the onset of the phase transition, for two dipole orientations, $\theta = 0°$ and $90°$, and various AR values. The determine $s_c(\theta)$ we use two independent methods. The first one, based on a double-line fit, identifies $s_c(\theta)$ as the point where the FWHM starts to grow, whereas the second method probes the visibility of the interference pattern [27, 41]. The visibility is more reliable for large ARs, where the system undergoes a three-dimensional phase transition and the side interference peaks have a larger contrast [27, 42]. Figure 4E shows $\Delta s_{\rm c} = s_{\rm c}(0°) - s_{\rm c}(90°)$ as a function of the AR. We find a substantial increase of $\Delta s_{\rm c}$ from negative to positive values, providing the opportunity to modify the phase diagram by tuning the strength and the sign of the DDI. In addition, we observe that $\Delta s_{\rm c}$ crosses zero at AR ≈ 1.2 (Fig. 4E). This value is surprising because, if the DDI affected only the onsite interaction, one should record the same symmetric condition as measured in the frozen gas regime, i. e. AR $= 1.07$ (dotted line in Fig. 4E). However, at AR $= 1.07$, we still observe an angle dependence of the phase transition with the MI phase favored for $\theta = 0°$ (Fig. 4D). This behavior could be explained if the DDI also affected the tunneling dynamics. In the eBH model, such a term appears in the form of a dipolar-interaction-driven-tunneling mechanisms, i. e. DIT, on top of the standard single-particle tunneling; see Eq. 1 and [29]. For our typical experimental parameters, the DIT is predicted to be on the order of a few percent of the single-particle tunneling and exhibits an angle dependence (Fig. 1F and inset in Fig. 4E), which leads for instance to a reduction of the overall tunneling for out-of-plane orientation ($\theta = 0°$) and thus to a shift of $s_{\rm c}(0°)$ to a smaller value. The presence of the DIT is consistent with our observations, as shown by the better agreement of our data with the mean-field calculations including the DIT (solid line in Fig. 4E) with respect to the calculations without DIT (dotted line in Fig. 4E). For completeness, we checked with Monte Carlo calculations that the observed behavior can not be explained by the NNI, as discussed in [27].

Quantum degenerate gases of magnetic Lanthanide atoms in optical lattices offer a new avenue to access the physics of

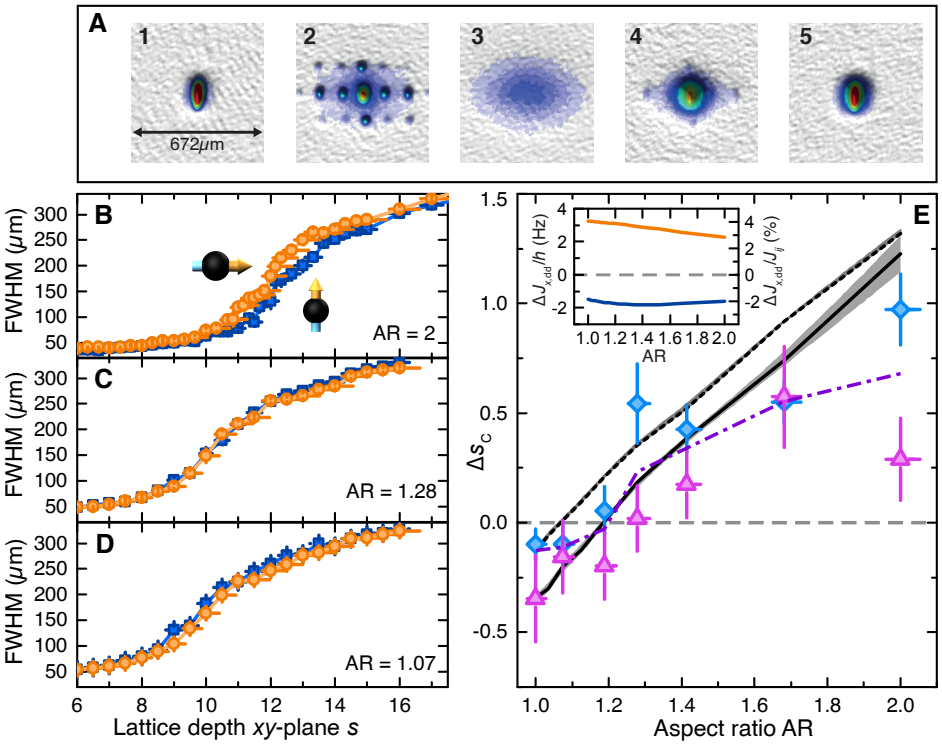

FIG. 4. **Superfluid-to-Mott-insulator transition.** (A) Time-of-flight absorption images of the atomic cloud at $\theta = \phi = 0°$ taken 27 ms after a sudden release from the 3D lattice with $s_{x,y,z} = s$ where $s = 0$, $s = 10$, $s = 22$ (A) 1 to 3, respectively and $s = 4$, $s = 0$ (A), 4 to 5, respectively. The distribution of the interference peaks (A2) reflects the anisotropy of the lattice in combination with the orientation of the reciprocal lattice with respect to the imaging light [27]. (B to D) The FWHM of the central interference peak as a function of the lattice depth in the xy-plane for AR $= 2; 1.28; 1.07$, with dipoles oriented along $\theta = 0°$ (blue squares) and $\theta = 90°$ (orange circles) with $\phi = 0°$. (E) Δs_c as a function of the AR. We extract $s_c(\theta)$ using both a double-line fit (triangles) and the visibility method (diamonds) [27]. The error bars for Δs_c represent the SEM from the fits and the dot-dashed line is the weighted mean of the two methods. We compare our data with mean-field calculations in presence (solid line) and absence of the DIT (dotted line). The grey shaded regions show the SEM, resulting from the resolution of the calculation[27]. The dashed line represents the purely contact interacting case. The inset shows the calculated values of the DIT along the x-direction, $\Delta J_{x,\mathrm{dd}}$, for $\theta = 0°$ (blue) and $\theta = 90°$ (orange) with $\phi = 0°$ and $s_{x,y} = 10$, which is close to the phase transition point, in units of frequency (left axis) and in units of the single-particle tunneling $J_{ij} = 80.5\,\mathrm{Hz}$ in the xy-plane (right axis).

strongly correlated systems for both bosonic and fermionic Hubbard dynamics in the presence of dipolar interactions, while building on the well-developed toolbox to prepare ultracold dense samples, and to manipulate and measure these atomic gases. We have realized the extended Bose-Hubbard Hamiltonian with anisotropic onsite and offsite interactions, which reveal themselves in the excitation spectrum and in the many-body dynamics of the system. Our results show how to control the Hamiltonian terms with the dipole orientation and accomplish the long-awaited observation of NNI in Hubbard dynamics. An outstanding challenge for future experiments is the realization of many-body states in the lattice with spontaneously broken spatial symmetry due to NNI, such as the checkerboard and stripe phase[17]. For our experimental parameters, the latter phase is expected to appear at temperatures in the few nK regime [27]. Dipolar interactions can be further increased by working with Feshbach molecules of magnetic Lanthanides, essentially doubling the magnetic dipole moment [43], and sub-wavelength lattices [44, 45]. Lanthanides offer unique opportunities to access the multitude of many-body phases predicted for dipolar quantum matter and are complemented by the remarkable experimental developments with heteronuclear molecules and Rydberg atoms [2].

We thank F. Meinert and H.-C.-Nägerl for fruitful discussions. The Innsbruck experimental group is supported by the Austrian Ministry of Science and Research (BMWF) and the Austrian Science Fund (FWF) through a START grant under project Y479-N20 and by the European Research Council (ERC) under project 259435. K.A. has been supported within the Lise-Meitner program of the FWF. The Innsbruck theory group is supported by the SFB FoQuS, by the ERC Synergy Grant UQUAM, and by the EU FET Proactive Initiative SIQS. The data leading to the histograms of Fig. 3D are presented in [27].

SUPPLEMENTARY MATERIALS

BEC production

We create a Bose-Einstein condensate (BEC) of about 1.5×10^5 ^{168}Er atoms by means of evaporative cooling in a crossed optical dipole trap (ODT) [12]. The cloud has typically a BEC fraction above 80 %, which is extracted by a two-dimensional bimodal fit to an absorption image of the atomic cloud after a time-of-flight (TOF) of 27 ms [12]. The cloud temperature is estimated to be about 70 nK. The ODT is operated at 1064 nm and is created by two beams, one propagating horizontally and one vertically. The beams cross at their respective focal points. The elliptic horizontal beam has a vertical (horizontal) waist of about 18 μm (117 μm) and the elliptic vertical beam has a waist of about 55 μm (110 μm) along (perpendicular to) the axis of the horizontal beam. The measured trap frequencies are $(\omega_x,\omega_y,\omega_z)=2\pi\times(29.0(6),22.2(4),165.2(5))$ Hz. We observe a lifetime of the trapped cloud of about 10 s.

The atomic cloud is spin-polarized in the lowest Zeeman sublevel ($J=6,m_J=-6$), where J denotes the total angular momentum quantum number and m_J is its projection along the quantization axis. The spin polarization already occurs in the magneto-optical trap [46] and is maintained in the ODT by applying a bias magnetic field with a fixed value of 0.40(1) G. As discussed below, the magnitude of this field is kept constant for all the experiments, whereas its orientation is varied to set the desired dipole orientation.

3D lattice setup

We describe the 3D lattice setup in the coordinate system given by the two horizontal lattice beams denoting the x and y-axis and the direction of gravity giving the z-axis (Fig. 1A, inset). The horizontal lattice beams are created by two retroreflected beams with a waist of about 160 μm and a wavelength $\lambda_x=\lambda_y=532$ nm. The vertical lattice beam has a waist of about 300 μm and a wavelength $\lambda_z=1064$ nm. The resulting 3D optical lattice is given by $V(x,y,z)=V_x\cos^2(k_x x)+V_y\cos^2(k_y y)+V_z\cos^2(k_z z)$, where V_i is the lattice depth in the i-direction and $k_i=2\pi/\lambda_i$ the corresponding lattice wavevector with $i=(x,y,z)$. Because of the different wavelengths, the atoms experience different recoil energies $\mathrm{E_{R},}_i$ in the xy-plane with respect to the vertical direction. The recoil energies given by $\mathrm{E_{R},}_i=h^2/(2m\lambda_i^2)$ are $\mathrm{E_{R},}_x=\mathrm{E_{R},}_y=h\times4.2$ kHz and $\mathrm{E_{R},}_z=h\times1.05$ kHz. Here, h is the Planck constant and m the mass of the Er atom. For convenience, we give the lattice depth in units of the corresponding recoil energy $s_i=V_i/\mathrm{E_{R},}_i$. The maximum lattice depth we can achieve is $(s_x,s_y,s_z)=(30,30,220)$. Because of the Gaussian profile of the lattice beams the atoms experience an additional harmonic confinement. At a typical 3D lattice depth of $(s_x,s_y,s_z)=(20,20,20)$ we measure $(\omega_x,\omega_y,\omega_z)=2\pi\times(34(1),31(1),43(1))$ Hz.

We note that the vertical lattice beam is tilted from the vertical axis by $\theta=10(2)^\circ$ and has an azimuthal angle of $\phi=5(5)^\circ$. This has two consequences: (a) The lattice spacings d_x and d_z are modified to $d_x=270(2)$ nm and $d_z=540(4)$ nm with respect to the $\lambda/2$ case and (b) the tilt of the wavefront of the vertical lattice beam gives rise to an additional potential difference between neighboring lattice sites along x of 200(40) Hz due to gravity. While (b) only leads to a broadening of the excitation resonances in the modulation spectroscopy measurements, (a) could in principle change the values of the extended Bose-Hubbard (eBH) terms. Therefore, we recalculate them considering our effective lattice spacings for a typical experimental condition of $(s_x,s_y,s_z)=(15,15,15)$. We find that the isotropic terms are reduced by 3 % while the anisotropic terms can differ between 2-6 %, depending on the dipole orientation and the direction of the observed process (see Table S1). This gives rise to a downshift of the phase transition point s_c of about 1 % for both $\theta=0^\circ$ and $\theta=90^\circ$. However, all these shifts are not resolvable within our statistical errors and can therefore safely be neglected.

TABLE S1. Difference of the eBH terms between the $\lambda/2$-spacing and the actual spacing given in percentage of the $\lambda/2$-case for three dipole orientations ($\theta=90^\circ$, $\phi=0^\circ$), ($\theta=90^\circ$, $\phi=0^\circ$), and $\theta=0^\circ$.

	$\theta=90^\circ,\phi=0^\circ$	$\theta=90^\circ,\phi=0^\circ$	$\theta=0^\circ$
U_s	3 %		
$J_{ij=x},J_{ij=z}$	3 %		
$J_{ij=y}$	0 %		
U_dd	6 %	−2 %	2 %
U	3 %	−2 %	3 %
ΔV_NNI	3 %	2 %	-
$\Delta J_{ij=x}$	3 %	2 %	3 %
$\Delta J_{ij=y}$	4 %	2 %	3 %
$\Delta J_{ij=z}$	3 %	2 %	3 %

Lattice depth calibration and onsite aspect ratio

To calibrate the depths of the horizontal lattice beams we use the standard Kapitza-Dirac diffraction method [47]. For the vertical lattice we use the technique of parametric heating, in which the atoms are excited from the first to the third lattice band [48, 49]. With these methods, we extract the lattice depths with an uncertainty of up to 4 %.

The onsite aspect ratio (AR) is defined in terms of a Gaussian approximation to the corresponding Wannier function: $\mathrm{AR}=l_z/l_{x,y}$, where $l_{x,y}=d_{x,y}/(\pi s_{x,y}^{1/4})$ and $l_z=d_z/(\pi s_z^{1/4})$ are the harmonic oscillator lengths associated with the lattice beams along x,y and z, respectively (Note that we use $s_x=s_y$ in our measurements). The uncertainty of the AR results from the uncertainty of the lattice depths and is about 1 %.

Because of the non S-state character of Er atoms in their electronic ground state, the atomic polarizability of Er has a tensorial contribution, which is about 3 % of the scalar one for

an off-resonant trapping light [50]. In our system this effect gives rise to a different lattice depth depending on the dipole orientation. For each lattice beam, we carefully studied this effect by comparing the measured lattice depth for the dipoles aligned parallel and orthogonal to the corresponding lattice beam. Our measurements reveal that the parallel orientation gives a deeper confinement of up to 4 % as compared to the orthogonal orientation. We account for this effect as a systematical error, which gives rise to asymmetric error bars in the AR in Fig. 2 (C and D) and Fig. 4E and in the *xy*-plane lattice depth in Fig. 4 (B to D) and Fig. S4 (A to F).

Loading of the 3D lattice

For our experiments the atoms are adiabatically loaded to the 3D lattice by an exponential ramp to the final value within 150 ms, during which the vertical ODT is linearly lowered to zero. To perform modulation spectroscopy, the horizontal ODT is switched off within 1 ms after the loading. For the measurement of the BEC depletion, we exactly reverse the described process. In the Mott-insulator (MI) phase we estimate a central density of two atoms per lattice site. The external harmonic confinement leads to a density distribution with a central doubly occupied Mott shell, consisting of up to 40 % of the total atoms, surrounded by a singly occupied shell. The external harmonic confinement is given by the sum of the ODT potentials and the Gaussian profiles of the lattice beams during the lattice loading. For our typical lattice depth condition $(s_x, s_y, s_z) = (20, 20, 20)$, the lifetime of the atomic sample in the lattice is $5(1)$ s. In addition, we observe a heating, which leads to a full depletion of the recovered BEC for a holding time in the lattice of about 1 s. The origin of this heating is not fully understood and might be due to frequency fluctuations of the 532 nm laser source. It should be noted that beside the case of AR = 2 the asymmetric lattice configuration (i.e. larger lattice spacing along the vertical direction) for our experimental condition leads to a quasi-two-dimensional system, since the tunneling rates along the vertical lattice are much smaller compared to those along the horizontal plane.

Control of the dipole orientation

The dipole orientation follows the direction of the magnetic field, which we control using three pairs of independent coils oriented perpendicular to each other. Each pair of coils is independently calibrated by performing radio-frequency spectroscopy, where resonant excitations to higher Zeeman sublevels can be used as a measure of the actual magnetic field at the position of the atoms. The dipole orientation can be changed from $\theta = 0^\circ$ to $\theta = 90^\circ$ and for any value of ϕ. Noise of the ambient magnetic field leads to fluctuations of the absolute angles θ and ϕ by about 1° around their set values. During the evaporative cooling sequence the dipoles are aligned at $\theta = 0^\circ$. Before loading the atoms into the 3D lattice, the dipole orientation is changed to the desired value in 38 ms, while the magnetic-field magnitude is kept constant.

Modulation spectroscopy in the MI

To probe the excitation gap in the MI we use a modulation spectroscopy technique [35, 36]. We sinusoidally modulate the power of one horizontal lattice beam with a typical total amplitude between 30 % and 40 %, and a modulation time between 50 ms and 100 ms. With this method, we resonantly create particle-hole excitations in the system [37]. These excitations manifest themselves as a resonant depletion of the recovered BEC because of the extra energy stored in the system. We record the remaining BEC fraction after ramping down the lattice as a function of the modulation frequency. The resulting loss spectrum is then fitted with a double-Gaussian function, whose centers give the excitation frequencies. The typical full width at half maximum (FWHM) of the resonant loss features is 1 kHz for excitations using the *x*-lattice beam and 0.8 kHz for the *y*-lattice beam. The width is mainly determined by the external harmonic confinement. We note that the difference in width between the two excitation directions is due to the tilt of the vertical lattice beam as discussed above.

We also measure the onsite interaction by using an alternative method, known as the collapse-and-revival technique [51]. Here, we first prepare the system at the onset of the SF-to-MI transition with a lattice depth of $(s_x, s_y, s_z) = (10, 10, 10)$ and we then suddenly quench the system to $(s_x, s_y, s_z) = (20, 20, 40)$ within 5 μs. As a result of the quench the system oscillates between the MI and the superfluid (SF) phase. Figure S1 shows the evolution of the FWHM of the central interference peak as a function of the holding time after the quench for two different dipole orientations $\theta = 0^\circ$ and $\theta = 90^\circ$. We observe up to four collapses and revivals and extract the onsite interaction from the oscillation frequency. For $\theta = 0^\circ$ ($\theta = 90^\circ$) we measure a frequency of $2.07(16)$ kHz ($2.98(5)$ kHz), which are consistent with the value of $2.15(3)$ kHz ($2.77(3)$ kHz) obtained with the modulation spectroscopy technique.

Analysis of the nearest-neighbor interaction (NNI)

To derive the NNI we perform a differential measurement based on modulation spectroscopy, in which the orientation of dipoles is fixed but the direction of excitation is changed between the horizontal lattice axes *x* and *y*. To explain the amount of energy needed to drive a particle-hole excitation we consider the situation where the dipoles are aligned with angles $\theta = 90^\circ$ and $\phi = 90^\circ$, as also illustrated in Fig. 3 (see main manuscript). Here we denote V^{att} (V^{rep}) the attractive (repulsive) value of V_{ij} for the bond direction *y* (*x*). At the starting configuration (Fig. 3A) the total energy is $E_{\mathrm{A}} = 12V^{\mathrm{att}} + 12V^{\mathrm{rep}}$. For an excitation along the *y*-axis the final energy of this configuration reads as $E_{\mathrm{B}} = U + 11V^{\mathrm{att}} + 12V^{\mathrm{rep}}$,

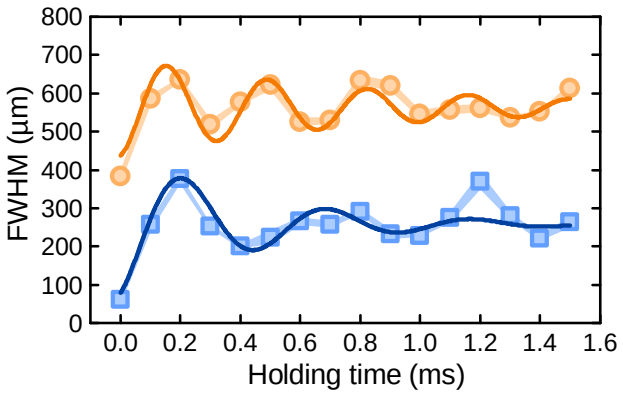

FIG. S1. **Measurement of U by the collapse-and-revival technique.** The FWHM of the central peak of the interference pattern is monitored as a function of the holding time after a sudden quench from the SF to the MI phase for an initial dipole orientation of $\theta = 0°$ (squares) and $\theta = 90°$ (circles). The latter measurement is vertically offset by 300 μm for a better visualization of the two data sets. Each point is obtained by two to four independent measurements and the shaded region indicates the SEM. The solid lines are the fits of a damped sine to the data, used to extract the oscillation frequency and hence U.

while for an x-excitation it is $E_C = U + 12V^{att} + 11V^{rep}$. From this consideration it becomes clear that the difference in energy $E_B - E_C = -V^{att} + V^{rep} = \Delta V_{NNI}$ purely reveals the NNI.

Analogously the same consideration can be applied for an initial dipole orientation of $\theta = 90°$ and $\phi = 0°$ leading to $\Delta V_{NNI} = -V^{rep} + V^{att}$. From the theory we expect $V^{rep}/h = 31.5\,\text{Hz}$, $V^{att}/h = -59.5\,\text{Hz}$ and thus $|\Delta V_{NNI}|/h = 91\,\text{Hz}$. Including the corrections arising from the modification of the lattice spacings due to the tilt of the vertical lattice beam (see above) $|\Delta V_{NNI}|/h$ changes to 89 Hz, even closer to our measured values.

In Fig. S2A we show two excitation spectra obtained using the method described above. The difference between the centers of the Gaussian fits to the data is found to be $72(30)\,\text{Hz}$ and corresponds to one data point of Fig. S2B, where all taken measurements are summarized. We believe that the fluctuation of ΔV_{NNI} along the data sets is mainly caused by relative drifts of the lattice depths during a differential measurement. We carefully check for systematic errors on ΔV_{NNI} using different initial lattice depths or atom numbers, but do not find an effect within our measurement resolution. The used lattice depths are $(s_x, s_y, s_z) = (15, 15, 30), (14, 18, 30)$, and $(20, 20, 40)$. The different depths can slightly modify ΔV_{NNI} by a maximum of 2 % which is not resolvable within our error bar.

Analysis of the SF-to-MI transition point

To study the SF-to-MI transition we probe the momentum distribution of the atoms as a function of the lattice depths [40]. In particular, we ramp simultaneously in 150 ms the power of the three lattice beams up to the final desired value while lowering the vertical ODT to zero. We then suddenly switch off all beams and let the atomic cloud expand for 27 ms. Here, we perform standard absorption imaging using a resonant 401 nm laser beam [12]. The imaging light propagates horizontally with an angle of 20° with respect to the x-lattice beam, ($\theta = 90°$, $\phi = -20°$). By increasing the lattice depth we observe a dramatic change in the momentum distribution, which is the textbook signature for the SF-to-MI transition [40]. In the SF phase the distribution of the interference peaks (Fig.4A2) reflects the anisotropy of the lattice in combination with the orientation of the reciprocal lattice with respect to the imaging light (see Fig. S3). In particular we find in total six first-order interference peaks: two in the vertical direction and four in the horizontal one. Along the vertical direction, the two peaks have half the spacing from the zero-momentum central peak with respect to the peaks resulting from the y-axis lattice. In the horizontal direction, we observe both the interference peaks from the y- and x-axis, since the imaging axis is not completely collinear to the x direction. When the lattice depth is further increased the system enters into the MI as can be seen in the momentum distribution by an increasing incoherent background (Fig. 4A3). An analysis of the observed momentum distribution for various final lattice depths $s_{x,y}$ can thus reveal the SF-to-MI phase transition point. For a quantitative study of the dependence of the phase transition point we repeat the experiment for the two angles $\theta = 0°$ and $\theta = 90°$ with $\phi = 0°$ and for various values of the AR. Beside the case of AR = 2 the physics of the SF-to-MI transition is effectively two-dimensional due to the negligible tunneling rate along the vertical lattice.

The critical value for the SF-to-MI transition, s_c, depends on the ratio of the total onsite interaction to the total tunneling rate. In presence of the dipole-dipole interaction (DDI), both terms depend on the dipole orientation, imprinting an angle dependence on the phase transition point $s_c(\theta)$, defined by the value of the horizontal lattice depth $s_{x,y} = s_x = s_y$. We study the phase transition for $\theta = 0°$ and $\theta = 90°$ and extract the difference in the critical point $\Delta s_c = s_c(0°) - s_c(90°)$.

In general we observe a smooth transition from the SF phase to the MI phase as expected for a trapped system with a spatially depending density. For this reason, the extraction of s_c is a delicate matter and we use two different methods [41]. The first method (a) is a double-line fit, which analyses the increase of the FWHM of the central interference peak along the horizontal direction as a function of $s_{x,y}$ (Figure S4, A to C). A weighted fitting function consisting of two smoothly connected lines is used to extract s_c, which thus corresponds to the knee of the experimental data. We apply the fit in a region from $s_{x,y} = 5$ to the values of $s_{x,y}$ for which the FWHM is 250 μm. In this region the experimental data are well approximated by the double-line fit.

The second method (b) is based on the visibility. Figure S4, D to E, shows the extracted visibility data for the same data as in (a). The visibility is calculated from a two-

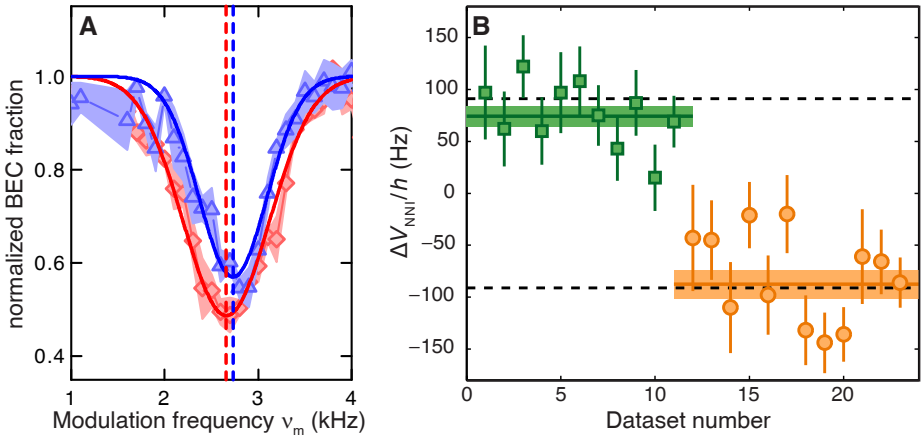

FIG. S2. **Measurements for the NNI.** (A) Excitation spectrum with modulation along x (diamonds) and y (triangles) with $\theta = 90°$ and $\phi = 90°$, forming one differential measurement. Each point is the average of about 5 independent measurements and the shaded region indicates the SEM. The solid lines are weighted Gaussian fits to the data. The dashed lines indicate the obtained resonance frequencies. (B) Set of differential measurements as presented in (A) for dipoles aligned with $\theta = 90°$ and $\phi = 90°$ (squares), $\theta = 90°$ and $\phi = 0°$ (circles). The solid lines are weighted fits with the shaded region being the SEM. The dashed lines are the theoretical expectations.

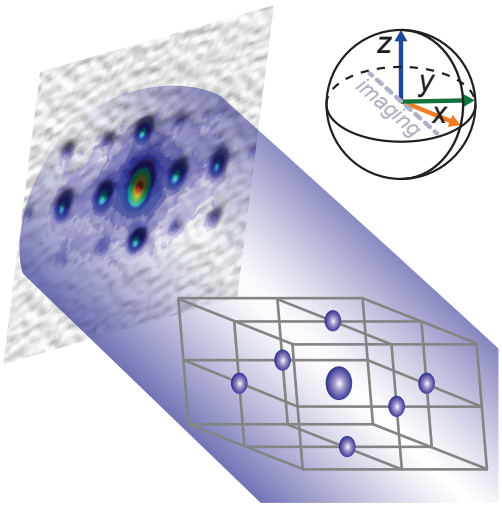

FIG. S3. **Observation of the interference peaks.** Visualization of the observed momentum distribution of the atoms in the SF phase released from the 3D lattice in TOF absorption imaging due to the orientation of the reciprocal lattice with respect to the imaging axis (see also inset)

dimensional (2D) fit consisting of eight gaussians: one for the central, six for the first-order interference peaks, and one for the broad incoherent background (see Fig. S2G). The visibility is defined as $\mathscr{V} = A/(A+B)$, where A stands for the mean amplitude of the first-order interference peaks and B for the mean value of the incoherent background at the positions of the interference peaks. We extract $\mathscr{V}$ as a function of $s_{x,y}$ and fit the whole dataset by the phenomenological function $\mathscr{V}(s_{x,y}) = C/(1+\exp(\alpha(s_{x,y}-s_c))) - \mathscr{V}_0$ (adapted from [41]). Here C, α, s_c, and $\mathscr{V}_0$ are fitting parameters, where s_c corresponds to the phase transition point.

For both methods, at large ARs, we observe a clear shift of s_c toward higher values for $\theta = 0°$ compared to $\theta = 90°$ (Fig. S4, A and D). This shift vanishes around AR ≈ 1.2 (Fig. S4, B and E), and changes sign for lower ARs (Fig. S4, C and F). We note that method (b), is more reliable at large ARs than at smaller ones, since in the latter case the phase transition has a 2D nature (negligible tunneling rate along z). Therefore, the interference peaks are broadened compared to the 3D case resulting in a lower contrast, which might leads to a systematic shift of $\mathscr{V}$. Method (a) can be applied to all ARs but it can be more sensitive to experimental drifts and interaction broadening since it is based on the measurement of the FWHM of the central peak.

Extended Bose-Hubbard model from microscopic Hamiltonian

Here we present the details of derivation of the eBH model Eq. 1 together with the expressions for all its coefficients in terms of microscopic parameters of the system (see, e. g. [52]).

The microscopic Hamiltonian of the considered system of polarized (magnetic) dipolar atoms has the form:

$$\hat{H}_{\rm tot} = \hat{H}_0 + \hat{H}_{\rm int}, \tag{S1}$$

where the first term

$$\hat{H}_0 = \int d\mathbf{r}\Psi^\dagger(\mathbf{r})[-\frac{\hbar^2\nabla^2}{2m} + V(\mathbf{r})]\Psi(\mathbf{r}) \tag{S2}$$

is the single-particle Hamiltonian with $\Psi(\mathbf{r})$ being a boson field operator, which describes the motion of an atom with mass m in the optical-lattice potential $V(\mathbf{r}) = V_x\cos^2(k_x x) + V_y\cos^2(k_y y) + V_z\cos^2(k_z z)$, and the second term

$$\hat{H}_{\rm int} = \frac{1}{2}\int d\mathbf{r}\int d\mathbf{r}'\Psi^\dagger(\mathbf{r})\Psi^\dagger(\mathbf{r}')U(\mathbf{r}-\mathbf{r}')\Psi(\mathbf{r}')\Psi(\mathbf{r})$$

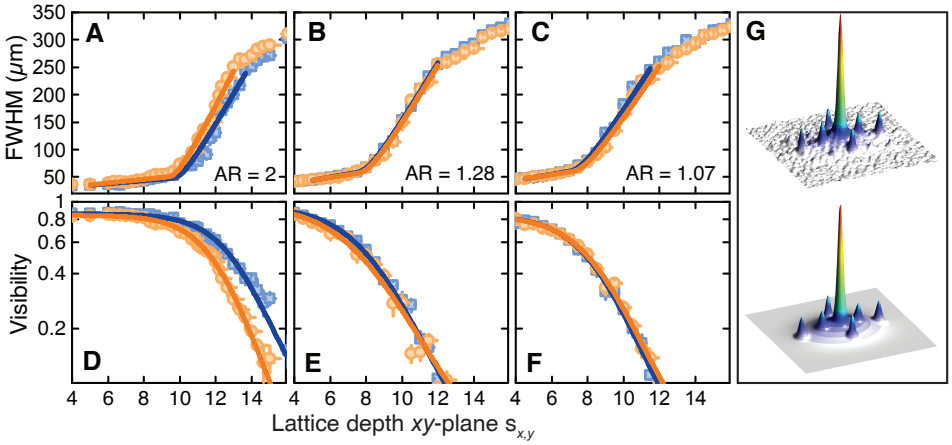

FIG. S4. Derivation of the phase transition point s_c. (A to F) The FWHM of the central interference peak and the visibility are displayed as a function of the final $s_{x,y}$ lattice depths for AR = 2 (A and D), 1.28 (B and E), and 1.07 (C and F), for dipole orientations $\theta = 0°$ (squares) and $\theta = 90°$ (circles). The solid lines show the corresponding fitting functions (see text). Each point is obtained from about 10 independent measurements. (G) Example of density distribution after TOF (top) and the corresponding 2D fit (bottom) used for the derivation of the visibility.

corresponds to the interatomic interaction. In the considered case, the interaction contains a short-range part, which can be modeled by a contact potential with the s-wave scattering length a_s, and the dipole-dipole interaction (see, e.g. [53])

$$U(\mathbf{r}-\mathbf{r}') = \frac{4\pi\hbar a_s}{m}\delta(\mathbf{r}-\mathbf{r}') + \frac{\mu_0\mu^2}{4\pi}\frac{1-3\cos^2\theta_{\mathbf{r}-\mathbf{r}'}}{|\mathbf{r}-\mathbf{r}'|^3}$$

with $\theta_{\mathbf{r}-\mathbf{r}'}$ being the angle between the relative position of two dipoles $\mathbf{r}-\mathbf{r}'$ and their polarization.

The Hamiltonian of Eq. S2 determines the single-particle band structure,

$$[-\frac{\hbar^2\nabla^2}{2m} + V(\mathbf{r})]u_{\alpha\mathbf{p}}(\mathbf{r}) = \varepsilon_\alpha(\mathbf{p})u_{\alpha\mathbf{p}}(\mathbf{r}),$$

where $u_{\alpha\mathbf{p}}(\mathbf{r})$ is the Bloch wavefunction corresponding to the band α and quasimomentum $\mathbf{p}$ from the Brillouin zone (BZ), defined by $-\pi/d_i < p_i/\hbar \leq \pi/d_i$ with $d_i = \pi/k_i$ being the lattice spacing along the i-direction, p_i the corresponding component of $\mathbf{p}$, and $\varepsilon_\alpha(\mathbf{p})$ is the corresponding energy. For our purposes it is more convenient to work with Wannier functions $\phi_{i,\alpha}(\mathbf{r}) = \sum_{\mathbf{p}\in BZ}\exp[-i\mathbf{p}(\mathbf{r}-\mathbf{R}_i)]u_{\alpha\mathbf{p}}(\mathbf{r})$, which are localized at different sites $\mathbf{R}_i$ of the lattice and orthogonal to each other with respect to both the lattice position i and the band index α, $\int d\mathbf{r}\phi^*_{i,\alpha}(\mathbf{r})\phi_{j,\beta}(\mathbf{r}) = \delta_{ij}\delta_{\alpha\beta}$. Using these functions as a single-particle basis in the bosonic field operator, $\Psi(\mathbf{r}) = \sum_{i,\alpha} b_{i,\alpha}\phi_{i,\alpha}(\mathbf{r})$, where $b_{i,\alpha}$ are the bosonic annihilation operators for particles on the site i in the band α, we can rewrite the initial Hamiltonian of Eq. S1 in terms of the operators $b_{i,\alpha}$ and $b^\dagger_{i,\alpha}$. To obtain the eBH model, we keep terms with operators for the lowest energy band only. Note that this approximation is legitimate because the interatomic interaction in our case is order of magnitudes less than the band gap such that the admixture of the higher bands can be neglected. From the remaining terms we then neglect those which contain square and higher power of exponentially small spatial overlaps of the Wannier functions from different sites (see, [52] for details). Denoting the operators and the Wannier functions for the lowest band as b_i, $b^\dagger_i$ and $\phi_i(\mathbf{r})$, respectively, we obtain

$$\begin{aligned} H = &-\sum_{\langle ij\rangle} J_{ij}(b^\dagger_i b_j + h.c) + \frac{U}{2}\sum_i n_i(n_i-1) + \sum_{\langle ij\rangle} V_{ij}n_i n_j \\ &-\sum_{\langle ij\rangle}\Delta J_{ij}[b^\dagger_i b_j(n_i+n_j-1) + h.c] \end{aligned} \tag{S3}$$

where $\langle ij\rangle$ denotes a pair of nearest-neighboring sites. The first two terms in this expression correspond to the standard Hubbard model with the single-particle hopping amplitude

$$J_{ij} = -\int d\mathbf{r}\phi^*_i(\mathbf{r})[-\frac{\hbar^2\nabla^2}{2m} + V(r)]\phi_j(\mathbf{r})$$

and the onsite interaction $U = U_s + U_{dd}$, where U_s comes from the contact interaction,

$$U_s = \frac{4\pi\hbar a_s}{m}\int d\mathbf{r}\,|\phi_i(\mathbf{r})|^4,$$

and U_{dd} from the dipole-dipole one,

$$U_{dd} = \frac{\mu_0\mu^2}{4\pi}\int d\mathbf{r}\int d\mathbf{r}'\,|\phi_i(\mathbf{r})|^2\frac{1-3\cos^2\theta_{\mathbf{r}-\mathbf{r}'}}{|\mathbf{r}-\mathbf{r}'|^3}|\phi_i(\mathbf{r}')|^2.$$

The third term in Eq. S3 corresponds to the NNI with

$$V_{ij} = \frac{\mu_0\mu^2}{4\pi}\int d\mathbf{r}\int d\,\mathbf{r}'\,|\phi_i(\mathbf{r})|^2\frac{1-3\cos^2\theta_{\mathbf{r}-\mathbf{r}'}}{|\mathbf{r}-\mathbf{r}'|^3}|\phi_j(\mathbf{r}')|^2$$

coming from the DDI (the contribution from the contact interaction is proportional to the square of the exponentially

small overlap and is therefore neglected). Note that the DDI also generates interactions V_{ij} beyond the nearest-neighbors, which decay as $\left|\mathbf{R}_i-\mathbf{R}_j\right|^{-3}$. The corresponding terms are neglected in the Hamiltonian of Eq. S3 because they are smaller and play only minor role in the spatially homogeneous phases (SF and MI) relevant for our experiment. These terms however will be definitely relevant for inhomogeneous phases like, for example, the stripe and the checker-board phases. Finally, the fourth term in Eq. S3 describes the density-induced tunneling (DIT) with the amplitude $\Delta J_{ij}=\Delta J_{ij,\mathrm{s}}+\Delta J_{ij,\mathrm{dd}}$ resulting from the contribution from the contact interaction

$$\Delta J_{ij,\mathrm{s}}=-\frac{4\pi\hbar a_s}{m}\int d\mathbf{r}\,|\phi_i(\mathbf{r})|^2\,\phi_i^*(\mathbf{r})\phi_j(\mathbf{r})$$

and from the dipole-dipole one

$$\Delta J_{ij,\mathrm{dd}}=-\frac{\mu_0\mu^2}{4\pi}\int d\mathbf{r}\int d\mathbf{r}'\,|\phi_i(\mathbf{r})|^2\,\frac{1-3\cos^2\theta_{\mathbf{r}-\mathbf{r}'}}{|\mathbf{r}-\mathbf{r}'|^3}\phi_i^*(\mathbf{r}')\phi_j(\mathbf{r}').$$

It should be mentioned that in our experiments we also have a shallow confining potential $V_{\mathrm{h}}(\mathbf{r})$. It can be taken into account by adding the term $\sum_i V_{\mathrm{h},i}\,n_i$ with $V_{\mathrm{h},i}=\int d\mathbf{r}|\phi_i(\mathbf{r})|^2V_{\mathrm{h}}(\mathbf{r})$ to the Hamiltonian of Eq. S3.

The above expressions, together with numerically computed Wannier functions, provide the theoretical values for the parameters J_{ij},U,V_{ij}, and ΔJ_{ij}. During the calculations, the singularity for $|\mathbf{r}-\mathbf{r}'|\to 0$ in the contributions from the DDI was resolved by performing the integration over $\theta_{\mathbf{r}-\mathbf{r}'}$ before integrating over $|\mathbf{r}-\mathbf{r}'|$. For our experimental conditions, the contributions from the DDI to the eBH parameters are typically smaller for U, in the same order of magnitude for ΔJ_{ij} and much larger for V_{ij} than those from the short-range contact interaction. However, they strongly depend on the form of the Wannier function $\phi_i(\mathbf{r})$, i.e. on the intensity and ratio of s_x, s_y, and s_z, and on the alignment of the dipoles relative to the lattice axes (see Fig. 1, D to F).

SF-to-MI transition in the mean-field (MF) approximation

In the MF approximation (see, e.g. [54–56]), the ground-state wavefunction of the system is written as a product state over sites:

$$|\Psi_G\rangle=\bigotimes_i\Big(\sum_{n=0}^{\infty}C_i^{(n)}|n\rangle_i\Big),$$

where $|n\rangle_i$ denotes the Fock state with n bosons on site i. The coefficients $\{C_i^{(n)}\}$ are the variational parameters subjected to the constraint $\sum_{n=0}^{\infty}\left|C_i^{(n)}\right|^2=1$, which can be determined by minimizing the energy $E_G=\langle\Psi_G|H|\Psi_G\rangle$. The SF phase is characterized by the local order parameter $\langle b_i\rangle=\langle\Psi_G|b_i|\Psi_G\rangle=\sum_{n=1}^{\infty}\sqrt{n}C_i^{(n-1)}C_i^{(n)}\neq 0$, which implies that $C_i^{(n)}$ are non-zero for several adjacent values of n. In contrast, in the MI phase $C_i^{(n)}$ are non-zero for only one value of n. In a spatially inhomogeneous system (e.g., in the presence of a trapping potential V_{h}), this value is site-independent, and the system has typically a layered structure in which the Mott states with different n ($n=1$ and 2 in our case) are separated by the SF phase.

It should be mentioned that, even though the MF approximation is known to overestimate the stability of the SF phase, here we are interested not in the phase boundary of the SF-to-MI transitions itself, but in the relative shift of this boundary when the dipolar polarization is changed from $\theta=0^\circ$ to $\theta=90^\circ$.

In calculating this shift, the MF method turns out to be reliable, as it is demonstrated on Fig. S5 where we present the results for the phase transition shift Δs_c in a spatially homogeneous system, obtained within quantum Monte Carlo (QMC) and MF methods. One sees practically no effects of quantum fluctuations on Δs_c, and this is why the MF method can be used for the quantitative description of our experimental results (Fig. 4E). To underline the role of the DIT in determining Δs_c, we analyze the effect of the NNI on the SF-to-MI transition point by using QMC studies of the eBH model with NNI, but without DIT. Fig. S5 shows that the inclusion of the NNI only slightly shifts Δs_c (compare dot-dashed and dot-dot-dashed line), and this shift turns out to be much smaller (5-6 times in our case) as the shift due to DIT (Fig. S5, solid line), despite the fact that the values of the NNI are much larger than those of the DIT. An insight into this counterintuitive result can be gained by considering the SF-to-MI transition in the MF approximation. One can easily see that within this approximation the contribution of the NNI to the energy of the system is the same for both phases. As a result, on the MF level the NNI does not affect the transition at all, and it is only the fluctuation effects beyond the MF which introduces the dependence of the transition point on the NNI. On the other hand, the DIT affects the transition already on the MF level and therefore, although being much smaller than the NNI, has nevertheless a much more pronounced effect on the shift of the transition.

Observability of the stripe phase

The stripe phase is an example of exotic quantum phases induced by the NNI, which is characterized by spontaneous translational symmetry breaking along one direction. It can be accessed in a deep optical lattice half-filled with atoms, when the NNI overwhelms the effects of single-particle tunneling and temperature. In this case, the onsite interaction is much larger than all the other parameters in the Hamiltonian, and prevents two atoms to be on the same lattice site. We therefore can consider atoms as hardcore bosons, such that the number of atoms on a lattice site can be only zero or one. We assume that the dipoles are polarized along the x-direction resulting in attractive V^{att} (repulsive V^{rep}) NNI for the bonds ij in the $x(y)$-direction, with $-V^{\mathrm{att}}=2V^{\mathrm{rep}}=2V$. To calculate the critical temperature for the stripe phase, we con-

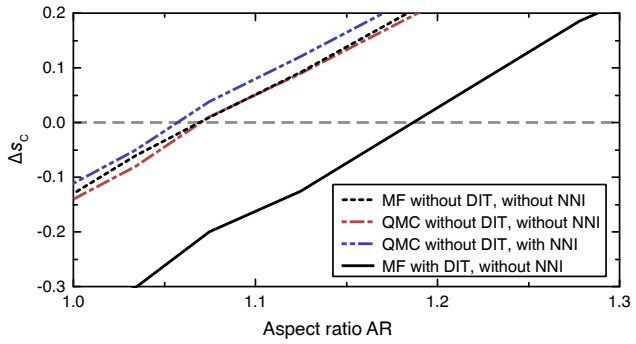

FIG. S5. **Effects of fluctuations, the NNI and the DIT on the shift of the phase transition Δs_c.** Theoretical calculations of the shift of the phase transition as a function of AR around the zero of Δs_c. The results for Δs_c in the spatially homogeneous case without DIT and NNI obtained within the MF (dotted line) and QMC (dot-dashed line) are similar. The effect of the NNI on Δs_c [compare QMC without (dot-dashed line) and with NNI (dot-dot-dashed line)] is much smaller than the effect of the DIT [compare MF without (dotted line) and with DIT (solid line).

sider typical experimental conditions with $s_x = s_y = 20$ and AR $= 1$. In such a lattice, we can ignore the DIT and the tunneling in the z-direction, and the single-particle tunneling amplitudes J_{ij} do not depend on the direction of the hopping, $J_{ij} = J = h \times 20.5\,\mathrm{Hz}$. We obtain $V = h \times 34\,\mathrm{Hz}$ and the NNI value for the bonds in the z-direction is $V/8 = h \times 4.25\,\mathrm{Hz}$. After neglecting this small coupling in the z-direction, the Hamiltonian for each xy-plane can now be written as

$$H_{xy} = -J \sum_{\langle ij \rangle} (b_i^\dagger b_j + h.c) + \sum_i (-2V n_i n_{i+\hat{e}_x} + V n_i n_{i+\hat{e}_y} - \mu n_i), \tag{S4}$$

where $b_i^\dagger$ and b_i are hard-core boson operators and $i + \hat{e}_x$ ($i + \hat{e}_y$) denotes the neighboring site of site i in the x (y) direction. We also add the chemical potential μ which is chosen as $\mu = -V$ to satisfy the condition of half-filling $\langle n_i \rangle = 1/2$. To determine the critical temperature of the transition into the stripe phases, we perform Quantum Monte Carlo calculations based on the worm algorithm for the Hamiltonian of Eq. S4, which is free from the negative sign problem. For the above parameters, the calculated value for the critical temperature is $T_c = 1.4J \simeq 1.5\,\mathrm{nK}$.

* Current adress: Department of Physics, Graduate School of Science and Engineering, Tokyo Institute of Technology, Meguro-ku, Tokyo, 152-8550 Japan

[1] T. Lahaye, C. Menotti, L. Santos, M. Lewenstein, and T. Pfau, Rep. Prog. Phys. **72**, 126401 (2009).
[2] M. Baranov, M. Dalmonte, G. Pupillo, and P. Zoller, Chem. Rev. **112**, 5012 (2012).
[3] P. G. de Gennes and J. Prost, *The Physics of Liquid Crystals* (Oxford Unversity Press, Oxford, 1995).
[4] R. E. Rosensweig, *Ferrohydrodynamics* (Cambridge University Press, New York, 1985).
[5] K. A. Dill, Biochemistry **29**, 7133 (1990).
[6] The magnetic DDI reads as $V_{\mathrm{DDI}}(r,\theta) = \frac{\mu_0 \mu^2}{4\pi} \frac{1-3\cos^2\theta}{r^3}$ where r stands for the distance between the two particles, θ for the angle between the dipole orientation and the interparticle axis, μ_0 for the vacuum permeability, and μ for the magnetic moment of the particles.
[7] B. Yan, S. A. Moses, B. Gadway, J. P. Covey, K. R. A. Hazzard, A. M. Rey, D. S. Jin, and J. Ye, Nature **501**, 521 (2013).
[8] P. Schauß, J. Zeiher, T. Fukuhara, S. Hild, M. Cheneau, T. Macrí, T. Pohl, I. Bloch, and C. Gross, Science **347**, 1455 (2015).
[9] A. Griesmaier, J. Werner, S. Hensler, J. Stuhler, and T. Pfau, Phys. Rev. Lett. **94**, 160401 (2005).
[10] A. de Paz, A. Sharma, A. Chotia, E. Maréchal, J. H. Huckans, P. Pedri, L. Santos, O. Gorceix, L. Vernac, and B. Laburthe-Tolra, Phys. Rev. Lett. **111**, 185305 (2013).
[11] B. Naylor, A. Reigue, E. Maréchal, O. Gorceix, B. Laburthe-Tolra, and L. Vernac, Phys. Rev. A **91**, 011603 (2015).
[12] K. Aikawa, A. Frisch, M. Mark, S. Baier, A. Rietzler, R. Grimm, and F. Ferlaino, Phys. Rev. Lett. **108**, 210401 (2012).
[13] K. Aikawa, A. Frisch, M. Mark, S. Baier, R. Grimm, and F. Ferlaino, Phys. Rev. Lett. **112**, 010404 (2014).
[14] M. Lu, N. Q. Burdick, S. H. Youn, and B. L. Lev, Phys. Rev. Lett. **107**, 190401 (2011).
[15] M. Lu, N. Q. Burdick, and B. L. Lev, Phys. Rev. Lett. **108**, 215301 (2012).
[16] A. Frisch, M. Mark, K. Aikawa, F. Ferlaino, J. Bohn, C. Makrides, A. Petrov, and S. Kotochigova, Nature **507**, 475 (2014).
[17] O. Dutta, M. Gajda, P. Hauke, M. Lewenstein, D.-S. Lühmann, B. A. Malomed, T. Sowiński, and J. Zakrzewski, Reports on Progress in Physics **78**, 066001 (2015).
[18] R. Micnas, J. Ranninger, and S. Robaszkiewicz, Rev. Mod. Phys. **62**, 113 (1990).
[19] J. Zaanen, Physica C **317**, 217 (1999).
[20] R. T. Scalettar, G. G. Batrouni, A. P. Kampf, and G. T. Zimanyi, Phys. Rev. B **51**, 8467 (1995).
[21] V. W. Scarola and S. Das Sarma, Phys. Rev. Lett. **95**, 033003 (2005).
[22] S. Wessel and M. Troyer, Phys. Rev. Lett. **95**, 127205 (2005).
[23] S. Yi, T. Li, and C. P. Sun, Phys. Rev. Lett. **98**, 260405 (2007).
[24] L. Pollet, J. D. Picon, H. P. Büchler, and M. Troyer, Phys. Rev. Lett. **104**, 125302 (2010).
[25] B. Capogrosso-Sansone, C. Trefzger, M. Lewenstein, P. Zoller, and G. Pupillo, Phys. Rev. Lett. **104**, 125301 (2010).
[26] C. Trefzger, C. Menotti, B. Capogrosso-Sansone, and M. Lewenstein, Journal of Physics B: Atomic, Molecular and Optical Physics **44**, 193001 (2011).
[27] Materials, methods, and additional theoretical background are available as supplementary material on Science Online.
[28] G. Mazzarella, S. M. Giampaolo, and F. Illuminati, Phys. Rev. A **73**, 013625 (2006).
[29] D.-S. Lühmann, O. Jürgensen, and K. Sengstock, New Journal of Physics **14**, 033021 (2012).
[30] O. Jürgensen, F. Meinert, M. J. Mark, H.-C. Nägerl, and D.-S. Lühmann, Phys. Rev. Lett. **113**, 193003 (2014).
[31] S. Trotzky, P. Cheinet, S. Fölling, M. Feld, U. Schnorrberger, A. M. Rey, A. Polkovnikov, E. A. Demler, M. D. Lukin, and I. Bloch, Science **319**, 295 (2008).

[32] A. Auerbach, *Interacting electrons and quantum magnetism* (Springer Science & Business Media, 2012).

[33] S. Müller, J. Billy, E. A. L. Henn, H. Kadau, A. Griesmaier, M. Jona-Lasinio, L. Santos, and T. Pfau, Phys. Rev. A **84**, 053601 (2011).

[34] For our lattice configuration the spherical point with $U_{\rm dd} = 0$ is shifted to AR $= 1.05$ when including corrections to the harmonic approximation.

[35] T. Stöferle, H. Moritz, C. Schori, M. Köhl, and T. Esslinger, Phys. Rev. Lett. **92**, 130403 (2004).

[36] C. Kollath, A. Iucci, T. Giamarchi, W. Hofstetter, and U. Schollwöck, Phys. Rev. Lett. **97**, 050402 (2006).

[37] S. R. Clark and D. Jaksch, New Journal of Physics **8**, 160 (2006).

[38] M. J. Mark, E. Haller, K. Lauber, J. G. Danzl, A. J. Daley, and H.-C. Nägerl, Phys. Rev. Lett. **107**, 175301 (2011).

[39] M. L. Wall, , and L. D. Carr, New Journal of Physics **15**, 123005 (2013).

[40] M. Greiner, O. Mandel, T. Esslinger, T. W. Hänsch, and I. Bloch, Nature **415**, 39 (2002).

[41] S. Ospelkaus, C. Ospelkaus, O. Wille, M. Succo, P. Ernst, K. Sengstock, and K. Bongs, Phys. Rev. Lett. **96**, 180403 (2006).

[42] For ARs < 2 tunneling along the z-axis is very small compared to the tunneling in the x and y directions because of the asymmetry of our lattice configuration, leading to an effectively two-dimensional SF-to-MI phase transition.

[43] A. Frisch, M. Mark, K. Aikawa, S. Baier, R. Grimm, A. Petrov, S. Kotochigova, G. Quéméner, M. Lepers, O. Dulieu, et al., Phys. Rev. Lett. **115**, 203201 (2015).

[44] W. Yi, A. J. Daley, G. Pupillo, and P. Zoller, New J. Phys. **10**, 073015 (2008).

[45] S. Nascimbene, N. Goldman, N. R. Cooper, and J. Dalibard, Phys. Rev. Lett. **115**, 140401 (2015).

[46] A. Frisch, K. Aikawa, M. Mark, A. Rietzler, J. Schindler, E. Zupanič, R. Grimm, and F. Ferlaino, Phys. Rev. A **85**, 051401 (2012).

[47] P. L. Gould, G. A. Ruff, and D. E. Pritchard, Phys. Rev. Lett. **56**, 827 (1986).

[48] J. H. Denschlag, J. E. Simsarian, H. Häffner, C. McKenzie, A. Browaeys, D. Cho, K. Helmerson, S. L. Rolston, and W. D. Phillips, Journal of Physics B: Atomic, Molecular and Optical Physics **35**, 3095 (2002).

[49] O. Morsch and M. Oberthaler, Rev. Mod. Phys. **78**, 179 (2006).

[50] M. Lepers, J.-F. Wyart, and O. Dulieu, Phys. Rev. A **89**, 022505 (2014).

[51] M. Greiner, O. Mandel, T. W. Hänsch, and I. Bloch, Nature **419**, 51 (2002).

[52] G. Mazzarella, S. M. Giampaolo, and F. Illuminati, Phys. Rev. A **73**, 013625 (2006).

[53] S. Yi and L. You, Phys. Rev. A **61**, 041604 (2000).

[54] D. Jaksch, C. Bruder, J. I. Cirac, C. W. Gardiner, and P. Zoller, Phys. Rev. Lett. **81**, 3108 (1998).

[55] M. P. A. Fisher, P. B. Weichman, G. Grinstein, and D. S. Fisher, Phys. Rev. B **40**, 546 (1989).

[56] S. Sachdev, *Quantum phase transitions* (Cambridge University Press, New York, 2000).

5.6. Publication: Realization of a Strongly Interacting Fermi Gas of Dipolar Atoms[†]

submitted for publication in Physical Review Letters
submitted 30 Mar 2018
DOI arXiv:1803.11445

S. Baier[1], D. Petter[1], J. H. Becher[1,⋆], A. Patscheider[1,2], G. Natale[1], L. Chomaz[1], M. J. Mark[1,2], F. Ferlaino[1,2]

[1] *Institut für Experimentalphysik, Universität Innsbruck, Technikerstraße 25, 6020 Innsbruck, Austria*
[2] *Institut für Quantenoptik und Quanteninformation, Österreichische Akademie der Wissenschaften, 6020 Innsbruck, Austria*
⋆ *Current address: Physikalisches Institut, Universität Heidelberg, Im Neuenheimer Feld 226, 69120 Heidelberg, Germany*

[†] The author of the present thesis developed the experimental procedures together with J-H. B., and D. P., performed the measurements together with J-H. B., D. P., A. P., L. C. and G. N., analyzed the data, and contributed strongly in writing the manuscript.

Realization of a Strongly Interacting Fermi Gas of Dipolar Atoms

S. Baier[1], D. Petter[1], J. H. Becher[1,†], A. Patscheider[1,2], G. Natale[1], L. Chomaz[1], M. J. Mark[1,2], F. Ferlaino[1,2,*]
[1] *Institut für Experimentalphysik, Universität Innsbruck, Technikerstraße 25, 6020 Innsbruck, Austria*
[2] *Institut für Quantenoptik und Quanteninformation, Österreichische Akademie der Wissenschaften, 6020 Innsbruck, Austria*

(Dated: April 2, 2018)

We report on the realization of a strongly interacting Fermi gas with a dipolar spin mixture of fermionic erbium. Employing a lattice-protection technique, we prepare deeply degenerate Fermi mixtures of the two lowest spin states and perform high-resolution Feshbach spectroscopy. We identify a comparatively broad Feshbach resonance and precisely map the inter-spin scattering length across the resonance. We show a remarkable collisional stability of the quantum mixture in the strongly interacting regime, providing a first step towards BEC-to-BCS studies in presence of dipole-dipole interaction.

The ability to prepare dipolar quantum gases of magnetic atoms [1–6] has led to the demonstration of fascinating, yet unexpected, phenomena, emerging from the peculiar traits of the dipole-dipole interaction (DDI) among particles. In bosonic systems, the DDI can dominate the system's behavior, leading to counter-intuitive effects, such as a d-wave-patterned collapse [7], droplet stabilization [8–10], or the emergence of roton excitations [11]. With fermions, many-body dipolar phenomena have been investigated only in spin-polarized systems. Here, the DDI competes with the Pauli pressure, rendering dipolar effects much more subtle, as e. g. their influence on the shape of the Fermi surface [12].

Magnetic atoms further realize high-spin systems, e. g. fermionic erbium (Er) has twenty available spin states in the lowest hyperfine manifold. Bosonic dipolar spinor gases have been investigated in remarkable experiments with magnetic Cr atoms [13–16] (see also Rb experiments [17, 18]), whereas the fermionic counterpart remains rather unexplored in the quantum regime. Scattering experiments with fermionic Dy mixtures slightly above quantum degeneracy, showed a large collisional stability against inelastic dipolar relaxation [19], enabling e. g. the production of long-lived spin-orbit-coupled gases via Raman excitations [20]. Near-degenerate gases of fermionic ground-state molecules have been used to study spin dynamics in lattices [21].

As yet, the realization of a two-component dipolar Fermi mixture with tunable interactions has remained elusive. Such a system is expected to give access to a variety of fascinating phenomena, from anisotropic quantum phases of matter, e. g. anisotropic Fermi liquids and BEC-to-BCS pairing [22, 23], to dipolar magnetism [24], but also extended Fermi-Hubbard models with direct off-site interactions [25]. A prime candidate for its realization is given by fermionic lanthanides that have a large magnetic moment. However, the astonishingly large density of Feshbach resonances (FRs) even in spin-polarized gases [26–28] raises the question of whether stable fermionic quantum mixtures with tunable contact and dipolar interactions can be realized with lanthanides.

We here report on a powerful platform to produce a two-component dipolar Fermi gas of pseudo-spin $1/2$ and demonstrate tunability of the inter-spin interactions. By using highly magnetic ^{167}Er atoms and a three-dimensional (3D) optical lattice as a tool for spin preparation, we perform high-resolution Feshbach spectroscopy and unambiguously identify the spin nature of the different FRs. Among the resonances, we find a well isolated and comparatively broad inter-spin FR and precisely measure the scattering length between the two spin states. By conducting scattering experiments, we reveal a remarkable collisional stability of the Fermi mixture in the strongly interacting regime.

Achieving a deterministic preparation of a spin-$1/2$ mixture and a precise control over the inter-spin interactions in highly-magnetic lanthanide atoms challenges experimental schemes. Indeed, the enormous density of FRs can cause collisional losses and severe heating, limiting the production and preparation of deeply degenerate mixtures at arbitrary magnetic fields (B), where hundreds of FRs might need to be crossed; see e. g. [20]. Moreover, state-selective preparation of a spin-$1/2$ system typically requires large B values for which the quadratic Zeeman effect lifts the degeneracy on the Zeeman splitting among consecutive sublevels [19, 29].

For these reasons, we establish a technique for collisional protection during the spin preparation; see Fig. 1. In a nutshell, the key production steps are: We first produce a spin-polarized degenerate Fermi gas (dFg) in an optical dipole trap (ODT) at low B (a1), we then load the atoms into the lowest band of a deep 3D optical lattice, which acts as a collisional shield (a2) [30, 31]. We then sweep to high B for spin preparation and perform radio-frequency (rf) transfer (a3), and sweep to the desired B and eventually melt the lattice (a4).

Experimentally, we prepare a spin-polarized dFg of ^{167}Er atoms in a crossed-beam ODT [5] (stage (a1); Fig. 1). All fermions occupy the lowest Zeeman state $|\downarrow\rangle \equiv |F = 19/2, m_F = -19/2\rangle$ of the ground-state manifold. Here, F is the total spin quantum number and m_F its projection along the quantization axis. A homogeneous magnetic field of $B = 0.6\,\mathrm{G}$ is applied along the vertical z direction to define the quantization axis and to maintain the spin polarization in the system. The sample typically contains $N = 2.4 \times 10^4$ atoms at about $T = 0.25\,T_\mathrm{F}$. Note that the ODT is shaped to optimize single-band loading of the optical lattice and yields $E_\mathrm{F} = k_\mathrm{B} \times T_\mathrm{F} = k_\mathrm{B} \times 170\,\mathrm{nK} = h \times 3.6\,\mathrm{kHz}$ [32]. Here, T_F is the Fermi temperature, h the Planck constant, and k_B the Boltzmann constant.

In the next step, we transfer the spin-polarized dFg into a 3D optical lattice (stage (a2); Fig. 1). We use a lattice geometry and a loading scheme similar to the one of our previous work [33]; for details see also Ref. [32]. In order to pin the atoms in a one-fermion-per-lattice-site configuration (unit filling), we use large lattice depths of about $(s_x, s_y, s_z) = (20, 20, 80)$, where s_i with $i \in \{x, y, z\}$ is given in units of the respective recoil energies, $\mathrm{E}_{\mathrm{R};x,y} = h \times 4.2\,\mathrm{kHz}$ and $\mathrm{E}_{\mathrm{R};z} = h \times 1.05\,\mathrm{kHz}$. After lattice loading, we obtain a single-component fermionic band-insulator (BI) of about 2.2×10^4 $|\downarrow\rangle$ atoms. By melting the lattice and re-loading the fermions into the ODT, we measure a temperature of $T \approx 0.3\,T_\mathrm{F}$ and extract a heating rate in the lattice as low as $\dot{T} = 0.03\,T_\mathrm{F}/\mathrm{s}$.

Our system is well described by a single-band extended Fermi-Hubbard model [25] with residual tunneling rates of $J_{x,y} = h \times 10.5\,\mathrm{Hz}$ and $J_z = h \times 0.001\,\mathrm{Hz}$, and nearest-neighbor interactions in the order of $\mathrm{h} \times 50\,\mathrm{Hz}$ [33]. We confirm the single-band population by performing standard band-mapping measurements [34] [35]. In the horizontal (xy) plane, we observe that the fermions occupy the lowest band and we do not record higher band occupation within our resolution; see Fig. 1(b) [36]. Along the z-axis, we detect a residual $< 5\,\%$ population in the first excited band, resulting from the fact that $E_\mathrm{F} > E_{\mathrm{R},z}$ [37]. Because of the Pauli exclusion principle, doubly-occupied sites (doublons) in a single band are strictly forbidden for identical particles ($|\downarrow\rangle$).

In the BI regime, the lattice is expected to provide a strong collisional protection to the particles, as previously observed with deeply-bound molecules [30, 31, 38]. As a first application, we use the lattice-protection technique to realize a spinor Fermi gas with pseudo-spin 1/2 (stage (a3); Fig. 1). For such $|\downarrow\rangle$–$|\uparrow\rangle$ mixtures, $|\uparrow\rangle \equiv |F = 19/2, m_F = -17/2\rangle$. Experimentally, we start with a $|\downarrow\rangle$ BI at $B = 0.6\,\mathrm{G}$ and then ramp B in 40 ms to a value of about 40 G, for which the quadratic Zeeman effect in ^{167}Er is large enough to lift the degenerate coupling of the individual spin levels [32]. After letting the field stabilize for 120 ms, we use a standard rf-sweep technique to transfer part of the atoms into the $|\uparrow\rangle$ state. By

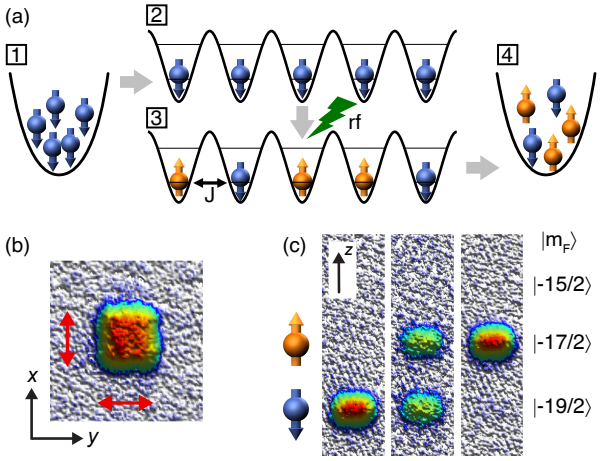

FIG. 1. Spin-1/2 dipolar fermions in a 3D optical lattice. (a) Sketch of the four key stages of our preparation scheme: spin-polarized dFg in an ODT (a1), single-component BI (a2), rf-preparation of a spin mixture in the lattice (a3), and spin-mixture in the ODT (a4). (b) Band population in the horizontal xy-plane, obtained by averaging 50 absorption images for a 12 ms time-of-flight (TOF). The red arrows indicate the first Brillouin zone of the lattice, i. e. $2\hbar\pi/d_{x,y}$ with $d_{x,y} = 266\,\mathrm{nm}$. (c) Spin-resolved band-mapping images after 9 ms of TOF in the vertical $z\tilde{x}$ plane, where $\tilde{x}$ accounts for the angle between the imaging beam and the y-axis of the lattice, for population imbalances $\delta = 1$ (left panel), 0.02 (middle panel), and -0.94 (right panel). The images are averages of about 20 absorption pictures. The spin states are separated along the z-direction by a Stern-Gerlach technique and are depicted by the blue and orange dipole, respectively.

tuning the rf-power, we can precisely control the population imbalance, $\delta = (N_\downarrow - N_\uparrow)/(N_\downarrow + N_\uparrow)$, in the mixture. Figure 1(c) shows exemplary spin-resolved absorption images of $|\downarrow\rangle$–$|\uparrow\rangle$ mixtures for various δ after B is swept back to low values [39]. At $\delta \approx -1$, we typically record $N_\uparrow = 1.6 \times 10^4$ $|\uparrow\rangle$ atoms. By reloading the atoms into the ODT, we extract a temperature of $T \approx 0.3\,T_\mathrm{F}$ (stage (a4); Fig. 1). For comparison, similar measurements in absence of the lattice clearly show a much lower atom number of $N_\uparrow = 0.6 \times 10^4$, proving the strength of our lattice-protection scheme to circumvent atomic loss [20] when cruising through the ultra-dense Feshbach spectrum [26].

Figure 2 shows the high collisional stability of the lattice-confined spin mixture with lifetimes of several seconds. In particular, we probe the atom number of $|\downarrow\rangle$ and $|\uparrow\rangle$ as a function of the holding time in the lattice; see Fig. 2(a). From an exponential fit to the data, we extract long lifetimes of $\tau_\downarrow = 31(3)\,\mathrm{s}$ and $\tau_\uparrow = 12.2(7)\,\mathrm{s}$. The measurements are carried out at $B = 3.99\,\mathrm{G}$, where no FRs occur [32]. We also observe that the lifetime of each spin state does not show a dependence on the population in the other state, i. e. on δ; see Fig. 2(b).

We note that, although very long for our purpose, we

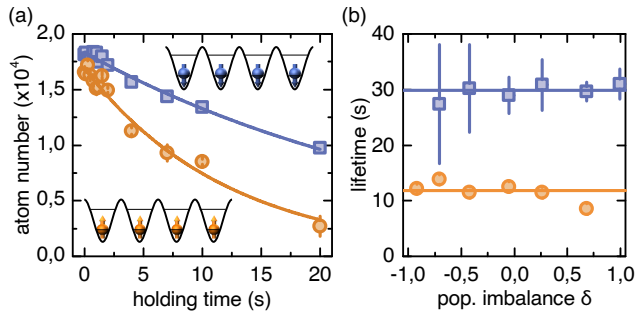

FIG. 2. Spin mixture of dipolar ^{167}Er in a 3D lattice. (a) Lifetime measurements for spin-polarized samples of $|\downarrow\rangle$ (squares) with $\delta = 1$ and of $|\uparrow\rangle$ (circles) with $\delta = -0.92$ at $B = 3.99\,\mathrm{G}$. Exponential decay functions (solid lines) are fitted to the respective data. (b) Lifetimes as a function of δ. Constant fits extract mean lifetimes across δ of $\bar{\tau}_\downarrow = 29.9(3)\,\mathrm{s}$ and $\bar{\tau}_\uparrow = 11.8(7)\,\mathrm{s}$. All error bars indicate the statistical uncertainty.

always record shorter lifetimes for a $|\uparrow\rangle$ BI with respect to the ones measured for a $|\downarrow\rangle$ BI. Differently from the $|\downarrow\rangle$ case, two-body relaxation processes for $|\uparrow\rangle$ are allowed. At our magnetic fields, this process converts Zeeman energy into a large enough kinetic energy to let the atoms escape from the lattice [13, 40], and requires the particles to collide at short distance (onsite) [19, 41]. In the spin-polarized cases (e. g. $\delta = -1$; $|\uparrow\rangle$), double occupancy necessarily involves population in higher bands since the Pauli exclusion principle forbids doublons in the lowest band. In our system, a continuous transfer of a small fraction of atoms into higher bands might be driven by intensity and frequency noise of the lattice beams [31]. In the case of $|\uparrow\rangle$ this would lead to subsequent fast relaxation and explain the observed difference in the lifetimes.

With the above described spin-preparation method, we are now able to conduct high-precision Feshbach spectroscopy in an ODT (stage (a4); Fig. 1) in search of interspecies loss features. For this, we first prepare the spin-1/2 mixture in a deep lattice and sweep B to the target value within 10 ms. After letting B stabilize for about 100 ms, we transfer the mixture back into the ODT, hold the atoms for 500 ms, and finally measure the spin populations, as previously described. We then repeat the measurement for different B values within the desired range. Figure 3 exemplifies the high-precision Feshbach spectroscopy for three values of δ within a narrow magnetic field range from $B = 550\,\mathrm{mG}$ to $750\,\mathrm{mG}$ with a resolution of 1 mG. A lower-resolution and larger-range scan is shown in Ref. [32].

As expected [26, 27], the atom-number trace as a function of B shows a high density of resonant loss features on top of a constant background. By controlling δ, we are able to distinguish the spin nature of each of the observed FRs. In the excerpt shown in Fig. 3, we identify three narrow homo-spin FRs in a pure $|\downarrow\rangle$ sample ((a), blue shading) and four in a quasi-pure $|\uparrow\rangle$ sample ((b), orange shading). In the spin-polarized cases, all FRs are narrow with measured widths of the order of our magnetic field stability of $\approx 1\,\mathrm{mG}$. Thanks to our lattice-preparation technique, the shape and the width of the FRs are not affected by the magnetic field ramps, namely we do not observe neither broadening nor fictitious asymmetry in the loss peaks. For the 50%-50% spin mixture ($\delta = 0$), we observe five additional inter-spin FRs (Fig. 3(c), green shading), where atoms in the two spin states are simultaneously lost. Because of the complicated scattering behavior of Er, standard coupled-channel methods to assign the leading partial-wave character of the FRs are currently not available [42]. However, the width of the FRs can give indications on the strength of the coupling between open and closed channels [43].

Among the observed inter-spin FRs, the one at about 0.68 G stands out from the forest of narrow FRs, as it is almost two orders of magnitude broader. This feature makes this FR a promising candidate for Fermi-gas experiments in the strongly interacting regime. A thorough understanding of the collisional properties and interactions in its proximity becomes thus crucial to assert the usefulness of this FR for such type of investigations. To reach a precise knowledge of the inter-spin scattering length, $a_{\downarrow\uparrow}$, we conduct modulation spectroscopy experiments in the 3D lattice to map the B-to-$a_{\downarrow\uparrow}$ conversion. This technique, which has been very powerful to precisely determine the scattering length in dipolar Bose-Einstein condensates [9, 33], allows to measure the onsite interaction energy $U_{\downarrow\uparrow}$. We prepare a spin-1/2 Fermi gas in a one-atom-per-lattice-site configuration (stage (a3); Fig. 1). When the frequency of the lattice-depth modulation is resonant with $U_{\downarrow\uparrow}/h$, the sample undergoes increased losses; for details see Ref. [32]. In our system, $U_{\downarrow\uparrow} = U_\mathrm{c} + U_\mathrm{dd}$ is the sum of the inter-spin contact interaction, U_c, and the DDI, U_dd. Thanks to the precise knowledge of U_dd for our lattice configuration [33] we are able to directly extract $a_{\downarrow\uparrow} \propto U_\mathrm{c} = U_{\downarrow\uparrow} - U_\mathrm{dd}$. Importantly, the angle dependence of the DDI makes our method sensitive to the sign of $a_{\downarrow\uparrow}$: By changing the orientation of the dipoles, we can tune U_dd from negative to positive values, which increases (decreases) the total energy $|U_{\downarrow\uparrow}|$ for positive (negative) $a_{\downarrow\uparrow}$ [32, 33].

Figure 4(a) shows $a_{\downarrow\uparrow}$ for various B values around the comparatively broad inter-spin FR of Fig. 3(c). The measured $a_{\downarrow\uparrow}$ follows the typical behavior at an isolated FR, demonstrating the tunability of $a_{\downarrow\uparrow}$ from positive to negative values. To obtain a precise B-to-$a_{\downarrow\uparrow}$ conversion, we fit the standard function $a_{\downarrow\uparrow}(B) = a_\mathrm{bg}\left(1 - \frac{\Delta}{B-B_0} - \frac{\Delta'}{B-B_0'}\right)$ to the data [43]. From the fit, we extract the background scattering length $a_\mathrm{bg} = 91(8)\,a_0$, the position of the comparatively broad FR $B_0 = 687(1)\,\mathrm{mG}$ and its width $\Delta = 58(6)\,\mathrm{mG}$. Note that our fitting function also accounts for a nearby inter-

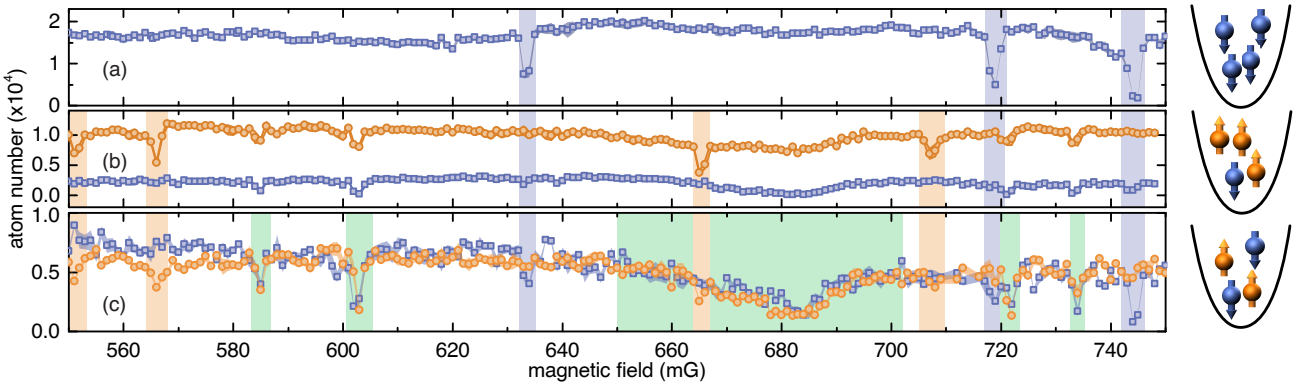

FIG. 3. High-resolution Feshbach spectroscopy with a 1 mG step size for three different population imbalances in an ODT (cartoons): atoms in $|\downarrow\rangle$ (squares) and $|\uparrow\rangle$ (circles) for $\delta = 1$ (a), -0.6 (b), and 0 (c) as a function of B. From the three datasets one can determine the spin nature of the FRs as indicated by the blue ($|\downarrow\rangle$), orange ($|\uparrow\rangle$), and green ($|\downarrow\rangle$–$|\uparrow\rangle$) shaded regions.

spin FR at $B_0' = 480\,\mathrm{mG}$ (out of range of Fig. 3 and 4) of width $\Delta' = 29(4)\,\mathrm{mG}$, whereas narrower inter-spin FRs are neglected. Based on the extracted values, we can give an estimate of the length parameter $R^* = \hbar^2/(m_{\mathrm{Er}}\Delta a_{\mathrm{bg}}\delta\mu)$, which characterizes the strength of a FR [43]. Here, m_{Er} is the mass of ^{167}Er. For the considered FR the differential magnetic moment between the open and closed channel, $\delta\mu$, is not known. For bosonic Er, we have previously measured a typical $\delta\mu \approx 3\,\mu_{\mathrm{B}}$ via molecular spectroscopy of a few molecular states [42]. By using this bosonic value we estimate $R^* \approx 1000 a_0$. Universal scattering behavior is expected for $a_{\downarrow\uparrow} > R^*$ [44].

In experiments with strongly interacting alkali Fermi gases of ^{40}K or ^{6}Li, the large collisional stability in two-component mixtures has been essential for observing e. g. fermionic superfluidity and molecular BECs [45]. As direct consequence of the Pauli principle, three-body recombination occurs primarily on the repulsive (BEC) side of a broad s-wave FR, where a weakly bound molecular level exists [46], whereas, on the attractive (BCS) side, large scattering lengths coexist with a remarkable collisional stability [47–50]. Such an asymmetry in the scattering behavior is identified as an essential attribute of BEC-to-BCS physics.

To investigate this aspect, we prepare an equally populated spin mixture ($\delta = 0$) in an ODT, following the scheme of Fig.1(a), and probe the time evolution of the spin population as a function of the holding time in the trap (stage (a4); Fig. 1) for various B across the FR. Exemplary decay curves are shown in Fig. 4(b-c). On the BEC side at $a_{\downarrow\uparrow} = 880(140)\,\mathrm{a_0}$, we observe a fast atomic decay of both $|\uparrow\rangle$ and $|\downarrow\rangle$ atoms (Fig. 4(b)). A simple exponential fit to the data gives lifetimes of $\tau_{1/e} \approx 150\,\mathrm{ms}$. In striking contrast, on the BCS side at $a_{\downarrow\uparrow} = -1500(500)\,\mathrm{a_0}$ (Fig. 4(d)), the spin mixture shows a remarkable collisional stability with lifetimes exceeding $\tau_{1/e} = 1200\,\mathrm{ms}$ (Fig. 4(c)).

To get deeper insights, we systematically study the initial decay rate, $\dot{N}/N_0$, as a function of B. We determine the rates by using a linear fit to the data for the initial time evolution. Figure 4(d) summarizes our results, plotted in terms of the dimensionless coupling constant $1/(k_F a_{\downarrow\uparrow})$ with k_F being the Fermi wave vector [32]. We clearly observe that the maximum in the loss rate is shifted to the repulsive side of the FR pole and that the Fermi mixture exhibits a remarkable stability in the unitary and strongly attractive regime. The observed shape of the loss rate reveals a remarkable similarity with measurements conducted with alkali fermions. It is interesting that the absolute values of the loss rates in ^{167}Er are not only qualitatively similar but also quantitatively very close to the ones measured in ^{40}K [49], with e. g. on the BCS side lifetimes of about one second in both cases.

The existence of a comparatively broad FR, our acquired precise knowledge of the scattering length, and the collisional stability in the strongly interacting regime make fermionic Er atoms a new promising system for accessing BEC-to-BCS crossover physics. Our mixture adds DDI to the alkali scenario, paving the way for studying Cooper pairs with large magnetic moments and strongly dipolar molecular BECs [22].

We thank R. Grimm, M. Greiner, and A. M. Rey for fruitful discussions. We acknowledge financial support through an ERC Consolidator Grant (RARE, no. 681432), FET Proactive project (RySQ, no. 640378) of the EU H2020, and a DFG/FWF (FOR 2247). LC is supported within a Marie Curie Project (DipPhase, no. 706809) of the EU H2020.

† Current address: Physikalisches Institut, Universität Heidelberg, Im Neuenheimer Feld 226, 69120 Heidelberg, Germany

* Correspondence and requests for materials should be addressed to F.F. (email: francesca.ferlaino@uibk.ac.at).

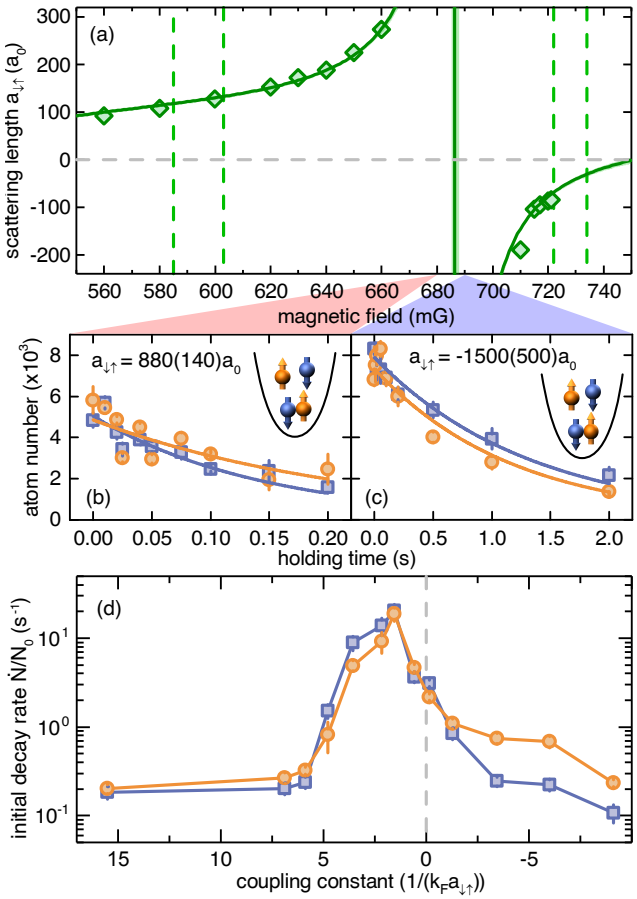

FIG. 4. Inter-spin scattering length and collisional behavior of the strongly interacting Fermi mixture (a) $a_{\downarrow\uparrow}$ extracted from modulation spectroscopy in the lattice; see text. Error bars are smaller than the size of the data points. Vertical dashed lines indicate the position of narrow inter-spin FRs as identified in Fig. 3(c). The solid line is a fit to the data (see text) with the fit statistical uncertainty indicated as shaded region. (b-c) Lifetimes of a spin mixture of $|\downarrow\rangle$ (squares) and $|\uparrow\rangle$ (circles) with $\delta = 0$ in an ODT for large positive $a_{\downarrow\uparrow}$ at 680 mG (b) and for large negative $a_{\downarrow\uparrow}$ at 690 mG. (d) Initial decay rate $\dot{N}/N_0$ of the normalized atom numbers as a function of $1/(k_F a_{\downarrow\uparrow})$ in the vicinity of the FR.

[1] A. Griesmaier, J. Werner, S. Hensler, J. Stuhler, and T. Pfau, Phys. Rev. Lett. **94**, 160401 (2005).
[2] M. Lu, N. Q. Burdick, S. H. Youn, and B. L. Lev, Phys. Rev. Lett. **107**, 190401 (2011).
[3] M. Lu, N. Q. Burdick, and B. L. Lev, Phys. Rev. Lett. **108**, 215301 (2012).
[4] K. Aikawa, A. Frisch, M. Mark, S. Baier, A. Rietzler, R. Grimm, and F. Ferlaino, Phys. Rev. Lett. **108**, 210401 (2012).
[5] K. Aikawa, A. Frisch, M. Mark, S. Baier, R. Grimm, and F. Ferlaino, Phys. Rev. Lett. **112**, 010404 (2014).
[6] B. Naylor, A. Reigue, E. Maréchal, O. Gorceix, B. Laburthe-Tolra, and L. Vernac, Phys. Rev. A **91**, 011603 (2015).
[7] T. Lahaye, J. Metz, B. Fröhlich, T. Koch, M. Meister, A. Griesmaier, T. Pfau, H. Saito, Y. Kawaguchi, and M. Ueda, Phys. Rev. Lett. **101**, 080401 (2008).
[8] H. Kadau, M. Schmitt, M. Wenzel, C. Wink, T. Maier, I. Ferrier-Barbut, and P. Tilman, Nature (London) **530**, 194 (2016).
[9] L. Chomaz, S. Baier, D. Petter, M. J. Mark, F. Wächtler, L. Santos, and F. Ferlaino, Phys. Rev. X **6**, 041039 (2016).
[10] M. Schmitt, M. Wenzel, F. Böttcher, I. Ferrier-Barbut, and T. Pfau, Nature (London) **539**, 259 (2016).
[11] L. Chomaz, R. M. W. van Bijnen, D. Petter, G. Faraoni, S. Baier, J. H. Becher, M. J. Mark, F. Waechtler, L. Santos, and F. Ferlaino, Nature Physics (2018), 10.1038/s41567-018-0054-7.
[12] K. Aikawa, S. Baier, A. Frisch, M. Mark, C. Ravensbergen, and F. Ferlaino, Science **345**, 1484 (2014).
[13] S. Hensler, J. Werner, A. Griesmaier, P. Schmidt, A. Görlitz, T. Pfau, S. Giovanazzi, and K. Rzażewski, Applied Physics B **77**, 765 (2003).
[14] B. Pasquiou, E. Maréchal, G. Bismut, P. Pedri, L. Vernac, O. Gorceix, and B. Laburthe-Tolra, Phys. Rev. Lett. **106**, 255303 (2011).
[15] A. de Paz, A. Sharma, A. Chotia, E. Maréchal, J. H. Huckans, P. Pedri, L. Santos, O. Gorceix, L. Vernac, and B. Laburthe-Tolra, Phys. Rev. Lett. **111**, 185305 (2013).
[16] S. Lepoutre, J. Schachenmayer, L. Gabardos, B. Zhu, B. Naylor, E. Marechal, O. Gorceix, A. M. Rey, L. Vernac, and B. Laburthe-Tolra, ArXiv e-prints (2018), arXiv:1803.02628 [cond-mat.quant-gas].
[17] M. Vengalattore, S. R. Leslie, J. Guzman, and D. M. Stamper-Kurn, Phys. Rev. Lett. **100**, 170403 (2008).
[18] Y. Eto, H. Saito, and T. Hirano, Phys. Rev. Lett. **112**, 185301 (2014).
[19] N. Q. Burdick, K. Baumann, Y. Tang, M. Lu, and B. L. Lev, Phys. Rev. Lett. **114**, 023201 (2015).
[20] N. Q. Burdick, Y. Tang, and B. L. Lev, Phys. Rev. X **6**, 031022 (2016).
[21] B. Yan, S. A. Moses, B. Gadway, J. P. Covey, K. R. A. Hazzard, A. M. Rey, D. S. Jin, and J. Ye, Nature **501**, 521 (2013).
[22] M. A. Baranov, M. Dalmonte, G. Pupillo, and P. Zoller, Chem. Rev. **112**, 5012 (2012).
[23] I. Bloch, J. Dalibard, and W. Zwerger, Rev. Mod. Phys. **80**, 885 (2008).
[24] D. M. Stamper-Kurn and M. Ueda, Rev. Mod. Phys. **85**, 1191 (2013).
[25] O. Dutta, M. Gajda, P. Hauke, M. Lewenstein, D.-S. Lühmann, B. A. Malomed, T. Sowiński, and J. Zakrzewski, Reports on Progress in Physics **78**, 066001 (2015).
[26] A. Frisch, M. Mark, K. Aikawa, F. Ferlaino, J. Bohn, C. Makrides, A. Petrov, and S. Kotochigova, Nature (London) **507**, 475 (2014).
[27] K. Baumann, N. Q. Burdick, M. Lu, and B. L. Lev, Phys. Rev. A **89**, 020701 (2014).
[28] T. Maier, H. Kadau, M. Schmitt, M. Wenzel, I. Ferrier-Barbut, T. Pfau, A. Frisch, S. Baier, K. Aikawa, L. Chomaz, M. J. Mark, F. Ferlaino, C. Makrides, E. Tiesinga, A. Petrov, and S. Kotochigova, Phys. Rev. X **5**, 041029 (2015).
[29] H. Schmaljohann, M. Erhard, J. Kronjäger, M. Kottke,

S. van Staa, L. Cacciapuoti, J. J. Arlt, K. Bongs, and K. Sengstock, Phys. Rev. Lett. **92**, 040402 (2004).
[30] K. Winkler, F. Lang, G. Thalhammer, P. v. d. Straten, R. Grimm, and J. H. Denschlag, Phys. Rev. Lett. **98**, 043201 (2007).
[31] A. Chotia, B. Neyenhuis, S. A. Moses, B. Yan, J. P. Covey, M. Foss-Feig, A. M. Rey, D. S. Jin, and J. Ye, Phys. Rev. Lett. **108**, 080405 (2012).
[32] Supplemental Material.
[33] S. Baier, M. J. Mark, D. Petter, K. Aikawa, L. Chomaz, Z. Cai, M. Baranov, P. Zoller, and F. Ferlaino, Science **352**, 201 (2016).
[34] A. Kastberg, W. D. Phillips, S. L. Rolston, R. J. C. Spreeuw, and P. S. Jessen, Phys. Rev. Lett. **74**, 1542 (1995).
[35] We decrease all lattice potential to zero within 1 ms, thus mapping the quasi momentum of the band to real momentum, which finally reveals the band population in TOF.
[36] The edges of the lowest band are smeared out because of the finite width of the in-situ cloud and due to an imperfect adiabatic switch-off of the lattice potentials [51].
[37] S. Will, PhD Thesis (2011).
[38] J. G. Danzl, M. J. Mark, E. Haller, M. Gustavsson, R. Hart, J. Aldegunde, J. M. Hutson, and H.-C. Nägerl, Nature Physics **6**, 265 (2007).
[39] Spin resolved imaging is performed via a Stern-Gerlach imaging with a 1-ms pulsed magnetic field gradient during TOF.
[40] A. de Paz, A. Chotia, E. Maréchal, P. Pedri, L. Vernac, O. Gorceix, and B. Laburthe-Tolra, Phys. Rev. A **87**, 051609 (2013).
[41] B. Pasquiou, G. Bismut, Q. Beaufils, A. Crubellier, E. Maréchal, P. Pedri, L. Vernac, O. Gorceix, and B. Laburthe-Tolra, Phys. Rev. A **81**, 042716 (2010).
[42] A. Frisch, M. Mark, K. Aikawa, S. Baier, R. Grimm, A. Petrov, S. Kotochigova, G. Quéméner, M. Lepers, O. Dulieu, and F. Ferlaino, Phys. Rev. Lett. **115**, 203201 (2015).
[43] C. Chin, R. Grimm, P. Julienne, and E. Tiesinga, Rev. Mod. Phys. **82**, 1225 (2010).
[44] M. Jag, M. Cetina, R. S. Lous, R. Grimm, J. Levinsen, and D. S. Petrov, Phys. Rev. A **94**, 062706 (2016).
[45] M. Inguscio, W. Ketterle, and C. Salomon, eds., *Proceedings of the International School of Physics "Enrico Fermi", Course CLXIV* (IOS Press, Amsterdam, 2007).
[46] D. S. Petrov, Phys. Rev. A **67**, 010703 (2003).
[47] K. Dieckmann, C. A. Stan, S. Gupta, Z. Hadzibabic, C. H. Schunck, and W. Ketterle, Phys. Rev. Lett. **89**, 203201 (2002).
[48] T. Bourdel, J. Cubizolles, L. Khaykovich, K. M. F. Magalhães, S. J. J. M. F. Kokkelmans, G. V. Shlyapnikov, and C. Salomon, Phys. Rev. Lett. **91**, 020402 (2003).
[49] C. A. Regal, M. Greiner, and D. S. Jin, Phys. Rev. Lett. **92**, 083201 (2004).
[50] S. Jochim, PhD Thesis (2004).
[51] M. Köhl, H. Moritz, T. Stöferle, K. Günter, and T. Esslinger, Phys. Rev. Lett. **94**, 080403 (2005).
[52] J. G. Conway and B. G. Wybourne, Phys. Rev. **130**, 2325 (1963).
[53] K. F. Smith and P. J. Unsworth, Proceedings of the Physical Society **86**, 1249 (1965).
[54] S. Baier et al., in preparation (2018).
[55] J. H. Becher, S. Baier, K. Aikawa, M. Lepers, J.-F. Wyart, O. Dulieu, and F. Ferlaino, Phys. Rev. A **97**, 012509 (2018).
[56] R. Jördens, N. Strohmaier, K. Günter, H. Moritz, and T. Essslinger, Nature (London) **455**, 204 (2008).

SUPPLEMENTAL MATERIAL

Spin-polarized degenerate Fermi gases

Our experimental protocol for the preparation of deeply degenerate Fermi gases (dFgs) of ^{167}Er follows the one described in Ref. [5]. The experiment starts with a narrow-line magneto-optical trap operated at 583 nm to prepare spin-polarized ^{167}Er atoms with $N = 1.2 \times 10^7$ atoms in the lowest hyperfine sublevel $|F = 19/2, m_F = -19/2\rangle$, where F is the total spin quantum number and m_F is its projection along the quantization axis. The atoms are then transferred to a horizontal optical dipole trap (ODT) operated at 1064 nm (ODT_{1064}). The aspect ratio $\mathrm{AR} = w_\perp/w_z$ of this trap can be tuned from 1.6 to 15 via a time-averaging potential technique [9] and allows to reach a good spatial mode overlap between the atomic cloud and the optical potential. Sub-sequentially the atomic cloud is compressed by reducing the AR and transferred to a counter propagating tight ODT operated at 1570 nm (ODT_{1570}) with a beam waist of about 15 μm. At this stage we typically have 1×10^6 atoms. During the evaporation procedure the atoms are further confined by a vertical ODT at 1570 nm with at waist of about 32 μm.

Following our previous work [5], we perform evaporative cooling based on elastic dipolar scattering among identical fermions. Dipolar cooling has been proven to be very efficient to produce samples in the deeply quantum degenerate regime [5, 20]. At the end of the evaporation we typically obtain a spin-polarized dFg with up to 6×10^4 atoms and temperatures of $T \leq 0.15\, T_\mathrm{F}$, with T_F being the Fermi temperature. At this stage the Fermi energy is $E_F = k_\mathrm{B} T_\mathrm{F} = k_\mathrm{B} \times 630\,\mathrm{nK} = h \times 13\,\mathrm{kHz}$. The final trap frequencies in ODT_{1570} are $(\nu_\perp, \nu_\parallel, \nu_z) = (286(3), 85(1), 255(3))$ Hz with $\parallel$ ($\perp$) corresponding to the axis along (perpendicular to) the horizontal beam and z indicating the axis of gravity. The magnetic field has a value of $B = 0.6$ G and is oriented along z, which sets the quantization axis of the atomic dipoles.

Preparation for lattice loading

For deeply dFgs the atoms fill the Fermi sea up to the Fermi energy $E_F = h\bar{\nu}(6N)^{1/3}$, where h is the Planck constant, $\bar{\nu}$ the geometric mean of the trap frequencies and N the atom number. Hence, the Fermi energy gives the relevant energy scale of the system. The number of populated bands, when the atoms are loaded to an optical lattice, thus crucially depends on the ini-

tial Fermi energy. Here, in first approximation, the Fermi energy can be compared to the lattice recoil energy $E_{\rm rec} = h^2/(2m\lambda^2)$, with m being the mass of ^{167}Er and λ the lattice wavelength. In particular, during the initial increase of the lattice potential higher bands become populated if $E_F > E_{\rm rec}$ [37].

To minimize the occupation of higher bands due to the loading procedure we reduce the Fermi energy of our sample. Here, we transfer the atoms back to a crossed ODT_{1064} within 510 ms, which allows for a convenient control on $\bar{\nu}$ via the dynamically adjustable AR. We optimize the ODT parameters by lowering $\bar{\nu}$ and N while keeping a low temperature of the sample. Best conditions for subsequent lattice loading are reached for $(\nu_\perp, \nu_\parallel, \nu_z) = (63(1), 36(2), 137(1))$ Hz and $N = 2.4 \times 10^4$ atoms corresponding to a Fermi energy $E_{\rm F} = k_{\rm B} \times 170\,\mathrm{nK} = h \times 3.6\,\mathrm{kHz}$. We note that for lower ν_z atoms get lost due to gravity.

Three-dimensional optical lattice

After preparation, we adiabatically load the spin-polarized dFg into a three-dimensional (3D) optical lattice, created by two retro-reflected 532 nm laser beams along the x- and y-axis and one retro-reflected 1064 nm vertical laser beam along the z axis; see Fig. S1. The lattice spacing are $d_{x,y} = 266\,\mathrm{nm}$ along the horizontal xy-plane and $d_z = 532\,\mathrm{nm}$ along the vertical z-axis [33]. We increase the lattice-beam intensities exponentially in 150 ms to the final value. With the available power, we reach maximum lattice depths of $(s_x, s_y, s_z) = (25, 25, 120)$, where s_i with $i \in \{x, y, z\}$ is given in units of the respective recoil energies, $\mathrm{E}_{\mathrm{R};x,y} = h \times 4.2\,\mathrm{kHz}$ and $\mathrm{E}_{\mathrm{R};z} = h \times 1.05\,\mathrm{kHz}$. Typical lattice depths used in the experiment are $(s_x, s_y, s_z) = (20, 20, 80)$ corresponding to band gaps of $h \times 32.8\,\mathrm{kHz}$ along x and y and $h \times 17.7\,\mathrm{kHz}$ along z. Subsequentially, the ODT beams are switched off in 10 ms and we additionally hold the atoms for 500 ms. This time is sufficient to remove residual atoms that have been pushed to higher bands of the optical lattice by the Fermi pressure. We note that when the atoms are loaded directly from ODT_{1570} we find up to 25 % of higher bands population, which in this case get strongly depopulated within 500 ms. A remaining fraction of 5 % in the higher band of the vertical lattice remains also for our most careful loading procedure; see main manuscript.

Zeeman energy for fermionic Er

Fermionic Er exhibits a hyperfine structure with a nuclear spin quantum number $I = 7/2$ that couples with the total electronic angular momentum J to the total angular momentum $\mathbf{F} = \mathbf{J} + \mathbf{I}$. In the lowest hyperfine manifold ($F = 19/2$) there are $2F + 1 = 20$ magnetic substates m_F resulting from the projection of $\mathbf{F}$ on the quantization axis. The lowest magnetic state $|F = 19/2; m_F = -19/2\rangle$ exhibits a magnetic moment of $\mu = m_F g_F \mu_B = -6.982804 \mu_B$ where $g_F = 0.735032$ is the Landé g-factor and μ_B is the Bohr magneton [52].

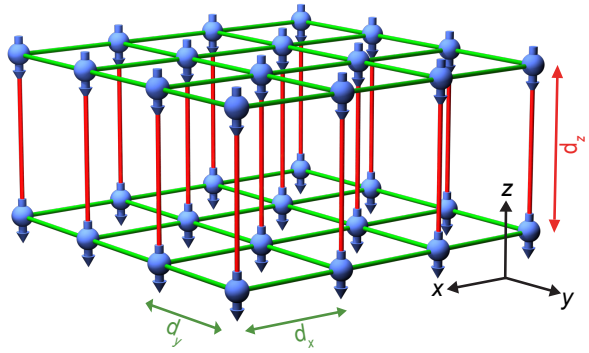

FIG. S1. Sketch of our lattice geometry. The coordinate system $\{x, y, z\}$ and the lattice constants d_x, d_y, and d_z are indicated.

The hyperfine energies can be calculated via exact diagonalization of the atomic Hamiltonian [53]. In Fig. S2 we plot the Zeeman substates of the lowest hyperfine manifold as a function of the magnetic field. At first glance it appears that the energies evolve linearly. However, at larger magnetic field due to the Paschen-Back effect J and I start to decouple. This leads to a quadratic term of the Zeeman energy for states $\sigma = m_F$ with $E_\sigma = q_{\rm qu}(\sigma^2 - F^2)$ and $q_{\rm qu} \propto B^2$. The deviation from the linear Zeeman energy becomes evident in the differential splitting $\Delta E_{\rm Z} = (E_\sigma - E_{\sigma+1}) - (E_{\sigma+1} - E_{\sigma+2})$ with $E_\sigma = q_{\rm li}\sigma + q_{\rm qu}(\sigma^2 - F^2)$ and $\sigma \in [-19/2, \ldots, 19/2]$ as shown in the inset of Fig. S2. The linear Zeeman effect $q_{\rm li}\sigma \propto B$ cancels out when $\Delta E_{\rm Z}$ is evaluated.

Preparation of a spin mixture in the lattice

For deterministic spin preparation of the two lowest spin states we use typically magnetic field values of $B = 40.51\,\mathrm{G}$ where $\Delta E_{\rm Z} = 42.6\,\mathrm{kHz}$, which is larger than the magnetic field noise at this field of $\approx 20\,\mathrm{kHz}$. This resembles an effective two level spin-1/2 system for spin-spin couplings and enables a deterministic spin preparation of the lowest two spin states via radio-frequency (rf)-techniques. To couple the two hyperfine sub-states we apply a rf-sweep by chirping the rf-frequency continuously from a value of $(\nu^\star + 30\,\mathrm{kHz})$ to $(\nu^\star - 30\,\mathrm{kHz})$ within about 10 ms, where $h \times \nu^\star$ corresponds to the difference in Zeeman energy of the two lowest spin states ($\Delta 1$; Fig. S2). We can prepare a well-reproducible mixture of $|\downarrow\rangle$ and $|\uparrow\rangle$ without populating the next higher

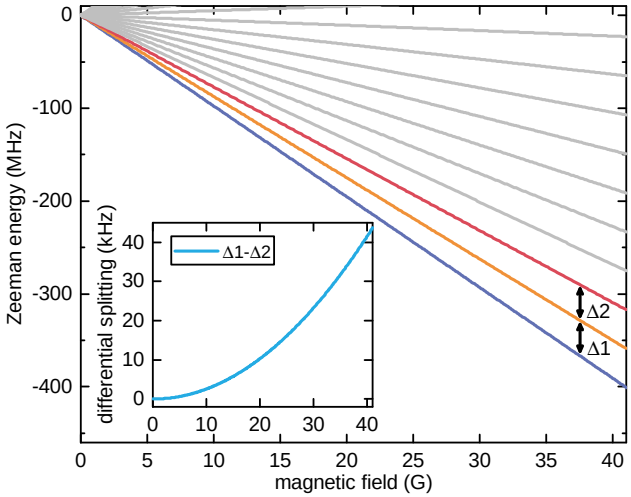

FIG. S2. Zeeman energy for the magnetic substates in the $|F = 19/2\rangle$ hyperfine manifold. For this work the energy splitting of the lowest three spin states $|{-19/2}\rangle \equiv |{\downarrow}\rangle$ (blue line), $|{-17/2}\rangle \equiv |{\uparrow}\rangle$ (orange line) and $|{-15/2}\rangle$ (red line) is of most relevance. Higher spin states are visualized by grey lines. The linear Zeeman effect dominates the energy evolution while in the differential splitting $\Delta E_{\mathrm{Z}} = \Delta 1 - \Delta 2$ (inset) the quadratic Zeeman effect is evident.

spin state. The population imbalance δ between the two spin states can be freely controlled by varying the power of the rf signal. In particular, also almost all the atoms can be transferred to $|{\uparrow}\rangle$ reaching up to $\delta = -0.94$ (see Fig. 1(c) in main manuscript). We note that, while our preparation technique in the lattice initially leads to a coherent superposition of the two spin states, additional measurements suggest a fast decoherence, leading to a projection of pure states on the individual lattice sites for experimental relevant time scales. In particular, we observe that coherently driven Rabi oscillations between the two spin states quickly damp within a few ms.

Lifetime of the spin mixture in a deep lattice

To conduct a clean measurement of the collisional properties of a spin mixture in the deep optical lattice it is important to fulfill the following requirements: (i) The spin mixture is in an insulating regime where the formation of doublons is suppressed via sufficiently large ratios of the onsite energy U to the tunneling rate J. The magnetic field is also well away from Feshbach resonances (FRs). (ii) The Zeeman energies do not have an equidistant spacing. In such a regime magnetization conserving spin exchange would lead to a change of the spin composition [15, 16, 21, 54].

Due to the high density of FRs the first requirement can be more conveniently achieved with low technical magnetic field noise, which ensures a higher stability of the magnetic field value. In our experiment this is given below 5 G where the noise is found to be ≈ 1 mG. The second requirement is matched for a sufficiently large magnetic field, where the quadratic Zeeman effect is strong enough to not be canceled by quadratic light shifts [55]. Best conditions are found at a magnetic field value of 3.99 G, which is used for the lifetime measurements of Fig. 2. At this field the measured onsite interaction $U = h \times 2.43(2)$ kHz exceeds by far the relevant tunneling rates $J_{x,y} = h \times 10.5$ Hz and no spin dynamics are observed.

State-resolved Feshbach spectroscopy

To identify the magnetic field regions where promising inter-spin FRs occur, we first perform a rough Feshbach scan in the $0 - 2$ G region for different population imbalances δ (Fig. S3). For this set of data we do not use our lattice-protection technique. Instead, the spin preparation, the magnetic-field ramps, and the Feshbach spectroscopy are directly performed in the ODT. As expected, without the lattice, the loss features present broadening and asymmetric shapes due to mere magnetic-field sweeps (e. g. losses during the sweeps).

For this measurement set, we first perform a Feshbach scan in a spin polarized gas in ODT_{1570} (Fig. S3, upper panel). We jump to the final magnetic field and hold for $t_{\mathrm{hold}} = 70$ ms before time-of-flight imaging. The trap frequencies are $(\nu_\perp, \nu_\parallel, \nu_z) = (324(1), 147(5), 259(4))$ Hz. The system has an initial temperature of $T = 0.18(1)\, T_{\mathrm{F}}$. Similar to Ref. [26], we observe a high density of loss features, which correspond to single-component ($|{\downarrow}\rangle$) FRs of high partial-wave character. We then repeat the magnetic-field scan in an almost pure $|{\uparrow}\rangle$ sample (Fig. S3, middle panel). Here, we use a resonant rf-pulse at 0.99 G to prepare a mixture with mainly $|{\uparrow}\rangle$ atoms. Then we jump on a purely $|{\downarrow}\rangle$ homo-spin FR located at 1.034 G to remove remaining $|{\downarrow}\rangle$ atoms. The measurement is performed in the more shallow ODT_{1064} to prevent too strong interspecies losses and $t_{\mathrm{hold}} = 500$ ms. For this trap the trap frequencies are $(\nu_\perp, \nu_\parallel, \nu_z) = (39(1), 37(1), 145(3))$ Hz and the initial temperature is $T = 0.35(1)\, T_{\mathrm{F}}$. We find new FRs, which mainly correspond to single-component $|{\uparrow}\rangle$ FRs. In a last scan we observe the loss features for a spin mixture prepared at 0.58 G in the same trap as for the pure $|{\downarrow}\rangle$ measurement with $t_{\mathrm{hold}} = 50$ ms (Fig. S3, lower panel). Here, the initial temperature is slightly increased due to the spin mixing to $T = 0.24(1)\, T_{\mathrm{F}}$. The individual homo-spin FRs are still visible while we also find new inter-spin $|{\downarrow}\rangle$–$|{\uparrow}\rangle$ FRs.

We analyze the three sets of data to extract the spin nature of the individual FRs. For several FRs, the entrance spin channel can be easily identified. In addition, we also observe overlapping FRs. Here, an exact assign-

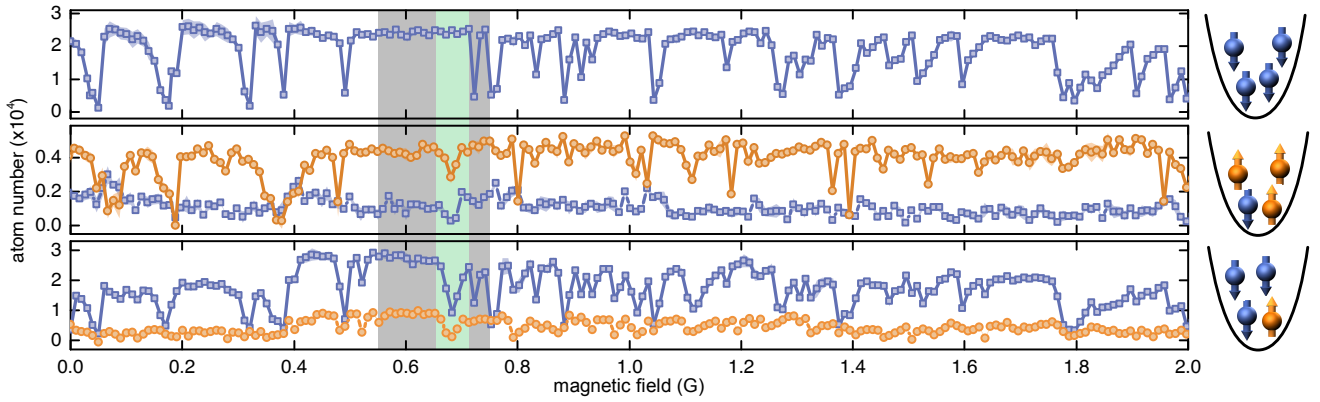

FIG. S3. Feshbach spectroscopy of a two-component spin mixture in an ODT (without the lattice-protection technique) for different population imbalances δ: $\delta = 1$ (upper panel), -0.54 (middle panel), 0.4 (lower panel). While the measurements for the upper and lower panel are performed in ODT_{1570} with $\bar{\nu} = 231(3)$ Hz, the data of the middle panel is measured in ODT_{1064} with $\bar{\nu} = 59(1)$ Hz. The shading around the data points indicates statistical uncertainties, which are often smaller than the data points. Due to the finite resolution of the scans of 10 mG it is possible that narrower FRs are not resolved. The grey shading shows the magnetic field region studied in the main manuscript with the green shading indicating the comparatively broad inter-spin FR.

ment requires a high-resolution magnetic-field scan and our lattice-protection technique; see main text. Among the forest of FRs recorded in the two-component mixture, we observe a promising inter-spin FR at about 700 mG, which remains rather isolated from other homo-spin FRs; see green shading in Fig. S3.

In a second set of measurements, we focus on the magnetic-field region around 700 mG and perform high-resolution Feshbach spectroscopy, taking advantage of a lattice-preparation scheme, as described in the main text. The lattice-protection technique is very powerful in removing technical broadening and artificial asymmetry of the loss peaks, as clearly appears from a comparison between the atom-number traces recorded with ODT-preparation (Fig. S3) and lattice-preparation schemes (Fig. 3). We note that the observed atomic losses can be mainly attributed to resonant three-body recombination collisions in the short-range potential. Inelastic two-body losses driven by the spin-non-conserving dipolar interactions are, in principle, also energetically allowed since $|\uparrow\rangle$ atoms are in an excited Zeeman state [43]. However, we do not expect this process to be enhanced at resonance.

We perform the measurements for Fig. 3 as follows. We prepare a spin mixture in the lattice at high B as described above and sub-sequentially ramp the field to the desired value within 10 ms. After letting the B stabilize for about 100 ms, the dipole trap beams are ramped up within 10 ms and we unload the atoms from the lattice back into the ODT_{1064} within 150 ms. At this stage, the sample contains $N \approx 1.6 \times 10^4$ atoms at $T \approx 0.3\,T_\mathrm{F}$ and the trap frequencies are $(\nu_\perp, \nu_\parallel, \nu_z) = (111.6(2), 35(1), 169.4(6))$ Hz. We record the spin population after a holding time of 500 ms.

Modulation spectroscopy with a fermionic spin mixture in the lattice

To measure the scattering length between two spin states of ^{167}Er we rely on a method, which we have already successfully implemented with ^{168}Er [33] and ^{166}Er [9]. It is based on the measurement of the onsite energy of two atoms in a deep optical lattice. Here, after preparing a spin mixture of $|\downarrow\rangle$ and $|\uparrow\rangle$ in the lattice we drive particle-hole excitations of neighboring atoms in different spin states by a resonant modulation of the horizontal lattice depths $s_{x,y}$. Note that for neighboring identical particles no single-band excitation will be observed due to the Pauli exclusion principle. A convenient method to measure double occupancies uses the coupling to a third spin state. Close to a molecular state of the original doublon components, the third spin state features a smaller inter-spin onsite energy and can thus be used to detect an initial double occupancy [56]. As in our system this method remains to be explored we detect doublons via an increased atom loss once doublons are created. We speculate that onsite dipolar driven relaxation is responsible for the observed loss [40]. Typically, we modulate the lattice depth for 1 s with a peak-to-peak amplitude of 30%. Maximum loss occurs when the modulation frequency ν_mod reaches the resonance condition ν_res (see Fig. S4). ν_res is directly related to the onsite energy via $U_{\downarrow\uparrow} = h \times \nu_\mathrm{res}$. Following our previous work the onsite energy $U_{\downarrow\uparrow}$ consists out of two contributions: the contact interaction U_c

$$U_\mathrm{c} = \frac{4\pi\hbar a_{\downarrow\uparrow}}{m_\mathrm{Er}} \int d\mathbf{r}\, |\phi_i(\mathbf{r})|^4 ,$$

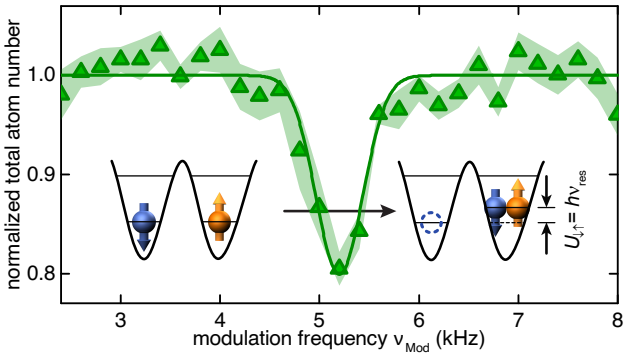

FIG. S4. Exemplary modulation spectroscopy measurement with a spin mixture of $|\downarrow\rangle$ and $|\uparrow\rangle$ in the deep lattice at $B = 650\,\mathrm{mG}$. The resonance condition determines ν_{res}, which is related to the onsite energy $U_{\downarrow\uparrow}$ (cartoon).

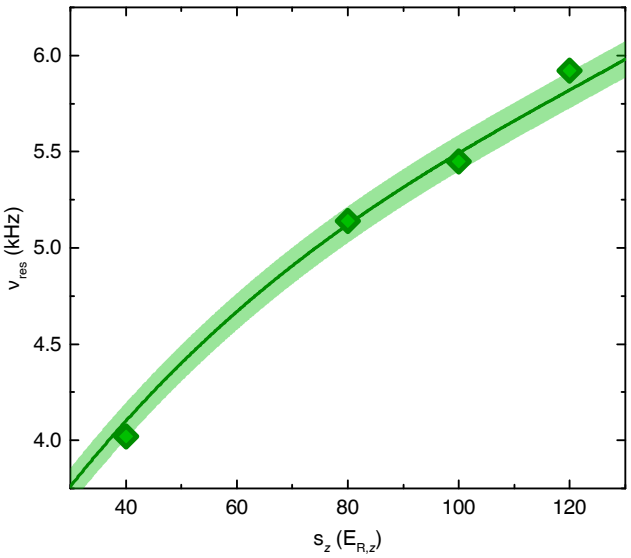

FIG. S5. Modulation resonance ν_{res} as a function of the vertical lattice power s_z for $s_{x,y} = 20$ at $B = 650\,\mathrm{mG}$. The solid line shows a fit with our theory to extract the scattering length $a_{\downarrow\uparrow}$. The shaded region accounts for the systematic uncertainty of the scattering length of $\pm 4\,a_0$ at 0.65 G, which results from our magnetic field fluctuations of $\pm 1\,\mathrm{mG}$.

and the DDI U_{dd}

$$U_{\mathrm{dd}} = \frac{\mu_0 \mu_\downarrow \mu_\uparrow}{4\pi} \int d\mathbf{r} \int d\mathbf{r}' \, |\phi_i(\mathbf{r})|^2 \, \frac{1 - 3\cos^2\theta_{\mathbf{r}-\mathbf{r}'}}{|\mathbf{r} - \mathbf{r}'|^3} \, |\phi_i(\mathbf{r}')|^2 \, .$$

Here, $\phi_i(\mathbf{r})$ denotes the Wannier function on site i, $|\mathbf{r} - \mathbf{r}'|$ is the interatomic distance and $\theta_{\mathbf{r}-\mathbf{r}'}$ corresponds to the angle between the polarization axis of the two dipoles with respect to their interparticle axis. The contact part depends on the inter-spin scattering length $a_{\downarrow\uparrow}$, the reduced Plank constant $\hbar$, and the mass m_{Er} of Er, while the DDI part is proportional to the vacuum permeability μ_0 and the magnetic moments of the two spin states $\mu_\downarrow$ and $\mu_\uparrow$. The contribution of nearest-neighbor interactions are minor and therefore neglected.

Both, the strength but also the sign of U_{dd} strongly depend on the dipole orientation and the aspect ratio (AR) of the onsite Wannier function. As specified in our earlier work [33] the AR is defined by the ratio of the onsite harmonic oscillator lengths $\mathrm{AR} = l_z/l_{x,y}$ with $l_i = d_i/(\pi s_i^{1/4})$ for $i \in \{x, y, z\}$. For our typical lattice parameters we find $\mathrm{AR} > 1$ and hence U_{dd} is negative (positive) for a dipole orientation out of (in) the xy-plane. In the experiment we can use this fact to determine the sign of the scattering length $a_{\downarrow\uparrow}$. First, we perform a modulation spectroscopy with a dipole orientation along z. The extracted resonance frequency deduces the energy gap $|U_{\downarrow\uparrow}|$ of the particle-hole excitation but does not give any information on the sign of the total onsite energy. We repeat the measurement at the same magnetic field with the dipoles oriented inside the xy-plane. The rotation of the dipoles leads to a more positive total onsite energy $U_{\downarrow\uparrow}$ and thus to a shift to larger (smaller) values of $|U_{\downarrow\uparrow}|$ corresponds to a positive (negative) sign of $U_{\downarrow\uparrow}$. With this method we determine the sign of the scattering length $a_{\downarrow\uparrow}$ for Fig. 4(a).

As a final test of our method we study the dependence of the onsite energy as a function of the lattice depth s_z (Fig. S5). Here, we fix the magnetic field, oriented along z, to 650 mG and vary the depth of the z lattice. We repeat the modulation spectroscopy for different values of s_z and extract ν_{res} for each measurement. A comparison to our theoretical model with $a_{\downarrow\uparrow}$ being the only free parameter reveals a nice agreement, confirming the validity of our modulation spectroscopy technique. Here, the fit gives a value for $a_{\downarrow\uparrow}$ of $225(2)\,a_0$.

The presented data in Fig. 4(a) for a given magnetic field B shows the mean of all experimental data sets, taken with different lattice parameters. Table 1 summarizes all experimental lattice parameters and the expected contribution of U_{c} (for $a_{\downarrow\uparrow} = 100\,a_0$) and U_{dd} from our theoretical model. From a given measurement of $U_{\downarrow\uparrow}$ the inter-spin scattering length can be evaluated by $a_{\downarrow\uparrow}/a_0 = (U_{\downarrow\uparrow} - U_{\mathrm{dd}}) \times 100/U_{\mathrm{c}}$.

Loss spectroscopy in the ODT at the inter-spin FR

For the measurements of the collisional properties of the fermionic spin mixture in the vicinity of the comparatively broad inter-spin FR (see Fig. 4(b-d)), we apply the following experimental procedure. We prepare a spin mixture with $\delta = 0$ in the deep 3D lattice and sweep to a magnetic field of $B = 3.99\,\mathrm{G}$. We then jump with the magnetic field to the final value and let it stabilize for 10 ms. We ramp up the ODT_{1064} beams in 10 ms and melt the lattice in 20 ms as to avoid losses to happen already during the ramp-down procedure. The final trap frequencies are $(\nu_\perp, \nu_\parallel, \nu_z) =$

(s_x, s_y, s_z)	AR	U_c/h (Hz)	U_{dd}/h (Hz)
$(20, 20, 40)$	1.68	2029	-441
$(20, 20, 60)$	1.52	2263	-396
$(20, 20, 80)$	1.41	2443	-350
$(20, 20, 100)$	1.34	2590	-307
$(20, 20, 120)$	1.28	2717	-265
$(15, 15, 80)$	1.32	2068	-223
$(22, 22, 80)$	1.45	2578	-399

TABLE I. Lattice parameters for the determination of $a_{\downarrow\uparrow}$ (Fig. 4(a)). The lattice depths (s_x, s_y, s_z) define the onsite Wannier function AR. From our theoretical model we evaluate the onsite energy contributions U_c and U_{dd} for an inter-spin scattering length of $a_{\downarrow\uparrow} = 100\,a_0$. Here, the dipoles are oriented along z. This values are used to extract the inter-spin scattering length from the measured total onsite energy $U_{\downarrow\uparrow}$.

$(111.6(2), 35(1), 169.4(6))$ Hz. For this trap we typically record $E_F \approx k_B \times 150\,\mathrm{nK}$ corresponding to a Fermi wave vector $k_F \approx \sqrt{2m_{Er}E_F}/\hbar = 1 \times 10^7\,\mathrm{m}^{-1}$. We then store the two-component mixture in the ODT_{1064} for a variable holding time and finally record the spin populations with Stern-Gerlach imaging.

We record the atom decay for various magnetic fields B across the FR. For each B, we extract an initial decay rate $\dot{N}/N_0$ by fitting a linear-decay function to the data, normalized to the initial atom number N_0. As fitting range, we include all data for which the atom number stays above a threshold of 75% of N_0. We checked that the extracted values of $\dot{N}/N_0$ do not change significantly when varying the threshold between $65-85\%$. An analysis of the full data using exponential fits also yields similar results.

Chapter 6

Conclusion and outlook

6.1. Conclusion

This thesis is dedicated to the study of dipolar phenomena in the cold and ultracold regime. It reports on effects of the long range and anisotropic dipole-dipole interaction (DDI) on the few- and many-body behavior of an atomic sample. To this aim, we have utilized erbium atoms, which combine the possibility for efficient laser cooling and trapping with a strongly magnetic character. Our success of bringing not only bosonic but also fermionic erbium atoms into the quantum degenerate regime has set the foundation for the observation of dipolar phenomena with different governing quantum statistics. Our studies have also faced the orbital anisotropy of erbium, an important feature of magnetic lanthanides. With the implementation of a three-dimensional optical lattice, we have transformed the experimental apparatus into a quantum simulator of condensed matter systems with long-range interactions. Being one among only a few dipolar experiments around the world has allowed us to constantly break fresh experimental grounds. Our efforts have rewarded us with the attainment of fascinating physical systems, such as dipolar Feshbach molecules, extended Hubbard models, or strongly interacting dipolar Fermi gases, and enabled observations of intriguing physical phenomena, such as universal and anisotropic elastic few-body scattering, chaotic inelastic scattering, or the altering of the quantum many-body phase transition from the superfluid to the insulating phase by the DDI.

In order to explore unknown territories, we have constantly upgraded the experimental apparatus as to enrich the possible research directions. A particular interesting prospect for our experiment is given by our recent successful preparation of extended Fermi Hubbard models with spin-mixtures of dipolar fermions, see Sec. 5.6. In the following section we will briefly discuss possible experiments along this lines that are on the way or that can be undertaken with our system.

6.2. Future investigations along the extended Fermi Hubbard model

Within the course of this thesis, we have successfully prepared deeply degenerate Fermi gases of ^{167}Er and have adiabatically transferred them into the lowest band of a three-dimensional optical lattice. A major advantage of our fermionic system arises from quantum statistics. For a spin-polarized gas, double occupancies on a single lattice site are forbidden, resulting in a single-component band insulator with high filling fraction and long lifetime. This clean preparation method together with the long-range dipolar character of the particles provides a very clean test bed for the study of quantum phenomena that are solely driven by offsite interactions. In addition, we can deterministically prepare individual spin states of ^{167}Er, which features the unprecedented large number of 20 spin states in the lowest hyperfine manifold, see Sec. 2.2.4. Our system gives exciting prospects for the studies of transport dynamics, lattice spin models, or resonant demagnetization dynamics as we will briefly discuss below.

Transport phenomena with spin-polarized dipolar fermions

In solid state systems, transport properties are closely linked to the underlying physical phenomena, such as high-temperature superconductivity, topological insulators, or disorder phenomena. Well-controlled ultracold atomic systems in optical lattices can serve as quantum simulators to investigate such phenomena via the study of transport dynamics. For the case of long-range interactions, the transport properties of the many-body state can be markedly influenced by the nearest-neighbor interaction (NNI) among particles. Such a system can be conveniently prepared with spin-polarized dipolar fermions in a deep optical lattice. The formed band insulator with high filling fraction gives ideal starting conditions for the study of transport properties via expansion measurements, see e. g. Ref. [Sch12b]. In order to expand, the atomic sample needs to locally break bonds of NNI between particles. This process is suppressed by simple energy arguments and hence the system is expected to show reduced expansion dynamics [San17]. As a result, a so-called *clustered state* is formed where neighboring particles tend to stick together. Interestingly, the reduction of expansion is expected to depend on the strength of the NNI, which in the case of dipolar interactions can be conveniently controlled via the angle of the dipoles with respect to the interparticle axis, see Eq. 3.2.

Extended spinor Fermi-Hubbard models

While already spin-polarized gases give exciting prospects for studies of peculiar quantum effects, the story can become even more intriguing when the spin degree of freedom is added to the system. Indeed, the availability of higher spin states allows to access lattice spin models, as represented by the extended spinor Fermi-Hubbard model.

For the Hamiltonian of Eq. 5.18 we have included all terms that conserve the total magneti-

zation, i. e. where $F^z_{\text{tot}} = \sum_i S^z_i = \text{const}$. In reality, the Hamiltonian can also feature terms that do not conserve F^z_{tot}, i. e. that lead to a demagnetization of the collective spin state. The offsite part of the Hamiltonian of this system reads as [Aue94, Zhu17]

$$H_{\text{offsite}} = H_{\text{cons}} + H_{\text{non-cons}} \tag{6.1}$$

where H_{cons} and $H_{\text{non-cons}}$ include the spin-conserving and spin-non-conserving terms, respectively. The effects of this terms will be discussed in the following. For the sake of simplicity, we will restrict the discussion to a one-dimensional systems, i. e. to a lattice chain of dipoles.

Spin conserving terms

The spin conserving offsite interaction terms read as

$$H_{\text{cons}} = \sum_{i<j,\sigma} V_0^{ij}(1 - 3\cos^2\theta_{\mathbf{r}-\mathbf{r}'}) \left[F^z_{\sigma_i} F^z_{\sigma_j} - \frac{1}{4}(F^+_{\sigma_i} F^-_{\sigma_j} + F^-_{\sigma_i} F^+_{\sigma_j}) \right] \tag{6.2}$$

with the general dipolar coupling strength

$$V_0^{ij} = \int d\mathbf{r} \int d\mathbf{r}' w_i^*(\mathbf{r}) w_j^*(\mathbf{r}') \left(\frac{\mu_0 (g_F \mu_B)^2}{4\pi} \frac{1}{|\mathbf{r} - \mathbf{r}'|^3} \right) w_i(\mathbf{r}) w_j(\mathbf{r}'). \tag{6.3}$$

As already discussed in Sec. 5.2.3, $F^z_{\sigma_i} F^z_{\sigma_j}$ represents the NNI while the term $F^+_{\sigma_i} F^-_{\sigma_j}$ gives rise to spin-conserving flip-flop dynamics among neighboring particles. This Hamiltonian has been studied in pioneering works by the groups of Jun Ye in Boulder and Bruno Laburthe-Tolra in Paris by exploring off-site driven spin exchange with spin-$^1/_2$ KRb molecules [Yan13] and with spin-3 bosonic chromium atoms [dP13b, Lep18]. With our experiment we have now reached the point where we can investigate such exotic spin models in the context of an unrivaled large spin-$^{19}/_2$ system.

The dynamics are expected to depend on various parameters. First of all, for a flip-flop process to take place, energy has to be conserved. Hence, the dynamics will strongly depend on the energy difference between adjacent spin states. In our system, this differential energy can conveniently be controlled via spin-dependent quadratic Zeeman and quadratic light shifts, see Sec. 5.2.3. With this tool at hand, we can switch on and off flip-flop dynamics at will. Further, the deterministic preparation of pure spin states will allow us to investigate in detail the spin-dynamics time scales for different initial spin states. Depending on the spin number, slower or faster time scales are expected, as follows from Eq. 5.17. Finally, the time scales are expected to be controllable via the dipole orientation $\theta_{\mathbf{r}-\mathbf{r}'}$. For dipoles aligned along to the lattice chain, $\theta_{\mathbf{r}-\mathbf{r}'} = 0°$, the dynamics should be twice as fast compared to a perpendicular orientation, $\theta_{\mathbf{r}-\mathbf{r}'} = 90°$, and spin-exchange should be absent at the magic angle $\theta_{\mathbf{r}-\mathbf{r}'} = 54.74°$.

Spin non-conserving terms

The spin non-conserving offsite interaction terms read as

$$H_{\mathrm{non-cons}} = -\sum_{i<j,\sigma} V_0^{ij}\Bigg(\frac{3}{4}\sin^2\theta_{\mathbf{r}-\mathbf{r}'}\left[e^{-2i\phi}F_{\sigma_i}^{+}F_{\sigma_j}^{+}+h.c.\right] + \frac{3}{4}\sin 2\theta_{\mathbf{r}-\mathbf{r}'}\left[e^{-i\phi}(F_{\sigma_i}^{z}F_{\sigma_j}^{+}+F_{\sigma_i}^{+}F_{\sigma_j}^{z})+h.c.\right]\Bigg). \tag{6.4}$$

Here, $\theta_{\mathbf{r}-\mathbf{r}'}$ and ϕ denote the polar and azimuthal angles, respectively, and V_0^{ij} is the general dipolar coupling strength, see Eq. 6.3. The first term of the Hamiltonian changes the magnetization of two atoms by ± 2 and the terms of the second line result in a change by ± 1. Magnetization changing terms are of particular interest as they allow to couple the spin and the orbital degree of freedom, assosciated to the famous Einstein-de-Haas effect, see e. g. Ref. [Lah09] for a review. In the case of lattice-confined particles, spin-orbit coupling can lead to excitations to higher lattice bands as beautifully demonstrated with onsite interacting $|S=3, m_s=3\rangle$ bosonic chromium atoms [dP13a]. However, offsite-driven spin demagnetization remains to be observed.

An offsite-driven demagnetization can occur when a resonant state is accessible. This scenario can emerge when the change of the NNI energy ($F_{\sigma_i}^{z}F_{\sigma_j}^{z}$), resulting from the spin flip, matches the respective Zeeman splitting. In our system this process requires very low magnetic field values well below 1 mG. The preparation of such a low magnetic field amplitude demands a very precise magnetic field control. In our experiment we have already successfully implemented an active magnetic field stabilization, see Appendix C. However, to reach the necessary magnetic field stability, further improvements have to be employed.

Interestingly, the strength of the terms in Eq. 6.4 show a peculiar angle dependence. In particular, the sign of the terms can be changed by adjusting the dipole orientation and for a parallel dipole orientation, i. e. $\theta_{\mathbf{r}-\mathbf{r}'} = 0°$, the demagnetization terms would vanish.

Appendix

A

Additional publications

A.1. Publication: Quantum-Fluctuation-Driven Crossover from a Dilute Bose-Einstein Condensate to a Macrodroplet in a Dipolar Quantum Fluid[†]

Phys. Rev. X **6**, 041039 (2016)
submitted 22 Jul 2016; published 22 Nov 2016
DOI 10.1103/PhysRevX.6.041039

Lauriane Chomaz,[1,2] Simon Baier,[1] Daniel Petter,[1] Manfred J. Mark,[1,2] Falk Wächtler,[3] Luis Santos,[3] F. Ferlaino[1,2]

[1] *Institut für Experimentalphysik, Universität Innsbruck, Technikerstraße 25, 6020 Innsbruck, Austria*
[2] *Institut für Quantenoptik und Quanteninformation, Österreichische Akademie der Wissenschaften, 6020 Innsbruck, Austria*
[3] *Institut für Theoretische Physik, Leibniz Universität Hannover, Appelstrasse 2, 30167 Hannover, Germany*

[†] The author of the present thesis developed the experimental procedures together with L. C., and D. P., performed the measurements and analyzed the data together with L. C., and D. P., and contributed in writing the manuscript. The theoretical calculations of this publication have been contributed by F. W., and L. S.

Quantum-Fluctuation-Driven Crossover from a Dilute Bose-Einstein Condensate to a Macrodroplet in a Dipolar Quantum Fluid

L. Chomaz,[1] S. Baier,[1] D. Petter,[1] M. J. Mark,[1,2] F. Wächtler,[3] L. Santos,[3] and F. Ferlaino[1,2,*]

[1]*Institut für Experimentalphysik, Universität Innsbruck, Technikerstraße 25, 6020 Innsbruck, Austria*

[2]*Institut für Quantenoptik und Quanteninformation, Österreichische Akademie der Wissenschaften, 6020 Innsbruck, Austria*

[3]*Institut für Theoretische Physik, Leibniz Universität Hannover, Appelstrasse 2, 30167 Hannover, Germany*

(Received 22 July 2016; revised manuscript received 15 September 2016; published 22 November 2016)

In a joint experimental and theoretical effort, we report on the formation of a macrodroplet state in an ultracold bosonic gas of erbium atoms with strong dipolar interactions. By precise tuning of the s-wave scattering length below the so-called dipolar length, we observe a smooth crossover of the ground state from a dilute Bose-Einstein condensate to a dense macrodroplet state of more than 2×10^4 atoms. Based on the study of collective excitations and loss features, we prove that quantum fluctuations stabilize the ultracold gas far beyond the instability threshold imposed by mean-field interactions. Finally, we perform expansion measurements, showing that although self-bound solutions are prevented by losses, the interplay between quantum stabilization and losses results in a minimal time-of-flight expansion velocity at a finite scattering length.

DOI: 10.1103/PhysRevX.6.041039

Subject Areas: Atomic and Molecular Physics, Quantum Physics

I. INTRODUCTION

The extraordinary success of ultracold quantum gases largely stems from the simplicity with which the physics at the many-body level can be controlled and described, allowing access to a wide range of theoretical models of general interest [1]. Notably, the actual many-body interactions are often very well captured via simple mean-field (MF) potentials, proportional to the local particle density n and accounting for the average mutual effect of all neighboring particles [1]. Moreover, short-ranged interactions, even if complex or unknown, can be simply accounted for via a contact potential and parametrized by the sole s-wave scattering length a_s, which in turn can be widely tuned by means of Feshbach resonances (FRs) [2]. The MF treatment of a Bose gas leads to the celebrated Gross-Pitaevskii equation (GPE) and Bogoliubov–de Gennes (BdG) spectrum of collective modes, which are very powerful in describing the physics of an ultracold bosonic gas: its ground-state properties as a Bose-Einstein condensate (BEC), as well as its dynamics [1].

Beyond the great achievements of dilute gases as a test bed for MF theories, the quest for beyond-MF effects has triggered great interest in the ultracold community. The general question of how the many-body ground state of bosons is modified by quantum fluctuations (QFs) of elementary excitations was first addressed by Lee, Huang, and Yang (LHY) in the 1950s [3]. The so-called LHY term, which accounts for the first-order correction to the condensate energy, scales for a contact-interacting gas as $a_s n\sqrt{n a_s^3}$. While in the weakly interacting regime the effect of QFs is negligible and difficult to isolate from MF contributions, it can be sufficiently amplified by increasing a_s via a FR. Based on this concept, recent experiments with alkali have observed clear shifts of the BdG spectrum and equation of state caused by the LHY term in strongly interacting Fermi [4–6] and Bose gases [7,8].

While in these measurements the LHY correction does not modify the qualitative behavior of the gas, it has been recently pointed out [9] that, in systems with competing interactions of different origin, the MF interaction can be made small and the LHY term dominant, so that the latter dictates the physics of the system, even in weakly interacting gases. In this regime, a novel phase of matter is expected to appear, namely, a liquidlike droplet state. For purely contact-interacting gases, this situation is hard to realize since it would require, for instance, Bose-Bose mixtures with coincidental overlapping FRs [9]. In contrast, dipole-dipole interaction (DDI) genuinely offers this possibility in a single-component atomic gas by competing with the isotropic MF contact interaction [10,11]. In the pure MF picture, a paradigm of the competition between DDI and contact interaction is embodied by the ability of quenching a dipolar BEC to collapse by varying $\varepsilon_{\mathrm{dd}} = a_{\mathrm{dd}}/a_s$, where

*Francesca.Ferlaino@uibk.ac.at

$a_{dd} = \mu_0\mu^2 m/12\pi\hbar^2$ is a characteristic length set by the DDI, with m the mass and μ the magnetic moment of the atoms [12,13]. Here, $\hbar$ stands for the reduced Planck constant and μ_0 for the vacuum permeability. In general, because of the special geometrical tunability of DDI with the external trapping potential and dipole orientation, the stability and phase diagram remarkably depend on $\lambda = \nu_\parallel/\nu_\perp$, where $\nu_\parallel$ ($\nu_\perp$) is the trapping frequency along (perpendicular to) the dipole orientation [11,12,14].

In parallel, recent breakthrough experiments with an oblate dysprosium (Dy) dipolar BEC ($\lambda > 1$) have shown that when quenching up ε_{dd}, the system, instead of collapsing, forms a metastable state of several small droplets [15,16]. This observation has triggered an intense debate on the nature of such a state and its underlying stabilization mechanism [17–23]. Eventually, Dy experiments indicated QFs as the origin of the stabilization [16], which were quickly confirmed by theoretical works [20–22]. Furthermore, these theoretical studies highlight the richness of the dipolar-gas phase diagram, in which a dilute-BEC, a multidroplet, and a single-droplet phase are found for distinct a_s, a_{dd}, atom number N, and λ. Up to now, droplet physics has only been investigated in a single setup, using Dy BEC and exploring a specific region of the phase diagram: In the considered pancake geometry ($\lambda > 1$), multiple stable solutions—single droplet or multidroplet—coexist, resulting in the formation of variable mesoscopic assemblies of a small droplet in the experiments.

In the present work, we (i) demonstrate the generality of droplet physics, by using a dipolar BEC of erbium (Er) atoms [24], (ii) quantitatively investigate the specific role played by QFs in dipolar systems, and (iii) explore a pristine region of the phase diagram, studying a cigar-shaped geometry ($\lambda \ll 1$), and observe the crossover from a dilute BEC to a single macrodroplet state when increasing ε_{dd}, as predicted in Refs. [21,22]. Given the complexity of the physics at play, we combine distinct measurements, based on the observations of the density distributions, collectives excitations, expansion dynamics, and lifetime of the dipolar quantum gas, which together offer a comprehensive picture of droplet physics. The exquisite control of the scattering length gained in our experiment, together with a direct comparison to parameter-free simulations including QF effects, ultimately enable us to depict in which way QFs dictate the physics at play, beyond proving their crucial stabilizing role.

II. EXPERIMENTAL PROCEDURES

The atomic properties of Er offer a privileged platform to explore a variety of interaction scenarios. Besides its strongly magnetic character and its many FRs [25], Er has several stable isotopes. This feature adds an important flexibility in terms of the choice of the background a_s [26]. In our early work on Er BECs, we employed the ^{168}Er isotope, which has a background a_s about twice as large as the dipolar length, $a_{dd} = 65a_0$ [27,28].

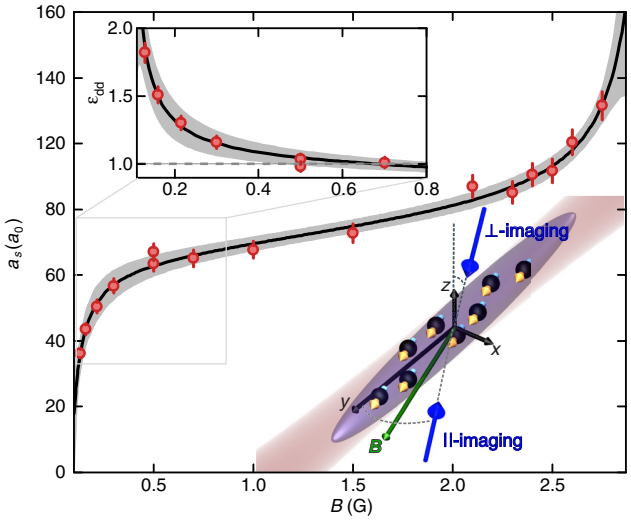

FIG. 1. Scattering length in ^{166}Er. a_s as a function of B. The data points (circles) are extracted from spectroscopic measurements in a lattice-confined gas and the solid line is a fit to the data with its statistical uncertainty (gray shaded region [30]). Upper inset: Zoom-in of ε_{dd} as a function of B. The gray dashed line marks $\varepsilon_{dd} = 1$; see also the other figures. The lower inset illustrates the geometry of our experimental setup, the relevant axes (x, y, z), the optical-dipole-trap beam (shaded region), the magnetic field orientation (green arrow) along which the dipoles are aligned, and the ∥- and ⊥-imaging view axes (blue arrows). The dashed lines picture the small angles of these axes to y and z [30].

In the work reported here, we produce and use a BEC of ^{166}Er in the lowest internal state. This isotope provides us with two major advantages. First, its background a_s is comparable to its dipolar length, $a_{dd} = 65.5a_0$, realizing $\varepsilon_{dd} = a_{dd}/a_s \approx 1$ without the need of Feshbach tuning. Second, ^{166}Er features a very convenient FR at ultralow magnetic-field values B. To precisely map a_s as a function of B, we use a spectroscopic technique based on the measurement of the energy gap of the Mott insulator state in a deep three-dimensional optical lattice [28,29]. A detailed description is given in the Supplemental Material [30]. Between 0 and 3 G, we observe a smooth variation of a_s, which results from two low-lying FRs whose centers are fitted to 0.05(5) and 3.0(1) G, respectively; see Fig. 1. This feature gives easy access into the $\varepsilon_{dd} > 1$ regime, allowing variation of ε_{dd} from 0.70(2) to 1.58(18) by changing B from 2.5 to 0.15 G; see Fig. 1 upper inset. By fitting our data [2], we extract $a_s(B)$ valid for B in the [0.15, 2.5]-G range, which we use throughout this paper [30].

We achieve Bose-Einstein condensation of ^{166}Er using an all-optical scheme very similar to Ref. [27] with cooling parameters optimized for ^{166}Er [30]. In short, we drive forced evaporative cooling at a magnetic field $B = 1.9$ G, corresponding to $a_s = 81(2)a_0$ [$\varepsilon_{dd} = 0.81(2)$]. In this phase, B is oriented along the vertical z axis. At the end of the evaporation, we obtain a BEC of $N = 1.2 \times 10^5$ atoms with a condensed fraction above 80%.

To reach the $\lambda \ll 1$ regime, we slowly modify, in the last step of the evaporation, the confining potential to the final cigar shape, with typical frequencies $(\nu_x, \nu_y, \nu_z) = [156(1), 17.2(4), 198(2)]$ Hz. Simultaneously, we decrease B to 0.8 G [$a_s = 67(2)a_0$] and then change the magnetic-field orientation to the weak trapping axis (y) while keeping its amplitude constant [30]. Finally, we ramp B to the desired target value (and equivalently a_s) in t_r [30], hold for a time t_h, and perform absorption imaging of our gas after a time-of-flight (TOF) of t_{TOF}. Two imaging setups are used in order to measure the density distribution integrated either along the dipoles (∥ imaging) or perpendicular to them (⊥ imaging) [30]. Figure 1 (lower inset) illustrates the final geometry of our system with $\nu_\parallel = \nu_y$, $\nu_\perp = \sqrt{(\nu_x^2 + \nu_z^2)/2}$, giving $\lambda = 0.097(3)$, and defines the relevant axes.

Here, we explore the properties of the system when the repulsive MF contact interaction is weakened enough to be overcome by the DDI ($\lambda \ll 1$, $\varepsilon_{\mathrm{dd}} > 1$), after adiabatically changing ($t_r \geq 45$ ms) or quenching ($t_r = 10$ ms) a_s to its target value [30]. For $t_r \geq 45$ ms, the system evolves following its ground state and gives access to the slow dynamics, whereas for the $t_r = 10$ ms case, we can probe the fast dynamics and study the relaxation towards an equilibrium. The key question is whether QFs protect the system from collapsing. Indeed, in this regime, the MF treatment would imply that the attractive BEC becomes unstable, leading to a twofold dramatic consequence [1]. First, some modes of the BdG spectrum acquire complex frequencies. Second, in a trap, the density distribution of the cloud undergoes a marked change on short time scales ($\lesssim 1/\nu_\perp$), described as a "collapse", which can develop into a rapid loss of coherence [12,31], and pattern formations, such as anisotropic atom bursts ("bosenova") and special d-wave-type structures, as observed in rubidium [32] and dipolar gases of chromium [12,13], respectively. This fast dynamics has been proved to be well encompassed by GPE simulation [13,14,33].

III. DENSITY DISTRIBUTION

In a first set of experiments, we study the stability of our dipolar Er BEC by probing the evolution of the TOF density distribution for different a_s. Figures 2(a)–2(c) show the absorption images acquired with ∥ imaging [Figs. 2(a)–2(c)] and the corresponding central cuts ($x = 0$) of the 2D column density profiles [Fig. 2(d)]. In striking contrast to the MF predictions, we observe that the system remains stable for a_s well below a_{dd}, with a central coherent core surviving for times much longer than $1/\nu_\perp$ (from several tens to hundreds of ms). The density distribution does not exhibit any special patterns, which is typical of a collapsing cloud [12,13,32].

For $a_s > a_{\mathrm{dd}}$ [Fig. 2(a)], the density distribution of the gas shows good agreement with the MF Thomas-Fermi (TF) profile on top of a broad Gaussian distribution,

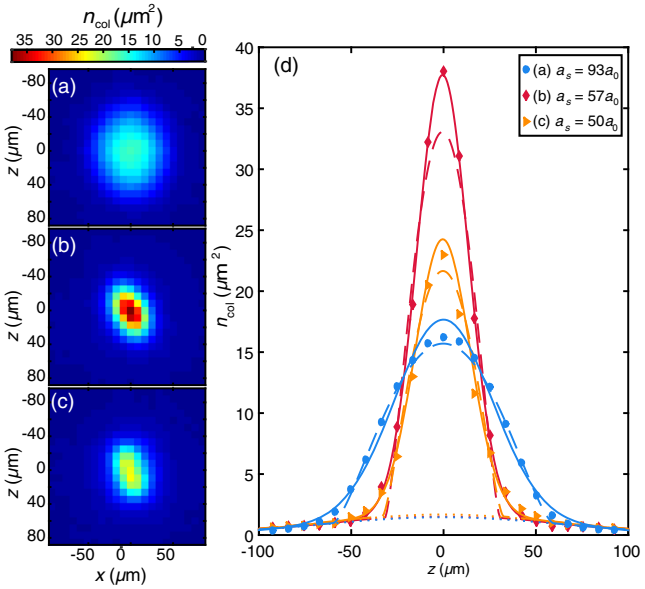

FIG. 2. Density profiles in the BEC-to-droplet crossover. (a)–(c) 2D column density distributions probed with ∥ imaging and (d) corresponding central cuts along the $x = 0$ line (dots) for $t_r = 10$ ms, $t_h = 6$ ms ($> 1/\nu_\perp$), and different a_s (see legend). Each distribution is obtained by averaging four absorption images taken after $t_{\mathrm{TOF}} = 27$ ms. In (d), the lines show the central cuts of the 2D bimodal fit results, the solid (dashed) lines showing the two-Gaussian (MF-TF plus Gaussian) distributions and the dotted lines the corresponding broad thermal Gaussian part.

accounting for the thermal atoms; see Fig. 2(d), dashed lines. When lowering a_s below a_{dd} [Fig. 2(b)], we observe a sharpening of the central core, whose profile starts to deviate from the MF-TF shape (see Ref. [30] for a quantitative description). When decreasing a_s even further [Fig. 2(c)], a similar bimodal structure holds on although the dense core loses atoms. Because of the high density reached, three-body (3B) collisions regulate the lifetime of the central core; see discussion below and Ref. [23]. We note that we observe a similar qualitative behavior of the density distribution when using an adiabatic ramp of a_s. However, the importance of the central peak is reduced as, in this case, losses already set in during the ramp.

In contrast with the behavior of the central core, the distribution of the thermal atoms, encompassed by the broad Gaussian function of the bimodal fits [see Fig. 2(d), dotted lines], remains mainly unaffected by the change of a_s, highlighting an absence of significant heating and population transfer, and thus an apparent decoupling of the evolution of the coherent and thermal parts.

For further analysis, we fit the data to a bimodal distribution made of the sum of two Gaussian functions, as it offers a smaller residue than the fit to the MF-TF distribution for $a_s \lesssim 70a_0$; see Fig. 2(d). We note that the beyond-MF effects on the density profile are expected to be more sophisticated than a Gaussian shaping. However,

theoretical studies show good agreement between the Gaussian ansatz and the full numerical solution for our parameter range [22,23].

Being a smoking gun for long-range phase coherence, the survival of a bimodal profile in the TOF distribution far beyond the MF instability threshold points to a persistent coherent behavior. This absence of a collapse advocates the outbreak of an additional stabilization mechanism, which we now further investigate by probing global properties of the gas.

IV. COLLECTIVE OSCILLATION

In a second set of experiments, we unveil the origin of the stabilization mechanism by studying the elementary excitations of the coherent cloud. This is a very powerful probe of the fundamental properties in quantum degenerate gases [1,34]. In particular, collapse is intimately related to the softening of some collective modes at the MF-instability threshold. We focus here on the axial mode, which is the lowest-lying excitation in the system above the dipole mode. It corresponds to a collective oscillation of the condensate length along y ($R_\parallel$) with frequency ν_{axial}. The axial oscillation comes along with a smaller-amplitude oscillation of the radial sizes in phase opposition; see Fig. 3(a). As a result, this mode has a mixed character between a compression and a surface mode [1]. The compression character is particularly relevant since it involves a change in the density and it is therefore sensitive to the LHY corrections [35].

We excite the axial mode either by ramping B during the final preparation stage or by transiently increasing the power of the vertical optical dipole trap beam, after ramping B to B_f. Here, $\nu_\parallel$ is abruptly changed from 17 Hz to typically 21 Hz, kept at this higher value for 8 ms, and finally set back to 17 Hz. Following the excitation, we let the cloud evolve for a variable t_h and image its TOF density distribution with $\perp$ imaging. To extract ν_{axial}, we probe the axial width $R_\parallel$ of the central coherent component of the gas [30] with t_h and fit it to a damped sine; see inset of Fig. 3(b).

Figure 3 shows the observed ν_{axial} normalized to the trapping frequency $\nu_\parallel$ [36] as a function of a_s for adiabatic [Fig. 3(b)] and nonadiabatic [Fig. 3(c)] ramps. Both cases exhibit a similar qualitative behavior. For $a_s > a_{\mathrm{dd}}$, the oscillations show a smooth dependence on $\varepsilon_{\mathrm{dd}}$, with ν_{axial} increasing by about 5% with an average value of $1.70\nu_\parallel$ [37]. When lowering a_s, the oscillation of the coherent part remains visible well below the $\varepsilon_{\mathrm{dd}} = 1$ threshold and ν_{axial} exhibits a marked increase. $\nu_{\mathrm{axial}}/\nu_\parallel$ grows up to 2.6(1) at $a_s = 54a_0$ for $t_r = 100$ ms [Fig. 3(b)]. For $t_r = 10$ ms [Fig. 3(c)], $\nu_{\mathrm{axial}}/\nu_\parallel$ first increases similarly to the adiabatic case [Fig. 3(b)], reaches a maximum of $\sim 2.13(7)$ at $57a_0$ ($\varepsilon_{\mathrm{dd}} = 1.15$), and finally decreases for even smaller a_s (open squares). The latter behavior can be explained by the fact that the larger quenches in the interaction excites additional high-energy modes while it drives the system away from the linear response regime [38]. A similar behavior is found from our theory predictions including the LHY term (see below), thus highlighting a qualitative agreement even in this small-a_s range.

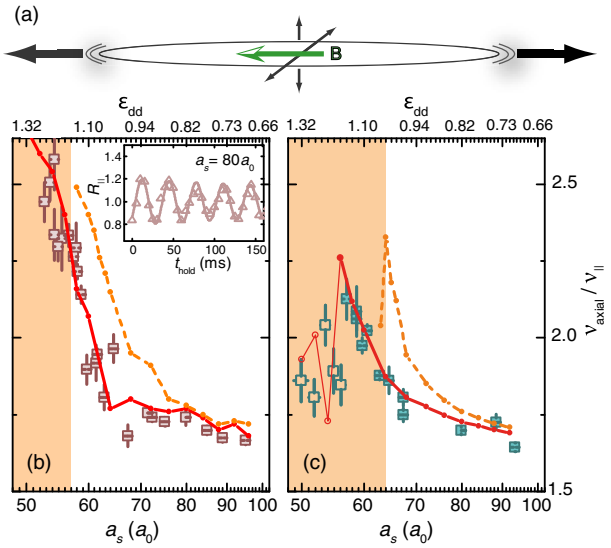

FIG. 3. Axial mode. (a) Illustration of the axial mode in our experimental setup. The black arrows sketch the oscillations of the widths of the coherent gas along the characteristic axes of the trap, with weights indicating their relative amplitudes. (b), (c) Measured $\nu_{\mathrm{axial}}/\nu_\parallel$ (squares) as a function of a_s together with the theoretical predictions, including (solid line) or not (dashed lines) the LHY term for $t_r = 100$ ms (b) and $t_r = 10$ ms (c). Theoretical predictions are obtained from RTE (see text) for a_s varied from $50a_0$ to $95a_0$. In the MF case, predictions fail for $a_s \leq a_c$ (orange area) due to the occurrence of the collapsing dynamics which rules out the collective excitation picture. $a_c = 57a_0$ [$a_c = 64a_0$] in (b) [(c)]. In (c), ν_{axial} cannot be reliably extracted for quenches to $a_s \leq 56a_0$, nor from the experiment (open squares) or from the LHY theory (open circles, thin line). The inset in (b) exemplifies a measurement of $R_\parallel$ (triangles) and its fit to a damped sine (solid line) for $a_s = 80a_0$. We typically fit 4–5 oscillations for all our a_s.

V. THEORY

To account for our observation and discern between the MF instability picture and QF mechanisms, we develop a beyond-MF treatment of our system at $T = 0$. The coherent gas is described here by means of the generalized nonlocal nonlinear-Schrödinger equation (gNLNLSE), which includes the first-order correction from QF effects, i.e., the LHY term, and 3B loss processes. The gNLNLSE reads as [20,23]

$$i\hbar\frac{\partial\psi}{\partial t} = \left[\hat{H}_0 + \mu_{\mathrm{MF}}(n,\epsilon_{dd}) + \Delta\mu(n,\epsilon_{dd}) - i\hbar\frac{L_3}{2}n^2\right]\psi, \tag{1}$$

where $\hat{H}_0 = [(-\hbar^2\Delta)/2m] + V(\boldsymbol{r})$ is the noninteracting Hamiltonian and $V(\boldsymbol{r}) = 2\pi^2 m \sum_{\eta=x,y,z} \nu_\eta^2 \eta^2$ the harmonic confinement. The MF chemical potential, $\mu_{\mathrm{MF}}[n(\mathbf{r}), \epsilon_{dd}] = gn(\mathbf{r}) + \int d^3r' V_{\mathrm{dd}}(\mathbf{r}-\mathbf{r}')n(\mathbf{r}')$, results from the competition between short-range interactions, controlled by the coupling constant $g = 4\pi\hbar^2 a_s/m$, and the DDI term with $V_{\mathrm{dd}}(\mathbf{r}) = [(\mu_0\mu^2)/4\pi r^3](1-3\cos^2\theta)$ and θ the angle sustained by $\mathbf{r}$ and the dipole moment μ. Here, $n(\mathbf{r}) = |\psi(\mathbf{r})|^2$. The beyond-MF physics is encoded in the LHY term, leading to an additional repulsive term in the chemical potential, $\Delta\mu(n, \epsilon_{dd}) = [32/(3\sqrt{\pi})]gn\sqrt{na^3}F(\epsilon_{dd})$. The function $F(\epsilon_{dd}) = \frac{1}{2}\int d\theta_k \sin\theta_k [1 + \epsilon_{dd}(3\cos^2\theta_k - 1)]^{5/2}$ is obtained from the LHY correction in homogeneous 3D dipolar BECs [39–41] using local-density approximation [42]. The last non-Hermitian term in Eq. (1) accounts for 3B loss processes [43]. In our calculations, we use the experimentally determined values of the 3B recombination rate of the condensate $L_3(a_s)$ [30].

As discussed in Refs. [22,23], due to the repulsive LHY term, Eq. (1) sustains stable ground-state solutions for any a_s and λ. For pancake traps ($\lambda > 1$), the solution of Eq. (1) is not unique. The phase diagram reveals three types of solutions: the one of a dilute BEC, a single droplet solution, and a third one, which separates the previous two phases, that corresponds to a metastable region of multidroplet states. The latter has been observed in Dy experiments [15]. However, the single-droplet solution appears difficult to access because of the overhead multidroplet state and the stringent 3B loss mechanisms. Remarkably, in cigar-shaped traps ($\lambda < 1$), Eq. (1) has only one possible solution. In the $\varepsilon_{\mathrm{dd}}$ parameter space, the corresponding wave function exhibits a smooth crossover from a dilute BEC to a single, high-density, macrodroplet solution for increasing $\varepsilon_{\mathrm{dd}}$. It is worth noting that the crossover physics, e.g., the formation and lifetime of the droplet state, is expected to crucially depend on the 3B collisional processes. In the following, we concentrate on the $\lambda < 1$ case, which corresponds to our experimental setting.

The continuous and smooth change of the static properties of the system with increasing $\varepsilon_{\mathrm{dd}}$ is consistent with our observations on the evolution from a dilute into an high-density state; see Fig. 2.

Based on Eq. (1), we theoretically investigate the dynamics of the coherent gas. In order to compare as close as possible the theory to our experimental results, we precisely account for the experimental sequence by performing real-time evolution (RTE) starting from the ground state of Eq. (1) at $a_s = 67a_0$ with $N = 1.2 \times 10^5$ atoms. We simulate a linear ramp in a_s from $67a_0$ to a variable final value of a_s in t_r, followed by a compression of the axial trap from $\nu_\parallel = 17.3$ to 21 Hz during 8 ms. We then record the axial width from the standard deviation of $n(\boldsymbol{r})$, $\sigma_y = \sqrt{\langle y^2 \rangle}$, as a function of the subsequent holding time. The evolution of σ_y is well fitted by a sinusoidal function, whose frequency constitutes our theoretical prediction of ν_{axial}.

In Fig. 3, we present our calculations with and without the LHY term. The MF simulations reveal a critical scattering length $a_c < a_{\mathrm{dd}}$ below which the system collapses, thus ruling out the collective mode excitation picture for $a_s < a_c$. This is in qualitative disagreement with the experimental observations. Moreover, for decreasing $a_s \geq a_c$, the MF predictions of ν_{axial} are sizably shifted compared to our measurements. In contrast, the experiment shows an excellent match with the theory including the LHY term, thus ruling out the MF scenario and demonstrating the crucial role played by QFs in stabilizing the system. Then, QFs qualitative modify the phase diagram and drive the formation of a special coherent state, namely, a single macrodroplet [20–23]. The lowering of $a_c = 57a_0$ found in Fig. 3(b) compared to Fig. 3(c) ($a_c = 64a_0$) arises from the more stringent interplay between QFs and 3B losses within this longer ramp, both mechanisms being able to drive the system out of the instability region.

VI. LOSS DYNAMICS

To further investigate the respective roles of 3B losses and QFs, we study the time evolution of the atom number of both the central core (N_{core}) and thermal (N_{th}) components along the BEC-to-droplet crossover. Since in the droplet regime the core density $n_{\mathrm{core}}(r)$ dramatically increases, 3B losses are expected to play an important role even for moderate and low values of L_3 [23]. Notwithstanding, 3B losses and QFs exhibit different power dependencies on $n(r)$ [see Eq. (1)] and, thus, the atom-loss dynamics should disclose their competition: while QFs tend to stabilize a high-density state, namely the droplet, 3B losses favor lower densities.

Figures 4(a) and 4(b) show N_{core} and N_{th}, extracted from the double-Gaussian fit as a function of a_s after a nonadiabatic [Fig. 4(a)] and adiabatic [Fig. 4(b)] change of a_s. Both cases show a similar evolution. When lowering a_s, N_{core} is first constant for $a_s > a_{\mathrm{dd}}$, then shows a sharp drop starting around $a_s \sim a_{\mathrm{dd}}$, and finally curves up for lower a_s. We note that in the adiabatic case, N_{core} decreases faster as compared to the nonadiabatic one and finally saturates around 7×10^3 at lower a_s. We attribute these to the longer timing involved, and we observe a similar trend as well as a similar saturation value for longer t_h [see, e.g., Fig. 4(c)].

Remarkably, N_{th} remains mainly unaltered over the whole range of a_s and the whole system does not show any appreciable heating. This suggests that the condensed atoms, which are ejected from in the core, leave the trap instead of being transferred to the thermal component, confirming a picture in which the thermal and the condensed component have uncoupled dynamics.

We now compare the experiment with the theory, which, as previously, precisely accounts for the experimental sequence and its timing by performing RTE along

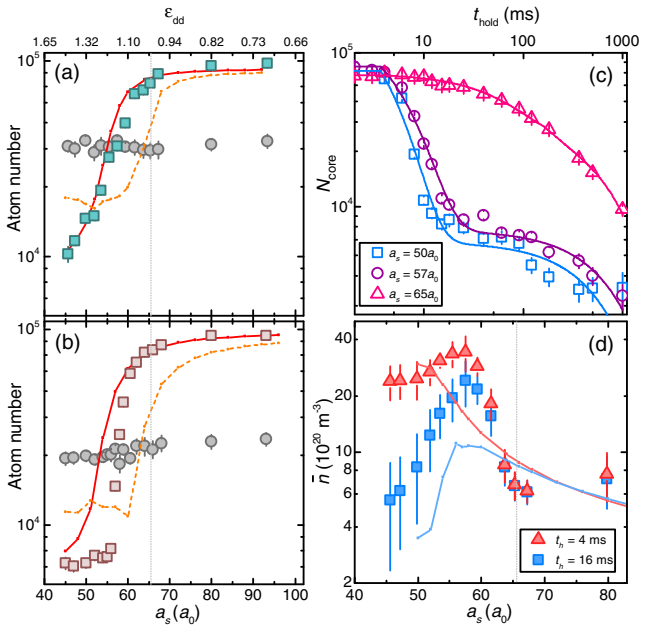

FIG. 4. Lifetime and *in situ* density of the high-density core. (a), (b) Measured $N_{\rm core}$ (squares) and $N_{\rm th}$ (circles) versus a_s after (a) a nonadiabatic ($t_r = 10$ ms, $t_h = 8$ ms) and (b) an adiabatic ($t_r = 45$ ms, $t_h = 0$ ms) ramp. The data show a better agreement with the theory with the LHY term (solid line) as compared to the MF theory (dashed line). (c) Time decay of $N_{\rm core}$ for $a_s = 65a_0$ (triangles), $57a_0$ (circles), and $50a_0$ (squares) after quenching a_s ($t_r = 10$ ms). We fit a double exponential function to the data (solid lines) [30]. (d) From the fit, we deduct the mean *in situ* density of the core $\bar{n}$ (see text) for $t_h = 4$ ms (triangles) and 16 ms (squares) and as a function of a_s. The error bars include the statistical errors on the fit and on L_3. The solid lines show results of the RTE including the LHY correction for $t_h = 0$ ms (red), $t_h = 25$ ms (blue).

Eq. (1). Here, we compute the final atom number $N = \int n(\boldsymbol{r}) d^3 r$ as a function of a_s with and without the LHY term. Remarkably, the observed evolution of $N_{\rm core}$ is very well reproduced by our beyond-MF calculations (solid lines), whereas in the absence of the LHY stabilization, the calculations predict losses in the condensed core to occur at values of a_s too large compared to the measured ones; see Figs. 4(a) and 4(b).

The observed evolution of $N_{\rm core}$ is well reproduced by our beyond-MF calculations (solid lines). The agreement is particularly remarkable for the quench [Fig. 4(a)] while it is slightly degraded in the adiabatic ramp [Fig. 4(b)], with an overestimation of the remaining $N_{\rm core}$ at small a_s. This can be explained by noting that, due to the longer time during which the losses set in, a more acute importance is given to L_3, and by considering the effects of QFs on its value. Indeed, it is of interest to note that many-body effects modify the 3B correlation function g_3 [44], leading to an enhanced loss rate. This then justifies the larger predicted $N_{\rm core}$ in our simulation based on the simple noninteracting value $g_3 = 1$ [30] compared to the experiment (we estimate $g_3 \sim 1.3$ for our typical parameters), and the increased discrepancy with decreasing a_s, where QFs are doomed to prevail. In contrast, the MF calculations deviate from the experiment with enhanced losses in the $a_s \sim a_{\rm dd}$ region. We note that the abrupt and high saturation of $N_{\rm core}$ at $a_s < a_{\rm dd}$, distinct from the experimental observations, is a signature of the collapse, reestablishing lower density in the gas via fast "explosive" dynamics.

Finally, we investigate the in-trap time evolution of $N_{\rm core}$ after quenching a_s in the droplet regime; see Fig. 4(c). Our measurements reveal three different time scales for the losses. At very short t_h (≈0–3.5 ms), $N_{\rm core}$ is roughly constant, which we attribute to the time needed for the high-density state to develop. It follows a fast decay (≈3.5–25 ms), in which the atoms are ejected from the high-density core via 3B losses, and witnesses the formation of a high-density coherent state. The steepness of this fast decay appears to critically depend on a_s, with a marked acceleration below the MF instability threshold. Then, the loss dynamics substantially slows down (≈25–1000 ms) while a coherent central core is still visible in the density profile (with $N_{\rm core} \sim 10^4$ atoms).

From the loss curves [Fig. 4(c)] and using the general 3B loss relation $(1/N_{\rm core})(dN_{\rm core}/dt_h) = -L_3 \bar{n}^2$, we are able to extract the mean *in situ* density $\bar{n} = \sqrt{\langle n_{\rm core}(r)^2 \rangle}$ of the high-density component in the BEC-to-droplet crossover. Here, we estimate $N_{\rm core}(t_h)$ and $(dN_{\rm core}/dt_h)$ from an empirical fit to our data and compute $\bar{n}$ using an independent measurement of the 3B loss coefficient L_3 [30]. Figure 4(d) shows our results for $t_h = 4$, 16 ms. We observe a prominent increase of $\bar{n}$ across the threshold $a_s \sim a_{\rm dd}$, and a surviving high-density state deep into the MF instability regime.

The formation of the droplet state is particularly visible for the $t_h = 4$ ms case. Here, $\bar{n}$ grows from $6.2(9) \times 10^{20}$ m^{-3} at $a_s = 67a_0$ to a maximum of $35(7) \times 10^{20}$ m^{-3} at $a_s = 57a_0$, while it is slightly reduced to $\sim 24 \times 10^{20}$ m^{-3} at $a_s \sim 46a_0$. This direct estimate of $\bar{n}$ advocates the activation of the LHY term when lowering a_s; additionally, its magnitude as well as its evolution are in good agreement with our simulations including the LHY correction.

Our results together with the good agreement between theory and experiments provide an alternative confirmation of the central role of beyond-mean-field physics. The lifetime of the high-density core reveals, on the one hand, the activation of the LHY term and the crossover toward a dense droplet state, and on the other hand, the counteracting role of 3B losses in regulating the maximum density in the droplet regime.

VII. EXPANSION DYNAMICS

Besides their dissimilar stability diagram, collective excitations, and density distribution, a dilute BEC in the

MF regime and a quantum droplet are also expected to exhibit a markedly different expansion dynamics. While the first is confined by an external trapping potential and thus freely expands in its absence, a droplet state is self-bound (SB) by its underlying interaction in analogy with the He-droplet case [20–23]. As in our previous discussions, the evolution from a trap-bound to a self-bound solution is expected to be regulated by the interplay between QFs and 3B loss processes.

We investigate the expansion dynamics of our system for various a_s. To preserve the high density of the coherent component, our measurements focus on short time scales with $t_r = 10$ ms and $t_h = 5$ ms. After preparing the system at the desired a_s, we abruptly switch off the optical dipole trap, let the gas expand for a variable t_{TOF}, and probe the cloud width using the ∥ imaging. We fit the observed density distribution to a double-Gaussian function, as previously described. To extract the width σ_η of the high-density core (n_{core}), we compute the second moments $\sigma_\eta^2 = \int \eta^2 n_{\mathrm{core}}(\boldsymbol{r}) d\boldsymbol{r}$ along $\eta = x, z$, where n_{core} is extracted from the double-Gaussian fit. Figure 5(a) exemplifies the TOF evolution of $\sigma_{\eta=x}$ at $a_s = 93a_0$, $64a_0$, and $55.5a_0$. When entering the $\varepsilon_{\mathrm{dd}} > 1$ regime, atoms in the high-density core exhibit a marked slowing-down of the expansion dynamics, which cannot be explained within the MF approach.

To systematically study this effect, we repeat the above measurements for different values of a_s (i.e., $\varepsilon_{\mathrm{dd}}$). From $\sigma_\eta(t_{\mathrm{TOF}})$, we extract the value of the expansion velocity v_η by fitting the data to $\sigma_\eta(t_{\mathrm{TOF}}) = \sqrt{\sigma_{\eta,0}^2 + v_\eta^2 t_{\mathrm{TOF}}^2}$. Figure 5(b) shows v_x in an $\varepsilon_{\mathrm{dd}}$ range from 0.7 to 1.5. When the system approaches the droplet regime with decreasing scattering length ($a_s < a_{\mathrm{dd}}$), v_x undergoes a strong reduction and drops to a minimum equal to $v_x = 0.40(2)$ μm/ms at about $56a_0$ ($\varepsilon_{\mathrm{dd}} \sim 1.17$). For further lowering of a_s, v_x starts to increase again. A similar behavior is observed for v_z. We note that only the high-density component reveals this intriguing dependency on a_s, whereas the thermal part shows an almost constant expansion velocity [45].

Considering the fit-free character of our simulations as well as the experimental challenge of accurately estimating the expansion velocities [46], we conclude that our observations agree well with the theory predictions including the LHY term; see solid line in Fig. 5(b). The TOF evolution is calculated using a multigrid numerical scheme [30]. We record the evolution of σ_η with t_{TOF} and extract the corresponding expansion velocities from the asymptotic behavior of $d\sigma_\eta/dt_{\mathrm{TOF}}$. Our simulations show a slowing-down with a minimum of $v_x = 0.32$ μm/ms at $a_s \sim 56a_0$ ($\varepsilon_{\mathrm{dd}} \sim 1.17$), followed by an increase at lower a_s. In contrast, calculations in the absence of beyond-MF corrections fail to reproduce the experimental data. Here, the velocity is first slightly more reduced above the MF instability threshold $\varepsilon_{\mathrm{dd}} \sim 1$ than is expected with LHY

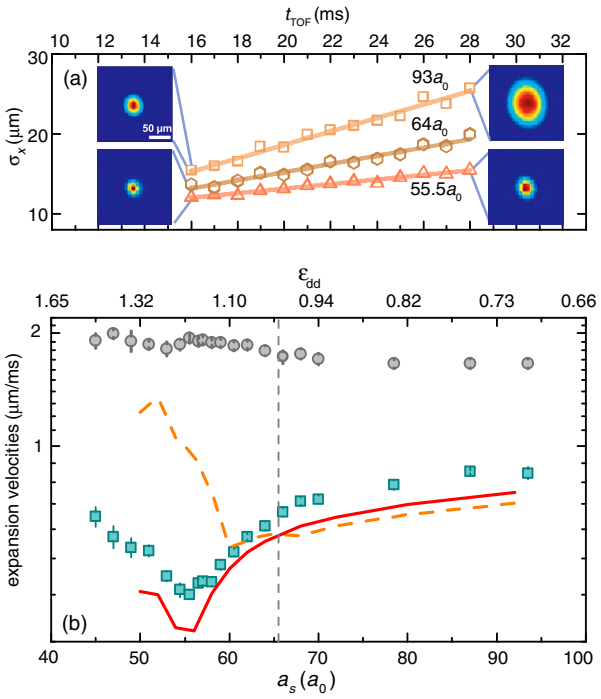

FIG. 5. Expansion dynamics across the BEC-to-droplet crossover. (a) TOF evolution of the width σ_x of the high-density component for $a_s = 93a_0$ (squares), $64a_0$ (circles), $55.5a_0$ (triangles). The lines are fit to the data using $\sigma_x(t_{\mathrm{TOF}}) = \sqrt{\sigma_{x,0}^2 + v_x^2 t_{\mathrm{TOF}}^2}$, from which we extract v_x. (b) v_x as a function of a_s (squares). For comparison, the a_s-independent expansion velocities of the thermal component are also shown (circles). The experimental data are in very good agreement with our parameter-free theory from RTE simulations including the LHY term (solid line) and rule out the MF scenario (dotted line). For clarity, we show only v_x; similar results are found for v_z.

corrections, it then already increases at this threshold. The first point relies on the trivial slowing-down of a BEC whose mean repulsion energy is weakened (by reducing a_s or decreasing its population N_{core}). The second point reveals a collapsing behavior that gives rise to an explosive evolution of the density profile. The minimal velocity is found here to be $v_x = 0.56$ μm/ms at $a_s = 68a_0$, which is a much higher value than both our experimental results and our theory predictions including the LHY correction.

The expansion behavior can be qualitatively well understood considering the so-called released, or internal, energy E_R. This is the energy of the system when subtracting the energy related to the confinement [1]. In the MF scenario, $E_R > 0$, as long as the ground state is stable. The BEC expands ballistically and v_η decreases for decreasing a_s and N. In the unstable regime, the expansion velocity depends crucially on the value of t_h at which the trap is switched off due to the occurrence of an *in situ* collapse dynamic. On the contrary, in the presence of QF, a stable ground state always exists. The sharp variability in t_h is expected to be

suppressed. Assuming a fixed N_{core} (i.e., no 3B losses), one can show that E_R decreases with decreasing a_s and eventually reaches $E_R < 0$ for $a_s < a_{\mathrm{SB}}$, marking the onset of the SB solution (e.g., $a_{\mathrm{SB}} = 56a_0$ for $N = 1.2 \times 10^5$) [30]. However, in stark contrast to the MF case, E_R increases with decreasing N_{core} in the droplet regime. We note that a_{SB} is then shifted to lower values when N_{core} gets reduced by 3B losses, thus affecting the lifetime of the self-bound solution.

The existence of a minimal expansion velocity is thus a direct consequence of the competition between the decrease of E_R for decreasing a_s at a fixed N_{core} and the increase of E_R for decreasing N_{core} in the droplet regime. In the crossover regime, the system smoothly evolves towards a fully self-bound state ($v_\eta = 0$) until 3B losses, occurring in the trap or in the initial phase of the expansion, set in to unbind the system and to reduce the lifetime of the droplet state.

VIII. CONCLUSION

In summary, we demonstrate the existence of the crossover from a dilute BEC to a quantum droplet state driven by QFs. Our experiments not only demonstrate that LHY stabilization is a general feature of strongly dipolar gases, but also thoroughly investigate the driving role of QFs in dictating the system properties, in particular, its collective mode, its atom losses, and expansion dynamics. This clear and quantitative demonstration of the impact of QFs in dipolar gases intrinsically relies on our unique and precise knowledge of a_s that alone enables a direct comparison to a parameter-free theory, which is based on a generalized GPE with LHY correction. Our combined experimental and theoretical results ultimately offer an experimental validation of the modeling proposed in Ref. [20] and thus of the latter results of Refs. [21–23].

ACKNOWLEDGEMENT

We thank M. Baranov, R. van Bijnen, R. N. Bisset, B. Blakie, E. Demler, R. Grimm, T. Pfau, and the Stuttgart Dy team for multiple useful discussions. We thank G. Faraoni for her support in the final stage of the experiment. The Innsbruck group thanks the European Research Council within the ERC Consolidator Grant RARE No. 681432. L. C. is supported within the Marie Curie Project DIPPHASE No. 706809 of the European Commission. The Hannover group acknowledges the support of the DFG (RTG 1729). Both groups acknowledge the support of the DFG/FWF (FOR 2247).

Note added in the proof.—A related work by M. Schmitt *et al.* recently appeared [47].

[1] L. Pitaevskii and S. Stringari, *Bose-Einstein Condensation* (Oxford University Press, Oxford, England, 2003).

[2] C. Chin, R. Grimm, P. S. Julienne, and E. Tiesinga, *Feshbach Resonances in Ultracold Gases*, Rev. Mod. Phys. **82**, 1225 (2010).

[3] T. D. Lee, K. Huang, and C. N. Yang, *Eigenvalues and Eigenfunctions of a Bose System of Hard Spheres and Its Low-Temperature Properties*, Phys. Rev. **106**, 1135 (1957).

[4] A. Altmeyer, S. Riedl, C. Kohstall, M. J. Wright, R. Geursen, M. Bartenstein, C. Chin, J. H. Denschlag, and R. Grimm, *Precision Measurements of Collective Oscillations in the BEC-BCS Crossover*, Phys. Rev. Lett. **98**, 040401 (2007).

[5] Y.-i. Shin, A. Schirotzek, C. H. Schunck, and W. Ketterle, *Realization of a Strongly Interacting Bose-Fermi Mixture from a Two-Component Fermi Gas*, Phys. Rev. Lett. **101**, 070404 (2008).

[6] N. Navon, S. Nascimbène, F. Chevy, and C. Salomon, *The Equation of State of a Low-Temperature Fermi Gas with Tunable Interactions*, Science **328**, 729 (2010).

[7] S. B. Papp, J. M. Pino, R. J. Wild, S. Ronen, C. E. Wieman, D. S. Jin, and E. A. Cornell, *Bragg Spectroscopy of a Strongly Interacting* ^{85}Rb *Bose-Einstein Condensate*, Phys. Rev. Lett. **101**, 135301 (2008).

[8] N. Navon, S. Piatecki, K. Günter, B. Rem, T. C. Nguyen, F. Chevy, W. Krauth, and C. Salomon, *Dynamics and Thermodynamics of the Low-Temperature Strongly Interacting Bose Gas*, Phys. Rev. Lett. **107**, 135301 (2011).

[9] D. S. Petrov, *Quantum Mechanical Stabilization of a Collapsing Bose-Bose Mixture*, Phys. Rev. Lett. **115**, 155302 (2015).

[10] T. Lahaye, C. Menotti, L. Santos, M. Lewenstein, and T. Pfau, *The Physics of Dipolar Bosonic Quantum Gases*, Rep. Prog. Phys. **72**, 126401 (2009).

[11] M. A. Baranov, M. Dalmonte, G. Pupillo, and P. Zoller, *Condensed Matter Theory of Dipolar Quantum Gases*, Chem. Rev. **112**, 5012 (2012).

[12] T. Koch, T. Lahaye, J. Metz, B. Fröhlich, A. Griesmaier, and T. Pfau, *Stabilization of a Purely Dipolar Quantum Gas against Collapse*, Nat. Phys. **4**, 218 (2008).

[13] T. Lahaye, J. Metz, B. Fröhlich, T. Koch, M. Meister, A. Griesmaier, T. Pfau, H. Saito, Y. Kawaguchi, and M. Ueda, *d-Wave Collapse and Explosion of a Dipolar Bose-Einstein Condensate*, Phys. Rev. Lett. **101**, 080401 (2008).

[14] J. Metz, T. Lahaye, B. Fröhlich, A. Griesmaier, T. Pfau, H. Saito, Y. Kawaguchi, and M. Ueda, *Coherent Collapses of Dipolar Bose-Einstein Condensates for Different Trap Geometries*, New J. Phys. **11**, 055032 (2009).

[15] H. Kadau, M. Schmitt, M. Wenzel, C. Wink, T. Maier, I. Ferrier-Barbut, and T. Pfau, *Observing the Rosensweig Instability of a Quantum Ferrofluid*, Nature (London) **530**, 194 (2016).

[16] I. Ferrier-Barbut, H. Kadau, M. Schmitt, M. Wenzel, and T. Pfau, *Observation of Quantum Droplets in a Strongly Dipolar Bose Gas*, Phys. Rev. Lett. **116**, 215301 (2016).

[17] K.-T. Xi and H. Saito, *Droplet Formation in a Bose-Einstein Condensate with Strong Dipole-Dipole Interaction*, Phys. Rev. A **93**, 011604 (2016).

[18] R. N. Bisset and P. B. Blakie, *Crystallization of a Dilute Atomic Dipolar Condensate*, Phys. Rev. A **92**, 061603 (2015).

[19] P. B. Blakie, *Properties of a Dipolar Condensate with Three-Body Interactions*, Phys. Rev. A **93**, 033644 (2016).

[20] F. Wächtler and L. Santos, *Quantum Filaments in Dipolar Bose-Einstein Condensates*, Phys. Rev. A **93**, 061603 (2016).

[21] R. N. Bisset, R. M. Wilson, D. Baillie, and P. B. Blakie, *Ground State Phase Diagram of a Dipolar Condensate with Quantum Fluctuations*, Phys. Rev. A **94**, 033619 (2016).

[22] F. Wächtler and L. Santos, *Ground-State Properties and Elementary Excitations of Quantum Droplets in Dipolar Bose-Einstein Condensates*, Phys. Rev. A **94**, 043618 (2016).

[23] D. Baillie, R. M. Wilson, R. N. Bisset, and P. B. Blakie, *Self-Bound Dipolar Droplet: A Localized Matter Wave in Free Space*, Phys. Rev. A **94**, 021602(R) (2016).

[24] Note that Er offers a system of intermediate dipolar strength ($a_{dd} = 65.5a_0$) between Cr ($a_{dd} = 15a_0$) and Dy ($a_{dd} = 132a_0$).

[25] A. Frisch, M. Mark, K. Aikawa, F. Ferlaino, J. L. Bohn, C. Makrides, A. Petrov, and S. Kotochigova, *Quantum Chaos in Ultracold Collisions of Gas-Phase Erbium Atoms*, Nature (London) **507**, 475 (2014).

[26] S. Baier *et al.* (to be published).

[27] K. Aikawa, A. Frisch, M. Mark, S. Baier, A. Rietzler, R. Grimm, and F. Ferlaino, *Bose-Einstein Condensation of Erbium*, Phys. Rev. Lett. **108**, 210401 (2012).

[28] S. Baier, M. J. Mark, D. Petter, K. Aikawa, L. Chomaz, Z. Cai, M. Baranov, P. Zoller, and F. Ferlaino, *Extended Bose-Hubbard Models with Ultracold Magnetic Atoms*, Science **352**, 201 (2016).

[29] M. J. Mark, E. Haller, K. Lauber, J. G. Danzl, A. J. Daley, and H.-C. Nägerl, *Precision Measurements on a Tunable Mott Insulator of Ultracold Atoms*, Phys. Rev. Lett. **107**, 175301 (2011).

[30] See Supplemental Material at http://link.aps.org/supplemental/10.1103/PhysRevX.6.041039 for further details on our experimental setup and procedure, on the data analysis performed, on our numerical simulations and on additional calculations using the Gaussian ansatz.

[31] J. L. Roberts, N. R. Claussen, S. L. Cornish, E. A. Donley, E. A. Cornell, and C. E. Wieman, *Controlled Collapse of a Bose-Einstein Condensate*, Phys. Rev. Lett. **86**, 4211 (2001).

[32] E. A. Donley, N. R. Claussen, S. L. Cornish, J. L. Roberts, E. A. Cornell, and C. E. Wieman, *Dynamics of Collapsing and Exploding Bose-Einstein Condensates*, Nature (London) **412**, 295 (2001).

[33] M. Ueda and H. Saito, *A Consistent Picture of a Collapsing Bose-Einstein Condensate*, J. Phys. Soc. Jpn. **72**, 127 (2003).

[34] R. Grimm, in *Ultra-Cold Fermi Gases*, Proceedings of the International School of Physics "Enrico Fermi", Course CLXIV, edited by M. Inguscio, W. Ketterle, and C. Salomon (2007) [arXiv:cond-mat/0703091].

[35] L. Pitaevskii and S. Stringari, *Elementary Excitations in Trapped Bose-Einstein Condensed Gases beyond the Mean-Field Approximation*, Phys. Rev. Lett. **81**, 4541 (1998).

[36] $\nu_{\|}$ is determined from the center-of-mass oscillations along y, which are simultaneously excited with the axial breathing mode.

[37] G. Bismut, B. Pasquiou, E. Maréchal, P. Pedri, L. Vernac, O. Gorceix, and B. Laburthe-Tolra, *Collective Excitations of a Dipolar Bose-Einstein Condensate*, Phys. Rev. Lett. **105**, 040404 (2010).

[38] We indeed observe a high-energy mode in which the high-density core splits and recombines in a damped oscillating manner.

[39] A. R. P. Lima and A. Pelster, *Quantum Fluctuations in Dipolar Bose Gases*, Phys. Rev. A **84**, 041604 (2011).

[40] A. R. P. Lima and A. Pelster, *Beyond Mean-Field Low-Lying Excitations of Dipolar Bose Gases*, Phys. Rev. A **86**, 063609 (2012).

[41] A. Boudjemâa, *Theory of Excitations of Dipolar Bose-Einstein Condensate at Finite Temperature*, J. Phys. B **48**, 035302 (2015).

[42] We note that the use of a generalized GPE, valid in the TF regime, can be extended beyond this regime as long as the LHY correction is dominated by short-wavelength excitations, whose momentum $\boldsymbol{q}$ fulfills $qR \gg 1$, where R is the size of the condensate along the direction of q. As discussed in detail in Refs. [20,22], this is the case for large droplet and ε_{dd} close to 1. Our experiments, performed in cigar-shaped traps with relatively large BECs, offer privileged conditions to be compared to generalized GPE predictions (in particular, enhanced compared to Refs. [15,16]). Indeed, we quantitatively estimate the validity of this approximation in our study by introducing an anisotropic cutoff, $q_c(\theta) = q_y\sqrt{\cos^2(\theta) + K^2\sin^2(\theta)}$, with K the aspect ratio of the BEC, assuming here an isotropic geometry around the dipole axis y, and θ denoting the angle $(y, \boldsymbol{q})$ [22]. For typical experimental parameters, e.g., $a_s = 58a_0$, $N = 5\times10^4$, we find an axial radius $R_y = 13\ \mu$m and $K = 7.5$. Introducing a typical cutoff value $q_yR_y = 25$, the cutoff LHY correction [i.e., taking momenta $q > q_c(\theta)$] equals ~0.8 of the value calculated in homogeneous space, demonstrating that short-wavelength excitations indeed have a dominant contribution and validating our approach. We note that, when decreasing a_s, long-wavelength excitations and unstable modes come to play a more significant role, and for this reason we consider our simulation reliable down to $a_s \geq 50a_0$.

[43] Yu. Kagan, A. E. Muryshev, and G. V. Shlyapnikov, *Collapse and Bose-Einstein Condensation in a Trapped Bose Gas with Negative Scattering Length*, Phys. Rev. Lett. **81**, 933 (1998).

[44] Yu Kagan, B. V. Svistunov, and G. V. Shlyapnikov, *Effect of Bose Condensation on Inelastic Processes in Gases*, Pis'ma Zh. Eksp. Teor. Fiz. **42**, 169 (1985).

[45] We observe a 14(9)% increase of v_{th} over the a_s range when decreasing a_s that we attribute to fit artifacts. First, the double Gaussian fit does not properly account either for the coherent or for the thermal parts of the gas which may result in cross talk in the fit of these components. Second, flaws in the partition in two components may occur, especially for

the configuration where both components have similar sizes (short TOF). We note that at long t_{TOF} the thermal sizes are nearly constant, while a trend in their evolution with a_s appears at short t_{TOF}. Because they are less subject to artifacts, the long t_{TOF} are expected to more reliably estimate v and we hence conclude that the observed slight heating is, at least mainly, an artifact.

[46] The observed slight overall shift of the experimental data compared to the theoretical predictions may be attributed to experimental artifacts coming from (i) the restricted range of t_{TOF} experimentally accessible, (ii) artifacts of the expansion fit arising, in particular, from the interplay of the two fit parameters, the empirical expression of the fit, or the finite range of expansion time [cf. (i)], or (iii) artifacts coming from the empirical double Gaussian fit used here to extract σ. This may lead to misassessment of the size of the coherent part and of its evolution with t_{TOF}.

[47] M. Schmitt, M. Wenzel, F. Böttcher, I. Ferrier-Barbut, T. Pfau, *Self-Bound Droplets of a Dilute Magnetic Quantum Liquid*, Nature (London) **539**, 259 (2016).

Quantum-fluctuation-driven crossover from a dilute Bose-Einstein condensate to a macro-droplet in a dipolar quantum fluid: Supplementary Material

L. Chomaz[1], S. Baier[1], D. Petter[1], M. J. Mark[1,2], F. Wächtler[3], L. Santos[3], F. Ferlaino[1,2*]
[1] *Institut für Experimentalphysik, Universität Innsbruck, Technikerstraße 25, 6020 Innsbruck, Austria*
[2] *Institut für Quantenoptik und Quanteninformation, Österreichische Akademie der Wissenschaften, 6020 Innsbruck, Austria*
[3] *Institut für Theoretische Physik, Leibniz Universität Hannover, Appelstr. 2, 30167 Hannover, Germany*
(Dated: October 18, 2016)

PACS numbers: 30.0, 67.85.-d, 03.75.Kk

Appendix: Supplementary material

1. Bose-Einstein condensation of ^{166}Er

We prepare an ultracold gas of the ^{166}Er isotope following a similar trapping and cooling scheme as the one employed for ^{168}Er [1, 2]. We load a crossed-ODT from a narrow-line MOT of 3×10^7 ^{166}Er atoms at about 10μK. At the end of the MOT sequence, the atoms are automatically spin-polarized in their lowest Zeeman sub-level [2]. The dipole orientation follows the one of the external applied magnetic field, $\boldsymbol{B}$. In our experiment, the latter is controlled by independent tuning of the components B_x, B_y, B_z along the experimental coordinate system (x, y, z), as defined in Fig. 1 (lower inset).

The ODT results from the crossing at their foci of two red-detuned laser beams at a wavelength of 1064 nm. One beam propagates horizontally along the y-axis, and the other propagates vertically and nearly collinear to the z-axis. The z-beam has a maximum power of 10 W and an elliptical profile defined by its waists of $(w_x^{(z)}, w_y^{(z)}) = (110, 55)\,\mu$m. The y-beam has a maximum power of 27 W, a vertical waist $w_z^{(y)} = 18\,\mu$m, and a tunable horizontal waist, $w_x^{(y)}$. The latter can be conveniently tuned from $1.57\,w_z^{(y)}$ to $15\,w_z^{(y)}$ by time averaging the frequency of the first-order deflection of an Acousto-Optic Modulator (AOM). This scanning scheme enables both an efficient loading of the MOT into the ODT ($> 30\%$ of the atoms are loaded) and an adiabatic and controlled tuning of the trap aspect ratio λ over a broad range. We achieve Bose-Einstein condensation of ^{166}Er atoms by means of evaporative cooling in the crossed ODT at $|\boldsymbol{B}| = B_z = 1.9\,\mathrm{G}$ ($a_\mathrm{s} = 80(2)\,a_0$). Typically, we first rapidly (in 600 ms) reduce the power and aspect ratio $w_x^{(y)}/w_z^{(y)}$ of the y-beam from 24 W to 4 W and 10 to 1.6, respectively. We further decrease the power of the y-beam from 4 W to 0.3 W in 3 s in an exponential manner and then exponentially increase the aspect ratio $w_x^{(y)}/w_z^{(y)}$ from 1.6 to 8 in 2.5 s. The final trap frequencies are typically of $(\nu_x;\nu_y;\nu_z) \sim (40; 40; 180)$ Hz. We finally obtain BECs of typically $N = 1.2\times10^5$ atoms with more than 80% condensed fraction and a temperature $T \sim 70$ nK. We typically measure N and the condensed fraction from a bimodal fit of the 2D column density distribution measured along $/\!/$-imaging with $t_\mathrm{ToF} = 27$ ms. T is extracted from the evolution of the thermal size of the bimodal fit with t_ToF varying from 14 to 28 ms.

2. Experimental setup and axes

In our setup we define the orthonormal (x, y, z)-coordinate system in the following way: the vertical axis z is aligned with gravity and the y axis with the horizontal ODT beam; see Fig. 1. The polarizing magnetic field is created by three orthogonal pairs of coils. These pairs of coils define an orthonormal (X, Y, Z)-coordinate system with $Z = z$ and (X, Y) rotated by a small angle θ as compared to (x, y). The magnetic field components B_X, B_Y, B_Z, each created by each pair of coils, can be controlled independently. We estimate θ to be about 15° by sensing directly the atomic cloud, as its dipolar character makes it sensitive both to the trap geometry and to the magnetic field direction.

The small tilt θ between the dipoles and y causes a small reduction of the mean DDI energy and corresponding small shifts of the expected characteristics compared to the one predicted for $\theta = 0$: the MF collapse threshold should appear at a lower a_s and, for a given a_s, $\nu_\mathrm{axial}/\nu_{/\!/}$ and v_η are shifted respectively down and up. We have experimentally evaluated the shift of ν_axial deep in the stable BEC regime ($|\boldsymbol{B}| = \sqrt{B_X^2 + B_Y^2} = 2\,\mathrm{G}$) to be of the order of 2% and in the droplet regime to be about 10 to 15%, as confirmed also by our theoretical predictions.

Finally, we also note a tilt between the $/\!/$-imaging beam and our reference frame, corresponding to an angle of $\theta_{/\!/,0}^\mathrm{im} \sim 28°$ compared to y and $\theta_{/\!/}^\mathrm{im} = 13°$ compared to Y in the xy-plane. The $\perp$-imaging axis is tilted by $\sim 15°$, mainly in the xz-plane. Such tilts shift the observed size compared to the ideal case of imaging along and perpendicular to the dipoles. Such an effect is not expected to impact the measurement of the collective frequencies, whereas it might bring a systematic shift of v_x because of a mixed projection of v_X and v_Y, the two first velocity components in the (X, Y, Z)-coordinate system, which are respectively perpendicular and along the dipoles.

* Francesca.Ferlaino@uibk.ac.at

In the theoretical calculations presented in the main text (Eq. (1), RTE and Gaussian ansatz), for simplicity, we do not account for these angles, whose effects are estimated to be smaller than our systematics.

3. Precision measurements of the a_s-to-B conversion in a three-dimensional optical lattice

Precise determination of the a_s-to-B conversion is a delicate issue, especially in the case of complex species, such as Er, for which comprehensive multi-channel calculations are still out of reach and the knowledge of a_s should thus rely on experimental investigations. We perform lattice modulation spectroscopy in a three-dimensional optical lattice. From the measurements of the energy gap in the Mott insulator state we extract $a_s(B)$. Our lattice experiments focuses in the region of low B-field $[0, 2.5\,\mathrm{G}]$ and are based on a lattice setup and procedure similar to the one described in Ref. [3]. In brief, after producing the BEC, we load the atoms in a three-dimensional optical lattice by exponentially increasing the lattice-beam power in 150 ms. The typical final depths are $(s_x, s_y, s_z) = (20, 20, 100)$, given in units of the respective recoil energies $h \times (4.2, 4.2, 1.05)\,\mathrm{kHz}$. At these lattice depths, the gas is in the Mott insulator state. We then vary $B = (0, 0, B_z)$ to the desired value by rapidly changing B_z in 2 ms, either just before or just after loading the lattice. We use the latter option for the smallest B values at which L_3 is enhanced because of its proximity to the near-zero-field resonance. In this case, we further hold 20 ms to make sure the magnetic field is fully established before performing the modulation.

To perform spectroscopy measurements, we sinusoidally modulate s_y at a variable frequency ν_m for 90 ms with a peak-to-peak amplitude of about 30%. Finally, we ramp down the lattice depths to zero in 150 ms, and measure the recovered condensed fraction as a function of ν_m from //-imaging ToF picture. For the smallest B values considered, we also ramp B back to 2 G in 2 ms before switching off the lattice-beams in order to again minimize 3B loss effects.

When varying ν_m, we observe a resonant depletion of the condensate due to particle-hole excitations. The resonance condition in the Mott-insulator regime is given by

$$h\nu_\mathrm{ex} = U_\mathrm{s} + U_\mathrm{dd} - V_\mathrm{dd}. \tag{A.1}$$

Here U_s, U_dd and V_dd are respectively the on-site contact interaction, the on-site dipolar interaction and the nearest-neighbor dipolar interaction along y in the corresponding extended Bose-Hubbard model. U_dd and V_dd can be accurately predicted from the knowledge of the lattice depths and dipole orientation and in our typical experimental condition, they are equal to $h \times -344.8\,\mathrm{Hz}$ and $h \times 31.5\,\mathrm{Hz}$ respectively. By subtracting the theoretical dipolar contributions to the measured frequency, we extract U_s, which is directly proportional to the scattering length a_s. A precise mapping of a_s in the ultralow B-field region is then obtained by repeating the above measurements at various B values; see Fig. 1.

In the low B-field region shown in Fig.1, our lattice spectroscopy reveals the presence of two FRs, one located at about zero B field and the other one at about 3 G. The existence and position of these two FRs agree with our Feshbach spectroscopy measurements performed in an harmonically trapped thermal cloud, where the maxima in 3B losses approximately pinpoint the resonance positions. In this measurement, further FRs are identified at 4.1 G and 5 G.

The scattering length of ^{166}Er can be parametrized by the following simple expression [4]

$$a_\mathrm{s}(B) = a_\mathrm{bg}(B)\left[1 + \sum_{i=1}^{4} \frac{\Delta B_i}{B - B_i}\right] \tag{A.2}$$

in which the specific positions (B_i) and widths (ΔB_i) of the two first resonances as well as the background scattering length are obtained from a fit to our lattice spectroscopy measurement. From the fit, we obtain $B_1 = 48(45)\,\mathrm{mG}$, $\Delta B_1 = 39(20)\,\mathrm{mG}$, $B_2 = 3.0(1)\,\mathrm{G}$, $\Delta B_2 = 110(35)\,\mathrm{mG}$. The B-dependent background scattering length $a_{bg}(B)$ accounts for the overlapping resonances and reads as $a_\mathrm{bg}(B) = 62(4) + kB$ with $k = 5.8(1.2)\,a_0/\mathrm{G}$. We also account for the small effect of the two next resonances, whose positions B_3, B_4 and widths $\Delta B_3, \Delta B_4$ are fixed to their estimates from the loss-spectroscopy measurements to 10 mG. We check that the precise values of this parameters has little effect on our empirical description along Eq. A.2 of a_s in the B-range of interest here, namely $[0, 2.5]\,\mathrm{G}$.

4. Ramps in scattering length

Our measurements rely on controlled variations of the scattering length $a_\mathrm{s}(B)$. In our experiments, we either adiabatically change a_s using $t_\mathrm{r} = 45\,\mathrm{ms}$ or we quench it using $t_\mathrm{r} = 10\,\mathrm{ms}$. The adiabatic condition for a_s reads as

$$\frac{1}{a_\mathrm{s}}\frac{\mathrm{d}a_\mathrm{s}}{\mathrm{d}t} \leq \min\left(\nu_x, \nu_y, \nu_z\right) = \nu_{/\!/} \text{ for } \lambda \ll 1 \tag{A.3}$$

As shown in Fig. S1, we use two different types of time variations of B and thus of a_s: (i) a simple linear ramp in B and (ii) we design a specific $B(t)$ variation in order to minimize the adiabaticity parameter $\frac{1}{a_\mathrm{s}}\frac{\mathrm{d}a_\mathrm{s}}{\mathrm{d}t}/\nu_{/\!/}$. The resulting a_s shows an exponential-type variation with t. The adiabaticity condition of Eq. (A.3) is more stringent for lower a_s. For ramping down to $a_\mathrm{s} = 48\,a_0$, we find that (i) verifies Eq. (A.3) for $t_\mathrm{r} \gtrsim 100\,\mathrm{ms}$ and (ii) for $t_\mathrm{r} \gtrsim 20\,\mathrm{ms}$. Data from Figs. 1, 3 and 4 (a, c-d) (resp. Figs. 2, 4 (b) and 5) use ramp (i) (resp. (ii)).

For our theoretical description, we use a linear change of $a_\mathrm{s}(t)$, similar to case (ii).

5. Determination of the three-body recombination rate coefficient

Since three-body inelastic losses play a crucial role in the many-body dynamics and lifetime of the droplet state, we run a dedicated set of measurements to determine L_3. We first prepare a non-degenerate thermal sample of Er atoms at $T = 490(10)\,\mathrm{nK}$ in an harmonic trap. We then record the decay of the atom number, N_{th}, as a function of t_{h} in a range from 0 to 1 s. N_{th} is obtained from a Gaussian fit to the measured density distribution.

To fit the time evolution of N_{th}, we use the integrated 3B rate equation, which reads as $\frac{1}{N_{\mathrm{th}}}\frac{\mathrm{d}N_{\mathrm{th}}}{dt_{\mathrm{h}}} = -L_3^{\mathrm{th}}\langle n^2\rangle$. Here, $\langle n^2\rangle$ is the mean square density on the cloud. To describe the scaling of $\langle n^2\rangle$ with N_{th}, we use its prediction for an ideal gas at thermal equilibrium at T whose state occupancies follow Boltzmann law and take into account the anti-evaporation effect [5]. Then L_3^{th} is extracted from a fit of $N_{\mathrm{th}}(t_{\mathrm{h}})$ along:

$$N_{\mathrm{th}}(t_{\mathrm{h}}) = \frac{N_0}{(1+3\gamma_0 N_0^2 t_{\mathrm{h}})^{1/3}} \tag{A.4}$$

where N_0 is the atom number at $t_{\mathrm{h}} = 0\,\mathrm{ms}$ and γ_0 is defined via the relation

$$L_3^{\mathrm{th}} = \sqrt{27}\,\gamma_0 \left(\frac{k_{\mathrm{B}}T}{2\pi m\bar{\nu}}\right) \tag{A.5}$$

with k_{B} the Boltzmann constant and $\bar{\nu} = (\nu_x\nu_y\nu_z)^{1/3}$.

We account for the a_{s}-dependence of L_3^{th} near a FR by repeating the measurement at different B. We check that the measured L_3^{th} does not depend on the $\boldsymbol{B}$ orientation and measure its B-dependency using $|\boldsymbol{B}| = B_y$ and for B varying in 0.1 to 1.9 G. Note that, due to the bosonization effect, the L_3 in a quantum degenerate bosonic gas is equal to $L_3^{\mathrm{th}}/3!$. Figure S2 shows L_3 in a quantum degenerate bosonic gas of ^{166}Er as a function of a_{s} using the measured a_{s}-to-B conversion. Despite the existence of many coupled molecular potential in Er, we measure a low $L_3(a_{\mathrm{s}})$, comparable to the typical values reported in alkali atoms. $L_3(a_{\mathrm{s}})$ varies between $1.7(3)\times10^{-40}\mathrm{m}^6/\mathrm{s}$ at $a_{\mathrm{s}} = 18(17)\,a_0$ and $3.2(3)\times10^{-42}\,\mathrm{m}^6/\mathrm{s}$ at $a_{\mathrm{s}} = 80(2)\,a_0$.

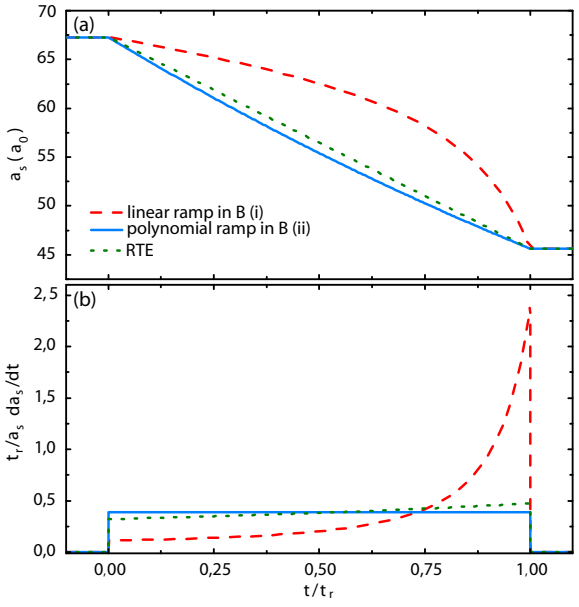

FIG. S1. Predicted evolution of the scattering length a_{s} (upper panel) and the adiabaticity parameter $\frac{1}{a_{\mathrm{s}}}\frac{\mathrm{d}a_{\mathrm{s}}}{\mathrm{d}t}/\nu_{//}$ (lower panel) over the ramp from $B = 0.8\,\mathrm{G}$ to the extreme $B_{\mathrm{f}} = 0.17\,\mathrm{G}$ ($a_{\mathrm{s}} = 45\,a_0$). The parameters are shown as a function of the normalized time t/t_{r} and the universal variation of the adiabaticity parameter is obtained from normalizing to $\nu_{//}t_{\mathrm{r}}$. We show the cases of three different ramps: a linear ramp in B (dashed red line) which is used in a first set of experiments (i), a polynomial ramp in B (solid blue line) which is used in a second set of experiments (ii), a linear ramp in a_{s} (dotted green line) which is used in the simulation (RTE).

6. Time-of-Flight measurements

For our ToF measurements, we abruptly extinguish the ODT in about 100 μs. In order to accurately image our gas while minimally influencing its dynamics during the expansion, we split the ToF in two parts. During a first part, lasting $t_{\mathrm{ToF}} - t_{\mathrm{B}}$, $\boldsymbol{B}$ remains unchanged and the dynamics occur at the original a_{s} and dipole orientation. At time t_{B} before the image is taken, $\boldsymbol{B}$ is modified both in amplitude and in direction, in order to correctly set the quantization axis for the imaging light to be σ_- polarized. The amplitude $|\boldsymbol{B}|$ of the imaging field is chosen constant

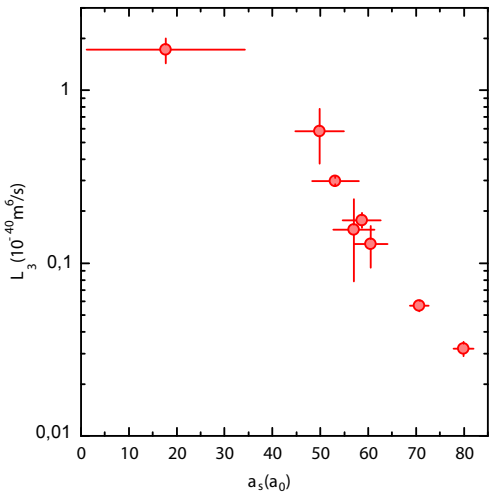

FIG. S2. Measured 3B recombination rate coefficient L_3 of a quantum degenerate gas of ^{166}Er as a function of a_{s} for B varying from 0.1 to 1.9 G. We extract L_3 from the measurement of L_3^{th} on a thermal gas at $T = 490(10)\,\mathrm{nK}$ using Boltzmann law and taking into account anti-evaporation effect; see text.

and equal to 0.31 G for all a_s considered. t_B is set to be 12 ms for //-imaging and 15 ms for ⊥-imaging where the change in $\boldsymbol{B}$ is more drastic for the typical dipole orientation (Y) used in this experiment.

We note that our resolution limit for both //- and ⊥-imaging is estimated to be $\gtrsim 3\,\mu$m. Moreover the effective pixel sizes are set to 8.4 μm and 3.1 μm in our setup. These limit the size of the structure we are able to observe as well as the minimal t_{ToF} we can use, which is typically $t_{ToF} \geq 16$ ms.

7. Averaging experimental density distribution

In order to obtain a better image quality and resolution, we typically average four experimental absorption images taken in the same condition and with the same experimental series (*i.e.* within less than a few hours interval). In order to average the images we first define a region of interest (ROI) of typically 300 μm × 300 μm containing the cloud shadow and translate the ROI to superimpose the cloud centers. To estimate the translation amplitudes for each individual image, we use the center from a simple Gaussian fit to the 2D density distribution ROIs. In this averaging process, we use a sub-grid resolution of 1/10 of a pixel to more accurately superimpose the centers. We fit the averaged density distribution after binning back to the original resolution. We note that fits on the sub-pixel resolved images give similar results.

8. Extracting the frequency of the collective modes

As stated in the main text, we focus on the axial mode, which reveals itself by a collective oscillation of the axial size $R_{//}$ of the BEC, along with smaller amplitude oscillations of the radial size in phase opposition. We extract its frequency ν_{axial} by studying the larger amplitude oscillation of $R_{//}$. For this, we probe the ToF density distribution of the gas with ⊥-imaging after a ToF of 30 ms. We focus on the sizes of the central, high-density component of the cloud, which we study as a function of t_h for different a_s. We note that the precise shape of the column density profile is expected to change as a function of a_s and this in a different way for the two axis x and y under observation in ⊥-imaging. This complicates the analysis, in particular compared to the //-imaging where both axes are nearly equivalent. Here, we extract the sizes of the central component, using various methods and select the most reliable method according to a_s. Typically, we use a bimodal MF TF plus Gauss fit for $a_s \geq 57\,a_0$. For $a_s \leq 57\,a_0$, we select a central region in the cloud and perform a simple Gaussian fit on it. Such a determination should give access to the variations, if not to its absolute value, of $R_{//}$ with t_h at fixed a_s and thus enables to determine ν_{axial}. In particular, we have checked that for large a_s, the two fits (Gaussian on a central region and MF-TF plus gaussian bimodal fits) give very similar and compatible values of ν_{axial}. For example for $a_s = 93\,a_0$ we find $\nu_{axial} = 30.65(4)$ Hz and 30.55(6) Hz for the MF-TF and Gaussian fit respectively. For $a_s = 60\,a_0$, we find respectively $\nu_{axial} = 36.1(3)$ Hz and 36.7(3) Hz.

To fit ν_{axial}, we use a damped-sine function of t_h. Typically we fit the evolution of $R_{//}$ for t_h varying from 0 to few hundreds of ms, depending on the damping rate observed. The upper value of t_h used is never less than 150 ms such that at least 4 to 5 oscillations are observed and fitted. We also note that for our shortest $t_r = 10$ ms we typically discard the first 4 ms of the evolution in order to ensure that the magnetic field is safely stabilized at its target value.

9. Bimodal fits of the density distribution in //-imaging.

To quantitatively analyse the experimental column density distribution imaged along //-imaging, we perform bimodal fits on the 2D averaged profiles $n_{//}(x, z)$. The bimodal fits are made of the sum of two peak distributions, describing respectively a high-density, coherent part and a thermal incoherent background. To account for the change of the profile of the density distribution across the BEC-to-droplet crossover, we use two types of fitting functions $f_{fit}(x, z)$: (i) A sum of a MF-TF and a Gaussian distribution, which account respectively for the coherent and the thermal part. For

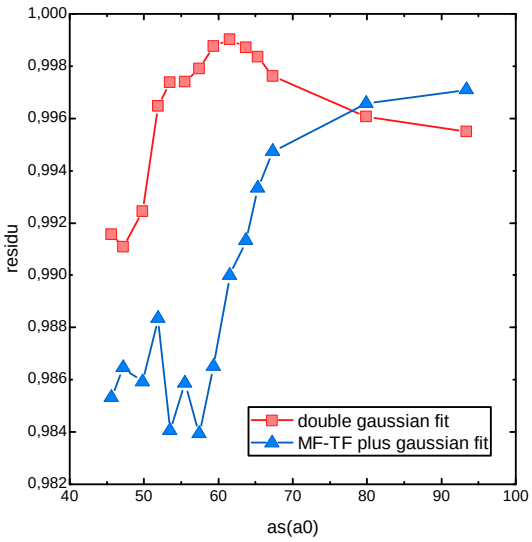

FIG. S3. Residues of the two bimodal fits used in our analysis of the //-images as a function of a_s for $t_r = 10$ ms and $t_h = 6$ ms: MF-TF plus Gauss fit (blue triangle) and double Gaussian fit (red square).

the integrated column density, the MF TF distribution writes $f_{\mathrm{TF}}(x,z) = \left(1 - \frac{(x-x_0)^2}{R_x^2} - \frac{(z-z_0)^2}{R_z^2}\right)^{3/2}$ [6].(ii) The sum of two Gaussian distributions. Typically the central Gaussian can be anisotropic with any orientation axis.

As expected, the thermal background is broader than the central coherent component and for the t_{ToF} considered its width is typically at least 1.6 times larger. It is first fitted by taking out the central part of the density distribution at radius typically smaller than 1.3 times its width.

The quality of the bimodal fit is evaluated by the norm of the residue $\rho = 1 - \frac{\int \mathrm{d}x\,\mathrm{d}z\,\left(n_{/\!/}(x,z) - f_{\mathrm{fit}}(x,z)\right)^2}{\int \mathrm{d}x\,\mathrm{d}z\,n_{/\!/}(x,z)^2}$. For both distributions, it satisfies $\rho > 0.98$.

The evolution of ρ with a_{s} informs us further on the physical properties our gas, as stressed in the main text in Sec. III. Fig. S3 shows the extensive variations of ρ, thus completing the data of Fig. 2 and the physical picture described there. First, as stated in Sec. III, by considering the agreement of MF-TF plus Gauss distribution, one is able to identify a deviation from the MF-TF behavior. Indeed ρ shows here a marked decrease when lowering a_{s} below a_{dd} from 0.997 to 0.985 and a further saturation around this value. On the contrary, the residue of the double Gaussian fit increases when lowering a_{s} below a_{dd} before decreasing again for a_{s} below $57\,a_0$, and remains above 0.99 over the whole range of a_{s}.

However, we point out that we are not able to distinguish, from the mere density profiles, between a MF or beyond-MF character of the deviation from MF-TF regime. Even though theoretical studies point out the difference in density profile expected by the arising of beyond-MF effects compared to the simple reduction of the MF interactions [7–10], bimodal fit agreement does not enable a reliable distinction. Indeed, the difference is minute and surely blurred by the presence of a thermal fraction. Hence, even though a more complex profile is expected, the double Gaussian fit agrees particularly well to our data and is here used to extract global properties of the system for further studies. We note that such a procedure has been also adopted in [11, 12] for the array of micro droplets, and the Gaussian ansatz has also been used in theoretical works [8, 9], in which the Gaussian solution shows a good approximation as compared to the much heavier numerical solution. To further prove the role of QFs in our paper, we extensively account for emblematic global properties that characterize the droplet physics (see Figs. 3, 4and 5).

10. Describing the atom number decay

In Figure 4 (c) and in the main text we have briefly described the evolution of the atom number in the coherent part N_{core} with t_{h}. There our aim was to extract the mean density and we did not expand on the mere description of the $N_{\mathrm{core}}(t_{\mathrm{h}})$.

We note that $N_{\mathrm{core}}(t_{\mathrm{h}})$ is well accounted for by a double exponential decay evolution of respective amplitude $N_0(1-p)$ and $N_0 p$. N_0 is the initial atom number. Each decay corresponds to a different time constant, respectively t_{fast} and t_{slow}, and starts after a different delay time, respectively t_{d} and t_{D}. We fix $t_{\mathrm{D}} = t_{\mathrm{d}} + 2t_{\mathrm{slow}}$. For $t_{\mathrm{r}} = 10\,\mathrm{ms}$ t_{d} is approximately constant and equal to 3.65 ms. The absence of evolution for $t_{\mathrm{h}} < t_{\mathrm{d}}$ indicates that the magnetic field may not have reached the target value in the first ms. For $t_{\mathrm{r}} = 45\,\mathrm{ms}$, t_{d} can be set to 0. t_{fast}, t_{slow} and p (and N_0) depend on a_{s}, typically decreasing with it. The evolution is illustrated in Fig. S4 for $t_{\mathrm{r}} = 10\,\mathrm{ms}$.

11. Gaussian Ansatz including L_3

A good qualitative (and to a large extent quantitative) insight in the physics of dipolar condensates in the presence of LHY stabilization may be gained from a simplified

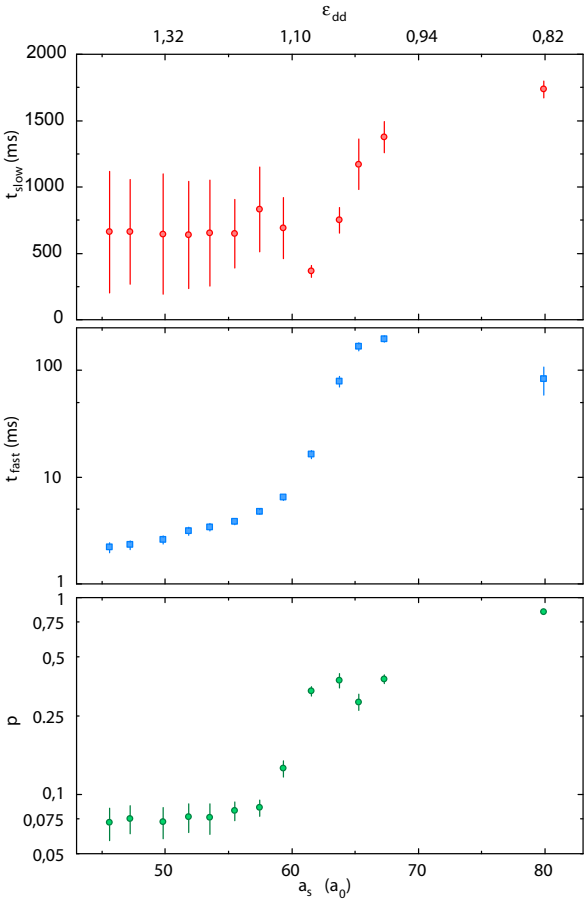

FIG. S4. Fit parameters for the evolution of $N_{\mathrm{core}}(t_{\mathrm{h}})$.

Gaussian ansatz of the form

$$\psi(\mathbf{r},t) = \sqrt{N(t)}e^{\mathrm{i}\phi(t)} \prod_{\eta=x,y,z} \frac{\mathrm{e}^{-\frac{\eta^2}{2w_\eta^2}+i\eta^2\beta_\eta(t)}}{\pi^{1/4}w_\eta^{1/2}}, \quad \text{(A.6)}$$

where the variational parameters are the number of atoms $N(t)$, the global phase $\phi(t)$, the widths w_η, and the phase curvatures β_η. The Lagrangian density reads:

$$\begin{aligned}\mathcal{L} =& \frac{i\hbar}{2}\left(\psi\frac{\partial\psi^*(\mathbf{r},t)}{\partial t} - \psi^*\frac{\partial\psi(\mathbf{r},t)}{\partial t}\right) + \frac{\hbar^2}{2m}|\nabla\psi(\mathbf{r},t)|^2 \\ &+ V(\mathbf{r})|\psi(\mathbf{r},t)|^2 + \frac{g}{2}|\psi(\mathbf{r},t)|^4 + \frac{2}{5}g_{\mathrm{LHY}}|\psi(\mathbf{r},t)|^5 \\ &+ \frac{1}{2}\int d^3r' V_{\mathrm{dd}}(\mathbf{r}-\mathbf{r}')|\psi(\mathbf{r},t)|^2|\psi(\mathbf{r}',t)|^2. \quad \text{(A.7)}\end{aligned}$$

We insert ansatz (A.6) into Eq. (A.7), obtaining the Lagrangian $L = \int d^3r\mathcal{L}$:

$$\begin{aligned}L = N&\left\{\hbar\dot{\phi} + \frac{\hbar}{2}\sum_\eta \dot{\beta}w_\eta^2 + \frac{m}{4}\sum_\eta \omega_\eta^2 w_\eta^2 \right. \\ &\left. + 2\,\frac{\hbar^2}{2m}\sum_\eta\left(\beta_\eta^2 w_\eta^2 + \frac{1}{4w_\eta^2}\right)\right\} \\ &+ N^2\left\{\frac{g(1+\epsilon_{dd}F(w_y/w_x, w_y/w_z))}{2(2\pi)^{3/2}\prod_\eta w_\eta}\right\} \\ &+ N^{5/2}\left\{\left(\frac{2}{5}\right)^{5/2}\frac{g_{LHY}}{\pi^{9/4}\prod_\eta w_\eta^{3(2}}\right\}, \quad \text{(A.8)}\end{aligned}$$

with

$$\begin{aligned}F(\kappa_x,\kappa_z) = &\frac{1}{4\pi}\int_0^\pi d\theta\sin\theta\int_0^{2\pi}d\phi \\ &\left[\frac{3\cos^2\theta}{\left(\kappa_x^2\cos^2\phi + \kappa_z^2\sin^2\phi\right)\sin^2\theta + \cos^2\theta} - 1\right]. \quad \text{(A.9)}\end{aligned}$$

The variational parameters are determined from the corresponding Euler-Lagrange equations [13]:

$$\frac{d}{dt}\left(\frac{\partial L}{\partial\dot{\lambda}}\right) - \frac{\partial L}{\partial\lambda} = \int d^3r\left[\Gamma\frac{\partial\psi^*}{\partial\lambda} + \Gamma^*\frac{\partial\psi}{\partial\lambda}\right], \quad \text{(A.10)}$$

where $\lambda = N, \phi, w_\eta, \beta_\eta$, and $\Gamma(\mathbf{r}) = -i\hbar\frac{L_3}{2}|\psi(\mathbf{r})|^4\psi(\mathbf{r})$. Introducing the dimensionless units $\tau = \tilde{\omega}t$, $w_\eta = \tilde{l}v_\eta$, $\tilde{l} = \sqrt{\hbar/m\tilde{\omega}}$, with $\tilde{\omega} = (\prod\omega_\eta)^{1/3}$, and after some algebra, we obtain a close set of equations for the Gaussian widths and the number of atoms:

$$\dot{N} = -\frac{3R}{\prod_\eta v_\eta^2}N^3, \quad \text{(A.11)}$$

$$\ddot{v}_\eta = -v_\eta\left[\frac{7R^2N^4}{\prod_{\eta'}v_{\eta'}^4} + \frac{2RN^2}{\prod_{\eta'}v_{\eta'}^2}\sum_{\eta''\neq\eta}\frac{\dot{v}_{\eta''}}{v_{\eta''}}\right] - \frac{\partial U}{\partial v_\eta}, \quad \text{(A.12)}$$

with $R = \frac{L_3}{\pi^3 3^{5/2}\tilde{\omega}\tilde{l}^6}$, and

$$\begin{aligned}U = &\frac{1}{2}\sum_\eta\left[v_\eta^{-2} + \left(\frac{\omega_\eta}{\tilde{\omega}}\right)^2 v_\eta^2\right] + \frac{2}{3}\frac{PQN^{3/2}}{\left(\prod_\eta v_\eta\right)^{\frac{3}{2}}} \\ &+ \frac{PN}{\prod_\eta v_\eta}\left(1 + \epsilon_{dd}F\left(\frac{v_y}{v_x}, \frac{v_y}{v_z}\right)\right), \quad \text{(A.13)}\end{aligned}$$

with $P = \sqrt{\frac{2}{\pi}}\frac{a}{\tilde{l}}$ and $Q = \frac{512\,F(\epsilon_{dd})}{25\sqrt{5}\pi^{\frac{5}{4}}}(a/\tilde{l})^{3/2}$.

Due to their simplicity, Eqs. (A.11) and (A.12) permit a much more flexible simulation of the exact experimental conditions and sequences compared to the obviously more exact but numerically much more cumbersome simulation of the gNLNLSE. We have checked that the results of the Gaussian ansatz approach are in excellent agreement both qualitative and to a large extent also quantitative to full simulations of the gNLNLSE, in what concerns lowest-lying excitations, atom losses, and expansion velocities.

12. Self-bound droplets

The Gaussian ansatz approach allows for an intuitive understanding of the degree of self-bound (SB) character of the system. As mentioned in the main text, a SB solution is characterized by a negative released energy, $E_{\mathrm{R}} < 0$. In absence of losses, we may evaluate E_{R} by means of the Gaussian Ansatz for the ground-state of a trapped BEC with scattering length a_{s} and fixed N. Figure S5 shows the results for E_{R} for different N values. Whereas E_{R} increases with growing N for large a_{s}, for small a_{s} in the droplet regime E_{R} increases with decreasing N. For each N there is a finite scattering length a_{SB} such that if $a_{\mathrm{s}} \leq a_{\mathrm{SB}}$ the droplet will be fully self-bound ($v_\eta = 0$). Given its N-dependence, a_{SB} shifts to lower values with decreasing N. 3B losses add a time dependence on N and thus on a_{SB} that governs the lifetime of the droplet state. We note that for small $(t_{\mathrm{r}}, t_{\mathrm{h}})$ E_{R} may change its sign during the ToF due to atom losses, i.e. a SB solution may unbind during the ToF. In our experiments, the interplay of losses and LHY stabilization leads to a minimal released energy, that translates into a minimal expansion velocity as shown in the main text.

13. Simulation of the ToF expansion using the gNLNLSE

ToF expansion is simulated using the gNLNLSE by means of a multi-grid method, i.e. dynamically enlarging the numerical grid following the expansion. This is necessary due to the obvious difference in length scales at the beginning and at the end of the ToF. We note that the precise description of the ToF dynamics is very relevant, since in contrast to standard cases, nonlinear dynamics

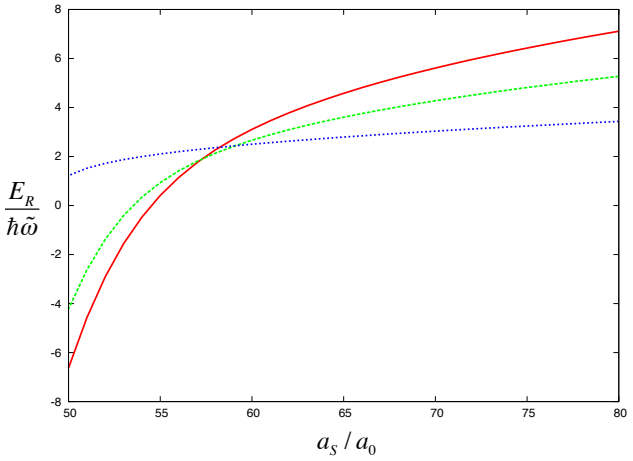

FIG. S5. Released energy E_R as a function of a_s for $N = 1.2 \times 10^5$ (solid), 5×10^4 (dashed), and 10^4 (dotted). Note that $E_R < 0$ indicates a SB solution.

and losses here may play an important role during the expansion, especially within the LHY stabilized regime.

[1] K Aikawa, A Frisch, M Mark, S Baier, A Rietzler, R Grimm, and F Ferlaino, "Bose-einstein condensation of erbium," Phys. Rev. Lett. **108**, 210401 (2012).

[2] A Frisch, K Aikawa, M Mark, A Rietzler, J Schindler, E Zupanič, R Grimm, and F Ferlaino, "Narrow-line magneto-optical trap for erbium," Phys. Rev. A **85**, 051401 (2012).

[3] S. Baier, M. J. Mark, D. Petter, K. Aikawa, L. Chomaz, Z. Cai, M. Baranov, P. Zoller, and F. Ferlaino, "Extended bose-hubbard models with ultracold magnetic atoms," Science **352**, 201–205 (2016).

[4] Cheng Chin, Rudi Grimm, Paul S. Julienne, and Eite Tiesinga, "Feshbach resonances in ultracold gases," Rev. Mod. Phys. **82**, 1225–1286 (2010).

[5] Tino Weber, Jens Herbig, Michael Mark, Hanns-Christoph Nägerl, and Rudolf Grimm, "Three-body recombination at large scattering lengths in an ultracold atomic gas," Phys. Rev. Lett. **91**, 123201 (2003).

[6] L. Pitaevskii and S. Stringari, *Bose–Einstein condensation* (Oxford University Press, Oxford, 2003).

[7] F. Wächtler and L. Santos, "Quantum filaments in dipolar bose-einstein condensates," Phys. Rev. A **93**, 061603 (2016).

[8] F Wächtler and L Santos, "Ground-state properties and elementary excitations of quantum droplets in dipolar bose-einstein condensates," arXiv:1605.08676 (2016).

[9] RN Bisset, RM Wilson, D Baillie, and PB Blakie, "Ground state phase diagram of a dipolar condensate with quantum fluctuations," arXiv:1605.04964 (2016).

[10] D Baillie, RM Wilson, RN Bisset, and PB Blakie, "Self-bound dipolar droplet: a localized matter-wave in free space," arXiv:1606.00824 (2016).

[11] Igor Ferrier-Barbut, Holger Kadau, Matthias Schmitt, Matthias Wenzel, and Tilman Pfau, "Observation of quantum droplets in a strongly dipolar bose gas," Phys. Rev. Lett. **116**, 215301 (2016).

[12] Holger Kadau, Matthias Schmitt, Matthias Wenzel, Clarissa Wink, Thomas Maier, Igor Ferrier-Barbut, and Tilman Pfau, "Observing the rosensweig instability of a quantum ferrofluid," Nature **530**, 194–197 (2016).

[13] Victo S. Filho, F. Kh. Abdullaev, A. Gammal, and Lauro Tomio, "Autosolitons in trapped bose-einstein condensates with two- and three-body inelastic processes," Phys. Rev. A **63**, 053603 (2001).

A.2. Publication: Anisotropic polarizability of erbium atoms[†]

Phys. Rev. A **97**, 012509 (2018)
submitted 20 Oct 2017; published 19 Jan 2018
DOI 10.1103/PhysRevA.97.012509

Jan Hendrik Becher,[1,⋆] Simon Baier,[1,⋆] Kiyotaka Aikawa,[1] Maxcence Lepers,[3] Jean-François Wyart,[3] Olivier Dulieu,[3] F. Ferlaino[1,2]

[1] *Institut für Experimentalphysik, Universität Innsbruck, Technikerstraße 25, 6020 Innsbruck, Austria*
[2] *Institut für Quantenoptik und Quanteninformation, Österreichische Akademie der Wissenschaften, 6020 Innsbruck, Austria*
[3] *Laboratoire Aimé Cotton, CNRS, Université Paris-Sud, ENS Paris-Saclay, Université Paris-Saclay, 91405 Orsay, France*

⋆ These authors contribute equally to this work.

Supplemental Material:

The theoretical dataset containing information on all dipole allowed transitions from the ground state, as used for the calculations within this publication, are available in Ref. [Bec18].

[†] The author of the present thesis developed the experimental procedures together with K. A., performed the measurements and analyzed the data together with J. H. B., and K. A., and contributed in writing the manuscript. The theoretical calculations of this publication have been contributed by M. L., J.-F. W. and O. D.

Anisotropic polarizability of erbium atoms

J. H. Becher,[1,*] S. Baier,[1] K. Aikawa,[1,†] M. Lepers,[2,‡] J.-F. Wyart,[2] O. Dulieu,[2] and F. Ferlaino[1,3,§]

[1]*Institut für Experimentalphysik, Universität Innsbruck, Technikerstraße 25, 6020 Innsbruck, Austria*

[2]*Laboratoire Aimé Cotton, CNRS, Université Paris-Sud, ENS Paris-Saclay, Université Paris-Saclay, 91405 Orsay, France*

[3]*Institut für Quantenoptik und Quanteninformation, Österreichische Akademie der Wissenschaften, 6020 Innsbruck, Austria*

(Received 20 October 2017; published 19 January 2018)

We report on the determination of the dynamical polarizability of ultracold erbium atoms in the ground and in one excited state at three different wavelengths, which are particularly relevant for optical trapping. Our study combines experimental measurements of the light shift and theoretical calculations. In particular, our experimental approach allows us to isolate the different contributions to the polarizability, namely, the isotropic scalar and anisotropic tensor part. For the latter contribution, we observe a clear dependence of the atomic polarizability on the angle between the laser-field-polarization axis and the quantization axis, set by the external magnetic field. Such an angle dependence is particularly pronounced in the excited-state polarizability. We compare our experimental findings with the theoretical values, based on semiempirical electronic structure calculations, and we observe a very good overall agreement. Our results pave the way to exploit the anisotropy of the tensor polarizability for spin-selective preparation and manipulation.

DOI: 10.1103/PhysRevA.97.012509

I. INTRODUCTION

Ultracold quantum gases provide many different degrees of freedom, which can be controlled to a very high precision. This makes them a reliable and versatile tool to study complex many-body phenomena in the laboratory [1]. Some of those degrees of freedom rely on the interaction between atoms and light. The strength of such an interaction depends on the atomic polarizability, which is a characterizing quantity of the specific atomic species under examination. Over the course of the last decades, tremendous progress has been made to develop theoretical methods and experimental protocols to determine the atomic polarizabilities, α_{tot}, with an increasing level of accuracy [2,3]. With the gained control over quantum systems, the precise determination of α_{tot} became even more fundamental with implications for quantum information processing, precision measurements, collisional physics, and atom-trapping and optical cooling applications. Calculations of α_{tot} require a fine knowledge of the energy-level structure and transition matrix elements, which is increasingly complex to acquire with the increasing number of unpaired electrons in the atomic species. For instance, alkali atoms with their single valence electron allow a determination of the static atomic polarizability with an accuracy below 1% [4,5] when the full atomic spectrum is taken into account.

In the case of the multielectron lanthanide atoms (Ln), which have been recently brought to quantum degeneracy (ytterbium (Yb) [6,7], dysprosium (Dy) [8,9], erbium (Er) [10,11]), the atomic spectrum can be very dense with a rich zoology of optical transitions, from being ultranarrow to extremely broad. Beside Yb with its filled shell, the other Ln show an electron vacancy in an inner and highly anisotropic electronic shell ($4f$ for all Ln besides lanthanum and lutetium), surrounded by a completely filled isotropic s shell. Because of this peculiar electronic configuration, such atomic species are often referred to as *submerged-shell atoms* [12,13].

Capturing the complexity of Ln challenges spectroscopic approaches and allows for stringent tests of *ab initio* calculations [14–20]. Besides being benchmark systems for theoretical models, Ln exhibit special optical properties, opening novel possibilities for the control, manipulation, and detection of Ln-based quantum gases [21,22]. One peculiar aspect of magnetic Ln is their sizable anisotropic contribution to the total atomic polarizability, originating from the unfilled $4f$ shell. Particularly relevant is the anisotropy arising from the tensor polarizability. This term gives rise to a light shift, which is quadratic in the angular-momentum projection quantum number, m_J, and provides an additional tool for optical spin manipulation, as recently studied in ultracold Dy experiments [23]. The anisotropy in the polarizability has been observed not only in atoms with large orbital-momentum quantum number, but also in large-spin atomic systems, such as chromium (Cr), [24,25] and molecular systems [26–29].

This paper reports on the measurement of the dynamical polarizability in ultracold Er atoms in both the ground state and one excited state for trapping-relevant wavelengths. Our approach allows us to isolate the spherically symmetric (scalar) and the anisotropic (tensor) contribution to the total polarizability. We observe that the latter contribution, although small in the ground state, can be very large for the excited state. Our

*Present address: Physikalisches Institut, Universität Heidelberg, Im Neuenheimer Feld 226, 69120 Heidelberg, Germany.

†Present address: Department of Physics, Graduate School of Science and Engineering, Tokyo Institute of Technology, Meguroku, Tokyo 152-8550, Japan.

‡Present address: Laboratoire Interdisciplinaire Carnot de Bourgogne, CNRS, Université de Bourgogne Franche-Comté, Dijon, France.

§Corresponding author: Francesca.Ferlaino@uibk.ac.at

results are in very good agreement with electronic structure calculations of the atomic polarizability, showing a gained control of the atom-light interaction in Er and its spectral properties.

II. THEORY OF DYNAMICAL POLARIZABILITY

To understand the concept of anisotropic polarizability, we first review the basic concepts of atom-light interaction [3,30]. When an isotropic medium is submitted to an external electric field, e.g., a linearly polarized light field, it experiences a polarization parallel to the applied electric field. However, in anisotropic media, an external electric field can also induce a perpendicular polarization, which in the atom-light-interaction language corresponds to a polarizability with a tensorial character. As we will discuss in the following, Er atoms can be viewed as an anisotropic medium because of their orbital anisotropy in the ground and excited states (nonzero orbital-momentum quantum number $L \neq 0$). The atomic polarizability is then described by a 3×3 tensor, $\mathscr{P}$. The total light shift experienced by an atomic medium exposed to an electric field $\vec{E}$ reads as

$$U = \tfrac{1}{2}\vec{E}^{\dagger}\mathscr{P}\vec{E}. \tag{1}$$

Equation (1) can be decomposed into three parts. For this, we define the scalar polarizability tensor $\mathscr{A}_s$ (diagonal elements), the vectorial polarizability tensor $\mathscr{A}_v$ (antisymmetric part of the off-diagonal elements), and the tensorial polarizability tensor $\mathscr{A}_t$ (symmetric part of the off-diagonal elements). Hence, a medium with polarizability tensor $\mathscr{P}$ placed into an electric field $\vec{E}$ feels the total light shift,

$$U = \tfrac{1}{2}\vec{E}^{\dagger}[\mathscr{A}_s + \mathscr{A}_v + \mathscr{A}_t]\vec{E}. \tag{2}$$

We now consider the case of an atom in its electronic ground state with nonzero angular-momentum quantum number J, its projection on the quantization axis m_J, and a total polarizability α_{tot} placed in a laser field of intensity $I = \frac{\epsilon_0 c}{2}|\vec{E}|^2$, polarization vector $\mathbf{u}$, and frequency $\omega = 2\pi\frac{c}{\lambda}$. Here, ϵ_0 is the vacuum permittivity, c is the speed of light, and λ is the wavelength of the laser field. For a given quantization axis, which is typically set by an external magnetic field, we furthermore define θ_k (θ_p) as the angle between the propagation [31] (polarization) axis of the laser field and the quantization axis (see inset in Fig. 1). As shown in Ref. [17], the tensor product of Eq. (2) can be developed and the total light shift can be expressed as the sum of the scalar (U_s), vector (U_v), and tensor (U_t) light shift as follows:

$$\begin{aligned} U(\omega) &= -\frac{1}{2\epsilon_0 c} I(r)\alpha_{\text{tot}} = U_s + U_v + U_t \\ &= -\frac{1}{2\epsilon_0 c} I(r)\Bigg[\alpha_s(\omega) + |\mathbf{u}^* \times \mathbf{u}| \cos\theta_k \frac{m_J}{2J}\alpha_v(\omega) \\ &\quad + \frac{3m_J^2 - J(J+1)}{J(2J-1)} \frac{3\cos^2\theta_p - 1}{2}\alpha_t(\omega)\Bigg]. \end{aligned} \tag{3}$$

For convenience, we have explicitly separated the tensor and vector term into two parts. The first part depends on the angles, J and m_J, and the second part on ω and J. We refer to the latter as the polarizability coefficients $\{\alpha_s,\alpha_v,\alpha_t\}$ for the scalar, vector, and tensor part, respectively.

Because of their J, $\mathbf{u}$, and angle dependence, U_v and U_t vanish for special configurations. In particular, U_v vanishes for any linear polarization since $\mathbf{u}^* \equiv \mathbf{u}$ is a real vector, and thus $|\mathbf{u}^* \times \mathbf{u}| = 0$, and for elliptical polarization at $\theta_k = \pm 90^\circ$. U_t vanishes for $\cos\theta_{p0} = \sqrt{1/3}$, i.e., for $\theta_{p0} = 54.7^\circ$, or for $J = 1/2$. The latter condition is always fulfilled by alkali atomic species, which indeed have zero tensor light shift in the ground state. As we will discuss later, this is an important difference between alkali and magnetic Ln, such as Dy and Er, which have $J = 8$ and $J = 6$ in the ground state, respectively. Finally, we note that U_t shows a quadratic dependence on m_J, which paves the way for a selective manipulation of individual Zeeman substates.

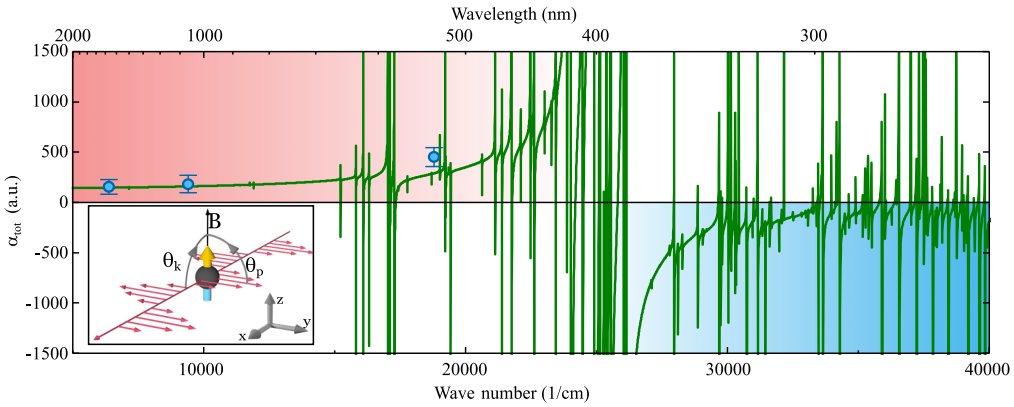

FIG. 1. Calculated (solid line) and measured (filled circles) atomic polarizability α_{tot} of Er in the ground state for $\theta_p = \theta_k = 90^\circ$ as a function of the light-field wave number and wavelength in atomic units. A divergence of the polarizability indicates an optical dipole transition. The finite amplitude of the peaks of the narrow transitions are an artifact caused by the finite number of calculated data points. The red and blue shadows indicate that there is a broad red-detuned region for long wavelengths without many resonances and also a mostly blue-detuned region in the ultraviolet range. The inset illustrates the configuration of angles θ_k and θ_p for the shown data. B denotes the orientation of the magnetic field.

The polarizability coefficients read as

$$\alpha_s(\omega) = -\frac{1}{\sqrt{3(2J+1)}}\alpha_J^{(0)}(\omega),$$
$$\alpha_v(\omega) = \sqrt{\frac{2J}{(J+1)(2J+1)}}\,\alpha_J^{(1)}(\omega), \quad (4)$$
$$\alpha_t(\omega) = \sqrt{\frac{2J(2J-1)}{3(J+1)(2J+1)(2J+3)}}\,\alpha_J^{(2)}(\omega),$$

where $\alpha_J^{(K)}(\omega)$, $K \in \{0,1,2\}$, is known as the coupled polarizability. To precisely calculate the value of the polarizability, it is necessary to know the parameters of each dipole-allowed transition, i.e., the energy of the transition $\hbar\omega_{JJ'}$ and the natural linewidth of the excited state $\gamma_{J'}$. In constant-sign convention [29], $\alpha_J^{(K)}(\omega)$ is indeed given by a sum-over-state formula over all dipole-allowed transitions ($\Delta J = 0,\pm 1$),

$$\alpha_J^{(K)}(\omega) = \sqrt{2K+1} \times \sum_{J'} (-1)^{J+J'} \times \begin{Bmatrix} 1 & K & 1 \\ J & J' & J \end{Bmatrix} |\langle J'||\mathbf{d}||J\rangle|^2 \times \frac{1}{\hbar}\mathrm{Re}\left[\frac{1}{\Delta^-_{J'J} - i\gamma_{J'}/2} + \frac{(-1)^K}{\Delta^+_{J'J} - i\gamma_{J'}/2}\right]. \quad (5)$$

Here, $|\langle J'||\mathbf{d}||J\rangle|$ is the reduced dipole transition element and $\Delta^{\pm}_{J'J} = \omega_{J'J} \pm \omega$. The curly brackets denote the Wigner 6-j symbol. Note that the imaginary part of the term in the squared brackets is connected to the off-resonant photon scattering rate. As will be discussed in the next section, a precise knowledge of the atomic spectrum is highly nontrivial for multielectron atomic species with submerged-shell structure and requires advanced spectroscopic calculations.

III. ATOMIC SPECTRUM OF ERBIUM

The submerged-shell electronic configurations of Er in its ground state reads as $[\mathrm{Xe}]4f^{12}6s^2$, accounting for a xenon core, an open inner f shell with a two-electron vacancy, and a closed s shell. The corresponding total angular momentum is $J = 6$, given by the sum of the orbital ($L = 5$) and the spin ($S = 1$) quantum number.

The calculated static polarizability of ground-state Er is 149 a.u. [32]. To calculate the dynamical one, $\alpha_{\mathrm{tot}}(\omega)$, we use Eqs. (3) and (5), based on the semiempirical electronic structure calculation from Ref. [18]. The result is shown in Fig. 1 for the case of light propagating along the x axis and linearly polarized along the y axis [$\theta_k = \theta_p = 90°$; see Fig. 1 (inset)]. Note that for this configuration, the vectorial contribution vanishes and the tensor part is maximally negative. The ground-state polarizability of Er is mainly determined by the strong optical transitions around 400 nm (see Supplemental Material [33]). The broadest transition is located at 401 nm with a natural width of $2\pi\times 29.7$ MHz [34]. Apart from the broad transitions, Er also features a number of narrow transitions. As indicated in Fig. 1 by the red-shaded region to the left of the strong resonances, i.e., for wavelengths above 500 nm, there is a large red-detuned region. To the right, i.e., for wavelengths below 380 nm, the atomic polarizability is mainly negative (blue-shaded region), which enables the realization of blue-detuned dipole traps for, e.g., boxlike potentials [35].

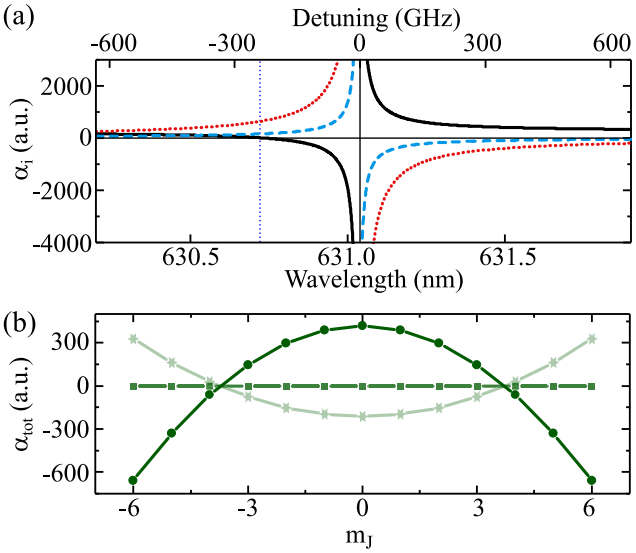

FIG. 2. Ground-state polarizability of Er in the proximity of a narrow optical transition at 631.04 nm with a linewidth of $2\pi\times 28$ kHz. (a) Polarizability coefficients α_s (solid line), α_v (dotted line), and α_t (dashed line) vs the laser-field wavelength. The vertical dotted line indicates the zero crossing of α_s. (b) Total polarizability α_{tot} as a function of m_J, identifying the different Zeeman sublevels of the ground-state manifold for $\theta_p = 90°$ (circles), $\theta_{p0} = 54.7°$ (squares), and $\theta_p = 0°$ (stars) calculated with Eq. (3) for $\theta_k = 90°$ at 630.7 nm, corresponding to the wavelength of the zero crossing of α_s.

As shown with Dy [23], narrow lines give prospects for state-dependent manipulation of atomic samples. We find that a promising candidate for spin manipulation is the transition coupling the ground state to the $J' = 7$ excited state at 631.04 nm with a natural linewidth of $2\pi\times 28$ kHz [36], which we investigate theoretically here. It is weak enough to allow near-resonant operation with comparatively low scattering rate and features large vector and tensor polarizabilities. Figure 2(a) shows the calculated values of α_s, α_v, and α_t of the ground state in the proximity of this optical transition, calculated with Eqs. (4) and (5). Interestingly, α_s has a sign opposite to α_v and α_t and crosses zero around 630.7 nm, where still very large vector (680 a.u.) and tensor (175 a.u.) polarizabilities persist. Such wavelengths are very interesting since they allow one to freely tune the total light shift by changing the polarization of the laser light. Figure 2(b) shows the total polarizability α_{tot} as a function of m_J calculated with Eq. (3) for the three angles $\theta_p \in \{0°, 54.7°, 90°\}$ at the zero crossing of the scalar polarizability for $\theta_k = 90°$. α_{tot} depends quadratically on m_J and can be tuned from positive to negative by changing θ_p, while keeping θ_k constant. By changing θ_k, the vertex of the parabola in Fig. 2 can be shifted towards higher or lower values of m_J, such that α_{tot} vanishes for a particular m_J state. Such a feature can, in principle, be used for a state-dependent manipulation or trapping of the atomic sample [37].

IV. MEASUREMENTS

To extract the polarizability of Er, we measure the light shift at three wavelengths: 532.26, 1064.5, and 1570.0 nm. In addition, we study the polarizability of one excited state, located at 17 157 $cm^{-1} \equiv 583$ nm with respect to the ground state for 1064.5 and 1570.0 nm. This optical line is particularly relevant for ultracold Er experiments since it is used as the laser-cooling transition in magneto-optical traps (MOT).

For the measurements, we initially cool down a sample of ^{168}Er in a MOT [38]. Here, the atoms are spin polarized to the lowest level of the ground-state Zeeman manifold ($J = 6$, $m_J = -6$). We then transfer the sample into a crossed-beam optical dipole trap at 1064 nm. We force evaporation by decreasing the power of the trapping laser following the procedure reported in [10] and cool the sample down to temperatures of several μK. All measurements of the light shift are performed at a magnetic offset field of 0.4 G. At this field, the Zeeman shift is large enough to have the atoms in a well-defined magnetic sublevel m_J so that Eq. (3) is valid.

A. Measurement of the ground-state polarizability

For the measurement of the polarizability at $\omega = 2\pi c/\lambda$, we load the thermal sample from the crossed-beam dipole trap into an optical dipole trap generated by a single focused beam, operating at the desired wavelength λ. Typical beam waists range from 18 to 46 μm. In this single-beam trap, the thermal sample reaches typical peak densities ranging from 10^{13} to 10^{14} cm^{-3} and temperatures of several μK. The propagation direction of the beam is illustrated in the inset of Fig. 1, i.e., with a magnetic field oriented along the z axis and $\theta_k = \theta_p = 90^\circ$.

We extract the corresponding light shift of the ground state by employing the standard technique of trap-frequency measurements. From the trapping frequencies, we infer the depth of the optical potential U, which in turn is related to $\alpha_{\rm tot}$ by Eq. (3). In harmonic approximation, for a Gaussian beam of power P, which propagates along the x axis with elliptical intensity profile $I(y,z) = I_0 \exp(-\frac{2y^2}{w_y} - \frac{2z^2}{w_z})$, beam waists w_y and w_z, and $I_0 = \frac{2P}{\pi w_y w_z}$, the depth of the induced dipole potential U_0 is related to the radial trapping frequencies by $\omega_i = \sqrt{-4U_0/(w_i^2 m)}$, where $i \in \{y,z\}$. m is the atomic mass, and $U_0 = -\frac{1}{2\epsilon_0 c}\alpha_{\rm tot}(\omega) I_0$. By combining the above expressions, we find the relation

$$\omega_i = \sqrt{\frac{4\alpha_{\rm tot} P}{\epsilon_0 c \pi w_y w_z w_i^2 m}}. \tag{6}$$

In Eq. (6), $\alpha_{\rm tot}$ is the only free parameter since we independently measure the w_i and P, as discussed later.

We measure the radial trapping frequencies along the y and the z axis by exciting center-of-mass oscillations and monitoring the time evolution of the position of the atomic cloud in time-of-flight images. To excite the center-of-mass oscillation, we instantly switch off the trapping beam for several hundreds of μs [39]. During this time, the atoms move due to gravity and residual magnetic field gradients. When the trapping beam is switched on again, the cloud starts to oscillate in the trap and we probe the oscillation frequencies $\nu_z = \omega_z/2\pi$ along the z axis and $\nu_y = \omega_y/2\pi$ along the y axis. In order to extract $\alpha_{\rm tot}$ from Eq. (6), we precisely measure the beam waists w_y and w_z. The most reliable measurements of the beam waists are performed by using the knife-edge method [40]. We measure the beam waists with an uncertainty of the order of 1%. Aberrations and imperfections of the trapping beams, however, introduce a systematic uncertainty in the measurement of the beam waists. We estimate a conservative upper bound for such an effect of 2 μm, which provides the largest source of uncertainty in the measurement of the polarizability. The corresponding systematic errors on $\alpha_{\rm tot}$ are up to about 35%. We measure the trap frequencies as a function of the laser powers P and we fit Eq. (6) to the measured frequencies, leaving $\alpha_{\rm tot}$ the only free fitting parameter.

We apply the above-described procedure to three different wavelengths of the trapping beam. The experimental and theoretical values for $\alpha_{\rm tot}$ are summarized in Table I. For completeness, we also give $\alpha_s^{\rm theor.}$. Comparatively speaking, at a wavelength of 1064.5 nm, we find that Er, as other Ln, exhibits a weaker polarizability as compared, for instance, to alkali atoms (e.g., 687.3(5) a.u. (calculated) for rubidium [41]). This is related to the submerged-shell electronic structure of Er and the so-called lanthanide contraction, resulting in valence electrons being more tightly bound to the atomic core, and so more difficult to polarize, than the single outermost electron of alkali atoms [18,42].

The comparison between the measured and calculated values shows an overall very good agreement, especially at $\lambda = 1064.5$ and 1570 nm. In this wavelength region, there are very sparse and weak optical transitions and the polarizability approaches its static value; see Fig. 1. At $\lambda = 532.26$ nm, we observe a larger deviation between experiment and theory. This can be due to the larger density of optical resonances in this wavelength region. Here, the calculated value of α_s is thus much more sensitive to the precise parameters of the optical line (i.e., energy position and strength). In addition, our theoretical model predicts a very narrow transition at 18 774 $cm^{-1} \equiv 532.7$ nm with a linewidth of $\gamma_{J'} = 6.2\times10^3$ s^{-1}.

We point out that as a result of our improved methodology to calculate transition probabilities, the theory value of $\alpha_s = 173$ a.u. at $\lambda = 1064.5$ nm is slightly larger than the one previously reported in [18]. In particular, our present calculations use a refined value of the scaling factor on monoelectronic transition dipole moments (Er^+) [43], which is now equal to 0.807.

As previously discussed, Ln exhibit an anisotropic light shift, arising from the sizable tensor contribution to the total polarizability [see Eq. (3)]. This distinctive feature has been experimentally observed in Dy in the proximity of a narrow optical transition [23]. Here, we address this aspect with Er atoms by measuring the light shift in the ground state and its angle dependence at 532.26 and 1064.5 nm. At these wavelengths, our theory predicts that α_t for the ground state is of the order of a few percent of α_s. To isolate this small contribution and to clear the systematic uncertainties, which could potentially mask the effect, we probe the tensor-to-scalar polarizability ratio as follows. We first prepare the ultracold Er sample in the lowest Zeeman sublevel ($m_j = -6$) in the optical trap, operated at the desired wavelength. We then extract the angle-dependent light shift by repeating the measurements of

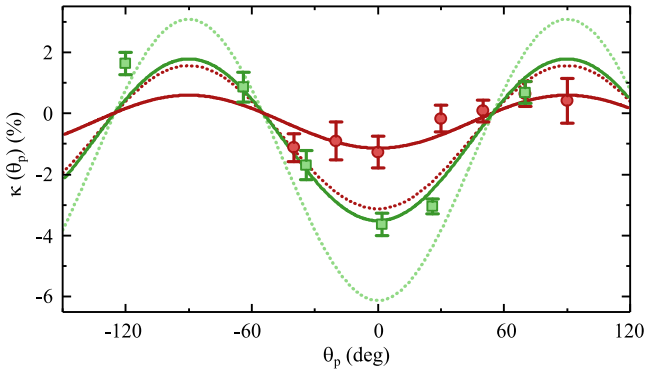

FIG. 3. Anisotropic polarizability of Er atoms in the ground state. The plot shows the relative change of the light shift at 532.26 nm (squares) and 1064.5 nm (circles) for $\theta_k = 90^\circ$ as a function of θ_p. The variation of the total light shift unambiguously reveals the tensor polarizability, which vanishes for an angle of $\theta_p \approx 54.7^\circ$. The lines are fits to the data with Eq. (3). The error bars indicate the statistical uncertainties from the trapping-frequency measurements. The dotted lines represent the theory prediction.

the trap frequencies for different values of θ_p. This is done by either rotating the magnetic field, while keeping an horizontal polarization of the trapping light, or by rotating the polarization axis of the trapping light at a constant magnetic field. In both measurements, we choose $\theta_k = 90^\circ$ such that the vector light shift vanishes. Hence, the total light shift comes only from α_s and α_t. Since the scalar light shift is independent of θ_p, a dependence of the total light shift on θ_p is only caused by α_t. We quantify this variation by the relative change of the light shift,

$$\kappa(\theta_p) = \frac{U - U_s}{U_s} = \frac{U_t}{U_s} = \frac{\omega(\theta_p)^2 - \omega(\theta_{p0})^2}{\omega(\theta_{p0})^2}$$
$$= \frac{3m_J^2 - J(J+1)}{J(2J-1)} \frac{3\cos^2\theta_p - 1}{2} \frac{\alpha_t}{\alpha_s}. \quad (7)$$

Note that the first factor in the second line of Eq. (7) is equal to one for $|J,m_J\rangle = |6,-6\rangle$, such that the peak-to-peak variation of $\kappa(\theta_p)$ corresponds to $\kappa_0 = 1.5 \times \frac{\alpha_t}{\alpha_s}$. Figure 3 shows $\kappa(\theta_p)$ for 532.26 and 1064.5 nm. At both wavelengths, the data show the expected sinusoidal dependence of κ on θ_p. We fit Eq. (7) to the data and extract κ_0 and α_t. Our results are summarized in Table I. The systematic uncertainties of α_t are obtained by error propagating the systematical errors of α_s. We observe that α_t for the ground state gives only a few-percent contribution to the total atomic polarizability. However, the corresponding tensor light shift for the typical power employed in optical trapping can already play an important role in spin-excitation phenomena in Er quantum gases [44].

Given the complexity of the Er atomic spectrum and the small tensorial contribution, the good agreement between the theoretical predictions of α_t and the experimental value for both investigated wavelengths is remarkable. The slightly smaller values extracted from the experiments can be due to additional systematic effects in the measurements. For comparison, we note that at 1064 nm, κ_0 for ground-state Er is slightly larger than the one for Dy, which was predicted to be around $\kappa_{0,\mathrm{Dy}}^{\mathrm{theor.}} = 1.1\%$ [15], and larger than the one of Cr atoms, which was calculated to be $\kappa_{0,\mathrm{Cr}}^{\mathrm{theor.}} = 0.5\%$ (at 1075 nm) [25] but was then measured to be significantly lower [24]. In Cr experiments, the tensorial contribution to the total light shift was then enhanced by using near-resonant light.

B. Measurement of the excited-state polarizability

Although small in the ground state, α_t is expected to be substantially larger in the excited state. Therefore, measuring the 583 nm excited-state polarizability provides a further test of the level calculations. To extract the excited-state polarizability, we measure the shift of the atomic resonance in the dipole trap. As is depicted in Fig. 4(a), the dipole trap induces a light shift not only to the ground state, but also to the excited state. To measure the excited-state light shift, we prepare the atomic sample as described above and apply a short pulse of a circularly polarized probe light at 583 nm to the sample. This light couples the ground-state $|J,m_J\rangle = |6,-6\rangle$ level to the $|J',m_J'\rangle = |7,-7\rangle$ sublevel of the excited-state manifold of energy 17 157 cm^{-1} ($[\mathrm{Xe}]4f^{12}6s6p(^3P_1)$). We find a resonant atom loss when the frequency of the probe light matches the energy difference between the ground and the excited state. By scanning the frequency of the probe light, we extract the resonance frequency. This frequency is shifted from that of the bare optical transition by the sum of the ground-state polarizability and the excited-state polarizability. Subtracting the ground-state shift reveals the light shift of the excited state. For this, we use the experimental values of the ground-state polarizability that are reported here and neglect the angle dependence thereof since its anisotropy is two orders of magnitude smaller than the anisotropy of the excited state.

TABLE I. Experimental and theoretical polarizabilities for Er of the ground state (0 cm^{-1}) and of the 583 nm excited state (17 157 cm^{-1}) for three laser wavelengths λ. α_{tot} for experiment and theory is given for the case $\theta_p = \theta_k = 90^\circ$. The relative change of the light shift κ_0 (see text) and the tensor polarizability coefficient α_t for the ground state and for the excited state are displayed. The polarizability is given in atomic units. To convert atomic units into SI units, use a factor of $\alpha[\mathrm{Hz/(W\,mm^{-2})}] = \alpha[\mathrm{a.u.}] \times 1.6488 \times 10^{-35}/2h\epsilon_0 c$. For $\alpha_s^{\mathrm{expt.}}$, we give statistical and systematic errors, respectively (see text).

E (cm^{-1})	λ (nm)	$\alpha_{\mathrm{tot}}^{\mathrm{expt.}}$ (a.u.)	$\alpha_{\mathrm{tot}}^{\mathrm{theor.}}$ (a.u.)	$\alpha_s^{\mathrm{theor.}}$ (a.u.)	$\kappa_0^{\mathrm{expt.}}$ (%)	$\kappa_0^{\mathrm{theor.}}$ (%)	$\alpha_t^{\mathrm{expt.}}$ (a.u.)	$\alpha_t^{\mathrm{theor.}}$ (a.u.)
0	532.26	$(430 \pm 8_{\mathrm{stat.}} \pm 80_{\mathrm{syst.}})$	317	308	(-5.3 ± 1)	−9.2	$(-15 \pm 3_{\mathrm{stat.}} \pm 6_{\mathrm{syst.}})$	−19
0	1064.5	$(166 \pm 3_{\mathrm{stat.}} \pm 61_{\mathrm{syst.}})$	176	173	(-1.8 ± 0.8)	−4.7	$(-1.9 \pm 0.8_{\mathrm{stat.}} \pm 1.2_{\mathrm{syst.}})$	−5.4
0	1570.0	$(163 \pm 9_{\mathrm{stat.}} \pm 36_{\mathrm{syst.}})$	162	159		−4.1		−4.3
		$\alpha_s^{\mathrm{expt.}}$ (a.u.)						
17157	1064.5	$(66.6 \pm 0.5_{\mathrm{stat.}} \pm 28_{\mathrm{syst.}})$		91	(-25.6 ± 1.6)	−29.7	$(-11.3 \pm 0.5_{\mathrm{stat.}} \pm 2.0_{\mathrm{syst.}})$	−18
17157	1570.0	$(-203 \pm 9_{\mathrm{stat.}} \pm 50_{\mathrm{syst.}})$		−254	(104 ± 6)	40.4	$(-141 \pm 9_{\mathrm{stat.}} \pm 19_{\mathrm{syst.}})$	−68.5

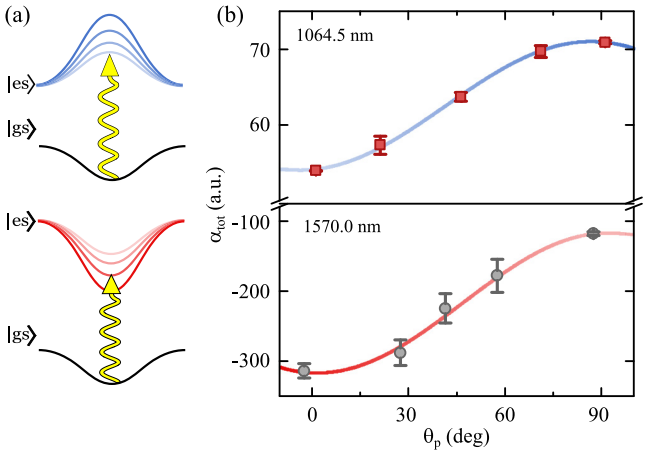

FIG. 4. 583 nm excited-state polarizability. (a) Illustration of the energy of atoms in an optical dipole trap with Gaussian shape. The upper (lower) panel indicates the case with the excited-state polarizability negative (positive). We measure the shift of the bare atomic resonance in the optical dipole trap (see text) for different values of θ_p (dark-to-light red and light-to-dark blue). This shift is given by the sum of the light shifts in the ground and in the excited state ($|J,m_J\rangle = |6,-6\rangle \rightarrow |J',m_{J'}\rangle = |7,-7\rangle$). To extract the excited-state light shift, we subtract the ground-state shift. (b) 583 nm excited-state polarizability for 1064.5 nm (red squares) and for 1570.0 nm (gray circles). The solid lines indicate fits to the data.

We repeat this measurement for various values of θ_p and find a large angle dependence, as we show in Fig. 4(b), for 1064.5 and 1570 nm. This is expected due to the highly anisotropic wave function of the $6p$ electron in the 583 nm excited state. From our data, similarly to the ground-state measurements, we extract both the scalar and the tensor polarizability coefficients. The results and the theoretical calculations are presented in the lower section of Table I. The scalar polarizability coefficient agrees within the error with the theoretical expectations, indicating a good understanding of the excited-state polarizability. The tensor polarizability coefficients qualitatively match well with the theoretical values. The quantitative disagreement by up to a factor of two is probably caused by uncertainties in the parameters of strong transitions close by.

V. CONCLUSION AND OUTLOOK

In this paper, we presented measurements of the scalar and tensor polarizability of Er atoms in the ground and the 583 nm excited state for three wavelengths. Our results qualitatively agree with our theoretical calculations of the polarizability and prove a good understanding of the level structure of Er. A similarly comprehensive picture of the correspondence between theoretical and experimental values of polarizability in Dy is still pending [8,15,23].

For 1064.5 and 1570.0 nm, we find excellent agreement of the scalar polarizability. For 532.26 nm, we observe that the measured value of α_s deviates from the calculated value, which we attribute to the proximity to optical transitions. The measured tensor polarizabilities at 532.26 and 1064.5 nm are of the order of a few percent with respect to the scalar polarizabilities and qualitatively agree with the theoretical values.

The polarizability of the 583 nm excited state was measured to be positive (negative) for 1064.5 nm (1570 nm), in agreement with the theory. Further it shows a large anisotropy due to the highly anisotropic electronic configuration around the core. Our measured values qualitatively agree with the calculations.

As was discussed, the anisotropic polarizability does not only depend on the angle between the quantization axis and the polarization of the light, but also gives rise to a m_J dependence of the total light shift. This can be of great importance for experiments with Ln since it allows for the deterministic preparation or the manipulation of spin states or for the realization of state- or species-dependent optical dipole traps.

ACKNOWLEDGMENTS

We thank R. Grimm, M. Mark, E. Kirilov, G. Natale, and V. Kokoouline for fruitful discussions. M.L., J.-F.W., and O.D. acknowledge support from "DIM Nano-K" under the project "InterDy," and from "Agence Nationale de la Recherche" (ANR) under the project "COPOMOL" (Contract No. ANR-13-IS04-0004-01). The Innsbruck group is supported through an ERC Consolidator Grant (RARE, No. 681432) and a FET Proactive project (RySQ, No. 640378) of the EU H2020. The Innsbruck group thanks the Deutsche Forschungsgemeinschaft/Wissenschaftsfonds FWF (FOR2247).

J.H.B. and S.B. contributed equally to this work.

[1] I. Bloch, J. Dalibard, and W. Zwerger, Rev. Mod. Phys. **80**, 885 (2008).

[2] K. D. Bonin and V. V. Kresin, *Electric-Dipole Polarizabilities of Atoms, Molecules, and Clusters* (World Scientific, Singapore, 1997).

[3] J. Mitroy, M. S. Safronova, and C. W. Clark, J. Phys. B **43**, 202001 (2010).

[4] P. Schwerdtfeger, *Table of Experimental and Calculated Static Dipole Polarizabilities for the Electronic Ground States of the Neutral Elements (in Atomic Units)*, Centre for Theoretical Chemistry and Physics (Massey University, North Shore City, New Zealand, 2015).

[5] M. D. Gregoire, I. Hromada, W. F. Holmgren, R. Trubko, and A. D. Cronin, Phys. Rev. A **92**, 052513 (2015).

[6] Y. Takasu, K. Maki, K. Komori, T. Takano, K. Honda, M. Kumakura, T. Yabuzaki, and Y. Takahashi, Phys. Rev. Lett. **91**, 040404 (2003).

[7] T. Fukuhara, Y. Takasu, M. Kumakura, and Y. Takahashi, Phys. Rev. Lett. **98**, 030401 (2007).

[8] M. Lu, N. Q. Burdick, S. H. Youn, and B. L. Lev, Phys. Rev. Lett. **107**, 190401 (2011).

[9] M. Lu, N. Q. Burdick, and B. L. Lev, Phys. Rev. Lett. **108**, 215301 (2012).

[10] K. Aikawa, A. Frisch, M. Mark, S. Baier, A. Rietzler, R. Grimm, and F. Ferlaino, Phys. Rev. Lett. **108**, 210401 (2012).
[11] K. Aikawa, A. Frisch, M. Mark, S. Baier, R. Grimm, and F. Ferlaino, Phys. Rev. Lett. **112**, 010404 (2014).
[12] R. V. Krems, G. C. Groenenboom, and A. Dalgarno, J. Phys. Chem. A **108**, 8941 (2004).
[13] C. B. Connolly, Y. S. Au, S. C. Doret, W. Ketterle, and J. M. Doyle, Phys. Rev. A **81**, 010702 (2010).
[14] X. Chu, A. Dalgarno, and G. C. Groenenboom, Phys. Rev. A **75**, 032723 (2007).
[15] H. Li, J.-F. Wyart, O. Dulieu, S. Nascimbène, and M. Lepers, J. Phys. B **50**, 014005 (2017).
[16] V. A. Dzuba, V. V. Flambaum, and B. L. Lev, Phys. Rev. A **83**, 032502 (2011).
[17] H. Li, J.-F. Wyart, O. Dulieu, and M. Lepers, Phys. Rev. A **95**, 062508 (2017).
[18] M. Lepers, J.-F. Wyart, and O. Dulieu, Phys. Rev. A **89**, 022505 (2014).
[19] D. Sukachev, S. Fedorov, I. Tolstikhina, D. Tregubov, E. Kalganova, G. Vishnyakova, A. Golovizin, N. Kolachevsky, K. Khabarova, and V. Sorokin, Phys. Rev. A **94**, 022512 (2016).
[20] A. Golovizin, E. Kalganova, D. Sukachev, G. Vishnyakova, D. Tregubov, K. Khabarova, V. Sorokin, and N. Kolachevsky, Quantum Electron. **47**, 479 (2017).
[21] M. Miranda, R. Inoue, Y. Okuyama, A. Nakamoto, and M. Kozuma, Phys. Rev. A **91**, 063414 (2015).
[22] N. Q. Burdick, Y. Tang, and B. L. Lev, Phys. Rev. X **6**, 031022 (2016).
[23] W. Kao, Y. Tang, N. Q. Burdick, and B. L. Lev, Opt. Express **25**, 3411 (2017).
[24] A. de Paz, A. Sharma, A. Chotia, E. Maréchal, J. H. Huckans, P. Pedri, L. Santos, O. Gorceix, L. Vernac, and B. Laburthe-Tolra, Phys. Rev. Lett. **111**, 185305 (2013).
[25] R. Chicireanu, Q. Beaufils, A. Pouderous, B. Laburthe-Tolra, É. Maréchal, L. Vernac, J.-C. Keller, and O. Gorceix, Eur. Phys. J. D **45**, 189 (2007).
[26] B. Neyenhuis, B. Yan, S. A. Moses, J. P. Covey, A. Chotia, A. Petrov, S. Kotochigova, J. Ye, and D. S. Jin, Phys. Rev. Lett. **109**, 230403 (2012).
[27] M. Deiß, B. Drews, B. Deissler, and J. Hecker Denschlag, Phys. Rev. Lett. **113**, 233004 (2014).
[28] P. D. Gregory, J. A. Blackmore, J. Aldegunde, J. M. Hutson, and S. L. Cornish, Phys. Rev. A **96**, 021402 (2017).
[29] R. Vexiau, D. Borsalino, M. Lepers, A. Orbán, M. Aymar, O. Dulieu, and N. Bouloufa-Maafa, Int. Rev. Phys. Chem. **36**, 709 (2017).
[30] F. Le Kien, P. Schneeweiss, and A. Rauschenbeutel, Eur. Phys. J. D **67**, 92 (2013).
[31] In fact, θ_k is the angle between the vector defined by $\mathbf{u}^* \times \mathbf{u}$ and the magnetic field. It changes sign when going from right to left circular polarization.
[32] This value is obtained using the improved calculations developed in this work and is slightly higher than the value 141 a.u. reported in Ref. [18].
[33] See Supplemental Material at http://link.aps.org/supplemental/10.1103/PhysRevA.97.012509 for the parameters of the transitions that were used to calculate the ground-state polarizability.
[34] A. Frisch, Ph.D. thesis, Innsbruck, Austria, 2014.
[35] B. Mukherjee, Z. Yan, P. B. Patel, Z. Hadzibabic, T. Yefsah, J. Struck, and M. W. Zwierlein, Phys. Rev. Lett. **118**, 123401 (2017).
[36] H. Y. Ban, M. Jacka, J. L. Hanssen, J. Reader, and J. J. McClelland, Opt. Express **13**, 3185 (2005).
[37] B. Yang, H.-N. Dai, H. Sun, A. Reingruber, Z.-S. Yuan, and J.-W. Pan, Phys. Rev. A **96**, 011602 (2017).
[38] A. Frisch, K. Aikawa, M. Mark, A. Rietzler, J. Schindler, E. Zupanič, R. Grimm, and F. Ferlaino, Phys. Rev. A **85**, 051401 (2012).
[39] The exact timing depends on the trap parameters.
[40] We use a mirror directly in front of the viewport of our science chamber and reflect the trapping beam such that we perform the measurement of the waists as close to the atomic sample as possible. We measure the beam diameter at different positions along the beam with a knife-edge method [45] and extract the waist with a fit to the measured beam diameters.
[41] B. Arora and B. K. Sahoo, Phys. Rev. A **86**, 033416 (2012).
[42] S. Cotton, in *Lanthanide and Actinide Chemistry* (Wiley, West Sussex, England, 2013), pp. 9–22.
[43] M. Lepers, Y. Hong, J. F. Wyart, and O. Dulieu, Phys. Rev. A **93**, 011401 (2016).
[44] S. Baier *et al.* (unpublished).
[45] J. M. Khosrofian and B. A. Garetz, Appl. Opt. **22**, 3406 (1983).

A.3. Publication: Observation of roton mode population in a dipolar quantum gas[†‡]

Nature Physics **14**, 442 (2018)
submitted 12 Dec 2017; published 05 Mar 2018
DOI 10.1038/s41567-018-0054-7

Lauriane Chomaz,[1] Rick M. W. van Bijnen,[2] Daniel Petter,[1] Giulia Faraoni,[1,3] Simon Baier,[1] Jan Hendrik Becher,[1] Manfred J. Mark,[1,2] Falk Wächtler,[4] Luis Santos,[4] F. Ferlaino[1,2]

[1] *Institut für Experimentalphysik, Universität Innsbruck, Technikerstraße 25, 6020 Innsbruck, Austria*
[2] *Institut für Quantenoptik und Quanteninformation, Österreichische Akademie der Wissenschaften, 6020 Innsbruck, Austria*
[3] *Dipartimento di Fisica e Astronomia, Università di Firenze, Via Sansone 1, 50019 Sesto Fiorentino, Italy*
[4] *Institut für Theoretische Physik, Leibniz Universität Hannover, Appelstrasse 2, 30167 Hannover, Germany*

[†] The author of the present thesis helped in performing the measurements, and contributed in writing the manuscript. The theoretical calculations of this publication have been contributed by R. v. B., F. W., and L. S.

[‡] The pre-print version of the publication is attached for online access of this thesis.

Observation of the Roton Mode in a Dipolar Quantum Gas

L. Chomaz[1], R. M. W. van Bijnen[2], D. Petter[1], G. Faraoni[1,3], S. Baier[1],
J. H. Becher[1], M. J. Mark[1,2], F. Wächtler[4], L. Santos[4], F. Ferlaino[1,2,*]
[1] *Institut für Experimentalphysik, Universität Innsbruck, Technikerstraße 25, 6020 Innsbruck, Austria*
[2] *Institut für Quantenoptik und Quanteninformation, Österreichische Akademie der Wissenschaften, 6020 Innsbruck, Austria*
[3] *Dipartimento di Fisica e Astronomia, Università di Firenze, Via Sansone 1, 50019 Sesto Fiorentino, Italy*
[4] *Institut für Theoretische Physik, Leibniz Universität Hannover, Appelstr. 2, 30167 Hannover, Germany*
(Dated: May 22, 2017)

The concept of a roton, a special kind of elementary excitation, forming a minimum of energy at finite momentum, has been essential to understand the properties of superfluid ^{4}He. In quantum liquids, rotons arise from strong interparticle interactions, whose microscopic description remains debated. In the realm of highly-controllable quantum gases, a roton mode has been predicted to emerge due to dipolar interparticle interactions despite of their weakly-interacting character. Yet it has remained elusive to observations. Here we report momentum-distribution measurements in dipolar quantum gases of highly-magnetic erbium atoms, revealing the existence of the long-sought roton. We observe the appearance of peculiar peaks at well-defined momentum matching the inverse of the tight confinement length as expected for dipolar rotons. Our combined theoretical and experimental work demonstrates unambiguously the roton softening of the excitation spectrum and provides a further step in the quest towards supersolidity.

Introduction

Quantum properties of matter continuously challenge our intuition, especially when many-body effects emerge at a macroscopic scale. In this regard, the phenomenon of superfluidity is a paradigmatic case, which continues to reveal fascinating facets since its discovery in the late 1930s [1, 2]. A major breakthrough in understanding superfluidity thrived on the concept of *quasiparticles*, introduced by Landau in 1941 [3]. Quasiparticles are elementary excitations of momentum k, whose energies ϵ define the dispersion (energy-momentum) relation $\epsilon(k)$.

To explain the special thermodynamic properties of superfluid ^{4}He, Landau postulated the existence of two types of low-energy quasiparticles: phonons, referring to low-k acoustic waves, and rotons, gapped excitations at finite k initially interpreted as elementary vortices. These two types of excitations were later unified in a unique dispersion relation [4], which continuously evolves from linear at low k (phonons) to parabolic-like with a minimum (roton) at a finite $k = k_{\mathrm{rot}}$. Neutron scattering experiments confirmed Landau's remarkable intuition [5]. In liquid ^{4}He, k_{rot} scales as the inverse of the interatomic distance. This manifests a tendency of the system to establish a local order, which is driven by the strong correlations among the atoms. Yet, the same strongly-correlated nature of helium handicaps a microscopic understanding from first principles of the roton properties [1, 6].

In the realm of low-temperature quantum physics, ultra-cold quantum gases realise the other extreme limit for which the interparticle interactions - and correlations - are weak, meaning that classically their range of action is much smaller than the mean interparticle distance [2, 7]. Because of this diluteness, roton excitations are typically absent in ordinary quantum gases, i. e. in Bose-Einstein condensates (BECs) with contact interactions [2]. However, the degree of tunability in BECs is remarkable and a roton-like softening has been induced in hybrid systems via cavity-mediated interactions [8], and in spin-orbit-coupled BECs [9] and quantum gases in shaken optical lattices [10] by engineering the single-particle dispersion relation.

About 15 years ago, the existence of a roton minimum was theoretically predicted in BECs with dipole-dipole interactions (DDI) [11, 12]. The DDI is long-range and anisotropic; in particular it can change sign depending on the dipole configuration, being attractive for head-to-tail dipoles and repulsive for side-by-side ones (Fig. 1a). Despite the weakly-interacting character of the gas, the roton minimum in dipolar BECs (dBECs) is genuinely interaction-induced as in superfluid ^{4}He. However, in contrast to helium, the dispersion minimum originates from the peculiar k-dependence of the DDI rather than from strong correlations (Fig. 1b).

The realisation of a roton minimum in dBECs would allow for an unprecedented degree of control and microscopic understanding of the roton properties unavailable in helium physics. This prospect has triggered remarkable theoretical works, devoted to unveil the special properties of the dipolar roton and to link them to experimental observables [13–27]. Despite the maturity achieved in the theoretical understanding, the observation of dipolar roton modes has remained so far an elusive goal. For a long time, the only dBEC available in experiments consisted of chromium atoms [28, 29], for which the achievable dipolar character is hardly sufficient to support a roton mode. With the advent of the more magnetic lan-

thanide atoms [30, 31], a broader range of dipolar parameters became available, providing new prospects for the observation of rotons.

A. Roton mode in dBECs and its signature

To elucidate the mechanism of rotonization in dBECs, it is instructive to first review the case of cylindrically symmetric pancake traps with the dipoles aligned along the symmetry axis z (Fig. 1e1) [11, 13, 15–27]. In this quasi-two-dimensional (q2D) geometry, we consider elementary excitations of planar momentum k, corresponding to in-plane density modulations of wavelength $2\pi/k$ (Fig. 1c-d). In a mean-field picture, the energy cost to create such an excitation, $\epsilon(k)$, arises from both kinetic and interparticle interaction contributions. The latter includes the contact interaction and the DDI, and the DDI changes sign with k because of the much stronger confinement along z. At low k, the repulsive nature of the in-plane DDI prevails, stiffening the dispersion relation (Fig. 1c). In contrast, for $k\ell_z \gtrsim 1$, ℓ_z being the transverse confinement length, the three-dimensional (3D) nature of the excitation is reestablished and the attractive part of the DDI dominates, softening $\epsilon(k)$ (Fig. 1d). This softening is counterbalanced by the contributions of the repulsive interactions, namely the contact interaction at positive scattering length a_s, and of the kinetic energy, increasing with k. For very large k, the kinetic energy cost prevails and $\epsilon(k)$ eventually bends up into a single-particle spectrum. For strong-enough DDI, the dipole-induced softening dominates at intermediate momenta, and $\epsilon(k)$ develops a minimum at $k_{\rm rot} \sim 1/\ell_z$ [11] (Fig. 1b).

Ultracold atoms allow to regulate the impact of the DDI in $\epsilon(k)$ by tuning the value of a_s through a Feshbach resonance (FR) [32]. This provides a powerful control knob for the roton physics that is absent in the ^{4}He case. The figure of merit is the parameter $\epsilon_{\rm dd} = a_{\rm dd}/a_s$, defined as the ratio between the dipolar length, $a_{\rm dd} = \mu_0\mu^2 m/12\pi\hbar^2$, and a_s. Here m is the mass and μ the magnetic moment of the atoms. Increasing $\epsilon_{\rm dd}$ (decreasing a_s) mitigates the energy cost for large-k excitations and the system can develop a roton minimum in $\epsilon(k)$. By further increasing $\epsilon_{\rm dd}$, the roton gap, $\Delta = \epsilon(k_{\rm rot})$, decreases and eventually vanishes (Fig. 1b). In the latter case, the system undergoes a *local* instability [18, 19] and develops a short-wavelength density modulation on the scale of $1/k_{\rm rot}$, , resembling the case of the expected superfluid-to-solid transition in overpressurized ^{4}He [33].

When the dBEC spectrum gets deeply rotonized (i. e. small Δ), the momentum distribution can be profoundly modified, providing a signature for the effect. In q2D geometries (Fig. 1e1), the excitation softening develops in plane - both in the x and y directions. This leads to a *radial* roton corresponding to a set of in-plane momenta $\boldsymbol{k}$ of $|\boldsymbol{k}| = k_{\rm rot}$. The privileged population of these modes translates into the emergence of a ring of radius $k_{\rm rot}$ in the momentum distribution (Fig. 1e2).

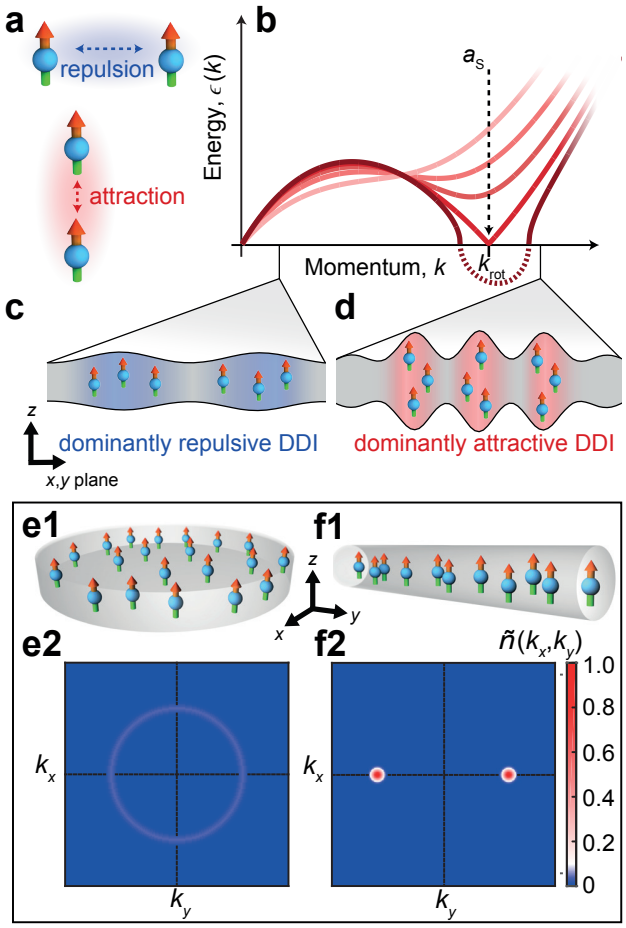

Figure 1 | Roton mode in a dBEC. **a**, dipole orientations with repulsive (blue) and attractive (red) DDI. **b**, illustration of the dispersion relation with real (solid lines) and imaginary (norm of the dotted line) parts of a dBEC in constrained geometries (see **e1-f1**) and varying a_s (dashed arrow) [11]. **c-d**, spatial density modulations associated to small- (**c**) and large-k (**d**) excitations. The shape along z and the color gradient illustrate the density modulation. The color code, following that of **a**, pictures the dominant DDI contribution to $\epsilon(k)$. In **b**, a roton emerges at $k_{\rm rot}$ when the attractive DDI prevails. In q2D geometries (**e1**), the roton in-plane momentum distribution shows a ring (**e2**). **f1** illustrates the advantageous q1D geometry, where the roton momentum distribution is double-peaked (**f2**). **e2** and **f2** have the same total population.

Here we extend the roton physics to a largely unexplored geometry: that of axially elongated dBECs with dipoles oriented orthogonally to the elongation axis y (Fig. 1f1). Although the above energy arguments equally apply to this quasi-one-dimensional (q1D) geometry, the axial elongation provides an important difference. Here, the system develops a *linear* roton mode corresponding

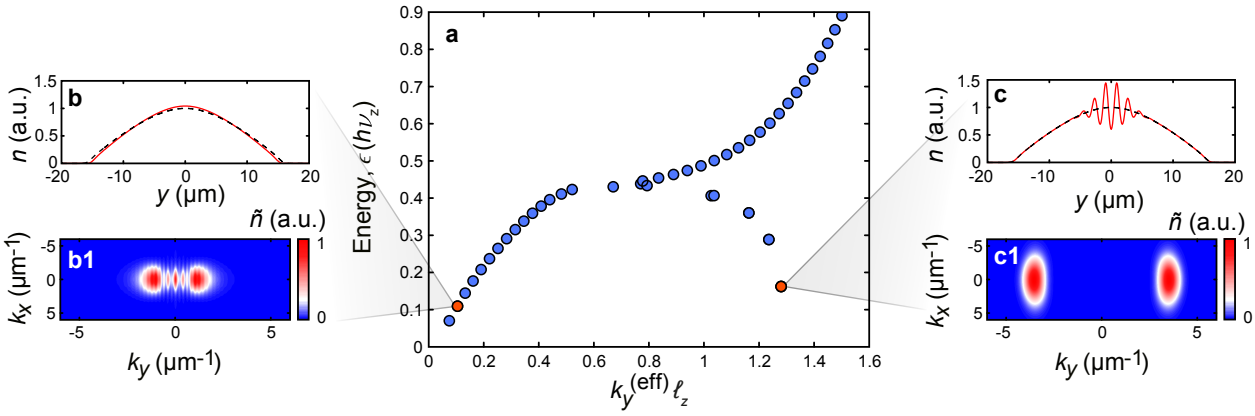

Figure 2 | BdG excitation spectrum. **a**, Excitation spectrum of the ground state of a BEC with $N = 50.000$ ^{166}Er atoms in a trap with $(\nu_x, \nu_y, \nu_z) = (267, 32, 456)$ Hz and scattering length $a_s = 43.75\, a_0$, obtained by numerically solving the BdG equations. Roton modes appear as isolated modes lying below the main branch of the spectrum, forming a 'roton finger'. The lowest roton mode and an exemplary phonon mode are highlighted, with panels **b**, **c** showing the corresponding excited state density modulation (with black dashed line the ground state, red solid line the excited state) and, **b1**, **c1**, the momentum distribution from 30 ms ToF expansion (Methods). **b, b1** phonon mode, **c, c1** roton mode.

to a narrow set of $\boldsymbol{k}$ with y component $k_y = \pm k_{\mathrm{rot}}$. As a consequence, the privileged population of this mode translates into two marked peaks in the momentum distribution (Fig. 1f2). This geometrical focusing of the roton population greatly enhances the visibility of the effect compared to the q2D case (Fig. 1e2-f2).

B. Rotonized dispersion relation in q1D dBECs

The existence of a roton minimum in our q1D geometry is well explained by a simplified model inspired from the uniform q2D calculations [11]. Here we consider that the condensate is trapped along x and z, with harmonic frequencies ν_x and ν_z, but homogeneous, i.e. unconfined, along the axis y. The physics of the dBEC is well captured by a non-local Gross-Pitaevskii equation (NLGPE) [2, 34], which contains the transverse confinement, the short-range interactions, and the DDI (Methods). Within the Thomas-Fermi (TF) approximation, the BEC density takes the simple form $n(x,z) = n_0\left(1-(x/X)^2-(z/Z)^2\right)$, with n_0 the homogeneous axial density [12] (Methods). The excitation spectrum is obtained from the linearisation of the NLGPE around the ground-state wavefunction $\sqrt{n(x,z)}$. Due to the homogeneity along y, the elementary excitations have a well-defined momentum k_y. Proceeding as in Ref. [11], we obtain an analytic form for $\epsilon(k_y)$ in the relevant case of 3D modes, i. e. for $k_y Z \gg 1$ (Methods). For dominant DDI ($\epsilon_{dd} \geq 1$), $\epsilon(k_y)$ indeed rotonizes. In the vicinity of the roton minimum the dispersion acquires a gapped quadratic form similar to that of helium rotons:

$$\epsilon(k_y)^2 \simeq \Delta^2 + \frac{2\hbar^2 k_{\mathrm{rot}}^2}{m}\frac{\hbar^2}{2m}(k_y - k_{\mathrm{rot}})^2 \qquad (1)$$

for $\epsilon_{\mathrm{dd}} \sim 1$. Here the roton momentum is $k_{\mathrm{rot}} = \sqrt{2mE_I}/\hbar$, with $E_I = 2gn_0(\epsilon_{dd}-1)/3$ and $g = 4\pi\hbar^2 a_s/m$, while its gap reads $\Delta = \sqrt{E_0^2 - E_I^2}$, with $E_0^2 = 2g\epsilon_{dd}n_0\frac{\hbar^2}{2m}\left(X^{-2}+Z^{-2}\right)$. Note that the TF radii X and Z can be evaluated as functions of $\nu_{x,z}$, ϵ_{dd} and gn_0 [12] and in particular $X^2, Z^2 \propto gn_0$. Then, close to the instability, $\Delta \simeq 0$, k_{rot} takes the simple form $k_{\mathrm{rot}} = \kappa/\ell_z$ with $\ell_z = \sqrt{\hbar/2\pi m\nu_z}$ and a geometrical factor κ that depends only on ν_z/ν_x (Methods). In the case $\nu_z/\nu_x = 1$, $\kappa = 1.74$.

To move beyond this simplified model and closer to realistic experimental conditions, we develop a numerical approach based on the 3D NLGPE for a generic anisotropic harmonic confinement of frequencies $\nu_{x,y,z}$ (Methods) [14]. For a quantitative understanding of the experiments, our numerical treatment also includes quantum fluctuations (i. e. local Lee-Huang-Yang (LHY) corrections) [35–41], finite temperature effects [37, 42], and three-body losses [43] (Methods). Our numerical platform offers rich possibilities to investigate the physics at play: it allows for real-time evolution of the quantum gas wavefunction, and provides access to the Bogoliubov-de Gennes (BdG) excitation spectrum.

The excitation spectrum is obtained by linearizing the NLGPE around a stationary state and numerically solving the resulting BdG equations (Methods) [44]. The calculated spectrum is qualitatively modified compared to that of an homogeneous system (Fig. 2). In order to depict the spectrum as a quasi-dispersion relation even in the presence of an axial confinement, we associate to each elementary excitation an effective momentum $k_y^{(\mathrm{eff})} = \langle k_y^2\rangle^{1/2}$ [17]. The spectrum is discrete with phonon-like collective modes at low $k_y^{(\mathrm{eff})}$. For higher

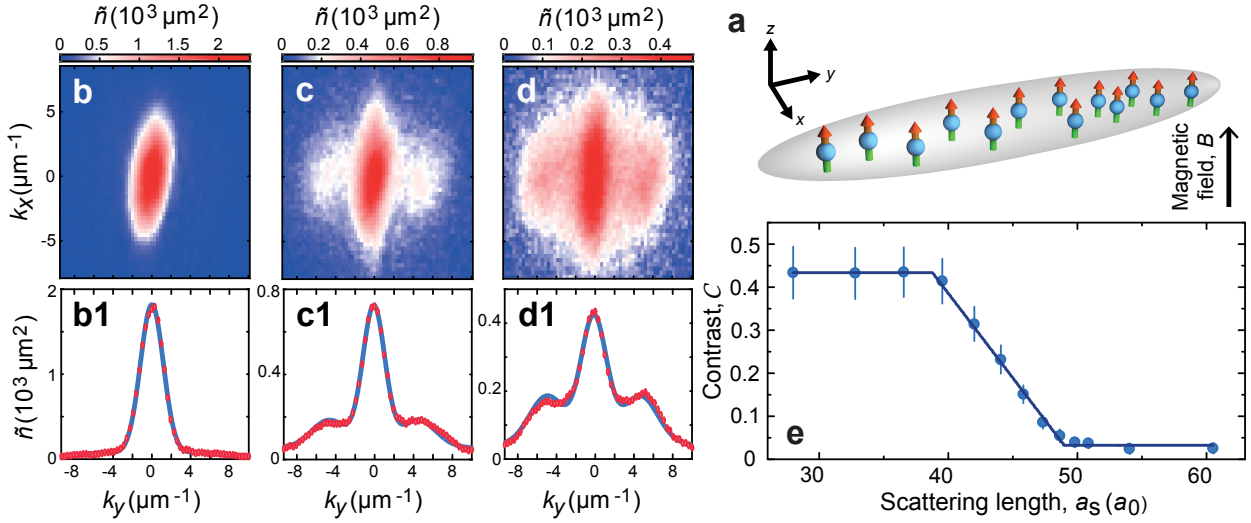

Figure 3 | Appearance of roton peaks in a q1D geometry. **a**, illustration of the in-trap Er BEC geometry, forming a cigar shape with y-elongation and dipoles aligned by an external uniform B-field along the z transverse direction. **b-d**, observed momentum distributions $\tilde{n}(k_x, k_y)$ obtained by averaging 15-to-25 absorption images with $(\nu_z, \lambda) = (456(1)\,\mathrm{Hz}, 14.4(4))$, $t_\mathrm{h} = 3\,\mathrm{ms}$ and for different a_s: **b**, $a_\mathrm{s} = 54a_0$, **c**, $a_\mathrm{s} = 44a_0$ and **d**, $a_\mathrm{s} = 37a_0$. **b1-d1** show the corresponding central cuts with $|k_x| < 3.5\mu\mathrm{m}^{-1}$ (red dots) and their fits with three-Gaussian distributions (blue lines), from which we extract k_rot and $\mathcal{C}$ (see text and Methods). **e**, evolution of $\mathcal{C}$ with a_s for $(\nu_z, \lambda) = (456(1)\,\mathrm{Hz}, 14.4(4))$ and $t_\mathrm{h} = 3\,\mathrm{ms}$ (dots). Error bars are deduced from the fit statistical uncertainties on the amplitudes $A_{*,0}$. We fit an empirically chosen linear step function to identify a_s^* (line).

$k_y^{(\mathrm{eff})}$ the spectrum flattens, but eventually bends upwards again due to the dominant kinetic energy. In our experimentally relevant q1D geometries, instead of developing a smooth minimum, roton excitations appear as isolated low-lying modes at intermediate momenta that depart from the overall spectrum [17]. These so-called roton fingers are related to confinement of the roton modes in the inhomogeneous BEC of profile $n_0(y)$ [16]. Using the local-density approximation in Eq. (1), the spatially-dependent spectrum $\epsilon(k, n_0(y))$ has a minimal roton gap at the trap center, translating into an effective confinement of the mode.

The confinement is evident from our BdG calculations, in which the lowest roton mode forms a short-wavelength density modulation localized at the trap center (Fig. 2c). This contrasts with phonon modes for which the modulation is delocalised over the entire condensate (Fig. 2b). Whereas the density modulation (Fig. 2c) and the finite-momentum peaks (Fig. 1f2) are signatures of the same effect, from now on we will focus on the latter aspect since it is the one we probe in the experiments via time-of-flight (ToF) expansion measurements [2]. Accordingly, we compute the momentum distribution from the ToF expanded densities associated with the selected modes (Fig. 2b1-c1) and observe that the roton mode indeed presents as two symmetric peaks localised at positions corresponding to $\pm k_\mathrm{rot}$.

To enrich the stationary-state picture, we additionally develop real-time evolution simulations of the 3D NL-GPE. This enables to fully account for the experimental procedure, as described in the next Section, as well as the effects due to finite temperature and atom losses (Methods). Also the real-time evolution shows a population of the roton mode with the same signatures as in Fig. 2c-c1, both in trap and in ToF. The extracted k_rot agrees well, within 10%, with the BdG approach in its validity regime, i. e. when a stationary dBEC state is found.

C. Roton peaks in quench experiments

Our experiment relies on the strong dipolar character of Er ($a_\mathrm{dd} = 65.5a_0$) and on the ability to fine tune a_s below a_dd. The experimental sequence starts with a ^{166}Er dBEC in a trap elongated along the y axis. The trap aspect ratio, $\lambda = \nu_z/\nu_y$, can span from about 4 to 30, corresponding to ν_z ranging from 150 Hz to 800 Hz. We note that ν_y and ν_z/ν_x are kept roughly constant to $\approx 30\,\mathrm{Hz}$ and ≈ 1.6, respectively (Methods). An external homogeneous magnetic field, B, defines the dipole orientation (magnetization) with respect to the trap axes and sets the values of a_s through a magnetic FR, centered close to $B = 0\,\mathrm{G}$. The precise B-to-a_s conversion has been measured in Ref. [39]. At the end of the preparation stage, we obtain a stable BEC at $a_\mathrm{s} = 61\,a_0$ ($\epsilon_\mathrm{dd} = 1.08$, $B = 0.4\,\mathrm{G}$) with transverse (z) magnetization (Fig. 3a) (Methods).

To access the roton regime, we suddenly quench a_s to

the desired lower value and we shortly hold the atoms in the trap for a time t_h, typically $t_\mathrm{h} = 3\,\mathrm{ms}$. We note that during t_h, B exponentially converges to its set value with a $1/e$-time of $0.98(5)\,\mathrm{ms}$ (Methods). We then release the atoms from the trap, change a_s back to approximately its initial value, and let the cloud expand for $t_\mathrm{f} = 30\,\mathrm{ms}$, after which we perform resonant absorption imaging. The imaging beam propagates transversely, i. e. nearly collinear with the z-axis. Hence the ToF images probe the two-dimensional density distribution of the expanded cloud, $n_\mathrm{f}(x, y, t_\mathrm{f})$. For t_f long enough to ignore the in-situ width of the cloud, $n_\mathrm{f}(x, y, t_\mathrm{f})$ maps the momentum distribution of the gas in trap, $\tilde{n}(k_x, k_y)$, assuming negligible interactions during the expansion. Our real-time simulations, accounting for the precise experimental sequence, confirm this assumption (Methods).

First we investigate $\tilde{n}(k_x, k_y)$ as a function of a_s for $(\nu_z, \lambda) = (456\,\mathrm{Hz}, 14.4)$, and $t_\mathrm{h} = 3\,\mathrm{ms}$. For large enough a_s, $\tilde{n}(k_x, k_y)$ shows a single narrow peak with an inverted aspect ratio compared to the trapped gas, typical of a stable BEC [2] (Fig. 3b). We define the center of the distribution as the origin of k. In contrast, when the system enters the dominantly dipolar regime by decreasing a_s , $\tilde{n}(k_x, k_y)$ changes fundamentally. We observe a sudden appearance of two symmetric finite-momentum peaks along the k_y axis, located at $\pm k_y^*$ and of similar shape (Fig. 3c-d). Beside their remarkable symmetry, these finite-momentum peaks also exhibit a high shot-to-shot reproducibility, as evidenced by their high contrast in the averaged distributions (Fig. 3c-d). The observed side peaks show the privileged population of specific high-momentum modes ($k_y = k_y^*$) in the excitation spectrum $\epsilon(k_y)$ of our trapped dBEC.

To quantitatively investigate the peak structures, we fit a sum of three Gaussian distributions to the central cuts of the average $\tilde{n}(k_x, k_y)$ (Fig. 3(b1-d1)) (Methods). From the fit we extract k_y^*, the amplitudes of the side and central peaks $A_{*,0}$, and derive the contrast of the side peaks, $\mathcal{C} = A_*/A_0$. Typical values of k_y^* are $\sim$ 4-5μm^{-1}. The evolution of $\mathcal{C}$ with a_s reveals an interesting behaviour (Fig. 3e). For large a_s, we observe an essentially zero and flat contrast. The residual $\mathcal{C} \sim 3\%$ arises from the usual thermal background and the imaging noise. With decreasing a_s, $\mathcal{C}$ first exhibits a sharp increase and then saturates to an upper value of about 40%. We define the onset of the finite-momentum excitation, a_s^*, as the value of a_s at which $\mathcal{C}$ starts to rise. For the (ν_z, λ) parameter here considered, we find $a_\mathrm{s}^* = 49.0(2)\,a_0$, corresponding to $\epsilon_\mathrm{dd} = 1.34(1)$.

Our ToF observations directly reveal the presence of the long-sought roton mode. The observed structures closely follow the predicted signature of this mode (Fig. 2c1). In addition, the fitted k_y^* are in very good agreement with the predicted k_rot from our theory (Sec. D). Finally, the high shot-to-shot repeatability of the remarkable peak structure in $\tilde{n}(k_x, k_y)$ suggests the persistence of a macroscopic phase coherence in the gas.

D. Properties of the roton excitation.

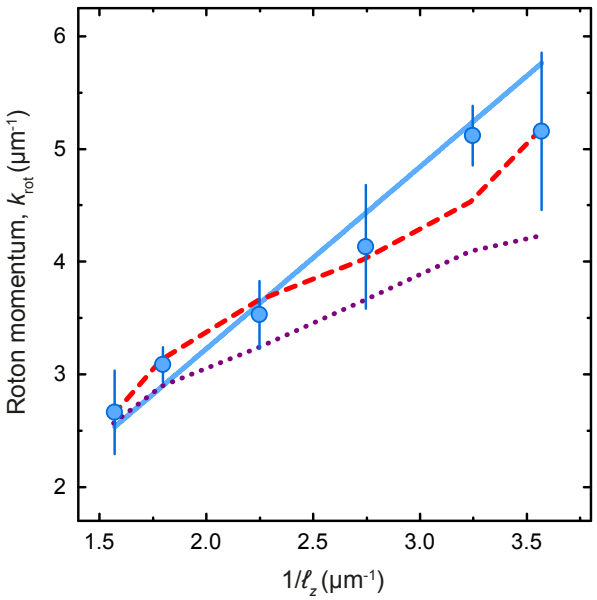

Figure 4 | Geometrical scaling of the roton momentum. Measured k_rot at the onset of a roton population $a_\mathrm{s} = a_\mathrm{s}^*$ in the quench experiment (dots) as a function of $1/\ell_z$. Error bars show the statistical uncertainty of the fit. Here short t_h ranging from 3 to 6 ms are used (Methods). The dotted and dashed lines show the theory predictions using the experimental parameters, from the analytic q1D model of Eq. (1) and from our real-time simulations reproducing the experimental procedure, respectively. Both theories use the a_s values being just below the predicted roton softening (Methods). The blue solid line shows a linear fit passing by the origin, to the data. The fitted slope is 1.61(4).

A major fingerprint of the roton mode in a dipolar gas is its characteristic dependence on the trap geometry. Its geometrical nature has been proven in various contexts, from pancake- [11, 13, 15–17] to our cigar-shaped traps (Sec. B), highlighting a universal scaling with $k_\mathrm{rot} \sim 1/\ell_z$. To experimentally investigate such geometrical properties in our elongated dBEC, we repeat the quench measurements for different trap parameters (ν_z, λ) and we extract the corresponding value of k_rot (Fig. 4) (Methods). Our data, plotted as a function of $1/\ell_z$, reveal a marked increase of k_rot, and a linear fit to the data gives a slope of 1.61(4). This value is remarkably close to the mean $k_\mathrm{rot}\ell_z = 1.59(15)$ calculated from our simple analytic model using the experimental parameters. To firmly tie our observation to the roton excitation, we perform real-time simulations of the NLGPE, accounting for the specific experimental sequences (Methods). The extracted parameter-free curve (dashed line in Fig. 4) is in excellent agreement with the data and also captures the smooth deviation from a linear slope

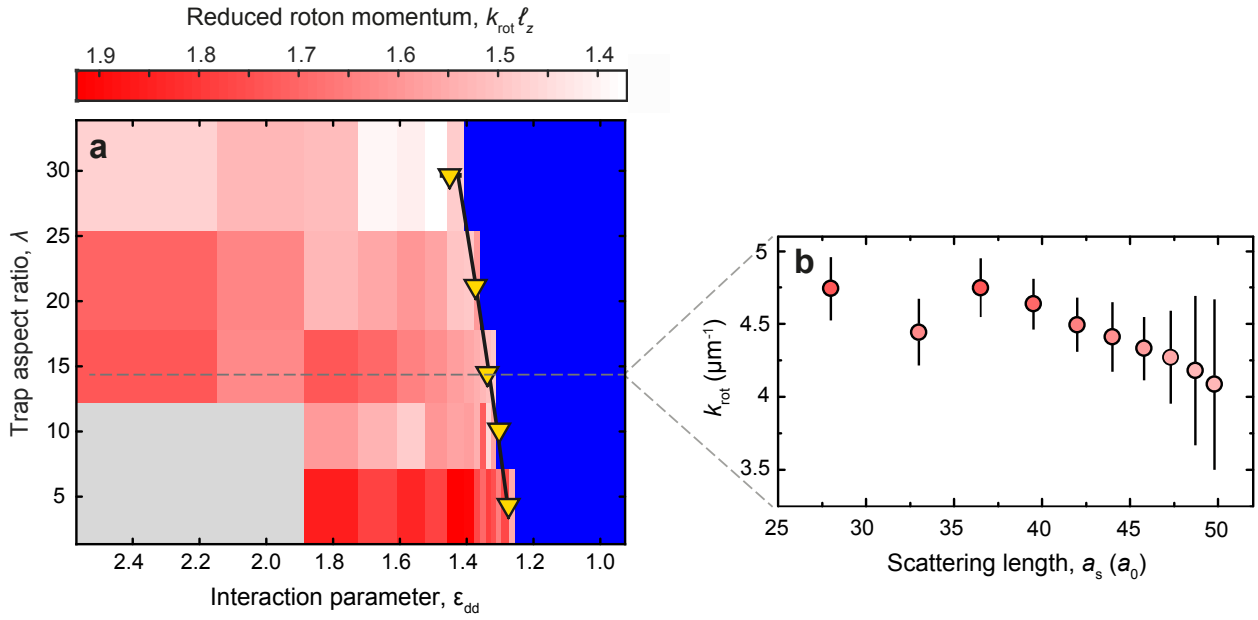

Figure 5 | Roton characteristic diagram. Summary of the measured roton properties as a function of $\epsilon_{\rm dd}$ and λ. Here short $t_{\rm h}$ ranging from 3 to 6 ms are used (Methods). The white-to-red colormap shows the reduced roton momentum $k_{\rm rot}\ell_z$. In the blue region no roton excitation is observed (e. g. Fig. 3b), and in the grey region we do not have a full set of data (Methods). The yellow triangles show the onset of the roton softening, $a_{\rm s}^*$, extracted from contrast measurements $\mathcal{C}$ at $t_{\rm h} = 3$ ms (e. g. Fig. 3d) and the solid black line is a linear fit to $a_{\rm s}^*(\lambda)$. **b**, $k_{\rm rot}$ as a function of $a_{\rm s}$ for the reference trap $(\nu_z, \lambda) = (456(1)\,\text{Hz}, 14.4(4))$, corresponding to the dashed line in **a**. Error bars show the statistical uncertainty of the fit.

reflecting the experimental details. The comparison between the experimental observations and our two complementary theories unambiguously establishes the rotonic nature of the finite-momentum peaks.

To gain further insights into the roton properties, we additionally investigate the effects of λ and $a_{\rm s}$. From all our measurements, we construct a characteristic diagram, presented in terms of the dimensionless parameters λ and $\epsilon_{\rm dd}$ (Fig. 5a). The former parameter governs the geometric competition between the attractive and repulsive parts of the DDI, and $\epsilon_{\rm dd}$ embodies the interplay between dipolar and short-range interactions (Methods). The white-to-red color scale indicates the values of the reduced roton momentum $k_{\rm rot}\ell_z$. Each column of the diagram shows the variation of $k_{\rm rot}\ell_z$ with λ, whereas each row gives the evolution of $k_{\rm rot}$ with $\epsilon_{\rm dd}$ for a given trap configuration. We observe $k_{\rm rot}\ell_z$ varying at most by $\approx 25\%$ along the lines and rows, which is on the order of our experimental precision. Close to the instability, both dependencies are expected to be mild as $k_{\rm rot}$ remains mainly set by its geometrical nature (see Secs. A, B and e. g. Refs.[11, 15]). The smooth dependence of $k_{\rm rot}$ with $a_{\rm s}$ is particularly relevant (Fig. 5b) as it contrasts the observed softening from a phonon instability in which the minimum in $\epsilon^2(k)$ is expected to appear at $k = 0$ and then move to larger values when lowering $a_{\rm s}$. From our analytic q1D model for the roton softening, we extract a residual increase of $k_{\rm rot}\ell_z$ of 17% from $a_{\rm s} = 44a_0$ to $37a_0$ in the geometry $(\nu_z, \lambda) = (457\,\text{Hz}, 14.3)$, similar to the experiments.

Besides the geometric determination of $k_{\rm rot}$, $\epsilon_{\rm dd}$ and λ control the roton gap Δ. In the experiment, we observe that the critical $\epsilon_{\rm dd}^* = a_{\rm dd}/a_{\rm s}^*$ for the onset of the roton population moves to larger values for more elongated traps (blue-to-red border and $\mathcal{C}$-measurements in Fig. 5). This increase can be explained by the following argument: a macroscopic roton population appears for small enough Δ (Methods). This condition is realised when the attractive DDI dominates over the total repulsive (contact and repulsive DDI) interaction. As the ratio of the attractive and repulsive contributions of the DDI depends on λ, so will $a_{\rm s}^*$. A larger λ favors the repulsive part of the DDI, thus weaker contact interactions are needed for a similar roton gap, explaining a lower $a_{\rm s}^*$. Predictions from our q1D model reproduce well the observed $a_{\rm s}^*$, both its variation direction and the actual values within 10% (Methods).

E. Discussion

In conclusion, we report on the observation of the long-sought roton mode in a dipolar BEC of Er atoms. Our investigations take advantage of an axially elongated geom-

etry, amplifying the roton signature in momentum space. Our results, combining experimental studies, numerical and analytic theories, unambiguously establish the roton softening of the excitation spectrum and the universal geometrical scaling $k_{\rm rot} \sim 1/\ell_z$ of the excitation.

Our work opens fascinating new ground for the study of roton physics in dipolar gases. In the future, it might be interesting to explore out-of-equilibrium dynamics of the roton mode, to spectroscopically access the roton gap, and to directly probe in-trap density modulated states. These density modulations, providing a signature of the roton softening in real space, are a precursor of a supersolid phase, in which a phase-coherent density-modulated ground-state would arise [45]. Although the density modulation is expected to be mean-field unstable against local collapses [46], quantum stabilization may prevent collapse as for the case of recently explored quantum droplets [37–41]. Future investigations may be directed in exploring, both in theory and experiment, the possibility of a stable supersolid state in dBECs.

[1] Balibar, S. The discovery of superfluidity. *Journal of Low Temperature Physics* **146**, 441–470 (2007).

[2] Pitaevskii, L. & Stringari, S. *Bose-Einstein condensation and superfluidity*, vol. 164 (Oxford University Press, 2016).

[3] Landau, L. D. The theory of superfluidity of helium II. *J. Phys. (Moscow)* **5**, 71 (1941).

[4] Landau, L. D. On the theory of superfluidity of helium II. *J. Phys. (Moscow)* **11**, 91 (1947).

[5] Henshaw, D. G. & Woods, A. D. B. Modes of atomic motions in liquid helium by inelastic scattering of neutrons. *Phys. Rev.* **121**, 1266–1274 (1961).

[6] Griffin, A. *Excitations in a Bose-condensed Liquid*. Cambridge Classical Studies (Cambridge University Press, 1993).

[7] Dalfovo, F. & Stringari, S. Helium nanodroplets and trapped Bose-Einstein condensates as prototypes of finite quantum fluids. *The Journal of Chemical Physics* **115**, 10078–10089 (2001).

[8] Mottl, R. *et al.* Roton-type mode softening in a quantum gas with cavity-mediated long-range interactions. *Science* **336**, 1570–1573 (2012).

[9] Ji, S.-C. *et al.* Softening of roton and phonon modes in a Bose-Einstein condensate with spin-orbit coupling. *Phys. Rev. Lett.* **114**, 105301 (2015).

[10] Ha, L.-C., Clark, L. W., Parker, C. V., Anderson, B. M. & Chin, C. Roton-maxon excitation spectrum of Bose condensates in a shaken optical lattice. *Phys. Rev. Lett.* **114**, 055301 (2015).

[11] Santos, L., Shlyapnikov, G. V. & Lewenstein, M. Roton-maxon spectrum and stability of trapped dipolar Bose-Einstein condensates. *Phys. Rev. Lett.* **90**, 250403 (2003).

[12] Giovanazzi, S. & O'Dell, D. H. J. Instabilities and the roton spectrum of a quasi-1d Bose-Einstein condensed gas with dipole-dipole interactions. *The European Physical Journal D - Atomic, Molecular, Optical and Plasma Physics* **31**, 439–445 (2004).

[13] Ronen, S., Bortolotti, D. C. E. & Bohn, J. L. Radial and angular rotons in trapped dipolar gases. *Phys. Rev. Lett.* **98**, 030406 (2007).

[14] Martin, A. D. & Blakie, P. B. Stability and structure of an anisotropically trapped dipolar Bose-Einstein condensate: Angular and linear rotons. *Phys. Rev. A* **86**, 053623 (2012).

[15] Blakie, P. B., Baillie, D. & Bisset, R. N. Roton spectroscopy in a harmonically trapped dipolar Bose-Einstein condensate. *Phys. Rev. A* **86**, 021604 (2012).

[16] Jona-Lasinio, M., Łakomy, K. & Santos, L. Roton confinement in trapped dipolar Bose-Einstein condensates. *Phys. Rev. A* **88**, 013619 (2013).

[17] Bisset, R. N., Baillie, D. & Blakie, P. B. Roton excitations in a trapped dipolar Bose-Einstein condensate. *Phys. Rev. A* **88**, 043606 (2013).

[18] Bohn, J. L., Wilson, R. M. & Ronen, S. How does a dipolar Bose-Einstein condensate collapse? *Laser Physics* **19**, 547–549 (2009).

[19] Parker, N. G., Ticknor, C., Martin, A. M. & O'Dell, D. H. J. Structure formation during the collapse of a dipolar atomic Bose-Einstein condensate. *Phys. Rev. A* **79**, 013617 (2009).

[20] Wilson, R. M., Ronen, S., Bohn, J. L. & Pu, H. Manifestations of the roton mode in dipolar Bose-Einstein condensates. *Phys. Rev. Lett.* **100**, 245302 (2008).

[21] Nath, R. & Santos, L. Faraday patterns in two-dimensional dipolar Bose-Einstein condensates. *Phys. Rev. A* **81**, 033626 (2010).

[22] Wilson, R. M., Ronen, S. & Bohn, J. L. Critical superfluid velocity in a trapped dipolar gas. *Phys. Rev. Lett.* **104**, 094501 (2010).

[23] Klawunn, M., Recati, A., Pitaevskii, L. P. & Stringari, S. Local atom-number fluctuations in quantum gases at finite temperature. *Phys. Rev. A* **84**, 033612 (2011).

[24] Bisset, R. N. & Blakie, P. B. Fingerprinting rotons in a dipolar condensate: Super-poissonian peak in the atom-number fluctuations. *Phys. Rev. Lett.* **110**, 265302 (2013).

[25] Blakie, P. B., Baillie, D. & Bisset, R. N. Depletion and fluctuations of a trapped dipolar Bose-Einstein condensate in the roton regime. *Phys. Rev. A* **88**, 013638 (2013).

[26] Jona-Lasinio, M., Łakomy, K. & Santos, L. Time-of-flight roton spectroscopy in dipolar Bose-Einstein condensates. *Phys. Rev. A* **88**, 025603 (2013).

[27] Natu, S. S., Campanello, L. & Das Sarma, S. Dynamics of correlations in a quasi-two-dimensional dipolar Bose gas following a quantum quench. *Phys. Rev. A* **90**, 043617 (2014).

[28] Griesmaier, A., Werner, J., Hensler, S., Stuhler, J. & Pfau, T. Bose-Einstein condensation of chromium. *Phys. Rev. Lett.* **94**, 160401 (2005).

[29] Beaufils, Q. *et al.* All-optical production of chromium Bose-Einstein condensates. *Phys. Rev. A* **77**, 061601 (2008).

[30] Lu, M., Burdick, N. Q., Youn, S. H. & Lev, B. L. Strongly dipolar Bose-Einstein condensate of dysprosium. *Phys. Rev. Lett.* **107**, 190401 (2011).

[31] Aikawa, K. *et al.* Bose-Einstein condensation of erbium. *Phys. Rev. Lett.* **108**, 210401 (2012).

[32] Chin, C., Grimm, R., Julienne, P. S. & Tiesinga, E.

Feshbach resonances in ultracold gases. *Rev. Mod. Phys.* **82**, 1225–1286 (2010).
[33] Schneider, T. & Enz, C. P. Theory of the superfluid-solid transition of ^{4}He. *Phys. Rev. Lett.* **27**, 1186–1188 (1971).
[34] Baranov, M. Theoretical progress in many-body physics with ultracold dipolar gases. *Physics Reports* **464**, 71 – 111 (2008).
[35] Lima, A. R. P. & Pelster, A. Quantum fluctuations in dipolar Bose gases. *Phys. Rev. A* **84**, 041604 (2011).
[36] Lima, A. R. P. & Pelster, A. Beyond mean-field low-lying excitations of dipolar Bose gases. *Phys. Rev. A* **86**, 063609 (2012).
[37] Wächtler, F. & Santos, L. Quantum filaments in dipolar Bose-Einstein condensates. *Phys. Rev. A* **93**, 061603 (2016).
[38] Ferrier-Barbut, I., Kadau, H., Schmitt, M., Wenzel, M. & Pfau, T. Observation of quantum droplets in a strongly dipolar Bose gas. *Phys. Rev. Lett.* **116**, 215301 (2016).
[39] Chomaz, L. *et al.* Quantum-fluctuation-driven crossover from a dilute Bose-Einstein condensate to a macrodroplet in a dipolar quantum fluid. *Phys. Rev. X* **6**, 041039 (2016).
[40] Wächtler, F. & Santos, L. Ground-state properties and elementary excitations of quantum droplets in dipolar Bose-Einstein condensates. *Phys. Rev. A* **94**, 043618 (2016).
[41] Bisset, R. N., Wilson, R. M., Baillie, D. & Blakie, P. B. Ground-state phase diagram of a dipolar condensate with quantum fluctuations. *Phys. Rev. A* **94**, 033619 (2016).
[42] Bisset, R. N. & Blakie, P. B. Crystallization of a dilute atomic dipolar condensate. *Phys. Rev. A* **92**, 061603 (2015).
[43] Kagan, Y., Muryshev, A. E. & Shlyapnikov, G. V. Collapse and Bose-Einstein condensation in a trapped Bose gas with negative scattering length. *Phys. Rev. Lett.* **81**, 933–937 (1998).
[44] Ronen, S., Bortolotti, D. C. E. & Bohn, J. L. Bogoliubov modes of a dipolar condensate in a cylindrical trap. *Phys. Rev. A* **74**, 013623 (2006).
[45] Pomeau, Y. & Rica, S. Dynamics of a model of supersolid. *Phys. Rev. Lett.* **72**, 2426–2429 (1994).
[46] Komineas, S. & Cooper, N. R. Vortex lattices in Bose-Einstein condensates with dipolar interactions beyond the weak-interaction limit. *Phys. Rev. A* **75**, 023623 (2007).
[47] Frisch, A. *et al.* Narrow-line magneto-optical trap for erbium. *Phys. Rev. A* **85**, 051401 (2012).
[48] Ahmadi, P., Timmons, B. P. & Summy, G. S. Geometrical effects in the loading of an optical atom trap. *Phys. Rev. A* **72**, 023411 (2005).
[49] Lahaye, T. *et al.* *d*-wave collapse and explosion of a dipolar Bose-Einstein condensate. *Phys. Rev. Lett.* **101**, 080401 (2008).
[50] van Bijnen, R. M. W., Parker, N. G., Kokkelmans, S. J. J. M. F., Martin, A. M. & O'Dell, D. H. J. Collective excitation frequencies and stationary states of trapped dipolar Bose-Einstein condensates in the Thomas-Fermi regime. *Phys. Rev. A* **82**, 033612 (2010).

- **Acknoledgements:** We thank M. Baranov and E. Demler for fruitful discussions and G. Natale for his support in the final stage of the experiment. This work is dedicated in memory of D. Jin and her inspiring example. The Innsbruck group is supported through a ERC Consolidator Grant (RARE, no. 681432) and a FET Proactive project (RySQ, no. 640378) of the EU H2020. LC is supported within a Marie Curie Project (DipPhase, no. 706809) of the EU H2020. FW and LS thank the DFG (SFB 1227 DQ-mat). All the authors thank the DFG/FWF (FOR 2247). Part of the computational results presented have been achieved using the HPC infrastructure LEO of the University of Innsbruck.

- **Competing Interests:** The authors declare that they have no competing financial interests.

- **Correspondence:** Correspondence and requests for materials should be addressed to F.F. (email: francesca.ferlaino@uibk.ac.at).

- **Author contributions:** FF, LC, DP, GF, MJM, JHB, SB conceived and supervised the experiment and took the experimental data. LC analysed them. RMWvB developed the BdG calculations. FW and LS performed the real time simulations. LS derived the q1D analytical model. LC, FF, RMWvB and LS wrote the paper with the contributions of all the authors.

METHODS

F. Production of ^{166}Er BECs

We prepare a ^{166}Er BEC similarly to Refs. [31, 39]. From a narrow-line magneto-optical trap with 3×10^7 ^{166}Er atoms, automatically spin-polarized in their absolute lowest Zeeman sub-level [47], at about 10μK, we directly load the atomic gas in a crossed optical dipole trap (ODT) with an efficiency of more than 30%. A uniform magnetic field, B, is permanently applied along the vertical z axis, fixing the dipole orientation, while its value is varied during the experimental sequence, to tune a_s (Method H). We achieve condensation by means of evaporative cooling in the crossed ODT at $B = 1.9\,\mathrm{G}$ ($a_s = 80(2)\,a_0$). During the evaporation procedure, we first change the power and then the ellipticity of one of the ODT beams (Method G). The final atom number, typically 10^5, and condensed fraction, typically 70%, are assessed by fitting the ToF absorption images of the gas to a bimodal distribution, sum of a TF profile and a broad Gaussian background.

G. Trapping geometries

The BEC is confined in a harmonic trapping potential $V(\mathbf{r}) = 2m\pi^2(\nu_x^2 x^2 + \nu_y^2 y^2 + \nu_z^2 z^2)$, characterized by the frequencies (ν_x, ν_y, ν_z). The ODT results from the crossing of two red-detuned laser beams of 1064 nm

wavelength at their respective focii. One beam propagates along the y-axis and is denoted hODTb; the other, called vODTb, propagates nearly collinear to the z-axis. The vODTb has a maximum power of 7 W and an elliptical profile with waists of 110 and 55 μm along x and y respectively. The hODTb has a maximum power of 24 W, a vertical waist $w_z = 18\,\mu$m, and a controllable horizontal waist, $w_x = \lambda' w_z$. The ellipticity λ' can be tuned from 1.57 to 15 by time averaging the frequency of the first-order deflection of an Acousto-Optic Modulator [48]. By adjusting independently λ' and the powers of the vODTb and of the hODTb , we can widely control the geometry of the trap in a dynamic manner. Precisely, ν_y is essentially set by the vODTb power, ν_z by that of the hODTb. ν_x is controlled by both the power and ellipticity of the hODTb, with $\nu_z/\nu_x \approx \lambda'$. The independent control of ν_y and ν_z yields an especially easy tuning of the relevant trap aspect ratio, $\lambda = \nu_z/\nu_y$, for our q1D geometry.

We use the tuning of the hODTb power and ellipticity to perform evaporative cooling to quantum degeneracy (Method F). After reaching condensation, we again modify the beam parameters to shape the trap into a favourable q1D configuration for observing the roton physics ($\nu_y \ll \nu_x, \nu_z$). The different trapping geometries probed in Figs. 3-5 are achieved by changing the hODTb power with $\lambda' = 1.57$ and the vODTb power set to its maximum so that ν_y and ν_z/ν_x are kept roughly constant. The corresponding $(\lambda, \nu_x, \nu_y, \nu_z)$ are calibrated via the excitation and probing of the center-of-mass oscillation of thermal samples and reported in Extended Data Table I. We note that the final atom number N, BEC fraction f, and temperature T after the shaping procedure depend on the final configurations, as detailed in Extended Data Table I. T is extracted from the evolution with the ToF duration t_f of the size of the background Gaussian in the TF-plus-Gaussian bimodal fit to the corresponding ToF images of gas. The values of $N_\mathrm{c} = fN$ and T are used for the initial states ψ_i of our real-time simulations (Method N).

H. Quench of the scattering length a_s

To control a_s we use a magnetic Feshbach resonance between ^{166}Er atoms in their absolute ground state, which is centered around $B = 0$ G. The B-to-a_s conversion has been previously precisely measured via lattice spectroscopy, as reported in Ref. [39]. Errors on a_s, taking into account statistical uncertainties of the conversion and effects of magnetic field fluctuations (e.g. from stray fields), are of 3-to-5 a_0 for the relevant a_s range 27-67 a_0 in this work. After the BEC preparation and in order to investigate the roton physics via an interaction quench, we suddenly change the magnetic field set value, B_set, twice. First we perform the quench itself and abruptly change B_set from 0.4 G ($a_\mathrm{s} = 61\,a_0$) to the desired lower value at the beginning of the hold in trap ($t_\mathrm{h} = 0$ ms). Second we prepare the ToF expansion and imaging conditions (see Method I) and abruptly change B_set from the quenched value to 0.3 G ($a_\mathrm{s} = 57\,a_0$) at the beginning of the ToF expansion ($t_\mathrm{f} = 0$ ms). Due to delays in the experimental setup, e.g. coming from eddy currents in our main chamber, the actual B value felt by the atoms responds to a change of B_set via $B(t) = B_\mathrm{set}(t) + \tau dB/dt$ [49]. By performing pulsed-radio-frequency spectroscopy measurements (pulse duration 100 μs) on a BEC after changing B_set (from 0.4 to 0.2 G), we verify this law and calibrate $\tau = 0.98(5)$ ms. As a consequence a_s is evolving during t_h and t_f. This effect is fully accounted in the experiment and simulations and, we report the roton properties as a function of the effective value of a_s at the end of t_h. We use t_h ranging from 3 to 6 ms. The lower bound on t_h comes from the time needed for a_s to effectively reach the regime of interest. Here we then consider the initial evolution for which $t_\mathrm{h}\nu_y$; $t_\mathrm{h}/\tau_\mathrm{coll} \ll 1$, $1/\tau_\mathrm{coll}$ being the characteristic collision rate. We estimate that τ_coll ranges typically from 40 to 90 ms in the initial BECs of Extended Data Table I at $a_\mathrm{s} = 61\,a_0$. We note that during the considered t_h, the atom loss remains below 25% for our less confined geometries $\nu_z \leq 600$ Hz and can go up 40% in the tightest traps of $\nu_z > 600$ Hz. We have checked that the roton, if it exists, has developed within this range of t_h. In Figs. 4-5, the parameter t_h is optimized for each a_s value to obtain the largest visibility of the roton peaks (largest $\mathcal{C}$).

I. Imaging procedure

The in-trap density modulation associated with the roton excitation has a characteristic wavelength of $d_y^* = 2\pi/k_\mathrm{rot} \sim 1\,\mu$m (e.g. Fig. 2c). This value is much smaller than the axial width of the cloud ($\sim 30\,\mu$m) and below our imaging resolution ($\sim 3.7\,\mu$m). In our experiments, we employ ToF expansion measurements, accessing the momentum distribution of the gas [2], to probe the roton mode population. We let the gas expand freely for $t_\mathrm{f} = 30$ ms, which translates the imaging resolution in space into a momentum resolution of $\sim 0.32\mu\mathrm{m}^{-1}$. This means that we can resolve the population of modulation modes with wavelength $\lesssim 20\,\mu$m and the roton mode of interest should be well detectable.

In the experiments, we record 2D absorption pictures of the cloud after ToF expansion by means of standard resonant absorption imaging on the atomic transition at 401 nm. The imaging beam propagates nearly vertically, with a remaining angle of $\sim 15^\mathrm{o}$ compared to the z-axis within the xz-plane. Thus the ToF images essentially probe the spatial density distribution $n_\mathrm{f}(x, y, t_\mathrm{f})$ in the xy plane. When releasing the cloud ($t_\mathrm{f} = 0$ ms), we change back B to $B = 0.3$ G (Method H). This change enables constant and optimal imaging conditions with a fixed probing procedure, i. e. a maximal absorption cross-section. In addition, the associated increase of a_s to 57 a_0 allows to minimize the time during which the evolution

happens in the small-a_s regime where roton physics develops. Thanks to this we are able to effectively probe the short-time evolution of the gas. In this work, we use the simple mapping:

$$\tilde{n}(k_x, k_y) = \left(\frac{\hbar t_f}{m}\right)^2 n_f\left(\frac{\hbar k_x t_f}{m}, \frac{\hbar k_y t_f}{m}, t_f\right), \quad (2)$$

which neglects the initial size of the cloud in the trap and the effect of interparticle interactions during the free expansion. Using real-time simulations (Method N), we simulate the experimental sequence and are able to compute both the real momentum density from the in-trap wavefunction and the spatial ToF distribution 30 ms after switching off the trap. Using the mapping of Eq. (2) and our experimental parameters, the two calculated distributions are very similar, and, in particular, the two extracted momenta associated with the roton signal agrees within 5%. This confirms that the interparticle interactions play little role during the expansion and justifies the use of Eq. (2).

J. Fit procedure for the ToF images

For each data point of Figs. 3-5, we record between 12 and 25 ToF images. By fitting a two-dimensional Gaussian distribution to the individual images, we extract their origin $(k_x, k_y) = (0, 0)$ and recenter each image. From the recentered images, we compute the averaged $\tilde{n}(k_x, k_y)$, from which we characterise the linear roton developing along k_y. To do so, we extract a one-dimensional profile $\tilde{n}_1(k_y)$ by averaging the one-dimensional cut of $\tilde{n}(k_x, k_y)$ of fixed k_x within $|k_x| \leq k_m = 3.5\mu m^{-1}$: $\tilde{n}_1(k_y) = \int_{-k_m}^{k_m} \tilde{n}(k_x, k_y)dk_x / \int_{-k_m}^{k_m} dk_x$. To quantitatively analyse the observed roton peaks, we fit a sum of three Gaussian distributions to $\tilde{n}_1(k_y)$. One Gaussian accounts for the central peak and its centre is imposed to $k_0 \sim 0$. The two other Gaussians are symmetrically located at $k_0 \pm k_y^*$, and we impose their size σ^* and amplitude A_* to be identical. We focus on the roton side peaks by constraining $k_y^* > 0.5\,\mu m^{-1}$ and $\sigma^* < 3\,\mu m^{-1}$. In all the figures, the statistical error of the fit is characterised by its 95 % confidence interval.

In order to analyze the evolution of the contrast $\mathcal{C}$ of the side peaks (see Fig. 3e and Fig. 5), we perform a second run of the fitting procedure, in which we constrain more strictly the value of k_y^*. The interval of allowed values is defined for each trapping geometry (Extended Data Table I) and is set from the results of the first run of the fitting procedure. We use the results of the (a_s, t_h)-configurations where the peaks are clearly visible (see Fig.5) and we set the allowed k_y^*-range to that covered by the 95% confidence intervals of the first-fitted k_y^* in these configurations. This constraint enables that, for $a_s > a_s^*$, the fitting procedure estimates the residual background population on the relevant momentum range for the roton physics.

In the ToF images, we qualitatively observe that the momentum distribution broadens (i. e. larger $\langle k_x^2 + k_y^2 \rangle$) when t_h increases and a_s decreases. This behaviour effectively limits the visibility of the roton peaks, and explains that the optimal t_h for the roton observation (see Method H) gets shorter for lower a_s. In Fig. 5, the grey region indicates the (a_s,λ)-configurations where the whole momentum distribution was observed to be too spread out even at the shortest $t_h = 3$ ms, so that the roton peaks could not be clearly detected. This region was then excluded and no full set of measurements is available. We note that, in this region of the diagram, $1/\ell_z$ is the smallest, making the blurring effect due to the distribution braodening more drastic, since the roton and BEC peaks are closer together. The non-detectability of roton peaks can also relate to the phase diagram characteristics. The small-a_s-small-λ region, corresponding to the grey area lies deeper in the roton regime (as embodied by the increase of a_s^* for decreasing λ, see main text). It is then possible that a larger number of modes are dynamically destabilized and populated, resulting in a blurring of the roton signal.

K. Generalized Gross–Pitaevskii equation

Our theory is based on an extended version of the NLGPE

$$i\hbar\frac{\partial\psi(\mathbf{r},t)}{\partial t} = \Big(-\frac{\hbar^2\nabla^2}{2m} + V(\mathbf{r}) + \int d\mathbf{r}' U(\mathbf{r}-\mathbf{r}')n(\mathbf{r}') + \Delta\mu[n] - i\hbar\frac{L_3}{2}n^2\Big)\psi(\mathbf{r},t) \quad (3)$$

$$\equiv \Big(\hat{H}_{GP}[\psi] - i\hbar\frac{L_3}{2}n^2\Big)\psi(\mathbf{r},t), \quad (4)$$

governing the evolution of a macroscopically occupied wavefunction $\psi(\mathbf{r}, t)$, with corresponding atomic density $n = |\psi(\mathbf{r}, t)|^2$ at position $\mathbf{r}$ and time t. The standard dipolar NLGPE includes the kinetic energy, external trap potential and the mean-field effect of the interactions. These correspond to the three first terms of Eq. (3), where the mean-field interaction potential takes the form of a convolution of n with the binary interaction potential

$$U(\mathbf{r}) = g\left(\delta(\mathbf{r}) + \frac{3\epsilon_{dd}}{4\pi}\frac{1-3\cos^2\theta}{|\mathbf{r}|^3}\right), \quad (5)$$

for two particles separated by $\mathbf{r}$ [34]. The first term corresponds to contact interactions between the particles with strength $g = \frac{4\pi\hbar^2 a_s}{m}$. The DDI gives rise to the second term, which depends on both the distance and orientation of the vector $\mathbf{r}$ compared to the polarisation axis (z axis) of the dipoles (angle θ). Most properties of dBECs are well captured by this standard NLGPE (mean-field) [2, 34].

Recent experimental and theoretical results, however, have established the importance of accounting for quan-

tum fluctuations in dipolar condensates [37–41]. Their effect can be included in the NLGPE in a mean field treatment through a Lee-Huang-Yang correction to the chemical potential, $\Delta\mu[n] = 32g(na_s)^{3/2}(1+3\epsilon_{\rm dd}^2/2)/3\sqrt{\pi}$, which is obtained under a local density approximation [35, 36]. The accuracy of this mean field treatment has been established, e.g., in Refs. [37, 40, 41], and has proven succesful in explaining recent experimental results [38, 39]. The final nonlinear term in the extended NLGPE accounts for three-body losses, with an experimentally determined loss parameter L_3, which is dependent on $a_{\rm s}$ and typically of the order $L_3 \simeq 10^{-41}{\rm m}^6{\rm s}^{-1}$, as reported in Ref. [39].

L. BdG spectrum calculations

Collective excitations of the dBEC are obtained by linearising the NLGPE around a stationary state ψ_0, which can be obtained by imaginary time propagation (Method N). We write $\psi = {\rm e}^{-{\rm i}\mu t/\hbar}(\psi_0 + \eta[u{\rm e}^{-{\rm i}\epsilon t/\hbar} - v^*{\rm e}^{+{\rm i}\epsilon t/\hbar}])$, where μ is the chemical potential associated with state ψ_0, and u, v are spatial modes oscillating in time with characteristic frequency $\epsilon/\hbar$ and $\eta \ll 1$ [44]. Inserting this ansatz in the NLGPE, and retaining only terms up to linear order in η we obtain the BdG equations

$$\begin{pmatrix} \hat{H}_{\rm GP}[\psi_0]+A & -A \\ A & -\hat{H}_{\rm GP}[\psi_0]-A \end{pmatrix}\begin{pmatrix} u \\ v \end{pmatrix} = \epsilon\begin{pmatrix} u \\ v \end{pmatrix}, \tag{6}$$

where the operator A, acting on a function f and evaluated at point $\mathbf{r}$, is defined as

$$(Af)(\mathbf{r}) = \int {\rm d}\mathbf{r}'\psi_0(\mathbf{r}')U(\mathbf{r}-\mathbf{r}')f(\mathbf{r}')\psi_0(\mathbf{r}) + \frac{16}{\sqrt{\pi}}ga_{\rm s}^{3/2}\left(1+\frac{3}{2}\epsilon_{\rm dd}^2\right)|\psi_0(\mathbf{r})|^3 f(\mathbf{r}). \tag{7}$$

The above equations constitute an eigenvalue problem, which we solve numerically using the Arnoldi method to obtain eigenmodes (u, v) and corresponding excitation energies ϵ. The equations presented here are a generalisation of the BdG equations for dipolar systems as derived in Ref. [44], to include the LHY correction for quantum fluctuations. The LHY term generally serves to stabilise the excitation spectrum, causing the roton instability point to shift to lower scattering lengths. The excited states shown in Fig. 2b-c correspond to the density $|\psi_0+\eta(u-v^*)|^2$, for particular pairs of (u, v) corresponding to phonon and roton modes. Even while the amplitude $\eta = 0.2$ of both modes is taken to be equal in Figs. 2b and 2c, the roton excitation (Fig. 2c) leads to markedly larger local density modulations than the phonon excitation (Fig. 2b). The ToF signatures in Fig. 2 are computed by letting the wave function of the excitation, $\eta(u-v^*)$, expand ballistically for 30ms, i.e. neglecting interactions during the expansion. The resulting density $|\eta(u-v^*)|^2$ is then plotted (Fig. 2b1, c1).

M. Analytical dispersion relation for an infinite axially elongated geometry

Equation (1) in the main text results from a similar procedure as that used in Ref. [11] for rotons in infinite q2D traps. We consider a dBEC homogeneous along y but harmonically confined with frequencies ν_x and ν_z along x and z. For sufficiently strong interactions the BEC is in the TF regime on the xz plane, in which the BEC wavefunction acquires the form $\psi_0(\boldsymbol{\rho}) = \sqrt{n(\boldsymbol{\rho})}$, with $n(\boldsymbol{\rho}) = n_0\left(1-(x/X)^2-(z/Z)^2\right)$, where X and Z are the TF radii, and $\boldsymbol{\rho} = (x, z)$. The calculation of n_0, X and Z is detailed at the end of this section.

Due to the axial homogeneity, the elementary excitations discussed in the previous section have a defined axial momentum k_y, and take the form $\delta\psi(\boldsymbol{r}, t) = u(\boldsymbol{\rho})e^{ik_y y - i\epsilon t/\hbar} - v(\boldsymbol{\rho})e^{-ik_y y + i\epsilon t/\hbar}$. We consider the GPE given by Eq. (3) without LHY correction and three-body losses, and insert the perturbed solution $\psi(\boldsymbol{r}, t) = (\psi_0(\boldsymbol{\rho}) + \eta\delta\psi(\boldsymbol{r}, t))\, e^{-i\mu t/\hbar}$. After linearization we obtain the BdG equations for $f_\pm(\boldsymbol{\rho}) = u(\boldsymbol{\rho}) \pm v(\boldsymbol{\rho})$:

$$\epsilon f_-(\boldsymbol{\rho}) = H_{kin} f_+(\boldsymbol{\rho}), \tag{8}$$

$$\epsilon f_+(\boldsymbol{\rho}) = H_{kin} f_-(\boldsymbol{\rho}) + H_{int}[f_-(\boldsymbol{\rho})], \tag{9}$$

where

$$H_{kin} f_\pm(\boldsymbol{\rho}) = \frac{\hbar^2}{2m}\left(-\nabla^2 + k_y^2 + \frac{\nabla^2\psi_0}{\psi_0}\right) f_\pm(\boldsymbol{\rho}), \tag{10}$$

$$H_{int}[f_-(\boldsymbol{\rho})] = 2\int d^3r' U(\boldsymbol{r}-\boldsymbol{r}')e^{-ik_y(y-y')} \psi_0(\boldsymbol{\rho})\psi_0(\boldsymbol{\rho}')f_-(\boldsymbol{\rho}'). \tag{11}$$

Employing $f_+(\boldsymbol{\rho}) = W(\boldsymbol{\rho})\psi_0(\boldsymbol{\rho})$, and for $k_y \gg 1/X, 1/Z$, we obtain the following equation for the function $W(\boldsymbol{\rho})$:

$$\begin{aligned} 0 = {} & 2gn_0\left(1-\tilde{x}^2-\tilde{z}^2\right)\left[\frac{1}{X^2}\frac{\partial^2 W}{\partial\tilde{x}^2} + \frac{1}{Z^2}\frac{\partial^2 W}{\partial\tilde{z}^2}\right] \\ & - gn_0(1+2\epsilon_{dd})\left[\frac{1}{X^2}\tilde{x}\frac{\partial W}{\partial\tilde{x}} + \frac{1}{Z^2}\tilde{z}\frac{\partial W}{\partial\tilde{z}}\right] \\ & + \left(\frac{2m}{\hbar^2}(\epsilon^2 - E(k_y)^2) - 2g\epsilon_{dd}n_0\left(\frac{1}{X^2}+\frac{1}{Z^2}\right)\right) \\ & - \frac{4m}{\hbar^2}gn_0(1-\epsilon_{dd})E(k_y)\left(1-\tilde{x}^2-\tilde{z}^2\right), \end{aligned} \tag{12}$$

where $\tilde{x} = x/X$, $\tilde{z} = z/Z$, $E(k_y) = \hbar^2k_y^2/2m$. For $\epsilon_{dd} = 1$ the last term of Eq. (12) vanishes. In that case, the lowest-energy solution is given by $W = 1$, whose eigenenergy builds, as a function of k_y, the dispersion $\epsilon_0(k_y)$ with

$$\epsilon_0(k_y)^2 = E(k_y)^2 + E_0^2, \tag{13}$$

with $E_0^2 = 2g\epsilon_{dd}n_0\frac{\hbar^2}{2m}\left(\frac{1}{X^2}+\frac{1}{Z^2}\right)$. In the vicinity of $\epsilon_{\rm dd} = 1$, the effect of the last term in Eq. (12) may be evaluated perturbatively, resulting in the dispersion

$$\epsilon(k_y)^2 \simeq \epsilon_0(k_y)^2 - 2E_I E(k_y), \tag{14}$$

with $E_I = \frac{2}{3} g n_0 (\epsilon_{dd} - 1)$.

This expression for the dispersion presents a roton minimum for $\epsilon_{dd} > 1$ at $k_{\rm rot} = \frac{1}{\hbar}\sqrt{2mE_I}$. Expanding Eq. (14) in the vicinity of the roton minimum, $\epsilon(k_y)^2 \simeq \epsilon(k_{\rm rot})^2 + \frac{1}{2}\left[\frac{d^2\epsilon^2(k_y)}{dk_y^2}\right]_{k_y=k_{\rm rot}}$, we obtain Eq. (1) of the main text, with $\Delta = \epsilon(k_{\rm rot}) = \sqrt{E_0^2 - E_I^2}$. At the instability, $\Delta = 0$, and $k_{\rm rot} = \frac{1}{\hbar}\sqrt{2mE_0}$.

Employing a similar procedure as in Ref. [12] we obtain that the BEC aspect ratio $\chi = Z/X$ fulfills:

$$\chi^2 \left[\frac{(1-\epsilon_{dd})(1+\chi)^2 + 3\epsilon_{dd}}{(1+2\epsilon_{dd})(1+\chi)^2 - 3\epsilon_{dd}\chi^2}\right] = \lambda_\perp^2, \qquad (15)$$

with $\lambda_\perp = \nu_x/\nu_z$ and

$$Z^2 = \frac{g n_0}{2\pi^2 m \nu_z^2}\left[(1+2\epsilon_{dd}) - \frac{3\epsilon_{dd}\chi^2}{(1+\chi)^2}\right] \qquad (16)$$

These two equations fully determine the TF solution for given ϵ_{dd}, gn_0, and the ratio ν_x/ν_z. By inserting the expressions of X^2 and Z^2 in E_0, we find for $\epsilon_{\rm dd} \simeq 1$:

$$E_0^2 = \frac{h^2\nu_z^2}{6}(1+\chi)^2\left(\lambda_\perp^2 + \frac{1}{1+2\chi}\right) \qquad (17)$$

whereas χ simplifies into $\chi = \lambda_\perp(1+\sqrt{1+1/\lambda_\perp})$. As a result, at the instability $k_{\rm rot}\ell_z$ depends only on the transverse confinement aspect ratio $\lambda_\perp$, and we obtain the geometrical factor κ introduced in the main text:

$$\kappa = k_{\rm rot}\ell_z = \left(\frac{2}{3}\right)^{1/4}\sqrt{1+\chi}\left(\lambda_\perp^2 + \frac{1}{1+2\chi}\right)^{1/4}. \qquad (18)$$

In order to better compare quantitatively with our quench experiments, we evaluate the 3D TF solution, $n = n_0(1-(x/X)^2-(y/Y)^2-(z/Z)^2)$ for the axially trapped condensate prior to the quench. We then use the central density n_0 and the TF radii X and Z in the evaluation of the roton spectrum above, employing the value of ϵ_{dd} after the quench. This procedure takes the quench of $a_{\rm s}$ into account by evaluating an initial (i. e. at $t_{\rm h} = 0\,$ms) *instantaneous* roton spectrum, within the assumption of an immediate change of $a_{\rm s}$. Further refinements might be required to fully describe the dynamical population of the roton mode, related to the roton softening of the time-dependent *instantaneous* excitation spectrum depicted in Method O. Yet, as being inspired from the latter concept, our approach allows for a better description of our experiments than purely stationary calculations.

The evaluation of the 3D TF solution is performed by following the procedure of Ref. [50]. We introduce the BEC aspect ratios: $\chi_x = Z/X$, and $\chi_y = Z/Y$. For a given ϵ_{dd}, these aspect ratios fulfil the equations:

$$\chi_x^2 \frac{A(\epsilon_{dd},\chi_x,\chi_y)}{C(\epsilon_{dd},\chi_x,\chi_y)} = \left(\frac{\nu_x}{\nu_z}\right)^2, \qquad (19)$$

$$\chi_y^2 \frac{B(\epsilon_{dd},\chi_x,\chi_y)}{C(\epsilon_{dd},\chi_x,\chi_y)} = \left(\frac{\nu_y}{\nu_z}\right)^2, \qquad (20)$$

where $A(\epsilon_{dd},\chi_x,\chi_y) = 1 + \epsilon_{dd}(F_1 - F_2 + F_3)$, $B(\epsilon_{dd},\chi_x,\chi_y) = 1 + \epsilon_{dd}(F_1 - F_2 - F_3)$, and $C(\epsilon_{dd},\chi_x,\chi_y) = 1 + \epsilon_{dd}(F_1 + 2F_2)$. Here we have introduced the functions:

$$F_1(\chi_x,\chi_y) = \int_0^1 du\left[\frac{3u^2}{\sqrt{\alpha^2-\beta^2}} - 1\right], \qquad (21)$$

$$F_2(\chi_x,\chi_y) = \int_0^1 du\left(\frac{3u^2-1}{2}\right)\left[\frac{3u^2}{\sqrt{\alpha^2-\beta^2}} - 1\right], \qquad (22)$$

$$F_3(\chi_x,\chi_y) = \int_0^1 du\left(\frac{9u^2(1-u^2)}{4}\right)\left[\frac{\sqrt{\alpha^2-\beta^2}-\alpha}{\beta\sqrt{\alpha^2-\beta^2}}\right], \qquad (23)$$

with $\alpha(\chi_x,\chi_y,u) = (\chi_x^2+\chi_y^2)(1-u^2)/2 + u^2$, and $\beta(\chi_x,\chi_y,u) = (\chi_x^2-\chi_y^2)(1-u^2)/2$. Once $\chi_{x,y}$ are determined one may then evaluate the TF radii:

$$X^2 = \frac{g n_0}{2\pi^2 m\nu_x^2} A(\epsilon_{dd},\chi_x,\chi_y), \qquad (24)$$

$$Y^2 = \frac{g n_0}{2\pi^2 m\nu_y^2} B(\epsilon_{dd},\chi_x,\chi_y), \qquad (25)$$

$$Z^2 = \frac{g n_0}{2\pi^2 m\nu_z^2} C(\epsilon_{dd},\chi_x,\chi_y), \qquad (26)$$

and the central density

$$n_0 = \frac{(15N)^{2/5}}{8\pi(ABC)^{1/5}}\frac{1}{(a_{\rm s}\tilde{l}^4)^{3/5}}, \qquad (27)$$

with $\tilde{l}^2 = \frac{\hbar}{2\pi m(\nu_x\nu_y\nu_z)^{1/3}}$.

Using this procedure and the experimental parameters (trap geometry and atom number), we calculate the values of $k_{\rm rot}$ shown in Fig. 4. These values are computed at a quenched $a_{\rm s}$ value taken to be just below the threshold for the roton softening. To estimate this threshold, we use here our full numerical platform based on the generalized NLGPE (Method N), as it is expected to better quantitatively capture the physical details of our experiments. Using our analytical model, we are also able to estimate a softening threshold in our quench experiment, corresponding to $\Delta = 0$ within the above-described simplified approach. The predicted threshold values, $a_{\rm s}^{\infty}$, in the experimentally relevant geometries are reported in Extended Data Table II. Despite of the local density approximation, and the limited validity of the approximate calculation of the roton spectrum performed above, which is restricted to the vicinity of $\epsilon_{dd} = 1$, we note that the results for $k_{\rm rot}$ and $a_{\rm s}^*$ are in very good agreement with our experimental results (see Figs. 4-5, Extended Data Table II)

N. Real-time evolution simulations

Our simulations of the NLGPE are performed using a split operator technique. The evolution operator over a time Δt ($\Delta t \to i\Delta t$ for imaginary time evolution) may be approximately split as $e^{-i\hat{H}\Delta t/\hbar} = e^{-i\hat{T}\Delta t/\hbar}e^{-i\hat{V}\Delta t/\hbar} + O(\Delta t^2)$. In this expression, $\hat{T}$ is the kinetic energy term, and $\hat{V}$ the potential energy. The effective potential energy for the evolution is given by the sum of external potential, inter particle interactions, local LHY correction, and three-body losses.

We first evaluate using imaginary time evolution the initial BEC wavefunction, $\psi_0(\boldsymbol{r})$, prior to the quench of a_s. The initial wavefunction for the subsequent real-time evolution is then constructed via $\psi_i = \psi_0 + \Delta\psi$, where $\Delta\psi$ accounts for thermal fluctuations, which we simulate by populating the eigenstates of the harmonic trap as in Refs. [37, 42]. Starting with this initial wavefunction ψ_i, we mimic as close as possible the conditions of our experiments, including ramping, holding, and ToF times. In particular, we include an exponential ramp of the magnetic field $B(t) = B_f + (B_i - B_f)e^{-t/\tau}$, with $\tau = 0.98$ms, and convert the magnetic field value to the scattering length a_s from the experimental measured relation. Moreover, for the value of the three-body loss coefficient L_3 we use a linear fit of the experimentally determined values.

The simulation of the ToF expansion is performed in two steps. First we use a multi-grid analysis in order to rescale the size of the numerical box as the cloud expands during the ToF expansion. After some expansion time the density drops significantly, and the subsequent evolution can be readily calculated via $e^{-i\hat{T}t/\hbar}$. Our numerics show clearly that the effect of nonlinearity is small during the first stages of the evolution, and hence that the ToF expansion indeed may be employed to image the momentum distribution of the condensate at the time in which the trap is opened.

We obtain the Fourier Transform of the wavefunction $\psi(\mathbf{r},\mathbf{t})$, $\tilde{\psi}(\mathbf{k},t)$, at different times, evaluating the integrated momentum distribution $\tilde{n}(k_y,t) = \int dk_x dk_z |\tilde{\psi}(\mathbf{k},t)|^2$. For a sufficiently large t, this momentum distribution shows clear roton side peaks. This is typically after a few ms, the exact t value depends on the gas characteristics (in particular T) and on a_s. We evaluate the roton momentum as the mean value of the momentum in the roton peak.

From the imaginary-time evolution simulations, we are also able to predict the a_s threshold for the roton softening (i. e $\Delta = 0$), as it is equivalent to the threshold for the instability of the BEC. To find the softening threshold, we then look for this instability boundary, which, in the imaginary-time, corresponds to the absence of mean-field stable solution [40, 41]. To do so, we proceed by steps. We start by calculating the ground-state solution for a given a_s that we know to be well within the stable regime. We then reduce a_s in small steps and successively calculate the corresponding ground-state solution using the solution of the previous step as starting condition. We do so until no mean-field stable solution can be found. The predicted instability threshold a_s^i is reported in Extended Data Table II. For the theory predictions shown in Fig. 4 (real-time evolution and analytical calculation (Method M)), we use quenched a_s values such that the instability boundary is just slightly crossed, meaning a_s is taken $1a_0$ smaller than the instability threshold a_s^i.

O. Privileged population of the roton mode in a quench of a_s and *instantaneous* excitation spectrum

It is interesting to note that, even in the presence of a finite roton gap Δ in the stationary excitation spectrum, the roton mode can still be selectively dynamically populated in a quench of a_s [27]. Indeed the quench can be viewed as performing a temporary destabilization of the mode of lowest energies in the stationary spectrum, and thus in particular of the roton mode. This can be grasped, based on our theoretical description, by decomposing the quench evolution in small time steps and linearising the NLGPE around the instantaneous state of the gas. As the local state differs from the ground state, the *instantaneous* spectrum is modified compared to the stationary one and the non stability of this state leads to pushing the spectrum down in energy, destabilizing the lowest energy modes. The dynamically populated modes are the ones that get instantly destabilized. Then the roton is favored in this respect as a local minimum in $\epsilon(k)$. Moreover, the flattening of the dispersion relation around $k_{\rm rot}$ makes the different modes in this region oscillate in phase. This might lead to a cooperative enhancement of the population at short t_h, as suggested in Ref. [27]. Note that our argument is based on a linear evolution assumption, which is expected to be valid at least for short t_h. The dynamical population of the roton mode is an intriguing problem, which we plan to further investigate in the future.

Extended Data Table I | dBEC parameters for the experimental measurements (Fig. 5). The typical statistical uncertainties on ν_x and ν_z are below 1 %, and can be up to 10 % for ν_y. The experimental repeatability results in 5-to-10 % shot-to-shot fluctuations of N, f and T.

λ	ν_x (Hz)	ν_y (Hz)	ν_z (Hz)	N (10^4)	f (%)	T (nK)
4.3	114	35	149	9	66	45
10.2	183	30	306	11	62	104
14.3	267	32	456	8.6	50	150
21.3	357	30	638	8.4	36	179
29.7	432	26	771	7	20	171

Extended Data Table II | Roton softening threshold for the experimental geometries (Table I), deduced from the $\mathcal{C}$ fits for the experimental onset of the population (a_s^*, also reported in Fig. 5), from the q1D analytical model (a_s^∞) and from imaginary time calculations (a_s^i). The theory and experiment values match well, yet with a noticeable stronger deviation for the (two) more elongated and tightest traps. We note that these latter cases depart more from the $\epsilon_{dd} = 1$ regime.

λ	ν_z (Hz)	a_s^* (a_0)	a_s^∞ (a_0)	a_s^i (a_0)
4.3	149	51.3	54	50
10.2	306	50.2	52.9	46
14.3	456	49	49.1	43
21.3	638	47.7	44.8	39
29.7	771	45.2	34.2	30

Appendix

B Optical setup improvements

Within this Appendix we discuss major experimental upgrades and improvements of the optical setup that have been implemented during the course of this thesis. For a description of the inital optical setup the reader is referred to Ref. [Fri14a].

Three-dimensional optical lattice

To perform experiments with erbium quantum gases in low dimensions, we implement a three-dimensional (3D) optical lattice. The optical lattice is created in a standard way. We retro-reflect the light of laser beams, which are focused on the position of the atoms. The formed standing wave effectively slices the atomic cloud along the lattice beams. This technique is applied along three (almost) orthogonal axes to form a crystal-like potential for the atoms. Our lattice is build with a special geometry: Two orthogonal horizontal green lattice beams at 532 nm[1] and one vertical infrared lattice beam at 1064 nm[2] create a cuboid lattice with a twice as large lattice constant along the vertical direction. The cuboid unit cell features lattice constants of $d_x = d_y = 266\,\mathrm{nm}$ and $d_z = 532\,\mathrm{nm}$, where x and y lie in the horizontal plane and depict the axis of the two green lattice beams, and z denotes the vertical axis oriented along the infrared lattice beam. The optical setup of our off-resonant trapping beams and resonant imaging beams is illustrated in Fig. B.1.

For the vertical lattice, we branch 1064 nm light from the horizontal optical dipole trap (ODT) setup [Fri14a]. The optical lattice potentials are applied at the very end of the forced evaporative cooling procedure, where the ODT has already reached low intensities and it becomes possible to branch off the light. A polarization maintaining high-power fibre[3] with a length of 3 m is used to clean the optical profile and delivers up to 6 W for the vertical lattice. The angle of the lattice beam with respect to the axis of gravity is $\approx 11^\circ$ and the waist at the position of the atoms is $\approx 300\,\mu\mathrm{m}$. At full power the harmonic confinement of the retro-reflected vertical lattice beam leads to radial trap frequencies of $\omega_r^{1064} \approx 2\pi \times 25\,\mathrm{Hz}$.

[1] laser light from model Verdi V10, 10 W at 532 nm, from Coherent
[2] laser light from model Mephisto MOPA, 42 W at 1064 nm, from Innolight (now Coherent)
[3] model LMA-PM-15, from NKT Photonics GmbH

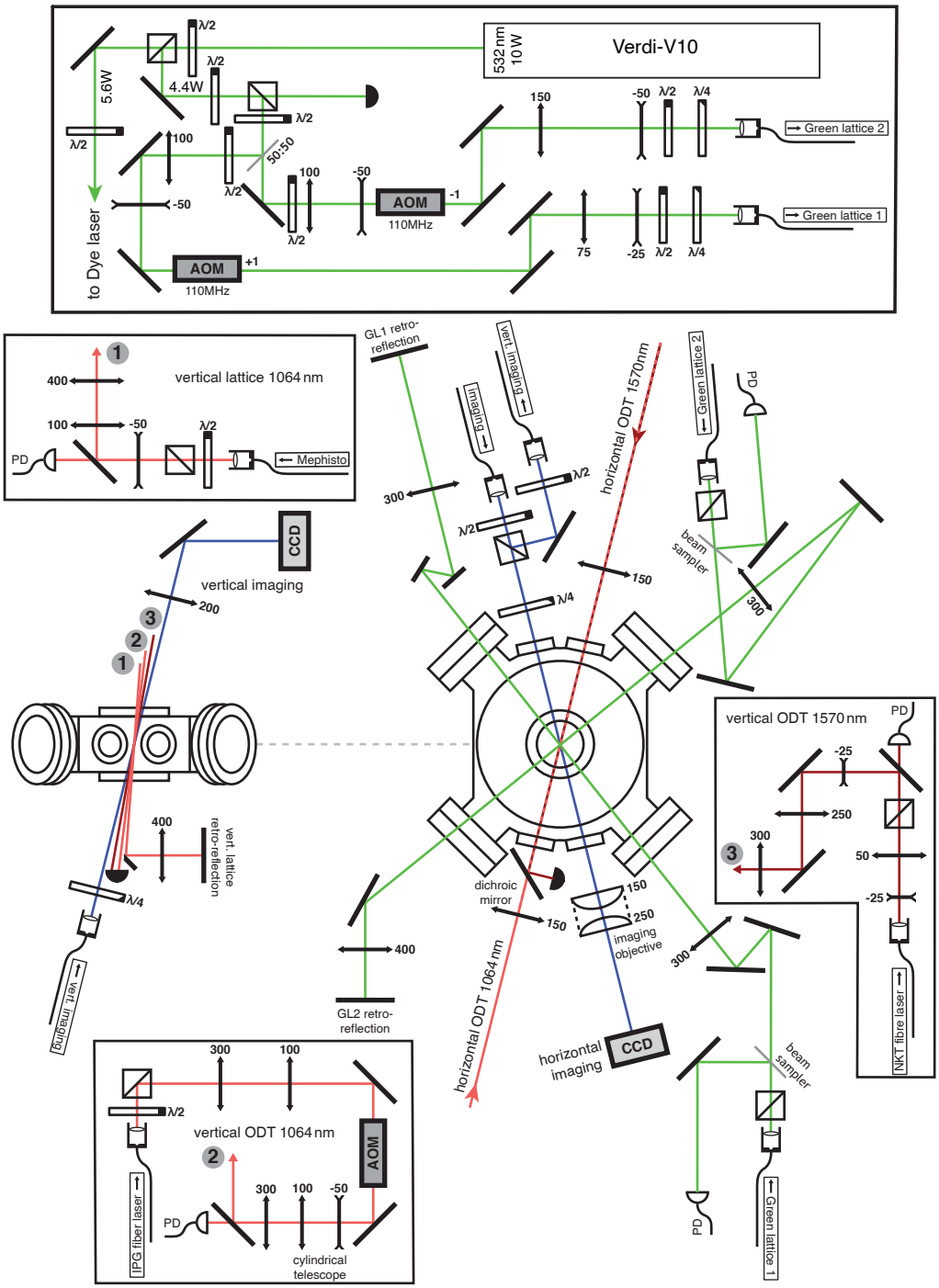

Figure B.1.: Overview of the laser setup for optical trapping, absorption imaging and lattice experiments. The laser beams intersect at the central point of the experimental chamber, shown from a side and a top view. For the horizontal optical lattice beams a diode-pumped solid state laser (Verdi) at 532 nm (green) is used. The vertical lattice utilizes 1064 nm (red) light from a single-mode master oscillator power amplifier (Mephisto MOPA). The lattice beams are created in a retro-reflecting configuration. The optical dipole trap beams operated at 1064 nm (red) and 1570 nm (dark red) are already introduced in Ref. [Fri14a] and shown here for completeness. Absorption imaging is performed with 401 nm (blue) light that is created by a frequency doubled diode laser (TA-SHG-pro). Figure adapted from [Fri14a].

The light for the horizontal lattice beams is prepared on a separate laser table, which is located next to the experimental table. The 532 nm-light is split into two paths and passes in each path through a large-aperture acusto-optic modulator[4] (AOM), which fulfill two purposes: First, they are used for an active stabilization of the lattice power and second, they prohibit interference effects of the lattice beams via a detuning of their respective laser frequencies to each other. Here, we use for the first green lattice beam the plus-first order and for the second green lattice beam the minus-first order of the respective AOM, leading to an absolute detuning of $\approx 220\,\mathrm{MHz}$. Then, the light is delivered to the experimental table via two 8 m polarization-maintaining fibres. The maximum deliverable power is limited due to stimulated Brillouin scattering [Ipp72] and reaches values of up to 1.2 W, respectively. In the future, shorter fibres could be implemented to increase the maximum available power. Monitoring photodiodes (PD) on the experimental table allow for an active stabilization of the laser power. The two green lattice beams are aligned such that they are orthogonal to each other and their respective focal waists are $\approx 160\,\mu\mathrm{m}$. At full power, the harmonic confinement of the retro-reflected green lattice beams leads to radial trap frequencies of $\omega_r^{532} \approx 2\pi \times 40\,\mathrm{Hz}$, respectively.

Reference [Fri14a] gives more details on the additional optical dipole traps and imaging beams.

Horizontal imaging

One of the most important technical requirements in ultracold atom experiments is a good performance of the optical imaging. For absorption imaging, resonant laser light illuminates the atoms and gets partially absorbed, which results in a reduction of the light intensity when it passes through the atomic cloud. This shadow-like signature is compared to a reference image and hence used to extract the density of the atoms, i. e. the optical depth. An important parameter is the resolution of this imaging technique, as it gives the limits on the size of observable structures within the atomic sample. Further, the quality can also be limited by technical noise on the image.

In our experiment, we typically image the atomic cloud after a certain time-of-flight (TOF), where the atoms have already expanded and reached a size of several tens of μm. Still, to extract most information from the absorption images, it is important to have a good performance in respect to the two relevant limitations: imaging resolution and imaging noise. To give an example where a good performance has proven to be of relevance, noise-correlation experiments can be mentioned. Here, pioneering works have shown that strongly correlated quantum phases can be observed via density-density correlations of atoms in momentum space in TOF experiments for high-resolution and low-noise images [Gre05, Föl05].

[4] model I-M110-2C10B6-3-GH26 AOM, from Gooch&Housego

Imaging resolution

The maximum possible imaging resolution for our horizontal imaging is given by our numerical aperture (NA), which is about 0.1. This value is set by the geometric size of the CF16 imaging viewport, see Fig. B.1. This NA results in a theoretical diffraction limit of 2.5 μm for our 401 nm imaging light. To reach this limit, we have implemented a self-designed imaging objective, which has replaced the former final lense before the horizontal CCD-camera, see Ref. [Fri14a]. The objective consists out of two achromatic doublets[5] mounted close to each other. The optimal combination of lenses has been found via ray-tracing simulations[6]. With the new objective the maximum imaging resolution is almost reached. The magnification of the final setup is 2.9.

Imaging noise

One major contribution to imaging noise arises from residual interference fringes. Interference fringes appear from scattering of the imaging light at defects or dust on optical components. As the original absorption image is compared to a reference image, which only differs by the absence of the atomic cloud, the fringes are expected to cancel after post processing. However, due to mechanical vibrations of the optical setup, it is possible that fringes slightly change in position or amplitude for the two subsequent images and hence do not vanish. The relevant parameter in this context is the timespan between the two images. A to long time interval between the pictures facilitates the manifestation of vibrations, which are typically governed by acoustic frequencies.

A reduction of this noise source for our imaging is tackled by exchanging the former CCD sensor by a fast CMOS camera[7]. The newly implemented CMOS model allows to improve the sampling rate of our imaging system by three orders of magnitude, reducing the timespan between the subsequent images from ≈ 100 ms to below 100 μs. This improvement results in a major suppression of residual fringes for the processed atomic picture, thus decreasing the noise level.

Further improvements

Throughout the coarse of this thesis we have constantly maintained and renewed the experimental setup. This minor technical updates have had the aim to reduce the daily maintenance necessities and to improve the performance and stability of the experiment.

Among these updates, the most important improvement, as compared to Ref.[Fri14a], relates

[5] model AC508-150 and -250, from Thorlabs

[6] software Zeemax Optics Studio

[7] scientific camera model Neo 5.5 sCMOS, front illuminated scientific CMOS, with 2560×2160 pixel resolution, $6.5 \times 6.5\,\mu m^2$ pixel size, 16 bit digitization, from Andor Technology

to the blue laser setup. The master laser was replaced by a commercial system[8] that can deliver up to 1.2 W of 401 nm light. This allowed us to remove the injection-locked slave laser for the Zeeman slower (ZS) setup, as the light can be transferred by an end-cap fiber[9] to the experiment. For best operation of the ZS about 200 mW laser power after the fiber is needed. With this setup, we find a nice long-term stability. In addition, we have replaced the injection-locked slave laser for the transversal cooling section by a similar homemade slave laser that delivers up to 300 mW, almost a factor of four more power than previously. With this transversal cooling section, we can increase the atom number trapped in the MOT by up to a factor of seven, as the perpendicular velocity spread of the atomic beam is reduced.

[8] TA-SHG-pro system, from Toptica Photonics AG
[9] model PMC-400Si, from Schäfter+Kirchhoff

Appendix

C Magnetic field stabilization

One of the most relevant requirements for our experiment is a precise and accurate control of the magnetic field. This control is from importance in different contexts:

- Particle interaction: As a result of the dense Feshbach spectrum with many narrow Feshbach resonances in lanthanides, see Chapter 4, tuning the scattering length a_s via such resonances requires a high level of control on the magnetic field. This control is especially needed in the strongly interacting regime, where small magnetic field changes can strongly affect a_s.

- Low field regime: An interesting direction with dipolar atoms is the study of phenomena emerging at very low magnetic field values, see Sec. 6.2. In this low-field region, a stable magnetic field is from particular interest, as the observed phenomena can be dramatically influenced if the noise reaches similar amplitudes as the bias field. Hence, the noise has to be reduced in a controlled manner.

- Dipole orientation: One of the major observables in our experiment is the dependence of the physical processes on the orientation of the dipoles with respect to the confinement geometry and to each other. Here, it is from particular importance to have the angle of the dipole orientation, i. e. the magnetic field orientation, well under control to reveal the underlying physics at play.

With this requirements in mind we have improved the magnetic field control along the three orthogonal directions in our experiment. While small drifts during the day (typically a few mG) can easily be calibrated and hence canceled, it is a major challenge to deal with magnetic field frequency noise, mainly coming from the power lines surrounding the experiment. This noise is related to the AC-frequency of the power line and shows frequency components at 50 Hz and multiple higher harmonics, and can have different influences for various experimental conditions:

- Long time effect: For experiments where we are interested in the properties of the atomic sample at timescales exceeding holding times of 20 ms, i. e. where also the oscillatory behavior of the lowest (50 Hz) noise component is covered, the magnetic field noise leads to an effective broadening of the applied magnetic field. Hence, one

has to take into account the magnetic field spread and the resulting spread of e. g. the scattering length a_s for a specific experiment.

- Dynamical effect: When the effects we want to observe occur at short timescales, the sinusoidal oscillation of the magnetic field has to be taken into account. While for large bias fields only oscillations of the noise *along* the bias field matters[1], for magnetic fields in the order of the amplitude of the noise all three axes have to be accounted. This proves to be particular striking when the noise oscillations of the different axis are not of the same amplitude and phase, leading to an oscillating rotation of the magnetic field direction as a function of time.

As a consequence, for certain measurements it is necessary to cancel this magnetic field noise in order to observe physical effects that are sensitive to the absolute magnetic field and the orientation of the dipoles.

Experimental setup

Our aim is to actively cancel the magnetic field noise along the three orthogonal axes. Therefore, we implement three sets of coils, which can be independently controlled via active stabilization servo-loops. For each axis we implement a pair of coils with two windings each on top of the already implemented compensation cage coils (see Ref. [Fri14a]). The coils are shaped rectangularly and have a geometric size of $1.2 \times 1.2 \times 0.85\,\mathrm{m}^3$. While the center of the coil pairs overlap with the center of the vacuum chamber in x and y, the center of the z-coils is shifted by 0.25 m in positive z-direction. For our lab coordinate system see Fig. 2.4.

For active feedback, we implement a three-axis magnetic field sensor[2] close to the experimental chamber. The sensor is about 10 cm away from the position of the atoms. The sensor signal is fed back to three PID-controllers, which actively regulate the current sent to the three cancellation coil pairs. In brief, the cancellation coils create a magnetic field that has the opposite sign but similar amplitude as the respective noise field, thus canceling the magnetic field noise along the three orthogonal axes. The output stage consists of three high-current operational amplifiers[3], capable to deliver a maximum current of ± 5 A each. With this we can reach magnetic field values of about ± 50 mG along x and y and about ± 100 mG along z. The PID-controllers are optimized for a frequency range below 1 kHz. For our experiment this marks the relevant range of noise-cancellation operation as higher frequency components are shielded by the steel chamber due to eddy currents and do not need to be compensated.

[1] The total magnetic field accounting for the field of three orthogonal axes is calculated by adding the quadratic components, i. e. $|B| = \sqrt{B_x^2 + B_y^2 + B_z^2}$. Hence, for a large bias field along one of the axis, e. g. B_x, the magnetic field noise along the other axes, which leads to small varying fields B_y and B_z, can be neglected.

[2] model Mag-03-MS-70, three-axis magnetic field sensor, noise $< 10\,\mathrm{pt}/\sqrt{\mathrm{Hz}}$, from Bartington Instruments

[3] model OPA549, from Texas Instruments

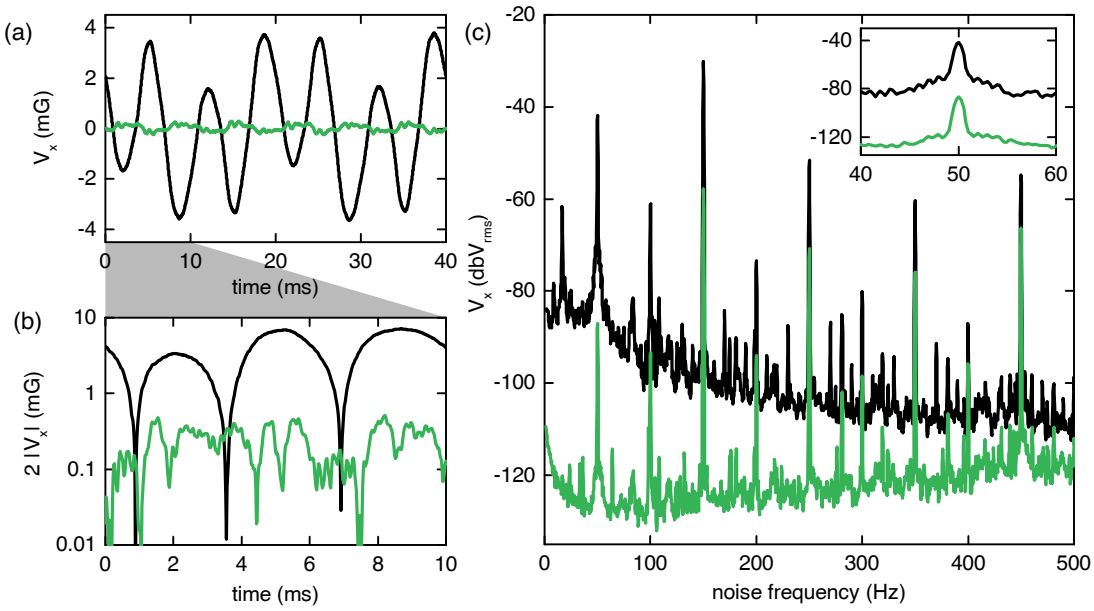

Figure C.1.: Performance of the magnetic-field-stabilization setup along the x-axis. The performance is measured with the magnetic field sensor, which is used for stabilization. Performance at the position of the atomic cloud might differ. Magnetic field fluctuation without (black) and with (green) active stabilization in the time domain (a-b) and frequency domain (c). (a) Amplitude of magnetic field noise and (b) normalized total amplitude in logarithmic scale within a narrower time window. (c) Frequency spectrum of the magnetic field fluctuations up to 500 Hz. On top of a smooth noise floor, 50 Hz and higher harmonics are the dominant frequency components. The inset shows a zoom-in into the 50 Hz region.

Performance

To investigate the performance of our magnetic-field-stabilization setup, we analyze the noise in time and frequency domain without and with active stabilization. The measurements are performed directly with the magnetic field sensor that is used within the feedback loop[4]. The magnetic field noise close to the atomic cloud is found to have peak-to-peak amplitudes of about 8 mG along x and y and about 2 mG along z. We note that, the lower noise amplitude along the z-axis results from a passive shielding by the massive optical table, which primarily affects the z-noise.

The total performance of our magnetic-field-cancellation setup, exemplary shown for the x-axis, is summarized in Fig. C.1. Similar performance is found along the other two axes. The initial peak-to-peak amplitude of ≈ 8 mG can be reduces below 1 mG when the stabilization is applied, see Fig. C.1(a-b). The most prominent frequency components are 50 Hz and 150 Hz, while also other frequency components are contributing, see Fig. C.1(c). Our magnetic field stabilization manages to reduce the noise amplitude by up to 45 db. At frequencies above 1 kHz the feedback loop acquires a π phase lag, resulting in an enhanced noise at this frequency components. This high-frequency oscillations can be neglected, as they are shielded by the steel chamber and do not reach the atomic sample.

[4] The magnetic field sensor reports the noise amplitude in voltage, where 14.3 mV correspond to 1 mG.

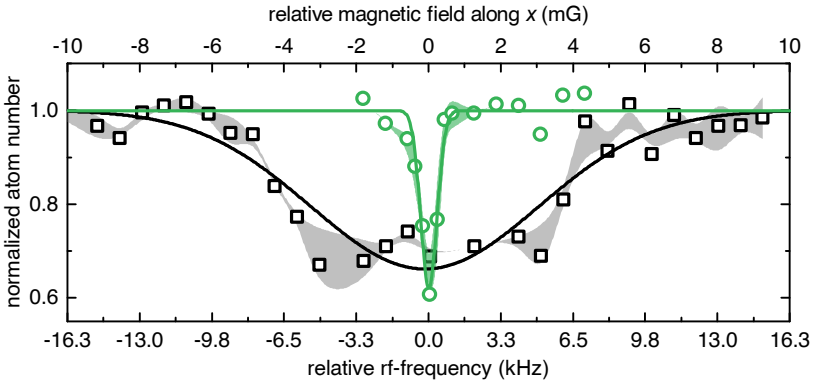

Figure C.2.: Performance of the magnetic-field-stabilization setup measured with ^{168}Er via Zeeman spectroscopy, see text. The measurements are performed for a bias field along the x-axis. The normalized atom number without (squares) and with (circles) active stabilization is plotted as a function of the frequency of the rf pulse, relative to the resonance frequency. The rf frequency can be converted into magnetic field via the knowledge of the Zeeman splitting, see Eq. 2.7. To estimate the peak-to-peak width of the noise, we use the $\pm 2\sigma$ width of the Gaussian fitting functions (solid lines). With this method we extract a noise amplitude without and with stabilization of 12.6(1.4) mG and 0.9(1) mG, respectively.

As an ultimate test of the performance, we measure the amplitude of the magnetic field noise directly with the atomic cloud. For the measurement we resonantly excite the atoms from the lowest to higher atomic Zeeman states by a radio-frequency (rf) pulse. The pulse lasts for 20 ms as to cover also the lowest frequency noise component (50 Hz). When the energy of the rf excitation matches the differential Zeeman energy, atom loss is encountered due to dipolar relaxation of populated higher spin states. The width of the resonant loss feature carries information on the magnetic field noise. In particular, it tells how much the magnetic field was drifting or oscillating during the rf spectroscopy. In turn, the width can be used as a measure of the performance of our magnetic field stabilization. Figure C.2 shows our measurements and reveals that the magnetic field noise across the atomic sample can be reduced below 1 mG along the x-axis. Similar performance is found along the two orthogonal directions. Our observations confirm the results of Fig. C.1. The achieved magnetic field stability is a promising starting point to investigate physical phenomena for which a precise magnetic field control is required.

Bibliography

[Aik12] K. Aikawa, A. Frisch, M. Mark, S. Baier, A. Rietzler, R. Grimm, and F. Ferlaino, *Bose-Einstein condensation of erbium*, Phys. Rev. Lett. **108**, 210401 (2012).

[Aik14] K. Aikawa, A. Frisch, M. Mark, S. Baier, R. Grimm, and F. Ferlaino, *Reaching Fermi degeneracy via universal dipolar scattering*, Phys. Rev. Lett. **112**, 010404 (2014).

[And87] P. W. Anderson, *The resonating valence bond state in la2cuo4 and superconductivity*, Science **235**, 1196 (1987).

[And95] M. H. Anderson, J. R. Ensher, M. R. Matthews, C. E. Wieman, and E. A. Cornell, *Observation of Bose-Einstein condensation in a dilute atomic vapor*, Science **269**, 198 (1995).

[And97] M. R. Andrews, C. G. Townsend, H.-J. Miesner, D. S. Durfee, D. M. Kurn, and W. Ketterle, *Observation of interference between two bose condensates*, Science **275**, 637 (1997).

[And17] L. Anderegg, B. L. Augenbraun, E. Chae, B. Hemmerling, N. R. Hutzler, A. Ravi, A. Collopy, J. Ye, W. Ketterle, and J. M. Doyle, *Radio frequency magneto-optical trapping of caf with high density*, Phys. Rev. Lett. **119**, 103201 (2017).

[And18] L. Anderegg, B. L. Augenbraun, Y. Bao, S. Burchesky, L. W. Cheuk, W. Ketterle, and J. M. Doyle, *Laser cooling of optically trapped molecules*, ArXiv e-prints 1803.04571 (2018).

[Ash76] N. Ashcroft and N. D. Mermin, *Solid state physics*, Hartcourt College Publishers, 1976.

[Aue94] A. Auerbach, *Interacting electrons and quantum magnetism*, Springer-Verlag, New York, 1994.

[Auz99] F. Auzel and P. Goldner, *Rare earth ions in the glass amplifying medium: A proposal for new doping precursors*, Mat. Sci. For. **315**, 34 (1999).

[Bai12a] S. Baier, *An optical dipole trap for erbium with tunable geometry*, Master's thesis, Faculty of Mathematics, Computer Science and Physics; University of Innsbruck (2012).

[Bai12b] D. Baillie and P. B. Blakie, *Magnetostriction and exchange effects in trapped dipolar Bose and Fermi gases*, Phys. Rev. A **86**, 023605 (2012).

[Bai16] S. Baier, M. J. Mark, D. Petter, K. Aikawa, L. Chomaz, Z. Cai, M. Baranov, P. Zoller, and F. Ferlaino, *Extended bose-hubbard models with ultracold magnetic atoms*, Science **352**, 201 (2016).

[Bak10] W. S. Bakr, A. Peng, M. E. Tai, R. Ma, J. Simon, J. I. Gillen, S. Fölling, L. Pollet, and M. Greiner, *Probing the superfluid–to–mott insulator transition at the single-atom level*, Science **329**, 547 (2010).

[Ban05] H. Ban, M. Jacka, J. Hanssen, J. Reader, and J. McClelland, *Laser cooling transitions in atomic erbium*, Opt. Express **13**, 3185 (2005).

[Bar08] M. Baranov, *Theoretical progress in many-body physics with ultracold dipolar gases*, Physics Reports **464**, 71 (2008).

[Bar12] M. A. Baranov, M. Dalmonte, G. Pupillo, and P. Zoller, *Condensed matter theory of dipolar quantum gases*, Chem. Rev. **112**, 5012 (2012).

[Bar14] J. F. Barry, D. J. McCarron, E. B. Norrgard, M. H. Steinecker, and D. DeMille, *Magneto-optical trapping of a diatomic molecule*, Nature **512**, 286 (2014).

[Bar15] R. Barends, L. Lamata, J. Kelly, L. García-Álvarez, A. G. Fowler, A. Megrant, E. Jeffrey, T. C. White, D. Sank, J. Y. Mutus, B. Campbell, Y. Chen, Z. Chen, B. Chiaro, A. Dunsworth, I.-C. Hoi, C. Neill, P. J. J. O'Malley, C. Quintana, P. Roushan, A. Vainsencher, J. Wenner, E. Solano, and J. M. Martinis, *Digital quantum simulation of fermionic models with a superconducting circuit*, Nature Comm. **6**, 7654 (2015).

[Bau14] K. Baumann, N. Q. Burdick, M. Lu, and B. L. Lev, *Observation of low-field Fano-Feshbach resonances in ultracold gases of dysprosium*, Phys. Rev. A **89**, 020701 (2014).

[Bec18] J. H. Becher, S. Baier, K. Aikawa, M. Lepers, J.-F. Wyart, O. Dulieu, and F. Ferlaino, *Anisotropic polarizability of erbium atoms: Supplemental material*, Phys. Rev. A **97**, 012509 (2018).

[Ber98] K. Bergmann, H. Theuer, and B. W. Shore, *Coherent population transfer among quantum states of atoms and molecules*, Rev. Mod. Phys. **70**, 1003 (1998).

[Ber17] H. Bernien, S. Schwartz, A. Keesling, H. Levine, A. Omran, H. Pichler, S. Choi, A. S. Zibrov, M. Endres, M. Greiner, V. Vuletić, and M. D. Lukin, *Probing many-body dynamics on a 51-atom quantum simulator*, Nature **551**, 579 (2017).

[Bis10] G. Bismut, B. Pasquiou, E. Maréchal, P. Pedri, L. Vernac, O. Gorceix, and B. Laburthe-Tolra, *Collective excitations of a dipolar Bose-Einstein condensate*, Phys. Rev. Lett. **105**, 040404 (2010).

[Bis12] U. Bissbort, F. Deuretzbacher, and W. Hofstetter, *Effective multibody-induced tunneling and interactions in the bose-hubbard model of the lowest dressed band of an optical lattice*, Phys. Rev. A **86**, 023617 (2012).

[Bla12] P. B. Blakie, D. Baillie, and R. N. Bisset, *Roton spectroscopy in a harmonically trapped dipolar Bose-Einstein condensate*, Phys. Rev. A **86**, 021604 (2012).

[Blo29] F. Bloch, *Über die quantenmechanik der elektronen in kristallgittern*, Zeitschrift für Physik **52**, 555 (1929).

[Blo99] I. Bloch, T. W. Hänsch, and T. Esslinger, *Atom laser with a cw output coupler*, Phys. Rev. Lett. **82**, 3008 (1999).

[Boh09a] J. L. Bohn, M. Cavagnero, and C. Ticknor, *Quasi-universal dipolar scattering in cold and ultracold gases*, New J. Phys. **11**, 055039 (2009).

[Boh09b] J. L. Bohn, R. M. Wilson, and S. Ronen, *How does a dipolar bose-einstein condensate collapse?*, Laser Phys. **19**, 547 (2009).

[Boh14] J. L. Bohn and D. S. Jin, *Differential scattering and rethermalization in ultracold dipolar gases*, Phys. Rev. A **89**, 022702 (2014).

[Bos24] S. N. Bose, *Plancks gesetz und lichtquantenhypothese*, Zeitschrift für Physik **26**, 178 (1924).

[Bou11] J. Bouchaud and M. Potters, *The oxford handbook of random matrix theory: Chapter 40*, Oxford Handbooks, 2011.

[Bra95] C. C. Bradley, C. A. Sackett, J. J. Tollett, and R. G. Hulet, *Evidence of Bose-Einstein condensation in an atomic gas with attractive interactions*, Phys. Rev. Lett. **75**, 1687 (1995).

[Bug04] C. Buggle, J. Léonard, W. von Klitzing, and J. T. M. Walraven, *Interferometric determination of the s and d-wave scattering amplitudes in* ^{87}Rb, Phys. Rev. Lett. **93**, 173202 (2004).

[Bur15] N. Q. Burdick, K. Baumann, Y. Tang, M. Lu, and B. L. Lev, *Fermionic suppression of dipolar relaxation*, Phys. Rev. Lett. **114**, 023201 (2015).

[Bur16] N. Q. Burdick, A. G. Sykes, Y. Tang, and B. L. Lev, *Anisotropic collisions of dipolar bose-einstein condensates in the universal regime*, New J. Phys. **18**, 113004 (2016).

[Cab17] C. R. Cabrera, L. Tanzi, J. Sanz, B. Naylor, P. Thomas, P. Cheiney, and L. Tarruell, *Quantum liquid droplets in a mixture of bose-einstein condensates*, Science (2017).

[Cam06] G. K. Campbell, J. Mun, M. Boyd, P. Medley, A. E. Leanhardt, L. G. Marcassa, D. E. Pritchard, and W. Ketterle, *Imaging the mott insulator shells by using atomic clock shifts*, Science **313**, 649 (2006).

[Car09] L. D. Carr, D. DeMille, R. V. Krems, and J. Ye, *Cold and ultracold molecules: science, technology and applications*, New J. Phys. **11**, 055049 (2009).

[Che16] L. W. Cheuk, M. A. Nichols, K. R. Lawrence, M. Okan, H. Zhang, and M. W. Zwierlein, *Observation of 2d fermionic mott insulators of* ^{40}K *with single-site resolution*, Phys. Rev. Lett. **116**, 235301 (2016).

[Chi05] C. Chin, T. Kraemer, M. Mark, J. Herbig, P. Waldburger, H.-C. Nägerl, and R. Grimm, *Observation of feshbach-like resonances in collisions between ultracold molecules*, Phys. Rev. Lett. **94**, 123201 (2005).

[Chi10] C. Chin, R. Grimm, P. Julienne, and E. Tiesinga, *Feshbach resonances in ultracold gases*, Rev. Mod. Phys. **82**, 1225 (2010).

[Chu86] S. Chu, J. E. Bjorkholm, A. Ashkin, and A. Cable, *Experimental observation of optically trapped atoms*, Phys. Rev. Lett. **57**, 314 (1986).

[Cla06] S. R. Clark and D. Jaksch, *Signatures of the superfluid to mott-insulator transition in the excitation spectrum of ultracold atoms*, New J. Phys. **8**, 160 (2006).

[Cla17] L. W. Clark, A. Gaj, L. Feng, and C. Chin, *Collective emission of matter-wave jets from driven bose-einstein condensates*, Nature **551**, 356 (2017).

[Con63] J. G. Conway and B. G. Wybourne, *Low-lying energy levels of lanthanide atoms and intermediate coupling*, Phys. Rev. **130**, 2325 (1963).

[Cor00] S. L. Cornish, N. R. Claussen, J. L. Roberts, E. A. Cornell, and C. E. Wieman, *Stable* ^{85}Rb *bose-einstein condensates with widely tunable interactions*, Phys. Rev. Lett. **85**, 1795 (2000).

[CS07] B. Capogrosso-Sansone, N. V. Prokof'ev, and B. V. Svistunov, *Phase diagram and thermodynamics of the three-dimensional bose-hubbard model*, Phys. Rev. B **75**, 134302 (2007).

[CS08] B. Capogrosso-Sansone, S. G. Söyler, N. Prokof'ev, and B. Svistunov, *Monte carlo study of the two-dimensional bose-hubbard model*, Phys. Rev. A **77**, 015602 (2008).

[CS10] B. Capogrosso-Sansone, C. Trefzger, M. Lewenstein, P. Zoller, and G. Pupillo, *Quantum phases of cold polar molecules in 2D optical lattices*, Phys. Rev. Lett. **104**, 125301 (2010).

[Cub03] J. Cubizolles, T. Bourdel, S. J. J. M. F. Kokkelmans, G. V. Shlyapnikov, and C. Salomon, *Production of long-lived ultracold* li_2 *molecules from a fermi gas*, Phys. Rev. Lett. **91**, 240401 (2003).

[Dah96] M. B. Dahan, E. Peik, J. Reichel, Y. Castin, and C. Salomon, *Bloch oscillations of atoms in an optical potential*, Phys. Rev. Lett. **76**, 4508 (1996).

[Dav95] K. B. Davis, M. O. Mewes, M. R. Andrews, N. J. van Druten, D. S. Durfee, D. M. Kurn, and W. Ketterle, *Bose-Einstein condensation in a gas of sodium atoms*, Phys. Rev. Lett. **75**, 3969 (1995).

[DeM99] B. DeMarco and D. S. Jin, *Onset of Fermi degeneracy in a trapped atomic gas*, Science **285**, 1703 (1999).

[Den15] X. Deng, C. Jia, and C.-C. Chien, *Sitewise manipulations and mott insulator-superfluid transition of interacting photons using superconducting circuit simulators*, Phys. Rev. B **91**, 054515 (2015).

[Don01] E. A. Donley, N. R. Claussen, S. L. Cornish, J. L. Roberts, E. A. Cornell, and C. E. Wieman, *Dynamics of collapsing and exploding bose-einstein condensates*, Nature **412**, 295 (2001).

[dP13a] A. de Paz, A. Chotia, E. Maréchal, P. Pedri, L. Vernac, O. Gorceix, and B. Laburthe-Tolra, *Resonant demagnetization of a dipolar bose-einstein condensate in a three-dimensional optical lattice*, Phys. Rev. A **87**, 051609 (2013).

[dP13b] A. de Paz, A. Sharma, A. Chotia, E. Maréchal, J. H. Huckans, P. Pedri, L. Santos, O. Gorceix, L. Vernac, and B. Laburthe-Tolra, *Nonequilibrium quantum magnetism in a dipolar lattice gas*, Phys. Rev. Lett. **111**, 185305 (2013).

[Dre17] D. Dreon, L. A. Sidorenkov, C. Bouazza, W. Maineult, J. Dalibard, and S. Nascimbene, *Optical cooling and trapping of highly magnetic atoms: the benefits of a spontaneous spin polarization*, J. Phys. B: At. Mol. Opt. Phys. **50**, 065005 (2017).

[Dür04] S. Dürr, T. Volz, A. Marte, and G. Rempe, *Observation of molecules produced from a bose-einstein condensate*, Phys. Rev. Lett. **92**, 020406 (2004).

[Dut15] O. Dutta, M. Gajda, P. Hauke, M. Lewenstein, D.-S. Lühmann, B. A. Malomed, T. Sowiński, and J. Zakrzewski, *Non-standard hubbard models in optical lattices: a review*, Rep. Prog. Phys. **78**, 066001 (2015).

[Ein05] A. Einstein, *Über einen die erzeugung und verwandlung des lichtes betreffenden heuristischen gesichtspunkt*, Annalen der Physik **322**, 132 (1905).

[Ein24] A. Einstein, *Quantentheorie des einatomigen idealen gases*, Akademie der Wissenschaften, Berlin, 1924.

[Fat06] M. Fattori, T. Koch, S. Goetz, A. Griesmaier, S. Hensler, J. Stuhler, and T. Pfau, *Demagnetization cooling of a gas*, Nature Phys. **2**, 765 (2006).

[Fat08] M. Fattori, C. D'Errico, G. Roati, M. Zaccanti, M. Jona-Lasinio, M. Modugno, M. Inguscio, and G. Modugno, *Atom interferometry with a weakly interacting bose-einstein condensate*, Phys. Rev. Lett. **100**, 080405 (2008).

[FB16] I. Ferrier-Barbut, H. Kadau, M. Schmitt, M. Wenzel, and T. Pfau, *Observation of quantum droplets in a strongly dipolar bose gas*, Phys. Rev. Lett. **116**, 215301 (2016).

[FB18] I. Ferrier-Barbut, M. Wenzel, F. Böttcher, T. Langen, M. Isoard, S. Stringari, and T. Pfau, *Scissors mode of dipolar quantum droplets of dysprosium atoms*, Phys. Rev. Lett. **120**, 160402 (2018).

[Fer10] F. Ferlaino, S. Knoop, M. Berninger, M. Mark, H. C. Nägerl, and R. Grimm, *Collisions of ultracold trapped cesium feshbach molecules*, Laser Phys. **20**, 23 (2010).

[Fey82] R. P. Feynman, *Simulating physics with computers*, International Journal of Theoretical Physics **21**, 467 (1982).

[Föl05] S. Fölling, F. Gerbier, A. Widera, O. Mandel, T. Gericke, and I. Bloch, *Spatial quantum noise interferometry in expanding ultracold atom clouds*, Nature **434**, 481 (2005).

[Föl06] S. Fölling, A. Widera, T. Müller, F. Gerbier, and I. Bloch, *Formation of spatial shell structure in the superfluid to mott insulator transition*, Phys. Rev. Lett. **97**, 060403 (2006).

[Fri12] A. Frisch, K. Aikawa, M. Mark, A. Rietzler, J. Schindler, E. Zupanič, R. Grimm, and F. Ferlaino, *Narrow-line magneto-optical trap for erbium*, Phys. Rev. A **85**, 051401 (2012).

[Fri13] A. Frisch, K. Aikawa, M. Mark, F. Ferlaino, E. Berseneva, and S. Kotochigova, *Hyperfine structure of laser-cooling transitions in fermionic erbium-167*, Phys. Rev. A **88**, 032508 (2013).

[Fri14a] A. Frisch, *Dipolar quantum gases of erbium*, Ph.D. thesis, Faculty of Mathematics, Computer Science and Physics of the University of Innsbruck (2014).

[Fri14b] A. Frisch, M. Mark, K. Aikawa, F. Ferlaino, J. L. Bohn, C. Makrides, A. Petrov, and S. Kotochigova, *Quantum chaos in ultracold collisions of gas-phase erbium atoms*, Nature **507**, 475 (2014).

[Fuk13a] T. Fukuhara, A. Kantian, M. Endres, M. Cheneau, P. Schauß, S. Hild, D. Bellem, U. Schollwöck, T. Giamarchi, C. Gross, I. Bloch, and S. Kuhr, *Quantum dynamics of a mobile spin impurity*, Nature Phys. **9**, 235 (2013).

[Fuk13b] T. Fukuhara, P. Schauß, M. Endres, S. Hild, M. Cheneau, I. Bloch, and C. Gross, *Microscopic observation of magnon bound states and their dynamics*, Nature **502**, 76 (2013).

[Gau13] A. L. Gaunt, T. F. Schmidutz, I. Gotlibovych, R. P. Smith, and Z. Hadzibabic, *Bose-einstein condensation of atoms in a uniform potential*, Phys. Rev. Lett. **110**, 200406 (2013).

[Gez08] A. Gezerlis and J. Carlson, *Strongly paired fermions: Cold atoms and neutron matter*, Phys. Rev. C **77**, 032801 (2008).

[Gór01] K. Góral, B.-G. Englert, and K. Rzążewski, *Semiclassical theory of trapped fermionic dipoles*, Phys. Rev. A **63**, 033606 (2001).

[Gór02] K. Góral, L. Santos, and M. Lewenstein, *Quantum phases of dipolar bosons in optical lattices*, Phys. Rev. Lett. **88**, 170406 (2002).

[Gre02] M. Greiner, O. Mandel, T. Esslinger, T. W. Hänsch, and I. Bloch, *Quantum phase transition from a superfluid to a Mott insulator in a gas of ultracold atoms*, Nature **415**, 39 (2002).

[Gre03] M. Greiner, C. A. Regal, and D. S. Jin, *Emergence of a molecular bose-einstein condensate from a fermi gas*, Nature **426**, 537 (2003).

[Gre05] M. Greiner, C. A. Regal, J. T. Stewart, and D. S. Jin, *Probing pair-correlated fermionic atoms through correlations in atom shot noise*, Phys. Rev. Lett. **94**, 110401 (2005).

[Gre13] D. Greif, T. Uehlinger, G. Jotzu, L. Tarruell, and T. Esslinger, *Short-range quantum magnetism of ultracold fermions in an optical lattice*, Science **340**, 1307 (2013).

[Gre16] D. Greif, M. F. Parsons, A. Mazurenko, C. S. Chiu, S. Blatt, F. Huber, G. Ji, and M. Greiner, *Site-resolved imaging of a fermionic mott insulator*, Science **351**, 953 (2016).

[Gri00] R. Grimm, M. Weidemüller, and Y. B. Ovchinnikov, *Optical dipole traps for neutral atoms*, Adv. At. Mol. Opt. Phy. **42**, 95 (2000).

[Gri05] A. Griesmaier, J. Werner, S. Hensler, J. Stuhler, and T. Pfau, *Bose-Einstein condensation of chromium*, Phys. Rev. Lett. **94**, 160401 (2005).

[Guh98] T. Guhr, A. Müller-Groeling, and H. Weidenmüller, *Random-matrix theories in quantum physics: common concepts*, Physics Reports **299**, 189 (1998).

[Guo16] M. Guo, B. Zhu, B. Lu, X. Ye, F. Wang, R. Vexiau, N. Bouloufa-Maafa, G. Quéméner, O. Dulieu, and D. Wang, *Creation of an ultracold gas of ground-state dipolar ^{23}Na^{87}Rb molecules*, Phys. Rev. Lett. **116**, 205303 (2016).

[Gup05] C. Gupta and N. Krishnamurthy, *Extractive metallurgy of rare earths*, CRC Press, 2005.

[Gus08] M. Gustavsson, E. Haller, M. J. Mark, J. G. Danzl, G. Rojas-Kopeinig, and H.-C. Nägerl, *Control of interaction-induced dephasing of bloch oscillations*, Phys. Rev. Lett. **100**, 080404 (2008).

[Had02] Z. Hadzibabic, C. A. Stan, K. Dieckmann, S. Gupta, M. W. Zwierlein, A. Görlitz, and W. Ketterle, *Two-species mixture of quantum degenerate bose and fermi gases*, Phys. Rev. Lett. **88**, 160401 (2002).

[Hag99] E. W. Hagley, L. Deng, M. Kozuma, J. Wen, K. Helmerson, S. L. Rolston, and W. D. Phillips, *A well-collimated quasi-continuous atom laser*, Science **283**, 1706 (1999).

[Har10] E. A. D. Hartog, J. P. Chisholm, and J. E. Lawler, *Radiative lifetimes of neutral erbium*, J. Phys. B **43**, 155004 (2010).

[Har15] R. A. Hart, P. M. Duarte, T.-L. Yang, X. Liu, T. Paiva, E. Khatami, R. T. Scalettar, N. Trivedi, D. A. Huse, and R. G. Hulet, *Observation of antiferromagnetic correlations in the hubbard model with ultracold atoms*, Nature **519**, 211 (2015).

[Hen17] T. Hensgens, T. Fujita, L. Janssen, X. Li, C. J. Van Diepen, C. Reichl, W. Wegscheider, S. Das Sarma, and L. M. K. Vandersypen, *Quantum simulation of a fermi-hubbard model using a semiconductor quantum dot array*, Nature **548**, 70 (2017).

[Her03] J. Herbig, T. Kraemer, M. Mark, T. Weber, C. Chin, H.-C. Nägerl, and R. Grimm, *Preparation of a pure molecular quantum gas*, Science **301**, 1510 (2003).

[HG15] S. Hacohen-Gourgy, V. V. Ramasesh, C. De Grandi, I. Siddiqi, and S. M. Girvin, *Cooling and autonomous feedback in a bose-hubbard chain with attractive interactions*, Phys. Rev. Lett. **115**, 240501 (2015).

[Hod05] E. Hodby, S. T. Thompson, C. A. Regal, M. Greiner, A. C. Wilson, D. S. Jin, E. A. Cornell, and C. E. Wieman, *Production efficiency of ultracold feshbach molecules in bosonic and fermionic systems*, Phys. Rev. Lett. **94**, 120402 (2005).

[Hon99] K. Honda, Y. Takahashi, T. Kuwamoto, M. Fujimoto, K. Toyoda, K. Ishikawa, and T. Yabuzaki, *Magneto-optical trapping of yb atoms and a limit on the branching ratio of the $^1P_1$ state*, Phys. Rev. A **59**, R934 (1999).

[Hou12] A. A. Houck, H. E. Türeci, and J. Koch, *On-chip quantum simulation with superconducting circuits*, Nature Phys. **8**, 292 (2012).

[Hub63] J. Hubbard, *Electron correlations in narrow energy bands*, Proc. Roy. Soc. London Ser. A **276**, 238 (1963).

[Hum85] R. E. Hummel, *Electronic properties of materials*, Springer-Verlag New York, 1985.

[Ilz18] P. Ilzhöfer, G. Durastante, A. Patscheider, A. Trautmann, M. J. Mark, and F. Ferlaino, *Two-species five-beam magneto-optical trap for erbium and dysprosium*, Phys. Rev. A **97**, 023633 (2018).

[Ing07] M. Inguscio, W. Ketterle, and C. Salomon (eds.), *Ultra-cold fermi gases*, IOS Press, Amsterdam, 2007.

[Ino18] R. Inoue, Y. Miyazawa, and M. Kozuma, *Magneto-optical trapping of optically pumped metastable europium*, ArXiv e-prints 1803.06475 (2018).

[Ipp72] E. P. Ippen and R. H. Stolen, *Controlling interactions between highly magnetic atoms with Feshbach resonances*, Appl. Phys. Lett. **21**, 539 (1972).

[Jak98] D. Jaksch, C. Bruder, J. I. Cirac, C. W. Gardiner, and P. Zoller, *Cold bosonic atoms in optical lattices*, Phys. Rev. Lett. **81**, 3108 (1998).

[Jen92] R. V. Jensen, *Quantum chaos*, Nature **355**, 311 (1992).

[JL13] M. Jona-Lasinio, K. Łakomy, and L. Santos, *Roton confinement in trapped dipolar bose-einstein condensates*, Phys. Rev. A **88**, 013619 (2013).

[Joc03a] S. Jochim, M. Bartenstein, A. Altmeyer, G. Hendl, C. Chin, J. H. Denschlag, and R. Grimm, *Pure gas of optically trapped molecules created from fermionic atoms*, Phys. Rev. Lett. **91**, 240402 (2003).

[Joc03b] S. Jochim, M. Bartenstein, A. Altmeyer, G. Hendl, S. Riedl, C. Chin, J. Hecker Denschlag, and R. Grimm, *Bose-einstein condensation of molecules*, Science **302**, 2101 (2003).

[Jör08] R. Jördens, N. Strohmaier, K. Günter, H. Moritz, and T. Esslinger, *A mott insulator of fermionic atoms in an optical lattice*, Nature **455**, 204 (2008).

[Jud61] B. R. Judd and I. Lindgren, *Theory of Zeeman effect in the ground multiplets of rare-earth atoms*, Phys. Rev. **122**, 1802 (1961).

[Jür14] O. Jürgensen, F. Meinert, M. J. Mark, H.-C. Nägerl, and D.-S. Lühmann, *Observation of density-induced tunneling*, Phys. Rev. Lett. **113**, 193003 (2014).

[Kad16] H. Kadau, M. Schmitt, M. Wenzel, C. Wink, T. Maier, I. Ferrier-Barbut, and T. Pfau, *Observing the rosensweig instability of a quantum ferrofluid*, Nature **530**, 194 (2016).

[Kha02] L. Khaykovich, F. Schreck, G. Ferrari, T. Bourdel, J. Cubizolles, L. D. Carr, Y. Castin, and C. Salomon, *Formation of a matter-wave bright soliton*, Science **296**, 1290 (2002).

[Koh59] W. Kohn, *Analytic properties of bloch waves and wannier functions*, Phys. Rev. **115**, 809 (1959).

[Köh05] M. Köhl, H. Moritz, T. Stöferle, K. Günter, and T. Esslinger, *Fermionic atoms in a three dimensional optical lattice: Observing fermi surfaces, dynamics, and interactions*, Phys. Rev. Lett. **94**, 080403 (2005).

[Köh06] T. Köhler, K. Góral, and P. S. Julienne, *Production of cold molecules via magnetically tunable feshbach resonances*, Rev. Mod. Phys. **78**, 1311 (2006).

[Kol06] C. Kollath, A. Iucci, T. Giamarchi, W. Hofstetter, and U. Schollwöck, *Spectroscopy of ultracold atoms by periodic lattice modulations*, Phys. Rev. Lett. **97**, 050402 (2006).

[Kot11] S. Kotochigova and A. Petrov, *Anisotropy in the interaction of ultracold dysprosium*, Phys. Chem. Chem. Phys. **13**, 19165 (2011).

[Kot14] S. Kotochigova, *Controlling interactions between highly magnetic atoms with Feshbach resonances*, Rep. Prog. Phys. **77**, 093901 (2014).

[Kra12] J. S. Krauser, J. Heinze, N. Fläschner, S. Götze, O. Jürgensen, D.-S. Lühmann, C. Becker, and K. Sengstock, *Coherent multi-flavour spin dynamics in a fermionic quantum gas*, Nature Phys. **8**, 813 (2012).

[Kra18] A. Kramida, Y. Ralchenko, J. Reader, and NIST ASD Team, *Nist atomic spectra database*, Tech. report, National Institute of Standards and Technology, Gaithersburg, MD., 2018.

[Küh00] T. D. Kühner, S. R. White, and H. Monien, *One-dimensional bose-hubbard model with nearest-neighbor interaction*, Phys. Rev. B **61**, 12474 (2000).

[Lad10] T. D. Ladd, F. Jelezko, R. Laflamme, Y. Nakamura, C. Monroe, and J. L. O'Brien, *Quantum computers*, Nature **464**, 45 (2010).

[Lah08] T. Lahaye, J. Metz, B. Fröhlich, T. Koch, M. Meister, A. Griesmaier, T. Pfau, H. Saito, Y. Kawaguchi, and M. Ueda, *d-Wave collapse and explosion of a dipolar Bose-Einstein condensate*, Phys. Rev. Lett. **101**, 080401 (2008).

[Lah09] T. Lahaye, C. Menotti, L. Santos, M. Lewenstein, and T. Pfau, *The physics of dipolar bosonic quantum gases*, Rep. Prog. Phys. **72**, 126401 (2009).

[Lan32] L. Landau, *On the theory of transfer of energy at collisions II*, Phys. Z. Sowjetunion **2**, 46 (1932).

[Lan41] L. Landau, *Theory of the superfluidity of helium II*, Phys. Rev. **60**, 356 (1941).

[Lan77] L. Landau and E. Lifshitz, *Quantum mechanics: Non-relativistic theory*, Butterworth-Heinemann, 1977.

[Law10] J. E. Lawler, J.-F. Wyart, and E. A. D. Hartog, *Atomic transition probabilities of Er I*, J. Phys. B **43**, 235001 (2010).

[Lee06] P. A. Lee, N. Nagaosa, and X.-G. Wen, *Doping a mott insulator: Physics of high-temperature superconductivity*, Rev. Mod. Phys. **78**, 17 (2006).

[Léo17] J. Léonard, A. Morales, P. Zupancic, T. Esslinger, and T. Donner, *Supersolid formation in a quantum gas breaking a continuous translational symmetry*, Nature **543**, 87 (2017).

[Lep14] M. Lepers, J.-F. Wyart, and O. Dulieu, *Anisotropic optical trapping of ultracold erbium atoms*, Phys. Rev. A **89**, 022505 (2014).

[Lep18] S. Lepoutre, J. Schachenmayer, L. Gabardos, B. Zhu, B. Naylor, E. Marechal, O. Gorceix, A. M. Rey, L. Vernac, and B. Laburthe-Tolra, *Exploring out-of-equilibrium quantum magnetism and thermalization in a spin-3 many-body dipolar lattice system*, ArXiv e-prints 1803.02628 (2018).

[Lew12] M. Lewenstein, A. Sanpera, and V. Ahufinger, *Ultracold atoms in optical lattices: Simulating quantum many-body systems*, Oxford University Press, 2012.

[Li16] X. Li and W. V. Liu, *Physics of higher orbital bands in optical lattices: a review*, Rep. Prog. Phys. **79**, 116401 (2016).

[Li17] J.-R. Li, J. Lee, W. Huang, S. Burchesky, B. Shteynas, F. C. Top, A. O. Jamison, and W. Ketterle, *A stripe phase with supersolid properties in spin–orbit-coupled bose–einstein condensates*, Nature **543**, 91 (2017).

[Lio72a] H. I. Liou, H. S. Camarda, and F. Rahn, *Application of statistical tests for single-level populations to neutron-resonance-spectroscopy data*, Phys. Rev. C **5**, 1002 (1972).

[Lio72b] H. I. Liou, H. S. Camarda, S. Wynchank, M. Slagowitz, G. Hacken, F. Rahn, and J. Rainwater, *Neutron-resonance spectroscopy. VIII. the separated isotopes of erbium: Evidence for dyson's theory concerning level spacings*, Phys. Rev. C **5**, 974 (1972).

[Lu10] M. Lu, S. H. Youn, and B. L. Lev, *Trapping ultracold dysprosium: A highly magnetic gas for dipolar physics*, Phys. Rev. Lett. **104**, 063001 (2010).

[Lu11] M. Lu, N. Q. Burdick, S. H. Youn, and B. L. Lev, *Strongly dipolar Bose-Einstein condensate of dysprosium*, Phys. Rev. Lett. **107**, 190401 (2011).

[Lu12] M. Lu, N. Q. Burdick, and B. L. Lev, *Quantum degenerate dipolar Fermi gas*, Phys. Rev. Lett. **108**, 215301 (2012).

[Luc18] E. Lucioni, L. Tanzi, A. Fregosi, J. Catani, S. Gozzini, M. Inguscio, A. Fioretti, C. Gabbanini, and G. Modugno, *Dysprosium dipolar bose-einstein condensate with broad feshbach resonances*, ArXiv e-prints 1803.10676 (2018).

[Lüh12] D.-S. Lühmann, O. Jürgensen, and K. Sengstock, *Multi-orbital and density-induced tunneling of bosons in optical lattices*, New J. Phys. **14**, 033021 (2012).

[Mad00] K. W. Madison, F. Chevy, W. Wohlleben, and J. Dalibard, *Vortex formation in a stirred bose-einstein condensate*, Phys. Rev. Lett. **84**, 806 (2000).

[Mai15] T. Maier, I. Ferrier-Barbut, H. Kadau, M. Schmitt, M. Wenzel, C. Wink, T. Pfau, K. Jachymski, and P. S. Julienne, *Broad universal feshbach resonances in the chaotic spectrum of dysprosium atoms*, Phys. Rev. A **92**, 060702 (2015).

[Man91] E. Manousakis, *The spin-1/2 heisenberg antiferromagnet on a square lattice and its application to the cuprous oxides*, Rev. Mod. Phys. **63**, 1 (1991).

[Mar78] W. C. Martin, R. Zalubas, and L. Hagan, *Atomic energy levels – The rare earth elements*, Tech. report, National Standard Reference Data System, 1978.

[Mar11] M. J. Mark, E. Haller, K. Lauber, J. G. Danzl, A. J. Daley, and H.-C. Nägerl, *Precision measurements on a tunable mott insulator of ultracold atoms*, Phys. Rev. Lett. **107**, 175301 (2011).

[Mar12] A. D. Martin and P. B. Blakie, *Stability and structure of an anisotropically trapped dipolar bose-einstein condensate: Angular and linear rotons*, Phys. Rev. A **86**, 053623 (2012).

[Mar13] A. L. Marchant, T. P. Billam, T. P. Wiles, M. M. H. Yu, S. A. Gardiner, and S. L. Cornish, *Controlled formation and reflection of a bright solitary matter-wave*, Nature Comm. **4**, 1865 (2013).

[Mat99] M. R. Matthews, B. P. Anderson, P. C. Haljan, D. S. Hall, C. E. Wieman, and E. A. Cornell, *Vortices in a bose-einstein condensate*, Phys. Rev. Lett. **83**, 2498 (1999).

[Maz17a] A. Mazloom, B. Vermersch, M. A. Baranov, and M. Dalmonte, *Adiabatic state preparation of stripe phases with strongly magnetic atoms*, Phys. Rev. A **96**, 033602 (2017).

[Maz17b] A. Mazurenko, C. S. Chiu, G. Ji, M. F. Parsons, M. Kanász-Nagy, R. Schmidt, F. Grusdt, E. Demler, D. Greif, and M. Greiner, *A cold-atom fermi–hubbard antiferromagnet*, Nature **545**, 462 (2017).

[McC06] J. J. McClelland and J. L. Hanssen, *Laser cooling without repumping: A magneto-optical trap for erbium atoms*, Phys. Rev. Lett. **96**, 143005 (2006).

[Meh63] M. L. Mehta and F. J. Dyson, *Statistical theory of the energy levels of complex systems. V*, J. Math. Phys. **4**, 713 (1963).

[Mei16] F. Meinert, M. J. Mark, K. Lauber, A. J. Daley, and H.-C. Nägerl, *Floquet engineering of correlated tunneling in the bose-hubbard model with ultracold atoms*, Phys. Rev. Lett. **116**, 205301 (2016).

[Mia14] J. Miao, J. Hostetter, G. Stratis, and M. Saffman, *Magneto-optical trapping of holmium atoms*, Phys. Rev. A **89**, 041401 (2014).

[Miy08] T. Miyakawa, T. Sogo, and H. Pu, *Phase-space deformation of a trapped dipolar Fermi gas*, Phys. Rev. A **77**, 061603 (2008).

[Mol14] P. K. Molony, P. D. Gregory, Z. Ji, B. Lu, M. P. Köppinger, C. R. Le Sueur, C. L. Blackley, J. M. Hutson, and S. L. Cornish, *Creation of ultracold* ^{87}Rb^{133}Cs *molecules in the rovibrational ground state*, Phys. Rev. Lett. **113**, 255301 (2014).

[Muk04] T. Mukaiyama, J. R. Abo-Shaeer, K. Xu, J. K. Chin, and W. Ketterle, *Dissociation and decay of ultracold sodium molecules*, Phys. Rev. Lett. **92**, 180402 (2004).

[Mül06] T. Müller, *Exploring excited bloch bands in optical lattices via stimulated raman transitions*, Master's thesis, Institut für Physik der Johannes Gutenberg-Universität Mainz (2006).

[Mül07] T. Müller, S. Fölling, A. Widera, and I. Bloch, *State preparation and dynamics of ultracold atoms in higher lattice orbitals*, Phys. Rev. Lett. **99**, 200405 (2007).

[Nat14] S. S. Natu, L. Campanello, and S. Das Sarma, *Dynamics of correlations in a quasi-two-dimensional dipolar bose gas following a quantum quench*, Phys. Rev. A **90**, 043617 (2014).

[Nay15] B. Naylor, A. Reigue, E. Maréchal, O. Gorceix, B. Laburthe-Tolra, and L. Vernac, *Chromium dipolar fermi sea*, Phys. Rev. A **91**, 011603 (2015).

[Ni08] K.-K. Ni, S. Ospelkaus, M. H. G. de Miranda, A. Peér, B. Neyenhuis, J. J. Zirbel, S. Kotochigova, P. S. Julienne, D. S. Jin, and J. Ye, *A high phase-space-density gas of polar molecules*, Science **322**, 231 (2008).

[Nor16] E. B. Norrgard, D. J. McCarron, M. H. Steinecker, M. R. Tarbutt, and D. DeMille, *Submillikelvin dipolar molecules in a radio-frequency magneto-optical trap*, Phys. Rev. Lett. **116**, 063004 (2016).

[Omr15] A. Omran, M. Boll, T. A. Hilker, K. Kleinlein, G. Salomon, I. Bloch, and C. Gross, *Microscopic observation of pauli blocking in degenerate fermionic lattice gases*, Phys. Rev. Lett. **115**, 263001 (2015).

[Osp06] C. Ospelkaus, S. Ospelkaus, L. Humbert, P. Ernst, K. Sengstock, and K. Bongs, *Ultracold heteronuclear molecules in a 3d optical lattice*, Phys. Rev. Lett. **97**, 120402 (2006).

[Par09] N. G. Parker, C. Ticknor, A. M. Martin, and D. H. J. O'Dell, *Structure formation during the collapse of a dipolar atomic bose-einstein condensate*, Phys. Rev. A **79**, 013617 (2009).

[Par15] J. W. Park, S. A. Will, and M. W. Zwierlein, *Ultracold dipolar gas of fermionic ^{23}Na^{40}K molecules in their absolute ground state*, Phys. Rev. Lett. **114**, 205302 (2015).

[Pas11a] B. Pasquiou, G. Bismut, E. Maréchal, P. Pedri, L. Vernac, O. Gorceix, and B. Laburthe-Tolra, *Spin relaxation and band excitation of a dipolar Bose-Einstein condensate in 2D optical lattices*, Phys. Rev. Lett. **106**, 015301 (2011).

[Pas11b] B. Pasquiou, E. Maréchal, G. Bismut, P. Pedri, L. Vernac, O. Gorceix, and B. Laburthe-Tolra, *Spontaneous demagnetization of a dipolar spinor bose gas in an ultralow magnetic field*, Phys. Rev. Lett. **106**, 255303 (2011).

[Pet04a] D. S. Petrov, *Three-boson problem near a narrow feshbach resonance*, Phys. Rev. Lett. **93**, 143201 (2004).

[Pet04b] D. S. Petrov, C. Salomon, and G. V. Shlyapnikov, *Weakly bound dimers of fermionic atoms*, Phys. Rev. Lett. **93**, 090404 (2004).

[Pet12] A. Petrov, E. Tiesinga, and S. Kotochigova, *Anisotropy-induced Feshbach resonances in a quantum dipolar gas of highly magnetic atoms*, Phys. Rev. Lett. **109**, 103002 (2012).

[Pet15] D. S. Petrov, *Quantum mechanical stabilization of a collapsing bose-bose mixture*, Phys. Rev. Lett. **115**, 155302 (2015).

[Pla06] M. Planck, *Vorlesung über die theorie der wärmestrahlung*, Verlag von J. A. Barth, Leibzig, 1906.

[Raj06] K. Rajan and L. F. Abbott, *Eigenvalue spectra of random matrices for neural networks*, Phys. Rev. Lett. **97**, 188104 (2006).

[Ran17] M. Rančić, M. P. Hedges, R. L. Ahlefeldt, and M. J. Sellars, *Coherence time of over a second in a telecom-compatible quantum memory storage material*, Nature Phys. **14**, 50 (2017).

[Rav18] C. Ravensbergen, V. Corre, E. Soave, M. Kreyer, S. Tzanova, E. Kirilov, and R. Grimm, *Accurate determination of the dynamical polarizability of dysprosium*, ArXiv e-prints 1801.05658 (2018).

[Reg03] C. A. Regal, C. Ticknor, J. L. Bohn, and D. S. Jin, *Creation of ultracold molecules from a fermi gas of atoms*, Nature **424**, 47 (2003).

[Roa02] G. Roati, F. Riboli, G. Modugno, and M. Inguscio, *Fermi-bose quantum degenerate* ^{40}K−^{87}Rb *mixture with attractive interaction*, Phys. Rev. Lett. **89**, 150403 (2002).

[Roa07] G. Roati, M. Zaccanti, C. D'Errico, J. Catani, M. Modugno, A. Simoni, M. Inguscio, and G. Modugno, ^{39}K *bose-einstein condensate with tunable interactions*, Phys. Rev. Lett. **99**, 010403 (2007).

[Ron07] S. Ronen, D. C. E. Bortolotti, and J. L. Bohn, *Radial and angular rotons in trapped dipolar gases*, Phys. Rev. Lett. **98**, 030406 (2007).

[Ron10] S. Ronen and J. L. Bohn, *Zero sound in dipolar fermi gases*, Phys. Rev. A **81**, 033601 (2010).

[Sac02] S. Sachdev, K. Sengupta, and S. M. Girvin, *Mott insulators in strong electric fields*, Phys. Rev. B **66**, 075128 (2002).

[Sag15] E. Saglamyurek, J. Jin, V. B. Verma, M. D. Shaw, F. Marsili, S. W. Nam, D. Oblak, and W. Tittel, *Quantum storage of entangled telecom-wavelength photons in an erbium-doped optical fibre*, Nature Phot. **9**, 83 (2015).

[Sal16] J. Salfi, J. A. Mol, R. Rahman, G. Klimeck, M. Y. Simmons, L. C. L. Hollenberg, and S. Rogge, *Quantum simulation of the hubbard model with dopant atoms in silicon*, Nature Comm. **7**, 11342 (2016).

[San03] L. Santos, G. V. Shlyapnikov, and M. Lewenstein, *Roton-maxon spectrum and stability of trapped dipolar Bose-Einstein condensates*, Phys. Rev. Lett. **90**, 250403 (2003).

[San17] L. Santos, private communication.

[Sch01] F. Schreck, L. Khaykovich, K. L. Corwin, G. Ferrari, T. Bourdel, J. Cubizolles, and C. Salomon, *Quasipure bose-einstein condensate immersed in a fermi sea*, Phys. Rev. Lett. **87**, 080403 (2001).

[Sch08] U. Schneider, L. Hackermüller, S. Will, T. Best, I. Bloch, T. A. Costi, R. W. Helmes, D. Rasch, and A. Rosch, *Metallic and insulating phases of repulsively interacting fermions in a 3d optical lattice*, Science **322**, 1520 (2008).

[Sch11] J. Schindler, *Characterization of an erbium atomic beam*, Master's thesis, Faculty of Mathematics, Computer Science and Physics; University of Innsbruck (2011).

[Sch12a] P. Schauß, M. Cheneau, M. Endres, T. Fukuhara, S. Hild, A. Omran, T. Pohl, C. Gross, S. Kuhr, and I. Bloch, *Observation of spatially ordered structures in a two-dimensional rydberg gas*, Nature **491**, 87 (2012).

[Sch12b] U. Schneider, L. Hackermüller, J. P. Ronzheimer, S. Will, S. Braun, T. Best, I. Bloch, E. Demler, S. Mandt, D. Rasch, and A. Rosch, *Fermionic transport and out-of-equilibrium dynamics in a homogeneous hubbard model with ultracold atoms*, Nature Phys. **8**, 213 (2012).

[Sch16] M. Schmitt, M. Wenzel, F. Böttcher, I. Ferrier-Barbut, and T. Pfau, *Self-bound droplets of a dilute magnetic quantum liquid*, Nature **539**, 259 (2016).

[Sem17] G. Semeghini, G. Ferioli, L. Masi, C. Mazzinghi, L. Wolswijk, F. Minardi, M. Modugno, G. Modugno, M. Inguscio, and M. Fattori, *Self-bound quantum droplets in atomic mixtures*, ArXiv e-prints 1710.10890 (2017).

[She10] J. F. Sherson, C. Weitenberg, M. Endres, M. Cheneau, I. Bloch, and S. Kuhr, *Single-atom-resolved fluorescence imaging of an atomic mott insulator*, Nature **467**, 68 (2010).

[Sin11] A. Singha, M. Gibertini, B. Karmakar, S. Yuan, M. Polini, G. Vignale, M. I. Katsnelson, A. Pinczuk, L. N. Pfeiffer, K. W. West, and V. Pellegrini, *Two-dimensional mott-hubbard electrons in an artificial honeycomb lattice*, Science **332**, 1176 (2011).

[Smi65] K. F. Smith and P. J. Unsworth, *The hyperfine structure of 167 Er and magnetic moments of 143, 145 Nd and 167 Er by atomic beam triple magnetic resonance*, Proc. Phys. Soc. **86**, 1249 (1965).

[Stö04] T. Stöferle, H. Moritz, C. Schori, M. Köhl, and T. Esslinger, *Transition from a strongly interacting 1d superfluid to a mott insulator*, Phys. Rev. Lett. **92**, 130403 (2004).

[Str02] K. E. Strecker, G. B. Partridge, A. G. Truscott, and R. G. Hulet, *Formation and propagation of matter-wave soliton trains*, Nature **417**, 150 (2002).

[Str03] K. E. Strecker, G. B. Partridge, and R. G. Hulet, *Conversion of an atomic fermi gas to a long-lived molecular bose gas*, Phys. Rev. Lett. **91**, 080406 (2003).

[Stu05] J. Stuhler, A. Griesmaier, T. Koch, M. Fattori, T. Pfau, S. Giovanazzi, P. Pedri, and L. Santos, *Observation of dipole-dipole interaction in a degenerate quantum gas*, Phys. Rev. Lett. **95**, 150406 (2005).

[Suk10] D. Sukachev, A. Sokolov, K. Chebakov, A. Akimov, S. Kanorsky, N. Kolachevsky, and V. Sorokin, *Magneto-optical trap for thulium atoms*, Phys. Rev. A **82**, 011405 (2010).

[Sya06] N. Syassen, T. Volz, S. Teichmann, S. Dürr, and G. Rempe, *Collisional decay of* ^{87}Rb *feshbach molecules at* 1005.8 G, Phys. Rev. A **74**, 062706 (2006).

[Tak14] T. Takekoshi, L. Reichsöllner, A. Schindewolf, J. M. Hutson, C. R. Le Sueur, O. Dulieu, F. Ferlaino, R. Grimm, and H.-C. Nägerl, *Ultracold dense samples of dipolar rbcs molecules in the rovibrational and hyperfine ground state*, Phys. Rev. Lett. **113**, 205301 (2014).

[Tan15] Y. Tang, A. Sykes, N. Q. Burdick, J. L. Bohn, and B. L. Lev, *s-wave scattering lengths of the strongly dipolar bosons* ^{162}*dy and* ^{164}*dy*, Phys. Rev. A **92**, 022703 (2015).

[Tan16] Y. Tang, A. G. Sykes, N. Q. Burdick, J. M. DiSciacca, D. S. Petrov, and B. L. Lev, *Anisotropic expansion of a thermal dipolar bose gas*, Phys. Rev. Lett. **117**, 155301 (2016).

[Tar12] L. Tarruell, D. Greif, T. Uehlinger, G. Jotzu, and T. Esslinger, *Creating, moving and merging Dirac points with a Fermi gas in a tunable honeycomb lattice*, Nature **483**, 302 (2012).

[Tay10] G. Tayebirad, A. Zenesini, D. Ciampini, R. Mannella, O. Morsch, E. Arimondo, N. Lörch, and S. Wimberger, *Time-resolved measurement of landau-zener tunneling in different bases*, Phys. Rev. A **82**, 013633 (2010).

[Tha06] G. Thalhammer, K. Winkler, F. Lang, S. Schmid, R. Grimm, and J. H. Denschlag, *Long-lived feshbach molecules in a three-dimensional optical lattice*, Phys. Rev. Lett. **96**, 050402 (2006).

[Tho04] N. R. Thomas, N. Kjærgaard, P. S. Julienne, and A. C. Wilson, *Imaging of s and d partial-wave interference in quantum scattering of identical bosonic atoms*, Phys. Rev. Lett. **93**, 173201 (2004).

[Tho05] S. T. Thompson, E. Hodby, and C. E. Wieman, *Ultracold molecule production via a resonant oscillating magnetic field*, Phys. Rev. Lett. **95**, 190404 (2005).

[Tho16] R. Thomas, K. O. Roberts, E. Tiesinga, A. C. J. Wade, P. B. Blakie, A. B. Deb, and N. Kjærgaard, *Multiple scattering dynamics of fermions at an isolated p-wave resonance*, Nature Comm. **7**, 12069 (2016).

[Tic08] C. Ticknor, *Collisional control of ground state polar molecules and universal dipolar scattering*, Phys. Rev. Lett. **100**, 133202 (2008).

[Tra12] A. Trabesinger, *Nature phys. insights - quantum simulation*, Nature Phys. **8**, 263 (2012).

[Tro08] S. Trotzky, P. Cheinet, S. Fölling, M. Feld, U. Schnorrberger, A. M. Rey, A. Polkovnikov, E. A. Demler, M. D. Lukin, and I. Bloch, *Time-resolved observation and control of superexchange interactions with ultracold atoms in optical lattices*, Science **319**, 295 (2008).

[Tru01] A. G. Truscott, K. E. Strecker, W. I. McAlexander, G. B. Partridge, and R. G. Hulet, *Observation of fermi pressure in a gas of trapped atoms*, Science **291**, 2570 (2001).

[Tru17] S. Truppe, H. J. Williams, M. Hambach, L. Caldwell, N. J. Fitch, E. A. Hinds, B. E. Sauer, and M. R. Tarbutt, *Molecules cooled below the doppler limit*, Nature Phys. **13**, 1173 (2017).

[Uli17] J. Ulitzsch, D. Babik, R. Roell, and M. Weitz, *Bose-einstein condensation of erbium atoms in a quasielectrostatic optical dipole trap*, Phys. Rev. A **95**, 043614 (2017).

[Vac17] V. Veljić, A. Balaž, and A. Pelster, *Time-of-flight expansion of trapped dipolar fermi gases: From the collisionless to the hydrodynamic regime*, Phys. Rev. A **95**, 053635 (2017).

[Vit17] N. V. Vitanov, A. A. Rangelov, B. W. Shore, and K. Bergmann, *Stimulated raman adiabatic passage in physics, chemistry, and beyond*, Rev. Mod. Phys. **89**, 015006 (2017).

[Wal13] M. L. Wall and L. D. Carr, *Dipole–dipole interactions in optical lattices do not follow an inverse cube power law*, New J. Phys. **15**, 123005 (2013).

[Wan37] G. H. Wannier, *The structure of electronic excitation levels in insulating crystals*, Phys. Rev. **52**, 191 (1937).

[Web03] T. Weber, J. Herbig, M. Mark, H.-C. Nägerl, and R. Grimm, *Bose-Einstein condensation of cesium*, Science **299**, 232 (2003).

[Wer05] J. Werner, A. Griesmaier, S. Hensler, J. Stuhler, T. Pfau, A. Simoni, and E. Tiesinga, *Observation of Feshbach resonances in an ultracold gas of ^{52}Cr*, Phys. Rev. Lett. **94**, 183201 (2005).

[Wig51] E. P. Wigner, *On a class of analytic functions from the quantum theory of collisions*, Ann. Math. **53**, 36 (1951).

[Wil10] R. M. Wilson, S. Ronen, and J. L. Bohn, *Critical superfluid velocity in a trapped dipolar gas*, Phys. Rev. Lett. **104**, 094501 (2010).

[Win07] K. Winkler, F. Lang, G. Thalhammer, P. v. d. Straten, R. Grimm, and J. H. Denschlag, *Coherent optical transfer of feshbach molecules to a lower vibrational state*, Phys. Rev. Lett. **98**, 043201 (2007).

[Wir10] G. Wirth, M. Ölschläger, and A. Hemmerich, *Evidence for orbital superfluidity in the p-band of a bipartite optical square lattice*, Nature Phys. **7**, 147 (2010).

[Xu03] K. Xu, T. Mukaiyama, J. R. Abo-Shaeer, J. K. Chin, D. E. Miller, and W. Ketterle, *Formation of quantum-degenerate sodium molecules*, Phys. Rev. Lett. **91**, 210402 (2003).

[Yan13] B. Yan, S. A. Moses, B. Gadway, J. P. Covey, K. R. A. Hazzard, A. M. Rey, D. S. Jin, and J. Ye, *Observation of dipolar spin-exchange interactions with lattice-confined polar molecules*, Nature **501**, 521 (2013).

[Yi01] S. Yi and L. You, *Trapped condensates of atoms with dipole interactions*, Phys. Rev. A **63**, 053607 (2001).

[Zen34] C. Zener, *A theory of the electrical breakdown of solid dielectrics*, Proc. Roy. Soc. London Ser. A **145**, 523 (1934).

[Zha18] X. W. Zhang, T. Lin, P. Zhang, H. C. Song, H. Jin, J. Xu, J. Xu, P. J. Wang, K. Y. Niu, and K. J. Chen, *Tunable quantum dot arrays as efficient sensitizers for enhanced near-infrared electroluminescence of erbium ions*, Nanoscale **10**, 4138 (2018).

[Zhu17] B. Zhu and A. M. Rey, private communication.

Acknowledgments

I have joined the ERBIUM experiment already during my master studies, and it turned out to be one of the best decisions I could make. Beside the great team spirit, which has remained curious and friendly during all the years, the experiment has been an exciting scientific working place, which enabled me to learn and discover intriguing physics at a constant pace. Already back at my master thesis work, I had the luck to contribute to a *worlds first* – the realization of a Bose-Einstein condensate of erbium. Greatly, this milestone only set the start to the following scientific journey with many more *worlds firsts*. Working with erbium, an element previously unstudied in the ultracold regime, imposed exciting challenges on our team and every scientific project added another piece of knowledge to our growing understanding. The access of physical phenomena in the quantum world requires a complex experimental setup and the contribution of many people. Here, I want to thank all the people that not only have been important for the success of our scientific visions, but also made the last five years a very enjoyable and exciting time.

First of all, I would like to thank my supervisor Francesca Ferlaino. She has introduced me to the fascinating world of ultracold atoms and has given me the opportunity to perform my thesis at the ERBIUM experiment. Her constant scientific curiosity and her strong will for making progress have enabled me to extract the most out of the last years. I have grown both scientifically as well as a person by realizing also my own ideas in the lab and by presenting our results on conferences around the world. I am grateful for her support during the various phases of my thesis work, and her support along my future scientific career.

During the last years the people within the ERBIUM team have changed almost completely and there are many people I want to thank for their assistance, patience and friendship. In the first phase of my thesis I could learn a lot from our two postdocs Kiyotaka Aikawa and Michael Mark, as well as from the *first generation* Phd student Albert Frisch. Kiyo gave me deep insights into the scientific world and his constant energy and focus to reveal the physics at play made a large impact on my scientific personality. Michael proved to be a master in solving every emerging problem and I enjoyed a lot his companion in the lab. Albert made an excellent job in designing and building the ERBIUM machine from scratch and his thorough work attitude and his way of documentation set the unquestioned base for the today still fully functional ERBIUM machine. I have learned a lot from his technical skills and his way of approaching physical problems.

The departure of the former ERBIUM members marked the start of the second phase of my thesis. New team members filled in and together we smoothly carried on our scientific ideas. Our senior scientist Manfred Mark constantly proves to be the important link for our coherently working DIPOLAR GROUP. It is hard to find a question about electronics he is

not able to answer, and his great technical skills are complemented by his ability to have for almost every question a Matlab script at hand. Our postdoc Lauriane Chomaz has a deep understanding about our experiment also from the theoretical side and her work and mindful ideas have been a great benefit for the whole team. Daniel Petter joined our team already during his master studies and has now become the person to ask for, when something in the lab decides to stop working. With the recent major upgrade by implementing a dynamical controllable spatial light modulator into the experiment, he turned to the new lead Phd student and I am confident that he will have a lot of fun working at the ERBIUM machine.

For one year our team obtained great support from the *borrowed* Phd students Giulia Faraoni and Jan Hendrik Becher. Especially the time spent with Jan Hendrik as part of TEAM SPIN in the lab – no matter if early in the morning or late in the night – is of fond memory. The *Hulk mode* turned out to be indispensable for efficient lab progress. To the new generation of Phd students Alexander Patscheider, and Gabriele Natale, who decided to stay in our team after their successful master thesis' with us, I wish the best of luck for their future scientific projects in the lab.

With the RARE experiment emerging, our team has grown larger and larger and I have enjoyed the delightful discussions and the time shared together. I will never forget our weekly *Besprechung&Breakfast* meetings and I have particularly enjoyed our yearly group retreats to conferences all around Europe.

All people within the ultracold-atoms research group, which was initially set up by Rudi Grimm, participate to the great environment in Innsbruck. Rudi took a special role during the initial phase of my thesis as he played an important supervisory role for our first scientific results. Despite that the ERBIUM team has relocated from the fourth to the second floor, we still keep a lively and most valuable scientific exchange with the teams of Rudi Grimm and also the teams of Hanns-Christoph Nägerl. In the lab area, behind almost every door you can most probably find someone who is an expert on something you are struggling with. I want to thank everyone for making work so enjoyable and instructive. Especially, I want to mention Michael Gröbner with whom I spent all my studies together and I am thankful for the uncountable discussions about physics and other things. Outside the lab I am grateful for the contact, time and friendship with past and current ultracold-atoms members.

Further, I want to thank my second supervisor Gerhard Kirchmair who always has an open ear to discuss about quantum physics outside the ultracold-atoms world. I am especially grateful for his encouragement towards my future scientific career.

A big *thank you* should also go to all our collaborators, which enriched our work with thoughtful discussions and striking ideas: George Bruun from Aarhus, John Bohn and Debbie Jin from Boulder, Svetlana Kotochigova and her team from Philadelphia, Eite Tiesinga from Maryland, Olivier Dulieu, Goulven Quéméner, Jean-François Wyart, and Maxcence Lepers from Orsay, the group of Tilman Pfau from Stuttgart, Peter Zoller, Mikhail Baranov, Marcello Dalmonte, Andreas Läuchli and many more from Innsbruck, the team of Markus Greiner from Harvard, Luis Santos and Falk Wächtler from Hannover, Antun Balaz and Vladimir Veljic from Belgrade, Axel Pelster from Kaiserslautern, as well as Ana Maria Rey and Bihui Zhu from Boulder. Certainly there are many more people who contributed in one

way or the other and I want to thank everyone for the great discussions at conference-calls or conferences and workshops around the world, from which I have learned a lot.

To be able to build, maintain and manage our experiments we also greatly rely on the non-scientific staff. The mechanical workshop with Armin Sailer, Anton Schönherr and Christoph Wegscheider, and the electronic workshop with Wolfgang Kratz, Wolfgang Kuen and Gerhard Hendl deliver almost everything needed from the technical side. The administrative support of our secretaries Christine Götsch-Obmascher, Nicole Jorda, Michaela Palz, Carina-Theresa Oberhöler, Carla Fantini, Gaby Holzer, Leonarda Garcia Lopez, and Silvia Bonazza eases our life significantly and enables us to focus on the physics component of our work.

My biggest thanks goes to my friends and my whole family. In particular, I want to thank my parents Reinhold and Julia, who have always supported my dreams and visions and also my brother, who has always been there for chats, sports and beer. In addition, I want to thank my uncle Gottfried for his constant support along my scientific career. However, this thesis truly belongs to my wife Katrin, who has always encouraged and pushed me to keep going. Your love and support is invaluable and I truly feel lucky that we will spend the rest of our lives together. Even though it seems that our newborn son Florian is now a bit taking over – I could not be happier.